ISSN 0031-8949
(ISSN 0281-1847)
ISBN 91-87308-17-7

Proceedings of the international workshop on

Acceleration and Radiation Generation in Space and Laboratory Plasmas

Kardamyli, Greece, August 29–September 4, 1993

Editors: R. Bingham
J. M. Dawson
T. Katsouleas
L. Stenflo

Recognized by the European Physical Society

Physica Scripta

Vol. T52 1994

Physica Scripta

Published jointly by

The Royal Danish Academy of Sciences and Letters in cooperation with the Danish Physical Society
The Delegation of the Finnish Academies of Science and Letters in cooperation with the Finnish Physical Societies
The Icelandic Scientific Society in cooperation with the Icelandic Physical Society
The Norwegian Academy of Science and Letters in cooperation with the Norwegian Physical Society
The Royal Swedish Academy of Sciences in cooperation with the Swedish Physical Society

Manuscripts
Shall be sent in triplicate – one original and two copies – to any of the editors. For full addresses see cover page 3.

Offprints
25 offprints of each paper will be supplied free of charge. Additional copies may be ordered at cost price.

Subscriptions
The Royal Swedish Academy of Sciences
Physica Scripta
Box 50005
S-104 05 Stockholm
Sweden

Subscription price
For 1994 (vols 49, 50 and T-volumes) the subscription price is DEM 1575. For subscribers in the Nordic Countries SEK 4725. For subscribers in USA, Canada and Mexico US $900.

Back numbers and single issues
Can be ordered separately. Price information on request.

Physica Scripta is delivered to some institutions in the former Soviet Union through a program initiated and administered by the European Physical Society. This program is funded by INTAS, the International Association for the promotion of cooperation with scientists from the independent States of the former Soviet Union. Members of INTAS are the European Union, Austria, Belgium, Denmark, Finland, France, Germany, Greece, Ireland, Italy, Luxemburg, the Netherlands, Portugal, Spain, United Kingdom, Sweden and Switzerland. (INTAS, Rue du Luxembourg 14A, 1040 Bruxelles, Belgique).

Typeset by Santype International Ltd and Printed in Great Britain by Lindsay Ross International Ltd., London and Oxon.

REPORT DOCUMENTATION PAGE

Form Approved
OMB No. 0704-0188

1. AGENCY USE ONLY (Leave blank)	2. REPORT DATE	3. REPORT TYPE AND DATES COVERED
	2-14-95	Final Technical Report - (2/1/93 - 1/31/94)

4. TITLE AND SUBTITLE Workshop on Acceleration and Radiation Generation in Space and Laboratory Plasmas - Aug. 29 - Sept. 4, 1993

5. FUNDING NUMBERS
N00014-93-1-0814

6. AUTHOR(S)
T. Katsouleas
R. Bingham
J. M. Dawson, L. Stenflo

7. PERFORMING ORGANIZATION NAME(S) AND ADDRESS(ES)
University of Southern Calfiornia
Dept. of Electrical Engineering-Electrophysics
Los Angeles, CA 90089-0484

8. PERFORMING ORGANIZATION REPORT NUMBER

9. SPONSORING/MONITORING AGENCY NAME(S) AND ADDRESS(ES)
Dr. Charles W. Roberson
Office of Naval REsearch
Code 3121 (1112AI)
800 N. Quincy St.
Arlington, VA 22217-5000

10. SPONSORING/MONITORING AGENCY REPORT NUMBER

11. SUPPLEMENTARY NOTES

12a. DISTRIBUTION/AVAILABILITY STATEMENT
Approved for public release: Distribution unlimited

12b. DISTRIBUTION CODE

13. ABSTRACT (Maximum 200 words)

Workshop proceedings - Papers presented at the International Workshop on Acceleration and Radiation Generation in Space and Laboratory Plasmas Kardamyli, Greece, August 29 - September 4, 1993.

14. SUBJECT TERMS
Space and laboratory plasmas, astrophysics, plasma physics lasers, space plasmas

15. NUMBER OF PAGES
156

16. PRICE CODE

17. SECURITY CLASSIFICATION OF REPORT	18. SECURITY CLASSIFICATION OF THIS PAGE	19. SECURITY CLASSIFICATION OF ABSTRACT	20. LIMITATION OF ABSTRACT
Unclassified	Unclassified	Unclassified	UL

GENERAL INSTRUCTIONS FOR COMPLETING SF 298

The Report Documentation Page (RDP) is used in announcing and cataloging reports. It is important that this information be consistent with the rest of the report, particularly the cover and title page. Instructions for filling in each block of the form follow. It is important to *stay within the lines* to meet *optical scanning requirements.*

Block 1. Agency Use Only *(Leave blank)*.

Block 2. Report Date. Full publication date including day, month, and year, if available (e.g. 1 Jan 88). Must cite at least the year.

Block 3. Type of Report and Dates Covered. State whether report is interim, final, etc. If applicable, enter inclusive report dates (e.g. 10 Jun 87 - 30 Jun 88).

Block 4. Title and Subtitle. A title is taken from the part of the report that provides the most meaningful and complete information. When a report is prepared in more than one volume, repeat the primary title, add volume number, and include subtitle for the specific volume. On classified documents enter the title classification in parentheses.

Block 5. Funding Numbers. To include contract and grant numbers; may include program element number(s), project number(s), task number(s), and work unit number(s). Use the following labels:

C	- Contract	PR	- Project
G	- Grant	TA	- Task
PE	- Program Element	WU	- Work Unit Accession No.

Block 6. Author(s). Name(s) of person(s) responsible for writing the report, performing the research, or credited with the content of the report. If editor or compiler, this should follow the name(s).

Block 7. Performing Organization Name(s) and Address(es). Self-explanatory.

Block 8. Performing Organization Report Number. Enter the unique alphanumeric report number(s) assigned by the organization performing the report.

Block 9. Sponsoring/Monitoring Agency Name(s) and Address(es). Self-explanatory.

Block 10. Sponsoring/Monitoring Agency Report Number. *(If known)*

Block 11. Supplementary Notes. Enter information not included elsewhere such as: Prepared in cooperation with...; Trans. of...; To be published in.... When a report is revised, include a statement whether the new report supersedes or supplements the older report.

Block 12a. Distribution/Availability Statement. Denotes public availability or limitations. Cite any availability to the public. Enter additional limitations or special markings in all capitals (e.g. NOFORN, REL, ITAR).

DOD	- See DoDD 5230.24, "Distribution Statements on Technical Documents."
DOE	- See authorities.
NASA	- See Handbook NHB 2200.2.
NTIS	- Leave blank.

Block 12b. Distribution Code.

DOD	- Leave blank.
DOE	- Enter DOE distribution categories from the Standard Distribution for Unclassified Scientific and Technical Reports.
NASA	- Leave blank.
NTIS	- Leave blank.

Block 13. Abstract. Include a brief *(Maximum 200 words)* factual summary of the most significant information contained in the report.

Block 14. Subject Terms. Keywords or phrases identifying major subjects in the report.

Block 15. Number of Pages. Enter the total number of pages.

Block 16. Price Code. Enter appropriate price code *(NTIS only)*.

Blocks 17. - 19. Security Classifications. Self-explanatory. Enter U.S. Security Classification in accordance with U.S. Security Regulations (i.e., UNCLASSIFIED). If form contains classified information, stamp classification on the top and bottom of the page.

Block 20. Limitation of Abstract. This block must be completed to assign a limitation to the abstract. Enter either UL (unlimited) or SAR (same as report). An entry in this block is necessary if the abstract is to be limited. If blank, the abstract is assumed to be unlimited.

ISSN 0031-8949
(ISSN 0281-1847)
ISBN 91-87308-17-7

Proceedings of the international workshop on

Acceleration and Radiation Generation in Space and Laboratory Plasmas

Kardamyli, Greece, August 29–September 4, 1993

Editors: R. Bingham
J. M. Dawson
T. Katsouleas
L. Stenflo

Recognized by the European Physical Society

EPS

Physica Scripta

Vol. T52 1994

Physica Scripta

Published jointly by

The Royal Danish Academy of Sciences and Letters in cooperation with the Danish Physical Society
The Delegation of the Finnish Academies of Science and Letters in cooperation with the Finnish Physical Societies
The Icelandic Scientific Society in cooperation with the Icelandic Physical Society
The Norwegian Academy of Science and Letters in cooperation with the Norwegian Physical Society
The Royal Swedish Academy of Sciences in cooperation with the Swedish Physical Society

Manuscripts
Shall be sent in triplicate – one original and two copies – to any of the editors. For full addresses see cover page 3.

Offprints
25 offprints of each paper will be supplied free of charge. Additional copies may be ordered at cost price.

Subscriptions
The Royal Swedish Academy of Sciences
Physica Scripta
Box 50005
S-104 05 Stockholm
Sweden

Subscription price
For 1994 (vols 49, 50 and T-volumes) the subscription price is DEM 1575. For subscribers in the Nordic Countries SEK 4725. For subscribers in USA, Canada and Mexico US $900.

Back numbers and single issues
Can be ordered separately. Price information on request.

Physica Scripta is delivered to some institutions in the former Soviet Union through a program initiated and administered by the European Physical Society. This program is funded by INTAS, the International Association for the promotion of cooperation with scientists from the independent States of the former Soviet Union. Members of INTAS are the European Union, Austria, Belgium, Denmark, Finland, France, Germany, Greece, Ireland, Italy, Luxemburg, the Netherlands, Portugal, Spain, United Kingdom, Sweden and Switzerland. (INTAS, Rue du Luxembourg 14A, 1040 Bruxelles, Belgique).

Typeset by Santype International Ltd and Printed in Great Britain by Lindsay Ross International Ltd., London and Oxon.

Physica Scripta Vol. T52 1994

Contents

Conference Participants

Foreword

Acceleration and Radiation Generation in Space and Laboratory Plasmas

Sixty-six leading researchers from ten nations gathered in the Homeric village of Kardamyli, on the southern coast of mainland Greece, from August 29–September 4, 1993 for the International Workshop on Acceleration and Radiation Generation in Space and Laboratory Plasmas. This Special Issue represents a cross-section of the presentations made at and the research stimulated by that meeting.

According to the Iliad, King Agamemnon used Kardamyli as a dowry offering in order to draw a sulking Achilles into the Trojan War. 3000 years later, Kardamyli is no less seductive. Its remoteness and tranquility made it an ideal venue for promoting the free exchange of ideas between various disciplines that do not normally interact. Through invited presentations, informal poster discussions and working group sessions, the Workshop brought together leaders from the laboratory and space/astrophysics communities working on common problems of acceleration and radiation generation in plasmas. It was clear from the presentation and discussion sessions that there is a great deal of common ground between these disciplines which is not at first obvious due to the differing terminologies and types of observations available to each community.

All of the papers in this Special Issue highlight the role collective plasma processes play in accelerating particles or generating radiation. Some are state-of-the-art presentations of the latest research in a single discipline, while others investigate the applicability of known laboratory mechanisms to explain observations in natural plasmas. Notable among the latter are the papers by Marshall *et al.* on *kHz* radiation in the magnetosphere; Barletta *et al.* on collective acceleration in solar flares; and by Dendy *et al.* on ion cyclotron emission.

The papers in this Issue are organized as follows:

In Section 1 are four general papers by Dawson, Galeev, Bingham *et al.* and Mori which serves as an introduction to the physical mechanisms of acceleration and radiation generation in plasmas. The next section includes state-of-the-art papers on laboratory accelerators driven by lasers (Nakajima *et al.*, Shukla, Johnson *et al.*), microwaves (Nishida *et al.*, Bogomolov *et al.*) and by particle beams (Ogata *et al.*). Also in this section are theoretical papers presenting new work on synchrotron like oscillations in plasma waves (Fedele) and two types of laboratory radiation sources, FEL's (Marshall *et al.*) and ionization fronts (Lai *et al.*), and Frantzeskakis *et al.* described the Hamiltonian analysis of a slow-wave autonomous cyclotron buncher. Section 3 contains papers on astrophysical plasmas, with the general presentations of Colgate and Krishnan. Kazanas and Krishnan address active galactic nuclei (AGNs). Thielheim discusses general acceleration mechanisms in rotating magnetized systems. Asseo discussed Langmuir solitons in pulsars and Blackman *et al.* treat magnetic reconnection relativistically. Su *et al.* analyze the possibility of plasma wave excitation and particle acceleration by neutrinos from supernovae. Dogiel *et al.* on cosmic ray scattering by MHD fluctuations.

The papers in Section 4 treat fusion plasmas (Dendy *et al.* and Lashmore-Davies *et al.*). Section 5, space plasmas, includes papers on acceleration processes in the magnetosphere (Anagnostopoulos and Marshall *et al.*) and the sun (Barletta *et al.*).

It is evident from the Workshop and the papers collected here that this is indeed a rich field of investigations and that both the natural and laboratory plasma communities can benefit from the cross-fertilization of ideas between them.

We wish to thank the authors and attendees for their contributions to the success of this workshop, Dr Philip Debenham and Dr David Sutter of the U.S. D.o.E. and Dr Charles Roberson of the U.S. O.N.R. for their financial support (Grants DE-FG03-93ER40776 and N00014-93-1-0814), and the ECC Twinning Grant SC1*-CT92-0773.

We appreciate the considerable local support from Mr Glegles and his staff at the Agricultural Bank of Greece. We thank Mr V. Tataronis, mayor of Kardamyli, and members of the Kardamyli organizing committee and the community for their incredible hospitality. The excellent work of the Conference Secretaries, Ms Shirin Mistry and Mrs Sheila Shield is gratefully acknowledged. Finally, a special thank you goes to Mr S. C. Katsouleas who is so much more than our local organizing chairman.

R. Bingham, Oxford, UK, T. Katsouleas, Malibu, CA, USA, J. M. Dawson, Los Angeles, CA, USA, L. Stenflo, Umeå, Sweden.

Physica Scripta. Vol. T52, 7–12, 1994

Plasma Accelerators

John M. Dawson

University of California, Los Angeles, Physics Department, 1–130 Knudsen Hall, Los Angeles, CA90024, U.S.A.

Received January 7, 1994; accepted April 22, 1994

1. Astrophysical plasma acceleration

In the early part of this century cosmic rays were discovered by physicists [1, 2]. At first they were identified only through the ionization they caused in air and were thought to be high energy γ-rays [3]. Later, because of the earth's magnetic effects on them and the tracks they left in cloud chambers, they were found to consist largely of very energetic charged particles [4]. The sun was ruled out as their source (except for a relatively low-energy component) because they rain down on the earth essentially isotropically. Studies showed that the intensity decreased like a power law of the energy [5]. Cosmic rays have been observed up to energies of 10^{20} eV [6]. It is clear from these observations that some mechanisms were accelerating charged particles to great energy at least within our own galaxy. Whatever the acceleration mechanisms are, they must involve electric and magnetic fields and almost certainly plasmas since plasmas are so prevalent throughout the universe.

The first plausible mechanism for cosmic ray acceleration was proposed by Fermi [7]. Clouds of gas and associated magnetic fields had been observed in space. Fermi proposed that by repeated reflections from the magnetic fields of these randomly moving clouds the particles would become energized; they would attempt to come to a temperature equivalent to that of the random motion of the gas clouds which is of course enormous because of their huge mass. Recently this mechanism has been generalized to include scattering of particles from waves that propagate in the interstellar plasmas and in shock waves surrounding supernova [8].

In 1968 pulsars [9] were discovered. It was soon found that these pulsars were rapidly rotating neutron stars which contained enormous magnetic fields ($\sim 10^{12}$ G); the magnetic dipole is generally not aligned with the axis of rotation. It was also found that the rate of spin of these stars was gradually slowing down and that this effect could be explained by the radiation a spinning dipole should emit. The neutron star emits very powerful electromagnetic waves. The fields of these waves (as well as the near fields of the dipole) are so large that charged particles are accelerated to cosmic ray energies by them. That such processes go on is clearly seen in the Crab nebula [10] (and other supernova remnants) where the presence of electrons of cosmic ray energies can be inferred from the synchrotron radiation they emit.

Radiation from other pulsar systems has also been observed to be very energetic. Cygnus X-3 [11] has been observed to be producing γ-rays with energies of at least 10^{15} eV, which implies that particles in this system are accelerated up to at least 10^{17} eV. This acceleration must take place within a region the size of the system (perhaps much smaller), i.e, in a region the size of the solar system or smaller. Some very powerful acceleration mechanism almost certainly involving plasma exists there.

On a much more modest scale, but nevertheless quite impressive, are the plasma particle acceleration processes observed on the sun. At times of large solar flares the acceleration of both ions and electrons are observed [12]. They are observed through the energetic particles that arrive at the earth, in γ-rays coming from the sun which must be due to nuclear collisions involving energies up to GeVs; through the emission of intense X-rays which indicate that electrons are accelerated to energies of a few hundred keV; and through bursts of microwave radiation which indicate that there are beams of relativistic electrons traveling through the solar atmosphere. Such events clearly show that in the solar plasma large energies can be stored (probably in the form of magnetic fields) and that this energy can be suddenly released with a substantial fraction of that energy going into accelerated particles (both ions and electrons).

All this evidence indicates that strong particle acceleration processes exist in astrophysical plasmas. Recent laboratory experiments have been successful in producing impressive accelerations in plasmas. These have illuminated some mechanisms that can be important acceleration processes. We will return to astrophysical plasma accelerators later, but for now we will turn to particle acceleration in laboratory plasmas.

2. Laboratory plasma accelerators

2.1. *Some history*

Here on earth there have been a number of proposals for using plasmas to accelerate particles. Quite a few of these proposals have been created and some serious experiments have been carried out. Many of these have not succeeded because of the perversity of plasmas. However, there have been some successes. Recently there has been spectacular success using the laser beat wave scheme.

In 1967 it was proposed [13] that dense, non-neutral, relativistic electron rings which were magnetically confined would trap ions; the plan was to trap many fewer ions than electrons. The idea was to accelerate the ring (which has a much larger charge-to-mass ratio than ions) by more-or-less conventional accelerator means. The trapped ions would be carried along and reach much higher energies than they could in standard accelerators of the same size. This scheme

was tried in the USSR [14] and US [15] but plasma problems with control and stability of the electron rings prevented it from achieving interesting results.

Another method that was tried was the so called Auto-Resonance Accelerator [16] in which an energetic electron beam is propagated through some slow wave structure. The waves on the beam are negative energy waves, exciting the waves decreases the energy of the beam. Bunches of ions introduced into the beam excite the negative energy waves which transfers energy to the ions and accelerates them. By a proper choice of parameters, the accelerated ions and the excited waves can be made to stay in phase so that acceleration continues (auto-resonance). Here again the perversity of plasmas, the many degrees of freedom they possess which can be excited, often lead to turbulent behavior; this has prevented the construction of a practical device.

2.2. *Plasma beat waves*

There have also been experiments in which acceleration was not the goal but in which substantial acceleration was observed. In particular in early experiments on inertial fusion, in which intense lasers illuminate plasmas, often a population of energetic electrons (hundreds of keV to MeV energies) was produced [17]. The production of such energetic electrons has been attributed to the production of high phase velocity plasma waves by parametric instabilities and by mode conversion. These waves are effective electron accelerators. Since these energetic electrons are detrimental to achieving inertial fusion, efforts have been made to suppress the wave generation by going to shorter wavelength lasers which penetrate to higher density plasma regions where collisional effects are stronger and prevent the wave growth [18]. These efforts have been successful in getting rid of the high energy electrons.

We now turn to a plasma accelerator that has been successful at least on a modest scale. The laser experiments suggested that one might be able to accelerate electrons to high energy by intentionally generating high phase velocity plasma waves. This lead to computer simulations and theoretical studies of the "laser wake field" and "laser beat wave" techniques for plasma acceleration of particles [19, 20]. For the laser beat wave scheme, two intense laser beams with different frequencies are incident on a plasma. The frequency difference of the two lasers is equal to the plasma frequency. The two beams have regions of constructive and destructive interference. The result is a series of intense light pulses moving through the plasma at the group velocity of light (assuming the laser frequency is large compared to the plasma frequency). The plasma electrons feel periodic light pressure forces ($\boldsymbol{J}_1 \times \boldsymbol{B}_2$ and $\boldsymbol{J}_2 \times \boldsymbol{B}_1$) which are at the plasma frequency. The plasma responds resonantly to these forces and large amplitude plasma oscillations build up. For the case of the laser wake field, there is a single light pulse less than half a plasma wave length long which leaves a wake of plasma oscillations behind it.

For the beat wave or laser wake field, the plasma waves have a phase velocity which is equal to the group velocity of light in the plasma; this is very close to the velocity of light $[v_g(\mathrm{EM}) = v_p(\mathrm{P}) = c(1 - \omega_p^2/\omega^2)^{1/2}]$. Furthermore, the electric field of these waves can be very large; the theoretical maximum E is $4\pi e^2 n_e c/\omega_p$ and is determined by wave breaking. The magnitude of this electric field is $E = n_e^{1/2}$ V/cm where n_e is in electrons per cm^3; for an electron density of 10^{16} per cm^3, this gives the enormous field of 10^8 V/cm. Theoretical studies show that as the intensity approaches this value, the relativistic mass increase of the electrons shifts the plasma frequency and resonance is lost [21]. Nevertheless, the intensity can be a substantial fraction of the maximum possible. Theoretical, computer simulation, and recently experimental studies, show that values of the order of 30% of the theoretical maximum value can be achieved.

Since the phase velocity of the plasma wave is slightly less than the speed of light, the accelerated electrons ultimately outrun the wave; there is a maximum energy [20] to which the electrons can be accelerated. By going to a frame moving with the phase velocity of the plasma wave, computing the energy of a particle just reflected by the wave, and then transforming the energy of such a reflected particle back to the lab frame, one can show that the maximum energy the electron can be accelerated to is $W = 2\varepsilon\gamma^2 mc^2$ where $\gamma = (1 - v_p^2/c^2)^{-1/2} = \omega/\omega_p$, ε is the ratio of the amplitude to the maximum possible.

As we mentioned earlier, there is a limit on the energy that the plasma beat wave can reach due to the fact that the phase velocity of the beat wave is slightly slower than the velocity of light. One would like to have a method to prevent the particles from out running the beat wave. Working on this problem and with his knowledge of surfing, Tom Katsouleas [20] came up with the idea of the surfatron. He realized that if one could make the particle move at a slight angle to the direction of the waves propagation, even if the particle was moving with the speed of light, it could stay in phase with the accelerating wave. This is similar to what a surfer does when he rides a wave; he goes at an angle to the wave so as not to outrun it and thus gets a much longer ride. He realized that one could achieve a similar effect with plasma waves if one put the plasma in a small $\boldsymbol{B}$ field perpendicular to the direction of propagation of the plasma wave. The sideways deflection of the particle by the magnetic field lead to its moving across a phase front and unlimited acceleration of properly phased particles could be achieved. There are many situations in which this type of surfing mechanism can result in very high energy particles, this is particularly true in astrophysics [22].

Some other important properties of the plasma beat wave scheme are the following:

1. Nonlinear effects in the plasma make the light waves self-focus; there is a limiting size to the focused beam of a few times c/ω_p.

2. The plasma wave is focusing for the accelerated particles over half the accelerating portion of the wave ($\frac{1}{4}$ wavelength).

3. The region of wave excitation and the length of the accelerating wake need not be very long since the exciting laser beams and the accelerated particles move along together (at almost the speed of light). Thus, turbulent effects do not have time to grow before the exciter and the accelerated particles have passed on; the turbulence is left behind and cannot catch up with the accelerated electrons.

Early experiments on the plasma beat wave showed clear evidence of the generation of the expected plasma wave [23]. Some experiments [24] showed evidence of energetic electron production ($\sim$1–2 MeV). However, systematic

demonstration of the acceleration process turned out to be a difficult experiment. This was largely due to subtle side effects (such as small stray non-reproducible magnetic fields associated with the plasma production).

2.3. *UCLA plasma Beat Wave Experiment*

UCLA has recently carried out a very successful Beat Wave Accelerator experiment [25]. A schematic of the experiment is shown in Fig. 1. A CO_2 laser is operated on two wavelengths, 10.59 μm and 10.29 μm. This gives beat resonance with the plasma frequency for a plasma density of roughly $n_e = 10^{16}$ per cm^3. The laser delivers 60 J in the 10.59 μm line and 10 J in the 10.29 μm line; the duration of the laser pulse is approximately 300 ps. The laser is focused into hydrogen gas at between 100 and 200 mTorr. At the focal spot the intensity rises to 10^{13}–10^{14} W per cm^2, which is enough to cause tunneling ionization (the laser field is comparable to the field binding the electrons to the atoms). The gas rapidly ionizes when the intensity goes above the critical field for tunneling ionization; full ionization takes about a ps (shown in Fig. 2); every atom undergoes ionization. The gas is thus converted to a plasma whose density is equal to the atomic density of the gas. Since the beating EM waves already exist in the plasma, the beat wave builds up rapidly to a large amplitude.

Since the plasma density is only 10^{-3} of the critical density, refraction by the plasma is negligible. The intensity is also below the critical intensity for self-focusing so the laser intensity is almost that given by focusing the light in the vacuum. Thus, the laser intensity is high and roughly constant over a Rayleigh length which is a little more than a cm for the lenses used. The diameter of the focal spot is 300 μ and the laser intensity at the spot is a few times 10^{14} W per cm^2. The γ_p associated with the phase velocity of the beat wave $[(1 - v_p^2/c^2)^{-1/2}]$ is 32.

A test electron beam at 2 MeV was focused into the beat wave region. This beam was generated by a commercial industrial linear accelerator; it produced a series of pulses, each one lasting about one ps and with bunches following each other at intervals of 100 ps. The situation is shown in Fig. 3. The electron bunches are not synchronized with the laser but since the laser pulse lasts 100 ps, an electron bunch will overlap the beat wave at some stage in its development. An electron bunch is sufficiently long to overlap many beat wave wavelengths; thus all possible phases of acceleration and deceleration are present. However, the peak energy achieved does depend on whether the bunch arrives during the build-up of the beat wave, at its peak, or in its decaying portion.

After the electrons leave the accelerating region, they enter an energy analyzer. This consists of a slit, a magnetic field that focuses electrons of different energies at different points, and a series of detectors which detect how many electrons are deflected to a certain detector. There is a dump for the unaccelerated electrons; this is specially shielded so that X-rays from the dump do not create spurious signals on the detectors. This set up is shown in Fig. 4.

Results from a series of experiments carried out in 1992–93 are shown on Figs 5 and 6. Figure 5 shows the number of electrons observed *vs.* energy for a large number of shots. You see there are electrons accelerated up to 30 MeV. There are also many electrons accelerated to a lesser extent; as mentioned above this is due to their phase in the beat wave as well as when the bunch comes with respect to the peak beat wave intensity. One even sees electrons that have been decelerated by the wave as expected.

The fact that electrons are accelerated to 30 MeV is very important. First this shows that electric fields are generated that are roughly 3 GeV per meter (the exact value depends on the length of the accelerating region and how the intensity varies with position in the focal spot region; these are not exactly known but the accelerating region is in the range of 1–2 cm). This is the largest coherent man-made accelerating field to date; it implies that the electron density

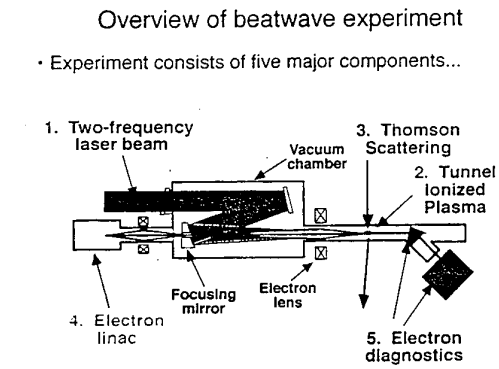

Fig. 1. Schematic of UCLA's BWA.

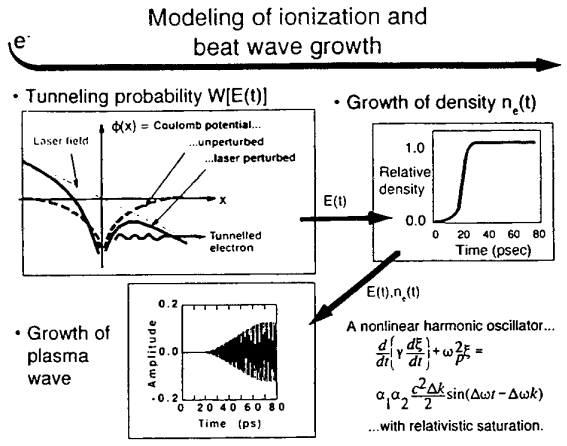

Fig. 2. Gas ionization by tunneling ionization showing 1 Ps ionization time.

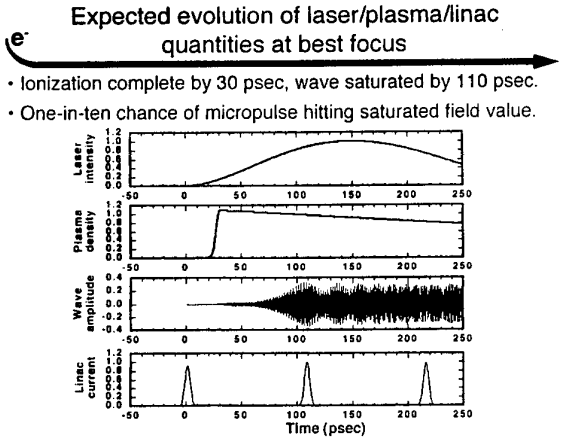

Fig. 3. Electron bunches entering the region of the BW.

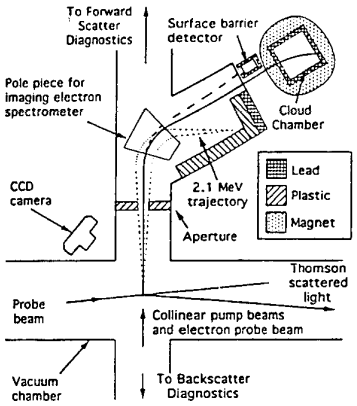

Fig. 4. Electron analyzer.

perturbation in the wave is ~30%. The second important aspect of achieving 30 MeV is that the electron γ is larger than γ_p of the wave. This means that in the wave frame the electron velocity has been reversed; in other words electron trapping by the wave has occurred. If the beat wave existed over a sufficient distance (~10 cm), the electrons would reach an energy of roughly 300 MeV at which point they would start to decelerate.

Figure 6 shows tracks made by accelerated electrons when a cloud chamber is placed at the location of one of the detectors. In this case the cloud chamber collected electrons at an energy of 5.6 MeV. The curvature is that expected for 5.6 MeV electrons in the magnetic field of the cloud chamber. From the density of tracks in the cloud chamber when the bending magnet is turned off, one can estimate the number of electrons captured by the wave and accelerated; it turns out to be a few per cent.

2.4. *Plasma wake field accelerators*

A second means of generating plasma waves for particle acceleration is by sending a bunch of high energy electrons through the plasma [26]. The bunch leaves a wake of longitudinal plasma waves behind it; the phase velocity of the waves matches the velocity of the bunch, which for relativistic electrons is very near the speed of light ($v_p = c[1 - \frac{1}{2}\gamma_e^2]^{1/2}$). For energies of 50 MeV, $\gamma_E = 100$, the phase velocity differs from c by only 5 parts in 10^5.

One might think that it is strange to use electrons to accelerate electrons; why not simply use the initial linear accelerator to accelerate the electrons to the desired energy? The answer to this is that the plasma can be used as a transformer; a bunch containing a large number of electrons can be used to accelerate a bunch containing many fewer electrons to a much higher energy. To do this the first bunch must be shaped so that its density increases from a small value at the front to a large value at the back where it falls rapidly to zero. If the bunch is much longer than c/ω_p, then as it enters a region of plasma, the plasma electrons are repelled out so as to keep the combination of the plasma and bunch almost neutral; very little electric field is produced to slow down the bunch. As the bunch leaves a region, the plasma is suddenly left in a non-neutral state and large plasma oscillations are generated. The situation is shown in Fig. 7. The ratio, R, of the electric field of the wave to that slowing down the driving bunch is

$$R = 2\pi l_b \omega_p / c,$$

where l_b is the bunch length. This so-called transformer ratio can easily be in the range of 10 to 100 so that the accelerated electrons can reach energy orders of magnitude larger than the driver bunch energy. This can be done in a short plasma region.

This method for accelerating electrons has been investigated extensively by means of computer modeling. Figure 8 shows some results obtained by J. J. Su at UCLA [27]. It

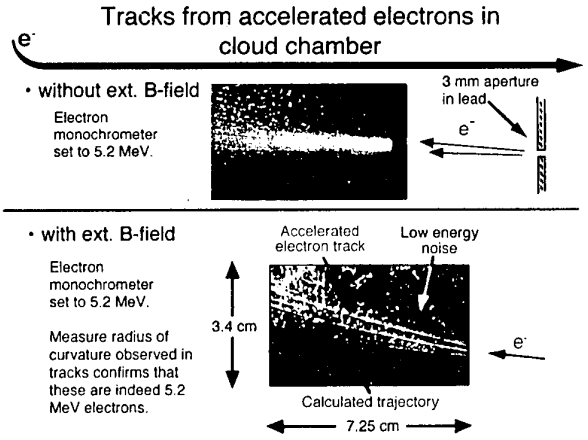

Fig. 6. Cloud chamber tracks.

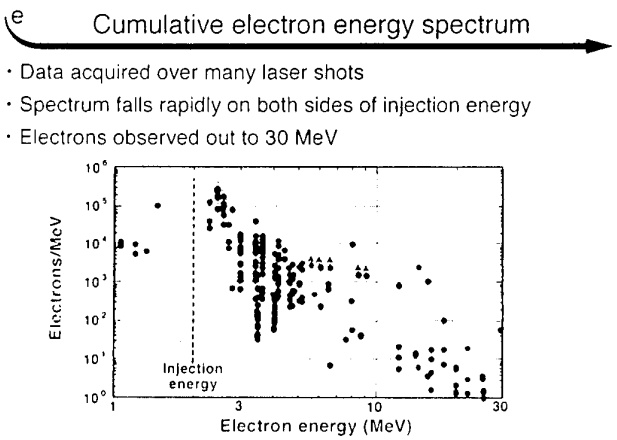

Fig. 5. Number of electrons *vs.* energy showing energies to 30 MeV.

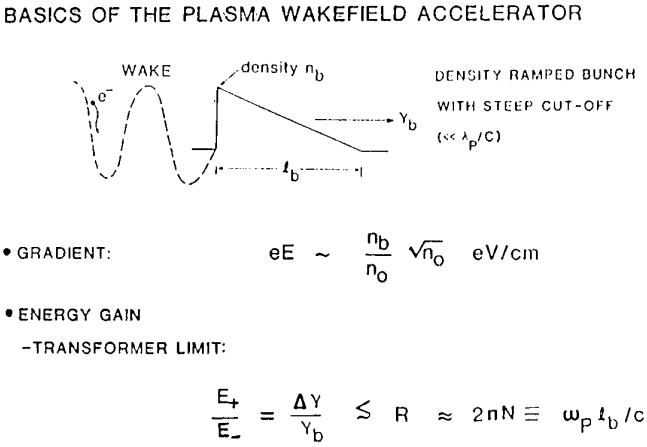

Fig. 7. WFA generating a large transformer ratio.

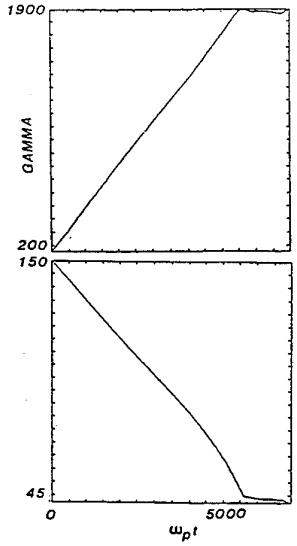

Fig. 8. Energy history of a test accelerated particle *vs.* time. (a) γ starts from 150 at $t = 0$ then increases to 1840 at $\omega_p t \simeq 6000$. (b) Energy loss of driving particles.

shows the slowing down of a driving bunch and the acceleration of trailing electrons for a one-dimensional simulation. Both the driving bunch and the accelerated electrons start out at 75 MeV ($\gamma = 150$). The driving bunch looses about 75% of its energy before it breaks up. The accelerated electrons accelerate up to essentially 1 GeV before the acceleration becomes ineffective.

Clearly if the above calculation is correct, a large fraction of a driving beam's energy can be converted into plasma wave energy which is effective for accelerating electrons (or positrons). Real systems are not one-dimensional and we must ask what happens for real bunches. To address this question, J. J. Su [28] has made two-dimensional simulations of the bunch evolution and the wakes generated. Figures 9 and 10 show some results from these simulations. Figure 9 shows what happens to the bunch if it is cold. One can clearly see the bunch soon begins to filament; if this happens the bunch is no longer effective for generating wakes suitable for accelerating particles. The time (or distance) for filamentation break-up is proportional to its γ to the one-half power, whereas the time (or distance) required for the bunch to loose most of its energy to the plasma wave is proportional to γ. Thus for high γ bunches the break-up would occur long before it had deposited its energy in the wake unless this filamentation can be suppressed. One way to overcome this effect is to give the electrons in the bunch a finite amount of transverse velocity (emissivity) so that the filaments disperse faster than they grow. It turns out that the driving bunch electrons only need 75 keV transverse energy spread, independent of the bunches total energy, to achieve this. Figure 10 shows the result of giving the bunch this much random transverse energy. There is no trace of the filamentation instability in this figure. Thus it appears that we can maintain a coherent bunch.

Another important question is the efficiency with which plasma wave energy can be converted to accelerated particle energy. This question applies to both the laser beat wave and the plasma wake field accelerator. This question was extensively investigated by Scott Wilks in his Ph.D. thesis at UCLA [29]. He finds that by proper choice of the accelerated bunch number and position in the wave, it can absorb a large fraction of the waves energy ($\sim$30%). It is also possible to do this while maintaining the quality of the bunches emittance if the diameter of the accelerated bunch is small compared to the diameter of the driving bunch. This insures that the accelerated electrons all see nearly the same accelerating field and their synchrotron oscillations cause them to further average the fields they see over the accelerated bunch. Even a small bunch is able to absorb energy from a much wider plasma wave just as electrons in a conventional linear accelerating cavity absorbs energy from the whole cavity. These problems were explored extensively in the Ph.D. theses of Su and Wilks, both theoretically and by computer simulation. Their results show that plasma accelerators can accelerate electrons or positrons without increasing the bunch emittance.

Often the question of emittance growth due to Coulomb scattering of the accelerated particles by the background plasma is raised. Because the particles very quickly reach highly relativistic velocities, these cross-sections are very small, only a small fraction of a Barn. Even for the fields already achieved in Joshi's experiment ($\sim$3 GV/m), one can

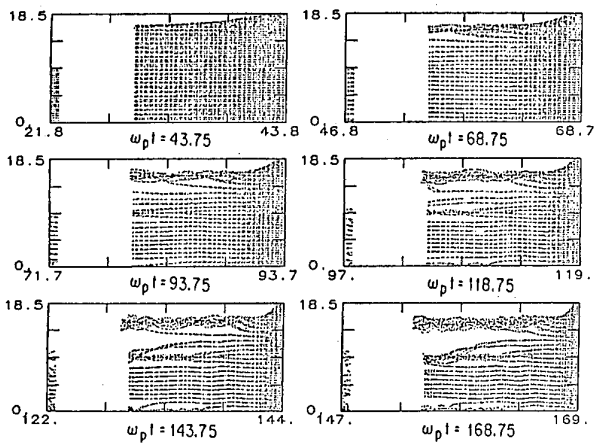

Fig. 9. The time development of monoenergetic driving and accelerated bunches in real space r *vs.* z at ($\omega_p t$ = 43.75, 68.75, 93.75, 118.75, 143.75, and 168.75). The filaments processed to coalesce into large filaments.

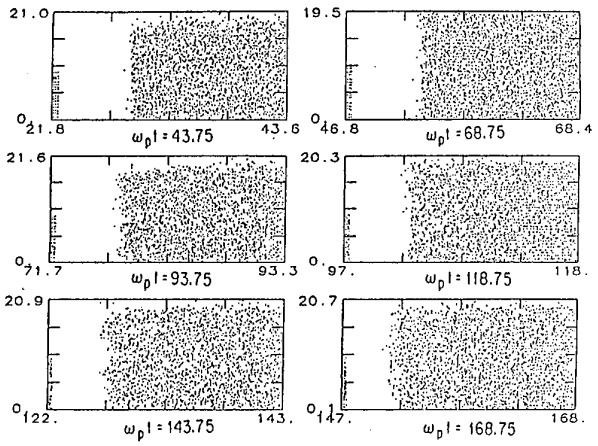

Fig. 10. Phase space p_r *vs.* r of the driving beam with an energy spread $T_\perp = 25$ keV.

reach energies of 10^{15} eV without appreciable scattering. These arguments do not mean that it will not be a difficult technological feat to accelerate a high quality beam without emittance growth, but only that the laws of physics allow it.

The idea of the plasma wake field, at least in is simplest form (no bunch shaping), has been tested by experiments. This was first done by Rosenzweig at Argon [30]. Subsequent tests were carried out at KEK by Nakanishi [31]. All these experiments have confirmed the predictions of the theory. What is called for now are experiments which will accelerate significant numbers of particles to substantially higher energies than they start with; experiments that test the ideas of achieving large transformer ratios, and experiments that demonstrate that the quality of the beam can be maintained during the acceleration process.

2.5. *Some closing remarks*

We have emphasized the acceleration of particles to very high energies using plasma wave accelerators in astrophysical situations and in laboratory experiments. However, there are many uses of modest energies in science, industry, and medicine. Plasma accelerators might provide very compact accelerators for these modest energies. This might be achieved without the high voltage that conventional accelerators need. This feature could open up many applications that are not now possible. One feature of these plasma accelerators that may find wide use is the fact that they can produce a series of very short electron bunches ($\sim 10\,\mu$), one coming every picosec or less. These could be used to make stroboscopic light and X-ray sources that can be used to diagnose very fast physical processes, such as the dynamics of chemical reactions.

Acknowledgements

The author would like to acknowledge the invaluable assistance of Chan Joshi in supplying him with results of the UCLA Beat Wave Experiment. He is also indebted to J. J. Su, Scott Wilks, and Tom Katsouleas for the contributions their works have made to this paper. The author would also like to thank Tom Katsouleas, Warren Mori and Bob Bingham for many stimulating and fruitful discussions. This work was supported by ONR, NSF, and LLNL.

References

1. Wilson, C. T. R., Proc. Camb. Phil. Soc. **11**, 52 (1900); Proc. Roy. Soc. **A68**, 151 (1901); **69**, 277 (1901).
2. Geitel, H., Phys. Zeits. **2**, 116 (1900–01); Elster, J. and Geitel, H., Phys. Zeits. **2**, 560 (1900–01).
3. Millikan, R. A. and Cameron, G. H., Phys. Rev. **28**, 851 (1926); Phys. Rev. **31**, 921 (1929).
4. Compton, A. H., Rev. Sci. Instr. **7**, 71 (1936); Phys. Rev. **50**, 1119 (1936).
5. Ginzburg, V. L. and Syrovatskii, S. I., "The Origin of Cosmic Rays", Translated by H. S. H. Massey (Edited by D. ter Haar) (Pergamon Press 1964).
6. Bird, D. J. *et al.*, Phys. Rev. Lett. **71**, 3401 (1993); Colgate, S. A., this conference; Sadoulet, B. and Cronin, W., "Subatomic Astronomy", Sky & Telescope, p. 25, January, 1992.
7. Fermi, E., Phys. Rev. **75**, 1169 (1949).
8. Wenzel, K. P. *et al.*, "The Interplanetary Shock Event of November 12, 1978: a comprehensive test of acceleration theory", Proc. 18th International Cosmic Ray Conference, Bangalore, **3**, 131 (1983); Kennel, C. F., "On the Relationship Between Collisionless Shock Structure and Energetic Particle Acceleration", in Radiation in Plasmas, Proc. Spring College on Radiation in Plasmas, p. 87, International Center for Theoretical Physics (Trieste) (World Scientific Publishing Co., Singapore 1984).
9. Ostriker, J. P. and Gunn, J. E., Astrophys. J. **157**, 1395 (1969); Gunn, J. E. and Ostriker, J. P., Astrophys. J. **160**, 979 (1970).
10. Coroniti, F. V. and Kennel, C. F., "Magnetohydrodynamic Model of the Crab Nebula and its Radiation", The Crab Nebula and Related Supernova Remnants (Edited by R. B. C. Henry and M. Kafatos) (Cambridge University Press, Cambridge, England 1985), p. 25.
11. Gamma-Ray Astronomy (Edited by H. S. W. Massey, R. D. Wills and A. W. Wolfendale) (Royal Society of London 1981); Mackeown, P. K. and Weekes, T. C., "Cosmic Rays from Cygnus X-3", Sci. Amer., p. 60, November 1985.
12. Clements, M. C. *et al.*, Astrophys. J. **409**, 465 (1993).
13. Veksler, V. I. *et al.*, in Proc. of the 6th International Conference on High Energy Accelerators, Cambridge, MA (Stanford Linear Accelerator Center Report No. SLAC-TRANS-0078) (1967).
14. Keefe, D., Research on the Electron Ring Accelerator, in Particle Accelerators, **Vol. I**, 1 (1970).
15. Keefe, D., "Collective-Effect Accelerators", Sci. Amer., p. 23, April 1972.
16. Sloan, M. L. and Drummond, W. E., Phys. Rev. Lett. **31**, 1234 (1974).
17. Kruer, W. L., "The Physics of Laser Plasma Interactions", Frontiers In Physics Lecture Note Series (Addison-Wesley Publishing Company, The Advanced Book Program 1988).
18. Ripin, B. H. and Kruer, W. L., "Inertial Confined Fusion Systems" in Plasma and Fluids – Physics Through the 1990s (National Academy Press, Washington DC 1986), p. 221–236.
19. Tajima, T. and Dawson, J. M., Phys. Rev. Lett. **43**, 267 (1979).
20. Katsouleas, T. *et al.*, "Plasma Accelerators", Proc. of the AIP Conference Number 130, "Laser Acceleration of Particles" (Malibu, CA, 1985) (Edited by C. Joshi and T. Katsouleas) (American Institute of Physics 1985), pp. 63–98.
21. Rosenbluth, M. and Liu, C. S., Phys. Rev. Lett. **29**, 701 (1972).
22. McClements, K. G., Su, J. J., Dawson, J. M. and Spicer, D. S., Lower Hybrid Resonance Acceleration of Electrons and Ions in Solar Flares and Associated Microwave Emission, Astrophys. J. **409**, 465 (1993).
23. Joshi, C., Clayton, C. E., Darrow, C. and Umstader, D., "Experimental Studies of Beat Wave Excitation of High Phase Velocity Space Charge Waves in a Plasma for Particle Acceleration", Proc. of the AIP Conference Number 130, "Laser Acceleration of Particles" (Malibu, CA, 1985) (Edited by C. Joshi and T. Katsouleas) (American Institute of Physics 1985), pp. 99–113.
24. Martin, F. *et al.*, Phys. Rev. Lett. **55**, 1652 (1985).
25. Clayton, C. E. *et al.*, Phys. Rev. Lett. **70**, 37 (1993).
26. Chen, P., Dawson, J. M., Huff, R. W. and Katsouleas, T., Phys. Rev. Lett. **54**, 693 (1985); Chen, P. and Dawson, J. M., "The Plasma Wake Field Accelerator", Proc. of the AIP Conference Number 130, "Laser Acceleration of Particles" (Malibu, CA, 1985) (Edited by C. Joshi and T. Katsouleas) (American Institute of Physics 1985), pp. 201–212.
27. Chen, P., Su, J. J., Dawson, J. M., Bane, K. L. F. and Wilson, P. B., Phys. Rev. Lett. **56**, 1252 (1986).
28. Su, J. J. *et al.*, IEE Transactions On Plasma Science **PS-15**, 192 (1987).
29. Wilks, S., Katsouleas, T., Dawson, J. M., Chen, P. and Su, J. J., IEE Transactions On Plasma Science **PS-15**, 210 (1987); Wilks, S., Ph.D. Thesis, UCLA (1989).
30. Rosenzweig, J. B. *et al.*, Phys. Rev. Lett. **61**, 98 (1988).
31. Nakanishi, H. *et al.*, "First Results of KEK Plasma Wakefield Accelerator Experiments" in the Proc. of the 14th International Conference on High Energy Accelerators, Part V, 202 (August 22–26, 1989, Tusuba, Japan) (Edited by D. Keefe) (Gordon and Beach Science Publishers, New York 1989).

Physica Scripta. Vol. T52, 13–19, 1994

Nonlinear Limits of Magnetic Reconnection

A. A. Galeev

Space Research Institute, Russia Academy of Sciences, 117810 GSP-7 Moscow, Russia

Received November 22, 1993; accepted January 28, 1994

Abstract

The present understanding of the magnetic field lines reconnection, both the externally driven and spontaneous ones, is reviewed. The discussion of the theory is centered around the nonlinear limitation of the reconnection rate. Modification of the magnetic field structure in the region of plasma outflow by the plasma current near the neutral X-line limits the reconnection rate to the value lower than that given by Petschek. In collisionless plasma the ion trapping by the space charge near the X-line imposes slightly weaker limitation. The structure of the dissipation region in the case of nonvanishing (sheared) magnetic field is described for the tearing mode reconnection and the implications of this analysis for the externally driven reconnection of the strained magnetic field lines are discussed.

1. Introduction: Limitations of the Petschek model of MHD reconnection

Reconnection of magnetic field lines was defined by Axford [1] as a change in the plasma elements which are connected by a given field line (Fig. 1). Plasma elements initially connected by magnetic field lines can become connected to different plasma elements, which are widely separated from the original plasma elements by a distance independent of the plasma resistivity (see more detailed discussion in Strauss [2]). We should mention also that the magnetic reconnection is accompanied by a change in the topology of the magnetic field lines frozen into the plasma flow everywhere

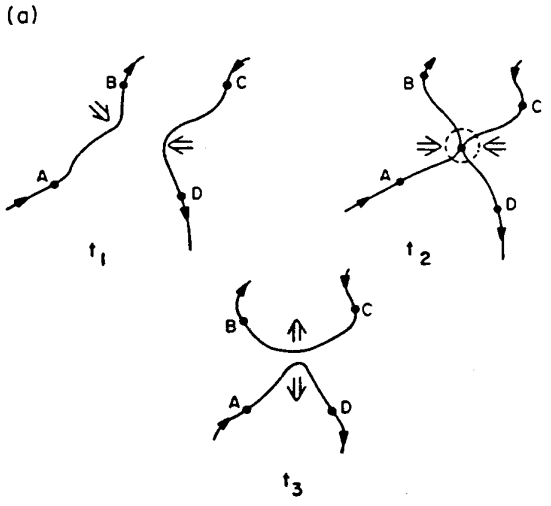

Fig. 1. At the time t_1 the magnetic field line defined by the fluid elements A and B approaches a more-or-less oppositely-directed field line defined by the fluid elements C and D. At the time t_2 the two field lines touch at some intermediate point between A and B and between C and D. At the time t_3 the connection between A and B and between C and D is broken and the field line defined by the fluid elements A and D moves away from the field line defined by the fluid elements B and C [1].

besides the singular planes, lines or points. The most popular model of the fast magnetic reconnection was proposed by Petschek [3] for the uniform two-dimensional magnetized plasma flow driven externally (Fig. 2). Here, the external uniform plasma flow coupled with the frozen magnetic field lines (I) provides the inflow of the magnetic field lines into the reconnection region (III) near the neutral X-line, where the frozen in condition is violated due to the finite plasma resistivity. The size of this region is defined solely by the boundary condition since the velocity of the external flow should be matched here with the velocity of the plasma diffusion into the reconnection region

$$u_z = \frac{c^2}{4\pi\sigma d_z}, \tag{1}$$

where u_z is the velocity of the external flow, c – the speed of light, σ – the plasma electrical conductivity, d_z – the half-thickness of the reconnection region. In the reconnection region the magnetic field lines reconnect in the manner described by Parker [4] and Sweet [5]. The reconnected field lines are exhausted from the sides of this region with about the Alfvén velocity in the external field and continue to flow along the $\pm x$-axis inside the region II bounded by the weak standing Alfvén shock waves, at which the magnetic field lines make an abrupt turn. The role of these shocks is to maintain the uniform inflow of plasma from the external region into the outflow region II with the Alfvén velocity in the uniform magnetic field $\boldsymbol{B}_{\mathrm{II}z}$ in this region,

$$u_z = \frac{B_{\mathrm{II}z}}{\sqrt{4\pi\rho}}, \tag{2}$$

where ρ is the plasma mass density.

In the regions I and II outside the reconnection region and the standing Alfvén waves the plasma current was assumed to be weak so that the magnetic field is described by the Laplace equation. The solution of this equation in the region I satisfying the boundary conditions $\boldsymbol{B}_{\mathrm{I}z} = \boldsymbol{B}_{\mathrm{II}z}$ at

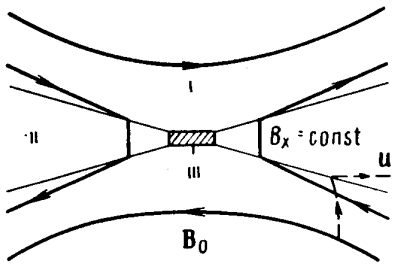

Fig. 2. The reconnection model in configuration with standing waves.

the standing Alfvén waves is

$$B_{1x} = -A\ell n(L/r) + B_0, \quad B_{1z} = +A\theta, \tag{3}$$

where (r, θ) are polar coordinates in the (z, x)-plane. The assumption of weakly disturbed magnetic field in the region I requires that

$$A\ell n\left(\frac{L}{d_z}\right) < \tfrac{1}{2}B_0, \tag{4}$$

so that the reconnection rate is bounded by the conditions (2) and (4)

$$u_z = \frac{\pi A}{2\sqrt{4\pi\rho}} < \frac{\pi V_A}{4\ell nRe_m}, \tag{5}$$

where we put $\theta \equiv \arctan(x/z) \simeq (\pi/2)$ for the weak Alfvén shocks.

The Petschek solution for the magnetic reconnection cannot be considered as self-consistent, since it neglects nonlinearities of the problem that are very important near the reconnection region [6, 7]. Indeed for an inflow velocity (5) much smaller than the Alfvén velocity of outflow the reconnection region can be represented as a rectangular box with the thickness $2d_z$ much smaller than the width $2d_x$ as follows from the plasma flow continuity equation:

$$u_z d_x \simeq V_A d_z \tag{6}$$

Then, the magnetic field jump across the current sheet in the reconnection region is related to the plasma current $j = \sigma E_y$ inside this region:

$$\tfrac{1}{2}\Delta B_x \equiv B_0 - \frac{2}{\pi}u_z\sqrt{4\pi\rho}\,\ell n\frac{L}{d_z} \simeq \frac{2\pi}{c}\sigma E_y d_z > 0, \tag{7}$$

where E_y is the steady electric field generated by the external plasma flow across the magnetic field. Under the condition (4) the plasma current in the reconnection region generates in the outflow region a magnetic field with a strength $B_z \sim B_0$ much bigger than that given by eqs (3) and (2) and with the opposite sign. The self-similar solutions found by Yeh and Axford [10] for the 2D reconnection flow near the X-line have the same problem. Recently Priest and Lee [8] have proposed a different solution for the plasma flow and magnetic field outside the reconnection region that matches both the reconnection region and the plasma outflow region without problems described above. The magnetic field configuration is described by the analytical solution of the Laplace equation with a cut $(-L, +L)$ along the x-axis [compare with eq. (3)]:

$$B_z + iB_x = iB_i[(z + ix)^2/L^2 + 1]^{1/2}. \tag{8}$$

We see that the plasma current at the edge of the reconnection region $j \sim B_x \to 0$ so that the magnetic field in the plasma outflow region is disturbed only near the edge resulting in a reversed current spike. In contrast to the Petschek model the magnetic field and plasma flow lines are strongly curved and there is a strong jet along the separatrix (YS-line in Fig. 3). The Alfvén shock wave (YH-line in Fig. 3) very slightly disturbs the magnetic field and plasma flow. Though this solution for the MHD flow outside the reconnection region is very attractive one should obtain, from first principles, a plasma current profile in the reconnection region that is consistent with the magnetic field configuration (8) near its border.

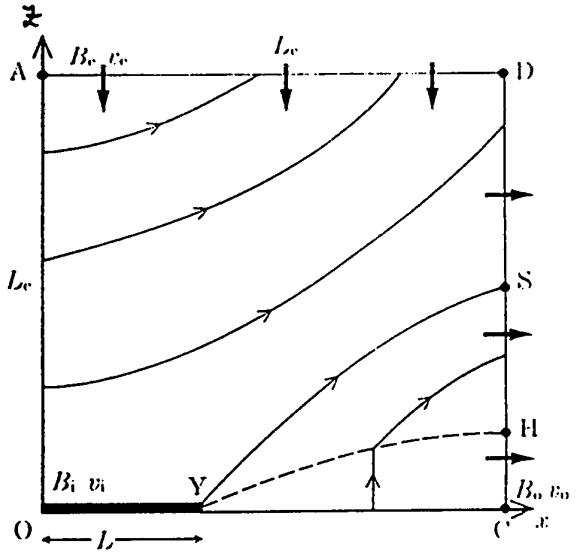

Fig. 3. The notation for reconnection with a highly curved flow [8].

In fact, the size of the reconnection region given by eq. (1) happens to be much smaller than the mean free path of plasma particles in most space applications. Therefore, we need to revise the physics of the collisionless magnetic reconnection in the close vicinity of the neutral X-line both for the driven reconnection [6, 7] and the explosive tearing reconnection [9]. Following the above cited papers we consider, in the next section, the structure of the dissipation region near the X-line in collisionless plasma and discuss such important issues as the inertial- and gyroresistivity, the electron-ion momentum coupling in the collisionless plasma near the neutral X-line. We also specify the upper limit for the collisionless reconnection rate caused by the space charge effect on the plasma flow near the X-line. Similar effects for the nonlinear tearing reconnection will be discussed in Section 3. Finally, in Section 4 we briefly review the collisionless reconnection in the weakly sheared magnetic field which is important both for the solar flares and the plasma dynamics in tokamaks.

2. Structure of the driven collisionless reconnection near the magnetic X-line

As we have described in the Introduction the magnetic field lines are frozen into the ideal MHD plasma flow everywhere besides the vicinity of magnetic X-line where the field lines decoupled from the stagnated plasma flow due to the collisional diffusion and reconnection. In collisionless plasma the magnetic field lines decouple from the plasma drifting in the crossed electric and magnetic field in the small area near the X-line where the particles are effectively unmagnetized. Following the work [7], we describe the externally generated vacuum magnetic field near the X-line by the expression (Fig. 4)

$$\boldsymbol{B} = B_0\left(\frac{z}{L_z}\boldsymbol{e}_x + \frac{x}{L_x}\boldsymbol{e}_z\right), \tag{9}$$

where $\boldsymbol{e}_\alpha$ is the unit vector along the α-axis and the plasma flows into the reconnection region along the $\pm z$-axis and out along the $\pm x$-axis. Therefore, $d_x > d_z$ [10].

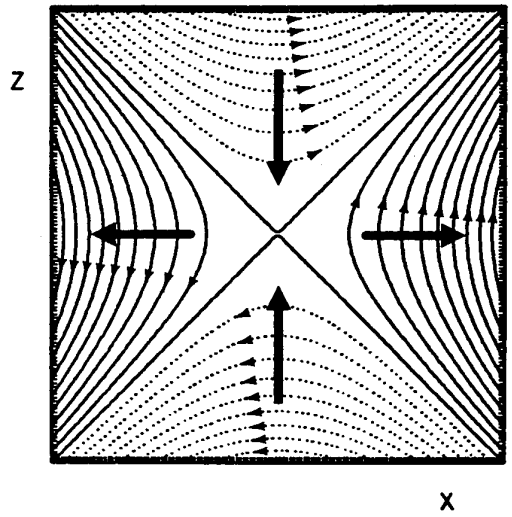

Fig. 4. Vacuum magnetic field configuration with the general direction of plasma flow indicated by the arrows [6].

2.1. *Reconnection in the hot plasma* ($v_{T_j} \gg cE_y/B$)

The size of the region near the X-line where the particles of given species j are unmagnetized is defined by the expressions [11]:

$$d_{zj} = \frac{v_{T_j}}{\Omega_{xj}(d_{zj})}, \quad d_{xj} = \frac{v_{T_j}}{\Omega_{zj}(d_{xj})}, \tag{10}$$

where $v_{T_j} = \sqrt{2T_j/m_j}$ is the thermal velocity of the particles of j-species with the temperature T_j and mass m_j, $\Omega_{\alpha j} = e_j B_\alpha/m_j c$ the cyclotron frequency in the α-component of the magnetic field (9), d_{zj} and d_{xj} are the half-thickness and the half-width of the unmagnetized region, respectively. With the help of the expression (9) we obtain, from eq. (10):

$$d_{zj} = \sqrt{\rho_j L_{zj}}, \quad d_{xj} = \sqrt{\rho_j L_{xj}}, \tag{11}$$

where $\rho_j = v_{T_j}/\Omega_j$ and $\Omega_j = e_j B_0/m_j c$ are the cyclotron radius of the thermal particles and their cyclotron frequency in the magnetic field $\boldsymbol{B}_0$ far from the X-line.

The reconnection electric field $E_y = -u_z B_0/c$ accelerates the ions and electrons freely in the region where they are unmagnetized driving the electrical current near the magnetic X-line. The finite life time of particles in this region limits their acceleration thus limiting the electric current to the value [12, 13]:

$$j_{yj} = \frac{n(d_{zj})e_j^2 \tau_j}{m_j} E_y, \tag{12}$$

where $\tau_j = d_{xj}/v_{T_j} \sim 1/\Omega_{jz}(d_{xj})$ is the lifetime of j-particles in the magnetic cusp region where they are unmagnetized, $n(d_{zj}) \simeq n_0 d_{zj}/L_z$ – the density of the j-plasma species in this region that was estimated from the conservation of the j-particles inflow into the latter with the electric drift velocity.

$$n \frac{cE_y}{B_x} = \text{const.} \tag{13}$$

The plasma resistivity due to the finite life time of particles in the current sheet is called the inertial resistivity and is very similar to the gyroresistivity of the Earth magnetotail plasma sheet.

The limit for the collisionless reconnection rate is set by the condition of the weak disturbance of the vacuum magnetic field in the plasma outflow region produced by the ion plasma current (12) that dominates the electron current [6]:

$$\frac{dB_z}{dx} = \frac{B_0}{L_x} - \frac{4\pi}{c} j_{yj} \frac{d_{zi}}{d_{xi}}. \tag{14}$$

Using expression (12) for the ion plasma current we find that, under the above specified condition, the reconnection rate is well below the Alfvén velocity:

$$u_z \simeq \frac{cE_y}{B_0} < v_A \frac{c}{\omega_{pi} L_x}, \tag{15}$$

where $v_A = B_0/\sqrt{4\pi n_0 m_i}$ is the Alfvén velocity in the external plasma flow.

It is important to note that in the collisionless plasma the reconnection rate can be limited by the plasma space charge in the reconnection region which is a consequence of the coupling of electron and ion momentums via the magnetic field [7]; see Fig. 5. In Fig. 5 the electrons and ions are accelerated by the electric field $E_y > 0$ in the opposite directions. As they turn and flow outward in the x-direction, they transfer their momentum to the magnetic field by bending the initially planar magnetic field in the negative and positive y-direction respectively. The chain of momentum transfer can be described by the relations [7]:

$$ne_j E_y \sim \frac{\partial}{\partial x} u_x(nu_y) \sim (\boldsymbol{B} \cdot \nabla) B_y. \tag{16}$$

As a result of this process the B_y component of the magnetic field is generated and the space charge can be accumulated under the action of the component of the reconnection electric field along the bent magnetic field lines to cancel the longitudinal electric field:

$$\boldsymbol{E} \cdot \boldsymbol{B} \equiv E_y B_y - (\boldsymbol{B} \cdot \nabla)\phi = 0, \tag{17}$$

where ϕ is the electrostatic field potential.

If the electrostatic electric field force in the plasma outflow direction (i.e. along the x-axis) exceeds the ion pressure force per particle the reconnection will stop since the ions will be trapped in the reconnection region. With the help of the relations (16) and (17) this condition takes a form:

$$e\phi/dx = \frac{4\pi e^2 n(d_{zi}) E_y^2 d_x}{B_x^2(d_{zi})} < \frac{T_i}{d_x}, \tag{18}$$

where the derivative along the magnetic field line $(\boldsymbol{B} \cdot \nabla) \simeq B_x/d_{xi} > B_z/d_{zi}$ due to the $B_z(x)$ – profile modification by the

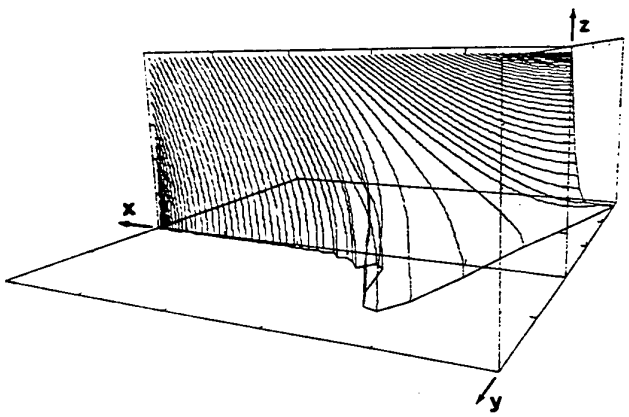

Fig. 5. A 3-D plot of the magnetic field lines [7].

plasma current [see eq. (14)].

$$u_z = c\frac{E_y}{B_0} < \beta_i^{1/2}\left(\frac{c}{\omega_{pi}L_x}\right)\left(\frac{L_x}{L_z}\right)^{1/2} V_A, \tag{19}$$

where $\beta_i = V_{Ti}^2/V_A^2$ is the ratio of thermal and magnetic pressures. Comparing the inequalities (15) and (19) we find that the electrostatic effects set a lower limit of the reconnection only in the low beta plasma ($\beta_i \ll 1$).

Finally, the above described reconnection due to the ion current dissipation is real since the electron diffusion through the area where electrons are unmagnetized is faster than that of ions:

$$c^2/4\pi\sigma_e\, d_{ze} > c^2 4\pi\sigma_i d_{zi}, \tag{20}$$

where $\sigma_i = n(d_{zj})e^2/m_j\Omega_{jz}(d_{xj})$ is the inertial plasma resistivity.

2.2. *Reconnection in the cold plasma* ($v_{Tj} \ll cE_y/B$)

In case of a very strong electric field reconnection the electric drift velocity near the X-line exceeds the ion thermal velocity:

$$V_{Ex,z} = \frac{cE_y}{B_{z,x}} \gg v_{Ti}.$$

In this limit the size of the region near the X-line where the ions are unmagnetized is given by the relations [6]:

$$d_z = \frac{V_{Ez}(d_z)}{\Omega_{ix}(d_z)}, \quad d_{xj} = \frac{V_{Ex}(d_x)}{\Omega_{iz}(d_x)} \tag{21}$$

or

$$d_z = \left(\frac{cE_y}{B_0\Omega}L_z^2\right)^{1/3}, \quad d_x = \left(\frac{cE_y}{B_0\Omega}L_x^2\right)^{1/3}. \tag{22}$$

The effective ion lifetime in the unmagnetized region is $\tau_i = |\Omega_{iz}(d_x)|^{-1}$, so that the ion electric current is given by expression (12). Therefore, we can use eq. (14) and the expressions (22) for d_x and d_z to obtain the limit for the reconnection rate from the condition of the B_z-magnetic field perturbation by the plasma current [6]:

$$u_z = c\frac{E_y}{B_0} < V_A\frac{c}{\omega_{pi}L_z^{1/3}L_x^{2/3}}. \tag{23}$$

As in the case of reconnection in a hot plasma the electrostatic electric field in the plasma outflow direction can stop the reconnection flow, if the electrostatic field strength exceeds the Lorentz force acting on the accelerated particles. Therefore, the reconnection rate is limited by the opposite condition [compare with condition (18)]:

$$\phi/\tilde{d}_x = \frac{4\pi e n(d_{zi})E_y^2 d_{zi}^2}{B_z^2(\tilde{d}_{xi})\tilde{d}_{xi}} < \frac{1}{c}v_y B_z(d_{xi}) \simeq E_y, \tag{24}$$

where, in contrast to the preceding section, the derivative along the magnetic field line is estimated as $(\boldsymbol{B}\cdot\nabla) \simeq B_z/d_{zi} \gg B_z/d_{xi}$ [see the relations (22)], and the x-size of the reconnection region $\tilde{d}_{xi}$ is corrected due to the B_z-profile modification, i.e.

$$B_z(\tilde{d}_{xi}) = B_z'\tilde{d}_{xi}, \quad \tilde{d}_{xi} = d_{xi}\left(\frac{B_0}{B_x'L_x}\right)^{2/3}, \tag{25}$$

where $B_x' \equiv dB_z(x)/dx$ is given by eq. (14).

However, using the relations (25) we find that the condition (24) is independent of the B_z-profile modification and certainly weaker than condition (23) [7].

$$\frac{\phi}{d_{xi}E_y} = \frac{\omega_{pi}L_z}{cV_A}\frac{cE_y}{B_0} < 1. \tag{26}$$

It is worthwhile noting that this higher limit for the magnetic reconnection could be reached only with a strong modification of the B_z-profile by the plasma current described by eq. (14) and relations (25):

$$\frac{B_z'L_x}{B_0} = 1 - \frac{\omega_{pi}L_x^{2/3}L_z^{1/3}}{cV_A}\frac{cE_y}{B_0}\left(\frac{B_z'L_x}{B_0}\right)^{1/3} \ll 1. \tag{27}$$

However, in this case one needs to find a nonlinear solution for the plasma flow outside the reconnection region instead of the linear solution given by Petschek [3].

3. Implications for the explosive tearing mode reconnection

Formation of the near-Earth neutral line followed by the rapid reconnection of the magnetic field lines was proposed by Hones [14], Russell and McPherron (1973) as the most plausible mechanism of the initiation of substorms in the Earth magnetospheric tail. By that time the theory of the linear tearing mode instability was developed for the Earth magnetospheric tail [15]. Later on the explosive growth of the finite amplitude ion tearing mode [16] was proposed by Galeev *et al.* [9] as a model of the rapid reconnection in the magnetospheric tail. The explosive growth of the ion tearing mode starts when the thickness of the magnetic island formed due to the magnetic reconnection exceeds the thickness of the region near the plane neutral sheet where the ions are unmagnetized (Fig. 4). Since the ion motion is now influenced by the z-component of the tearing mode magnetic field we include the latter into the Harris magnetic field model:

$$\boldsymbol{B} = B_0\tanh(z/L)\boldsymbol{e}_x + B_1(t)\Psi(|z|)\sin kx\boldsymbol{e}_z, \tag{28}$$

where $\Psi(|z|) = [1 + \tanh(|z|/L)/kL]\exp(-k|z|)$, L – the thickness of the unperturbed current sheet, $\boldsymbol{k} = k\boldsymbol{e}_x$ – the wave vector of the tearing mode and the magnetic field of the tearing mode was calculated using the external solution of the linear tearing mode equation for the y-component of the vector potential, A_1 [15]:

$$A_1(x, z, t) = -[B_1(t)\Psi(|z|)/k]\cos kx. \tag{29}$$

Here, we limit ourselves to the moderately nonlinear tearing mode characterized by the weak B_{1x} and E_{1y} fields in the reconnection region:

$$B_{1x} \simeq \frac{B_1(t)}{k^2L^2}(1 - k^2L^2) \ll B_0,$$

$$E_{1y} \simeq \frac{\Psi(|z|)\partial B_1(t)}{kc\partial t} \ll (v_{Ti}/c)B_{1z}. \tag{30}$$

In this limit the ion tearing mode growth is described by the equation [9]:

$$\frac{\partial}{\partial t}\frac{1}{8\pi}\int_{-\infty}^{\infty}\int_{-\pi/k}^{\pi/k}\left[\left|\frac{dA_1}{dz}\right|^2 + k^2|A_1|^2 - \frac{2|A_1|^2}{L^2\cosh^2(z/L)}\right]dx\,dz$$
$$= -\sum_j\int_{-dz_j}^{dz_j}\int_{-dx_j}^{dx_j} j_{1y}E_{1y}\,dx\,dz, \tag{31}$$

where the dimensions d_{zj} and d_{xj} of the reconnection region and the electric current j_{1j} are defined by the expressions (11) and (12). Using all these expressions we rewrite eq. (31)

in the form (see details in [9]):

$$\frac{1}{\Omega_i b_1^2}\frac{\partial b_1}{\partial t} = \frac{\pi}{4}\frac{c^2}{\omega_{pi}^2 L^2 \varepsilon_i}\frac{1-k^2L^2}{kL} \tag{32}$$

where $b_1 = B_1(t)/B_0$.

Equation (32) describes the explosive tearing mode reconnection in the range of mode amplitudes b_1 limited from below by the condition $kd_{xi} < 1$ for the transition into the nonlinear growth and from above by the condition (15) for the weak modification of the $B_z(x)$ profile. Comparing the magnetic field models (9) and (28) we find that in the last model we can put $L_x = 1/kb_1\Psi$ in expression (11) for d_x and write the first condition in the form:

$$kd_x = \sqrt{k\rho_i/b_1}\,\Psi < 1. \tag{33}$$

The second condition (15) with the help of the eq. (32) can be written as

$$\frac{\pi}{4}\frac{b_1}{k^2L^2\varepsilon_i\Psi}\frac{1-k^2L^2}{kL} < 1. \tag{34}$$

Combining the inequalities (33) and (34) we find that the explosive growth is possible only near the instability threshold: $1 - k^2L^2 \ll 1$, so that $\Psi \simeq 1$ for $\varepsilon_i \ll 1$. From the relations (23) and (34), in turn, follows that $b_1 < \varepsilon_i^{1/2}$. Finally, comparing the relations (11) and (22) for d_{xi} one can show that the transition from the moderately nonlinear tearing mode defined by the conditions (30) to the strongly nonlinear mode in the opposite case cannot take place within the range of the mode amplitude b_1 defined by the inequalities (33) and (34). This means that the strongly nonlinear tearing mode discovered by Pritchett [17] under the conditions opposite to those in (30) in his two-dimensional numerical simulations should be stabilized in the real three-dimensional configuration by the positive space charge near the X-line blocking the ion flow [7].

4. Magnetic reconnection in the nonvanishing magnetic field

Up to now our discussion of magnetic reconnection was limited to the two-dimensional models in which the magnetic field strength turns to zero at the neutral X-line where the field lines reconnect. In this section we consider the magnetic reconnection in the nonvanishing magnetic field. For the sake of simplicity we limit ourselves to the case of a strong guiding magnetic field

$$\boldsymbol{B} = B_0\boldsymbol{e}_y + \boldsymbol{B}_\perp(\boldsymbol{r}, t), \quad |\boldsymbol{B}_\perp| \ll B_0, \tag{35}$$

which is typical both for the solar corona magnetic field [18, 19] and the laboratory fusion devices such as tokamaks [20].

4.1. *Spontaneous reconnection of sheared magnetic field lines*

Magnetic reconnection in a nonvanishing magnetic field was studied first in applications to the laboratory fusion devices where it takes the form of a specific plasma instability in the sheared magnetic field [11, 12]. To illustrate the physics of such reconnection we further simplify the magnetic field model (35) reducing it to the plane sheared magnetic field described by the generalized Harris model [22]:

$$\boldsymbol{B} = B_\perp \tanh\frac{X}{L}\,\boldsymbol{e}_z + B_0\boldsymbol{e}_y. \tag{36}$$

The structure of the dissipation region, in this case, becomes quite complicated. First, the tearing mode in the sheared magnetic field is coupled to the drift mode [23, 24]. Therefore, it should be described by both vector and scalar potentials in the form:

$$\{A_\parallel, \phi\} = \{A_\parallel(x), \phi(x)\}\exp(-i\omega t + i\boldsymbol{k}\cdot\boldsymbol{r}), \tag{37}$$

where $\boldsymbol{k} = (0, k_y, k_z)$ and $x = X - X_s$ with X_s defined by the condition $k_\parallel \equiv (\boldsymbol{k}\cdot\boldsymbol{B}) = 0$ for the resonant magnetic surface. Electrons and ions moving along the magnetic field lines with thermal velocities fall into Cherenkov resonance ($\omega = k_\parallel v_\parallel$) with the propagating drift tearing mode dissipating its energy due to the Landau damping. The width of the resonance region for the particles of the jth species follows from the Cherenkov resonance condition

$$\delta_j = \left|\frac{\omega_{*e}}{k_\parallel'(x)v_{Tj}}\right| \sim \frac{\rho_j L_s}{L}, \tag{38}$$

where $\omega_{*e} \sim k_z\rho_j v_{Tj}/L$ is the frequency of the drift-tearing mode, $k_\parallel'(x) \equiv dk_\parallel/dx$, $L_s \simeq B_0 L/B_\perp$. However, Cherenkov interaction of particles with the mode is limited to the distance $\delta_e \ll \delta_\phi = \sqrt{\rho_i\delta_i} \ll \delta_i$ from the resonant magnetic surface where the longitudinal electric field of the mode

$$E_\parallel(x) = \frac{i\omega}{c}A_\parallel - ik_\parallel(x)\phi(x) \tag{39}$$

has not been shortcircuited by the charged particles motion along the magnetic field lines (see Fig. 6). Here, $\phi(x)$ is given by [23, 24]:

$$\phi(x) = \frac{\omega A_\parallel}{k_\parallel c}\left[\frac{ix^2}{2\delta_\phi^2}\int_0^{\pi/2}\exp\left(-\frac{ix^2}{2\delta_\phi^2}\cos\theta\right)\sqrt{\sin\theta}\,d\theta\right],$$
$$\delta_\phi = \sqrt{\delta_i\rho_i} < \delta_i. \tag{40}$$

The growth of the drift tearing mode is described by the Maxwell equation for the vector potential

$$\frac{d^2A_\parallel}{dx^2} - k^2A_\parallel - \frac{2k_z^2}{k^2L^2}\cosh^{-2}\left(\frac{x+X_s}{L}\right)A_\parallel = -\frac{4\pi}{c}j_\parallel, \tag{41}$$

where

$$\frac{4\pi}{c}j_\parallel = -\sum_j\frac{4\pi e_j^2 n}{T_j c^2}\int_{-\infty}^{+\infty}\frac{(\omega-\omega_{*j})v_\parallel^2 f_{0j}(v_\parallel)}{\omega - k_\parallel(x)v_\parallel + i0}\,dv_\parallel \times\left(A_\parallel - \frac{ck_\parallel(x)}{\omega}\phi(x)\right)$$

is the electric current driven by the localized electric field of the mode near the resonant magnetic surface. Dividing both sides of this equation by its external solution (29) for the tearing mode vector potential $A_\parallel(x)$ and integrating the result across the resonant magnetic surface we obtain the

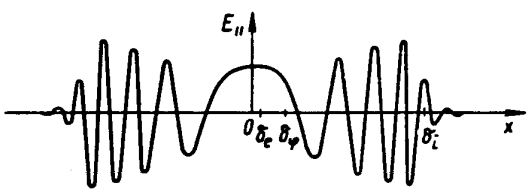

Fig. 6. The longitudinal electric field profile $E_\parallel(x)$ in the region of the Cherenkov resonance.

dispersion relation:

$$\Delta' = -\frac{\pi^{1/2}\omega_{pe}^2}{c^2}\frac{i(\omega-\omega_{*e})}{|k'_{\parallel}(0)|v_{T_e}} + 0.75\frac{\omega_{pi}^2}{c^2}\left(1+\frac{T_i}{T_e}\right)\delta_\phi e^{-i(\pi/4)} \quad (42)$$

where $\Delta' = (1-k^2L^2)/kL^2$ is a measure of the free energy for the particular case of the magnetic field model (35). The second term here stabilizes the instability in the strongly sheared magnetic field ($L/L_s \geqslant \sqrt{m_e/m_i}$).

The nonlinear development of the drift-tearing modes in toroidal fusion devices such as tokamaks strongly differs from that in space plasma. In tokamaks the resonant magnetic surfaces are discretely spaced due to discreteness of the poloidal and toroidal wave numbers. Therefore, the single mode nonlinear growth is of interest in this case. Cherenkov interaction of electrons with the single mode is quenched first when the width, w, of the magnetic island becomes larger than the width, δ_e, of Cherenkov interaction region for electrons. However, this cannot stabilize the instability since the resonant ions outside the magnetic island still dissipate the mode energy. The mode grows approximately linearly with time at this stage until it stops when the magnetic island width, w, exceeds the width, δ_ϕ, of the region where the mode electric field $E_\parallel$ is localized [22]. In case of MHD tearing instability both the mode energy dissipation and the mode electric field are localized in the same region near the resonant magnetic surface with the width, δ_ϕ, depending on the collisional resistivity [21]. Therefore, the tearing mode grows exponentially until the width, w, of the magnetic island becomes comparable with the width, δ_ϕ, of the dissipation region and then continues to grow linearly in time due to finite plasma resistivity [20].

In space plasma with dimensions exceeding, by many orders of magnitude, the characteristic microscopic scales such as the particles Larmor radius ρ_j or their inertial length c/ω_{pj} the resonant magnetic surfaces are spaced so closely that the magnetic islands near the different resonant surfaces overlap already at very small amplitudes of the modes (see Fig. 7). Therefore, the magnetic field lines become stochastic [25] and diffuse across the undisturbed magnetic surfaces. The diffusion coefficient depends on the amplitudes B_k of the tearing modes:

$$D = \sum_k \frac{|B_k|^2}{B_0^2}\int_0^\infty \exp\{-ik_\parallel[x(0)]s - k'^2_\parallel Ds^3/6\}\,ds. \quad (43)$$

The width of the layer of the stochastic field lines near the resonant magnetic surface can be estimated from this equation using the diffusion law $\Delta x^2 = Ds$:

$$\delta_{st} \sim (D/k'_\parallel)^{1/3}. \quad (44)$$

It is obvious that the electric field potential will be spread at least in this region. In fact, the width of the longitudinal electric field localization region, δ_ϕ, also grows with the tearing mode amplitudes [26]:

$$\delta_\phi \simeq \delta_{st}^{3/4}\,\delta_i^{1/4}. \quad (45)$$

Therefore, Cherenkov interaction of electrons with the mode weakens when $\delta_{st} > \delta_\phi$, i.e. for $\delta_{st} > \delta_i$. In this limit the resonant electrons are spread over the distance δ_{st} across the magnetic surface bigger than the width δ_i of the electric field localization region. Therefore the dispersion relation modifies as

$$\Delta' \simeq -\frac{i\omega_{pe}^2}{c^2}\frac{\omega}{|k'_\parallel|\delta_{st}v_{T_e}}\delta_i, \quad (46)$$

and the tearing mode energy density grows explosively under some special conditions (see details in [26]).

4.2. *Driven magnetic reconnection of strain-wrapped magnetic field lines*

Gold [27] first pointed out that the convective motion of photospheric plasma causes the twisting and strain-wrapping of the coronal loop magnetic field lines embedded by its ends into the photospheric plasma. The strained magnetic field lines then relax via magnetic reconnection to a state with a lower energy producing the solar flare. By this process only the energy of strained magnetic field lines released and the potential part of the magnetic field stays unchanged since it is generated by the under photospheric currents. Parker [19] has shown that if the magnetic field lines winding pattern varies along the magnetic field then there is no plasma equilibrium and the reconnection should change this pattern to reach the equilibrium state (Fig. 8). The reconnection can proceed with any rate lower than given by Petschek [3] for the MHD model:

$$u_\perp \leqslant V_{Aj}/\ell n Re_m \quad (47)$$

where V_{Aj} is the Alfvén velocity in the magnetic field B_j generated by the longitudinal currents in the coronal loop [28]. According to Parker [29], the role of the shuffling of the

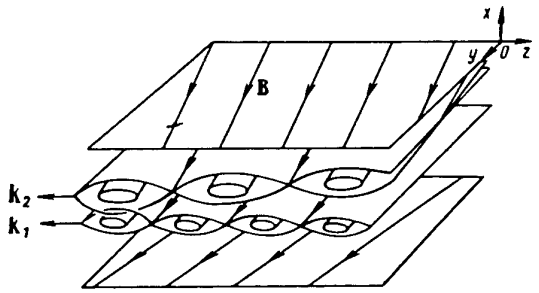

Fig. 7. The magnetic surface splitting in the case of the two tearing modes with finite amplitudes and close wave vectors and their overlapping.

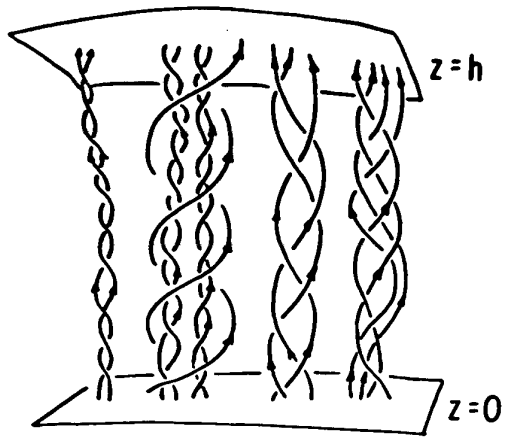

Fig. 8. A sketch of some of the forms of twisted and wrapped field lines that may occur in the unidirectional field as a consequence of shuffling the footpoints of the lines of force (at $z = 0$) [19].

footpoints of coronal field lines is to maintain the field stress that reduces the thickness of the current sheet in opposition to the diffusion in a resistive plasma.

5. Conclusion

All models of the fast magnetic reconnection required to explain the observational data in space and laboratory plasma are based on the Petschek's idea that the reconnection of magnetic field lines takes place in a so small region that the resistive magnetic field diffusion matches the MHD reconnection flow in the vicinity of the reconnection region. In general the theoretical conception of the fast MHD reconnection was confirmed by the numerical simulation for the driven reconnection near the X-line and in the non-vanishing magnetic field [2], as well as for the spontaneous explosive tearing mode reconnection in collisionless plasma [30]. However, recently it was noted [6, 7] that the electric current flowing in the reconnection region destroys the structure of the magnetic field in the plasma outflow region for fast enough reconnection, thus limiting the applicability of such models to slower reconnection rates.

Therefore, a truly nonlinear solution for the plasma flow through both the external and reconnection regions has to be constructed to find out whether the nonlinear effects limit the reconnection rate to a value much smaller than that given by Petschek [3].

For the case of the driven collisionless reconnection of the strained magnetic field lines [27, 29] the structure of the dissipation region was not studied yet to obtain a realistic rate of such driven reconnection.

References

1. Axford, W. I., "Magnetic Reconnection in Space and Laboratory Plasmas" (Edited by W. Hones, Jr.) (AGU, Washington D.C. 1984), Geophysical Monograph 30, pp. 1–8.
2. Strauss, H. R., Astrophys. J. **381**, 508 (1991).
3. Petschek, H., in: "AAS-NASA Symposium on Physics of Solar Flares" (NASA SP-50 1964), p. 425.
4. Parker, E. N., J. Geophys. Res. **62**, 509 (1957).
5. Sweet, P. A., in: "Electromagnetic Phenomena in Cosmical Physics" (Edited by B. Lehnert) (Cambridge University Press 1958); I.A.U. Symp. No. 6, pp. 123–134.
6. Burkhart, G. R., Drake, J. F. and Chen, J., J. Geophys. Res. **96**, 11539 (1991).
7. Drake, J. F. and Burkhart, G. R., Geophys. Res. Lett. **19**, 1077 (1992).
8. Priest, E. R. and Lee, L. C., J. Plasma Phys. **44**, 337 (1990).
9. Galeev, A. A., Coroniti, F. V. and Ashour-Abdalla, M., Geophys. Res. Lett. **5**, 707 (1978).
10. Yeh, T. and Axford, W. I., J. Plasma Phys. **4**, 207 (1970).
11. Laval, G. R., Pellat, R. and Vuillemin, M., in: "Plasma Phys. and Controlled Nucl. Fusion Res." (IAEA, Vienna 1966), Vol. 2, p. 259.
12. Biskamp, D. and Schindler, K., Plasma Phys. **13**, 1013 (1971).
13. Rusbridge, M. G., Plasma Phys. **13**, 33 (1971).
14. Hones, E. W. Jr., in: "Dynamics of the Magnetosphere" (Edited by S.-I. Akasofu) (D. Reidel Publishing Co., Dordrecht 1979), p. 599.
15. Coppi, B., Laval, G. and Pellat, R., Phys. Rev. Lett. **16**, 1207 (1966).
16. Schinder, K., J. Geophys. Res. **79**, 2803 (1974).
17. Pritchet, P. L., Phys. Fluids **B4**, 3371 (1992).
18. Parker, E. N., Astrophys. J. Suppl. **8**, 177 (1963).
19. Parker, E. N., Astrophys. J. **174**, 499 (1972).
20. Rutherford, P. H., Phys. Fluids **16**, 1903 (1973).
21. Furth, H. P., Killin J. and Rosenbluth, M. N., Phys. Fluids **6**, 459 (1963).
22. Galeev, A. A., Zeleny, L. M. and Kuznetsova, M. M., JETP Lett. **41**, 387 (1985).
23. Bussac, M. N., Edery, D., Pellat, R. and Soule, J. L., Phys. Rev. Lett. **40**, 1500 (1978).
24. Coppi, B., Mark, J. W., Sugiama, L. and Bertin, G., Phys. Rev. Lett. **42**, 1058 (1979).
25. Rosenbluth, M. N., Sagdeev, R. Z., Taylor, J. B. and Zaslavskii, G. M., Nucl. Fusion **6**, 297 (1966).
26. Galeev, A. A., Sov. J. Plasma Phys. **18**, 645 (1992).
27. Gold, T., in: "AAS-NASA Symposium on the Physics of Solar Flares" (NASA Spec. Publ., SP-50 1964), p. 389.
28. Galeev, A. A., Rosner, R., Serio, S. and Vaiana, G. S., Astrophys. J. **243**, 301 (1981).
29. Parker, E. N., Astrophys. J. **407**, 342 (1993).
30. Terasawa, T., J. Geophys. Res. **86**, 9007 (1981).

Physica Scripta. Vol. T52, 20–27, 1994

Particle Acceleration in Lower-Hybrid Cavitons

R. Bingham[1], J. J. Su[2], V. D. Shapiro[3], V. Shevchenko[3], S. Ma[4], J. M. Dawson[4] and V. N. Tsytovich[5]

[1] Rutherford Appleton Laboratory, Chilton, Didcot, Oxon, OX11 0QX, UK
[2] National Central University, Chung-Li, Taiwan
[3] Dept. Electrical and Computer Eng., University of California, San Diego, La Jolla, CA 92091, U.S.A.
[4] Dept. of Physics, University of California, Los Angeles, CA 90024, U.S.A.
[5] General Physics Institute, Moscow, Russia

Received November 22, 1993; accepted February 14, 1994

Abstract

In this paper we investigate particle acceleration resulting from the relaxation of unstable ion ring distributions, producing strong wave activity at the lower hybrid frequency. It is shown that strong lower hybrid wave turbulence collapses in configuration space producing density cavities containing intense electrostatic lower hybrid wave activity. The collapse of these intense nonlinear wavepackets saturate by particle acceleration producing energetic electron and ion tails. There are several mechanisms whereby unstable ion distributions could be formed in plasmas, including reflection at perpendicular shocks, tearing modes, and loss cone depletion.

Numerical simulations of ion ring relaxation processes, obtained using a $2\frac{1}{2}$-D fully electromagnetic, relativistic particle in cell code are discussed. We apply the results to the problem of explaining energetic particle production in solar flares. The results show the simultaneous acceleration of both electrons and ions to very high energies: electrons are accelerated to energies in the range 10–500 keV, while ions are accelerated to energies of the order of MeV's. Our simulations also show wave generation at the electron cyclotron frequency. The strong turbulence collapse process leads to a highly filamented plasma producing many localized regions for particle acceleration of width $\simeq 10\lambda_{De}$.

1. Introduction

A particle-in-cell (PIC) simulation code is used to investigate wave activity and electron acceleration resulting from the presence of a dilute population of monoenergetic gyrating ions. We suggested that ion distributions of this type could exist downstream of collisionless perpendicular shocks, tearing instabilities and mirror magnetic fields in the solar atmosphere, pointing out that evidence for the existence of such shocks is provided by type II radio bursts and coronal mass ejections. The ion ring speed in our simulation was about one third of the Alfvén speed, and the ring density was 30% of the total ion density. The initial plasma beta was about 10^{-3}, consistent with conditions in the flaring solar corona. We found that the mean square electron speed parallel to the magnetic field increased by a factor of ten during the simulation, and showed no sign of leveling off (the mean square perpendicular electron speed rose by a much smaller factor). After 600 plasma periods, the flux of deka-keV electrons was already sufficient to produce the hard X-ray emission observed in a typical flare. We concluded that anisotropic ion distributions might be responsible for electron acceleration in flares, via the intermediate process of lower-hybrid wave generation. This work is complementary to previous studies of lower-hybrid collapse [1, 2, 3].

Waves with frequencies around the lower-hybrid frequency are likely to be excited whenever there is a deficiency of ions with small pitch angles, or when ions are drifting perpendicular to the magnetic field: such distributions are found in both laboratory and space plasmas. A velocity space ring distribution, for example, may be created artificially in the presence of magnetic fields by energetic particle injection, or resonant heating by electromagnetic waves [4]. Other mechanisms, which could be relevant to natural plasmas, include ion reflection at perpendicular shocks [5], magnetic reconnection [6, 7] and the interaction of a high velocity neutral gas with a magnetized plasma [8]. Naturally occurring ion rings are known to exist downstream of the earth's bow shock [9], in the earth's radiation belts [10] and plasma sheet [11], and in the vicinity of comets [12]. Ion loss cone distributions, which exhibit similar instabilities to ring distributions, also occur in natural magnetic mirror systems, such as auroral field lines [13]. Indeed, anisotropic ions are found in virtually every plasma which is accessible to *in situ* measurements.

A number of different wave modes can be excited by ring or loss cone distributions. Parallel-propagating ion cyclotron waves are excited at frequencies below the ion gyrofrequency: in this limit, the ring and background ions are "magnetized", in the sense that there is at least one Larmor orbit in one wave period. Lower-hybrid waves are excited at frequencies lying between the ion and electron gyrofrequencies, in which case the ions are unmagnetized and the electrons magnetized. Ion acoustic-like instabilities also exist, but these are only possible if the electron temperature is significantly greater than the ion temperature or if there is a relative drift between electrons and ions [14]. The linear theory of wave generation by ion ring distributions has been summarized by Mikhailovskii [15], while the quasi-linear theory of the loss cone instability has been treated by Galeev [16]. A unified formalism of the parametric (i.e. nonlinear) instabilities associated with lower-hybrid waves has been developed by Tripathi, Grebogi and Liu [17], who dealt primarily with three wave decay processes and nonlinear ion or electron Landau damping associated with a pump wave near the lower-hybrid frequency. Tripathi *et al.* [17] were concerned with radio frequency heating of tokamaks, but their analysis can also be applied to situations in which the lower-hybrid mode is generated *in situ* by an unstable ion distribution.

In a strongly turbulent plasma, the modulational instability may cause a lower-hybrid wave to collapse. Normally, the lower-hybrid instability results in the generation of waves in the region of wavevector space where dissipation (i.e. Landau damping) is negligible: this, in fact, is a pre-

requisite for wave growth. The modulational instability, however, causes waves to cascade to shorter wavelengths, leading to wave collapse and subsequently particle energization by Landau and transit time damping. As a result of wave collapse, direct energy transfer to both electrons and ions can take place.

In this paper we use a PIC code to investigate the acceleration process outlined above. In Section 2 we suggest various mechanisms whereby ion ring or loss cone distributions might develop in the flaring solar atmosphere. We also summarize the theory of lower-hybrid wave collapse, outlining the process which enables electrons and ions to be simultaneously accelerated. In Section 3 we present simulation results which show the effects of ion ring relaxation on the electron distribution and the background ion distribution.

2. Flare Acceleration Model

2.1. *Formation of ion ring distributions*

It has been suggested that energetic gyrating ions could be produced by perpendicular shocks, generated by the super-Alfvénic motion of magnetic flux tubes emerging from the photosphere. We showed that such flux tubes could dissipate energy at a sufficient rate to power the impulsive phase of one particular flare. It should be stressed however, that the validity of the results do not rely on the existence of perpendicular shocks: it is possible that ions rings could also result from magnetic reconnection, which is generally assumed to be the primary mechanism of energy release in flares. Simulations by Leboeuf, Tajima and Dawson [6] have shown that tearing modes produce cross field ion drifts, Ma [18] has carried out full particle in cell simulations of the tearing instability and confirmed the generation of anisotropic ion velocity distributions, which form rings or cross field drifts.

Processes involved in magnetic reconnection are best illustrated with the magnetic neutral sheet configuration, where an infinite current sheet is centered at $x = 0$, generating oppositely directed magnetic field lines on either side. This configuration is stable against ideal MHD perturbations. However, in the vicinity of $x = 0$ where the **B** field vanishes, resistive dissipation, electron inertia, and anomalous dissipation due to plasma collective interactions become important, giving rise to a tearing instability in a boundary layer in which magnetic flux tubes on one side of the neutral sheet can tear, diffuse and connect to those on the other side. The growth rate of the tearing instability is governed by the detailed mechanism of dissipation. Resistive dissipation gives rise to a slow tearing, while electron inertia gives rise to a fast tearing. As the tearing grows, magnetic islands characterised by X and 0 points in the magnetic field lines are formed, and an electric field in the z-direction is induced near the X and 0 points. This **E** field then gives rise to an $\mathbf{E} \times \mathbf{B}$ drift that drags particles toward $x = 0$ near an X-point and away from an 0-point. When a stationary state is reached as a result of nonlinear coalescence of magnetic islands, cold fluid that bring together the magnetic fields of opposite polarities flow toward the X-point at a fraction of the Alfvén speed, and are accelerated as they go across the neutral region, and flow out at the Alfvén speed along the y-axis toward the adjacent 0-points, forming standing shocks.

With this magnetic reconnection configuration, a direct particle acceleration mechanism due to the inductive electric field can be identified for a neutral sheet where the ion Larmor radius (using the asymptotic magnetic field strength) is smaller than the sheet dimension. Outside the neutral sheet, the ions are magnetized. As they $\mathbf{E} \times \mathbf{B}$ drift toward the X-point, some of them, become unmagnetized since the **B** field is weaker. As a particle enters the neutral region, it is accelerated in the z-direction by the inductive **E** field. The energy gained by the particle depends on how long it will stay in the neutral region before it gets out to be remagnetized. Therefore, slow ions are more likely to be accelerated with this mechanism.

2.2. *Lower-hybrid wave collapse and particle acceleration*

Wave collapse, predicted by Zahkarov [19] as the nonlinear stage of the modulational instability, plays a dominant role in the dynamics of strong turbulence. Collapse leads to the explosive-like compression of cavities (regions of high wave energy density from which plasma is expelled by wave pressure). The process of collapse results in the transformation of the wave spectrum to larger wavenumbers, producing small scale structures called cavitons, within which the waves are trapped. These waves are absorbed by resonant particles, and a quasi-steady state is eventually reached in which the pumping of wave energy into the system (e.g. from an unstable ion distribution) is balanced by wave absorption (i.e. Landau damping). It has been shown that lower-hybrid waves can become modulationally unstable, and eventually collapse [1, 2]. The mechanism leading to the modulational instability is the nonlinear coupling of lower-hybrid waves with the much lower frequency quasi-neutral density perturbations of ion acoustic waves. The result is a filamentation of the high frequency field, and the formation of elongated nonlinear wavepackets aligned with the magnetic field, the signature of which is a density depletion.

The modulational instability results in the creation of lower-hybrid wave with $k_\parallel \neq 0$, in addition to slowly varying magnetic structures. Waves with $k_\parallel \simeq \omega_{lh}/3v_e$, where v_e is the electron thermal speed, are efficiently absorbed by resonant electrons in the bulk of the distribution. The same waves have perpendicular wavenumbers $k_\perp \simeq k \simeq \omega_{lh}/3v_i$, where v_i is the ion thermal speed, and can thus be absorbed by (un-magnetized) bulk ions. As a result, simultaneous acceleration of electrons in the parallel direction and ions in the perpendicular direction can occur. Particle acceleration prevents further growth of the pump lower-hybrid wave, thus causing it to saturate.

We will first consider the linear theory of the modulational instability for a pump wave, ϕ_0, where ϕ_0 is the electrostatic wave potential, with a frequency close to the lower-hybrid frequency, and polarized in the plane perpendicular to the magnetic field coupled to the two lower-hybrid satellites, $\phi^\pm$, referred to as the Stokes$^-$ and anti-Stokes$^+$ modes such that

$$\mathbf{k}_\pm = \mathbf{k}_0 \pm \mathbf{k}, \tag{3}$$

$\mathbf{k}_0$ and $\mathbf{k}$ being the initial pump wave and low frequency mode respectively, $\mathbf{k}_\pm$ are the satellite modes.

The equations describing the coupling of the high frequency lower-hybrid potential, ϕ, to the low frequency density perturbation, δn, are given by Shapiro *et al.* [1, 2]:

$$-\frac{2i}{\omega_{LH}}\frac{\partial}{\partial t}\Delta\phi - R^2\Delta^2\phi + \frac{M}{m}\frac{\omega_{LH}^2}{\omega_{ce}}\phi + \frac{M}{m}\frac{\partial^2\phi}{\partial z^2} = -i\frac{M}{m}\frac{\omega_{LH}}{\omega_{ce}n_0}(\nabla\phi\times\nabla\delta n)_z, \tag{4}$$

$$\frac{\partial^2\delta n}{\partial t^2} - \frac{T_e+T_i}{M}\Delta\delta n = +\frac{i\omega_{pe}^2}{4\pi M\omega_{ce}\omega_{LH}}\Delta(\nabla\phi^*\times\nabla\phi)_z, \tag{5}$$

where $\Delta = (\partial^2/\partial x^2) + (\partial^2/\partial y^2)$ is the transverse Laplace operator and

$$R = \left(\frac{3T_i}{\omega_{LH}^2 M} + \frac{2T_e}{\omega_{ce}^2 m}\frac{\omega_{pe}^2}{(\omega_{pe}^2+\omega_{ce}^2)}\right)^{1/2}.$$

The nonlinear term in equation (4), namely $\nabla\phi\times\nabla\delta n$, is of a vortex type and it vanishes for perturbations that are one dimensional in the plane perpendicular to the magnetic field [$(\partial/\partial x) = 0$, $(\partial/\partial y) = 0$]. In one dimension the resulting nonlinearity is smaller by the factor (m_e/m_i), the vortex nonlinearity is due to the density variation as a result of the electron drift velocity across the magnetic field given by $v_{De} = -(c/B^2)(\nabla\phi\times\mathbf{B}_0)$. Since this drift occurs in the background of the low frequency density inhomogeneity, δn, due to the low frequency ion acoustic mode, it gives rise to a high frequency density variation in the form

$$n_e \simeq \frac{1}{i\omega_{LH}}\nabla\cdot\delta n v_{De}. \tag{6}$$

The nonlinear term that couples the slow mode with the high frequency oscillations in eq. (5) is due to the ponderomotive force acting on the electrons. In deriving eqs (4) and (5) we have neglected the polarization drift and parallel motion of the electrons and ions. The ratio of these terms to the vortex nonlinearity is of the order of (m/M), therefore the vortex nonlinearity is the dominant term. It is clear from the nature of $\nabla\phi\times\mathbf{B}_0$ that at least two plane waves or a standing wave must be considered. Due to the appearance of the vortex type of nonlinearity in both eqs (4) and (5) the typical threshold wave amplitude for the modulational instability and collapse is less than the wave amplitudes for the Langmuir modulational instability by the factor (m/M). Equations (4) and (5) can be regarded as the equivalent Zakharov equations for lower-hybrid collapse.

The dispersion relation describing the modulational instability of a pump wave, ϕ_0, decaying into two lower-hybrid sidebands, $\phi^{\pm}$, and a low frequency mode, δn, defined by the complex amplitudes in the form

$$\phi_0 = \phi_0\exp\left(i\left(k_{0\perp}r_\perp - \tfrac{1}{2}\omega_{LH}k_0^2R^2t + \frac{\omega_{pe}^2\omega_{LH}}{2k_0^2c^2}t\right)\right), \tag{7}$$

$$\phi^{\pm} = \phi^{\pm}\exp\left[i\left((\mathbf{k}_0\pm\mathbf{k})\cdot\mathbf{r} - \tfrac{1}{2}\omega_{LH}(\mathbf{k}_0\pm\mathbf{k})^2R^2t + \frac{\omega_{pe}^2\omega_{LH}}{2(\mathbf{k}_0\pm\mathbf{k})^2c^2}t - \frac{M}{m}\frac{k_\parallel^2\omega_{LH}t}{2(\mathbf{k}_0\pm\mathbf{k})^2}\mp\omega t\right)\right], \tag{8}$$

$$\delta n = \tfrac{1}{2}\delta n\exp i(\mathbf{k}\cdot\mathbf{r} - \omega t) + c.c. \tag{9}$$

can be obtained from eqs (4) and (5) and has the following form

$$\omega^2 - k^2\frac{T}{M} = -k_0^2|\phi_0|^2\frac{\omega_{pe}^2[\mathbf{k}\times\mathbf{k}_o]_z^2}{8\pi n_0 m\omega_{ce}^2}\times\left[\frac{1}{|\mathbf{k}+\mathbf{k}_0|^2}\frac{\omega_{LH}}{(\delta_+ + \omega)} + \frac{1}{|k-k_0|^2}\frac{\omega_{LH}}{(\delta_- - \omega)}\right] \tag{10}$$

where

$$\delta_\pm = \tfrac{1}{2}\omega_{LH}\left[|\mathbf{k}_0\pm\mathbf{k}|^2R^2 - k_0^2R_0^2 - \frac{\omega_{pe}^2}{|\mathbf{k}_0\pm\mathbf{k}|^2c^2} + \frac{\omega_{pe}^2}{k_0^2c^2} + \frac{M}{m}\frac{k_\parallel^2}{|\mathbf{k}_0\pm\mathbf{k}|^2}\right]$$

are the frequency mismatches between the Stokes and anti-Stokes satellites and the pump wave. From eq. (10) we see that there is no instability for co-planar wave vectors, i.e. $\mathbf{k}\|\mathbf{k}_0$.

Equations (10) can be solved to yield the following threshold value of the pump electric field strength, E_0, and growth rate, γ, sufficiently above threshold namely

$$\frac{|E|^2}{4\pi n_0 T_e} > \frac{m}{M}\frac{\omega_{ce}^2}{\omega_{pe}^2}\frac{k^2+k_0^2}{2k_0^2}\delta_0, \tag{11}$$

$$\gamma \approx \omega_{LH}\left(\frac{|E_0|^2}{2\pi n_0 T_e}\frac{\omega_{pe}^2}{\omega_{ce}^2}\frac{M}{m}\frac{k_0^2}{k_0^2+k^2}\right)^{1/2}, \tag{12}$$

where

$$\delta_0 = \frac{1}{2}\left(k^2R^2 - \frac{\omega_{pe}^2}{(k_0^2+k^2)c^2} + \frac{\omega_{pe}^2}{k_0^2c^2} + \frac{M}{m}\frac{k_\parallel^2}{(k_0^2+k^2)}\right).$$

The instability results in the modulation of the pump intensity with the typical perpendicular and longitudinal space scales, $L_\perp$ and $L_\parallel$ respectively, being given by

$$L_\perp \sim k_\perp^{-1} \sim R\left(\frac{4\pi n_0 T_e}{|E_0|^2}\frac{m}{M}\frac{\omega_{ce}^2}{\omega_{pe}^2}\right)^{1/2} \tag{13}$$

and

$$L_\parallel \sim \frac{L_\perp^2}{R}\sqrt{\frac{M}{m}} \tag{14}$$

with $L_\perp \ll L_\parallel$.

The modulation of the electric field intensity results in cavity formation on a time scale $t \sim \gamma^{-1}$ where the growth rate γ is given by eq. (12).

Bingham *et al.* [20] have extended this analysis by showing that the low frequency mode could also be a magnetosonic wave. In this case, strong magnetic field perturbations develop perpendicular to the ambient field, leading finally to wave collapse and the cascading of waves to larger parallel wavenumbers, $k_\parallel$. This also occurs even if the initial lower-hybrid wave has $k_\parallel = 0$. Due to the modulational instability, two "satellite" waves are excited. The presence of these satellites causes a modulation of the lower-hybrid wave amplitude. The magnetic field develops fine structure, created by long wavelength, low frequency magnetosonic waves, which parametrically couple the initial lower-hybrid wave to its satellites.

Bingham *et al.* [20] have shown that the threshold wave level for the instability of lower-hybrid waves modulated by

low frequency magnetosonic waves is given by

$$\frac{|E|^2}{8\pi n T_e} = \frac{1}{8\pi}\frac{\omega_{lh}^2}{k_0^2 c^2}\frac{m_p}{m_e}\frac{k_\parallel^2}{k_0^2}\frac{k_\perp}{k_{0\perp}}\frac{B^2}{nT_e} \simeq \frac{1}{\beta_e}\frac{\omega_{lh}^2}{k_0^2 c^2}, \tag{15}$$

where β_e is the electron plasma beta, and $k_{0\perp}$, $k_\perp$ are respectively the perpendicular components of the lower-hybrid pump wave and the magnetosonic wave.

Contrary to the Langmuir modulational instability, which develops pancake like structures with $L_\parallel \ll L_\perp$, i.e. the plane of the pancake is perpendicular to the magnetic field, lower-hybrid cavitons are cigar shaped aligned along the magnetic field.

3. Simulations results

Particle simulations were carried out using ISIS, a fully electromagnetic, relativistic particle-in-cell code. There are two space dimensions and three velocity dimensions, with the undisturbed magnetic field $\boldsymbol{B}_0$ lying in the coordinate (x, y) plane: there is a small angle between $\boldsymbol{B}_0$ and the x-axis. The ratio m_p/m_e is taken to be 400. Time and space are measured in units of the electron plasma period $1/\omega_{pe}$ and the plasma skin depth c/ω_{pe} respectively (ω_{pe} is the electron plasma frequency). In terms of these dimensionless independent variables, Maxwell's equations and the equations of motion are independent of the absolute values of the particle masses. Periodic boundary conditions are imposed, so that no particles are lost from the system. A detailed description of ISIS has been provided by Su [21].

The ion distribution consists of a Maxwellian core and a hot ring perpendicular to the magnetic field:

$$f_i(v_\parallel, v_\perp) = \frac{n_c}{(2\pi)^{3/2}v_c^3} + \exp\left(-\frac{v_\parallel^2 + v_\perp^2}{2v_c^2}\right) + \frac{n_r}{4\pi^2 v_r v_c^2}\exp\left(-\frac{v_\parallel^2 + (v_\perp - v_r)^2}{2v_c^2}\right), \tag{16}$$

where v_r is the ring speed, v_c is the core ion thermal speed, and n_c, n_r are the densities of core ions and ring ions respectively. $v_\parallel$ and $v_\perp$ are the ion speeds parallel and perpendicular to the magnetic field. The normalization of the ring part of the distribution in eq. (16) is only correct if $v_r \gg v_c$. The core ions, ring ions, and electrons are all assigned the same initial temperature. The electron thermal speed, v_e, is set equal to $0.034c$: with a realistic electron mass, this would correspond to an initial temperature of about 800 eV. It should be remembered, however, that m_p/m_e is artificially small, and so there is a degree of flexibility in relating a thermal speed to a temperature.

The other parameters of the simulation are: the density ratio of ring ions to core ions, n_r/n_c, taken to be 3/7, the ring speed is set equal to $20v_c$ ($\equiv v_e$); and the electron gyrofrequency, ω_{ce}, is twice ω_{pe}. In terms of the simulation parameters, the Alfvén speed is given by

$$v_a = v_c\frac{\omega_{ce}}{\omega_{pe}}\frac{c}{v_e} \simeq 60v_c, \tag{17}$$

i.e. about three times the ring speed. If the ring was created as a result of ion reflection at a perpendicular shock, v_r would be greater than v_a. Alternatively, if the ring arose from a reconnection process, we would expect v_r to be rather less than v_a. Finally, if the ions are initially isotropic but develop a loss cone distribution, it is reasonable to suppose that a broad range of "ring" velocities will be present, although ions with speeds in excess of v_a are likely to be scattered into the loss cone by ion cyclotron wave turbulence [22]. The value of v_r/v_a chosen for the simulation is therefore quite reasonable. The chosen number density of ring ions is rather high, but, with a ring speed of $20v_c$, it corresponds to an energy density which is less than 5% of $B^2/8\pi$, and is therefore perfectly consistent with a magnetic origin. The mechanism whereby magnetic field energy is transferred to gyrating ions could involve either shock dissipation or reconnection.

Numerical solutions of eqs (4) and (5) have been carried out using a pseudo-spectral code to investigate two and three dimensional collapse, Fig. 1(a)–(d) represents solutions in terms of the lower-hybrid electric field amplitude and density perturbation, Figs 1(a)–(d) represent different times.

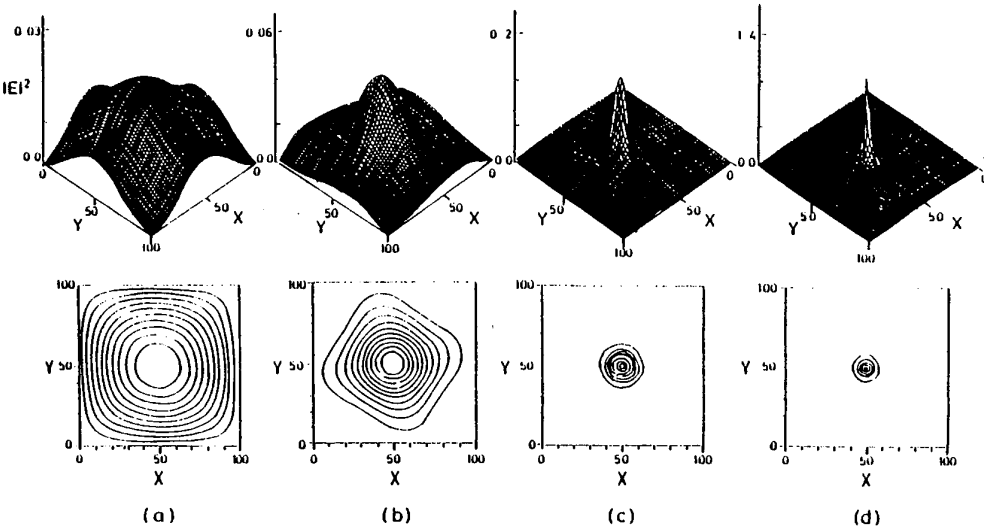

Fig. 1. Dynamics of 2D collapse, spatial structure of electric field and contours of equal densities of the cavity (a) $t = 0 \cdot |\delta n|_{MAX} = 0.031$; (b) $t = 230 \cdot |\delta n|_{MAX} = 0.06$; (c) $t = 335 \cdot |\delta n|_{MAX} = 0.25$; (d) $t = 360 \cdot |\delta n|_{MAX} = 0.38$.

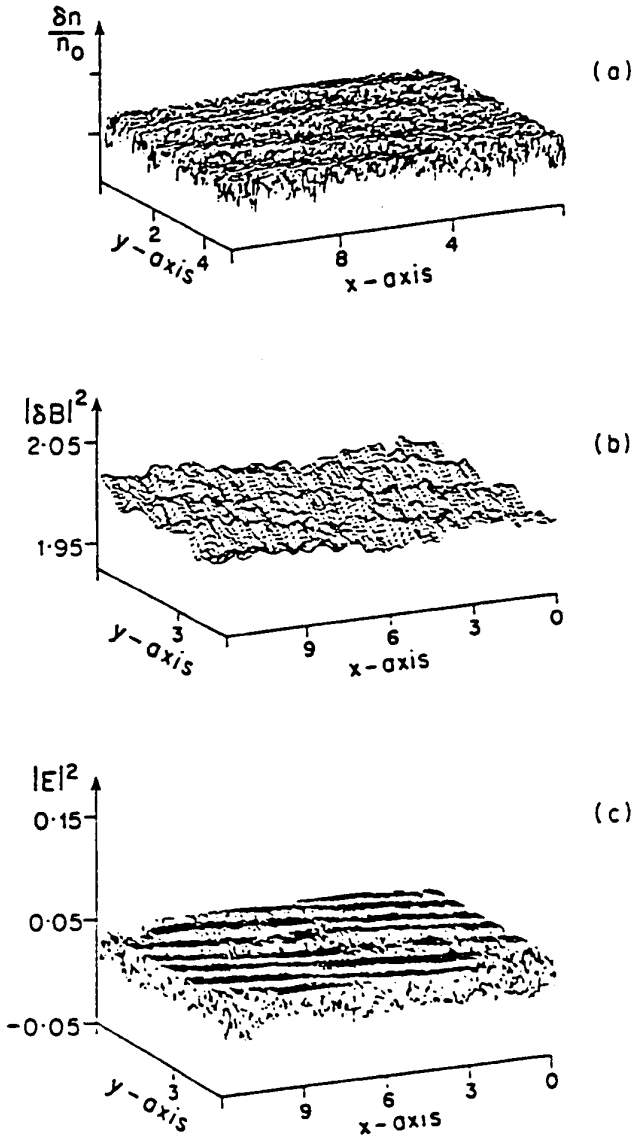

Fig. 2. (a) Low frequency density; and (b) magnetic field; (c) cavitons, arising from the high-frequency electric field envelope. Dark regions are regions of most intense waves located in regions of depleted density. x and y are in units of the plasma skin depth, c/ω_{pe}.

A full description of the 2 and 3-D simulations are given in Ref. [2].

It is clear that the wave energy density increases as the density perturbation decreases. In the 3-D numerical solutions the longitudinal size of the cavities in the z or magnetic field direction is still greater than the transverse scale size. It also appears that it is easier to initialize the collapse processes in 3-D than in 2-D [2]. There is clear evidence from the simulations using ISIS that the acceleration of electrons and ions can be attributed to nonlinear effects associated with density cavitons in the plasma. An analysis of the regions where energetic particles are created, reveals the presence of collapsing wavepackets. These regions also contain intense wave activity as seen in Fig. 2(a, b, c) which shows the signature of the modulational instability.

As expected the regions of high wave intensity correspond to regions of low density. These structures are elongated along the magnetic field direction with perpendicular and parallel dimensions of the order $10\lambda_D$ and $100\lambda_D$ respectively (λ_D being the Debye length). Figure 3 shows the directions of energetic electrons created within these localized structures showing that the acceleration of electrons is thus highly filamented and field aligned.

The parallel electron distribution is shown in Fig. 4. For a time corresponding to $t = 300\omega_{pe}^{-1}$, there is a well developed beam which indicates that strong wave particle trapping is taking place within the caviton.

Energetic ions are also observed to originate within the caviton structures and shown in Fig. 5, the final ion distribution is clearly nonthermal consisting of energetic particles in the perpendicular directions some heating and acceleration also occurs in the parallel direction, but to a much lesser extent. Simultaneously to observing energetic electrons and ions intense microwaves are also observed to be generated within these cavitons or hot spots.

The structure of the cavitons never gets much smaller than about $10\lambda_D$ or one ion gyro-radius, this is in contrast to the fluid theory which predicts collapse down to about λ_D. However, the simulations are fully self-consistent with the damping of the waves playing a major role in the minimum size of the cavitons. The acceleration process inside the cavity cannot be simple quasi-linear diffusion

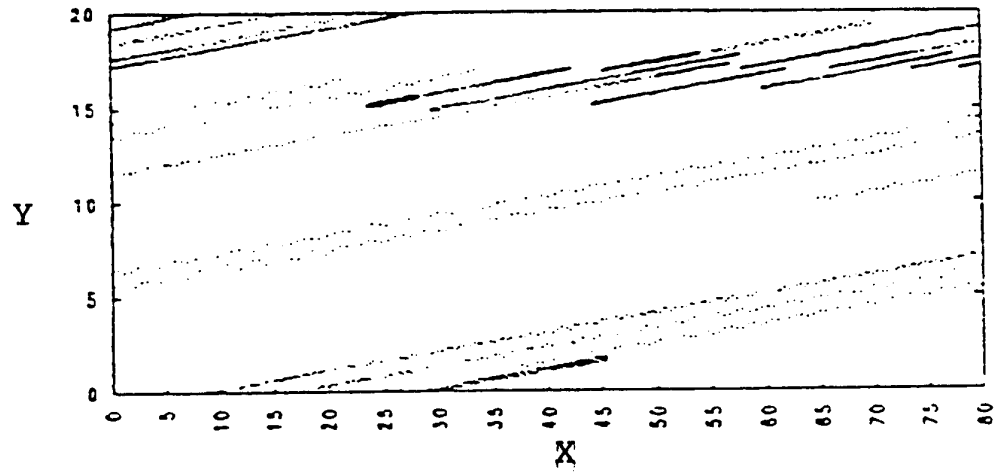

Fig. 3. Directions of energetic electrons in the x–y plane, showing parallel trajectory and filamentary structure of electrons.

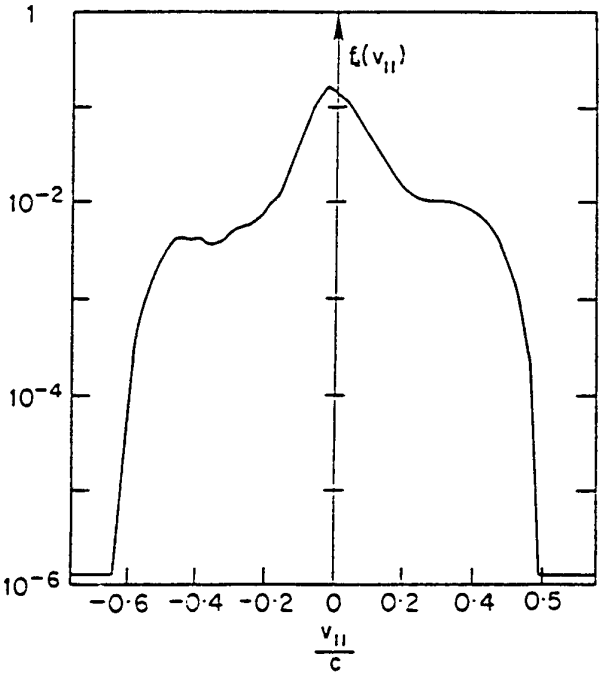

Fig. 4. Parallel electron velocity distribution function for the time $t = 300\omega_{pe}^{-1}$.

since this would not produce a positive slope in the electron distribution function. It is probable that the structure acts more like a coherent wave with particles interacting more strongly with the wave through transit time damping or transitional damping. In this case electrons which are in phase with the oscillations inside the structure can gain more energy per interaction than would be allowed with a quasi-linear treatment. The particles are therefore accelerated more effectively than would be expected from the quasi-linear theory. Strong trapping effects may be taking place which can also alter the distributions significantly. Strong coupling between the particle populations and the waves is taken place inside the cavitons as the wavenumber is decreasing rapidly, coming more into resonance with the bulk of the distribution. This damping is a very effective saturation mechanism which prevents collapse to very small dimensions.

Figure 6 shows the time evolution of the electric field energy density $|E|^2$, the electron energy, and the ion ring energy, all in dimensionless units. Both the field energy and the electron energy at first increase linearly with time, then grow exponentially in the periods $\omega_{pe}t = 350$–550 and $\omega_{pe}t = 1000$–1300. At the end of the simulation, we find that approximately 10% of the ring energy has been transferred to the electrons and core ions, while less than 1% of the energy is stored in all the waves generated. The low instananeous wavelevel is due to strong particle absorption. It can be seen that wave saturation occurs at $\omega_{pe}t \simeq 600$ and $\omega_{pe}t \simeq 1300$.

The time evolution of the parallel electron distribution, f_e, up to $\omega_{pe}t = 1200$ is depicted in Fig. 7. f_e is plotted as a function of the dimensionless parallel momentum $\gamma v_{||}/c$ (γ being the Lorentz factor).

The period of exponential wave growth clearly corresponds to the period of rapid electron acceleration. After about $\omega_{pe}t = 600$, the central core of the electron distribution becomes hotter, and the maximum electron speed continues to increase, eventually reaching $0.8c$ at $\omega_{pe}t = 1300$ (corresponding to an energy of 340–1000 keV, depending on the simulation electron mass). From f_e we can compute the rate at which electrons with $\frac{1}{2}m_e v_{||}^2$ greater than ε_0 are flowing out of the acceleration site per unit area:

$$F(\varepsilon_0) = 2\pi \int_{\sqrt{2\varepsilon_0/m_e}}^{\infty} v_{||}\, dv_{||} \int_0^{\infty} v_\perp\, dv_\perp\, f_e(v_{||}, v_\perp). \tag{18}$$

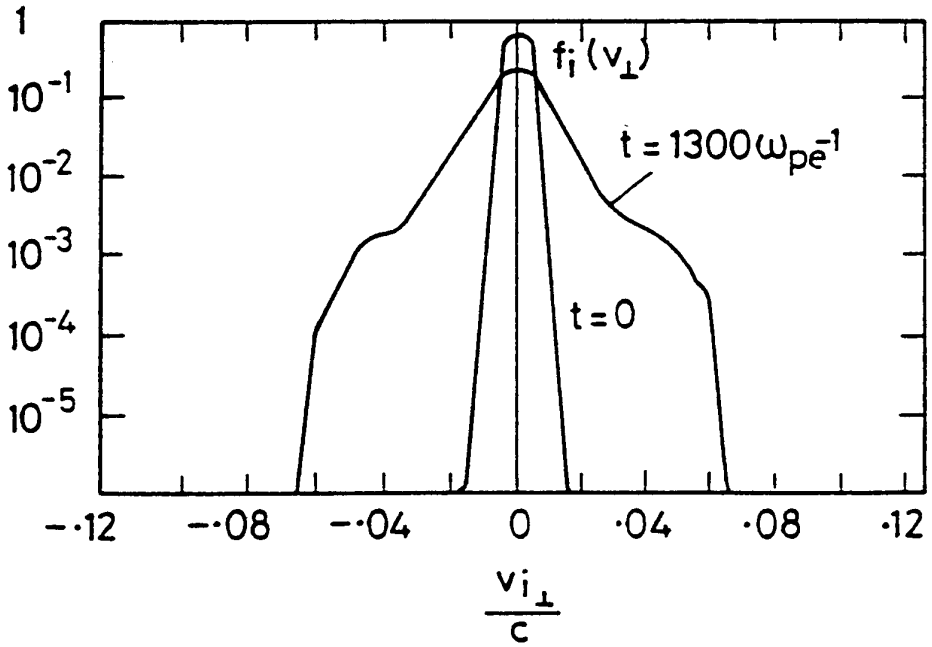

Fig. 5. Transverse ion velocity distribution function for times $t = 0$ and $t = 1300\omega_{pe}^{-1}$.

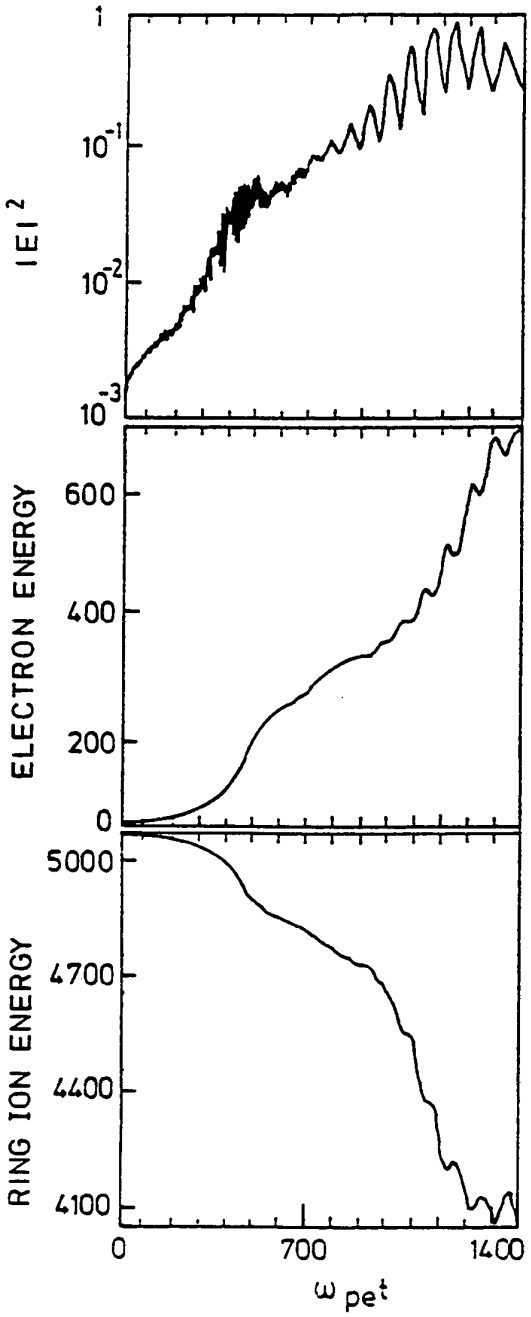

Fig. 6. Time evolution of wave energy density, electron energy and ring ion energy up to $\omega_{pe}t = 1500$. Dimensionless energy units are used.

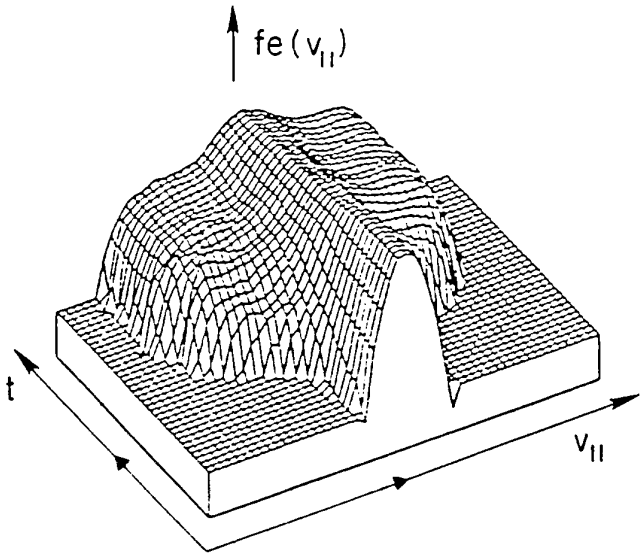

Fig. 7. Time evolution of the parallel electron distribution, plotted as a function of $\gamma v_{||}/c$, up to $\omega_{pe}t = 1200$.

$F(\varepsilon_0)$ is plotted for the first 1200 plasma periods of the simulation in Fig. 8. F is normalized to $2\pi nc$. $\varepsilon_0 = 20\,\text{keV}$ and m_e is set equal to its true value. Taking $n = 10^{10}\,\text{cm}^{-3}$, we find that by $\omega_{pe}t \simeq 1200$ the flux has risen to 1.4×10^{18} electrons $\text{cm}^{-2}\,\text{s}^{-1}$. The time profile of F is similar to that of the electron energy, insofar as the flux increases rapidly during the periods of exponential wave growth.

Figure 5 shows the distributions of core ions in v_y space at $t = 0$ and $\omega_{pe}t = 1300$. The final distribution is clearly nonthermal, with a mean energy much larger than the initial thermal energy. The distribution of v_z velocities is similar. Some heating and acceleration also occurs in the parallel direction, but to a much lesser extent. If $m_p = 400m_e$, where m_e is the true electron mass, the fastest ions in Fig. 5 have energies of around 450 keV (several times the initial energy of the ring ions). If, on the other hand, we set $m_p = 1200m_e$ (consistent with an initial temperature of 800 eV), we find that a significant number of protons have energies in excess of 1 MeV.

The electric field power spectrum at various times during the simulation are shown in Fig. 9. The intense low frequency spikes in (a) and (d) are purely electrostatic, and occur at about twice the lower-hybrid resonance frequency: the fact that emission at this frequency dominates the spectrum early in the simulation indicates the importance of lower-hybrid wave generation in the acceleration process. In the high frequency range, emission occurs predominantly at the electron cyclotron frequency at $\omega_{pe}t \simeq 400$, and close to the upper hybrid frequency $\omega_{uh} = (\omega_{pe}^2 + \omega_{ce}^2)^{1/2}$ at $\omega_{pe}t \simeq 1200$. We have not determined the polarization and propa-

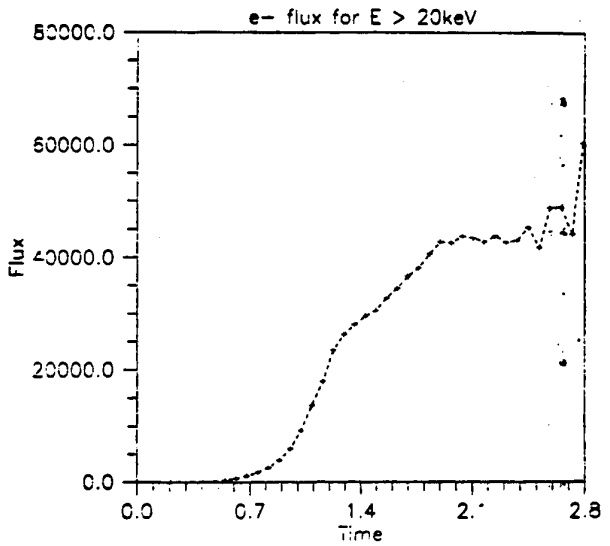

Fig. 8. Escaping flux of electrons, F, with energies above 20 keV, up to $\omega_{pe}t = 1200$. The flux is normalized to $2\pi nc$. Thus, if $n = 10^{10}\,\text{cm}^{-3}$, $F \simeq 1.4 \times 10^{18}$ electrons $\text{cm}^{-2}\,\text{s}^{-1}$ at $\omega_{pe}t = 1300$.

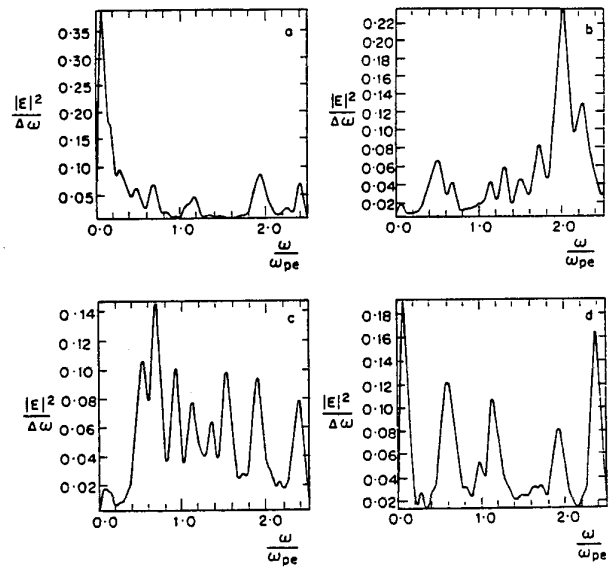

Fig. 9. Electric field power spectrum at $\omega_{pe}t = 0.350$ (a), 400 (b), 800 (c), and 1200 (d). The intense low frequency spikes in (a) and (d) occur at about the lower hybrid resonance frequency: In the microwave range, emission occurs predominantly at the electron cyclotron frequency at early times, and at the upper hybrid frequency at later times.

gation direction of these emission features, and so their identification is uncertain. However, the spike $\omega = \omega_{ce}$ has a magnetic component, and it may be the signature of a perpendicular-propagating electromagnetic cyclotron wave [23]. The spike at $\omega = \omega_{uh}$, on the other hand, appears to represent a Bernstein mode.

4. Conclusions

We have presented a comprehensive numerical model of particle acceleration in lower-hybrid cavitons the waves being generated by an anisotropic ion distribution. We have argued that there are several viable mechanisms whereby unstable (ring-like) ion distributions could be generated: the ubiquitous presence of anisotropic ions in both laboratory and space plasmas suggests very strongly that lower-hybrid turbulence occurs in most plasmas. Ion ring and loss cone distributions can excite waves close to the lower-hybrid resonance frequency. If the lower-hybrid wave amplitude is sufficiently high, the wave becomes modulationally unstable, cascading to shorter wavelengths and Landau damping on parallel-propagating electrons and perpendicular-propagating ions takes place. Lower-hybrid wave collapse can thus, uniquely, lead to the simultaneous acceleration of electrons and ions within cavitons. Particle simulation results show that the relaxation of an ion ring, containing only a small fraction of the magnetic field energy can give rise to fluxes of electrons and ions in the MeV range of energies for the parameters used in the simulation. Furthermore, the accelerated electrons produce bursts of high frequency wave emission close to the electron cyclotron frequency, with narrow bandwidths. Unlike the electron cyclotron maser instability, which is driven by a loss cone-type anisotropy, these waves are driven by an electron distribution with a nonthermal tail along the parallel direction. In a future paper we intend to study this instability in more detail, identifying in particular the polarization of wave emission at ω_{ce} and its harmonics.

The process of particle acceleration outlined above is ubiquitous to all plasmas and will play a major role in areas such as the aurora, bow-shocks, solar flares [24, 25] and supernovae remants.

Acknowledgements

This work was supported by NATO grant CGR 910316, NSF grant PHY 91-21052, and EC grant SC1-CT920773. The particle simulations were carried out at the San Diego Duper-computer Center.

References

1. Shapiro, V. D. and Shevchenko, V. I., in: "Handbook of Plasma Physics" (Edited by M. N. Rosenbluth and R. Z. Sagdeev) (Elsevier, Amsterdam 1984), Vol. 2, p. 123.
2. Shapiro, V. D. *et al.* Phys. Fluids **B5**, 3148 (1993).
3. Musher, S. L. and Sturman, B. I., Pisma Zh. Eksp. Teor. Fiz. **22**, 537 (1975).
4. Lashmore-Davies, C. N. and Dendy, R. O., Phys. Fluids **B1**, 1565 (1989).
5. Papadopoulos, K., Proc 1st Internat. School Plasma Ap., ESA sp.161 (Noordwijk: ESA 1981), p. 313.
6. Leboeuf, J. N., Tajima, T. and Dawson, J. M., Phys. Fluids **25**, 784 (1982).
7. Drake, J., private communication (1992).
8. Formisano, V., Galeev, A. A. and Sagdeev, R. Z., Planet. Space Sci. **30**, 491 (1982).
9. Paschmann, G., Sckopke, N., Bame, S. J. and Gosling, J. T., Geophys. Res. Lett. **9**, 881 (1982).
10. Liu, A. T. Y., McEntire, R. W., Sibeck, D. G. and Krimigis, S. M., J. Geophys. Res. **95**, 20839 (1990).
11. Chen, J., Burkhart, G. R. and Huang, C. Y., Geophys. Res. Lett. **17**, 2237 (1990).
12. Johnson, A. D., in: "Solare and Planetary Plasma Physics" (Edited by B. Buti) (World Scientific, Singapore 1990), p. 209.
13. Gorney, D. J., Clark, A., Croley, D., Fennell, J., Luhmann, J. and Mizera, P., J. Geophys. Res. **86**, 83 (1981).
14. Fried, B. D. and Gould, R. W., Phys. Fluids **4**, 139 (1961).
15. Mikhailovskii, A. B., "Theory of Plasma Instabilities" (Consultants Bureau, New York 1974), Vol. 1.
16. Galeev, A. A., J. Plasma Phys. **1**, 104 (1967).
17. Tripathi, V. K., Grebogi, C. and Lui, C. S., Phys. Fluids **20**, 1525 (1977).
18. Ma, S., private communication (1993).
19. Zakharov, V. E., Soviet Phys. JETP **35**, 908 (1972).
20. Bingham, R., Shapiro, V. D., Tsytovich, V. N., de Angelis, U., Gilman, M. and Shevchenko, V. I., Phys. Fluids **B3**, 1728 (1991).
21. Su, J. J., UCLA Institute of Plasma and Fusion Research Report, PPG-1301 (1989).
22. Kennel, C. F. and Petschek, H. E., J. Geophys. Res. **71**, 1 (1966).
23. Akhiezer, A. I., Akhiezer, I. A., Polovin, R. V., Sitenko, A. G. and Stepanov, K. N., Plasma Electrodynamics (Oxford: Pergamon 1975) Vol. 1.
24. McClements, K. G., Su, J. J., Bingham, R., Dawson, J. M. and Spicer, D. S., Solar Phys. **130**, 229 (1990).
25. McClements, K. G., Su, J. J., Bingham, R., Dawson, J. M. and Spicer, D. S., Astrophys. J. **409**, 465 (1993).

Physica Scripta. Vol. T52, 28–35, 1994

Overview of Laboratory Plasma Radiation Sources

W. B. Mori

Departments of Physics and Electrical Engineering, University of California, Los Angeles, Los Angeles, CA 90024-1547, USA

Received January 7, 1994; accepted May 7, 1994

Abstract

We give an overview of plasma phenomena which can either alter the frequency spectrum of an already existing source of radiation or generate radiation from another energy source. These phenomena include parametric instabilities, harmonic generation, photon acceleration and FEL's.

1. Introduction

The development of plasma-based radiation sources is a rapidly expanding field in plasma physics research [1]. The emergence of this field is due to the potential of plasma-based coherent radiation sources to provide tunable radiation spanning many wavelengths and pulse durations. Such unique sources could have applications in a range of topics including spectroscopy, radar, chemistry, medical imaging, and plasma diagnostics.

This research could also have implications to the field of astrophysics, where radiation is the main diagnostic of an astrophysical object or event. The physical phenomenon upon which the plasma radiation sources are based could be occurring naturally in space, and thus be either altering the radiation or generating it. As a result, the detected radiation spectrum may not be the same as that generated at the source.

In this article we give an overview of the physical mechanisms upon which plasma-based radiation sources are based. The phenomena described are Raman scattering, harmonic generation from Raman backscatter, relativistic effects and critical surface interactions, photon acceleration in plasma waves and ionization fronts, and unconventional FEL's.

2. Raman scattering

In Raman scattering [2] an incident electromagnetic wave decays into another electromagnetic wave and an electron plasma wave. The physical mechanism can be understood as follows. The incident wave scatters off a thermal plasma wave. The ponderomotive force (or light pressure) arising from the beat pattern of the incident and scattered electromagnetic waves then reinforces the plasma wave. The incident wave then rescatters off the reinforced plasma wave. Therefore, the scattered wave and the plasma wave grow as the feedback loop continues. It is clear from the above mechanism that ω and $\boldsymbol{k}$ matching is required:

$$\omega_0 = \omega_p + \omega_s,$$

$$\boldsymbol{k}_0 = \boldsymbol{k}_p + \boldsymbol{k}_s,$$

where the subscripts 0, p, s denote the incident, plasma and scattered waves respectively. The scattered wave can propagate in all 4π steradians with the direction of plasma wave being determined from $\boldsymbol{k}$ matching. We briefly review two extreme scattering angles, 180° and 0°.

2.1. *Raman backscatter*

When the scattered electromagnetic wave propagates in the opposite direction to the incident wave, the Raman instability is called Raman backscatter (RBS). In this case the phase velocity of the plasma wave is

$$v_{\phi p} = \frac{\omega_0 - \omega_s}{|k_0| + |k_s|} \cong \frac{\omega_p}{2k_0} \ll c$$

where c is the speed of light. The instability can be modeled [2] by a wave equation for A_s and a harmonic oscillator equation for δn

$$\left(-\frac{\partial^2}{\partial t^2} + \frac{\partial^2}{\partial x^2} - n_0\right) A_s = \delta n A_0, \tag{1}$$

$$\left(\frac{\partial^2}{\partial t^2} + 1\right) \delta n = \frac{\partial^2}{\partial x^2} (A_0 A_s), \tag{2}$$

where A_s is the vector potential of the scattered wave, δn is the density perturbation of the plasma wave, and n_0 is the background density. We neglect the plasma temperature and normalize time to ω_p^{-1}, distance to c/ω_p and current to ecn_0. Using these equations the temporal growth can be derived as, $\delta n \propto e^{\gamma_0 t}$ where

$$\gamma_0 = \frac{1}{2}\sqrt{\frac{\omega_0}{\omega_p}}\frac{eA_0}{mc^2}\omega_p.$$

Theoretical and experimental work on RBS has examined the effects of bandwidth and coherence of the pump [3]. The instability is found to be suppressed if the bandwidth and the reciprocal of the coherence time is greater than the growth rate. This work is relevant to space plasmas, where the radiation is not necessarily coherent.

The importance of RBS to space and astrophysical plasmas is that it could lead to significant absorption of the source radiation, even when the source radiation frequency is much greater than the plasma frequency, ω_p. The absorbed energy will ultimately be deposited into the plasma when the plasma wave breaks. We comment that an FEL can be viewed as RBS in the frame of the beam.

2.2. *Raman forward scatter*

When the scattered electromagnetic wave propagates in the same direction as the incident wave the Raman instability is called Raman forward scatter (RFS). In this case the phase velocity of the plasma wave is very close to the speed of light

$$v_{\phi p} = \frac{\omega_0 - \omega_1}{k_0 - k_1} = c\sqrt{1 - \frac{\omega_p^2}{\omega_0^2}} \cong c.$$

Therefore, RFS can generate relativistic electrons. The analysis for RFS is easiest in a Galilean system moving at the speed of light because all the waves have phase velocities near c. After making a transformation to the variables $\psi \equiv t - (x/c)$, $\tau \equiv t$, the model equations become [4]

$$2\frac{\partial}{\partial\tau}\frac{\partial}{\partial\psi}A = A(1-\phi), \tag{3}$$

$$\left(\frac{\partial^2}{\partial\tau^2}+1\right)\phi = \frac{A^2}{2}, \tag{4}$$

where ϕ is the electrostatic potential. A difference between RBS and RFS is that for RFS, in addition to the down shifted scattered wave, there is an upshifted scattered wave, $\omega_s = \omega_p + \omega_0$. Therefore, RFS is a 4-wave instability and is sometimes referred to as a modulational instability [2]. The temporal growth rate is

$$\gamma_0 = \frac{1}{\sqrt{8}}\left(\frac{\omega_p}{\omega_0}\right)^2\frac{eA_0}{mc^2}\omega_p.$$

The possible importance of RFS to space plasmas is that it can generate both frequency broadening via spectral cascading and relativistic electrons via wavebreaking. The amount of broadening is limited to $\Delta\omega \cong 2\omega_0$. The energy of the electrons depends on the plasma density and is roughly given by

$$\varepsilon \cong 2\left(\frac{\omega_0^2}{\omega_p^2}\right)mc^2.$$

3. Harmonics

An intense electromagnetic wave propagating in a plasma can generate harmonics from several nonlinear mechanisms. These include relativistic mass effects, the $V \times B$ force, Raman backscatter and resonance absorption. The first three effects require linearly polarized waves and only generate odd harmonics.

3.1. *Relativistic and $V \times B$ harmonics in underdense plasmas*

An electron oscillating in an electromagnetic wave in vacuum executes the well known figure-eight plus drift motion. The velocity of this motion can be decomposed into odd harmonics in the transverse direction and even harmonics in the longitudinal direction. This harmonic content is due to the relativistic mass nonlinearities. Sarachik and Schappert [5] made a detailed study of the harmonic content generated from radiation scattering off a single electron. It may seem that the odd harmonic content of an electromagnetic wave in a plasma could be ascertained by assuming that the harmonics scattered from a single electron in the forward direction add coherently. However, in an underdense plasma the density bunching from the longitudinal part in the figure-eight motion creates a source term which almost exactly cancels the relativistic mass corrections [6]. To illustrate this, we calculate the third harmonic [7] by expanding the current source term in the wave equation to only third order in the vector potential,

$$\left(\frac{-1}{c^2}\frac{\partial}{\partial t^2}+\frac{\partial^2}{\partial x^2}\right)A = \frac{n}{\gamma}A \cong (n_0+\delta n)A(1-\tfrac{1}{2}A^2)$$
$$= n_0 A + (\delta n - \tfrac{1}{2}n_0 A^2)A. \tag{5}$$

As just discussed there are two source terms for the third harmonic. The δnA term caused by the $V \times B$ longitudinal bunching and the $-\frac{1}{2}n_0 A^3$ term from the relativistic mass corrections. If $A = a_{\perp 0}\cos\psi_0$ and $\psi_0 \equiv k_0 x - \omega_0 t$, then it can be shown that [7]

$$\delta n = \frac{-k_0^2 a_{\perp 0}^2}{-4\omega_0^2+1}\cos 2\psi_0 \cong O(a_{\perp 0}^2)$$

and

$$\tfrac{1}{2}A^2 = \tfrac{1}{4}a_{\perp 0}^2(1+\cos 2\psi_0) \cong O(a_{\perp 0}^2)$$

where each source term is $O(a_{\perp 0}^2)$. However, the total third harmonic source term is

$$(\delta n - \tfrac{1}{2}A^2)A = \frac{3}{8}\frac{1}{-4\omega_0^2+1}a_{\perp 0}^2\cos 3\psi_0 \cong 0\left(a_{\perp 0}^2\frac{\omega_p^2}{\omega_0^2}\right) \tag{6}$$

where the source terms almost cancel, with their difference being ω_p^2/ω_0^2 times smaller than each term separately.

The amplitude of the third harmonic can be calculated by substituting the total source term, eq. (6), into the wave equation, eq. (5). This gives

$$a_3 = \frac{3}{64}\frac{a_{\perp 0}^3}{-4\omega_0^2+1} \tag{7}$$

from which the ratio of the power in third harmonic. P_3, to that in the fundamental can be calculated,

$$\frac{P_3}{P_1} = \left(\frac{9}{64}\right)^2\frac{a_{\perp 0}^4}{(-4\omega_0^2+1)^2} \simeq \left(\frac{9}{256}\right)^2 a_{\perp 0}^4\frac{\omega_p^4}{\omega_0^4} \tag{8}$$

For $a_{\perp 0} < 1$ and underdense plasmas $[(\omega_p/\omega_0) \ll 1]$, the harmonic conversion efficiency is, therefore, very low.

The harmonic conversion efficiency can be calculated for arbitrarily large pump strengths [7, 8] in the underdense limit and the result is

$$\frac{P_3}{P_1} = \left(\frac{9}{256}\right)^2\frac{a_{\perp 0}^4}{(1+a_{\perp 0}^2/2)^3}\frac{\omega_p^4}{\omega_0^4}. \tag{9}$$

Therefore, P_3/P_1 cannot be increased to large values by simply increasing $a_{\perp 0}$. It can also be shown that $P_{n+2}/P_n \simeq P_3/P_1$ for all n.

As the plasma density is increased, the amplitude of the harmonics increases. This occurs because there are more charges to radiate. Near critical density, i.e., when $\omega_p = \omega_0$, a further enhancement occurs because the magnetic field vanishes and this prevents $V \times B$ density bunching. A fully nonlinear analysis provides the simple result that at critical density [7]

$$\frac{P_n}{P_1} = \frac{1}{n^4}. \tag{10}$$

Therefore, coherent harmonic generation in underdense plasma is energetically insignificant.

3.2. *Relativistic and $V \times B$ harmonics from overdense plasmas*

As just shown, the lowest order harmonic source term is proportional to

$$(\delta n - \tfrac{1}{2}A^2)A. \tag{11}$$

In the underdense limit $\delta n \simeq \frac{1}{2}A^2$ so harmonic generation was small. At critical density $\delta n \to 0$ because the magnetic

field vanishes. However, even in this case, harmonic generation is not significant. The level of harmonics can be increased if the radiation impinges an overdense plasma, because the number of radiators is large. The harmonics are generated by nonlinear currents within a skin depth of the critical surface, and the harmonics are reflected [9]. In this case the dominant source term is δn because the electric field, and hence, the $\frac{1}{2}A^2$ term is shielded by the plasma.

A lowest order analysis predicts that when radiation impinges on a step function density profile with plasma density n_0, i.e., $\omega_p \simeq \omega_0$, the power in the third harmonic is [9]

$$\frac{P_3}{P_1} \simeq \frac{1}{10} A_{1\perp 0}^4 \frac{\omega_0^4}{\omega_{p0}^4}. \tag{12}$$

Calculating the power in the higher harmonics and a fully nonlinear analysis is difficult, so to determine these we resort to particle-in-cell simulations. Typical results are shown in Fig. 1, where P_n/P_1 is plotted as a function of $A_{1\perp 0}$ for $(\omega_{p0}^2/\omega_0^2) = 50$. The value of P_3/P_1 given by eq. (12) is shown by the solid line. The theoretical analysis is invalid for $A_{1\perp 0}\,\omega_0/\omega_{p0} > 1$, which is where the simulation results lie below the solid line.

We find that the harmonic conversion efficiency is significantly increased if the step function density profile is replaced by a gradual ramp. We believe the increase is due to the increased width of the skin depth.

Researchers in Los Alamos observed even harmonic generation [10] from a critical surface in both experiments and simulations. In this case, the harmonics were caused by the anharmonic nature of surface plasma waves generated by resonant absorption at the sharp plasma-vacuum interface.

3.3. *Harmonics from Raman Backscatter*

Coupled equations were given earlier which model Raman Backscatter (RBS). These equations were derived in the small $A_{1\perp 0}$ limit. Recently, Esarey and Sprangle [11] showed that if higher order terms are kept, nonlinear RBS of linearly polarized waves could generate odd harmonics. For illustrative purposes, we consider only the lowest order nonlinearities and identify the terms which generate the third harmonic. The modified coupled equations are

$$\left(\frac{-1}{c^2}\frac{\partial^2}{\partial t^2} + \frac{\partial^2}{\partial x^2}\right)A \equiv LA = \frac{n}{\gamma} A \simeq (n_0 + \delta n)A(1 - \tfrac{1}{2}A^2) \tag{13}$$

and

$$\left(\frac{\partial^2}{\partial t^2} + \omega_p^2\right)\delta n \simeq \frac{\partial}{\partial x}\frac{1}{\gamma}\frac{\partial}{\partial x}\gamma \simeq \frac{\partial}{\partial x}(1 - \tfrac{1}{2}A^2)\frac{\partial}{\partial x}\frac{A^2}{2}. \tag{14}$$

Recall that in linear RBS, a light wave decays into a plasma wave and a reflected light wave. The plasma wave has a frequency at ω_p and therefore, by ω matching, the reflected light wave has a frequency at $\omega_0 - \omega_p$. Furthermore, from k matching the plasma wave has a k of $\simeq 2k_0$. In nonlinear RBS higher order couplings result from the RHS's of eqs (13) and (14),

$$(L - n_0)A_s \simeq \frac{\delta n}{2} A_0^3 \tag{15}$$

and

$$\left(\frac{\partial^2}{\partial t^2} + \omega_p^2\right)\delta n = -\frac{\partial}{\partial x}\left(\tfrac{1}{2}A^2\frac{\partial}{\partial x}\frac{A^2}{2}\right). \tag{16}$$

In order for an instability to occur, each wave must still be a normal mode. So, if δn has a frequency of ω_p, then A_s has a frequency of $3\omega_0 - \omega_p \simeq 3\omega_0$. From k matching this requires that δn have a k at $k_p = k_s - 3k_0$, i.e., $k_p = 6k_0$. Therefore, nonlinear RBS of the third harmonic can be viewed as the decay of three pump photons into a plasma wave and a single scattered photon. The plasma wave is driven by the various combinations of $A_s A_0^3$ terms in eq. (15). Therefore, the scaling of the growth rate with A_0 can be quickly ascertained as $\gamma_0 \propto A_{1\perp 0}^3$. Similar arguments can be used to show that the growth rate of the nth harmonic is proportional to $A_{1\perp 0}^n$. Sprangle and Esarey's calculation is fully nonlinear but is only valid for strongly-coupled (no space charge effects) RBS.

This instability is probably not important in plasmas because the higher harmonics are generated with large k's, i.e., $2nk_0$. These plasma waves will be heavily Landau damped for typical plasma densities and temperatures unless the instability is in the strongly coupled regime. This mechanism may, however, generate harmonics during FEL-type interactions.

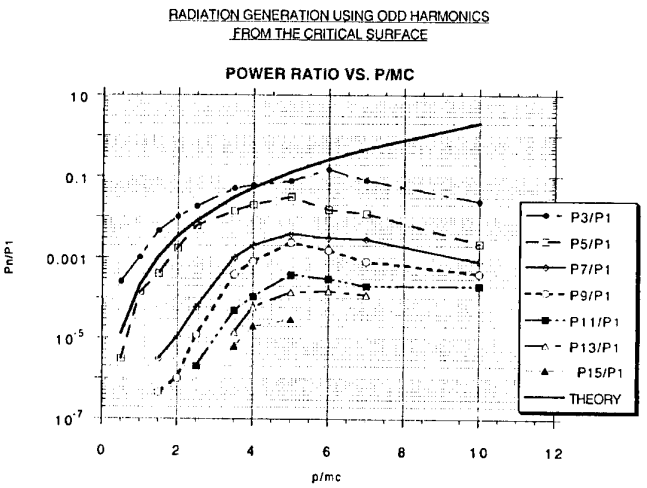

Fig. 1. Harmonic conversion efficiency for an incident wave upon a plasma slab with density 50 times the critical density, plotted against the incident wave's amplitude. The solid line is the theoretical prediction of eq. (12).

4. Photon acceleration

Upshifting existing sources of radiation by temporally altering the dielectric function of a medium is the oldest plasma-based concept. When the dielectric function varies only in time, then the wave number remains fixed and only the frequency changes [12]. Larger upshifts occur when the dielectric function depends on the variable x-ct rather than time alone, where c is the speed of light. In this case both the frequency and the wave number increase. We concentrate on this case because it provides the largest upshifts.

The rate of upshift and some physical insight can be obtained by considering two phase fronts of a wave moving in the same direction as a moving dielectric boundary. This

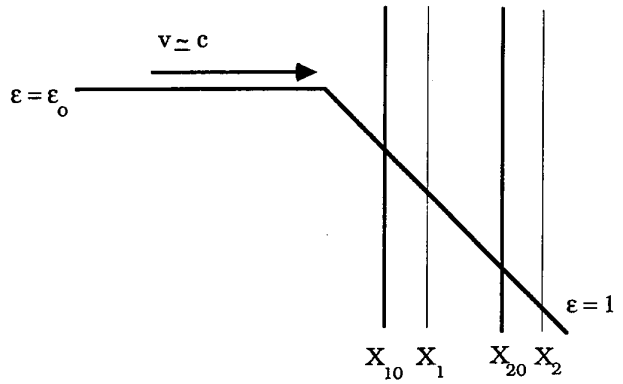

Fig. 2. Schematic of two phase fronts moving down a dielectric function gradient.

is depicted in Fig. 2. The positions of two neighboring phase fronts at $t = t_0$ are labeled as X_{10} and X_{20}. After a time Δt these fronts have moved to positions X_1 and X_2, given by

$$X_1 = X_{10} + \Delta t v_{\phi 1} \tag{17}$$

and

$$X_2 = X_{20} + \Delta t v_{\phi 2} \tag{18}$$

where $v_{\phi 1}$ and $v_{\phi 2}$ are the phase velocities of light at the respective positions in the dielectric boundary. The boundary is assumed to be moving at c, so that a negligible phase slippage occurs between the boundary and phase fronts. Therefore, each front moves at the phase velocity corresponding to its local value of ε, $v_\phi = 1/\sqrt{\varepsilon}$. Subtracting X_2 from X_1 gives

$$\lambda = X_2 - X_1 = \lambda_0 + \lambda_0 \, \Delta t \, \frac{\partial v_\phi}{\partial x} \tag{19}$$

or rewriting this in terms of the frequency gives

$$\frac{1}{\omega}\frac{\partial \omega}{\partial t} = -c\varepsilon \frac{\partial}{\partial x}\frac{1}{\sqrt{\varepsilon}} \tag{20}$$

as the rate of frequency upshifting. Therefore, as a wave moves along with a dielectric boundary, its frequency increases if the dielectric function has a negative slope. The plasma dielectric function can be varied in this manner by a variety of ways. These include a relativistic plasma wave, an ionization front, a recombination front, and a relativistic electron beam.

4.1. *Relativistic plasma waves*

The moving dielectric boundary could be a plasma wave with a phase velocity near the speed of light, i.e., a relativistic plasma wave. In such a wave the plasma density is modulated as

$$n = n_0 + \delta n \cos (k_p x - \omega_p t)$$

where $\omega_p/k_p \simeq c$. The dielectric function for an electromagnetic wave of frequency ω_0 is $\varepsilon = (1 - \omega_p^2/\omega_0^2)$ which can be written as

$$\varepsilon = 1 - \frac{\omega_{p0}^2}{\omega_0^2}\left(1 + \frac{\delta n}{n_0}\cos (k_p x - \omega_p t)\right) \tag{21}$$

when the density is modulated by a plasma wave. Substituting this into eq. (20) and assuming a very underdense plasma gives

$$\frac{1}{\omega}\frac{\partial \omega}{\partial t} = \frac{\omega_{p0}}{2}\frac{\omega_{p0}^2}{\omega^2}\frac{\delta n}{n}\sin (k_p x - \omega_p t) \tag{22}$$

for the rate of frequency upshift. This result was first obtained by Wilks *et al.* [13], and the mechanism was called photon acceleration because of the analogy with particle acceleration in relativistic plasma waves. The disperson relation for light in a plasma is analogous to the relativistic relationship between energy and momentum for a particle

$$\omega^2 = \omega_p^2 + c^2 k^2 \tag{23}$$

and

$$E^2 = m^2 c^4 + c^2 p^2. \tag{24}$$

Therefore, the group velocity of light in a plasma, $v_g = c^2(k/\omega) = c\sqrt{1 - \omega_p^2/\omega^2}$, can be identified as the velocity of a photon in a plasma. If the photon is accelerated then its velocity (v_g), momentum (k), and energy (ω), should all increase. Furthermore, when a short pulse is placed in a plasma wave, the pulse's energy increases at the expense of the plasma wave's energy. This is analogous to beam loading of particles in plasma waves [14]. In addition, it can be shown that the number of photons is conserved so that the increase in energy is proportional to the increase in frequency of each photon.

This process is probably not important in space and astrophysical plasmas because the amount of upshift is limited. The photons eventually outrun the plasma wave, limiting the upshift [9] to

$$\left[1 + 2\left(2\frac{\delta n}{n_0}\right)^{1/2} + 4\frac{\delta n}{n_0}\right]\omega_0$$

where ω_0 is the initial frequency.

4.2. *Ionization fronts*

Another moving dielectric boundary is an ionization front, where ahead of the front is unionized gas and behind the front is newly formed plasma. Radiation is upshifted when radiation is either counterpropagating or copropagating with respect to the front. When examining the counterpropagating geometry, it is useful to consider the situation in the front's frame. This is depicted in Fig. 3. In this frame the front is a stationary boundary which emits electrons and ions away from the incident radiation with a velocity v_f. The analysis is a boundary value problem with the boundary conditions that transverse electric and magnetic fields be continuous and that the transverse current vanish at the boundary. The boundary condition for the current is required because the plasma at the boundary, having just been created, cannot have any transverse velocity. Since there are three boundary conditions, there must be three modes besides the incident wave. These are a reflected, a transmitted, and a free streaming wave. The free streaming wave exists because the plasma is streaming. In this frame each of these waves has the same frequency as the incident wave. The incident wave has been doppler upshifted to $\omega_f = (1 + v_f/c)\gamma_f \omega_i \simeq 2\gamma_f \omega_i$ where $\gamma_f \equiv (1 - v_f^2/c^2)^{-1/2}$. On the other hand, the plasma frequency $\omega_p \equiv (4\pi e^2 n/m)^{1/2}$ is a

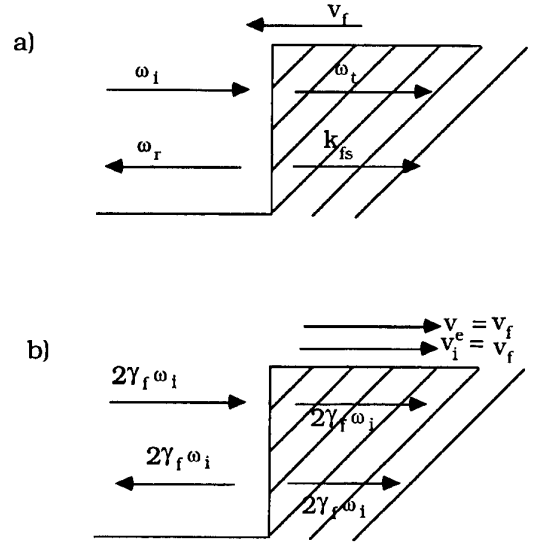

Fig. 3. A schematic for an incident electromagnetic wave impinging a front in the (a) lab frame and (b) front's frame.

Lorentz invariant because the density and the mass both increase by the factor γ_f. The transmitted wave is evanescent if $\omega_f < \omega_p$. Therefore, the front is called overdense if $\omega_f < \omega_p$ and underdense if $\omega_f > \omega_p$.

The generated frequencies can be determined by transforming the ω's and k's back to the lab frame. The k of each wave in the front's frame is determined from the respective dispersion relations of each wave. The incident and reflected waves have the dispersion relation for a wave in vacuum, i.e., $k = \pm\omega/c$, the transmitted wave has the dispersion relation in plasma, i.e, $k = \sqrt{\omega^2 - \omega_p^2}/c$ (recall ω_p is a Lorentz invariant) and the free streaming wave has the dispersion relation $k = (\omega/v_f)$. Upon transforming these ω's and k's back to the lab frame, we obtain

$$\omega_r = \frac{\left(1 + \frac{v_f}{c}\right)}{\left(1 - \frac{v_f}{c}\right)}\omega_i \cong 4\gamma_f^2\omega_i, \tag{25}$$

$$\omega_t \cong \left(1 + \frac{1}{4}\frac{\omega_p^2}{\omega_i^2}\right)\omega_i, \tag{26a}$$

$$k_t \cong \left(1 - \frac{1}{4}\frac{\omega_p^2}{\omega_i^2}\right)\frac{\omega_i}{c}, \tag{26b}$$

$$\omega_{fs} = 0 \tag{27a}$$

and

$$k_{fs} \cong \frac{\omega_i}{2c}. \tag{27b}$$

Therefore, the reflected wave has the double Doppler factor just as from a moving mirror and the free streaming mode becomes a static magnetic field.

In 1967, Semenova [15] and in 1978 Lampe *et al.* [16], calculated the reflection coefficient when the ionization front is overdense. They found that the power reflectivity is unity, but that the reflected energy is lower than the incident energy by the double Doppler factor $4\gamma_f^2$ because the pulse is compressed. The pulse compression occurs because the number of cycles in the pulse is conserved and each cycle is now shorter. In this overdense case most of the incident energy is deposited into the static magnetic field.

In the underdense case the reflectivity becomes negligible for fronts with realistic profiles. However, in 1991 [17], it was shown that large upshifts occur from the transmitted wave for underdense fronts. This is seen in eq. (26). Interestingly, when the large upshifts occur, i.e., when $\frac{1}{4}\omega_p^2/\omega_i^2 \gg 1$, the wavenumber is negative and hence the "transmitted" wave exits the plasma in the direction of the front. The physical reason for this is that when $\frac{1}{4}\omega_p^2/\omega_i^2 > 1$, the plasma becomes dense enough so that in the front's frame, the group velocity of the transmitted wave is less than v_f. Therefore, upon transforming back to the lab's frame, the energy of this wave is actually travelling backwards. In the underdense case, the power in the transmitted wave is equal to the incident power. As before, the energy in this mode is less than the incident energy by the frequency upshift factor and most of the energy resides in the magnetic field (if $\frac{1}{4}\omega_p^2/\omega_i^2 \gg 1$). Frequency upshifts from overdense and underdense fronts have been verified in simulations [17], and upshifts from underdense front have been observed in experiments [18].

The above mechanisms still occur for non-ideal fronts. The reflection coefficient for the overdense case and the transmission coefficient for the underdense case are insensitive to the spatial gradient of the front [16, 17, 19]. For finite gradients, the static magnetic field phase mixes and the energy in this mode is converted to thermal energy.

Radiation can also be upshifted for arbitrary angles of incidence. The co-propagating case [13, 20–22] can be viewed as the later half of the counterpropagating case. When radiation is reflected, it acquires half of the $4\gamma_f^2$ upshift going up the front (counterpropagating) and the other half going down (co-propagating) the front. The difference is that for finite gradient fronts, the radiation instantly is upshifted moving up the front, while it may take a long time (distance) to move down the front because both the radiation and the front are moving together at c. The co-propagating case has also been observed in experiments [20], and it is similar to photon acceleration in plasma waves [13]. The difference is that the plasma wave has energy while the ionization front does not. Therefore, radiation pulses can gain energy from the plasma wave with photon number being conserved. This is not the case for ionization fronts. Savage *et al.* [18], considered upshifting guided waves. Their results can be used to obtain upshifts for waves with arbitrary angles of incidence because waves in a waveguide are plane waves bouncing in the guide at various angles.

The generated frequencies can also be calculated in the lab frame by requiring that the wave's phases be equal to within a constant at the front [16]. This is necessary in order that the electric and magnetic fields be continuous at the front. The phase of a wave is defined to be

$$\omega_l t \pm k_l x$$

where $\pm$ refers to the direction of the wave. The position of the front is $x = v_f t$ (the front is moving to the left), so the phase of wave l is

$$(\omega_l \pm k_l v_f)t.$$

The continuity of the phase of a wave to that of the incident wave requires

$$(\omega_l \mp k_l v_f) = (\omega_i + k_i v_f) = C_i. \tag{28}$$

Therefore, any new wave must fall along a straight line with slope $\pm v_f$ in an ω and k diagram. Furthermore, the generated waves must intersect the dispersion relation of waves in either vacuum or plasma.

This ω and k diagram technique is particularly useful for determining the number of, the frequency of, and the propagation direction of waves generated by an ionization front in a magnetized plasma [23]. We illustrate [23] this in Fig. 4, where such diagrams are used for magnetic fields oriented perpendicular and parallel to the propagation direction of the front. The diagram shows that two additional modes are generated in a magnetized plasma. This necessitates additional boundary conditions. For the $\perp$ case, these are that the charge density and the parallel current must vanish at the front. For the $\parallel$ case, the conditions are continuity of electric and magnetic fields in the other transverse polarization planes.

The frequency of the reflected wave is unchanged. The transmitted wave is relatively unchanged as well for small values of ω_c/ω_p where ω_c is the cyclotron frequency. However, if ω_c/ω_p is large, as may very well be the case in astrophysical plasmas, then the upshifts can be substantially different in a magnetized plasma. For sufficiently large values of ω_c/ω_p, the incident radiation can be upshifted to ω_c. Details can be found in reference [23] by C. H. Lai *et al.*, and in the paper by C. H. Lai *et al.*, in this volume. In the earlier paper the reflection and transmission coefficients are calculated, and in the later paper the effects of non-ideal fronts are considered.

Photon acceleration in ionization fronts may be important in space plasmas. It could be energetically important and because it is a linear process, it does not depend sensitively on the coherence of the initial radiation. If the ionization front has a non-constant v_f, then the frequency of the

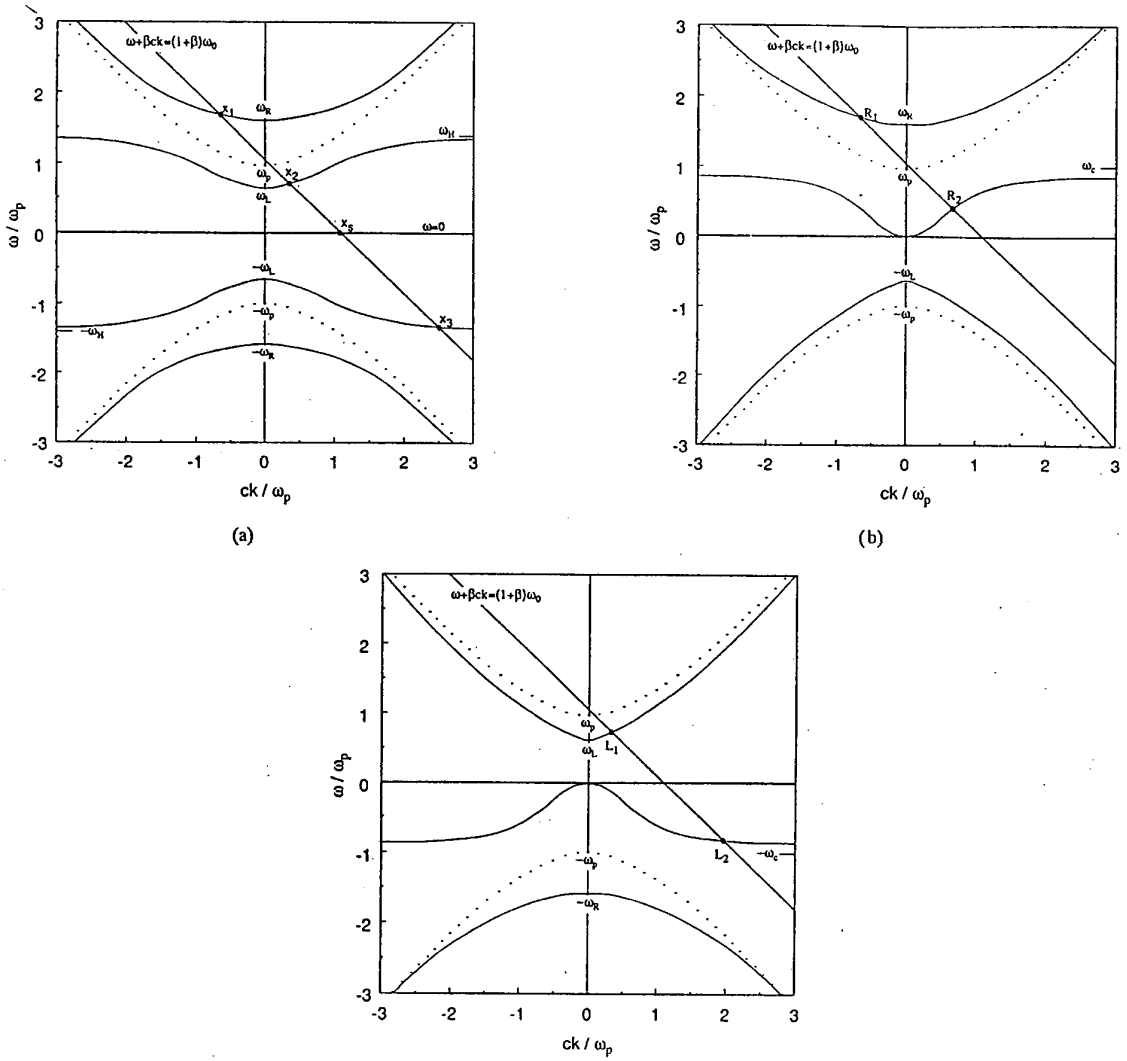

Fig. 4. (a) Dispersion relations for the plasma in a perpendicular magnetic field. The dotted curve is for the unmagnetized case. The three intersections (X_1, X_2 and X_3) of $\omega + \beta ck = (1 + \beta)\omega_0$ with the upper and lower branches gives solutions for the three transmitted modes, and X_s denotes the streaming mode with zero frequency in the lab frame, $\omega_c/\omega_p = 1$, $\gamma_f = 1000$. (b) Dispersion relations for the plasma in a parallel magnetic field for R waves. The dotted curve is for the unmagnetized case. The two intersections (R_1 and R_2) of $\omega + \beta ck = (1 + \beta)\omega_0$ with the upper and lower branches gives solutions for the two transmitted modes. $\omega_c/\omega_p = 1$, $\gamma_f = 1000$. (c) Dispersion relation for the plasma in a parallel magnetic field for L waves, the dotted curve is for the unmagnetized case. The two intersections (L_1 and L_2) of $\omega + \beta ck = (1 + \beta)\omega_0$ with the upper and lower branches give solutions for the two transmitted modes. $\omega_c/\omega_p = 1$, $\gamma_f = 1000$. (We define $\beta \equiv v_f/c$).

reflected wave will broaden. However, as seen in eq. (26a), the frequency of the transmitted wave will not be affected.

4.3. *Electron beam*

We briefly mention that another possible moving dielectric boundary could be an electron beam. A relativistic electron beam would act identically as a relativistic moving mirror. In a laboratory it is not possible to create an overdense electron beam. However, in space, such dense electron beams may exist. The requirement is that in the rest frame of the beam the incident radiation must be less than the plasma frequency. In its own frame, the beam's density is n_0/γ_b where n_0 is the beam density in the lab frame. Therefore, the requirement for an overdense beam is

$$\omega_i' = 2\gamma_b \omega_i < \omega_p \equiv \frac{\omega_{p0}}{\gamma^{1/2}} \tag{29}$$

where $\omega_{p0} \equiv 4\pi e^2 n_0/m$. This can be rewritten as

$$\omega_i < \frac{\omega_{p0}}{2\gamma_b^{3/2}}. \tag{30}$$

A critical difference between a moving mirror, i.e., an electron beam, and an ionization front is that the mirror contains kinetic energy while the ionization front does not. Therefore, a reflection from a moving mirror conserves photon number and amplifies the energy of the incident pulse.

We note that an underdense electron beam could also upshift radiation via the transmitted wave just as an ionization front does. This transmitted wave exists inside the beam. If it eventually exits the beam while the beam (dielectric boundary) is moving, it will lose the upshift. This is not a problem when upshifting from ionization fronts because in general the ionization stops; and then the radiation exits through a stationary boundary.

5. Free electron lasers

In a free electron laser (FEL) the kinetic energy of an electron beam is converted into coherent radiation. The radiation is generated when electrons are wiggled and lasing occurs when this radiation leads to bunching of the electron beam. In the conventional FEL mechanism, wiggling is caused by static magnets and gain requires good beam quality, i.e., emittance and brightness. The electrons can also be wiggled by a counterpropagating electromagnetic wave. In addition, high gain requires dense beams to be transported through the wiggler over long distances.

Plasmas may have applications in FEL's in both the focusing and the wiggling of the electron beam. Coherent magnetic fields are unlikely to exist in space (magnetic fields generated by ionization fronts could possibly act as wigglers). However, coherent plasma oscillations of relativistic space charge waves could provide large wiggling forces [24]. The electrons will wiggle with a velocity of $\delta nc/n$ where $\delta n/n$ is the amplitude of the wave. Two geometries have been proposed and these are discussed in Ref. [25].

When an electron beam with a density greater than the plasma density propagates in a plasma, it expels the plasma electrons leaving only an ion channel. The space charge of the beam is neutralized and the beam is pinched by the $V \times B$ force from its own azimuthal magnetic field [26]. The focusing force scales as $3 \times 10^9 n_0$ Gauss/cm, where n_0 is the plasma density in units of cm^{-3}. This focusing could guide dense beams over long distances. Furthermore, the betatron oscillations resulting from this focusing could themselves act as a wiggler. This is called the ion-channel FEL and details can be found in Refs [27] and [28]. Recently, Chen and Dawson [29] proposed that FEL radiation will be generated when an electron beam propagates obliquely to a preformed density channel. The beam creates an ion channel but because of the density ripple, the electrons are wiggled at a much shorter wavelength than in the ion-channel FEL. This scheme is called the ion-ripple FEL.

Whether plasma FEL mechanisms are important in space will depend on plasma uniformity and whether high energy electron beams and coherent plasma waves exist. Most likely, these mechanisms could provide incoherent radiation but not gain.

6. Summary

In summary, we have briefly reviewed some, but certainly not all, plasma mechanisms that could either alter already existing radiation or generate new radiation. These include parameter instabilities, harmonic generation, photon acceleration, and novel FEL's.

Acknowledgements

This work was supported by DOE Grants DE-FG03-91-ER12114, DE-FG03-92-ER40727, and LLNL Tasks No. 20 and 32. Much of this work was done in collaboration with T. Katsouleas, C. H. Lai, C. Joshi, J. M. Dawson, C. D. Decker, R. L. Savage, Jr., W. P. Leemans, S. C. Wilks, and N. DeMoraes.

References

1. IEEE Trans. Plasma Sci., Special Issue on Generation of Coherent Radiation Using Plasmas **PS-21** (1993) and references therein.
2. Forslund, D. W. *et al.*, Phys. Fluids **18**, 1002 (1975); Forslund, D. W. *et al.*, Phys. Fluids **18**, 1017 (1975); Drake, J. F. *et al.*, Phys. Fluids, **17**, 778 (1974).
3. Laval, G. *et al.*, Phys. Fluids **20**, 2049 (1977); Pesme, D. *et al.*, UCRL-JC-105479 (1990).
4. Mori, W. B. *et al.*, Phys. Rev. Lett. **72**, 1482 (1994); Antonsen, T. M. and Mora, P., Phys. Rev. Lett. 69, 2204 (1992); Krall, J. *et al.*, Phys. Rev. **E48**, 2157 (1993).
5. Sarachik, E. S. and Schappert, G. T., Phys. Rev. **D10**, 2738 (1970).
6. Sprangle, P. *et al.*, Phys. Rev. **A41**, 4463 (1990).
7. Mori, W. B. *et al.*, IEEE Trans. Plasma Sci. **PS-21**, 110 (1993); Leemans, W. P. *et al.*, Phys. Rev. **A46**, 1091 (1992).
8. Esarey, E. *et al.*, IEEE Trans. Plasma Sci. **PS-21**, 95 (1993); Rax, J. M. and Fisch, N. J., Phys. Rev. Lett. **69**, 772 (1992); Rax, J. M. and Fisch, N. J., IEEE Trans. Plasma Sci. **PS-21**, 105 (1993).
9. Wilks, S. C. *et al.*, IEEE Trans. Plasma Sci. **PS-21**, 120 (1993).
10. Carman, R. L. *et al.*, Phys. Rev. Lett. **46**, 29 (1981).
11. Esarey, E. and Sprangle, P., Phys. Rev. Lett. **67**, 2021 (1991).
12. Yablonvich, E., Phys. Rev. Lett. **31**, 877 (1975); Jiang, C. L., IEEE Trans. Antennas Propagat. **AP-23**, 83 (1975); Wilks, S. C. *et al.*, Phys. Rev. Lett. **61**, 337 (1988).
13. Wilks, S. C. *et al.*, Phys. Rev. Lett. **62**, 2600 (1989).
14. Katsouleas, T. *et al.*, Part. Accel. **22**, 81 (1987).
15. Semenova, V. I., Sov. Radiophys. **10**, 559 (1967).
16. Lampe, M. *et al.*, Phys. Fluids, **21**, 42 (1978).
17. Mori, W. B., Phys. Rev. **A44**, 5118 (1991).
18. Savage, R. L. Jr. *et al.*, Phys. Rev. Lett. **68**, 946 (1992); Savage, R. L. Jr. *et al.*, IEEE Trans. Plasma Sci. **PS-21**, 5, (1993).
19. Mori, W. B., UCLA PPG-1467 (1989).

20. Wood, W. M. *et al.*, Phys. Rev. Lett, **67**, 3523 (1991); Wood, W. M. *et al.*, IEEE Trans. Plasma Sci. **PS-21**, 20 (1993).
21. Esarey, E. *et al.*, Phys. Rev. A. **44**, 3908 (1991).
22. Gildenberg, V. B. *et al.*, IEEE Trans. Plasma Sci. **PS-21**, 34 (1993).
23. Lai, C. H. *et al.*, IEEE Trans. Plasma Sci. **PS-21**, 45 (1993).
24. Yan, Y. T. and Dawson, J. M., Phys. Rev. Lett. **57**, 1959 (1986).
25. Joshi, C. *et al.*, IEEE J. Quantum Electron **QE-23**, 1571 (1987).
26. Budker, G. I., Proc. of the CERN Symp. on High Energy Accelerators and Pion Physics, Geneva: CERN Service, d'Information, 1956, p. 68.
27. Whittum, D. H. *et al.*, Phys. Rev. Lett. **64**, 2511 (1990).
28. Chen, K. R. *et al.*, IEEE Trans. Plasma Sci. **PS-18**, 837 (1990).
29. Chen, K. R. and Dawson, J. M., Phys. Rev. Lett. **68**, 29 (1992); Chen, K. R. and Dawson, J. M., IEEE Trans. Plasma Sci. **PS-21**, 151 (1993).

Physica Scripta. Vol. T52, 36–39, 1994

Thermal Wave Model for Nonlinear Longitudinal Dynamics of a Relativistic Charged Particle Bunch in Cold Plasmas

R. Fedele and V. G. Vaccaro

Dipartimento di Scienze Fisiche, Università di Napoli "Federico II" and INFN Sezione di Napoli, Mostra d'Oltremare Pad.20, I-80125 Napoli, Italy

Received November 22, 1993; accepted January 28, 1994

Abstract

We study the longitudinal dynamics of a relativistic charged particle bunch through a cold, unmagnetized plasma, within the framework of the recently proposed thermal wave model for relativistic charged particle beam propagation. We show that, under the action of both a purely electrostatic plasma wave potential well and the plasma wake potential (self-interaction), the longitudinal bunch dynamics is governed by a nonlinear Schrödinger equation for a complex wave function whose squared modulus is proportional to the longitudinal bunch density. This wave model, for which the diffraction parameter is represented here by the longitudinal emittance, allows us to study synchrotron-like oscillations in the plasma wave potential well as well as to obtain a longitudinal envelope equation which includes the self-interaction. Furthermore, we show that a soliton solution for the bunch density is possible and it results to be the natural asymptotic evolution of a modulational instability occurring when the bunch propagates in the plasma under the action of the self-force only.

1. Introduction

Recently a quantum-like description of optics and dynamics of charged particle beams, (the so-called thermal wave model for relativistic charged particle beam propagation), has been proposed in the literature [1] and successfully applied to a number of physical problems such as beam dynamics in both conventional accelerating machines [2–5] and new plasma-based particle accelerator schemes [6]. In particular, this quantum-like description has been given both for transverse aberrations of a quadrupole lens with sextupole and octupole deviations [2–4] and for self-consistent nonlinear interaction between the plasma wake field and the driving relativistic electron (positron) beam [6]. In addition, this model seems appropriated for describing nonlinear longitudinal dynamics in particle accelerators giving, in particular, a wave picture for coherent instability [5].

In this paper, according to the previous work [1–6], we suggest to study the nonlinear longitudinal dynamics of a relativistic charge particle bunch in a cold, unmagnetized plasma, supposing that it propagates under the action of both a purely electrostatic plasma wave and the plasma wake potential. To this end, we propose a sort of nonlinear Schrödinger (NLS) equation for a complex wave function Ψ, the so called beam wave function (bwf), whose squared modulus gives the longitudinal density profile of the beam.

2. Hamiltonian of relativistic charge particle motion in a cold plasma

2.1. *Single particle dynamics in a plasma wave*

Let us consider the motion of charged particle of charge $q > 0$ with velocity $\beta c (\beta \approx 1)$ along x-direction in a cold, unmagnetized plasma where a plasma wave is present. We assume that the electric field associated with the plasma wave, with phase velocity $v_\phi \approx c$ is given by:

$$\boldsymbol{E}_{p0} = \hat{\boldsymbol{x}} E_{p0} \sin \phi(t), \tag{2.1}$$

where $\hat{\boldsymbol{x}}$ is the unitary vector along the x-axis. The particle will be accelerated or decelerated by the electric field, depending on the initial relative phase between particle and wave. In general, this interaction causes the particle to slip in phase relative to the plasma wave. However, there is a particular phase ϕ_s, called synchronous phase, for which the particle does not change its energy and remains locked in phase with the wave. By following the standard treatment of the single particle motion well known in particle accelerators [7, 8], we introduce a phase displacement $\tilde{\phi}$ with respect to the synchronous one, so that:

$$\phi = \tilde{\phi} + \phi_s \equiv k_p x + \phi_s, \tag{2.2}$$

where k_p is the plasma wave number ($k_p \equiv \omega_p/c$, ω_p being the plasma frequency) which in the following is supposed to be a constant and x is the longitudinal particle displacement with respect to the synchronous position.

By denoting with $\mathscr{P} \equiv (\Delta E/E_0) = (E - E_0)/E_0$ the relative variation of the particle energy E ($E_0 = m_0 \gamma c^2$ being the synchronous particle energy), we get:

$$\frac{dx}{ds} = \frac{1}{\gamma^2} \mathscr{P} \tag{2.3}$$

$$\frac{d\mathscr{P}}{ds} = \frac{qE_{p0}}{m_0 \gamma c^2} [\sin (k_p x + \phi_s) - \sin \phi_s] \tag{2.4}$$

where $s = ct$, $\gamma = (1 - \beta^2)^{-1/2}$. It is easy to prove that (2.3) and (2.4) can be obtained from the following dimensionless Hamiltonian:

$$H = \frac{\mathscr{P}^2}{2\gamma^2} + U_w, \tag{2.5}$$

where

$$U_w \equiv \frac{qE_{p0}}{m_0 \gamma c^2 k_p} [(k_p x - \sin k_p x) \sin \phi_s + \cos k_p x \cos \phi_s] \tag{2.6}$$

(plasma wave potential well).

For very small phase displacement, i.e. $|\tilde{\phi}| \ll 1$ (linear case), (2.6) becomes:

$$U_w \approx \frac{\gamma^2}{2} K_p x^2 + \text{const.}, \tag{2.7}$$

where

$$K_p \equiv -\frac{qE_{p0}k_p \cos\phi_s}{m_0\gamma^3 c^2}. \tag{2.8}$$

Note that, since we are concerning with non-modulated plasma wave number (usually in conventional accelarating machines the radio waves are frequency-modulated), it is necessary but not sufficient that ϕ_s satisfies the condition $\sin\phi_s = 0$, namely $\phi_s = n\pi$, with n integer. Thus, if $E_{p0} > 0$, a phase-stability criterion can be established from (2.8) for which $\cos\phi_s < 0$ ($\cos\phi_s > 0$) corresponds to stability (instability). Consequently, for getting synchronous phase it is sufficient to choose

$$\phi_s = (2n+1)\pi. \tag{2.9}$$

In the linear approximation (2.7), any non-synchronous particle will execute phase oscillations around ϕ_s. This way, by considering the single particle dynamics of each charged particle of a bunch injected in the plasma, in principle it is possible to describe statistically the particle distribution in the phase-space during the interaction with the plasma wave, according to the usual methods developed in particle accelerators [7, 8].

2.2. *Collective effects*

According to the standard description of the plasma wake field excitation (self-interaction) [9], when a charge particle bunch of length σ is much greater than the plasma wavelength $\lambda_p \equiv 2\pi/k_p$ is injected in an overdense cold plasma, we have:

$$en_1(x, s) \simeq qn_b(x, s), \tag{2.10}$$

where e is the absolute value of the electron charge and $n_1(x, s)$ and $n_b(x, s)$ are the plasma number density perturbation ($n_1 \ll n_p$, n_p being the unperturbed plasma number density) and the bunch number density, respectively. In addition, we assume that our bunch is transversally flat. Consequently, the wake potential is proportional to n_1 [9], and the effective potential energy u_s associated with the particles of the bunch is given by:

$$u_s = -\frac{q^2 m_0 c^2}{e^2}\frac{n_b(x, s)}{n_p}. \tag{2.11}$$

This energy can be put in the following dimensionless form:

$$U_s = -\frac{u_s}{m_0\gamma c^2} = -\frac{q^2}{e^2\gamma}\frac{n_b(x, s)}{n_p}. \tag{2.12}$$

Note that the bunch particles can be thought as independent particles but singularly subjected to a mean field given by (2.12).

2.3. *Combined effects*

In order to describe the particle motion in the plasma wave in the presence of the self-interaction given by the plasma wake field, we assign the following dimensionless Hamiltonian:

$$H = \frac{\mathscr{P}^2}{2\gamma^2} + U_w + U_s. \tag{2.13}$$

Hamilton's equations become now the following:

$$\frac{dx}{ds} = \frac{\partial H}{\partial \mathscr{P}} = \frac{1}{\gamma^2}\mathscr{P}, \tag{2.14}$$

$$\frac{d\mathscr{P}}{ds} = -\frac{\partial H}{\partial x} = \frac{qE_{p0}}{m_0\gamma c^2}[\sin(k_p x + \phi_s) - \sin\phi_s] + \frac{q^2}{e^2\gamma n_p}\frac{\partial n_b}{\partial x}, \tag{2.15}$$

where (2.6) and (2.12) have been used. Equations (2.14) and (2.15) are fully similar to the motion equations which hold in particle accelerators for longitudinal charged particle dynamics when the interaction between the bunch and the surrounding medium is produced by both a RF cavity and a purely reactive longitudinal coupling impedance [10].

3. Wave equation for longitudinal dynamics

In order to find an equation which describes the longitudinal evolution of the bunch, by taking into account both its thermal spreading (longitudinal emittance) and its interaction with the surrounding medium (plasma wave potential well and plasma wake potential), we use the recently proposed thermal wave model for particle beam propagation [1], which has been successfully applied to a number of physical situations in particle accelerators [2–5] and in plasma physics [6]. In particular, according to the formalism developed in Ref. [5], we introduce in (2.13) the following correspondence rules:

$$\mathscr{P} \to \hat{\mathscr{P}} \equiv -i\varepsilon\frac{\partial}{\partial x} \quad H \to \hat{H} \equiv i\varepsilon\frac{\partial}{\partial s} \tag{3.16}$$

where ε is the longitudinal beam emittance. Consequently, the following Schrödinger-like equation for a complex function $\Psi(x, s)$, the so-called beam wave function (bwf), can be assumed

$$i\varepsilon\frac{\partial\Psi}{\partial s} = \hat{H}\Psi \tag{3.17}$$

where $\hat{H} = (\hat{\mathscr{P}}^2/2\gamma^2) + (U_w + U_s) \equiv (\hat{\mathscr{P}}^2/2\gamma^2) + U$, namely:

$$i\varepsilon\frac{\partial\Psi}{\partial s} = -\frac{\varepsilon^2}{2\gamma^2}\frac{\partial^2\Psi}{\partial x^2} + (U_w + U_s)\Psi. \tag{3.18}$$

Equation (3.18) describes the evolution of the bwf whose squared modulus is related to the bunch density in the following way. Let us introduce the transverse number density of the bunch $\Sigma_b \equiv \int_{-\infty}^{\infty} n_b(x, s)\,dx = \text{const.}$ (number of particles per unit transverse section), we assume that

$$n_b(x, s) = \Sigma_b|\Psi(x, s)|^2, \tag{3.19}$$

provided that the following normalization is satisfied:

$$\int_{-\infty}^{\infty}|\Psi(x, s)|^2\,dx = 1. \tag{3.20}$$

This means that with (3.19) we have assumed that $|\Psi|^2$ represents the normalized longitudinal density profile of the bunch.

For the linearized plasma wave potential well [see eq. (2.7)] and by using (2.12) and (3.19), (3.18) becomes:

$$i\tilde{\varepsilon}\frac{\partial\Psi}{\partial s} = -\frac{\tilde{\varepsilon}^2}{2}\frac{\partial^2\Psi}{\partial x^2} + \tfrac{1}{2}K_p x^2\Psi - \frac{q^2}{e^2}\frac{\Sigma_b}{n_p\gamma^3}|\Psi|^2\Psi \tag{3.21}$$

where $\tilde{\varepsilon} \equiv \varepsilon/\gamma^2$. This wave equation, given for the present problem within the framework of the thermal wave model for particle dynamics, is a modified form of the well known nonlinear Schrödinger equation (NLS) [11] describing a number of very important nonlinear phenomena in physics [11, 12]. In particular, an analogous form of (3.21) seems to govern the nonlinear longitudinal dynamics in particle accelerators when both RF cavities and a reactive longitudinal coupling impedance are taken into account, as it has been recently pointed out [5].

3.1. *Particle distribution in the plasma wave potential well (synchrotron-like oscillations)*

In this section we want to determine the particle distribution in the configuration space when in the (3.21) the self-interaction term (wake potential) is negligible compared to the harmonic one. This means that the bunch is not dense enough to introduce appreciable effects of self-interaction. So that, (3.21) reduces to:

$$i\tilde{\varepsilon}\frac{\partial\Psi}{\partial s} = -\frac{\tilde{\varepsilon}^2}{2}\frac{\partial^2\Psi}{\partial x^2} + \tfrac{1}{2}K_p x^2\Psi. \tag{3.22}$$

A complete set of eigenfunctions associated to (3.22) is:

$$\Psi_m(x, s) = \frac{\exp\left[-\dfrac{x^2}{4\sigma^2(s)}\right]}{[2\pi\sigma^2(s)2^{2m}(m!)^2]^{1/4}} H_m\left(\frac{x}{\sqrt{2}\,\sigma(s)}\right) \times \exp\left[i\frac{x^2}{2\tilde{\varepsilon}\rho(s)} + i(1+2m)\Phi(s)\right]. \tag{3.23}$$

In (3.23) the function $\sigma(s)$, $\rho(s)$ and $\Phi(s)$ are solutions of the following system of differential equations

$$\frac{d^2\sigma}{ds^2} + K_p\sigma - \frac{\tilde{\varepsilon}^2}{4\sigma^3} = 0, \tag{3.24}$$

$$\frac{1}{\rho} = \frac{1}{\sigma}\frac{d\sigma}{ds}, \tag{3.25}$$

$$\frac{d\Phi}{ds} = -\frac{\tilde{\varepsilon}}{4\sigma^2}. \tag{3.26}$$

and $H_m(x)$ are the Hermite-polynomials with m a non-negative integer. Note that $|\Psi_m|^2$ for $m = 0$ (fundamental mode) gives a Gaussian particle distribution. Remarkably, it can be easily proved that (3.24) is completely equivalent to

$$\frac{d^2\sigma^2}{ds^2} + 4K_p\sigma^2 = 4\mathscr{E}, \tag{3.27}$$

where

$$\mathscr{E} = \frac{1}{2}\left(\frac{d\sigma}{ds}\right)^2 + \frac{\tilde{\varepsilon}^2}{8\sigma^2} + \tfrac{1}{2}K_p\sigma^2 = \text{const.}, \tag{3.28}$$

Note that it is easy to recognize that: (a) σ can be defined also in terms of the following quantum-like rms of x (bunch length), namely

$$\sigma(s) = \left[\int_{-\infty}^{\infty} x^2|\Psi_0(x, s)|^2\,dx\right]^{1/2}; \tag{3.29}$$

(b) equation of $\sigma(s)$, (3.27), i.e. (3.24), describes synchrotron-like oscillations; (c) the quantity $(\sigma_p^2/2\gamma^4) \equiv \frac{1}{2}(d\sigma/ds)^2 + (\tilde{\varepsilon}^2/8\sigma^2)$ appearing in (3.28) can be also introduced in terms of the following quantum-like definition of the rms linear momentum (bunch momentum spread):

$$\sigma_p = \left[\varepsilon^2\int_{-\infty}^{\infty}|\partial\Psi_0/\partial x|^2\,dx\right]^{1/2}; \tag{3.30}$$

(d) the quantity $\mathscr{E}$ can be also given by the following quantum-like definition (total averaged energy associated with the longitudinal bunch motion):

$$\mathscr{E} \equiv \int_{-\infty}^{\infty}\Psi_0^*\hat{H}\Psi_0\,dx. \tag{3.31}$$

The equilibrium condition $d^2\sigma/ds^2 = 0$ gives, from (3.24)

$$\sigma_0 = \frac{1}{\gamma^2\sqrt{|K_p|}}\sigma_{p0}, \tag{3.32}$$

where σ_0 and σ_{p0} are the equilibrium value of σ and σ_p. Since for the present case the bwf is Gaussian, in obtaining (3.32) we have introduced the minimum value $\sigma_0\sigma_{p0} = \varepsilon/2$ of the product $\sigma\sigma_p$ consistently with the following quantum-like uncertainty principle which holds in the framework of the thermal wave model [1–6]:

$$\sigma\sigma_p \geqslant \frac{\varepsilon}{2}. \tag{3.33}$$

3.2. *Envelope equation with self-interaction*

In this section we find an aberrationless solution of (3.21) following the standard techniques of nonlinear e.m. wave optics [12]. We look for a solution of (3.21) in the form:

$$\Psi(x, s) = \frac{e^{-x^2/4\sigma(s)}}{\sqrt[4]{2\pi\sigma^2(s)}}e^{i\theta(x, s)} \tag{3.34}$$

where the eikonal has been supposed as:

$$\theta(x, s) = \frac{x^2}{2\tilde{\varepsilon}\rho(s)} + \Phi(s). \tag{3.35}$$

By substituting (3.34) and (3.35), separating the real part from the imaginary one, and expanding $|\Psi|^2$ up to the second-power of x (aberrationless approximation) we get an equation system for the effective particle bunch length $\sigma(s)$, the curvature radius of the wavefront $\rho(s)$, and the phase $\Phi(s)$. Therefore:

$$\frac{d^2\sigma}{ds^2} + K_p\sigma - \frac{\xi}{\sigma^2} - \frac{\varepsilon^2}{4\gamma^4\sigma^3} = 0 \tag{3.36}$$

where $\xi \equiv (q^2/e^2)(\Sigma_b/\sqrt{2\pi}\,\gamma^3 n_0) > 0$. We first observe that in the limit of negligible self interaction ($\xi \approx 0$), (3.36) gives the envelope equation for the synchrotron-like motion [see eq. (3.24)]. Let us consider now the equilibrium condition, namely $d^2\sigma/ds^2 = 0$, when the self interaction is not negligible. In this case (3.36) gives:

$$\alpha\left(\frac{\sigma}{\sigma_0}\right)^4 - \delta\left(\frac{\sigma}{\sigma_0}\right) - 1 = 0 \tag{3.37}$$

where $\alpha \equiv K_p/|K_p|$ and $\delta = \xi/(|K_p|\sigma_0^3)$. Since $\sigma(s)$ is a positive function and ξ is a positive constant, it can be easily seen that (3.37) is possible only for $\alpha = 1$. Consequently, we conclude that the equilibrium solutions σ_0' associated with (3.36) exist only for $K_p > 0$, namely $\phi_s = (2n+1)\pi$, and

satisfy the condition

$$\sigma_0' > \sigma_0 . \tag{3.38}$$

This means that the competition between the effect on the particles due to the plasma wave potential well and the self interaction produces, in correspondence with the synchronous phase, a new equilibrium condition which results in a bunch lengthening according to (3.38). For $\delta \ll 1$ and $\alpha = 1$ the solution of (3.37) is approximately $\sigma_0' \approx (1 + \delta/4)\sigma_0$, but, as the self-interaction becomes more and more important, the bunch lengthening becomes more and more significant. For example, for $\delta = 1$, $\sigma_0' \approx 1.22\sigma_0$, for $\delta = 10$, $\sigma_0' \approx 2.19\sigma_0$, and for $\delta = 100$, $\sigma_0' \approx 4.64\sigma_0$.

3.3. *Modulational instability*

We now analyze the response of the system to a small perturbation in the bunch distribution under the action of the self-interaction only (the plasma wave is considered switched off). In the case (3.21) assumes the following form

$$\mathrm{i}\frac{\partial \Psi}{\partial s} + P\frac{\partial^2 \Psi}{\partial x^2} + Q|\Psi|^2\Psi = 0. \tag{3.39}$$

For this generic cubic-NLS a small perturbation is unstable (stable) if the following condition (Lighthill criterion) is satisfied [11, 12]:

$$PQ > 0 \quad (PQ < 0). \tag{3.40}$$

Consequently, for the (3.39) with $P = \tilde{\varepsilon}/2$ and $Q = q^2\Sigma_b/(e^2 n_p \gamma^3 \tilde{\varepsilon})$ we have only instability with respect to a small density perturbation. This is formally identical to the so-called modulational instability of an e.m. wave packet travelling in a nonlinear medium [11, 12] and for the present case it describes the self-bunching of the particle bunch under the action of its plasma wake potential.

3.4. *Soliton solution*

Still considering the plasma wave switched off, a solitary solution of (3.39) with $P = \tilde{\varepsilon}/2$ and $Q = q^2\Sigma_b/(e^2 n_p \gamma^3 \tilde{\varepsilon})$ is found by looking for a solution of the following envelope form:

$$\Psi(x, s) = G(x - \beta_0 s)\mathrm{e}^{\mathrm{i}k_0 x - \mathrm{i}\omega_0 s} \tag{3.41}$$

with k_0 and ω_0 real numbers. According to the general theory of NLS equation [11], the condition $PQ > 0$, satisfied by (3.39), is the right condition to have solitons. The soliton-like solution for the beam density, which satisfies (3.19) and (3.20) is thus:

$$n_b(x, s) = \frac{q^2}{e^2}\frac{\gamma\Sigma_b^2}{4n_p\varepsilon^2}\operatorname{sech}^2\left[\frac{q^2}{e^2}\frac{\gamma\Sigma_b}{2n_p\varepsilon^2}(x - \beta_0 s)\right], \tag{3.42}$$

$$k_0 = \frac{\gamma^2\beta_0}{\varepsilon};$$

$$\omega_0 = \frac{\varepsilon}{2\gamma^2}k_0^2 - \left(\frac{q^2}{e^2}\frac{\gamma\Sigma_b}{2n_p\varepsilon^2}\right)^2.$$

4. Remarks and conclusions

In this paper, we have described the nonlinear longitudinal dynamics of a relativistic charged particle bunch in cold, unmagnetized plasmas within the context of the recently proposed thermal wave model for relativistic charged particle beam propagation [1]. We have shown that the nonlinear interaction between the bunch and the surroundings (plasma wave potential well and plasma wake fields) is governed by an appropriate NLS equation [eq. (3.21)], fully similar to that one which holds for the propagation of an e.m. bunch in a nonlinear medium in paraxial approximation. In this analogy, our system satisfies Lighthill criterion (modulational instability [11, 12]), and the density can assume a soliton-like profile. Physically, a sort of competition between the diffractive energy (i.e. thermal energy) and the self energy is established. We have instability when the self energy term overcomes the diffraction one. According to Section 3.4 a soliton formation would be the natural evolution of the initial beam density modulation toward a self bunching which asymptotically gives a soliton-like envelope wave train. We finally observe that the present treatment has allowed us to describe the phase-slip oscillations (synchrotron-like oscillations) of the particle bunching in the plasma wave potential well as well as to obtain a longitudinal envelope equation including self-interaction.

References

1. Fedele, R. and Miele, G., Nuovo Cimento **D13**, 1527 (1991).
2. Fedele, R. and Miele, G., Phys. Rev. **A46**, 6634 (1992).
3. Fedele, R., Miele, G. and Galluccio, F., "A Numerical Check of the Thermal Wave-Model for Charged Particle-Beam Dynamics", INFN/TC-93/12, to be published in Proc. 1993 Particle Accelerator Conference. Washington D.C. May 17–20, 1993.
4. Fedele, R., Galluccio, F. and Miele, G., Phys. Lett. **A185**, 93 (1994).
5. Fedele, R., Miele, G., Palumbo, L. and Vaccaro, V. G., Phys. Lett. **A179**, 407 (1993).
6. Fedele, R. and Shukla, P. K., Phys. Rev. **A44**, 4045 (1992).
7. Sands, M., "The Physics of Electron Storage Rings", SLAC Report 121 (1971).
8. Lawson, J., "The Physics of Charged Particle Beams" (Clarendon, Oxford 1988), 2nd ed.
9. Chen, P., Part. Acc. **20**, 171 (1986).
10. Zotter, B., "Collective Effects – General Description", CAS Proc., CERN 85-19, November 1985, pp. 415–431.
11. Whitham, G. B., "Linear and Nonlinear Waves" (J. Wiley, New York 1974).
12. Akhmanov, S. A., Sukhuorukov, A. P. and Khokhlov, R. V., Sov. Phys. Usp. **93**, 609 (1968).

Physica Scripta. Vol. T52, 40–50, 1994

A Slow-Wave Autonomous Cyclotron Buncher: Exact Hamiltonian Analysis and Simplified Helical Model

D. J. Frantzeskakis

Department of Physics, Applied Physics Division, University of Athens, Panepistimiopolis, T.Y.P.A. Buildings, 157 71 Athens, Greece

and

K. Hizanidis and J. L. Vomvoridis

Department of Electrical and Computer Engineering, Electroscience Division, National Technical University of Athens, 9 Iroon Polytechniou, Zografou, 157 73, Athens, Greece

Received November 22, 1993; accepted January 28, 1994

Abstract

A nonlinear theory has been developed for the generation of perfect azimuthal bunching on a beam with axial initial electron velocity by slow radiation fields generated by the interaction itself, under conditions of the anomalous Doppler shift. The dynamics of the beam is formulated in the framework of a Hamiltonian analysis and the helical equations of motion are derived along with the two exact invariant quantities of the system in hand. Utilizing time separation a simplified set of equations is derived which compares favourably with the exact model at least for small initial pitch ratios. The simplified model is then utilized for calculating the properties of an electron beam buncher. The latter is also optimized to maximize the generated transverse momentum.

1. Introduction

A beam of free electrons, with each individual electron propagating along, and gyrating around, a static magnetic field, is at the well-known cyclotron resonance with an electromagnetic wave, when the wave frequency, Doppler-shifted in the electron frame of reference, is approximately equal to the electron gyrofrequency (or its harmonics, when the amplitude of the wave fields is non-uniform in a direction perpendicular to the magnetostatic field). When this cyclotron condition is satisfied, extended energy exchange between the electron beam and the radiation fields is possible, in a way that coherent emission could be obtained at the expense of the electron kinetic energy.

Among the cyclotron resonance interactions a prominent role is played by the Cyclotron-Resonance Maser (CRM), or Electron-Cyclotron Maser (ECM) [1–3]. In this interaction, the wave electric field affects the relativistic mass factor of the electrons and consequently the relativistic electron gyrofrequency, so that a bunch is formed in the transverse momentum vector of the electrons and the associated electron current in turn drives the wave fields. The technologically most advanced variant of the CRM is the gyrotron, characterized by a negligible Doppler shift. Gyrotron devices have succeeded in demonstrating production of megawatt power at the upper range of the microwave frequency spectrum [4–9]. An increase of the frequency into the infrared spectrum appears promising by the Cyclotron Auto-Resonant Maser (CARM), the CRM variant employing a large Doppler shift [5, 10–13]. In addition, other interactions based on cyclotron resonance are the Weibel instability, in which the wave magnetic field affects the axial velocity of the electrons and consequently the Doppler-shift term, resulting again the transverse bunching [14], as well as the peniotron instability, based on a systematic shift in the electron guiding centre, under the action of the wave fields [15].

In all these interactions, the free energy of the electrons resides in the transverse motion, and, therefore, transverse momentum must be imparted upon the beam electrons, either at the beam source, or by, e.g. a magnetic wiggler. These processes increase beam temperature and for this reason it appears that an interaction employing transverse wave fields at cyclotron resonance with a beam having initially only longitudinal velocity might be able to be proved more attractive than, e.g. the gyrotron. Notice that such electron beams can be produced with high degree of monoenergeticity by a Pierce gun, for instance. The investigation of this possibility, as well as the estimation of the expected performance of devices based on this interaction, has been the subject of an ongoing research programme at the National Technical University of Athens (Greece).

Employing basic principles [16] one can study whether and under what conditions an axial velocity beam can be used to generate radiation at the electron cyclotron resonance. Denoting by $\boldsymbol{E}_\perp$ and $\boldsymbol{B}_\perp$ the (rotating) transverse electric and magnetic field vectors of the wave, respectively, and by $\boldsymbol{v}_0$ the axial initial electron velocity, it can be immediately seen from the term $\boldsymbol{E}_\perp + \boldsymbol{v}_0 \times \boldsymbol{B}_\perp$ in the Lorentz force equation that when $|\boldsymbol{E}_\perp|/|\boldsymbol{B}_\perp| < |\boldsymbol{v}_0|$, then the acceleration of the electrons is coparallel with the electric field. If, at the same time, the magnetostatic field has the appropriate value for cyclotron resonance, the synchronous rotation of electrons and wave fields has as a result that, whichever amount of transverse velocity is developed on the electrons they remain in phase with the wave electric field. This holds true for all electrons, and therefore, in the transverse current that is thus developed, all electrons contribute equally and by the full amount of their transverse velocity. Thus, the transverse electric current density of the beam electrons is the maximum possible. In view of this resonance condition, the electron contribution to the current density rotates with the wave, remaining continuously antiparallel to the wave electric field. Therefore, they feed energy to the wave under the most favourable conditions.

Based on these observations, a nonlinear analysis [16–19] has been developed, based on the study of electron trajectories in a large amplitude plane wave at steady state. It has indicated that impressive efficiencies, approaching 100%, can be reached, at reasonable interaction lengths. In addition, the linear theory has been developed, using a fluid model to represent the electron beam, both for the cases of an oscillator [20] and an amplifier [21]. The linear results indicate substantial linear growth rates and moderate requirements for the starting current, as well as a weak mode competition.

The work cited in [16–19] is based on a simplified model, in which the radiation fields are assumed with constant transverse components and no axial components. In the present work, the model has been extended and all these dependencies are taken into account. Equations of motion, describing the dynamical behaviour of the electron beam, have been obtained, by means of the rigorous Hamiltonian formalism, and integrated in an appropriate (helical) coordinate system. It is readily shown from the analysis that slow waves are necessary for the interaction and that, due to limitations in the attainable rf field amplitudes, the resulting efficiency is not as high as originally envisaged. In this way, it is concluded that the prospects of directly using this interaction for high power generation (e.g. for heating of tokamak plasmas) are not so attractive.

An alternate application of a beam with axial initial electron velocity at cyclotron resonance with radiation fields of low amplitudes is proposed and analysed in this paper: the autonomous beam buncher. The idea is based on the fact that the radiation fields, generated by the beam, are able to impart transverse momentum on the electrons in perfect phase correlation with the wave. For such an application the efficiency needs not to be high (just enough to compensate for all losses), since the objective is the bunching of the electron beam and not the direct generation of high power radiation. Such high power radiation is expected to be generated subsequently and at high efficiency, when the power resident in this bunched beam is extracted in an attached appropriate cyclotron resonance device.

The present paper is arranged as follows: In Section 2 the physical model is defined. The equations of motion governing the nonlinear dynamics of a test beam, as well as the two constants of the motion are derived in Section 3. In Section 4 the separation of the time scales which lead to the simplified model is presented along with a comparison between the latter and the exact analysis. The requirements for the autonomous beam buncher are obtained in Section 5, by investigating the properties of the first invariant. The analysis yields the appropriate range of values of the input parameters (e.g. the frequency mismatch and the radiation field amplitude), as well as the expected values of the output parameters (e.g. the transverse momentum and the efficiency). An optimization procedure is also performed in the same Section, in order to define the optimal design values. Finally in Section 6 the main results are summarized.

2. The physical model

In the physical model under consideration, the electron beam is treated as a test beam, which is initially unmodulated, that is, no high-frequency fields have affected the beam prior to its entry into the interaction region. The beam is also assumed to be monoenergetic, and with vanishingly small initial transverse velocity for each constituent electron. This assumption is valid in view of the high quality of the available electron beams. Finally, the beam is supposed to be infinitesimally thin; although this seems to be an unrealistic hypothesis, one should note that the evolution of any real beam can conceptually be treated as an appropriate average of the evolution of the constituent filamentary beams. Under these assumptions, the subsequent evolution of the beam, can be described in terms of the motion of each electron. In particular, the momentum, $\boldsymbol{p}$, the transverse position, $\boldsymbol{r}_\perp$, and the axial position, z, inside the interaction region are obtained by

$$\frac{d}{dt}\boldsymbol{p} = -\frac{e}{\gamma m}(\gamma m\boldsymbol{E} + \boldsymbol{p} \times \boldsymbol{B}), \tag{2.1a}$$

$$\frac{d}{dt}\boldsymbol{r}_\perp = \frac{1}{\gamma m}(\boldsymbol{p} - p_z \boldsymbol{e}_z), \tag{2.1b}$$

$$\frac{d}{dt}z = \frac{p_z}{\gamma m}, \tag{2.1c}$$

where $-e$ and m are the electron charge and the rest mass, respectively, γ the relativistic factor, defined by $\gamma^2 = 1 + (p/mc)^2$ with c the speed of light in vacuo, and $(\boldsymbol{E}, \boldsymbol{B})$ are the electric and magnetic fields governing the electron motion. In eqs (2.1) the time t is used as an independent variable. They can be immediately modified, to employ z as the independent variable, by using the transformation $\mathrm{d}z = (p_z/\gamma m)\,\mathrm{d}t$, with $p_z = \boldsymbol{p} \cdot \boldsymbol{e}_z$.

The electric and magnetic fields governing the electron motion consist of the following components:

(*i*) A uniform static magnetic field, $\boldsymbol{B}_0$, which is directed along the axis of the filamentary beam, given by $\boldsymbol{B}_0 = B_0 \boldsymbol{e}_z$. Notice that the constant magnetic induction, B_0, provides both for beam guiding and for interaction at the cyclotron resonance.

(*ii*) The radiation electric field, $\boldsymbol{E}$, and magnetic field, $\boldsymbol{B}$, which represent a component of a guided mode, with right-circular polarization (for angular frequency $\omega > 0$) and with forward propagation (for wavenumber $k > 0$), given by

$$\boldsymbol{E} = E_\perp(\boldsymbol{e}_x \sin\phi - \boldsymbol{e}_y \sin\phi) + (-kE_\perp + \omega B_\perp)(x\cos\phi + y\sin\phi)\boldsymbol{e}_z, \tag{2.2a}$$

$$\boldsymbol{B} = B_\perp(\boldsymbol{e}_x \cos\phi + \boldsymbol{e}_y \sin\phi) + \left(-kB_\perp - \frac{\omega}{c^2}E_\perp\right)(-x\sin\phi + y\cos\phi)\boldsymbol{e}_z. \tag{2.2b}$$

In eqs (2.2), $(E_\perp, B_\perp)$ are the amplitudes of the transverse components, $\phi = \omega t - kz$ is the wave phase, with t being the time, (x, y, z) are the Cartesian spatial coordinates and $(\boldsymbol{e}_x, \boldsymbol{e}_y, \boldsymbol{e}_z)$ the corresponding unit vectors. The quantities $E_\perp$, $B_\perp$, ω and k are assumed to be constant. These fields represent locally a Taylor expansion in x and y (the transverse displacements of an electron from its initial position) of any guided mode, so that all dominant effects are included under the cyclotron resonance. The fields of eqs (2.2) refer to arbitrary (hybrid) eigenmodes and include as special cases the TE (when $E_\perp/cB_\perp = 1/n$) and TM (when $E_\perp/cB_\perp = n$) waves, where $n = kc/\omega$ is the refractive index (the inverse of the normalized phase velocity).

In order to analyse the dynamical behaviour of the electron beam, it is convenient to express the equations of motion in a rotating helical coordinate system, which can be defined by the unit vectors e_1, e_2, e_3, where

$$e_1 = e_x \sin\phi - e_y \cos\phi, \tag{2.3a}$$

$$e_2 = e_x \cos\phi + e_y \sin\phi, \tag{2.3b}$$

$$e_3 = e_z. \tag{2.3c}$$

This system is thus affixed to the wave, so that at any instant and at any point $\boldsymbol{E}\cdot\boldsymbol{e}_1 = E_\perp$ and $\boldsymbol{B}\cdot\boldsymbol{e}_2 = B_\perp$, while the position vector $\boldsymbol{r}$ and the mechanical momentum $\boldsymbol{p}$ can be expressed in the helical system as $\boldsymbol{r} = r_1\boldsymbol{e}_1 + r_2\boldsymbol{e}_2 + r_3\boldsymbol{e}_3$ and $\boldsymbol{p} = p_1\boldsymbol{e}_1 + p_2\boldsymbol{e}_2 + p_3\boldsymbol{e}_3$ respectively. Notice that the helical components r_1, r_2, r_3 (and p_1, p_2, p_3) are related to the Cartesian ones through the relation,

$$\boldsymbol{h} = \mathbf{R}\cdot\boldsymbol{c}, \tag{2.4}$$

where $\boldsymbol{h}$ and $\boldsymbol{c}$ are the column vectors of the helical and Cartesian components respectively of either the position or momentum vector, and $\mathbf{R}$ is the rotation matrix,

$$\mathbf{R} = \begin{pmatrix} \sin\phi & -\cos\phi & 0 \\ \cos\phi & \sin\phi & 0 \\ 0 & 0 & 1 \end{pmatrix}. \tag{2.5}$$

3. The dynamical equations and the constants of the motion

In analysing the dynamical behaviour of the beam electrons, we adopt the Hamiltonian formalism which is particularly suitable in such cases. The fields are now expressed in terms of the potential functions $(\boldsymbol{A}, \Phi)$, which in cylindrical coordinates (r, θ, z), attain the following form.

$$\boldsymbol{A} = A_\perp \cos(\phi-\theta)\boldsymbol{e}_r - \frac{\omega E_0}{kc^2} r \sin(\phi-\theta)\boldsymbol{e}_z + \left[\frac{r}{2}B_0 + A_\perp \sin(\phi-\theta)\right]\boldsymbol{e}_\theta, \tag{3.1}$$

$$\Phi = -E_0 r \sin(\phi-\theta). \tag{3.2}$$

The first part of the last (azimuthal) term in eq. (3.1) is responsible for the axial, constant magnetic field. On the other hand, the amplitudes $A_\perp$, E_0, are in general functions of the transverse coordinates r and θ. For simplicity, we assume cylindrical symmetry in $A_\perp$ and E_0. In this case, using the expressions for fields in the previous section, one easily obtains the following equations,

$$A_\perp(r) = A_{\perp_0} \exp\left[\frac{r^2}{2}\left(k^2 - \frac{\omega^2}{c^2}\right)\right], \tag{3.3}$$

$$B_\perp(r) = \frac{\omega}{k}\frac{E_\perp(r)}{c^2} + \left(k - \frac{\omega^2}{k^2c^2}\right)A_\perp(r) \tag{3.4}$$

and

$$E_\perp(r) = E_0 + \omega A_\perp(r), \tag{3.5}$$

where $A_{\perp_0}$ can be an arbitrary constant amplitude. It is immediately evident from the expressions eqs (3.3)–(3.5) that, to zero order in $\rho \equiv \omega r/c$ [i.e. $r^2(k^2 - \omega^2/c^2)/2 = \rho^2(n^2-1)/2$], the field amplitudes are constant while the next significant contribution is proportional to ρ^2.

The Hamiltonian of an electron in the electromagnetic field as given by eqs (3.1) and (3.2) is,

$$H = c\Big\{m^2c^2 + [P_r + eA_\perp(r)\cos(\phi-\theta)]^2 + \left[P_z - \frac{e\omega E_0}{kc^2} r\sin(\phi-\theta)\right]^2 + \left[\frac{P_\theta}{r} + \frac{m\Omega r}{2} + eA_\perp(r)\sin(\phi-\theta)\right]^2\Big\}^{1/2} + eE_0 r\sin(\phi-\theta), \tag{3.6}$$

where P_r, P_θ, P_z are the canonical momenta conjugate to r, θ, z respectively and $\Omega = eB_0/m$. Using now, as a generating function of a canonical transformation $(P_r, P_\theta, P_z; r, \theta, z) \to (P_r', P_\theta', P_z'; r', \theta', z')$, the expression,

$$F(z, P_z', t) = \left(z - \frac{\omega}{k}t\right)P_z' \tag{3.7}$$

one easily obtains the new Hamiltonian, H', which is now a constant of the motion, since it does not contain the time explicitly,

$$H' = -cm\omega e_0 r\sin(kz'+\theta) - c\frac{P_z'}{n} + \Big\{m^2c^2 + [P_r + mca_\perp(r)\cos(kz'+\theta)]^2 + \left[P_z' + \frac{m\omega}{n} re_0 \sin(kz'+\theta)\right]^2 + \left[\frac{P_\theta}{r} + \frac{m\Omega r}{2} - mca_\perp(r)\sin(kz'+\theta)\right]^2\Big\}^{1/2}, \tag{3.8}$$

where $P_z' = P_z$ is the conjugate to $z' = z - \omega t/k$ and the rest of the conjugate pairs are identically equal to the old ones. In eq. (3.8) the normalized amplitudes $e_0 = eE_0/m\omega c$ and $a_\perp(r) = eA_\perp(r)/mc$ have been used. The first term in the r.h.s. of eqs (3.6) and (3.8) is the total energy, $mc^2\gamma$, of a relativistic electron.

The apparently six-dimensional dynamical system represented by the Hamiltonian H', eq. (3.8), [the phase space, $(P_z', z'; P_r, r; P_\theta, \theta)$ is six-dimensional] can be further reduced to a four-dimensional one, since the spatial canonical variables z' and θ enter solely in the combined form $kz' + \theta$. By choosing as a generating function of a canonical transformation $(P_r, P_\theta, P_z'; r, \theta, z') \to (P_r'', P_z''; r'', \theta'', z'')$ the expression

$$F(z', \theta, P_z'', P_\theta'') = \left(z' + \frac{\theta}{k}\right)P_z'' + \theta P_\theta'', \tag{3.9}$$

one finally has for the new Hamiltonian H'' (numerically equal to the constant of the motion H'),

$$H'' = c\Big\{m^2c^2 + [P_r + mca_\perp(r)\cos(kz'')]^2 + \left[P_z'' + \frac{m\omega}{n} re_0\sin(kz'')\right]^2 + \left[\frac{P_z''}{kr} + \frac{P_\theta''}{r} + \frac{m\Omega r}{2} - mca_\perp(r)\sin(kz'')\right]^2\Big\}^{1/2} - cm\omega e_0 r\sin(kz'') - c\frac{P_z''}{n}, \tag{3.10}$$

where $P_z'' = P_z$ is conjugate to $z'' = z' + \theta/k = z - (\omega t - \theta)/k$ and the conjugate pair (P_r, r) remains the same as before. The canonical momentum P_θ'' in eq. (3.10) is apparently a second constant of the motion since its conjugate spatial position, θ'', does not explicitly enter in the Hamiltonian. One can relate P_θ'' back to the original canonical variables as follows,

$$P_\theta'' = P_\theta - \frac{P_z}{k}. \tag{3.11}$$

The two constants of the motion we found can be expressed in terms of the mechanical momenta in the rotating helical coordinate system P_1, P_2, P_3 and the respective spatial variables r_1, r_2, ϕ. Expressing the helical variables in normalized form, i.e. $u_1 = p_1/mc$, $u_2 = p_2/mc$, $u_3 = p_3/mc$, $\rho_1 = \omega r_1/c$ and $\rho_2 = \omega r_2/c$, one can easily obtain

$$\frac{\omega}{mc^2} P'' = \rho_1 u_2 - \rho_2 u_1 - \frac{u_3}{n} - \tfrac{1}{2}a(\rho_1^2 + \rho_2^2) - \left(a_\perp + \frac{e_0}{n^2}\right)\rho_1, \tag{3.12}$$

where $\rho^2 = \rho_1^2 + \sigma_2^2 = \omega^2 r^2/c^2$, $a = \Omega/\omega$ and

$$\frac{H'}{mc^2} = \gamma - \frac{u_3}{n} + e_0\left(1 - \frac{1}{n^2}\right)\rho_1, \tag{3.13}$$

with the relativistic energy, γ, defined by

$$\gamma^2 = 1 + u_1^2 + u_2^2 + u_3^2. \tag{3.14}$$

It should be mentioned that, as far as the normalized transverse fields $\varepsilon(\rho) = eE_\perp/m\omega c$ and $b(\rho) = eB_\perp(r)/m\omega$ are concerned, they are related to the normalized amplitude $a_\perp(\rho)$ through the expression

$$nb(\rho) - \varepsilon(\rho) = a_\perp(\rho)(n^2 - 1) = (n^2 - 1)a_{\perp_0} \exp\,[\rho^2(n^2 - 1)/2], \tag{3.15}$$

with $a_{\perp_0} = eA_{\perp_0}/mc$, which is the normalized version of eq. (3.4). Furthermore, e_0 is related to $a_\perp$ and ε through,

$$a_\perp(\rho) + e_0 = \varepsilon(\rho). \tag{3.16}$$

In this work, we use as constants of the motion the quantities $I_1 = H'/mc^2$ (i.e. the generalized Hamiltonian) and $I_2 = \omega P_\theta''/mc^2$ (basically, the action associated with the helical motion), which [via eqs (3.15) and (3.16)] are given by,

$$I_1 = \gamma - \frac{u_3}{n} + e_0(1 - 1/n^2)\rho_1 \tag{3.17}$$

and

$$I_2 = \rho_1 u_2 - \rho_2 u_1 - \tfrac{1}{2}a\rho^2 - \frac{u_3}{n} - [a_\perp(\rho) + e_0/n^2]\rho_1. \tag{3.18}$$

The two-degree of freedom Hamiltonian $H''(r, z'', P_r, P_z'')$, eq. (3.10), can be used as the basis of a dynamical system of four equations of motion. However, for the purpose of this paper and for reasons of convenience that the helical system provides to the physical system in hand, we use and integrate numerically the equations of motion in their helical form. This may add additional dynamical variables to follow in time, but it is algebraically much easier. The constants of the motion, eqs (3.17) and (3.18) are used as a diagnostic tool in our numerical integration. The shorter Hamilton's system of equations will prove to be useful in dealing with an ensemble at initial condition and in studying in detail the transverse thermalization of the electron beam. However, this will be a subject for future investigation.

The equations of motion in the helical system and in normalized form are,

$$\frac{d\rho_1}{d\tau} = \frac{u_1 + (\gamma - nu_3)\rho_2}{\gamma}, \tag{3.19a}$$

$$\frac{d\rho_2}{d\tau} = \frac{u_2 - (\gamma - nu_3)\rho_1}{\gamma}, \tag{3.19b}$$

$$\frac{du_1}{d\tau} = -\frac{a - (\gamma - nu_3)}{\gamma} u_2 + \frac{\varepsilon - nb}{\gamma}\rho_1 u_2 - \varepsilon + b\frac{u_3}{\gamma} + O_1(\epsilon^3), \tag{13.9c}$$

$$\frac{du_2}{d\tau} = \frac{a - (\gamma - nu_3)}{\gamma} u_1 - \frac{\varepsilon - nb}{\gamma}\rho_1 u_1 + O_2(\epsilon^3), \tag{3.19d}$$

$$\frac{du_3}{d\tau} = -b\frac{u_1}{\gamma} + (n\varepsilon - b)\rho_2 + O_3(\epsilon^3). \tag{3.19e}$$

The relativistic energy, $\gamma = (1 + u_1^2 + u_2^2 + u_3^2)^{1/2}$, also evolves according to the equation,

$$\frac{d\gamma}{d\tau} = -\varepsilon\frac{u_1}{\gamma} + \frac{n\varepsilon - b}{\gamma}\rho_2 u_3 + O(\epsilon^3). \tag{3.20}$$

The terms O_1, O_2, O_3 and O are higher order terms which stay idle for field strengths of the order $\varepsilon \cong 10^{-2}$. They are given by the following expressions (with $\chi = x\omega/c$ and $\psi = y\omega/c$):

$$O_1(\varepsilon^3) = \frac{u_3}{n\gamma} f(\rho)(\chi^2 \sin^2\phi + \psi^2 \cos^2\phi), \tag{3.21a}$$

$$O_2(\varepsilon^3) = \frac{u_3}{n\gamma} f(\rho)(\chi^2 - \psi^2)\sin\phi\cos\phi, \tag{3.21b}$$

$$O_3(\varepsilon^3) = -\frac{\rho_1}{n\gamma} f(\rho)(\rho_1 u_2 + \rho_2 u_1), \tag{3.21c}$$

and

$$O(\varepsilon^3) = -\frac{u_3}{n\gamma} f(\rho)\left(\rho_1\rho_2 \cos 2\phi - \frac{\rho^2}{2}\sin 2\phi\right) \times (u_2 \cos 2\phi - u_1 \sin 2\phi) \tag{3.22}$$

where

$$f(\rho) = \frac{1}{\rho}\frac{d\varepsilon(\rho)}{d\rho} + \varepsilon(\rho) - nb(\rho). \tag{3.23}$$

It is evident that in the case of guided TE $[\varepsilon(\rho)/b(\rho) = n]$ waves with $\varepsilon(\rho)$, and $b(\rho)$ constant, these higher order terms vanish identically. However, these terms represent a small correction to the arbitrary case, hence in the present analysis and numerical integration these terms will not be considered.

The equations of motion, obtained in the Section by use of the Hamiltonian formalism, can be interpreted using the Lorentz force $d\boldsymbol{p}/dt = -e(\boldsymbol{E} + \boldsymbol{v} \times \boldsymbol{B})$, keeping in mind the helical structure of the coordinate system, which gives rise to inertial terms proportional to $d\phi/dt = (\gamma - nu_3)/\gamma$. Considering first the equations for u_1, u_2, the first terms give the combined action of the magnetostatic field and the inertial effects, with the leading coefficients representing the normalized frequency mismatch, $(\Omega_0/\gamma - \omega - kv_z)/\omega$. The second terms give the contribution from the B_z component of the wave, at the instantaneous position ρ_1 of the electron. The remaining terms in the equation for u_1 arise from $\boldsymbol{E}_\perp + \boldsymbol{v}_z \times \boldsymbol{B}_\perp$. This contribution, being always in the direction $\boldsymbol{E}_\perp$, affects the momentum component u_1 only. In the equation for u_3 the terms are, respectively, the contribution from $\boldsymbol{v}_\perp \times \boldsymbol{B}_\perp$ and $\boldsymbol{E}_z$, the latter evaluated at the instantaneous position, ρ_2. Similarly, the equation for γ demonstrates the contributions $\boldsymbol{v}_\perp \cdot \boldsymbol{E}_\perp$ and $\boldsymbol{v}_z \cdot \boldsymbol{E}_z$, the latter evaluated at the position ρ_2.

The significance of the axial components of the wave fields can be assessed from the way these components appear in eqs (3.19)–(3.20). The component $\boldsymbol{B}_z$, represented by the terms involving ρ_1, affects explicitly only the transverse dynamics by means of an additional contribution to the frequency mismatch. However, taking ρ_1 at the Larmor orbit, $\rho_1 \simeq u_2/a$, and using as typical values $u_2 \sim 1$, $E_\perp =$ 100 kV/cm at 100 GHz (i.e. $\varepsilon = 10^{-2}$) and $a \sim \gamma \sim 1$, this additional contribution falls below 1% and, therefore, can be neglected in comparison to the frequency mismatch (a few times 1%).

On the other hand, the contribution of E_z, whenever such a component is present, appears to be much more significant. This component, proportional to ρ_2, affects explicitly the axial momentum and the relativistic energy, hence it allows for energy exchange also via E_z. It also affects implicitly, via the expression $\gamma - nu_3$, the frequency mismatch, which is the dominant term of transverse dynamics. Furthermore, if its contribution were omitted, e.g. by artificially setting $\rho_2 = 0$, then the first constant of the motion would read $I_1 = \gamma - u_3/n$.

4. Separation of time scales and the simplified model

The helical spatial coordinates ρ_1, ρ_2 can be combined into a complex entity (phasor) $\mathring{\rho} = \rho_1 + j\rho_2$, which evolves according to the equation,

$$\frac{d}{d\phi}(\mathring{\rho}\, e^{j\phi}) = \frac{\mathring{u}\, e^{j\phi}}{\gamma - nu_3} = \mathring{f}\, e^{j\phi}, \tag{4.1}$$

where $\mathring{u}$ is the transverse momentum phasor $u_1 + ju_2$ and $d\phi = (\gamma - nu_3)\, d\tau/\gamma$. This equation is merely a combination of eqs (3.19a) and (3.19b). By successive partial integration eq. (4.1) yields,

$$\mathring{\rho} = -\sum_{m=0}^{\infty} j^{m+1} \frac{d^m \mathring{f}}{d\phi^m}. \tag{4.2}$$

Separation of time scales is possible if the normalized field amplitudes ε_0, b_0 [equal to $\varepsilon(\rho = 0)$, $b(\rho = 0)$, respectively] as well as the quantities $a - \gamma + nu_3$ are considered as small quantities (of order ε, $\varepsilon \cong 10^{-2}$). It is important to notice that, indeed, the quantity $a - \gamma + nu_3$ is small since $\gamma = a + nu_3$ is the normalized version of the cyclotron resonance condition, eq. (2.6). One can easily observe that the dynamical equations for $\mathring{u}$, eqs (3.19c) and (3.19d), exhibit a slow evolution rate because of the presence of quantities of order ϵ in the r.h.s.:

$$\frac{d\mathring{u}}{d\tau} = -\frac{\gamma\varepsilon_0 - b_0 u_3}{\gamma} + j\frac{a - \gamma + nu_3 - (\varepsilon_0 - nb_0)\rho_1}{\gamma}\mathring{u}. \tag{4.3}$$

The magnitude of $\mathring{u}$, $|\mathring{u}|$, is, therefore, of order ε if, initially ($\tau = 0$) is so. Equation (4.2) implies that the leading contribution in the sum is of order ε, that is,

$$\mathring{\rho} = -j\frac{\mathring{u}}{\gamma - nu_3} + \frac{\gamma}{\gamma - nu_3}\frac{d}{d\tau}\left|\frac{\mathring{u}}{\gamma - nu_3}\right| + O(\varepsilon^m,\ m \geqslant 2),$$

or, utilizing eq. (4.3),

$$\mathring{\rho} = -j\frac{\mathring{u}}{\gamma - nu_3} - \frac{\gamma\varepsilon_0 - b_0 u_3}{(\gamma - nu_3)^2} + O(\varepsilon^m,\ m \geqslant 2). \tag{4.4}$$

To order ϵ^2, eq. (4.3) can now be rewritten as follows

$$\frac{d\mathring{u}}{d\tau} = \frac{\gamma\varepsilon_0 - b_0 u_3}{\gamma} + j\frac{a - \gamma + nu_3}{\gamma}\mathring{u} + O(\varepsilon^m,\ m \geqslant 3). \tag{4.5}$$

The first and second terms in the r.h.s. are the $O(\epsilon)$ and $O(\epsilon^2)$ terms, respectively. The dynamical equation for u_3 and γ, [eqs (3.19e) and (3.20)] can now be reexpressed with ρ_2 taken from eq. (4.4).

$$\frac{du_3}{d\tau} = -\frac{u_1}{\gamma}\left(b_0 + \frac{n\varepsilon_0 - b_0}{\gamma - nu_3}\gamma\right) + O(\varepsilon^m,\ m \geqslant 3) \tag{4.6}$$

and

$$\frac{d\gamma}{d\tau} = -\frac{u_1}{\gamma}\left(\varepsilon_0 + \frac{n\varepsilon_0 - b_0}{\gamma - nu_3}u_3\right) + O(\varepsilon^m,\ m \geqslant 3). \tag{4.7}$$

Equations (4.4)–(4.7) imply that the transverse helical coordinates evolve slowly with a rate which is proportional to the normalized field amplitudes ε_0, b_0 and the resonance frequency mismatch $a - \gamma - nu_3$. The axial momentum and the relativistic energy, γ, on the other hand, evolve much slower with a rate which is roughly proportional to the square of the normalized field amplitudes and frequency mismatches.

The first constant of the motion, K_1, of the simplified model ($K_1 \simeq I_1$) can be readily obtained from eqs (4.6) and (4.7) or, alternatively, from the original expression, eq. (3.17),

$$K_1 = \gamma - \frac{u_3}{n} + O(\varepsilon^m,\ m \geqslant 2). \tag{4.8}$$

If one now eliminates the time from eq. (4.7) and the imaginary part of eq. (4.5), and utilizes eq. (4.8) one can readily obtain

$$\frac{du_2}{d\gamma} = \frac{(\gamma - nu_3)(\gamma - a - nu_3)}{\varepsilon_0\gamma - b_0 u_3}. \tag{4.9}$$

This equation yields the following second constant of the motion for the simplified model, K_2,

$$K_2 = u_2 + \int_{\gamma_0}^{\gamma} d\gamma' \frac{[\gamma' - nu_3(\gamma')][\gamma' - a - nu_3(\gamma')]}{\varepsilon_0\gamma' - b_0 u_3(\gamma')}. \tag{4.10}$$

The main issue to be considered next is to check the validity of the results obtained by our simplified analysis.

This is affected by solving numerically for the electron trajectories, as they are obtained from eqs (4.4–(4.7). In addition, results are presented, in which the electron trajectories are calculated from the equations of motion in the exact radiation fields [eqs (3.19)–(3.20)]. In all cases, the radiation fields have been taken with the values $\varepsilon = 0.01$ and $b = 0.0078$. For reference purposes we note that e.g. at 100 GHz these values correspond to $E_\perp = 9.3$ MV/m and $B_\perp = 24$ mT. The beam is assumed to be quite relativistic, with $\gamma_0 = 2$, corresponding to a voltage of 511 KV. This choice has been made having in mind a potential application of the beam in a buncher, as it is further elaborated in the next Section. The refractive index, n, (the inverse of the wave phase velocity) is selected to maximize $u_\perp$ (as described in detail in the next Section), hence its reference value is taken to be $n = 1.73$. For the sake of completeness we choose initial values for the transverse momentum such that the pitch ratio, namely $\alpha = u_\perp/|u_{30}|$, takes the values of 0.0 and 0.5 (Figs 1–2 and 3–4 respectively). The normalized frequency mismatch, $\delta = \Delta = n\beta_0 - 1 - a/\gamma_0$, in both cases is taken to be 0.0414.

In Figs 1 and 3 we plot the exact constants of the motion (I_1 and I_2) against their respective values the simplified model provides (apparently, not invariant quantities anymore within that model), as well as the constants of the motion of the simplified analysis (K_1 and K_2) against their respective values according to the exact analysis. In this way we are in a position to assess the validity of the simplified model with a high degree of certainty. In Figs 2 and 4 the exact model is contrasted with the simplified one as far as the dynamics of the motion is concerned. Therefore the helical components of both momenta and radial displacements, as well as the relativistic factor are contrasted.

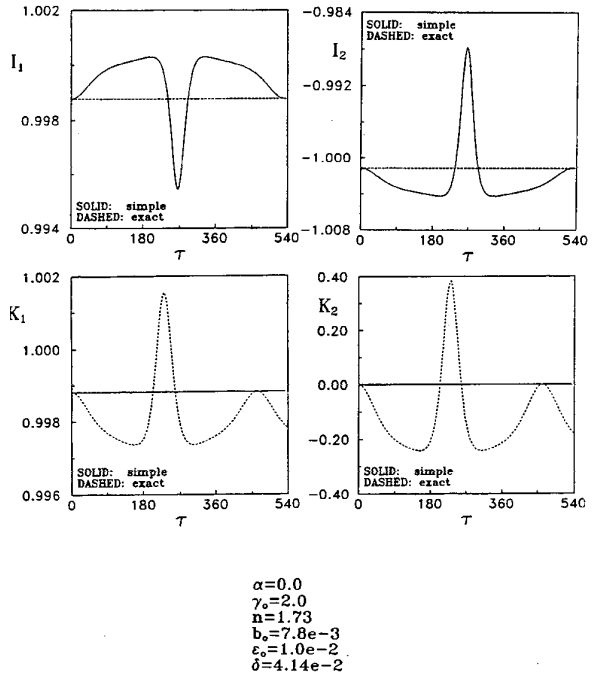

Fig. 1. Exact constants of the motion (I_1 and I_2) against their respective values in the simplified model and constants of the motion of the simplified analysis (K_1 and K_2) against their respective values according in the exact model, for a pitch ratio $\alpha = 0.0$.

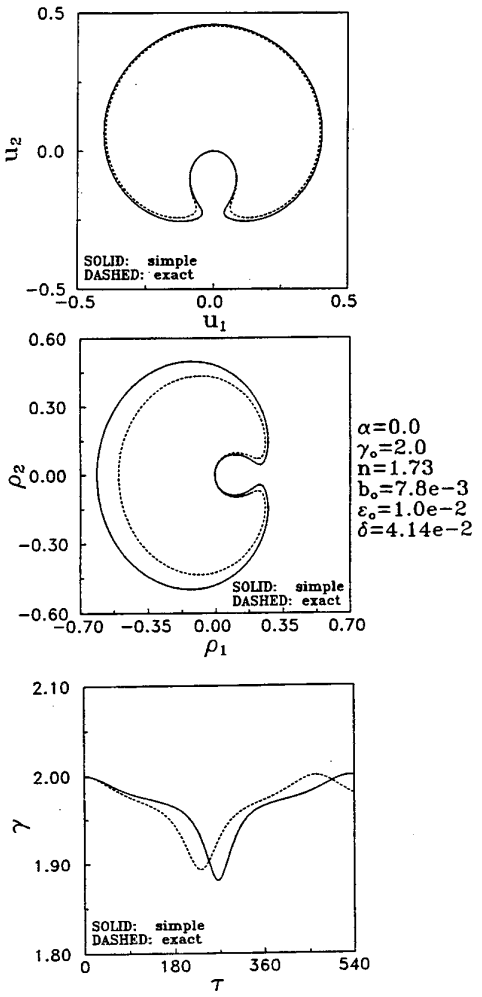

Fig. 2. Trajectories of electrons on the transverse planes (u_1, u_2) and (ρ_1, ρ_2) and temporal evolution of the relativistic factor, γ, for a pitch ratio $\alpha = 0.0$.

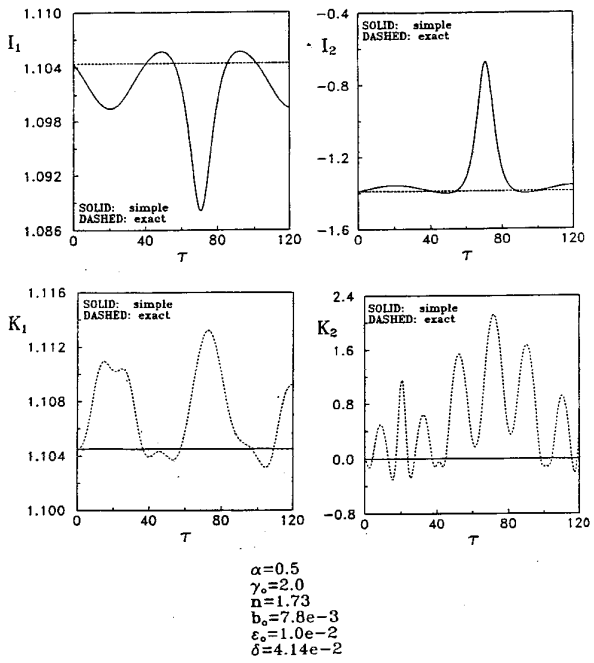

Fig. 3. Exact constants of the motion (I_1 and I_2) against their respective values in the simplified model and constants of the motion of the simplified analysis (K_1 and K_2) against their respective values according in the exact model, for a pitch ratio $\alpha = 0.5$.

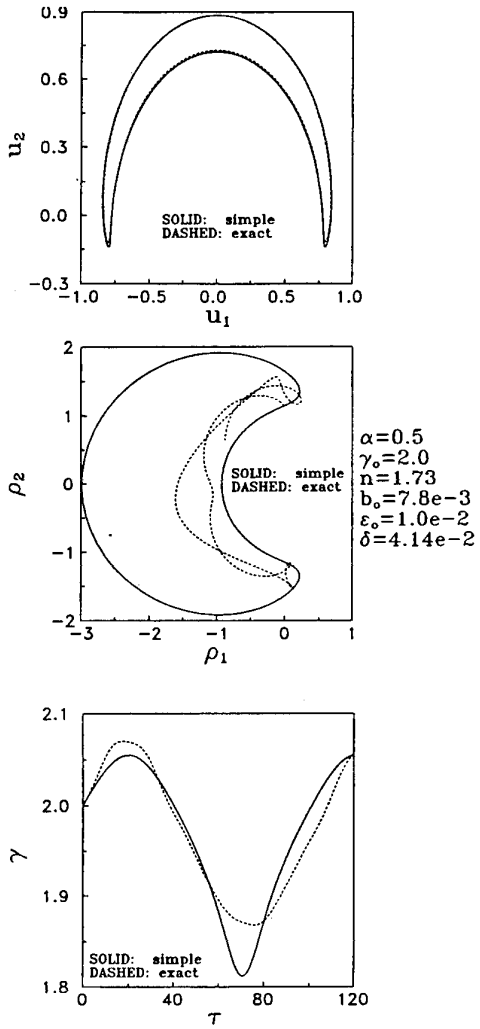

Fig. 4. Trajectories of electrons on the transverse planes (u_1, u_2) and (ρ_1, ρ_2) and temporal evolution of the relativistic factor γ for a pitch ratio $\alpha = 0.5$.

It is evident from the respective figures that at zero initial pitch ratio (which is the case for the application in hand) the agreement is remarkably good as far as the helical momentum is concerned. The small deviations between the two models, as far as the radial displacement and the relativistic factor is concerned, are rather insignificant (the disagreement in γ is less than 1%). The agreement in momenta and to a lesser degree in γ, persists even for a high value of the initial pitch ratio, such as $\alpha = 0.5$. The radial displacement the simplified model predicts is, however highly overestimated (Fig. 4). For applications that require high initial pitch ratio this defect does not pose a major problem since higher radial displacements correspond to a rather conservative prediction for most of the applications (they are undesirable).

5. Operation regime of the beam buncher

The first approximate constant of motion, K_1, which has an evolution rate of order $O(\varepsilon^3)$, allows for u_3 to be expressed in terms of γ and the initial values, i.e., $u_3 = n(\gamma - \gamma_0) + u_{30}$ (the subscript "0" indicates the initial values). The most important information to be obtained from the first constant of the motion K_1 is related to the direction in which the evolution of the beam proceeds. It can be seen that in coordinates $u_3 - \gamma$, the invariance of K_1 corresponds to trajectories represented by a straight line with slope $1/n$ (Fig. 5). Along this straight line, physically acceptable is only the segment for which $u_\perp^2 \geqslant 0$, represented by the inequality $\gamma^2 \geqslant 1 + u_3^2$. Having in mind the initial condition $u_\perp = 0$, $u_3 = u_{30}$, then in order for the system to operate at the expense of the beam, γ must fall below $\gamma_0 = \gamma(u_{30})$. The limiting case is the tangent one with corresponding minimum value of K_1 given by $nK_{1\min} = (n\gamma_0 - u_{30})_{\min} = (n^2 - 1)^{1/2}$. Thus, comparing the slopes of the straight line and the hyperbola $\gamma = (1 + u_3^2)^{1/2}$, one obtains

$$\frac{1}{n} < \frac{d}{du_3}(1 + u_3^2)^{1/2}\bigg|_0 = \frac{u_3}{\gamma}\bigg|_0 = \frac{u_{30}}{\gamma_0} = \beta_0. \tag{5.1}$$

Since $\beta_0 < 1$, a direct result of eq. (5.1) is that slow waves, $n > 1$, must be involved, that is waves with phase velocity $\omega/k < c$. This case corresponds to the anomalous Doppler shift, with

$$kv_z - \omega \approx -\frac{\Omega}{\gamma} > 0. \tag{5.2}$$

Upon considering the case of axial initial velocity, the initial condition for u_2 is $u_{20} = 0$. In this case, the second invariant, K_2, has the value $K_2 = 0$ and u_2 can directly be obtained by means of the integral term appearing in eq. (4.10). To perform the integration the integrand has to be expressed in powers of the denominator. For this purpose we introduce an auxiliary variable ξ, which is the natural parameter by which, e.g. the relativistic factor can be described. Its relation to γ is given by

$$\xi = \frac{1 - ng}{1 - \beta_0 g}\frac{\gamma - \gamma_0}{\gamma_0}, \tag{5.3}$$

where g is the ratio of the field amplitudes given by $g = b_0/\varepsilon_0$ and $\beta_0 = u_{30}/\gamma_0$ is the initial electron velocity. Using

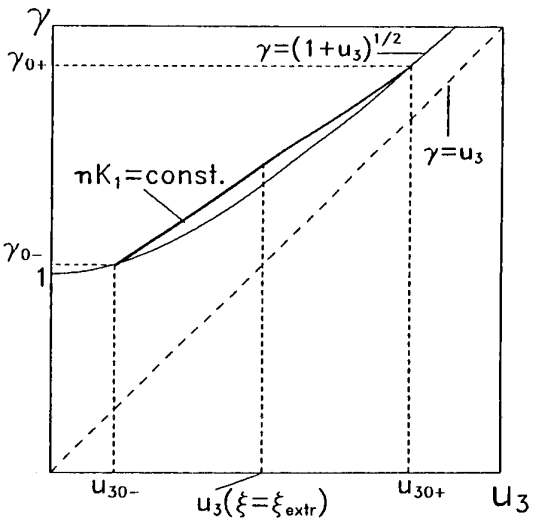

Fig. 5. Variation of the relativistic energy, γ, with the axial momentum u_3, with the invariance of nK_1. For vanishingly small initial transverse velocity $u_\perp$, trajectories are allowed only on the straight line $nK_1 = \text{const.}$ A reduction of γ below its initial value, corresponds to u_{30+} as the proper starting point, while $u_\perp$ attains its maximum value when $\xi = \xi_{extr}$.

this definition for ξ, and for $u_{20} = 0$, upon expressing the linear combinations $\gamma - nu_3$ and $\varepsilon_0\gamma - b_0 u_3$ appearing in the equations of motion in terms of the first invariant, eq. (4.10) yields,

$$u_2(\xi) = \frac{(n^2-1)^2}{(\varepsilon_0 - nb_0)^3} \times \left\{\frac{s_0^2}{2}\xi^2 + \left[s_0 + \frac{a(\varepsilon_0 - nb_0) - 2nK_1(n\varepsilon_0 - b_0)}{n^2-1}\right] \times s_0\xi - nK_1(n\varepsilon_0 - b_0) \times \frac{a(\varepsilon_0 - nb_0) - nK_1(n\varepsilon_0 - b_0)}{n^2-1} \ln(1+\xi)\right\}, \quad (5.4)$$

where $s_0 = \varepsilon_0\gamma_0 - b_0 u_{30}$. Note that initially $\xi = \xi_0 = 0$.

Using eq. (4.8) it is easy to verify that the transverse mechanical momentum $u_\perp = (u_1^2 + u_2^2)^{1/2} = (\gamma^2 - 1 - u_3^2)^{1/2}$ can also be expressed in terms of the aforementioned auxiliary variable ξ. In this way, one can readily obtain

$$u_\perp^2(\xi) = \frac{n^2-1}{(\varepsilon_0 - nb_0)^3} s_0^2(2\xi_{extr} - \xi)\xi, \quad (5.5)$$

where a quantity ξ_{extr} has been introduced to render $u_\perp$ in relatively compact form. This quantity is given by

$$\xi_{extr} = \frac{(\varepsilon_0 - nb_0)(\gamma_0 - nu_{30})}{(n^2-1)s_0}. \quad (5.6)$$

Note that at $\xi = \xi_{extr}$, $u_\perp$ attains its maximum value.

Using the expressions (5.4) and (5.5) one can immediately obtain the dependence of u_1, from the relation $u_1^2(\xi) = u_\perp^2 - u_2^2$. This relation renders the equations of motion integrable, since now all quantities are expressed as functions of ξ. The consequences of the integrability of the system in the design of an autonomous beam buncher will now be discussed. For the sake of convenience we suppress the subscript "0" in both ε_0 and b_0.

In order to choose the appropriate range of values of the normalized field amplitude ε, such that at the output $u_\perp$ is maximum, we consider the case in which $|\xi|$, as well as the normalized frequency mismatch $\Delta = n\beta_0 - 1 + a/\gamma_0$ are small quantities. The assumption $\Delta \ll 1$ describes the requirement that the interaction takes place close to cyclotron resonance. On the other hand, it has been shown that ξ should not approach ξ_{extr}, in order for our model to be valid. In addition, we expect that ξ should remain a small quantity, since its development is directly produced by the radiation fields, for which $\varepsilon, b \ll 1$. Therefore, in eq. (5.4) the Taylor expansion of $\ln(1+\xi)$ is employed, and terms are kept only up to order ξ^2 and $\xi\Delta$. In addition, in eq. (5.5), ξ is neglected compared to ξ_{extr}. The result is

$$u_\perp(\xi) = \gamma_0(n^2-1)^{1/2}\left|\frac{1-\beta_0 g}{1-ng}\right|(2|\xi_{extr}||\xi|)^{1/2}, \quad (5.7)$$

$$|u_2(\xi)| = \frac{1}{2\varepsilon}\gamma_0^2(n^2-1)\left|\frac{1-\beta_0 g}{1-ng}\right| \times \left|\frac{n\beta_0 - 1}{1-ng}\right|\left|\frac{2\xi_{extr}}{n\beta_0 - 1}\Delta - |\xi|\right||\xi|, \quad (5.8)$$

where $\xi_{extr} = -\mathrm{sgn}(\xi)|\xi_{extr}|$, has been taken into account.

It is readily seen from eq. (5.7) that $u_\perp$ is an increasing function of $|\xi|$ with infinite slope at $|\xi| = 0$. Since our objective is to have the largest possible $u_\perp$ at the end of the interaction, $|\xi|$ should also have the largest possible value, which is the one with $|u_1| = u_\perp$. On the other hand, near $|\xi| = 0$, $|u_2|$ increases at a slower rate, since it varies linearly (or quadratically). Nevertheless, this quantity eventually reaches $u_\perp$. This occurs both because of the large coefficient ε^{-1} in $|u_2|$ and because, for larger values of $|\xi|$, $u_\perp(\xi)$ becomes flatter due to the square-root dependence. The value of $|\xi|$ at which $u_\perp(\xi) = |u_2(\xi)|$, cannot be exceeded, since otherwise u_1^2 would acquire nonphysical negative values. Thus the interaction gives the maximum $u_\perp$ for the values of ξ for which $u_\perp(\xi) = |u_2(\xi)|$. This equality holds when ε is given by

$$\varepsilon = A\left|\left(\frac{\Delta}{n\beta_0 - 1} - \tfrac{1}{2}y^2\right)\right| y, \quad (5.9)$$

with

$$y^2 = |\xi/\xi_{extr}|$$

and

$$A = \frac{\gamma_0(n\beta_0 - 1)^2}{\sqrt{2}(n^2-1)^{1/2}|1-\beta_0 g|}. \quad (5.10)$$

It is apparent from eq. (5.9), as well as from Fig. 6, where ε as a function of y has been plotted, that the slope of ε depends on the sign of Δ. One may distinguish two cases. The first case refers to $\Delta \leqslant 0$. There, ε is a monotonously increasing function of y, which means that for every choice of the normalized field amplitude ε, one corresponding value of y is obtained. In particular, if ε increases, e.g. from the value ε_1 to ε_2, the value of y also increases, from the corresponding to point A to point B for $\Delta < 0$, or from point C to point D for $\Delta = 0$. In addition, if ε remains constant and Δ becomes less negative, again the corresponding values of y become larger (from A to C or from B to D). On the other hand, if $\Delta > 0$, then $\varepsilon(y)$ is no more monotonous, exhibiting a local maximum $\varepsilon = \varepsilon_{cr}$ at the point $y = y_{cr}$, where $d\varepsilon/dy = 0$. The characteristic values $(y_{cr}, \varepsilon_{cr})$ can easily be

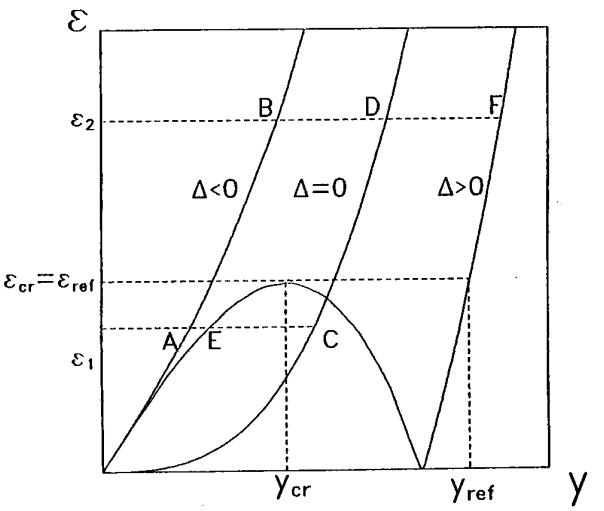

Fig. 6. Normalized electric field amplitude, ε, as a function of the parameter y (which is proportional to the transverse momentum), for negative, zero or positive frequency mismatch.

found to be

$$y_{cr} = [\tfrac{2}{3}\Delta/(n\beta_0 - 1)]^{1/2}, \tag{5.11}$$

$$\varepsilon_{cr} = A[\tfrac{2}{3}\Delta/(n\beta_0 - 1)]^{1/2}. \tag{5.12}$$

If $\varepsilon = \varepsilon_1 < \varepsilon_{cr}$ the value of y corresponds to point E, but as soon as the value ε_{cr} is reached, a sudden discontinuity occurs, from the value y_{cr}, given by eq. (5.11), to the value $2y_{cr}$. For even longer values of ε, the corresponding value of y increases even further, but at a slower rate, since the curve $\varepsilon(y)$ of eq. (5.9) is already very steep. If Δ is more positive, the values of y are larger, but at the same time the critical value ε_{cr} is also larger.

As has been mentioned in the introduction, the objective of this paper is to investigate the potential of an axial velocity beam to generate slow waves and at the same time to become azimuthally bunched. Clearly, the larger its transverse momentum, the more useful such a bunched beam is expected to be. Accordingly, we are interested to have at the end of the interaction the largest possible value of y, since $y \propto \xi^{1/2} \propto u_\perp$. At the same time technological constraints limit the acceptable values of ε to about $\varepsilon \simeq 10^{-2}$ (corresponding e.g. to electric fields of 10 MV/m and frequencies of about 100 GHz). Besides, the very applicability of eqs (4.4)–(4.7) is limited to values $\varepsilon \ll 1$. Finally, to have the cyclotron resonance dominate the interaction, the normalized frequency mismatch Δ should also be of the order of a few percent. For all these reasons, the combination of a large value of y with a not too large value of ε appears to require $\Delta > 0$ and $\varepsilon = \varepsilon_{cr}$, in order to produce $y = 2y_{cr}$. However one would expect that at $\varepsilon = \varepsilon_{cr}$ a singular point would appear in the electron trajectories, in particular a saddle (X-point). It is well known that near a saddle the trajectories are highly sensitive to small deviations in the initial conditions. Thus, including these considerations, one should treat the values $\varepsilon = \varepsilon_{cr}$ and $y = y_{cr}$ rather as indicators for the magnitude of the required input and expected output. Summing up, a potential design of a beam buncher should use as reference values (around which an optimization could be performed) the following:

(a) A small positive frequency mismatch, $\Delta \gtrsim 0$.

(b) A radiation field amplitude corresponding to somewhat above $\varepsilon_{ref} = \varepsilon_{cr}$.

(c) An expected output transverse momentum corresponding to somewhat above $y_{ref} = 2y_{cr}$.

Using these conclusions one can associate the reference value of the normalized radiation fields, the reference value of the output transverse momentum $u_\perp$ and the corresponding efficiency $\eta = (\gamma_0 - \gamma)/(\gamma_0 - 1)$ to the electron beam input (i.e. γ_0 or β_0) and radiation field dispersion characteristics n or n^{-1}). Recalling that $\Delta = n\beta_0 - 1 - a/\gamma_0$ is the frequency mismatch normalized to ω, the results are:

$$u_\perp = f(\gamma_0, n)|\varepsilon - \beta_0 b|^{1/3}, \tag{5.13}$$

$$\Delta = \frac{6}{f(\gamma_0, n)}|\varepsilon - \beta_0 b|^{2/3}, \tag{5.14}$$

$$\eta = \frac{16\gamma_0}{(\gamma_0 - 1)(n^2 - 1)f(\gamma_0, n)}|\varepsilon - \beta_0 b|^{2/3}. \tag{5.15}$$

These relations indicate a simple scaling of $u_\perp$, Δ and n with the amplitude of the radiation fields. In particular, typical values of the radiation fields (e.g. $|E_\perp + v_\parallel \times B_\perp| \simeq$ 3 MV/m) at 300 GHz correspond to values $|\varepsilon - \beta_0 b| \simeq 10^{-3}$, so that $u_\perp$ is expected of the order of 0.1, while Δ and η are expected of the order of 1%. The exact values of these quantities depend on the relative values of γ_0 and n, as expressed primarily by the function $f(\gamma_0, n)$. This function is defined by

$$f(\gamma_0, n) = 2\left(4\gamma_0 \frac{nu_{30} - \gamma_0}{n^2 - 1}\right)^{1/3}$$

$$= 2[4\gamma_0^2\gamma_{ph}^2(\beta_0 - \beta_{ph})]^{1/3}, \tag{5.16}$$

where the last expression is obtained by using the phase velocity $\beta_{ph} = 1/n$ and the corresponding relativistic factor $\gamma_{ph} = (1 - \beta_{ph})^{-1/2} = n/(n^2 - 1)^{1/2}$. It can be immediately seen that $f \geqslant 0$, for $\beta_0 \geqslant \beta_{ph}$, since then the requirement for the anomalous Doppler shift is satisfied. For $\gamma_0 \geqslant \gamma_{ph}$, the function f is monotonously increasing with γ_0, while as function of n it has a maximum when

$$n = \frac{\gamma_0 + 1}{u_{30}}. \tag{5.17}$$

Recalling that our objective is to provide the theoretical background for the design of a buncher for cyclotron resonance applications, it appears that the choice of n from this relation would be optimal, since it maximizes the output, $u_\perp$. However, it turns out that this choice is not particularly suited to high-frequency applications, since it requires too high magnetostatic fields. This can be seen from the definition of Δ, which gives

$$|a| = nu_{30} - \gamma_0 - \gamma_0\Delta. \tag{5.18}$$

For the choice of eq. (5.17), the dominant term in this relation gives $nu_{30} - \gamma_0 = 1$ for any value of γ_0. Recalling the definition $a = eB_0/m\omega = \Omega_0/\omega$, this means that $\omega \simeq |\Omega|$, limiting the operation frequency to values of the order of 100 GHz. To be able to extend the operation of the buncher into the submillimeter regime, values of $nu_{30} - \gamma_0$ below unity have to be chosen (but not too close to zero, to avoid the presence of the competitive axial TWT interaction). Sure enough such values would reduce the value of $u_\perp$ obtained by the interaction, but this reduction is expected to be small, in view of the third-root dependence in eq. (5.16).

In order to quantify these arguments and at the same time present the results of eqs (5.13)–5.15) graphically in a way which is both compact and easy to use, we introduce the normalized magnetostatic field at exact cyclotron resonance (i.e. when $\Delta = 0$). In view of eq. (5.18), this quantity is defined by

$$a_0 = nu_{30} - \gamma_0 \tag{5.19}$$

and can serve to give the refractive index n [or the wave phase velocity $n^{-1} = u_{30}/(a_0 + \gamma_0)$] needed for a given beam. This quantity is important in two aspects: First, apart from the small term $\gamma_0\Delta$ in eq. (5.18), $|a| = a_0$, so that a_0^{-1} ($\simeq \omega/|\Omega_0|$) gives by what factor the nonrelativistic gyrofrequency is multiplied. Second, in eq. (5.19) n is a linear function of a_0, which for $a_0 = 0$ gives the value $n = \gamma_0/u_{30}$ (for which the axial resonance is present and $u_\perp = 0$), while $a_0 = 1$ corresponds to the value of eq. (5.17) (which maximizes $u_\perp$). Values $a_0 > 1$ are in principle acceptable, but of no interest, since they correspond to both $u_\perp < u_{\perp_{max}}$ and $\omega/|\Omega_0| > 1$.

Using the parameter a_0 instead of the refractive index, in Fig. 7 we present the dependence on a_0 of the transverse

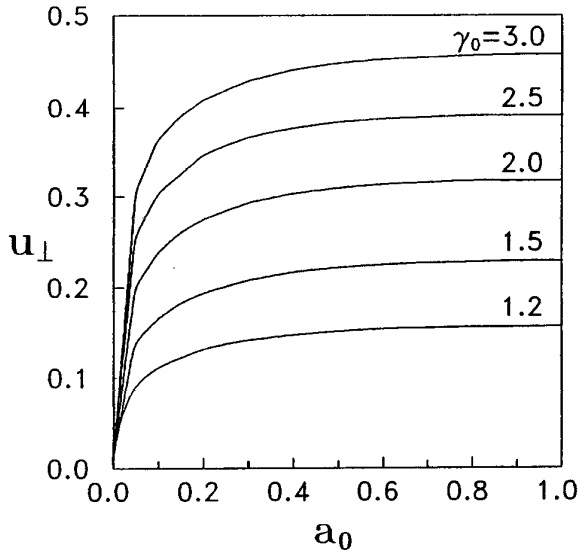

Fig. 7. Normalized transverse momentum $u_\perp$ generated by the interaction, for various values of the beam energy, γ_0, as function of the normalized magnetostatic field at resonance, for appropriate choice of the normalized frequency mismatch, Δ, with the normalized radiation field amplitude at the value $|\varepsilon - \beta_0 b| = 10^{-3}$.

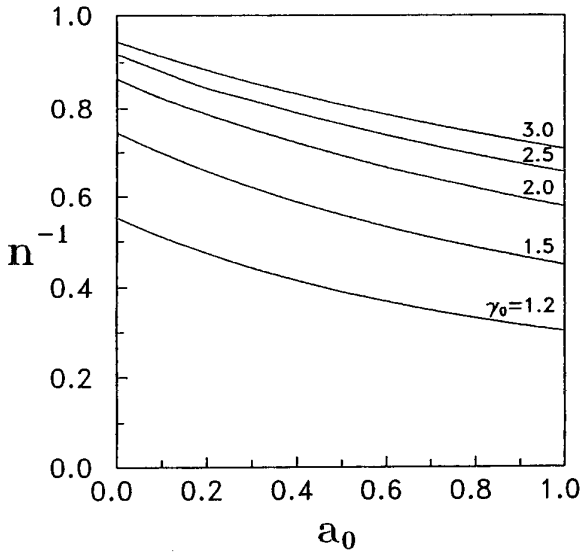

Fig. 8. Normalized phase velocity $1/n$ needed for the interaction, for various values of the beam energy, γ_0, as function of the magnetostatic field at resonance.

momentum $u_\perp$ produced by the interaction, for various values of the relativistic factor γ_0 (or, of the beam voltage $V_b = (\gamma_0 - 1) \times 511\,\mathrm{KV}$). For concreteness we have chosen $|\varepsilon - \beta_0 b| = 10^{-3}$ as a typical value for the normalized radiation field amplitude, while for other values the simple (third-root) scaling of eq. (5.19) can be directly applied. In Fig. 7 it is noted that a higher-voltage beam produces more transverse momentum. The most important feature is however the relative insensitivity of $u_\perp$ with a_0. Sure enough, the maximum of $u_\perp$ appears when $a_0 \simeq 1$ [i.e. when eq. (5.17) is satisfied], but even as far away as at $a_0 = 0.1$ (i.e. for $\omega \simeq 10\Omega_0$) the relative reduction of $u_\perp$ is only 20% of the maximum. This indicates the suitability of the buncher for high-frequency operation.

As has been discussed earlier, this interaction requires slow waves for autonomous operation. The necessary dimensionless phase velocity can be obtained directly from eq. (5.19), *viz.* $n^{-1} = u_{30}/(a_0 + \gamma_0)$. This relation is presented in Fig. 8 for various values of γ_0. For $a_0 = 0$, the curves give the phase velocity for the axial (TWT-type) interaction, which is an obvious competitor. However, the curves are the steepest for small values of a_0, indicating that, perhaps even at $a_0 = 0.1$, this resonance can be avoided. Furthermore, for higher voltage beams, high phase velocities, approaching the speed of light, are needed. Such waves are easier to produce, since they require a milder retarding structure.

As the final step in the assessment of the beam buncher, we discuss the requirements for the magnetostatic field (or a) and the expected electronic efficiency, η. The latter is already given by eq. (5.15), while the former requires some detuning from exact cyclotron resonance. The detuning is obtained from the definition of the frequency mismatch, which gives $|a| - a_0 = \gamma_0 \Delta$, with Δ given by eq. (5.14). The curves of $\gamma_0 \Delta$ and η are presented in Fig. 9 for $|\varepsilon - \beta_0 b| = 10^{-3}$ (the typical value) and for $\gamma_0 = 2$. This choice of γ_0 is dictated by the fact that both $\gamma_0 \Delta$ and η have at $a_0 = 1$ a relative maximum at $\gamma_0 = 2$. Hence this value of γ_0 gives the typical dependence of these quantities. Again, for other values of $|\varepsilon - \beta_0 b|$ the simple scaling law of eqs (5.14) and (5.15) can be immediately applied.

6. Discussion

In this paper we have investigated the potential of an axial velocity electron beam, to generate slow waves and to become azimuthally bunched. According to the model discussed in Section 2, the electron beam is considered to be initially unmodulated, monoenergetic, with no initial transverse velocity of each constituent electron, infinitesimally thin and at low current, to be treated as test beam. The electrons are acted upon by a guided mode, under conditions of cyclotron resonance. The dynamical behaviour of the electron beam is described by means of the equations of motion, which have been found (Section 3) to be integrable, since they exhibit two integrals of motion [see eqs (3.1) and (3.4)]. In Section 4 the first invariant gives the conditions for the beam voltage to decrease below its initial value. For ini-

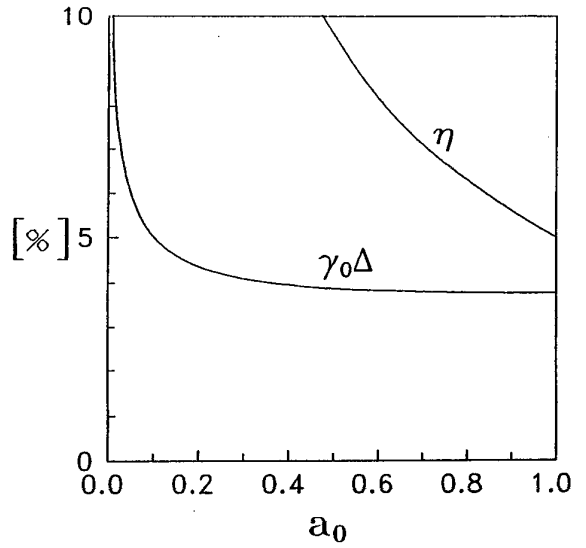

Fig. 9. Required normalized detuning of the magnetostatic field, $\gamma_0 \Delta$, and expected electronic efficiency, η, as function of the normalized magnetostatic field at resonance, for $\gamma_0 = 2$ and $|\varepsilon - \beta_0 b| = 10^{-3}$.

tially vanishing transverse electron momentum ($u_{\perp_0} = 0$), this occurs when the participating waves have phase velocities less than the speed of light in vacuum (refractive index $n = kc/\omega > 1$). The necessary conditions correspond to the anomalous Doppler shift. The appropriately normalized expression for the frequency mismatch Δ and the radiation field amplitudes ε and b have been obtained. It was found (Section 5) that generation of substantial transverse momentum is possible, especially if $\Delta > 0$, and after performing an appropriate optimization to maximize $u_\perp$, expressions for the expected output transverse momentum, as well as for the associated efficiency and the required normalized frequency mismatch, have been obtained given by eqs (5.13)–(5.15). A significant parameter, a_0, was introduced to present the normalized magnetostatic field at cyclotron resonance. It was shown that even when $a_0 \ll 1$, which leads to substantial frequency upshift, the interaction still generates significant amounts of transverse momentum. In addition it was found that, especially when a highly relativistic beam is used, a wave phase velocity just below the speed of light is needed, facilitating the construction of the necessary retarding structure.

In conclusion, in this paper we have demonstrated that, in spite of the drawback represented by the requirement for slow waves, the Autonomous Beam Buncher appears to be an interesting device which can be easily analyzed on the basis of a simplified model developed and assess in this work. This device,

– takes advantage of the high quality of electron beams with no initial transverse electron velocity,

– is able to generate its own radiation fields,

– requires only moderate rf electric fields to produce a perfect azimuthal bunch.

Acknowledgements

This work has been supported in part by the Commission of the European Communities (Directorate General XII, Fusion Programme). Part of this work has been performed at the Centre de Recherches en Physique des Plasmas (CRPP) of the Ecole Polytechnique Federale de Lausanne during the secondment of one author (J.L.V.), supported by a mobility contract with the Fusion Programme. Constructive discussions with Drs M. Q. Tran and T. M. Tran of CRPP, as well as with Dr C. N. Lashmore-Davies of AEA Fusion, Culham Laboratory, and Dr A. Phelps of the University of Strathclyde are kindly acknowledged.

References

1. Lindsay, P. A., Int. J. Electron. **33**, 289 (1972).
2. Hirshfield, J. L. and Granatstein, V. L., IEEE Trans. Microwave Theory Tech. **MTT-25**, 522 (1977).
3. Sprangle, P. and Dropot, A. T., IEEE Trans. Microwave Theory Tech. **MTT-25**, 528 (1977).
4. Flyagin, V. A. Gaponov, A. V., Petelin, M. I. and Yalpatov, V. K., IEEE Trans. Microwave Theory Tech. **MTT-25**, 514 (1977).
5. Bratman, V. L., Ginzburg, N. S., Nusinovich, G. S., Petelin, M. I. and Strelkov, P. S., In. J. Electron. **51**, 541 (1981).
6. Granatstein,V. L., *et al.* IEEE Trans. Nucl. Sci. **NS-32**, 2957 (1985).
7. Kreischer, K. E., Danly, B. G., Schutkeker, J. B. and Temkin, R. J., IEEE Trans. Plasma Sci. **PS-13**, 364 (1985).
8. Baird, J. M., in "High-Power Microwave Sources" (Edited by V. L. Granatstein and I. Alexeff), (Artech House, Boston-London, 1987), Ch. 4.
9. Granatstein, V. L., in "High-Power Microwave Sources" (Edited by V. L. Granatstein and I. Alexeff) (Artech House, Boston-London 1987), Ch. 5.
10. Vomvoridis, J. L., Int. J. Electron., **53**, 528 (1977).
11. Bratman, V. L., Denisov, G. G., Ginzburg, N. S. and Petelin, M. I., IEEE J. Quantum Electron. **QE-19**, 282 (1983).
12. Fliflet, A. W., Int. J. Electron. **61**, 1049 (1986).
13. Wang, Q. S., *et al.*, Int. J. Infrared Millimeter Waves **12**, 297 (1991).
14. Chu, K. R. and Hirshfield, J. L., Phys. Fluids **21**, 461 (1978).
15. Lashmore-Davies, C. N., Phys. Fluids **B4**, 1047 (1992).
16. Vomvoridis, J. L., IEEE Trans. Nucl. Sci. **NS-30**, 3124 (1983).
17. Ginzburg, N. S., Izv. Vyssh. Uchebn. Zaved. Radiofiz. **22**, 470 (1979); [Sov. Radiophys. Quantum Electron. **22**, 323 (1979)].
18. Kho T. H. and Lin, A. T., Phys. Rev. **A38**, 2883 (1988).
19. Vomvoridis, J. L. and Hambakis, M. A., Int. J. Electron. **71**, 167 (1991).
20. Vomvoridis, J. L. and Iatrou, C. T., Int. J. Electron. **71**, 145 (1991).
21. Iatrou, C. T. and Vomvoridis, J. L., Int. J. Electron. **71**, 493 (1991).
22. Fliflet, A. W. and Manheimer, W. M., Phys. Rev. A **39**, 3432 (1989).

Physica Scripta. Vol. T52, 51–57, 1994

Excitation of Fast Langmuir Wave and Strong Langmuir Turbulence by Two Microwaves: Theory and First Experimental Results

Ya. L. Bogomolov, Yu. Ya. Brodsky, A. M. Feigin, A. G. Litvak, A. O. Perminov and S. P. Shlepnev

Institute of Applied Physics, Russian Academy of Sciences, Nizhny Novgorod, Russia

Received November 22, 1993, accepted January 28, 1994

Abstract

The physical processes that determine limiting parameters of a fast Langmuir wave (FLW) excited by beatings of two electromagnetic waves in plasma are discussed. The typical situation under the conditions of the microwave experiment, when the striction nonlinearity is predominant, is considered. The plasma transition into the strong turbulence state due to the FLW excitation is demonstrated. The dependence of both FLW and strong Langmuir turbulence parameters on a pumping amplitude is obtained. The estimations of microwave experiment are produced. The first experimental results of the FLW excitation by two microwaves are presented.

1. Introduction

The goal of the present paper is to investigate physical processes that determine limiting parameters of laser beat-wave accelerators, and primarily, maximal achievable parameters of a fast Langmuir wave (FLW). This is proposed to achieve by studying excitation of an FLW in homogeneous collisionless plasma by beatings of two microwaves, frequencies of which ω_1 and ω_2 exceed by many times plasma electron frequency ω_p, and $(\omega_1 - \omega_2)$ is close to ω_p: $(\omega_1 - \omega_2) \cong \omega_p$.

The use of microwave radiation gives the possibility to perform experiments with comparatively large spatial ($l \geqslant 1$ cm) and temporal ($T \geqslant 10^{-6}$ s) scales at rather small-sized set-ups and to apply sufficiently simple and reliable diagnostic tools.

The theoretical investigations that have been performed show that a limiting amplitude of the FLW is determined by its modulation instability, which leads to plasma transition into the strongly turbulent state. A distinctice feature of the strong Langmuir turbulence (SLT) excited that way is the presence of a wide inertial interval in its spatial spectrum, since the phase velocity of the initially excited FLW is close to the light velocity c. Besides, the fact that the plasma is practically completely transparent for microwaves (its electron density is low as compared to the critical density) makes the reverse influence of the processes initiated in plasma on the pumping essentially weaker. Thus, there is the possibility to excite an SLT with "controlled" parameters and investigate within one experiment both the processes of FLW and SLT excitation in a rather wide range of parameters.

2. Theoretical model

2.1. *Problem formulation*

The scheme of a beat-wave accelerator is quasi-unidimensional "by birth". That gives the opportunity to evaluate parameters of microwave experiment based on the results of studying the unidimensional theoretical problem. Of great importance in the problem interesting for us is the question about the mechanism of plasma nonlinearity. The use of very strong sources of electromagnetic radiation for FLW excitation leads, within the frames of the unidimensional model, to predominance of the relativistic nonlinearity, whereas in the case of "moderate" pumping amplitudes the nonlinear plasma properties are determined by striction. The evaluation basing on the results presented in this paper shows that this very situation is characteristic for the microwave generators used in our first experiments (see Section 4).

Finally, another feature for developing the theoretical model is plasma's being collisionless. Thus, in the present paper we have the possibility to limit ourselves to the analysis of the unidimensional model for collisionless plasma, nonlinear properties of which are determined by striction.

2.2. *Description of pumping. Role of spatial plasma dispersion*

The source of excitation of an FLW,

$$\boldsymbol{E} = \boldsymbol{x}^0[E(x, t) \exp(\mathrm{i}\omega_0 t - \mathrm{i}\kappa_0 x) + c.c.],$$

within the scheme of a beat-wave accelerator is nonlinear current at frequency $\omega_0 = \omega_1 - \omega_2$ excited in plasma with electromagnetic waves

$$\boldsymbol{E}_{1,2} = \boldsymbol{y}^0[E_{1,2} \cdot \exp(\mathrm{i}\omega_{1,2} t - \mathrm{i}\kappa_{1,2} x) + c.c.].$$

In the case of $\omega_1, \omega_2 \gg \omega_p$, when the dielectric plasma permittivity for electromagnetic waves $\varepsilon_{1,2} = 1 - \omega_p^2/\omega_{1,2}^2$ is close to unity, the expression for the density of the nonlinear current has the following form [1]:

$$\boldsymbol{j} = \boldsymbol{x}^0 \mathrm{i} e\omega_0^2 E_1 E_2^* \exp(\mathrm{i}\omega_0 t - \mathrm{i}\kappa_0 x)/\pi m(\omega_1 + \omega_2)^2 c.$$

The wave number $\kappa_0 = \kappa_1 - \kappa_2 \cong \omega_0/c$ is so small, compared to the characteristic parameter of spatial dispersion r_d^{-1}, $\kappa_0 r_d \cong v_T/c \ll \ll 1$, that traditionally, when describing excitation of an FLW with beatings of two electromagnetic waves, spatial distribution is not taken into account (see, e.g., [2]). However, from the standpoint of searching for maximum achievable parameters of an FLW, the account of spatial distribution is of principle importance, since the relation between dispersion and nonlinearity determines the characteristics of FLW's modulation instability: maximum increment of instability and optimal – growing with highest rate – spatial scale of Langmuir waves λ_{opt}. Since the optimal scale of instability becomes lower as the pumping

grows, in the case of not very low amplitudes of electromagnetic waves the following inequality is fulfilled:

$$\lambda_{opt} \ll \lambda_0, \tag{1}$$

where $\lambda_0 = 2\pi/\kappa_0$ is the length of the FLW.

Due to that, a good approximation for development of the theoretical model is the approximation of the homogeneous FLW field ($\kappa_0 \to 0$). The corresponding condition for the amplitude of the pumping is given in Section 3.2 of the present paper. Above, we have used the following denotations: v_T and r_d are thermal velocity and Debye radius of the plasma electrons, respectively, and e and m are their charge and mass.

2.3. *System of equations for dimensionless values*

The mathematical model corresponding to the physical concept presented above includes the equations for the "slow" amplitude of the Langmuir waves' electric field in plasma $E(x, t)(|\dot{E}/E| \ll \omega_0)$ and for striction perturbations of plasma particle density $\delta n(x, t) = N(x, t) - N_0$ ($N_0 =$ *const.* is non-perturbed plasma density). Besides, for the benefit of SLT study it is sensible to include into consideration the equation for the unidimensional (within our approximation) function of plasma electron distribution $f(v, t)$ aiming both for the theoretical analysis of possible influence of interaction of Langmuir waves with resonance electrons on the efficiency of pumping interaction with plasma, and for revealing the possibility of SLT diagnostic by means of measuring the electron distribution function[1].

As a result, we obtain the following set of equations for dimensionless values:

$$i\frac{\partial e}{\partial \tau} - \frac{\partial^2 e}{\partial \xi^2} - \varepsilon e + ne = -d - \hat{\gamma} e, \tag{2}$$

$$\frac{\partial^2 n}{\partial \tau^2} - \frac{\partial^2 n}{\partial \xi^2} = \frac{\partial^2 |e|^2}{\partial \xi^2} - \hat{\Gamma}\frac{\partial n}{\partial \tau}, \tag{3}$$

$$\frac{\partial F}{\partial \tau} = \frac{\partial}{\partial u}\left[\frac{1}{u}|e_\kappa|^2_{\kappa=\alpha/u}\frac{\partial F}{\partial u}\right]. \tag{4}$$

Here,

$$e(\xi, \tau) = \frac{\omega_0}{\omega_p}\left(\frac{3M}{4m}\right)^{1/2}\frac{E(x, t)}{E_p}, \; n(\xi, \tau) = \frac{\delta n(x, t)}{N_0}\cdot\frac{\omega_0^2}{\omega_p^2}\frac{3M}{4m},$$

$$F(u, \tau) = f(v, t)/f_0, \; f_0 = \frac{256\pi}{3}\frac{N_0}{v_T}\left(\frac{m}{M}\right)^{11/6}\left(\frac{\omega_p}{\omega_0}\right)^{10/3}(6L)^{-5/3},$$

$$d = \frac{\omega_0^3}{\omega_p^2\omega_1\omega_2}\frac{e}{mc}\frac{|E_1||E_2|}{E_p}\left(\frac{3M}{4m}\right)^{3/2}, \tag{5}$$

$$\varepsilon = \frac{3M}{4m}\frac{\omega_0^2}{\omega_p^2}\left(1 - \frac{\omega_0^2}{\omega_p^2}\right), \; u = \frac{v}{v_0}, \; v_0 = v_T\left(6L\frac{\omega_0^2}{\omega_p^2}\sqrt{\frac{M}{m}}\right)^{1/3},$$

$$\alpha = \frac{1}{8\pi}\left(6L\frac{\omega_0^2}{\omega_p^2}\sqrt{\frac{M}{m}}\right)^{2/3}, \; \tau = \frac{\omega_p^2}{\omega_0^2}\frac{2m}{3M}\omega_0 t,$$

$$\xi = \frac{2\omega_p}{3\omega_0}\left(\frac{m}{M}\right)^{1/2}\frac{x}{r_d}, \; E_p = \frac{2mv_T\omega_0}{e}.$$

A numerical investigation of eqs (2)–(4) was performed in an interval of dimensionless length, L, that many times exceeded all the characteristic spatial scales of the physical problem under consideration. The unbounded medium was modeled by means of selecting periodic boundary conditions at the ends of the L interval. In this method of numerical investigation the parameters $\hat{\gamma}$ and $\hat{\Gamma}$, that describe collisionless dissipation of the energy of Langmuir and ion-acoustic waves, are given by the following relations:

$$\frac{1}{L}\int_{-L/2}^{L/2}\hat{\gamma}\cdot e(\xi, \tau)\exp(-i\kappa\chi_0\xi)\,d\xi = \gamma_\kappa \cdot e_\kappa(\tau), \tag{6}$$

$$\gamma_\kappa = -\frac{1}{\kappa^2}\left(\frac{\partial F}{\partial u}\right)_{\kappa=\alpha/\kappa},$$

$$\frac{1}{L}\int_{-L/2}^{L/2}\hat{\Gamma}\frac{\partial n}{\partial \tau}\exp(-i\kappa\chi_0\xi)\,d\xi = \Gamma_\kappa\cdot\frac{\partial n_\kappa}{\partial \tau}, \tag{7}$$

$$\Gamma_\kappa = \sqrt{\frac{\pi}{8}}\kappa\chi_0\left[\sqrt{\frac{m}{M}} + \left(\frac{T_e}{T_i}\right)^{3/2}\exp\left(-\frac{3}{2} - \frac{T_e}{2T_i}\right)\right].$$

Here, $e_\kappa(\tau)$ and $n_\kappa(\tau)$ are spatial Fourier harmonics of Langmuir and ion-acoustic waves,

$$\{e_\kappa(\tau), n_\kappa(\tau)\} = \frac{1}{L}\int_{-L/2}^{L/2}\{e(\xi, \tau), n(\xi, \tau)\}\exp(-i\kappa\chi_0\xi)\,d\xi,$$

$\chi_0 = 2\pi/L$ is a dimensionless minimal "step" of the numerical calculation in the space of wave numbers (κ-space), M and T_i are mass and temperature of plasma ions. Note that an FLW within the constructed model corresponds to the zeroth spatial harmonic of Langmuir waves, $e_0(\tau)$.

3. Theoretical results

3.1. *Results of numerical calculations and their interpretation*[2]

The main physical feature of the model under consideration is revealed when the time dependence of the complete energy density of Langmuir waves, W, is investigated. A typical form of such a dependence is given in Fig. 1 for the case, when there is no dissipation of energy ($\hat{\gamma} = \hat{\Gamma} = 0$, curve (a)), and when there is damping of Langmuir and ion-acoustic waves (curve (b)). Figure 1 shows also the time dependence of the squared amplitude of the FLW (curves (c) and (d)) for the two cases mentioned above. An amazing feature of the analyzed physical system is its coming into the quasi-stationary state even when there is no damping in the system (curve (a)). This feature is manifested under all the circumstances. Specifically, the system also comes into the quasi-stationary state when the energy of Langmuir waves is noticeably dissipated (curve (b)).

The reason for such behavior of the plasma becomes clear when we analyze the time dependencies of real amplitude a_0 (curves (c) and (d) in Fig. 1) and phase φ_0 (Fig. 2) of the FLW, $e_0(\tau) = a_0(\tau)e^{-i\varphi_0(\tau)}$. The results given in Fig. 1 permit us to divide the process running in the plasma into three consequent stages.

[1] It is readily seen that, under the conditions considered here, variation of the plasma ion distribution function can be neglected.

[2] We limit the scope of the present paper to investigation of the case of precise resonance, when the beating frequency ω_0 is equal to plasma electron frequency ω_p. The corresponding case for this situation is $\varepsilon = 0$ in eq. (2). One can state that the case with $\varepsilon \neq 0$ can be fully analyzed qualitatively basing on the results for the case of precise resonance that are given further.

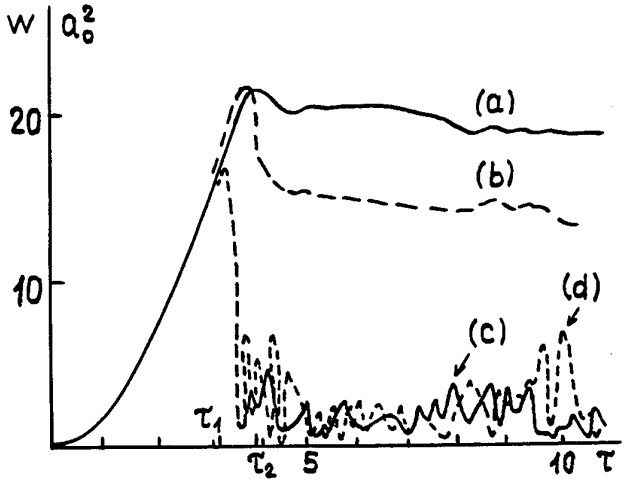

Fig. 1. The total energy density of Langmuir waves (a, b) and energy density of FLW (c, d) *vs.* time. The pumping is $d = 1.27$; the absorption of ion-acoustic waves is insignificant ($T_e/T_i = \infty$); the absorption of Langmuir waves is negligible for curves (a, c) ($M/m = \infty$) and is significant for curves (b, d) ($M/m = 10^4$). The parameter M/m determines the ν_m value for set pumping value (see eqs (11) and (10)).

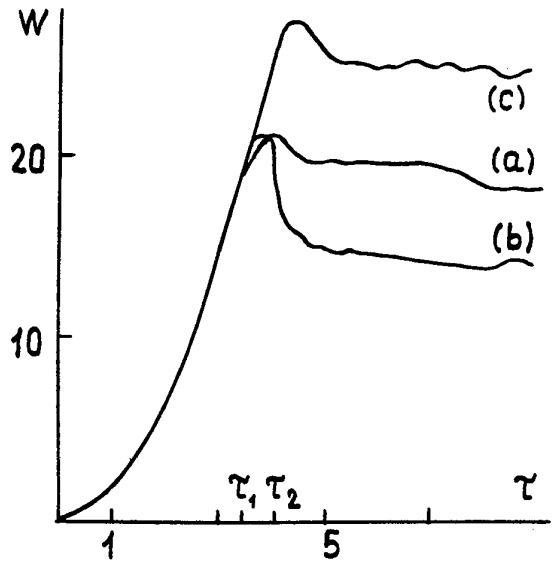

Fig. 3. The total energy density of Langmuir waves vs. time under different absorption of ion-acoustic waves; $d = 1.27$; $T_e/T_i = \infty$ (a, b) and $T_e/T_i = 3$ (c); $M/m = \infty$ (a) and $M/m = 10^4$ (b, c).

At the first stage, $0 \leqslant \tau \leqslant \tau_1$, an FLW is resonantly excited in plasma: density of the energy of Langmuir waves $W = a_0^2$ is density of the energy of the FLW. As the result, the amplitude of the FLW becomes sufficiently high for the modulation instability to come into play. Development of the instability takes place at the second stage, when $\tau_1 \leqslant \tau \leqslant \tau_2$, by this the amplitude of the FLW, a_0, reaches its maximum and then sharply decreases. At the third, "quasi-stationary" stage (when $\tau \geqslant \tau_2$) the value of a_0 undergoes chaotic oscillations, and the density of the FLW energy is an insignificant part of the total energy density of Langmuir waves W.

The dependence $\varphi_0(\tau)$ shown in Fig. 2 explains both the system's coming into the quasi-stationary state (including the absence of dissipation), and the reason for disastrously fast destruction of the FLW at the second stage of the process. It is seen that one of the consequences of development of the modulation instability is the nonlinear shift of the FLW phase, φ_0[3], from the "linear" value, $\varphi_0 = \pi/2$, set at the first stage of the process. The value $\varphi_0 = \pi/2$ corresponds, within the model of eqs (2–7), to the maximally efficient of transfer of the pumping energy to the fast Langmuir wave.

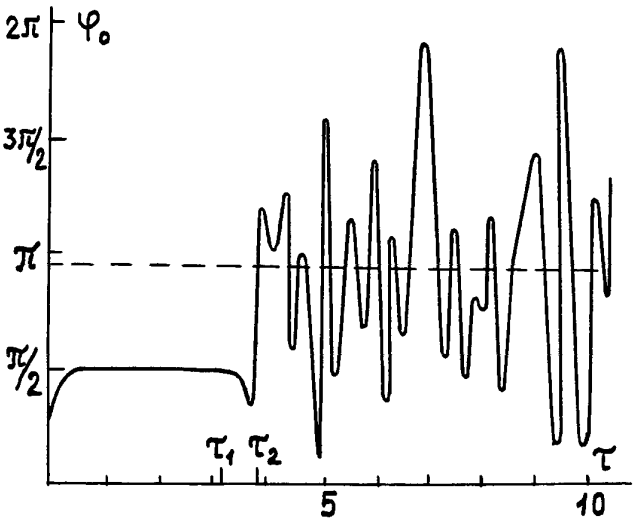

Fig. 2. The FLW phase *vs.* time, $d = 1.27$, $M/m = 10^4$, $T_e/T_i = \infty$.

The shift of phase, φ_0, is caused by interaction of the FLW with other Langmuir harmonics growing as the FLW instability increases. As a result, the phase synchronism between the FLW and the pumping is broken. The value of φ_0 undergoes strong oscillations changing from 0 to 2π. If there is no dissipation in the system, the average over several oscillations value is $\bar{\varphi}_0 = \pi$. That means that in spite of continuous energy exchange between the FLW and the pumping, at the third stage the pumping is, upon the average, "disconnected" from the Langmuir waves. In the presence of dissipation (this very case corresponds to dependence $\varphi_0(\tau)$ in Fig. 2) value $\bar{\varphi}_0$ differs from π such that the energy entering the system would compensate the damping-caused losses.

Those facts are verified by the dependence $W(\tau)$ shown in Fig. 3 for two different ratios of the temperatures of electrons and ions of the plasma. Curve (c) corresponds to $T_e/T_i = 3$, and curve (a) is given for the sake of comparison and calculated for strongly non-isothermal plasma with $T_e/T_e \to \infty$. In the first case the ion-acoustic waves excited during development of the modulation instability are strongly damping, therefore the nonlinear shift of phase, φ_0, that leads to disconnection of the pumping takes place at a noticeably higher density of the energy of Langmuir waves[4].

Figure 4 shows instant spatial spectra of Langmuir waves at the time moments corresponding to the first [Fig. 4(a)],

[3] The phase φ_0 is counted from the initial phase of the beat wave.

[4] Equation (2) yields that $d\varphi_0/d\tau \sim (n \cdot e)_0$, where

$$(ne)_0 = \frac{1}{L}\int_{-L/2}^{L/2} ne \, d\xi.$$

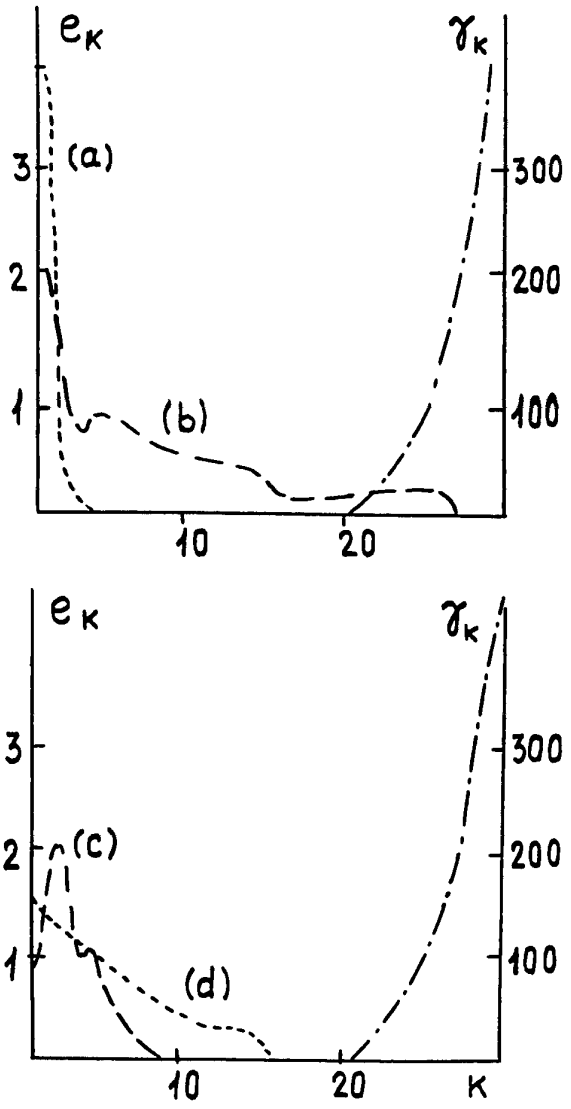

Fig. 4. Evolution of spatial spectrum of Langmuir waves; $d = 1.27$, $M/m = 10^4$, $T_e/T_i = \infty$; (a) $-\tau = 3.15$, (b) $-\tau = 3.975$, (c) $-\tau = 4.425$, (d) $-\tau = 5.1$. Dash-and-dotted line is for the dependence of the linear Landau damping coefficient γ_k on the spatial harmonic number k.

second [Fig. 4(b)] and third [Figs 4(c) and 4(d)] stages of the process. It is seen that after the FLW has grown resonantly at the first stage, at the second, shortest stage the spectrum promptly becomes richer, reaches its maximum width [Fig. 4(b)] and goes into the region of strong Landau damping of Langmuir waves. It is at the second stage, when the time dependence of ν_{eff},

$$\nu_{\text{eff}} = \sum_{\kappa} \gamma_{\kappa} a_{\kappa}^2 \Big/ \sum_{\kappa} a_{\kappa}^2,$$

that characterizes efficiency of energy transfer from Langmuir waves to plasma electrons (Fig. 5) has a sharp maximum. Further evolution of the spectrum [Figs 4(c) and 4(d)] goes in the region of wave numbers, where dissipation is almost absent. By this, $\nu_{\text{eff}} \ll \nu_{\text{m}}$ (see Fig. 5, $\tau > \tau_2$). That corresponds to weak interaction of the FLW with the pumping at the third stage of the process. In other words, the strong Langmuir turbulence excited in plasma in such a way proves to be practically disconnected from the pumping, and the plasma is in the quasi-stationary strongly turbulent state. As the result, the time-averaged spatial spectrum of the Langmuir turbulence (see Fig. 6) in this state has three clearly separate regions: in the "pumping region" $\kappa \leqslant \kappa_{\text{opt}}$ the amplitude of spectral harmonics is weakly dependent on κ; in the "damping region" $\kappa \geqslant \kappa^*$[5] the spectrum is sharply truncated. A significant feature of the way to excite a strong plasma turbulence that we consider here is the presence of a sufficiently wide inertial interval $\kappa_{\text{opt}} \leqslant \kappa \leqslant \kappa_0^*$. That gives the possibility to vary the parameters of the turbulence studies in a wide range by means of changing the pumping amplitude.

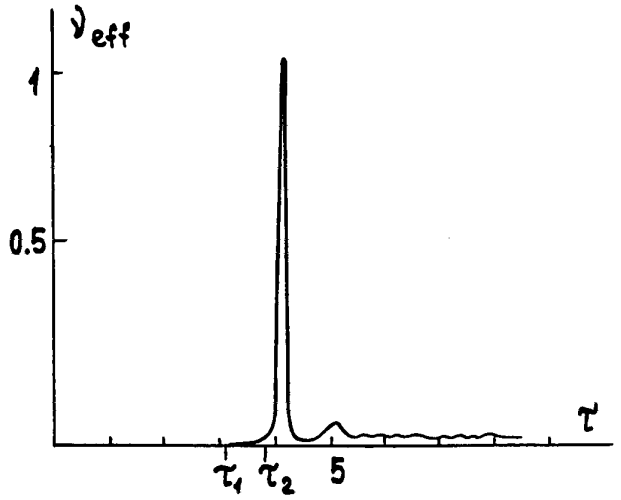

Fig. 5. Efficient Langmuir wave absorption coefficient *vs.* time; $d = 1.27$, $M/m = 10^4$, $T_e/T_i = \infty$.

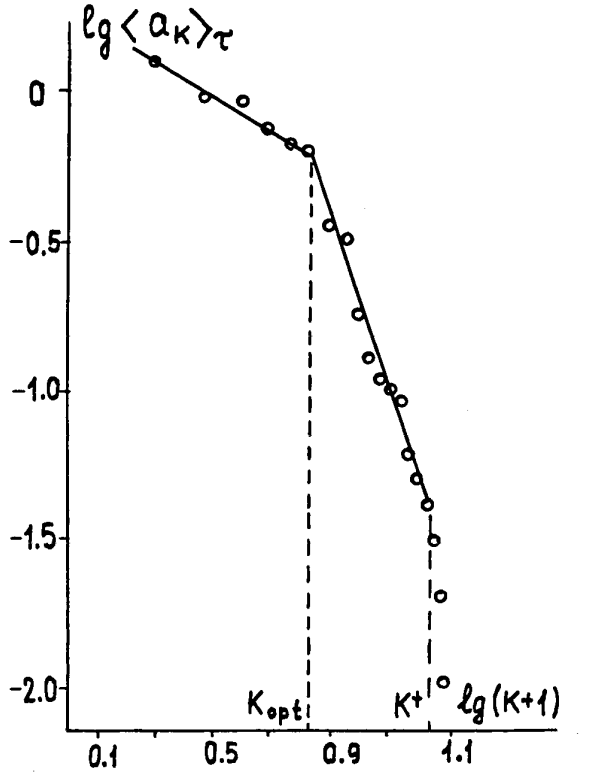

Fig. 6. Time-averaged spatial spectrum of the Langmuir turbulence; $d = 1.27$, $M/m = 104$, $T_e/T_i = \infty$.

[5] In various variables κ^* corresponds to wave number $\kappa r_d = 0.25$.

3.2. *Analytical results and estimations*

The pattern of excitation of an FLW and evolution of an SLT in plasma that has been presented is based on numerical investigation of eqs (2–7), as well as on the analytical results obtained by us. The analytical analysis is grounded upon the fact that the process development goes in three stages, which was revealed during numerical calculations. Besides, the following physical suppositions also correlated with the results of the numerical investigation were made:

1. The "regular" life-time of the FLW is limited by the moment $\tau = \tau_m$, when the amplitude of the "most unstable" Langmuir harmonic (with wave number $\kappa = \kappa_{opt}$) is compared with the FLW amplitude.

2. The saw-shaped "release" of the energy of Langmuir waves into the electron component of the plasma at the second stage (see the dependence $\nu_{eff}(\tau)$ in Fig. 5) is forerun by formation of a quasi-periodic nonlinear "caviton" structure in plasma, which has period $l \cong \lambda_{opt}$ being the optimum scale of the modulation instability[6].

3. Parameters of a single caviton in the structure (amplitude, characteristic width, nonlinear frequency shift) are interrelated in the same way, as in the case of a "free" Langmuir soliton [3].

These suppositions permit us to obtain approximate analytical expressions for the "life-time" of an FLW, τ_m, its limiting amplitude, a_m, optimal scale of the modulation instability, $\lambda_{opt} = 2\pi/\kappa_{opt}$, maximal value of decrement of Langmuir waves' energy dissipation, ν_m, value of dissipated energy, W_d, and average density of the energy of Langmuir waves in the quasi-stationary state, $\overline{W}$.

We will omit intermediate expressions, since the scope of the paper is limited, and give further dependencies of the mentioned values on parameters of the pumping and nonperturbed characteristics of plasma:

$$\tau_m \cong (\Lambda/d)^{1/2}, \tag{8}$$

$$a_m \cong (\Lambda d)^{1/2}, \tag{9}$$

$$\lambda_{opt} \cong 2\pi/(\Lambda d)^{1/3}, \tag{10}$$

$$\nu_m \approx 20\gamma_{\kappa^*} q^2 \exp(-q), \tag{11}$$

$$W_d \approx \frac{\nu_m}{\gamma_{\kappa^*}} a_m^2, \; \overline{W} \approx a_m^2\left(1 - \frac{\nu_m}{\gamma_{\kappa^*}}\right). \tag{12}$$

Here,

$$\Lambda = \ln(\sqrt{2}\, d/a_n^2)$$

characterizes the excess of pumping, d, over the level of thermal noises, a_n^2, q is set by the ratio of wave numbers, $\chi_0 \kappa_{opt}$ and $\chi_0 \kappa^*$, that determine the boundaries of the inertial interval in the SLT spectrum,

$$q \cong 3\left(\frac{2\kappa^*}{\kappa_{opt}}\right)^{2/3},$$

γ_{κ^*} is Landau damping decrement at $\kappa = \kappa^*$ in the "damping region" in κ-space. Relations (8–10) give the possibility to write explicitly the condition of applicability of the model under consideration, which was discussed in Section 2.

Comparison of eq. (8) with the life-time of the FLW found in [4] for the case of predominance of relativistic nonlinearity leads to upper limitation for the pumping power: the "striction" model can be used for $P \leqslant P_b$,

$$P_b(W) \cong 10^6 \frac{S_\perp}{\lambda_{1,2}^2}\left(\frac{10}{T_e(\text{eV})} \cdot 10^5 \frac{m}{M}\right)^{3/2}. \tag{13}$$

Here, $P = \sqrt{P_1 \cdot P_2}$, where P_1 and P_2 are powers (in Watts) of the used generators of electromagnetic radiation at the frequencies ω_1 and ω_2, $S_\perp$ is the area of the transverse cross-section of the electromagnetic beam in the plasma, and T_e is the temperature of plasma electrons in electron-Volts. When we were obtaining eq. (13) it was assumed that $\Lambda = 15$. For the generators of the 3-cm wavelength band that were used by us (see Section 4), the electromagnetic beam with its transverse cross-section $S_\perp \cong 200\,\text{cm}^2$ and argon plasma with the temperature $T_e \cong 10$ eV we have, from eq. (13),

$$P_b \cong 3.5 \cdot 10^7 \text{ (W)}.$$

Note that for the experiments using radiation of CO_2 lasers (see, e.g. [5]) eq. (13) yields, for hydrogen plasma with $T_e \cong 30\,\text{eV}$, the value of "boundary" density of radiation flow q_b:

$$q_b = P_b/S_\perp \cong 10^{14}\ (\text{W/cm}^2).$$

We find the lower limitation for the pumping power from eqs (1) and (10):

$$P(W) > (\gg) 3.5 \cdot 10^{11} \frac{S_\perp}{\lambda_1^2}\left(\frac{v_T}{c}\right)^4. \tag{14}$$

For the conditions of a microwave experiment (see Section 4) we obtain from here

$$P > (\gg) 2 \cdot 10^3 \text{ W},$$

and for the CO_2-laser experiment,

$$q > (\gg) 2 \cdot 10^9 \text{ W/cm}^2.$$

The two latter conditions are, certainly, rather "soft". Note also that unlike condition (13), requirement (14) is not of principle importance for the model consideration; its breach does not result in a qualitative change of the physical scheme of the phenomenon.

4. Microwave experiment: description of the set-up and first experimental results

Figure 7 shows the scheme of the experimental set-up. Magnetrons (1) and (2) radiate electromagnetic waves with frequencies $f_1 = 13\,\text{GHz}$ and $f_2 = 9\,\text{GHz}$ and with maximum output power of radiation $2 \cdot 10^5$ W, $7 \cdot 10^5$ W, respectively. Duration of the generators' pulses is 10^{-5} s. Radiation of the magnetrons is injected into a common waveguide line by means of a wave mixer (5), and is focused into a vacuum chamber (8) through a horn (6) and a lens (7). Diameter of the transverse cross-section of the electron beam in the focal plane is 15 cm. To make efficiency of transportation of the microwave power into the chamber higher, we use matching components: super-critical waveguide (4) in a "shoulder" of

[6] Collisionless damping of the "field" component of cavitons leads to destruction of the regular plasma-field structure by the end of the second stage of the process.

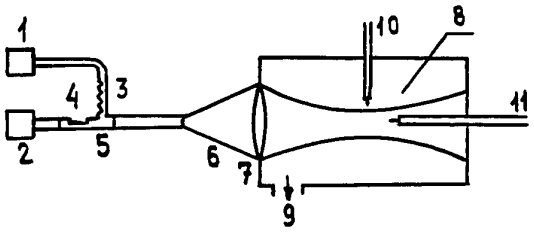

Fig. 7. Scheme of the experimental set-up.

the magnetron with frequency 13 GHz and filter (3) that prevents radiation with frequency 13 GHz from penetration into the "shoulder" of the magnetron with frequency 9 GHz. After the chamber had been degassed (with pump (9) in Fig. 7) down to the pressure of 10^{-5} Torr, it was filled with argon to the working pressure $3 \cdot 10^{-3}$ Torr. The plasma was produced by means of an HF inertial discharge. The special shape of the electrodes of the HF inductor gave the possibility to produce plasma with a high degree of homogeneity both along the chamber axis and in the transverse direction. Plasma density was controlled by means of a Langmuir probe (10) and varied during the work of the inductor (pulse duration 1 μs) from 10^{12} to 10^{11} cm^{-3}. Figure 8 shows the time dependence of the ion current to the Langmuir probe, which was proportional to plasma density. Changing the time interval between the leading front of the plasma pulse and the pulse of microwave radiation we had the possibility to study interaction of the microwave radiation and plasma with various density.

In the first experiments that were performed we used for diagnostic of Langmuir waves an antenna (11), the signal from which was transmitted to an HF receiver, and then, to an oscillograph. The bandwidth of the receiver was 10 MHz and could be tuned within the frequency range ~400 MHz near the beat frequency ω_0. Figure 9 shows the time dependence of the pumping microwave pulse (upper curve) and a typical signal from the antenna (lower curve). It is seen that the grown of the Langmuir waves begins after the microwave generators have been turned on. We specially studied the dependence of efficiency of excitation of Langmuir waves on detuning between the beat frequency of electromagnetic waves ω_0 and plasma electron frequency ω_p. The results of this study are presented in Fig. 10 as the dependence of the amplitude of the signal from the antenna (11) in relative units on plasma density (for the difference between magnetron frequencies 4020 MHz, $P_1 \cong 4 \cdot 10^5$ W, $P_2 \cong 8 \cdot 10^4$ W). Finally, Fig. 11 shows the frequency spectrum of the signal from the antenna in the case of the precise

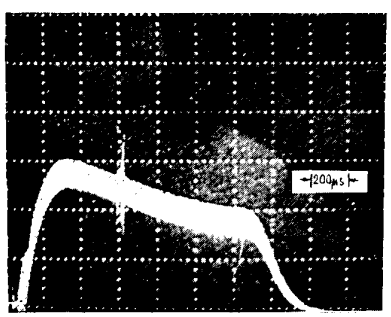

Fig. 8. Typical time dependence of ion current to the Langmuir probe.

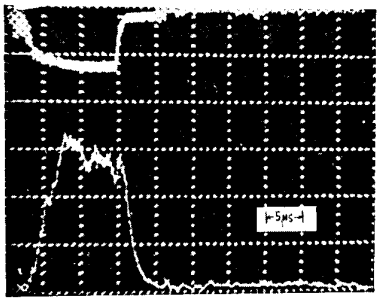

Fig. 9. Typical time dependence of the magnetron pulse (upper curve) and typical signal from antenna (11 in Fig. 7).

resonance of beat frequency ω_0 with plasma frequency ω_p for two values of pumping power, P. Curve (a) corresponds to $P \cong 4 \cdot 10^5$ W, curve (b) to $P \cong 1.8 \cdot 10^5$ W.

These results give the possibility to suppose that when two magnetrons are working synchronously, Langmuir oscillations are excited in plasma. This is evidenced, first of all, by the resonance character of the dependence shown in Fig. 10. Besides, it is seen from Fig. 11 that the width of the spectrum of the received signal exceeds many times the width of radiation of microwave generators (~1 MHz) shown in the figure as a black line.

This makes it possible to believe that the received signal is not the result of direct mixing of the pumping microwave at the double layer that appears in plasma near the antenna.

However, for accurate correlation of the above theoretical concepts with the experimental results one should perform a series of additional measurements. In this aspect of primary importance are dependencies of the parameters of the antenna signal on the pumping power, as well as spatio-temporal characteristics of electric fields in plasma. Those measurements require certain modification of our set-up, first, improvement of the waveguide line parameters in order to eliminate electric breakdowns in waveguides at $P_1 \geqslant 5 \cdot 10^5$ W.

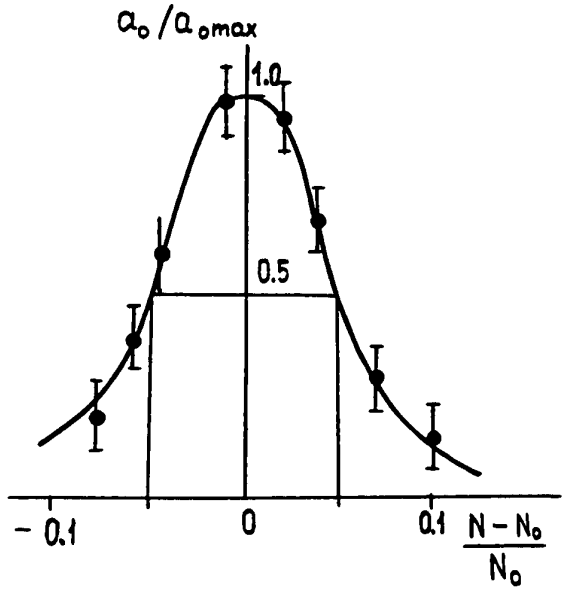

Fig. 10. The amplitude of the signal from the antenna *vs.* plasma density; $f_1 - f_2 = 4020$ MHz, $P \cong 1.8 \cdot 10^5$ W.

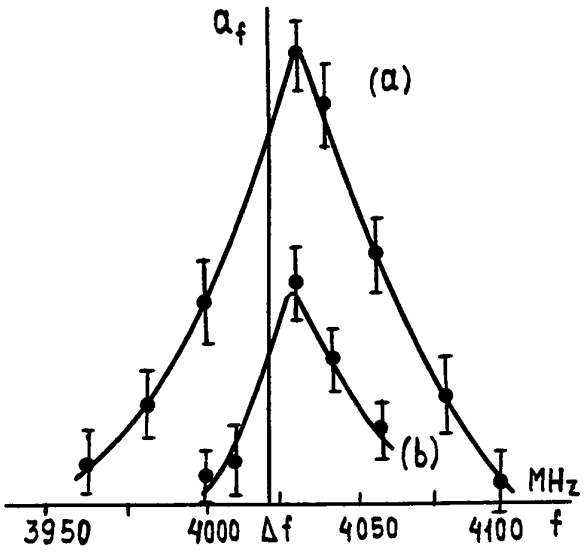

Fig. 11. Frequency spectrum of the signal from the antenna, $\omega_1 - \omega_2 = \omega_p$, $P \cong 4 \cdot 10^5$ W (curve (a)) and $P \cong 1.8 \cdot 10^5$ W (curve (b)).

Acknowledgements

The work presented is supported by the Russian Foundation for Fundamental Investigations, Project #93-02-837 and was partly supported by the Soros Foundation Grant awarded by the American Physical Society.

References

1. Litvak, A. G., Izv. VUZov, Radiofizika **7**, 2 (1964).
2. Tang, C., Sprangle, P. and Sudan, K., Phys. Fluids **28**, 1974 (1985).
3. Rudakov, L. I., Doklady, Akad. Nauk SSSR, **207**, 821 (1972).
4. Bogomolov, Ya. L., Litvak, A. G. and Feigin, A. M., Pis'ma Zh. Eksp. Teor. Fiz. **45**, 1 (1987).
5. Clayton, C. *et al.*, Phys. Rev. Lett. **70**, 37 (1993).

Physica Scripta. Vol. T52, 58–60, 1994

A Measurement of Space-Charge Fields in a Microwave Free Electron Laser

T. C. Marshall and M. A. Cecere

Department of Applied Physics, Columbia University, New York City 10027, U.S.A.

Received November 22, 1993; accepted January 28, 1994

Abstract

We report on the measurement of the electrostatic fields between the space charge bunches, done in an operating Free Electron Laser (FEL) at Columbia University. The FEL uses a 600 kV, 100 A electron beam and a helical undulator with period of 4 cm to produce a few MW of radiation at 24 GHz (12.5 mm). The FEL is operated in the exponential gain regime, and amplifies a signal of several kW which is provided by a magnetron. A specially designed and calibrated probe, described herein, is used to determine the electrostatic fringing field near the electron beam, which is then corrected to give the field within the beam. A field ~60 kV/cm was measured when the FEL power was ~1 MW, and is in the range which is predicted by numerical simulation of the theory.

1. Introduction

In this paper we report on measurements of the space charge field in the bunches of the FEL. Ordinarily, what is of interest in FEL physics is the power produced by the device, or its gain. However, a new scheme [1] has been proposed for a type of IFELA (inverse FEL Accelerator) which takes advantage of the space charge fields between the bunches of electrons in the FEL. In the conventional IFELA, a certain fraction of the electrons are trapped in a "bucket" which is then accelerated by manipulation of the undulator period and/or field; this was recently studied with success in an experiment [2]. In the new version, the IFEL-BWA (Beat Wave Accelerator), the primary electron beam is a low energy but high intensity beam which produces a powerful microwave FEL interaction and bunching; the accleration occurs when a separate bunch of higher-energy "test-electrons" is inserted into the FEL bunches. These "test" electrons may then be accelerated in the FEL space charge field by increasing the phase velocity of the FEL bunches (the ponderomotive wave phase velocity). This can be done by slowly changing the radius of the drift tube wall, for example. Since no measurements of the space charge field have been reported, we now do this measurement in order to establish more firmly some of the underpinnings of the IFEL-BWA.

In our Raman FEL at Columbia, the phase velocity of the beat (ponderomotive) wave is

$$v_p = \frac{\omega_s}{k_s + k_w} + \frac{\omega_p}{\gamma^{3/2}(k_s + k_w)}, \tag{1}$$

where k_s is the laser wavenumber, k_w is the undulator wavenumber, ω_p is the beam plasma frequency, and γ is the beam energy factor. Equation (1) describes the unstable "slow space charge wave" FEL interaction. Experimentally, we use the FEL interaction (1) to grow a wave to saturation power level and bunch the electron beam; then the drift tube radius is tapered so as to vary k_s and thereby v_p. (For the low energy electron beam, the FEL radiation wavelength is long, and so the "laser wave" must satisfy the relation

$$k_s = (\omega_s^2/c^2 - k_\perp^2)^{1/2}, \tag{2}$$

where $k_\perp$ involves the diameter of the drift tube; thus a variable radius waveguide causes a varying k_s.) If the high energy electrons are then injected into the bunches at the correct phase and with the phase velocity of the beat wave at the electron velocity, they can be accelerated by the space charge if the drift tube radius is tapered. In [1], a calculation is done for a microwave FEL, similar to the one described here, and it was found that the field gradient can be as high as 250–500 kV/cm. In this experiment, the current density is lower than that used for the example, and we expect lower accelerating fields.

Figure 1 is a schematic of the microwave FEL experiment [3]. The FEL can be operated either as an oscillator, or as a travelling wave amplifier (TWA) of 24 GHz radiation provided by a magnetron. The magnetron power (measured by a calibrated power meter) is injected from rectangular waveguide into a cylindrical drift tube via a 9 mm ID transition section. In this section, the waveguide excites only the circular TE11 mode (all others are cutoff) which then propagates through the taper and into the FEL. In the opposite direction, a cutoff section which passes the electron beam is adjusted to reinforce maximum microwave power in the forward direction. The undulator is a bifilar helix, 4 cm period, which incorporates a "tapered" initial section so that the electron orbit opens up into a spiral gradually. The electron beam is about 4 mm diameter and is centered into the

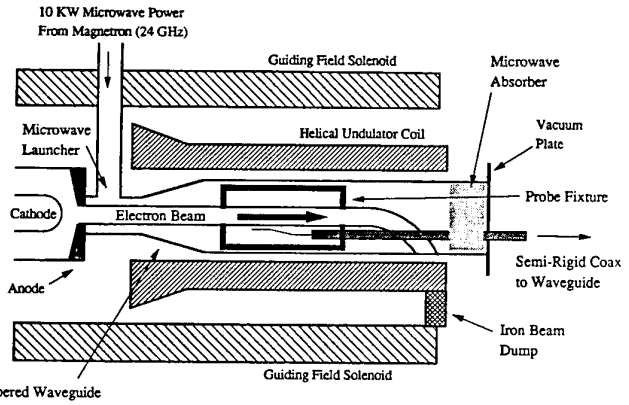

Fig. 1. Schematic of the microwave FEL [3]; the electrostatic probe is located 65 cm downstream along the undulator, toward the end of the solenoid. A drift tube having 24 mm ID was used in this experiment.

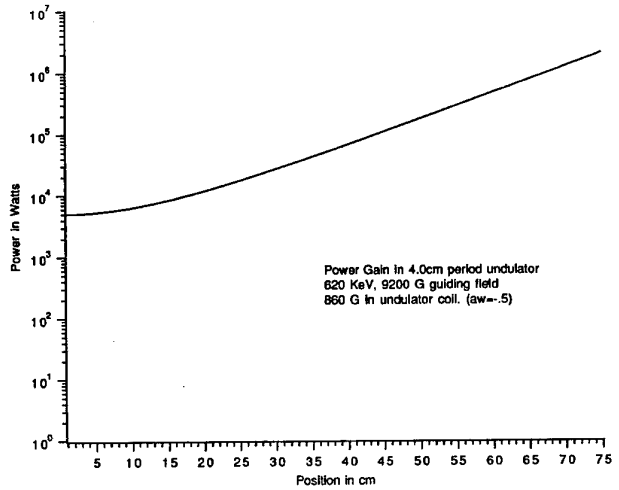

Fig. 2. Computed growth of FEL signal power along the undulator, taking the magnetron input power to be 5 kW and the undulator field to be 860 G ($a_w = 0.5$), beam energy = 620 kV, and guiding field = 9200 G.

24 mm ID stainless steel drift tube (cylindrical waveguide) by taking "witness plate" shots. A solenoidal field of 0.9 T is provided for beam transport; this is necessary in view of the high current density ($\sim 2\,\mathrm{kA/cm^2}$) and low energy ($\sim 600\,\mathrm{kV}$) of the electron beam.

The performance of the device as a FEL is well modelled by a numerical program [4] which computes the growth of the FEL power along the electron beam. The electron beam is modelled in 1D, but the field equations are 2D and therefore include the filling factor.

$$\frac{\mathrm{d}\gamma_j}{\mathrm{d}z} = -\frac{k_s a_s a_w}{\gamma_j}\sin\psi_j + \frac{2\omega_p^2}{k_s c^2} \times (\langle\cos\psi\rangle \sin\psi_j - \langle\sin\psi\rangle\cos\psi_j), \tag{3}$$

$$\frac{\mathrm{d}\psi_j}{\mathrm{d}z} = k_w\left(1 - \frac{\gamma_r^2}{\gamma_j^2}\right) + \frac{k_s a_s a_w}{\gamma_j^2}\cos\psi_j, \tag{4}$$

$$\left(\nabla_\perp^2 + 2ik_s\frac{\partial}{\partial z}\right)u(r, z) = -\frac{\omega_p^2 a_w}{c^2}\left\langle\frac{\mathrm{e}^{-\mathrm{i}(\psi-\phi)}}{\gamma}\right\rangle. \tag{5}$$

Here, γ_j stands for the energy factor of the jth electron, ψ_j is its phase, a_s and a_w are the normalized vector potentials of the radiation and wiggler fields, and u is the amplitude of the TE11 mode of a circular waveguide. Figure 2 shows a typical calculation of power growth along the FEL, starting from an input of 10 kW, of which one half couples to the right circularly polarized wave. It is worth noting, from a theoretical point of view, that it makes sense to use a long-wavelength FEL to drive the charge bunches, as the Raman contribution to the axial electric field scales as ω_p^2/k_s.

2. The axial space charge electric field measurements

The code itself can be consulted for a printout of the space charge field. In Figure 3 we show the computed distribution of electrons over phase, obtained as the amplified 24 GHz FEL wave nears saturation. One can see that about 1/3 of the electrons in the simulation are bunched into a rather narrow spread of phase (about 0.5 radian out of 2π). This is what produces the strong axial electric field.

Figure 4 is a schematic of a probing device which measures the electrostatic field. The device is positioned near the

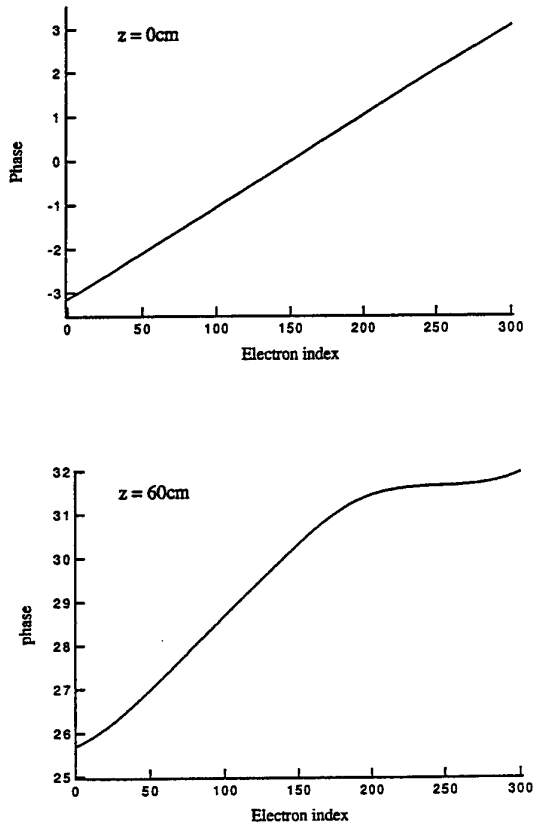

Fig. 3. The distribution of electrons (very closely spaced dots) in phase, as computed from the code, at $z = 0$ (above) and $z = 60$ cm (below) on the undulator. Appreciable bunching occurs near the (arbitrary) phase of 31.5 radians.

end of the FEL, where the magnetron signal has been amplified to about 1 MW level. The microwaves are absorbed by an absorbing baffle which is placed in front of a disk of metal. The metal disk prevents microwaves from entering the device; however, a 5 mm hole permits the bunched electron beam to pass through but not the microwaves. A small coaxial probe, with its 5 mm long central wire oriented parallel to the z-direction, is located a few mm behind the disk and about 1.5 mm from the edge of the electron beam. Before assembly, the probe is calibrated by picking up the transverse electric component of the magnetron wave in the empty drift tube (this field is 2 kV/cm for injected magnetron power of 10 kW). The coaxial probe is held in a lucite jig which also has a hole for the electron beam to pass out of. The device picks up zero field when the

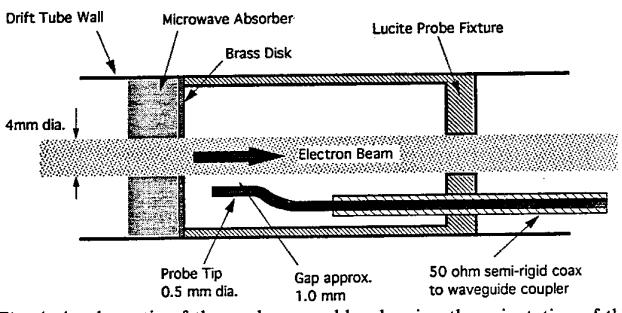

Fig. 4. A schematic of the probe assembly, showing the orientation of the probe which picks up the axial space charge field component. The scale is such that the diameter of the drift tube is 24 mm.

magnetron is on but the beam is off; the pickup is also zero when both magnetron and electron beam are on but the undulator field is zero. Now, it is well known [5] that the bunches of electrons which pass through the device will eventually cause a powerful rf signal to build up downstream of the metal disk. For this reason, we locate the probe close to the metal disk, and place additional microwave absorber behind the coaxial probe.

The coax line from the probe is passed through a vacuum seal and is fastened onto a coax-waveguide coupler. This generates 24 GHz signal in a section of 24 GHz waveguide. An isolator and an attenuator are positioned before a calibrated microwave crystal detector which is itself electrostatically isolated from the system. All the measured fields we report from the probe are referred to the probe response calibrated from the magnetron power in the empty drift tube as described above. The detector responds to power launched by the probe.

Figure 5 shows a typical shot; on it are shown the diode voltage signal (negative-going), the magnetron signal monitored at the input of the FEL (above) and the output of the electrostatic probe (below). For this shot, the undulator field is set at 860 G, which is too low to sustain oscillation, so the FEL is operated as a travelling wave amplifier. (If the field is increased to 950 G, the FEL will oscillate even with the magnetron off). The signal from the probe varies widely, so our measurements relate to a range of observations relating to the peak signal recorded. From the figure, one sees that the magnetron power is switched on just before the high voltage is applied to the cathode, and remains on throughout the shot. The diode voltage in this shot is "flat" for a time ~50–100 nsec, but rises appreciably toward the end of the pulse. Amplification occurs over a certain range of diode voltage swing, and fails when the electron energy is too high (last 50 nsec of the diode voltage pulse).

The power emitted by the FEL was measured by withdrawing the probe device, so that the FEL radiates via a conical horn across the room to another microwave horn which conveys a much-attenuated signal to a shielded room. There, the FEL signal is compared with the signal from the magnetron only, radiating in the same geometry; since the magnetron signal can be quantified using our power meter, we can infer the FEL power. The FEL oscillator produces in excess of 6 MW. The FEL TWA produces about 2 MW. From the code (Fig. 2), we estimate that at the location of the probe, the FEL power level is nearly 1 MW.

At this 1 MW power level, the probe field readings are in the range of 12 kV/cm RMS at the probe location, which is about 1.5 mm beyond the electron beam radius of 2 mm. The probe is oriented so that it senses the axial component of the fringing electrostatic field from the space charge wave on the electron beam. The solutions of space charge waves on an electron "plasma cylinder" can be represented in terms of Bessel functions of imaginary argument [6], from which we obtain that the electrostatic field at the probe location is approximately 27% of the axial component of field referred to the electron beam. Thus, at the 1 MW level, we estimate the electrostatic field actually present in the beam bunches to be ~60 kV/cm peak amplitude. This is to be compared with the results from the FEL Raman code: when the FEL power reaches the 1 MW level, the code predicts an axial electric field of peak amplitude ~45 kV/cm. If the FEL power were to grow to 20 MW, its optimum predicted saturation level in this device, then the peak electrostatic field on-axis from the space charge bunches should be about 150 kV/cm.

These fields are consistent with the assumptions set forth in reference [1]. In that paper, it was found that by using a higher electron beam current density (8.4 kA/cm^2), it should be possible to achieve an accelerating field of roughly 0.5 MV/cm, thereby using the space charge field in a microwave FEL to accelerate a secondary bunch of electrons to much higher energy.

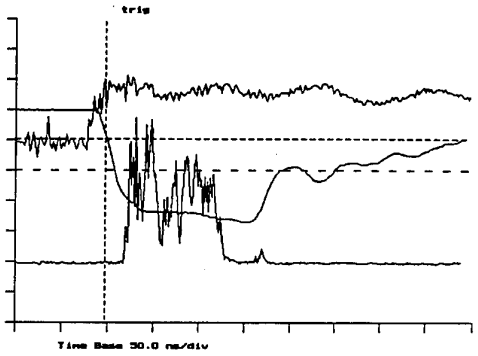

Fig. 5. Top: magnetron power monitor, showing magnetron turns on when the diode voltage appears. Middle: Accelerator voltage at the diode, approximately negative 600 kV on cathode. Lower: electrostatic probe signal. Vertical scale is in arbitrary units of detector voltage.

Acknowledgement

This research was supported by the U.S. Department of Energy, grant 02-91ER40669.

References

1. Cai, S. Y. and Bhattacharjee, A., Phys. Rev. **A42**, 4853 (1990).
2. Wernick, Iddo and Marshall, T. C., Phys. Rev. **A46**, 3566 (1992).
3. Lin, LiYi and Marshall, T. C., Phys. Rev. Lett. **70**, 2403 (1993).
4. See for example, Cai, S. Y., Bhattacharjee, A. and Marshall, T. C., IEEE J. of Quantum Electronics **QE-23**, 1651 (1987).
5. Wurtele, J. S., Bekefi, G., Chu, R. and Xu, K., Phys. Fluids **B2**, 401 (1990).
6. Heald M. A. and Wharton, C. B., in "Plasma Diagnostics with Microwaves" (John Wiley 1965), p. 176.

Physica Scripta. Vol. T52, 61–64, 1994

A Proof-of-principle Experiment of Laser Wakefield Acceleration

K. Nakajima, T. Kawakubo, H. Nakanishi and A. Ogata

National Laboratory for High Energy Physics, Tsukuba, Ibaraki, Japan

Y. Kato, Y. Kitagawa, R. Kodama, K. Mima, H. Shiraga, K. Suzuki and T. Zhang

Institute of Laser Engineering, Osaka University, Osaka, Japan

Y. Sakawa and T. Shoji

Plasma Science Center of Nagoya University, Nagoya, Japan

Y. Nishida and N. Yugami

Utsunomiya University, Utsunomiya, Japan

and

M. Downer, D. Fisher, B. Newberger and T. Tajima

The University of Texas at Austin, Austin, Texas, U.S.A.

Received November 22, 1993; accepted January 28, 1994

Abstract

A principle of the laser wakefield particle acceleration has been tested by the Nd : glass laser system with the peak power of 30 TW and the pulse duration of 1 ps. The particle acceleration up to 18 MeV/c has been demonstrated by injecting 1.0 MeV/c electrons emitted from a solid target by an intense laser impact. The corresponding field gradient achieves 1.7 GeV/m.

1. Introduction

Recently there has been a great interest in laser-plasma accelerators as next generation particle accelerators because of their potential for ultrahigh accelerating gradients and compact size compared with conventional accelerators. It is known that the laser pulse is capable of exciting a plasma wave propagating at a phase velocity close to the velocity of light by means of beating two-frequency laser pulses or an ultrashort laser pulse [1]. These schemes came to be known as the Beat Wave Accelerator (BWA) for the beating laser driver or as the Laser Wakefield Accelerator (LWFA) for the short pulse laser driver. Experimental activities around the world have focused on the BWA scheme using CO_2 and Nd : glass lasers [2], primarily becase of lack of intense ultrashort pulse lasers. A possible advantage in the BWA is efficient excitation of plasma waves due to resonance between the beat frequency of two lasers and the plasma frequency. On the other hand, a fine adjustment of the beat frequency with the plasma frequency is necessary. In the mean time, the LWFA does not rely on the resonant excitation of plasma waves so that a fine tuning of the plasma density is not absolutely necessary. Excitation of the plasma wave turns out to be more efficient in the LWFA than the BWA as the laser intensity increases over $\sim 10^{18}$ W/cm^2 for a Nd glass laser. Furthermore a new prospect of the LWFA are proposed, that is called "self-modulated-LWFA" [3] in which the self-modulation of the laser pulse is accompanied by the resonant excitation of wakefields behind the pulse. If practical and controllable, this scheme will have significant advantages in laser-plasma acelerators. In the LWFA scheme, however, no experiment is reported on the wakefield excitation and its acceleration of particles.

2. Nd : Glass laser system

The recent progress in ultrashort intense laser allows us to test the principle of the laser wakefield acceleration. In our experiment, the laser pulse with the peak power of 30 TW and the pulse duration of 1 ps is delivered by the Nd : glass laser system at Osaka University [4]. The laser system is schematically shown in Fig. 1. This laser system is based on the technique of chirped pulse amplification [5]. A low

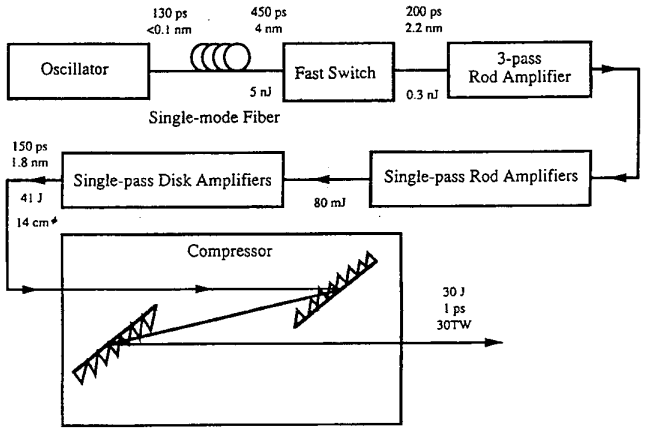

Fig. 1. Schematic diagram of the 1 ps Nd : glass laser system.

energy pulse of 20 nJ with 130 ps duration from the mode-locked oscillator is passed through a single mode fiber of a 1.85 km length to produce a linear frequency chirp. The long linearly chirped pulse with 450 ps duration and 4 nm bandwidth at exit of the fiber is split into two parts each of which is amplified to the maximum energy of 40 J through each broad bandwidth amplifier-chain. One of amplified pulses with 200 ps duration and 1.8 nm bandwidth is compressed to 1 ps duration by a pair of gratings. The other uncompressed pulse is focused on the solid target to produce an electron beam.

3. Experimental setup

The experimental setup is schematically shown in Fig. 2. The laser beam with a 140 mm diameter from the compression stage is focused by a 3.1 m focal length lens of f/22 into the vacuum chamber filled with a He gas to a spot size of 80 μm. The peak intensity of the order of 10^{17} W/cm^2 can be achieved so that a fully ionized plasma can be created in a fast time scale ($\leqslant$10 fs) due to the tunneling ionization process. The threshold intensity for the onset of tunneling ionization is 8.8×10^{15} W/cm^2 for He^{2+} ion [6]. With a 10 TW laser pulse focused into the He gas, the fully ionized plasma can be produced over more than 60 mm around the beam waist. The compressor grating-pair, the 10° mirror and the focusing lens are installed in the vacuum vessel connected to the vacuum chamber for the experiment. These vacuum chambers are evacuated down to $\sim 10^{-5}$ Torr with two turbo molecular pumps.

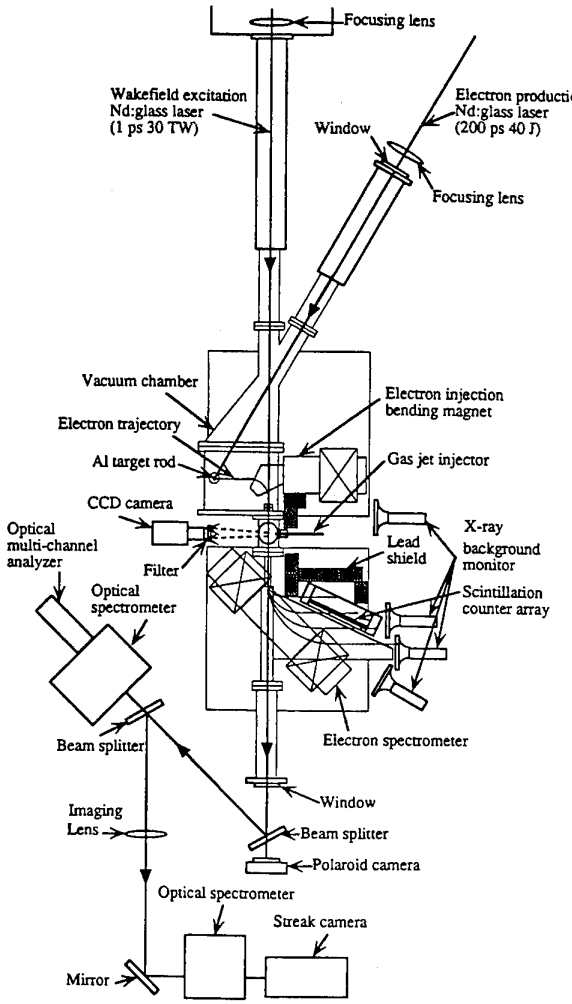

Fig. 2. Schematic of the experimental setup.

Recombination emission from the focal region plasma is imaged onto a charge-coupled-device (CCD) camera to measure the length of the plasma channel. Far-field patterns of the transmitted laser light is probed by a Polaroid film at the exit of the vacuum chamber. The transmitted 1 ps laser pulse is analyzed by the spectrometer-optical multichannel analyzer with a spectral resolution of 1 nm and imaged into the spectrometer-streak camera combination with a time resolution of 0.6 ps and a spectral resolution of 0.33 nm. The optical multichannel analyzer is used for measuring an integrated blueshifting of the laser frequency in the ionization front with a time scale of $\leqslant$10 fs. The spectrometer-streak camera detects a spectral shift resolved with respect to the time axis so that the electron density gradient proportional to the wakefield should be observed as a spectral oscillation of which amplitude represents amplitudes of excited plasma waves. A time profile of the streak image gives a direct observation of the laser pulse form modulated by interaction with the plasma. For the high density plasma experiment, a He gas was filled with the supersonic gas jet injector modified from the automobile fuel injector. For a low density plasma, a gas was statically filled with the flow controlled valve.

Electrons for acceleration are produced from an aluminum solid target irradiated by the amplified 200 ps laser pulse. The *P*-polarized laser beam with 140 mm diameter is focused with a 1.6 m focal length lens to a spot size of 40 μm diameter on the aluminum rod of 6 mm diameter. The peak intensity then exceeds 10^{16} W/cm^2 for 20 J irradiation which is sufficient to induce stimulated Raman scattering instabilities. The target rod of 60 mm length is mounted on the plunger head inside the vacuum chamber and vertically shifted by a 0.5 mm step in each shot to replace an ablated surface into a fresh surface shot by shot. Hot electrons emitted from the target are injected into the waist of the 1 ps pulse laser beam through the 90° bending magnet with an appropriate edge angle so as to achieve double focusing of an electron beam. Since the electron beam duration is as short as the 200 ps laser pulse duration, the optical path length of the 200 ps laser pulse is adjusted to a relative time delay of the 1 ps laser pulse arriving at the interaction point so that the 1 ps laser pulse should overlap with electrons at the focus within $\pm$100 ps. Electrons trapped by wakefields are accelerated in the beam waist of twice the Rayleigh length $\approx$10 mm. The momentum of electrons are analyzed by the dipole field of the magnetic spectrometer placed in the exit of the interaction chamber. This spectrometer covers the momentum range of 6–19.5 MeV/c at the dipole field of 3.9 kG. Upon exiting the vacuum chamber through a 30 μm thick Capton window, electrons are detected by the array of 32 scintillation counters each of which is assembled with a 3 mm thick, 10 mm wide, 60 mm long plastic scintillator coupled to a $\frac{1}{2}$-in. photomultiplier. Pulse heights of the detector are measured by the fast multichannel CAMAC ADCs gated by the trigger pre-pulse in coincidence with the laser pulse. The momentum resolution of the spectrometer is typically 1.0 MeV/c per channel at the 3.9 kG bending field. Figure 3 shows the momentum calibration plot for each

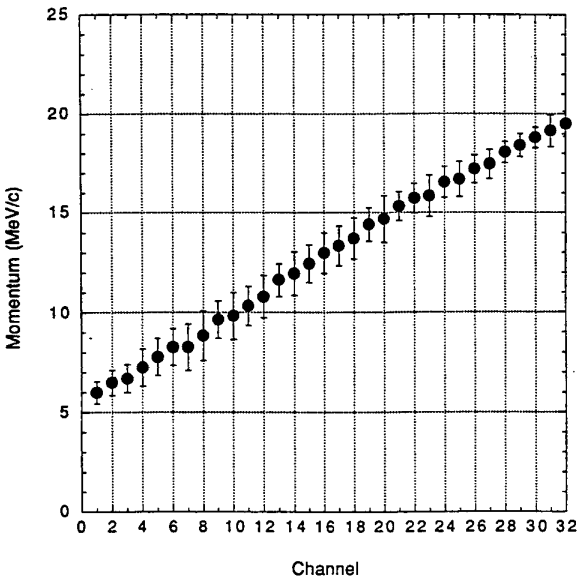

Fig. 3. Momentum calibration of the electron spectrometer obtained from the magnetic field mapping.

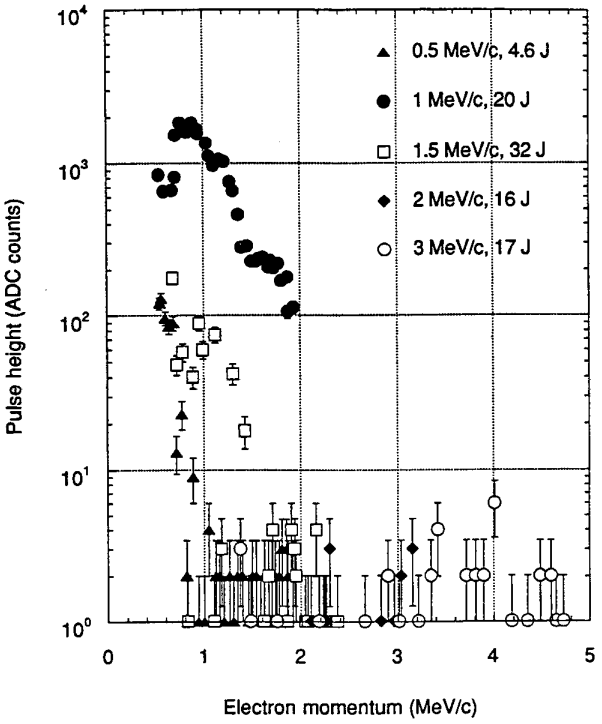

Fig. 4. Momentum distributions of electrons produced by the 200 ps laser pulse at the injection bending field set to 0.5, 1.0, 1.5, 2.0 and 3.0 MeV/c.

channel of the spectrometer. The background X-rays are detected by 4 scintillation counters ($180 \times 160 \times 5\,mm^3$) placed around the vacuum chamber to monitor electron intensity. The vacuum chamber is shielded by 4 mm thick lead sheets to reduce the flux of background X-rays. The back of the detector is entirely surrounded by 50 mm thick lead bricks so that the background output can be reduced to be less than a few counts for all ADC channels.

4. Results and discussion

In the beginning of this experiment, the electron production has been carried out by using only the 200 ps laser pulse. The momentum distribution of produced electrons was measured with the spectrometer for the injection bending field set to 0.5, 1.0, 1.5, 2.0 and 3.0 MeV/c. The data are summarized in Fig. 4. The flux of electrons above 2 MeV/c ($\approx$1.6 MeV kinetic energy) is negligibly small. A number of electrons along with numerous X-rays were produced above the pulse energy of 20 J corresponding to $\sim 10^{16}\,W/cm^2$. This result implies a good agreement with simulation and experimental results of Raman forward scattering instability [7]. For the injection bending field set to 340 G, the intensity of a hot electron beam with momentum of 0.88 ± 0.3 MeV/c was estimated to be more than 10^4 in the interaction region.

In the acceleration experiment the injected momentum of electrons was lower than 1 MeV/c. The noise level has been measured by taking the data for either shot of the 200 ps pulse or the 1 ps pulse. No energetic electrons above 2 MeV/c were observed when only the 200 ps pulse was injected into the target, although a large X-ray signal was detected in the monitor detector. The background level of the detector was not larger than a few ADC counts when only the 1 ps pulse was injected into a gas (160 mTorr He). There was no significant contribution to the detectable signal due to self-trapping of the background plasma electrons and X-ray emission in the plasma. No energetic electrons were observed when both the 200 ps pulse and the 1 ps pulse were injected into an evacuated chamber (5.2×10^{-5} Torr).

All data of electron momentum distribution are shown in Fig. 5. These data points were obtained from shots accompanying an ample signal level in X-ray monitoring detectors. We observed several candidate data points contributed by electrons accelerated up to higher than 6 MeV/c when the gas was injected at the back-pressure of 8 atm. The

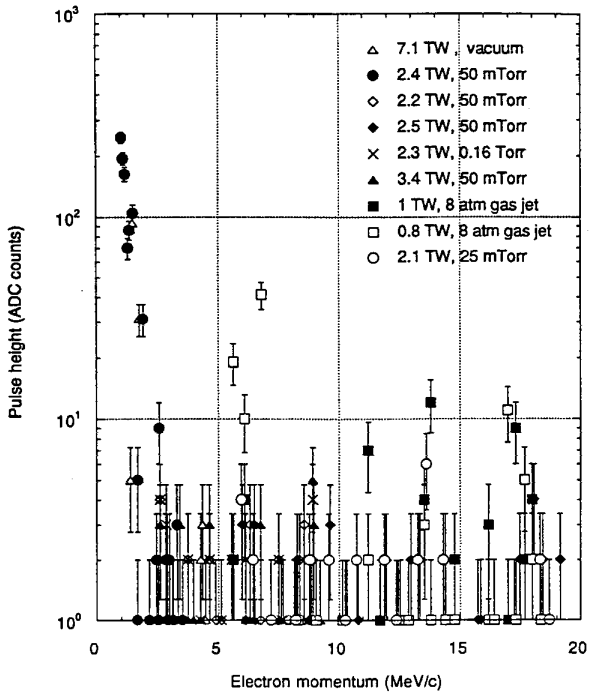

Fig. 5. Momentum distributions of electrons accelerated by wakefields of the 1 ps laser pulse at various powers and gas pressures.

highest momentum of the accelerated electrons was 17.7 ± 0.5 MeV/c. This implies an accelerating gradient of more than 1.7 GeV/m. The linear plasma fluid theory predicts the accelerating gradient of 2.5 GeV/m in the plasma wave excited by a 1 ps Nd : glass laser with the peak intensity of 10^{18} W/cm^2 at the plasma electron density of 2.4×10^{15} cm^{-3}. The simulation indicates that an estimate of the number of electrons accelerated up to more than 6 MeV/c was ~0.4% of the injected electrons with the momentum of 1 MeV/c for the maximum gradient of 1.7 GeV/m.

These results have been not yet conclusive because of lack of the number of the laser shots reproduced in a constant condition. It may be necessary to measure the streak spectrum of the laser pulse and the blueshifts due to the laser-plasma interaction simultaneously with the electron acceleration.

5. Conclusions

Electrons have been observed to be accelerated up to 18 MeV/c when 1 MeV/c electrons emitted by intense laser irradiation on the solid target were injected to the gas jet plasma produced by the 1 ps laser pulse. Momentum of electrons produced by impact of the 200 ps laser pulse was lower than 2 MeV/c. No electrons of higher than 2 MeV/c were detected when only 1 ps laser pulse was focused into the gas or when the 1 ps laser pulse was focused in vacuum with electron injection. We concluded that injected electrons were accelerated in the wakefield excited by the 1 ps laser pulse. A direct measurement of the wakefield in the plasma is pursued.

References

1. Tajima, T. and Dawson, J. M., Phys. Rev. Lett. **43**, 267 (1979); Gorbunov, L. M. and Kirsanov, V. I., Zh. Eksp. Teor. Fiz. **93**, 509 (1987) [Sov. Phys. JETP **66**, 290 (1987)]; Sprangle, P. *et al.*, Appl. Phys. Lett. **53**, 2146 (1988).
2. Clayton, C. E. *et al.*, Phys. Rev. Lett. **54**, 2343 (1985); Ebrahim, N. A., Phys. Canada **45**, 178 (1989); Dangor, A. E. *et al.*, Physica Scripta **T30**, 107 (1990); Kitagawa, Y. *et al.*, Phys. Rev. Lett. **68**, 321 (1992); Amiranov, F. *et al.*, Phys. Rev. Lett. **68**, 3710 (1992); Clayton, C. E. *et al.*, Phys. Rev. Lett. **70**, 37 (1993).
3. Andreev, N. E. *et al.*, Zh. Eksp. Teor. Fiz. **55**, 551 (1992) [JETP Lett., **55**, 571 (1992)]; Krall, J. *et al.* (to be published in Phys. Rev. E).
4. Yamakawa, K. *et al.*, Opt. Lett. **16**, 1593 (1991).
5. Maine, P. *et al.*, IEEE J. Quantum Electron. **QE-24**, 398 (1988).
6. Ammosov, M. V., Delone, N. B. and Krainov, V. P., Zh. Eksp. Teor. Fiz. **91**, 2008 (1986) [Sov. Phys. JETP **64**, 1191 (1986)]; Pentrante, B. M. and Bardsley, J. N., Phys. Rev. **A43**, 3100 (1991).
7. Joshi, C. *et al.*, Phys. Rev. Lett. **47**, 1285 (1981); Estabrook, K. and Kruer, W. L., Phys. Fluids **26**, 1892 (1983); Aithal, S. *et al.*, Phys. Fluids **30**, 3825 (1987).

Physica Scripta. Vol. T52, 65–68, 1994

Excitation of Wakefield and Electron Acceleration by Short Microwave Pulse

Yasushi Nishida, Shiroh Kusaka* and Noboru Yugami

Department of Electrical and Electronic Engineering, Utsunomiya University, 2753 Ishii-machi, Utsunomiya, Tochigi 321, Japan

Received November 22, 1993; accepted January 28, 1994

Abstract

Non-linear large amplitude ion wave excitation by short microwave pulse at the resonance absorption region has been observed. The maximum amplitude of the wave is $\delta n/n \approx 40\%$ in peak-to-peak, when a short microwave pulse of the order of or less than a period of ion oscillation ($\tau_i = 2\pi/\omega_{pi}$) is used. The excited wave propagates to lower density regions and its velocity is a function of its amplitude, $v \propto (\delta n/n_0)^{2.2-2.7}$. At the same time, a strong electron wave is excited after shut-off of the incident microwave pulse and high energy electrons are emitted and accelerated by the excited electron wave wakefield.

1. Introduction

Recent interests of charged particle accelerators are focused on producing much higher acceleration gradient than the present conventional accelerators which have typical acceleration gradient of about 10–20 MeV/m. Plasma based accelerators have been investigated for the last decade and some of new acceleration schemes, including a plasma wakefield accelerator (PWFA), a plasma beat wave accelerator (PBWA) and a $\mathbf{v}_p \times \mathbf{B}$ accelerator (including surfatron), have been proposed and successfully demonstrated in their proof of principle experiments [1]. In addition, a possibility of the charged particle acceleration using a transverse electric field supplemented by a weak external, static magnetic field in parallel to the fluctuating magnetic field has also been discussed [2]. Some of the experimental results based on the above mentioned schemes have shown to give higher acceleration gradients than the conventional methods have. In the plasma based accelerators, it might be easy to achieve more than 100 MeV/m in the acceleration gradient for electrons or positrons or to realize 1 GeV particles within a 10 m accelerator.

A laser wakefield accelerator (LWFA), which has been proposed originally by T. Tajima and J. Dawson [3] and extensively investigated to propose the concept of optical guiding by P. Sprangle *et al.* [4], is one of new mechanism. In this scheme a large amplitude plasma wave is produced by injecting a high intensity laser pulse, the width of which is less than a period of plasma oscillation ($\tau_{pe} = 2\pi/\omega_{pe}$), into the plasma. Ponderomotive force of the laser field acts on the plasma electrons. As the laser fields propagate with a group velocity $\mathbf{v}_g$ in the plasma, the velocity of the resultant large amplitude plasma wakefield is equal to $\mathbf{v}_g$. The advantage of this scheme is the excitation of the plasma wave is that it is independent of the plasma density, that is, non-resonance excitation.

In this paper we like to present experimental results of exciting large amplitude wakefields by injecting short fall-off time microwave pulse in a resonance absorption region. At the same time, large amplitude wakefields in the ion wave regime have also been observed, after shut-off of the short microwave pulse. In these, the pulse width of a period of ion oscillation ($\tau_i = 2\pi/\omega_{pi}$) is the key for exciting wakefields with a velocity much less than the speed of light. Although the exciter of the wakefield, the microwave pulse, does not propagate, remaining in the resonance region, the excited wave propagates with a velocity much larger than that of ion acoustic waves after shutting off the rf field. The excited wakefield has a maximum amplitude up to about $\delta n/n_0 = 40\%$. Such a large amplitude wave has rarely been observed in the ion wave regime except for the ion wave soliton [5] or ion wave wakefield [6], carried out in a double plasma device. The maximum amplitude in these cases is about 20%. Therefore, the wave is also useful for studying strong nonlinear wave phenomena including strong wave-particle interaction.

2. Experimental setup

A schematic view of the experimental apparatus is shown in Fig. 1. Cylindrical, nonuniform argon plasma was produced by pulse discharge (discharge duration of 3 msec and 10 Hz repetition) in a stainless-steel chamber of 1 m length by 60 cm diameter covered with multidipole magnets for a plasma confinement. Acrylic resin board located at far end of the chamber from the horn antenna prevents the microwave reflection in minimum inside the chamber. Typical

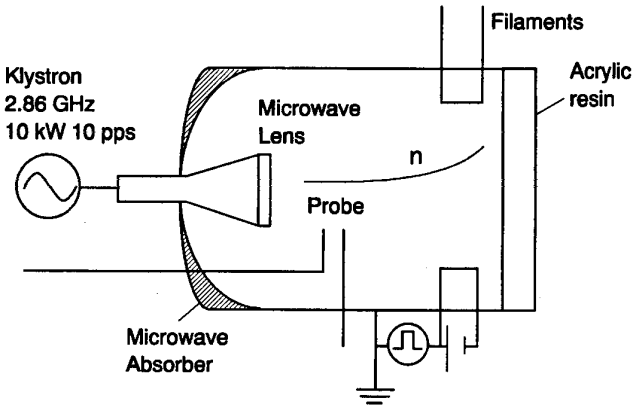

Fig. 1. Schematic view of the experimental apparatus.

* Present address: Tokyo Electric Power Co. Ltd.

plasma parameters are the maximum plasma density $n_e \approx 2 \times 10^{11}\,\mathrm{cm}^{-3}$, electron temperature $T_e \approx 3$–$5\,\mathrm{eV}$, ion temperature $T_i \approx T_e/10$ in an argon gas pressure $\approx 4 \times 10^{-4}$ Torr. The typical density gradient scale length in the axial direction (z-direction) $L_z = (\partial \ln n/\partial z)^{-1} \approx$ 100–150 cm and in the radial direction $L_r = (\partial \ln n/\partial r)^{-1} \approx$ 100–200 are observed. All the plasma parameters including fluctuating wave forms are diagnosed by Langmuir probes with tip of 1 mm length by 0.5 mm diameter, which is made of semirigid cable. Probes are biased in an electron saturation current region when the density fluctuations are observed.

The p-polarized microwave with frequency $f = \omega/2\pi = 2.86\,\mathrm{GHz}$ and a maximum power of 10 kW is irradiated from a horn antenna located at the lower end of plasma density toward the higher density area. The pulse width of the rf wave ranges from 60 ns to 1 μsec in FWHM, and a typical fall-off time, τ_{fall}, from 80–200 ns, where τ_{fall} is defined as the time difference between 10% and 90% of the maximum of the rf power. The pulse shape is not necessarily Gaussian and the fall-off time can become larger than the pulse width.

3. Experimental results and discussion

When a narrow rf pulse is applied, a large amplitude electron plasma wave can be excited at the critical layer where $\omega = \omega_{pe}$ is satisfied. A typical wave form observed at the critical layer is shown in Fig. 2. Here, the top trace shows the electron density fluctuations, the middle trace shows the electric field fluctuations measured through the crystal detector and the bottom trace refers to the incident microwave pulse. Note that the detector used for measuring the electric field fluctuation has a frequency response in the range of 0.01–18 GHz (model HP-463), so that the low frequency fluctuations caused by the waves with frequencies in the ion wave regime were not detected, only the envelope of the electron plasma wave was. A large amplitude electron plasma wave, shown in the middle trace, can run down the plasma density gradient. At the same time high energy electron emission ($\varepsilon > 50\,\mathrm{eV}$, ε is the maximum energy) has been observed as well within this duration (not shown here), that are accelerated by the large amplitude electron plasma waves excited near the critical layer. Here, the incident microwave pulse should have a width of about an ion plasma wave period or less, otherwise the present wave cannot be excited. The electrons could be pushed out as a bunch of electrons by the ponderomotive force of the electromagnetic wave localized near the critical layer. After turn-off of the microwave pulse the positive space charge remains there, and the resultant ambipolar Coulomb force can drive ion waves. Thus, the traveling electron bunch could excite the wakefield in the ion wave regime successively in space. This situation is quite similar to previous results [6], in which a bunch of ions is employed to excite the ion wave wakefield. Therefore, the wave velocity should be very close to the traveling velocity of the electron bunch.

Figure 2 also shows density fluctuations, n, at a resonance point ($n_c = 1.0 \times 10^{11}\,\mathrm{cm}^{-3}$) detected by the probe (upper traces) corresponding to different injection of microwave pulse (lower traces). The incident rf waves denoted by (a), (b) and (c) have pulse widths of 60, 250 and 400 ns with fall-off

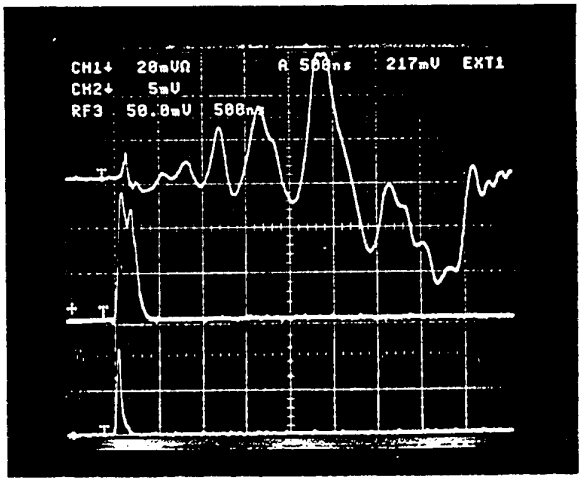

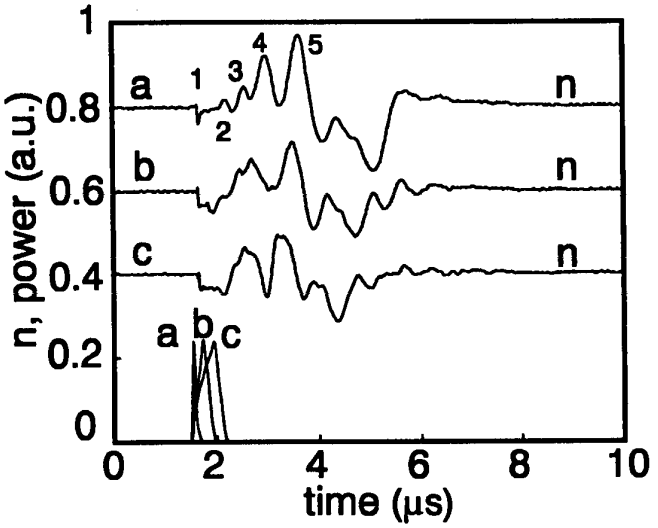

Fig. 2. Typical wave forms excited by the short microwave pulse. Top: Oscilloscope trace of the electron density fluctuation in the top trace, the envelope of the high frequency electric field fluctuation, $|E^2|$, ($f \geq 10\,\mathrm{MHz}$) in the middle trace and the envelope of the incident microwave pulse in the bottom trace. Bottom: The density fluctuations at the resonance region irradiating with rf pulses with various fall-off times, τ_{fall}. a: $\tau_{fall} = 80$ ns, pulse width = 60 ns. b: $\tau_{fall} = 170$ ns, pulse width = 250 ns. c: $\tau_{fall} = 180$ ns, pulse width = 400 ns.

times of 80, 170 and 180 ns, respectively. The maximum power of all these is 4.5 kW. The maximum amplitude, $\delta n/n_0$, of (a), (b) and (c) are 0.38, 0.28 and 0.23, respectively. All waveforms in the density indicate that large amplitude density fluctuations are excited after shutting off the microwave. Density dips due to ponderomotive force can be seen just when the rf pulse is irradiated. Numbers from 1–5 denoted in the trace (a) indicate indexes for later convenience to explain the characteristics of these waves.

Hereafter, we concentrate on the lower frequency fluctuations. The relation between the fall-off time of the rf pulse (τ_{fall}) and the amplitude $\delta n/n_0$ is shown in Fig. 3. Larger amplitude waves (>30%) are excited when the microwave pulse with shorter fall off time, $\tau_{fall} < 120$ ns, is irradiated. This result can be explained by the relation between the period of the ion wave oscillation (τ_{pi}) and the fall-off time (τ_{fall}) as the explanation of the mechanism for the wakefield excitation. The ion plasma frequency, ω_{pi}, calculated by using the experimental parameters, is estimated to be $\approx 6 \times 10^7\,\mathrm{s}^{-1}$, correponding to a period of ion wave oscil-

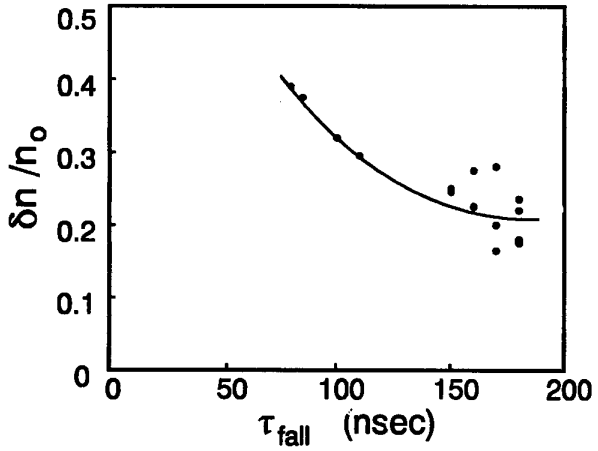

Fig. 3. Maximum amplitude of $\delta n/n_0$ as a function of fall-off time τ_{fall}.

lation of $\tau_{pi} \approx 100$ ns. A large amplitude wave is excited when the fall-off time is less than the characteristic time of the ion oscillation.

In the theory of the LWFA, the irradiated laser pulse propagates with the group velocity v_g in the plasma, therefore the generated wakefields propagate after the laser pulse has passed by. There are differences between the experiments and the LWFA theory. The velocity of the wakefield can be decided by the dispersion relation, because the effective velocity of the rf pulse for excitation is zero at the resonance point, the exciting layer. The excited wave is an ion wave because the fall-off time (τ_{fall}) of the incident rf field has a relation $\tau_{pe} \ll \tau_{fall} \leqslant \tau_{pi}$. Therefore, we can say that our experiments have demonstrated the special case of the LWFA ($v_g \to 0$).

Figure 4 shows a time-space distribution of the fluctuation obtained by scanning the probe in the z-direction. The waves were excited at the resonance point ($z \approx 22$ cm) and propagated toward the lower density region. The first wave, which is denoted 1 in Fig. 2, is excited at the same time as the rf waves are shut off and propagates faster than the other waves (2–5). The velocity of the first wave is estimated to be $v_1 = (1\text{–}5) \times 10^7$ cm/s. This should be the electron plasma wave because the electron thermal velocity of the plasma is estimated to be $v_{th} = 1 \times 10^8$ cm/s calculated by the plasma parameters. The other waves, marked 2–5, have different characteristics in the propagation.

Figure 5(a) shows the velocity of the waves as a function of z. The waves propagate to the lower density region decreasing their velocity. In the area $z \leqslant 18$ cm, the waves have a constant velocity, $v = (4\text{–}5) \times 10^5$ cm/s, which is the estimated ion acoustic velocity in this region. Here, the velocity of the ion acoustic wave c_s, is defined by

$$c_s = \sqrt{\frac{k_B T_e}{M}}, \tag{1}$$

where M and k_B are the ion mass and Boltzmann constant, respectively. Therefore, these density fluctuations would be the ion acoustic waves, at least in this area.

Figure 5(b) shows the relation between the velocity of the waves and their amplitude to explain the characteristics of the propagation. Symbols □ and ■ represent the 4th and 5th peaks in Fig. 2, respectively. The dependence $v \propto (\delta n/n_0)^{2.2}$ is observed in the 5th wave and for the 4th wave $v \propto (\delta n/n_0)^{2.7}$. In the experiments of the ion acoustic solitons, a similar dependence, $v \propto (\delta n/n_0)^2$, has been reported,

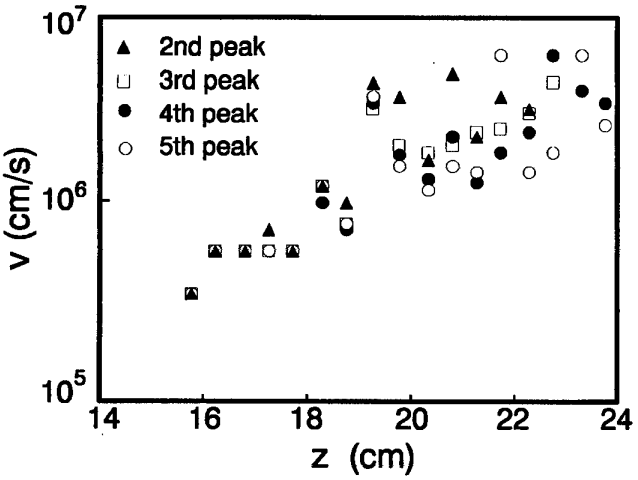

Fig. 5(a). Relation between the velocity of the waves and the position z.

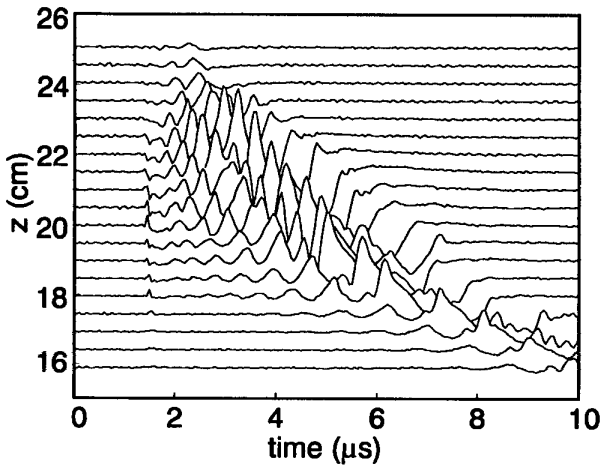

Fig. 4. Temporal-spatial distribution of the waves.

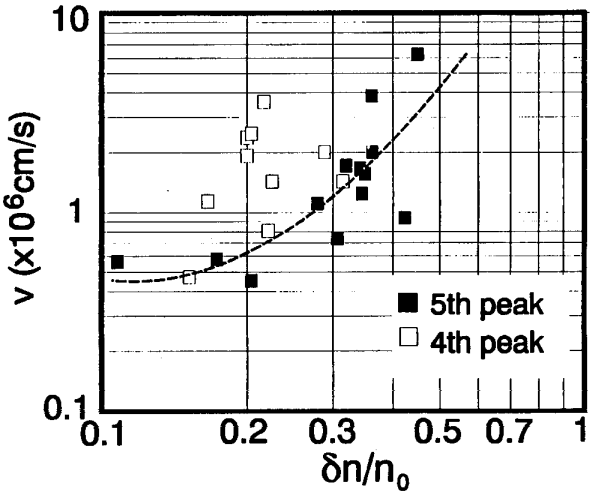

Fig. 5(b). Propagation velocity as a function of the amplitude of the wave $\delta n/n_0$. 4th wave: $v \propto (\delta n/n_0)^{2.7}$, 5th wave: $v \propto (\delta n/n_0)^{2.2}$.

although there are no precise theories of such large amplitude solitons. Therefore, the excited waves may have some characteristics of ion acoustic solitons.

4. Conclusion

We have observed the wakefield excited in both the electron wave regime and the ion wave regime by irradiating a microwave pulse with shorter fall-off time compared with the period of ion oscillation in the resonance absorption region. When an rf pulse with the fall-off time of 70 ns is applied, an electron wave is excited and high energy electrons, that are presumably accelerated by the electron wave, are observed. After the electron wave has been damped out, a large amplitude wakefield in the ion wave regime is observed to reach an amplitude of about $\delta n/n_0 = 40\%$. The amplitude of the wakefield in the ion wave regime decreases with increasing falling time of the rf pulse. The excited wakefield propagates with a velocity larger than that of the ion acoustic wave, and the velocity is proportional to the square of the amplitude. The results show fairly good agreement with the theory of the wakefield. However, we need more precise theoretical investigations on the wakefield in the ion wave regime.

Acknowledgements

A part of the present work is supported by the Grant-in-Aid from the Ministry of Education, Science and Culture, Japan.

References

1. Nishida, Y., Yugami, N., Onihashi, H., Taura, T. and Otsuka, K., Phys. Rev. Lett. **66**, 1854 (1991), and references therein.
2. Takeuchi, S., Sakai, K., Matsumoto, M. and Sugihara, R., Phys. Lett. **A122**, 257 (1987); IEEE Trans. Plasma Sci. **PS-15**, 251 (1987).
3. Tajima, T. and Dawson, J. M., Phys. Rev. Lett. **43**, 267 (1979).
4. Sprangle, P., Esarey, E., Ting, A. and Joyce, G., Appl. Phys. Lett. **53**, 2146 (1988).
5. Nishida, Y., Yoshida, K. and Nagasawa, T., Phys. Fluids **B5**, 722 (1993), and references therein.
6. Nishida, Y., Okazaki, T., Yugami, N. and Nagasawa, T., Phys. Rev. Lett. **66**, 2328 (1991).

Physica Scripta. Vol. T52, 69–72, 1994

Plasma Wakefield Acceleration Experiments Using Twin Linacs

A. Ogata, H. Nakanishi, T. Kawakubo, M. Arinaga, K. Nakajima and D. Whittum

National Laboratory for High Energy Physics (KEK), Oho, Tsukuba, Japan

Y. Yoshida

Institute of Scientific and Industrial Research, Osaka University, Mihogaoka, Ibaraki, Japan

T. Ueda and T. Kobayashi

Nuclear Engineering Research Laboratory, Faculty of Engineering, The University of Tokyo, Tokai-mura, Ibaraki-ken, Japan

H. Shibata

Research Center for Nuclear Science and Technology, The University of Tokyo, Tokai-mura, Ibaraki-ken, Japan

and

N. Yugami and Y. Nishida

Department of Electrical and Electronic Engineering, Utsunomiya University, Utsunomiya, Japan

Received November 22, 1993; accepted January 28, 1994

Abstract

A collinear wakefield test facility using two linacs with a common test section is constructed. Beams from one linac excite wakefields in a test medium such as a plasma, while beams from the other linac witness the wakefields. The time interval between the two beams is controllable with an accuracy of ~1 psec. Plasma wakefield acceleration experiments were conducted using this facility.

1. Introduction

Plasma wakefield acceleration is one of the methods which are proposed in order to obtain an acceleration gradient high enough for the next generation of linear colliders [1]. The concept has been first tested experimentally in 1988 at the Argonne National Laboratory (ANL) [2]. More recently, gradient of 20 MeV/m has been produced by a train of bunches from the 500 MeV linac at KEK [3]. Two experiments aiming at a gradient on the order of 0.1–1 GeV/m are now planned at ANL [4] and at the Budker Institute of Nuclear Physics in Novosibirsk [5].

The experiments reported in this paper do not aim at renewing the acceleration gradient record. They aim at accumulating basic data of this acceleration instead. A new collinear wakefield test facility was constructed for this purpose [6], which is unique in that it consists of two identical but independent linacs which are called twin-linacs, while in other wakefield accelerators one linac generates both the driving and witness beams. Beams from one linac excite wakefields in a plasma, while beams from the other linac witness the wakefields. Because these two beams are different in their energies, they are easily separated by a bending magnet. The time interval between the two beams is controllable with an accuracy of ~1 psec.

This paper consists of four sections. Following the present section of introduction, experimental apparatus, experimental results with discussion and conclusions are described in this order.

2. Experimental apparatus

A schematic diagram of the twin linacs is shown in Fig. 1. Each linac can generate beams in three schemes; an isolated single bunch, a 476 MHz bunch train or a 2856 MHz bunch train. Only single isolated bunches were used in these experiments. Because the two beams have different energies, the beamlines were joined in a configuration inverse to that of an energy analyser. They consist of achromatic lines as shown in Fig. 1, each of which has two dipole magnets and one quadrupole magnet. The two lines share one dipole magnet BM3, i.e., the two lines merge at BM3. Particles with the design energy are focused on the quadrupole magnets (QM1 and QM2 in Fig. 1). The off-energy particles are dispersed by the first dipoles (BM1 and BM2 in Fig. 1), and focused again onto BM3 by QM1 and QM2. Each line

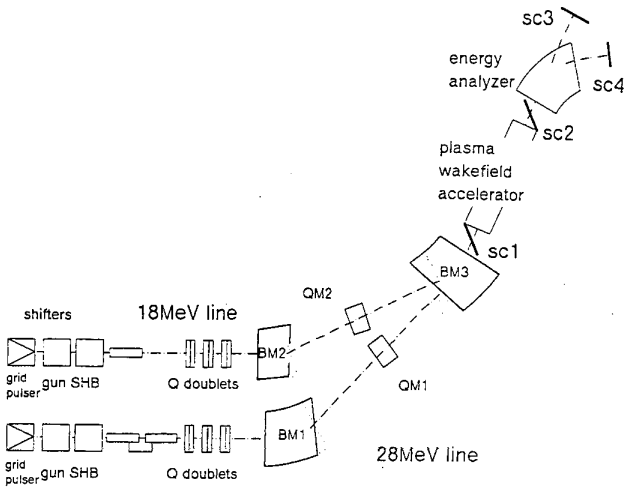

Fig. 1. Schematic diagram of the wakefield accelerator and positions of four phosphor screens SC1 to SC4.

has three pairs of doublet quadrupoles upstream, enabling fine tuning of the lattice. The fringe angles of the dipoles are designed so that the β, β' variables at the entrance of the BM1 and BM2 are transposed as β, $-\beta'$ at the exit of the BM3. This configuration transports the entire drive beam into the test region without loss due to energy dispersion. It is also possible to introduce witness beams with good energy resolution by inserting a vertical slit at the position of the quadrupole magnet.

Plasmas are produced in a chamber with 0.3 m diameter and 1 m length by pulse discharges between four lumps of LaB_6 cathodes and the chamber [8]. The cathodes are heated by a 10 V–80 A direct current source. The discharge pulse has a voltage of 80–120 V, a current of 10–20 A, a duration of 2 ms and a rate of 6.25 Hz equal to the linac beam repetition rate. The multi-dipole field of permanent magnets, 1 kG at the inner surface of the water-cooled chamber, is applied to confine the plasma. The chamber is evacuated to the order of 10^{-7} Torr, and the working gas of $1\text{–}3 \times 10^{-3}$ Torr filled the chamber at the plasma production. The plasma density was controlled both by the gas flow controller, the cathode temperature and the discharge voltage. The plasma density and temperature are measured by a Langmuir probe. The plasma density distribution was fairly homogeneous both in longitudinal and transverse directions.

To isolate the linacs from the test section, we adopted differential pumping. Previous experience on plasma lens experiments informed us that argon gas is quite harmful to the ion pumps used in the linac main ducts [7]. Nitrogen was therefore adopted as a working gas in these experiments. It was found however that the nitrogen gas reacts with the cathodes to shorten their lifetime. Plasmas with relatively low density, $1\text{–}3 \times 10^{11}\,\mathrm{cm}^{-3}$, were used in these experiments.

A 45° bending magnet at the end of the plasma chamber measured the beam energy, giving a displacement of $-55.8\,\mathrm{keV\,mm}^{-1}$. Four phosphor screens, SC1 through SC4, measured transverse profiles, whose positions are also given in Fig. 1.

The energies of the drive beams and test beams were 26.76 MeV and 15.98 MeV, respectively, and the respective charges in each bunch were 300 pC and 15–30 pC. Vertical and horizontal beam sizes of the drive bunch at SC1 are 1.99 mm and 0.94 mm, respectively, and those of the test bunch were 0.79 mm and 0.70 mm. Transverse centroids of the two beams coincided at SC1, but they differed 0.5 mm vertically and 0.2 mm horizontally at SC2. Emittance of the test bunch, calculated from beam sizes at three screen positions, were vertically 0.467 μm and horizontally 0.994 μm.

3. Experimental results and discussion

Beam images on SC4 were observed as a function of time delay between drive and test bunches. A remarkable observation is a periodical, horizontal split of the test bunch, which is shown in Fig. 2. Such an effect would be expected given the incomplete overlap of the two beams. The horizontal distribution is assumed to be sum of two Gaussian distributions. Delay dependence of the centroids of the two components obtained by the least square fit is given in Fig. 3. As for the vertical distribution, the mean and the standard deviation are calculated, which are given in Fig. 4 as position and spread.

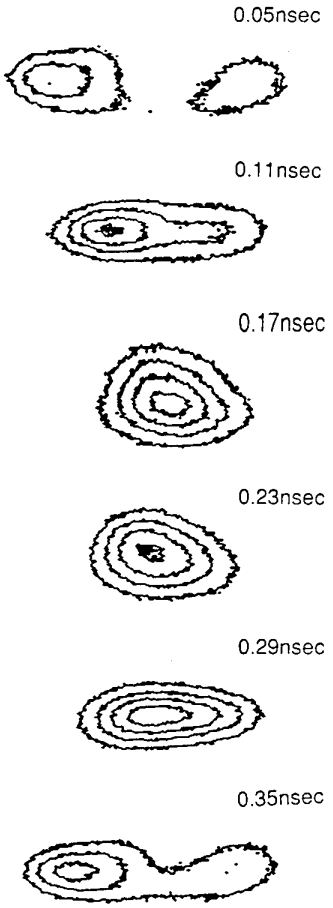

Fig. 2. Typical images on SC4 showing horizontal split of test bunches.

The delay dependences experimentally obtained were fit to the equation

$$f(t) = e^{-t/\tau}[a_1 \sin(\omega t + \phi_1) + a_2 \sin(2\omega t + \phi_2)].$$

The sin $2\omega t$ term is phenomenological, included to improve the fit. The following are findings and their interpretations in this equation.

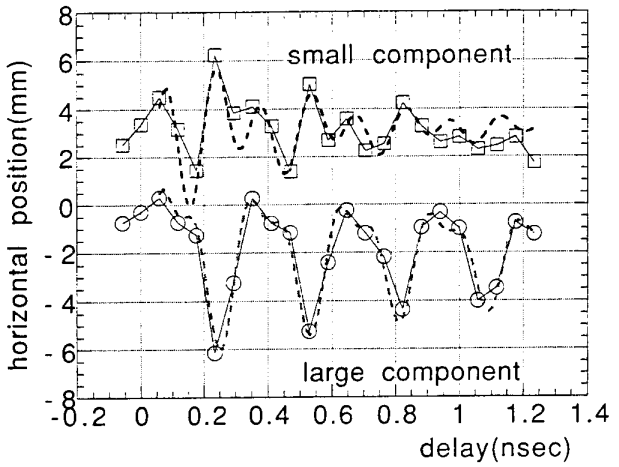

Fig. 3. Delay dependence of the horizontal centroid shift of two components.

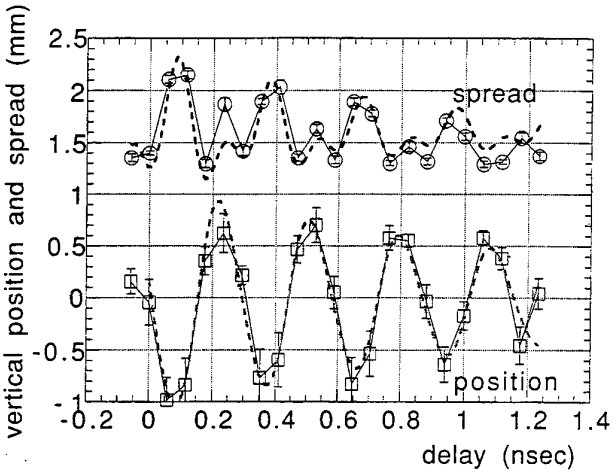

Fig. 4. Delay dependence of the vertical position and spread.

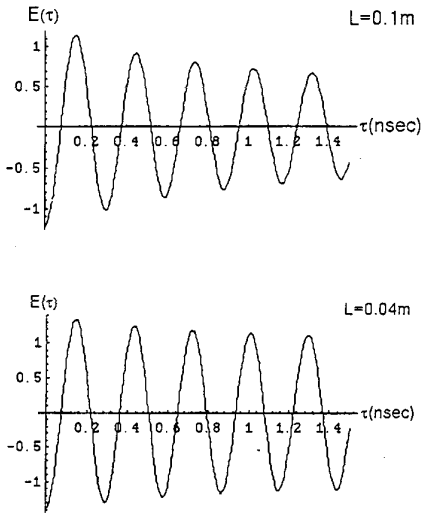

Fig. 5. Calculated total field experienced by a test bunch as a function of delay τ. $\omega_0 = 21.9\,\mathrm{GHz}$, $L_0 = 1\,\mathrm{m}$, $L = 0.1\,\mathrm{m}$, and $L = 0.04\,\mathrm{m}$.

Plasma frequency: The plasma density derived from the ω value of the delay dependence of the vertical position is $1.46 \times 10^{11}\,\mathrm{cm}^{-3}$. This is quite consistent with the value given by the Langmuir probe, $1.5 \times 10^{11}\,\mathrm{cm}^{-3}$.

Damping time of plasma oscillation: τ should give the damping time of the oscillation. Figure 4 gives the damping time of the oscillation in the vertical position as 3.69 nsec. This is too fast compared with the theoretical prediction. The previous experiments also gave the damping time nearly equal to the collision time, on the order of μsec [9]. This false damping in the present experiments can be attributed to the heterogeneity of the plasma density distribution as following. The plasma density and the resultant plasma frequency at the ends of the plasma column is lower than those at the plasma center. The test bunches suffer from the phase difference of the plasma oscillation, which becomes more severe as the time difference becomes longer. The phase difference tends to offset the positive and negative effects of the wakefield to decrease the amplitude of the oscillation.

Let us start from a simple assumption to simulate the damping. The plasma density is assumed to depend on the distance z along the beam axis as

$$n(z) = n_0[1 - \exp(z/L)], \quad 0 < z < L_0/2.$$

It is also assumed that the dependence is symmetrical at the chamber center whose total length is L_0. We refer with L to the thickness of the boundary layer. The plasma oscillation caused by a drive bunch should be given by a simple relation:

$$f(z, \tau) = \cos \omega(z)\tau,$$

where $\omega(z) \sim n(z)^{1/2}$. The longitudinal wakefield experienced by a test bunch is proportional to $n(z) \cos \omega(z)\tau$. The total field experienced by a test bunch with a specific delay time, τ, is the integration along the distance,

$$E(\tau) \sim 2 \int_0^{L_0/2} n(z) \cos[-\omega(z)\tau]\, \mathrm{d}\tau.$$

They are plotted as a function of τ in Fig. 5 for two cases of L_0 values, which successfully explains the experimental results. The decay time shown in the figure, 3.69 nsec, corresponds to a thickness of ~0.065 m in this model.

Acceleration or longitudinal wakefield: The horizontal positions on the screen at the exit of the energy analyser are varied both by the transverse and longitudinal wakefields, though the vertical position is varied only by the transverse wakefield. If we can eliminate the effects of the transverse wakefield, we can obtain the energy changes due to the longitudinal wakefields. The Panofski-Wentzel theorem permits this elimination based on the $\pi/2$ difference between these two wakefields. Let us forget the cos $2\omega t$ term and consider only the sin $(\omega t + \phi_1)$ term. The vertical position of Fig. 4 is approximated as

$$\sin(21.96t - 0.249),$$

where t is in nsec. The small component of Fig. 3 is approximated as

$$\sin(21.15t - 1.22) = \sin(21.15t - 0.249 - 0.97),$$

while the large component is

$$\sin(22.47t - 0.85) = \sin(22.47t - 0.249 - 0.60).$$

The coefficients of t, 21.96, 21.15 and 22.47, are regarded as the same values. Using the equality

$$a_t \sin(\omega t + \phi_1) + a_l \cos(\omega t + \phi_1)$$
$$= (a_l^2 + a_t^2)^{1/2} \sin(\omega t + \phi_1 + \psi), \quad \tan\psi = a_l/a_t,$$

we can derive the ratio between longitudinal and transverse wakes a_l/a_t from the ψ values. The small component gives $a_l/a_t = \tan(-0.97) = -1.45$ while the large component gives -0.684.

We can now derive the maximum amplitudes of longitudinal wakefields from the horizontal displacement. The small component and the large component give 62 keV and 60 keV, respectively. A linear theory [8] predicts the maximum longitudinal wakefield as 60.5 keV/m. The parameters assumed in the derivation are plasma density $n_p = 1.5 \times 10^{11}\,\mathrm{cm}^{-3}$, transverse beam size $\sigma_z = 2\,\mathrm{mm}$, longitudinal

beam size $\sigma_z = 3$ mm and charge of a bunch 200 pC. This is consistent with the experimental results.

4. Conclusion

Plasma wakefield acceleration experiments were conducted on a collinear wakefield test facility. Beam images were observed as a function of time delay between drive and test bunches at the end of an energy analyser. A periodic, horizontal split of the test bunch was observed. The plasma oscillation period was consistent with the plasma density measured by a Langmuir probe. However, a $2\omega_p$ component also appeared in the oscillation. The plasma oscillation decayed with a very short time constant; a few nsec, which can be attributed to the plasma heterogeneity. The horizontal displacement is caused both transverse and longitudinal wakefields. Separating the two effects using the Panofski-Wenzel theorem, we found that the energy change caused by the longitudinal field was consistent with the predictions of linear theory.

References

1. Chen, P., Dawson, J. M., Huff, R. W. and Katsouleas, T., Phys. Rev. Lett. **54**, 693 (1985).
2. Rosenzweig, J. *et al.*, Phys. Rev. Lett. **61**, 98 (1988).
3. Ogata, A. in "AIP Conf. Proc. 279; Advanced Accelerator Concepts", Port Jefferson, New York, 1992 (Edited by J. Wurtele) (American Institute of Physics, New York 1993) p. 420.
4. Rosing, M. *et al.*, in "1992 Linear Accelerator Conf. Proc.", Ottowa, 1992 (Edited by C. R. Hoffman) (AECL-10728, 1992) p. 79.
5. Militsyn, B. L. *et al.*, Phys. Fluids **B5**, 2714 (1993).
6. Nakanishi, H. *et al.*, Nucl. Instr. Meth. **A328**, 596 (1993).
7. Nakanishi, H. *et al.*, Phys. Rev. Lett. **66**, 1870 (1991); Yoshida, Y. *et al.*, Part. Accel. **39**, 77 (1992).
8. Nakajima, K., *et al.*, Nucl. Instr. Meth. **A292**, 12 (1990).
9. Ogata, A. *et al.*, Part. Accel. **39**, 33 (1992).

Physica Scripta. Vol. T52, 73–76, 1994

Laser Wakefield Generation in Magnetized Plasmas

P. K. Shukla

Institut für Theoretische Physik IV, Fakultät für Physik und Astronomie, Ruhr–Universität Bochum, D-44780 Bochum, Germany

Received November 22, 1993; accepted January 28, 1994

Abstract

Multi-dimensional equations for the plasma wakefields in the presence of an intense coherent electromagnetic wave in magnetized plasmas are derived. For a given electromagnetic wave envelope, the axial electric fields of plasma waves are obtained for a one-dimensional model problem in which all the waves are aligned either along or across the magnetic field lines. It is found that the presence of an external magnetic field can significantly enhance the strength of the plasma wakefields when the magnetic field aligned right-hand circularly polarized electromagnetic (CPEM) wave or transversely propagating O-mode radiation is used for the excitation purposes.

1. Introduction

The development of charged particle acceleration technology is very essential because a conventional accelerating structure is not capable of producing a gradient much higher than 100 MeV/m. Therefore, it is highly desirable to look for alternative practical schemes which could yield higher accelerating gradients.

It is widely thought that plasma-based accelerators can provide a breakthrough for the next generation of charged particle acceleration to ultrahigh energies within a compact space. A plasma-based accelerator concept is a promising collective acceleration scheme, which makes use of exciting highly relativistic phase velocity large amplitude electrostatic waves in plasmas. The latter could support orders of magnitude higher accelerating field gradients than conventional accelerators can produce.

The excitation of electron plasma waves can be accomplished by a number of schemes including a plasma beat-wave accelerator [1] (PBWA), a plasma wakefield accelerator [2] (PWFA), and a laser-wakefield accelerator [3] (LWFA). In the PBWA scheme, a large amplitude plasma wave is resonantly excited by the beats of two relatively low power, long pulse laser beams with a frequency difference equal to the electron plasma frequency. The PBWA utilizes a low energy, high current bunched relativistic electron beam as a driver travelling through the plasma in which the longitudinal wave is left behind the electron bunch. In the LWFA, a short, intense, single-frequency laser pulse produces plasma wakefields as it propagates through the plasma. In all these three schemes, a trailing bunch of electrons can be injected into accelerating phase of the excited plasma waves, so that the energy can be transferred from the plasma wave to the electrons. A comprehensive review of high energy laser plasma accelerators has been presented by Tajima [4]. Some recent laboratory experiments have conclusively demonstrated the feasibility of charged particle acceleration by the process of PBWA [5, 6] and PWFA [7, 8].

The LWFA is attractive because recent technology has made possible the generation of picosecond laser pulses having intensities of 10^{18} W/cm^2 and beyond. Such intense laser pulses could produce the accelerating field whose magnitude is of the order of 30 GV/m. Many theoretical investigations [9–13] have presented the profiles of wakefields in the presence of ultra-short intense laser pulses in an unmagnetized plasma.

In this paper, we present an investigation [14] of the electrostatic plasma wave generation by a large amplitude coherent electromagnetic wave in electron-ion as well as electron-positron plasmas embedded in an external magnetic field. It is found that the guide magnetic field can enhance the maximum electric field gradient of the wakefield.

The manuscript is organized as follows: In Section 2, we present the two-field description of multi-dimensional plasma waves in the presence of the ponderomotive force of magnetic field-aligned CPEM waves in magnetized plasmas. The contributions of space and time derivative ponderomotive forces are incorporated. In Section 3, we calculate the profile and the maximum potential of the wakefields for a model problem in which all the waves are aligned along the magnetic field lines. In Section 4, we consider the generation of upper-hybrid wakefields by an ordinary mode radiation propagating across the magnetic field lines. Our results are summarized in Section 5.

2. Wakefield generation by CPEM waves

We consider the nonlinear propagation of a large amplitude right-hand circularly polarized electromagnetic wave in an electron-ion (or an electron-positron) plasma embedded in an external magnetic field $B_0\hat{z}$. The electric field of the electromagnetic wave is of the form $\boldsymbol{E} = E(\hat{x} + i\hat{y}) \exp(i\boldsymbol{k}\cdot\boldsymbol{r} - i\omega t) + compl.\ conj.$ For electromagnetic wave propagation along $B_0\hat{z}$, the frequency ω and the wave vector $\boldsymbol{k} = \hat{z}k$ are related by the dispersion relation

$$\omega^2 = k^2c^2 + \sum_{j=e,\,i(p)} \omega_{pj}^2\,\omega/(\omega + \omega_{cj}), \tag{1}$$

where $\omega_{pj} = (4\pi n_j q_j^2/m_j)^{1/2}$ and $\omega_{cj} = q_j B_0/m_j c$ are the plasma and gyrofrequencies, n_j, q_j and m_j are, respectively, the number density, the charge, and the mass of the particle specie j (equals e for electrons and p for positrons), and c is the speed of light. We note that eq. (1) is valid for $|\omega + \omega_{cj}| \gg kv_{tj}$, where $v_{tj} = (T_j/m_j)^{1/2}$ is the thermal velocity and T_j is the temperature, and it does not hold when the wave frequency is very close to the electron gyrofrequency. Furthermore, in an electron-positron plasma, $m_e = m_p \equiv m$ and $q_e = -q_p = -e$, where e is the magnitude of the electron charge.

The nonlinear interaction between circularly polarized electromagnetic waves and the background plasma can give rise to an envelope of high-frequency waves. The ponderomotive force of the latter can excite multi-dimensional

plasma waves whose dynamics is governed by

$$\partial_t n_{j1} + n_{j0}\nabla\cdot v_{j\perp} + n_{j0}\partial_z v_{jz} = 0, \tag{2}$$

$$(\partial_t^2 + \omega_{cj}^2)v_{j\perp} = -\frac{q_j}{m_j}\partial_t\nabla_\perp(\phi + \phi_{pj}) + \frac{q_j}{m_j}\omega_{cj}\hat{z}\nabla(\phi + \phi_{pj}), \tag{3}$$

$$\partial_t v_{jz} = -\frac{q_j}{m_j}\partial_j\phi - F_{jz}, \tag{4}$$

and

$$\nabla^2\phi = -4\pi\sum_j q_j n_j, \tag{5}$$

where $n_{j1}(= n_j - n_0 \ll n_0)$ is the number density perturbation, n_0 is the unperturbed particle number density, v_j is the fluid velocity, ϕ is the ambipolar potential associated with plasma slow motions. For right-hand CPEM waves, the perpendicular (to $B_0\hat{z}$) component of the ponderomotive potential is

$$\phi_{pj} = \frac{q_j|E|^2}{m_j(\omega + \omega_{cj})^2}, \tag{6}$$

whereas the parallel component of the ponderomotive force reads [15]

$$F_{jz} = \left[\partial_z + \frac{k\omega_{cj}}{\omega(\omega + \omega_{cj})}\partial_t\right]\frac{q_j^2|E|^2}{m_j^2\omega(\omega + \omega_{cj})}. \tag{7}$$

The second term on the right-hand side of eq. (7) is the time derivative of the radiation pressure associated with CPEM waves in magnetized plasmas.

First, we derive the relevant equation for the right-hand CPEM wave driven electron plasma waves in magnetized plasmas with fixed ion background. Thus, combining eqs (2)–(4) we obtain

$$(\partial_t^2 + \omega_c^2)\partial_t^2 N_e = \frac{q_e}{m_e}[(\partial_t^2 + \omega_c^2)\partial_z^2 + \partial_t^2\nabla_\perp^2]\phi + \left\{(\partial_t^2 + \omega_c^2)\partial_z\left[\partial_z - \frac{k\omega_c}{\omega(\omega - \omega_c)}\partial_t\right] + \frac{\omega}{\omega - \omega_c}\partial_t^2\nabla_\perp^2\right\}\frac{e^2|E|^2}{m_e^2\omega(\omega - \omega_c)}, \tag{8}$$

where $N_e = n_{e1}/n_0$, $\omega_c = eB_0/m_e c$ and $\omega^2 = k^2c^2 + \omega_p^2\omega/(\omega - \omega_c)$ with $\omega_p^2 = 4\pi n_0 e^2/m_e$. On using Poisson's equation (5), we can write eq. (8) as

$$[(\partial_t^2 + \omega_c^2)(\partial_t^2\nabla^2 + \omega_p^2\partial_z^2) + \omega_p^2\partial_t^2\nabla_\perp^2]\phi = \left\{(\partial_t^2 + \omega_c^2)\partial_z\left[\partial_z - \frac{k\omega_c}{\omega(\omega - \omega_c)}\partial_t\right] + \frac{\omega}{\omega - \omega_c}\partial_t^2\nabla_\perp^2\right\}\frac{e\omega_p^2|E|^2}{m_e\omega(\omega - \omega_c)}. \tag{9}$$

Equation (9) describes the generation of multi-dimensional electron plasma waves by the envelopes of right-hand CPEM waves. For the plasma wave propagation along the guide magnetic field $B_0\hat{z}$, eq. (9) reduces to

$$(\partial_t^2 + \omega_p^2)\partial_z\phi = \left[\partial_z - \frac{k\omega_c}{\omega(\omega - \omega_c)}\partial_t\right]\frac{e\omega_p^2|E|^2}{m_e\omega(\omega - \omega_c)}. \tag{10}$$

It is instructive to mention that (9) and (10) with $\omega_c = -\omega_c$ also hold for the left-hand circularly polarized electromagnetic wave.

Next, we focus our attention on the generation of multi-dimensional plasma waves by intense circularly polarized EM waves in an electron-positron plasma in which there is no distinction between the right- and left-hand polarization. Here, the relevant driven plasma wave equation, which is derived from eqs. (2)–(5), is of the form

$$[(\partial_t^2 + \omega_c^2)(\partial_t^2\nabla^2 + 2\omega_p^2\partial_z^2) + 2\omega_p^2\partial_t^2\nabla_\perp^2]\phi = \left\{(\partial_t^2 + \omega_c^2)\partial_z\left[\partial_z - \frac{k}{\omega}\frac{\omega^2 + \omega_c^2}{\omega^2 - \omega_c^2}\partial_t\right] + \frac{\omega^2}{\omega^2 - \omega_c^2}\nabla_\perp^2\partial_t^2\right\}\frac{2e\omega_p^2|E|^2\omega_c}{m_e(\omega^2 - \omega_c^2)\omega}, \tag{11}$$

where $\omega^2 = k^2c^2 + 2\omega_p^2\omega^2/(\omega^2 - \omega_c^2)$. It is of interest to note that for $B_0 = 0$ the right-hand side of eq. (11) vanishes. Clearly, nonthermal plasma waves in an electron-positron plasma can be generated by CPEM waves only when an external magnetic field is present. When all the waves are aligned along the external magnetic fields, eq. (11) reduces to

$$(\partial_t^2 + 2\omega_p^2)\partial_z\phi = \left[\partial_z - \frac{k}{\omega}\frac{\omega^2 + \omega_c^2}{\omega^2 - \omega_c^2}\partial_t\right]\frac{2e\omega_p^2|E|^2\omega_c}{m_e(\omega^2 - \omega_c^2)\omega}, \tag{12}$$

which governs the generation of electrostatic plasma waves in magnetized electron-positron plasmas.

3. Wakefield profiles in the presence of CPEM waves

In order to show the influence of the external magnetic field on the CPEM driven plasma wave potentials, we consider a model problem of wave propagation along the guide magnetic field. We assume the excitation process to be stationary in the frame moving with the group velocity $(=\hat{z}v_g)$ of the CPEM waves. Thus, in a new frame $\xi = z - v_{ge}t$, eq. (10) becomes

$$(\partial_\xi^2 + k_e^2)\phi = \left[1 + \frac{kv_{ge}\omega_c}{\omega(\omega - \omega_c)}\right]\frac{e\omega_p^2|E|^2}{m_e\omega(\omega - \omega_c)v_{ge}^2}, \tag{13}$$

where $k_e = \omega_p/v_{ge}$ and $v_{ge} = kc^2/[\omega + \omega_c\omega_p^2/2(\omega - \omega_c)^2]$.

Similarly, in an electron-positron plasma, we can write eq. (12) in the stationary frame $\xi = z - v_{gp}t$ as

$$(\partial_\xi^2 + k_p^2)\phi = \left[1 + \frac{kv_{gp}}{\omega}\frac{(\omega^2 + \omega_c^2)}{(\omega^2 - \omega_c^2)}\right]\frac{2e\omega_p^2|E|^2\omega_c}{m_e(\omega^2 - \omega_c^2)\omega v_{gp}^2}, \tag{14}$$

where $k_p = \sqrt{2}\,\omega_p/v_{gp}$ and $v_{gp} = kc^2/[\omega + 2\omega_c^2\omega_p^2/(\omega^2 - \omega_c^2)^2]$.

A solution of eq. (13) is

$$\phi = k_e\left[1 + \frac{kv_{ge}\omega_c}{\omega(\omega - \omega_c)}\right]\frac{e}{m_e\omega(\omega - \omega_c)} \times \int_\xi^0 |E|^2(\xi')\sin[k_e(\xi - \xi']\,d\xi', \tag{15}$$

where the boundary conditions, $\phi = \partial\phi/\partial\xi = 0$ at $\xi = 0$ have been used.

For an electron-positron plasma, a solution of eq. (14) is

$$\phi = k_p\left[1 + \frac{kv_{gp}}{\omega}\frac{(\omega^2 + \omega_c^2)}{(\omega^2 - \omega_c^2)}\right]\frac{e\omega_c}{m_e(\omega^2 - \omega_c^2)\omega} \times \int_\xi^0 |E|^2(\xi')\sin[k_p(\xi - \xi')]\,d\xi'. \tag{16}$$

Let us suppose that short (compared with $\lambda_p = 2\pi c/\omega_p$) CPEM pulse envelope is given by $E = E_0 \sin(\pi\xi/L)$ for $-L \leqslant \xi \leqslant 0$ and $E = 0$ otherwise [11], where L is the pulse length. Hence, eq. (15) yields

$$\phi_e \simeq C_e \frac{|E_0|^2}{4}\left\{1 - \frac{1}{(k_e^2 - 4\pi^2/L^2)} \times \left[k_e^2 \cos(2\pi\xi/L) - \frac{4\pi^2}{L^2}\cos(k_e\xi)\right]\right\}, \quad (17)$$

where $C_e = [1 + kv_{ge}\omega_c/\omega(\omega - \omega_c]e/m_e\omega(\omega - \omega_c)$. For $L \ll \lambda_p$, eq. (17) gives $\phi_e \simeq (C_e/8)(k_e E_0)^2 g(\xi)$, where $g(\xi) = \xi^2 - 2(L/2\pi)^2[1 - \cos(2\pi\xi/L)]$. The functional $g(\xi)$ maximizes at $\xi = L$. Thus, the maximum value of the potential is

$$\phi_{em} \simeq (C_e/8)(k_e LE_0)^2. \quad (18)$$

Comparing eq. (18) with the wakefield potential (ϕ_0) in an unmagnetized plasma [11], we find that the two are in the ratio $\phi_{em}/\phi_0 \approx \eta_e$, where

$$\eta_e = \frac{c^2}{v_{ge}^2}\left[1 + \left(1 - \frac{X}{1-Y}\right)^{1/2}\frac{Y}{1-Y}\frac{v_{ge}}{c}\right]\frac{1}{1-Y}, \quad (19)$$

where $\phi_0 = (e/8m_e\omega^2)(2\pi LE_0/\lambda_p)^2$, $X = \omega_p^2/\omega^2$, $Y = \omega_c/\omega$, and $v_{ge}/c = [1 - X/(1-Y)]^{1/2}/[1 + XY/2(1-Y)^2]$.

In a magnetized electron-positron plasma, eq. (16) gives

$$\phi_p \simeq (C_p/8)(k_p E_0)^2 g(\xi), \quad (20)$$

where $C_p = [1 + kv_{gp}(\omega^2 + \omega_c^2)/\omega(\omega^2 - \omega_c^2)]e\omega_c/m_e\omega(\omega^2 - \omega_c^2)$. The maximum value of ϕ_p is

$$\phi_{pm} \simeq (C_p/8)(k_p LE_0)^2 \equiv \eta_p\phi_0, \quad (21)$$

where

$$\eta_p = 2\frac{c^2}{v_{gp}^2}\left[1 + \left(1 - \frac{2X}{1-Y^2}\right)^{1/2}\frac{1+Y^2}{1-Y^2}\frac{v_{gp}}{c}\right]\frac{Y}{1-Y^2}, \quad (22)$$

and $v_{gp}/c = [1 - X/(1-Y^2)]^{1/2}/[1 + 2XY^2/(1-Y^2)^2]$.

We have numerically examined the variation of η_e and η_p against Y for a fixed value of $X = 10^{-4}$. The results are depicted in Figs 1–3. It is seen from Figs 1 and 2 that η_e increases (decreases) for the right-hand (the left-hand) CPEM wave with the increase of ω_c. On the other hand, Fig. 3 exhibits the enhancement of wakefields in magnetized electron-positron plasmas. Clearly, the magnetic field has a substantial influence on the maximum potential of the wakefields that are excited by the right-hand circularly polarized electromagnetic waves propagating along the external magnetic field.

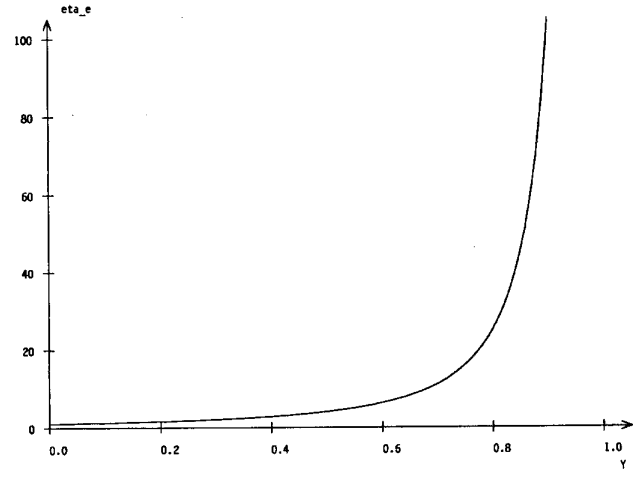

Fig. 1. η_e *vs.* Y for $X = 10^{-4}$ and the right-hand circularly polarized EM wave.

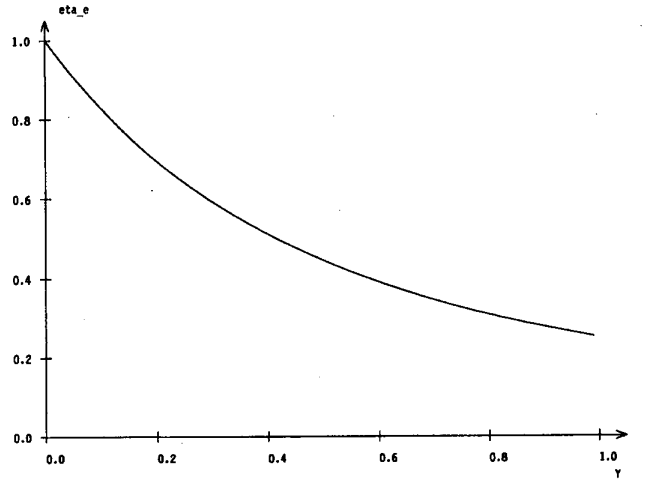

Fig. 2. η_e *vs.* Y for $X = 10^{-4}$ and the left-hand circularly polarized EM wave.

4. Wakefield generation by an ordinary mode radiation

In this section, as an illustration, we consider the generation of transversely (to $B_0\hat{z}$) propagating upper-hybrid wakefields by a large amplitude ordinary (O) mode radiation in electron-ion plasmas embedded in an external magnetic field. The extension of our work to multi-dimensional situation is straightforward.

The ordinary electromagnetic wave is characterized by the alignment of the wave electric field in the direction of the equilibrium magnetic field $B_0\hat{z}$. The wave magnetic field will then be in the y direction. For purely perpendicular propagation, the linear dispersion relation for the O-mode in a cold plasma model is given by

$$\omega^2 = k^2c^2 + \omega_{pe}^2. \quad (23)$$

where $\boldsymbol{k} \equiv k\hat{x}$ is the wave vector. It follows that the wave does not contain resonance and does not even involve B_0

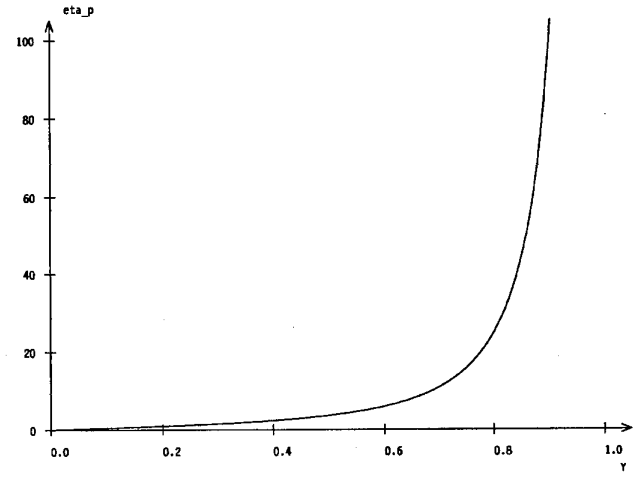

Fig. 3. η_p *vs.* Y for $X = 10^{-4}$. We note that there is no distinction between the right- and left-hand circularly polarized electromagnetic waves in magnetized electron-positron plasmas.

explicitly. This happens because the O-mode electric field is polarized along $B_0 \hat{z}$.

The upper-hybrid wakefield in an electron-ion plasma is produced by the nonlinear Lorentz force. By combining the electron continuity and momentum equations with Poisson's equation, we readily obtain [16]

$$(\partial_t^2 + \omega_H^2)\phi = \frac{\omega_p^2}{4\omega^2}\frac{e}{m_e}|E_z|^2, \tag{24}$$

where $\omega_H = (\omega_p^2 + \omega_c^2)^{1/2}$ is the upper-hybrid resonance frequency and E_z is the magnetic field aligned electric field of the O-mode radiation.

Thus, in a new frame $\xi = x - v_{g0}t$, eq. (24) becomes

$$(\partial_\xi^2 + k_u^2)\phi = \frac{\omega_p^2}{4\omega^2 v_{g0}^2}\frac{e}{m_e}|E_z|^2, \tag{25}$$

where $k_u = \omega_H/v_{g0}$ and $v_{g0} = kc^2/\omega$. The structure of (25) is similar to (13). Therefore, for a given pulse envelope of the form $E_z = E_{z0}\sin(\pi\xi/L)$ for $L \leqslant \xi \leqslant 0$ and $E_z = 0$ otherwise, the maximum value of the upper-hybrid wakefield potential is

$$\phi_u \simeq \frac{\omega_p^2 L^2}{32\omega^2 v_{g0}^2}\left(1 + \frac{\omega_c^2}{\omega_p^2}\right)\frac{e}{m_e}|E_{z0}|^2. \tag{26}$$

It follows that for $\omega_c \gg \omega_p$, the maximum gradient of the upper-hybrid wakefield is rather pronounced.

The upper-hybrid wakefields can also be generated in a magnetized electron-positron plasma. For this case, (25) and (26) remain valid, but ω_p^2 has to be defined as $8\pi n_0 e^2/m_e$, which is the sum of the squared electron and positron plasma frequencies.

The study of multi-dimensional wakefield generation by an intense extra-ordinary electromagnetic mode is under consideration and the results shall be presented elsewhere.

5. Discussion and conclusions

In this paper, we have considered the generation of wakefields by a single frequency, intense electromagnetic wave in magnetized plasmas. We have derived three-dimensional plasma wave equations in the presence of CPEM waves in an external magnetic field. Here, two cases have been explored. The first case deals with the excitation of electrostatic plasma waves in plasmas with fixed ion background, whereas the second one focuses on the generation of plasma waves in an electron-positron plasma. For both cases, choosing the CPEM pulse profile, we have obtained expressions for the magnetic field-aligned wakefields. It is found that the strength of the latter is considerably enhanced in the presence of right-hand CPEM waves whose frequency is close to the electron gyrofrequency. Furthermore, we have also demonstrated the possibility of upper-hybrid wakefield excitation by a large amplitude O-mode radiation propagating across the magnetic field lines. The electromagnetic wave driven large amplitude wakefields can then be exploited for accelerating electrons to very high energies in laboratory and astrophysical plasmas.

Acknowledgements

The author is grateful to Lennart Stenflo for valuable collaboration and discussions. He also thanks Andreas Kopp for his help in producing the figures.

This work was supported by the Commission of the European Economic Community through the SCIENCE (Twinning and operations) program under contract No. SC1-CT92-0773.

References

1. Tajima, T. and Dawson, J. M., Phys. Rev. Lett. **43**, 267 (1979).
2. Chen, P., Dawson, J. M., Huff, R. W. and Katsouleas, T., Phys. Rev. Lett. **54**, 693 (1985); ibid. **55**, 1537 (1985).
3. Gorbunov, L. M. and Kirsanov, V. I., Zh. Eksp. Teor. Fiz. **93**, 509 (1987) [Sov. Phys. JETP **66**, 290, (1987)].
4. Tajima, T., Laser Part. Beams **3**, 351 (1985).
5. Kitagawa, Y. *et al.*, Phys. Rev. Lett. **68**, 48 (1992).
6. Clayton, C. E. *et al.*, Phys. Rev. Lett. **70**, 37 (1993).
7. Rosenzweig, J. B. *et al.*, Phys. Rev. Lett. **61**, 98 (1988).
8. Nakanishi, H. *et al.*, Phys. Rev. Lett. **66**, 1870 (1990).
9. Berezhiani, V. I. and Murusidze, I. G., Phys. Lett. **A148**, 338 (1990); Physica Scripta **45**, 87 (1992).
10. Bulanov, S. V., Kirsanov, V. I. and Sakharov, A. S., Fiz. Plazmy **16**, 935 (1990) [Sov. J. Plasma Phys. **16**, 543 (1990)].
11. Ting, T., Esarey, E. and Sprangle, P., Phys. Fluids **B2**, 1390 (1990).
12. Abramyan, L. A., Litvak, A. G., Mironov, V. A. and Sargeev, A. M., Zh. Eksp. Teor. Fiz. **102**, 1816 (1992) [Sov. Phys. JETP **75**, 978 (1992)].
13. Bingham, R., de Angelis, U., Amin, M. R., Cairns, R. A. and McNamara, B., Plasma Phys. Control. Fusion **14**, 557 (1992).
14. Shukla, P. K., Phys. Fluids **5**, 3088 (1993).
15. Karpman, V. I. and Washimi, H., J. Plasma Phys. **18**, 173 (1977); Shukla, P. K. and Stenflo, L., Phys. Fluids **29**, 2479 (1986); Washimi, H., J. Phys. Soc. Jpn **58**, 3960 (1989).
16. Shukla, P. K., Phys. Fluids **27**, 407 (1984).

Physica Scripta. Vol. T52, 77–81, 1994

Plasma Wakefield Generation by Multiple Short Pulses

D. A. Johnson[1], R. A. Cairns[1], R. Bingham[2] and U. de Angelis[3]

[1] School of Mathematical and Computational Sciences, University of St. Andrews, St. Andrews, Fife KY16 9SS, UK.
[2] Rutherford Appleton Laboratory, Chilton, Didcot, Oxon. OX11 0QX, UK.
[3] Department of Physical Sciences, University of Napoli, Italy

Received November 22, 1993; February 14, 1994

Abstract

It is shown that large amplitude Langmuir waves, produced as a wake by short electromagnetic pulses in a plasma, can be generated effectively by a series of short pulses. The nonlinear nature of the Langmuir waves means that a given total energy in the electromagnetic wave is much more effective when delivered in a series of pulses than in a single short pulse. The present analysis treats the generation of the Langmuir wave in both electron-proton and electron-positron-proton plasmas.

A plot of phase trajectories shows that the correct phasing of the pulses leads to a dramatic improvement of the wake-field amplitude. For maximum amplification, the pulse maximum of each of the trailing pulses should be spatially coincident with the minimum of the wake-field potential.

1. Introduction

Present day linear electron accelerators can achieve accelerating fields of the order of a few MV/m. This technology would require huge acceleration distances (~ 100 km) to produce particle energies of the order of 1 TeV, which is the next energy regime of interest to particle physicists [1–3]. The concept of plasma-based accelerators has achieved much attention in recent years since plasmas are capable of supporting large electric fields (~ 100 GV/m) [4]. Hence, a plasma-based accelerator would require an acceleration distance of ~ 10 m to produce particles at 1 TeV energies. Such an accelerator relies on the generation of large amplitude longitudinal plasma waves with a phase velocity close to the velocity of light. Several mechanisms have been proposed for generating these waves in a plasma. The Plasma Beat Wave Accelerator (PBWA) [5] drives the plasma wave by the beating of two electromagnetic waves. The Plasma Wakefield Accelerator (PWFA) [4] scheme uses a bunched relativistic electron beam to drive the Langmuir oscillation in the plasma. A third scheme, the Laser Wakefield Accelerator (LWFA) [5] uses a single high intensity short pulse of laser radiation to excite the plasma wave. Of these schemes, the Beat Wave Accelerator has received the most attention [6].

Progress in laser technology in recent years has made compact terawatt laser systems possible. These systems can supply short ($\leqslant 1$ ps) pulses of high intensity ($\geqslant 10^{18}$ W/cm^2) radiation with energies $\sim$ 100J [7]. At such high intensities, the quiver velocity of electrons in the laser field becomes relativistic and the interaction with a plasma is highly nonlinear. The LWFA scheme has received attention recently using laser intensities in this ultra-high regime to generate relativistic Langmuir waves in a plasma.

It has been shown [8] that the efficiency of a single short laser pulse in generating a wake plasmon depends upon the shape of the pulse envelope and the length of the pulse. For pulses longer than a plasma wavelength, pulse distortion, due to the reaction of the plasma wave on the pulse, has been observed in simulations.

In this paper we present an analysis of the interaction of a train of short laser pulses with an underdense plasma. The analysis shows that it is possible, by phasing the laser pulses correctly with respect to the plasma wave, to excite resonantly a highly relativistic plasma wave with correspondingly high field gradients in the plasma. This suggests that a given pulse energy may be used much more effectively in a series of pulses than as a single pulse to generate a wake plasmon. This is a result of the nonlinearity of the plasma waves, as we now show.

We base our analysis on a well-known model [9] which combines one-fluid, cold relativistic hydrodynamics with Maxwell's equations to simulate the plasma and laser pulse respectively. The model employs the "quasi-static" and envelope approximations to obtain a set of two coupled nonlinear equations describing the self-consistent evolution of $\boldsymbol{a}_0$, the vector potential of the laser pulse envelope, and Φ, the scalar potential of the plasma wake-field.

We start from the equation for electron momentum,

$$\frac{\partial \boldsymbol{p}}{\partial t} + v_z \frac{\partial \boldsymbol{p}}{\partial z} = -e\left(\boldsymbol{E} + \frac{1}{c}\boldsymbol{v} \times \boldsymbol{B}\right) \tag{1}$$

where

$$\boldsymbol{p} = m_0 \gamma \boldsymbol{v}, \quad \gamma = (1 + p^2/m_0^2 c^2)^{1/2}, \tag{2}$$

$$\boldsymbol{E} = -\frac{1}{c}\frac{\partial \boldsymbol{A}_\perp}{\partial t} - \hat{\boldsymbol{z}}\frac{\partial \phi}{\partial z}; \; \boldsymbol{B} = \nabla \times \boldsymbol{A}_\perp; \; \boldsymbol{A}_\perp = \hat{\boldsymbol{x}}A_x + \hat{\boldsymbol{y}}A_y, \tag{3}$$

in which $\boldsymbol{A}_\perp$ is the vector potential of the electromagnetic pulse, ϕ the scalar potential due to charge separation in the plasma and m_0 and $\boldsymbol{v}$ are the usual electron rest mass and velocity respectively.

We normalise the potentials,

$$\frac{e}{m_0 c^2}\boldsymbol{A}_\perp \equiv \boldsymbol{a}(z, t); \quad \frac{e}{m_0 c^2}\phi \equiv \Phi \tag{4}$$

and split the relativistic γ into the product of transverse and longitudinal parts,

$$\gamma = \gamma_a \gamma_\parallel \tag{5}$$

where

$$\gamma_a = (1 + a^2)^{1/2}; \quad \gamma_\parallel = (1 - \beta^2)^{-1/2} \tag{6}$$

and $\beta = v_z/c$.

We can now derive the longitudinal component of the electron momentum equation and combine it with the equation of continuity, Poisson's equation and Maxwell's wave equation for the laser pulse to form a 1-D model.

In the envelope approximation we then assume a pulse of the form

$$a(z, t) = \tfrac{1}{2} a_0(\xi, \tau) e^{-i\theta} + c.c., \tag{7}$$

where the amplitude function, a_0, is now cast in the frame of the moving laser pulse, $\theta = \omega_0 t - k_0 z$, ω_0 and k_0 being the central frequency and wave-number, $\xi = z - v_g t$ and $v_g = \partial\omega_0/\partial k_0$ is the group velocity. τ is a slow time-scale such that

$$a_0^{-1} \frac{\partial^2 a_0}{\partial \tau^2} \ll \omega_0^2. \tag{8}$$

The final equations for a_0 and Φ are obtained on application of the "quasi-static" approximation to give,

$$\frac{\partial^2 \Phi}{\partial \xi^2} = \frac{\omega_{p0}^2}{c^2} G, \tag{9}$$

$$2i\omega_0 \frac{\partial a_0}{\partial \tau} + 2c\beta_0 \frac{\partial^2 a_0}{\partial \tau\, \partial \xi} + \frac{c^2 \omega_{p0}^2}{\omega_0^2} \frac{\partial^2 a_0}{\partial \xi^2} = -\omega_{p0}^2 H a_0 \tag{10}$$

where

$$G = \frac{\sqrt{\gamma_\parallel^2 - 1}}{\beta_0 \gamma_\parallel - \sqrt{\gamma_\parallel^2 - 1}}, \quad H = 1 - \frac{\beta_0}{\gamma_a(\beta_0 \gamma_\parallel - \sqrt{\gamma_\parallel^2 - 1})}. \tag{11}$$

The model is valid for electromagnetic pulses of arbitrary polarization and intensities $|a_0|^2 \geqslant 1$.

To simplify the theory we use the approximation that the group velocity of the electromagnetic wave can be taken to be c, in which case the electrostatic potential is generated according to the equation

$$\frac{d^2\Phi}{d\xi^2} = \frac{1}{2} \frac{\omega_p^2}{c^2} \left\{ \frac{\gamma_a^2}{(1 + \Phi)^2} - 1 \right\}. \tag{12}$$

For a mixture of electrons, positrons and protons eq. (12) becomes,

$$\frac{d^2\Phi}{d\xi^2} = \frac{1}{2} \frac{\omega_p^2}{c^2} \left\{ \frac{\gamma_a^2}{(1 + \Phi)^2} - \frac{\Gamma \gamma_a^2}{(1 - \Phi)^2} - (1 - \Gamma) \right\} \tag{13}$$

where Γ is the positron to electron density ratio.

When $a = 0$, $\gamma_a = 1$ and a first integral of eq. (12) is easily found, namely

$$u^2 + \frac{1}{1 + \Phi} + \Phi = K, \tag{14}$$

where K is a constant and

$$u = \frac{c}{\omega_p} \frac{d\Phi}{d\xi}. \tag{15}$$

Similarly a first integral of eq. (13) can be found, namely

$$u^2 + \frac{1}{1 + \Phi} - \frac{\Gamma}{1 - \Phi} - (1 - \Gamma)\Phi = K_0. \tag{16}$$

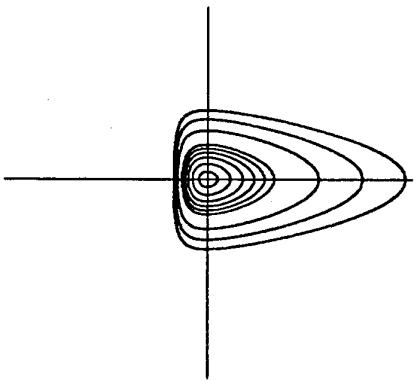

Fig. 1. The trajectories in $u - \Phi$ space generated by eq. (14) for varying values of the constant K. When $K = 1$, the trajectory is a fixed point at the origin and as the value of K increases, the trajectories become increasingly distorted from the linear circular orbits. Notice the bunching of the trajectories as the minimum value of Φ is approached.

The curves generated by eqs (14, 16) are illustrated in Figs 1 and 2.

Now suppose that we can approximate a short pulse by a δ-function,

$$\gamma_a^2 = 1 + 2A\delta(\zeta - \zeta_0), \tag{17}$$

where A is a positive number. The effect of such a δ-function pulse is to produce an impulsive change in u, of magnitude

$$\Delta u = \frac{A}{(1 + \Phi)^2}. \tag{18}$$

If we start from the equilibrium state $\Phi = u = 0$ and apply such a pulse, then we get

$$K = 1 + A^2 \tag{19}$$

and if $A \gg 1$, the maximum value of Φ is approximately A^2.

If, on the other hand, we use a series of pulses, each with a rather smaller value of A, we can exploit the Φ dependence of the impulses given by eq. (18) and drive the system each time it passes through a minimum value of Φ. In this way each successive pulse produces a larger jump in u and there

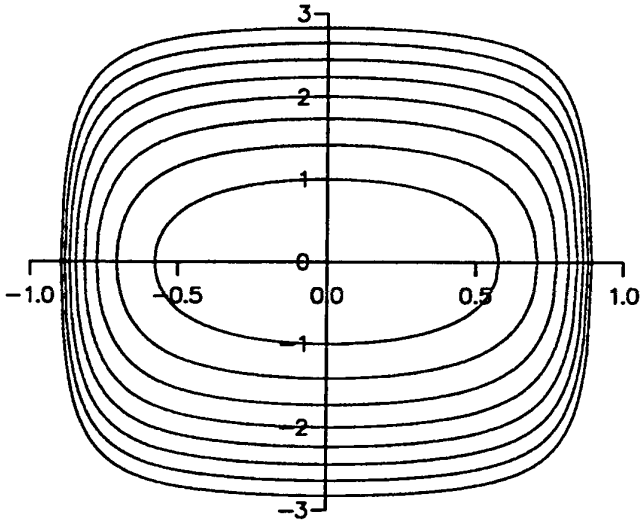

Fig. 2. The trajectories in $u - \Phi$ space generated by eq. (16), with $\Gamma = 1$, for values of the constant K_0 from 2 to 10.

is a rapid increase in the maximum value of Φ. To show just how strong this effect can be, we note that for large K the maximum and minimum values of Φ are, approximately,

$$\Phi_{max} = K,$$
$$\Phi_{min} = -1 + 1/K. \tag{20}$$

If we apply the impulse when the wave is passing through Φ_{min}, we get

$$\Delta u = AK^2 \tag{21}$$

and the new value of K is

$$K_1 = A^2K^4 + K - 1 + \frac{1}{K}$$
$$\approx A^2K^4. \tag{22}$$

if A is of order 1 and K is large. Thus, once we get into the large K regime, there is the potential for extremely rapid growth of the electrostatic wave amplitude with successive pulses.

These simple considerations indicate how the nonlinearity of the behaviour of the electrostatic potential may be exploited by using short pulses to drive up the wave amplitude at a point in its cycle where they are very effective in increasing the amplitude.

We now present some numerical results for the wake-fields generated by different combinations of short pulses. In what follows, the laser pulses are defined by their peak amplitude, Gaussian rise and fall coefficients and the position of the peak in the pulse frame. The time for the simulation is scaled in terms of the plasma period, $T_p = 2\pi/\omega_{p0}$. The spatial scale is the plasma wavelength, $\lambda_p = 2\pi c/\omega_{p0}$ and the space coordinate is ξ, the position in the frame moving with the laser pulse(s). The electric wake-field in the plasma is plotted as the normalised quantity $E_w = e|E|/m_0 c\omega_{p0}$. The vector potential, $\boldsymbol{a}$, and scalar potential, Φ, are normalised according to their previous definitions.

Figure 3 shows the interaction of a single Gaussian pulse with an under-dense homogeneous plasma. The pulse amplitude and profile have been chosen to represent a pulse of sufficient intensity to drive a relativistic Langmuir wave in the plasma. The wake-field generated has an amplitude $E_w = 0.85$. Such a wake-field set up in the plasma may then interact with a trailing particle beam or laser pulse. The structure of the resultant wake-field after the second interaction depends heavily on the phase of the plasma wave at the interaction site. This phase sensitivity means that the second pulse may either give energy to or take energy from the plasma wave. The case where energy is transferred to the trailing pulse is referred to as "Photon Acceleration" or "Beam Loading" and leads to a frequency upshifting of the pulse. Figure 4 shows a sample output from our numerical code in which the plasma wake-field is partially cancelled by the trailing pulse. As our code works in the envelope approximation, the frequency spread within each pulse cannot be illustrated. However, our interpretation of this result is that the energy of the plasma oscillation is transferred to the trailing pulse in the form of an upshifting of the frequency spread.

If the energy from the trailing pulse is transferred to the plasma, it drives a larger (and more strongly nonlinear) longitudinal wave. We now give some results to show the effect

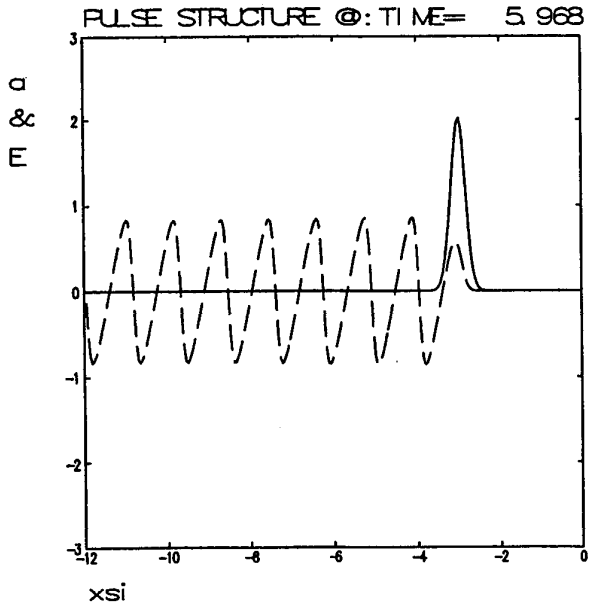

Fig. 3. Simulation results showing the magnitude of the normalised vector potential $|a_0|$ (solid line) and wake-electric field E_w (dashed curve). The spatial coordinate is $\xi = z - v_g t$ normalised to the plasma wavelength, λ_p. The parameter values are $|a_0^{in}| = 2.0$, $\omega_{p0}/\omega_0 = 0.05$, $t = 6T_p$, Gaussian rise and fall coefficients $\sigma = \pi/2 \times c/\omega_{p0} = 0.25\lambda_p$.

of splitting the energy of a single pulse into multiple pulses to drive a larger plasma wave.

Figure 5 shows the case where the energy of the pulse in Fig. 3 is split equally into two shorter pulses. The wake-field generated in the plasma is now $E_w = 2.3$, which is a factor of 2.5 times higher than that generated in Fig. 3. The accompanying phase plot of u *vs.* Φ, Fig. 6, shows the structure as predicted by our analysis. The leading pulse excites an oscillation which, when "kicked" at the correct point in its cycle by the second pulse interaction, is amplified. This phase diagram shows that in this case the impulse occurs at the point in the cycle where Φ is very close to its minimum

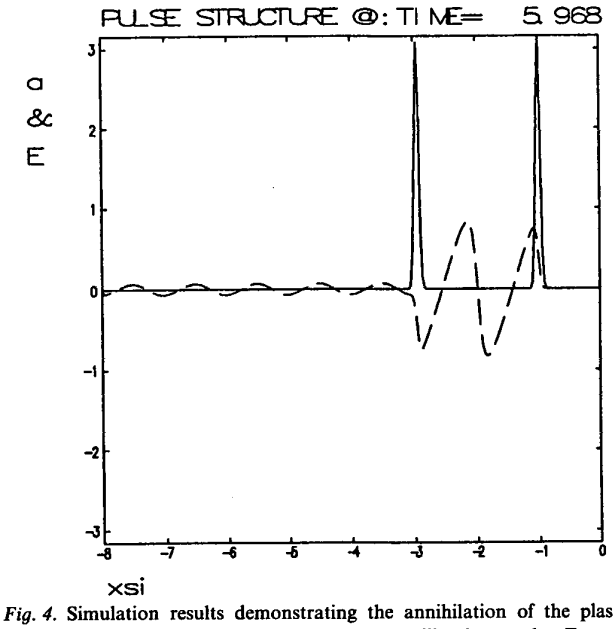

Fig. 4. Simulation results demonstrating the annihilation of the plasma wake structure, i.e. Photon Acceleration, by a trailing laser pulse. For each pulse $|a_0^{in}| = \sqrt{10}$, $\sigma = \pi/10 \times c/\omega_{p0} = 0.05\lambda_p$, $\omega_{p0}/\omega_0 = 0.05$ and $t = 6T_p$.

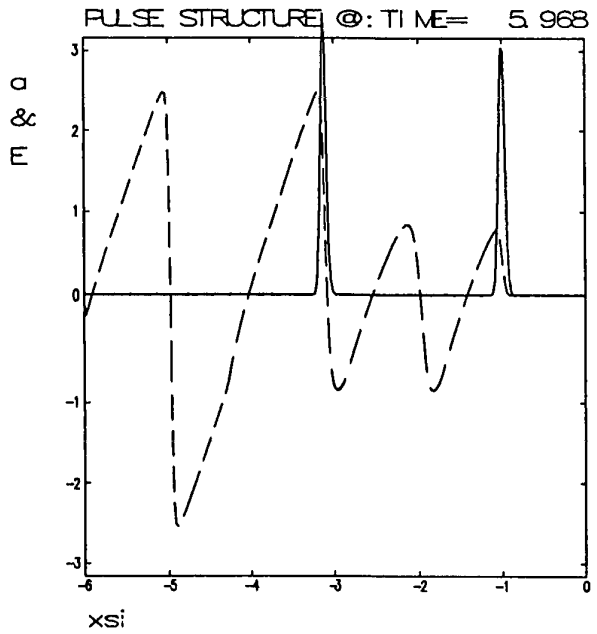

Fig. 5. Simulation to illustrate the amplification of the electric wake-field when a trailing laser pulse is positioned such that it interacts with the plasma at the point where the electrostatic potential has a minimum. Again, $|a_0^{in}| = \sqrt{10}$, $\sigma = 0.05\lambda_p$, $\omega_{p0}/\omega_0 = 0.05$ and $t = 6T_p$.

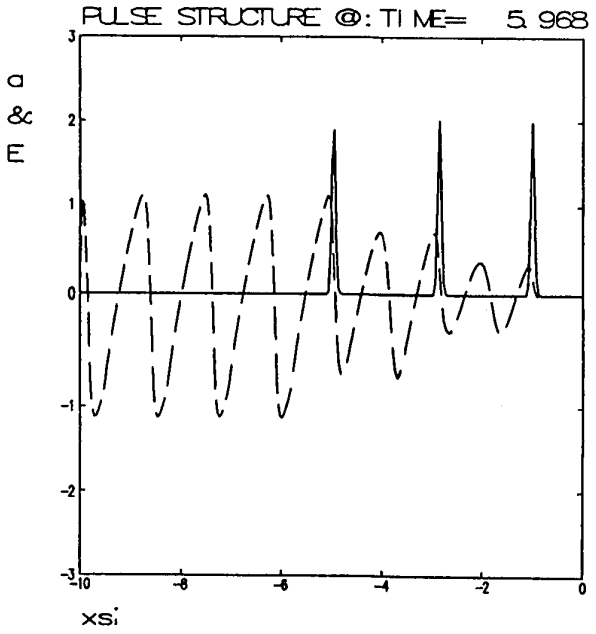

Fig. 7. Simulation of a train of 3 identical pulses, phased so that each of the trailing pulses interacts with the plasma electrons at the point where the electrostaic potential, Φ, has a local minimum. The parameter values are $|a_0^{in}| = 2.0$, $\sigma = 0.05\lambda_p$, $\omega_{p0}/\omega_0 = 0.05$ and $t = 6T_p$.

value and according to our analysis imparts the maximum amplification to the wake-field oscillation.

The demonstration of this effect leads one to ask whether a whole train of such pulses could be used to excite plasma waves up to the wave-breaking limit. In a real system, phasing such trains of pulses accurately is likely to be a limiting factor. Figure 7 shows the effect of a train of 3 pulses of equal energy in generating a wake-field. The total energy in the three pulses is of the order of 60% of the energy of the pulse used in Fig. 3. The excited electric wake-field has an amplitude $E_w \approx 1.15$, which is 35% larger than the field generated with the single pulse. The phase diagram, Fig. 8, again shows that the successive impulses to the system are applied very close to the local minimum value of the potential function, Φ, where the neighbouring phase trajectories are bunched closest together.

In conclusion, we have presented an analysis and some numerical graphics to demonstrate the increased efficiency of using multiple laser pulses in the generation of relativistic plasma wake-fields. The maximum wake amplitude is obtained when ultrashort pulses are arranged in such a way that they interact with the plasma electrons at the local minimum of the electrostatic potential generated by the preceding pulse(s). The multiple pulse scheme demonstrates that several short pulses is better than one pulse with the same total energy.

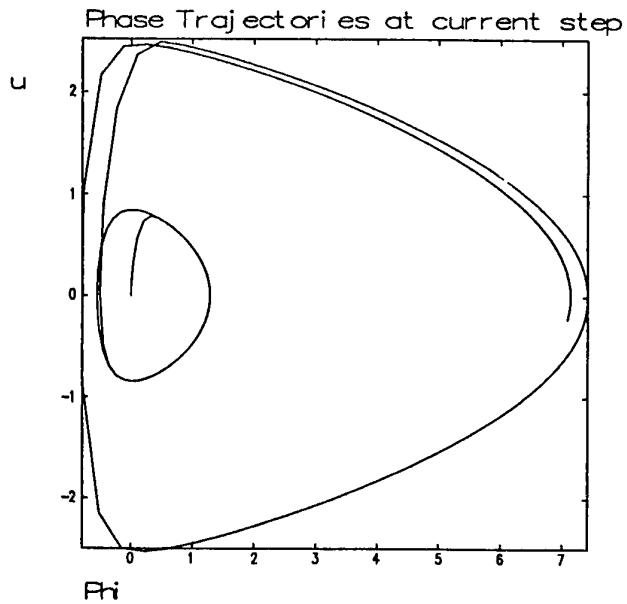

Fig. 6. The corresponding phase space trajectories for Fig. 5 which show the two impulses given to the plasma electron oscillation. The orbits excited are those with K values 1.7 and 6.3.

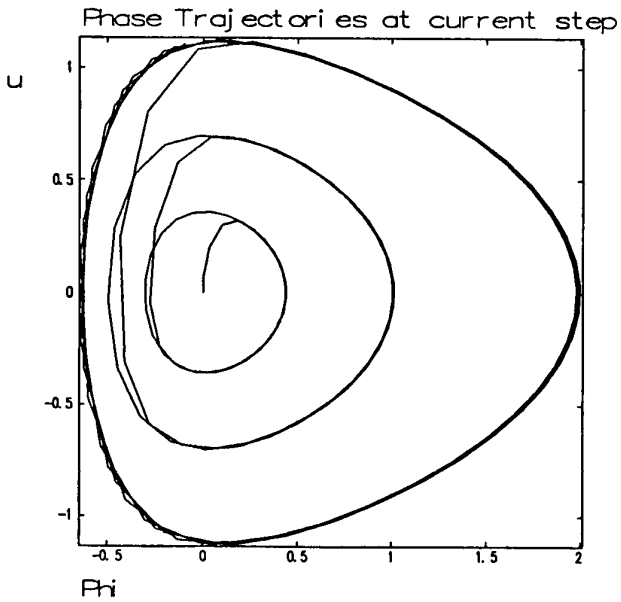

Fig. 8. The corresponding phase trajectories for Fig. 7. The orbits correspond to the approximate K values $1\frac{1}{6}$, $1\frac{1}{2}$ and $2\frac{1}{3}$.

It has been suggested previously [4, 10, 11] that multiple pulses might be used and some analysis has been carried out [12]. However, the novel phase plane analysis presented here shows more clearly than eariler work just how the nonlinear structure of the equations is such as to make excitation by a series of correctly placed pulses a very effective way of generating a high amplitude wakefield.

Acknowledgements

This work was supported by the Science and Engineering Research Council and European Commission Science Grant No: SCI/CT920773.

References

1. The Challenge of Ultra-high Energies, Proceedings of ECFA-RAL meeting, Oxford, September 1982.
2. The Generation of High Fields for Particle Acceleration to Very High Energies, Proceedings of the CAS-ECFA-INFN workshop, Frascati, September 1984.
3. Brianti, G., Physics Reports **225**, 79 (1993).
4. Chen, P., Dawson, J. M., Huff, R. W. and Katsouleas, T., Phys. Rev. Lett. **54**, 693 (1985).
5. Tajima, T. and Dawson, J. M., Phys. Rev. Lett. **43**, 267 (1979).
6. Joshi, C., Mori, W. B., Katsouleas, T., Dawson, J. M., Kindeland, J. M. and Forslund, D. W., Nature **311**, 525 (1984); Clayton, C., Joshi, C., Darrow, C. and Umstadter, K., Phys. Rev. Lett. **54**, 2343 (1985); Dangor, A. E., Bradshaw, A. D., Bingham, R., Evans, R. G., Edwards, C. B. and Tover, W. T., in "Laser Acceleration of Particles", AIP Conf. Proc. 130, (Edited by C. Joshi and T. Katsouleas) (New York 1987); Amiranoff, F. *et al.*, Phys. Rev. Lett. **68**, 3710 (1992); Joshi, C. *et al.*, in: "Advanced Accelerator Concepts", AIP Conf. Proc. 279, (Edited by J. S. Wurtele) (New York 1993).
7. Strickland, D. and Mourou, G., Opt. Commun. **56**, 216 (1985); Maine, P., Strickland, D., Bado, P., Pessot, M. and Mourou, G., IEEE J. Quantum Electron. **24**, 398 (1988); Perry, M. D., Patterson, F. G. and Weston, J., Opt. Lett. **15**, 1400 (1990).
8. Bingham, R., de Angelis, U., Amin, M. R. and Cairns, R. A., Plasma Physics and Controlled Fusion **34**, 557 (1992).
9. de Angelis, U., Physica Scripta **T30**, 210 (1990).
10. Rax, J.-M. and Fisch, N. J., Phys. Fluids **B5** (7), 2578 (1993).
11. Nakajima, K., Phys. Rev. **A45**, 1149 (1992).
12. Berezhiani, V. I. and Murusidze, I. G., Physica Scripta **45**, 87 (1992).

Physica Scripta. Vol. T52, 82–86, 1994

Simulations of the Interaction between a Light Wave and an Ionization Front in a DC Magnetic Field

C. H. Lai, T. C. Katsouleas

Department of Electrical Engineering-Electrophysics, University of Southern California, Los Angeles, CA 90089-0484, U.S.A.

and

W. B. Mori

UCLA, Departments of Physics and Electrical Engineering, Los Angeles, CA 90024, U.S.A.

Received January 7, 1994; accepted April 13, 1994

Abstract

We use a 1-D particle-in-cell simulation code to investigate the interaction of a light wave with a step relativistic ionization front in the presence of an applied D.C. magnetic field either perpendicular or parallel to the incident wave. It is seen that four transmitted waves are generated in each case. The frequency upshifts and transmission coefficients of those transmitted waves are measured from the simulation and compared to theoretical predictions. Furthermore, the phenomenon of a density ripple associated with the free streaming mode in the perpendicular case is also observed in the simulation, and the modulation rates ($\Delta n/n_0$) are close to theoretical values.

1. Introduction

The interaction between a relativistic ionization front, i.e. a moving plasma/gas boundary, and an electromagnetic wave impinging upon it has been investigated for the past 25 years. Most of this work has been concerned with unmagnetized laboratory plasmas while the interaction of ionization fronts in astrophysical plasmas (e.g. near pulsars) may occur in a strongly magnetized environment. The effect of magnetic fields on the frequency and transmission of light through ionization fronts is the subject of this paper.

In the 1960's, Semenova [1] and in the 1970's Lampe *et al.* [2] showed that the $(1+\beta)/(1-\beta)$ double Doppler upshifts and pulse compressions that arise when reflecting from a moving mirror also arise from unmagnetized overdense ionization fronts. In recent work it has been shown both theoretically [3] and experimentally [4] that significant upshifts and pulse compressions are also possible from radiation impinging upon underdense ionization fronts. For underdense fronts ($\omega_p < \gamma(1+\beta)\omega_0$), the upshift factor of the transmitted wave [3] is given by $(1+\omega_p^2/4\omega_0^2)$ rather than the double Doppler factor, where $\omega_p = (4\pi n_0 e^2/m_e)^{1/2}$ is the plasma frequency and ω_0 is the incident wave frequency. If a D.C. magnetic field is present either perpendicular or parallel to the front's propagation direction, it has been found [5] that additional transmitted waves are generated. The frequency upshifts and transmission coefficients are also altered due to the D.C. magnetic field. Furthermore, for a perpendicular D.C. magnetic field, the free streaming mode has both a static magnetic field and a density ripple. The density ripple could be easier to detect by using laser scattering diagnostics [5].

In this paper we briefly review the theoretical results of Ref. [5] and then present 1-D particle-in cell simulations of the effects of an applied DC magnetic field on the underdense front interactions. Simulation results are compared to the theoretical predictions of Ref. [5] and good agreement is found. Four tranmitted modes are clearly seen from power spectrums in both magnetic field orientations. For the perpendicular case, we also observe the density ripple of the free streaming mode and the measured $\Delta n/n_0$ is very close to the theoretical value.

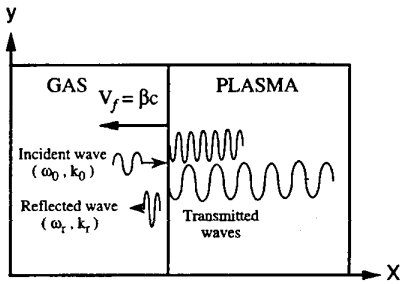

Fig. 1. The geometry of an ionization front moving from right to left towards the incident wave. The D.C. magnetic field is in the z-direction for the perpendicular case or in the x-direction for the parallel case.

2. Review of theoretical predictions

We consider an electromagnetic wave, linearly polarized in the y-direction, propagating in positive the x-direction impinging upon an ionization front moving in the opposite direction. This is schematically shown in Fig. 1. A D.C. magnetic field $\boldsymbol{B}_0$ is applied in the z-direction (for the perpendicular case) or the x-direction (parallel case). At the ionization front there are reflected and transmitted waves. The reflected wave has a frequency of $(1+\beta)^2\gamma^2\omega_0 \approx 4\gamma^2\omega_0$. For an unmagnetized underdense plasma, there is only one transmitted wave and one free streaming mode. The former has a tunable frequency $\omega_{out} = \omega_0(1+\omega_p^2/4\omega_0^2)$, while the latter is a spatially periodic D.C. magnetic field in the lab frame [1–3].

The transmitted wave frequencies can be obtained by requiring continuity of phase between each wave at the front and using the dispersion relations of each wave [5]. The dispersion relations in a magnetized plasma are [6]

$$\frac{c^2k^2}{\omega^2} \equiv \varepsilon = 1 - \frac{\omega_p^2}{\omega^2} \times \frac{\omega^2 - \omega_p^2}{\omega^2 - \omega_h^2} \quad (x\text{-wave}) \tag{1}$$

and $\omega = 0$ (the free streaming mode) for perpendicular $\boldsymbol{B}_0$ and

$$\frac{c^2k^2}{\omega^2} \equiv \varepsilon = 1 - \frac{\dfrac{\omega_p^2}{\omega^2}}{1 \mp \dfrac{\omega_c}{\omega}} \tag{2}$$

for parallel $\boldsymbol{B}_0$. $\mp$ refer to the R/L waves, respectively; $\omega_h^2 = \omega_p^2 + \omega_c^2$ is the upper hybrid frequency and $\omega_c = eB_0/cm_e$ is the electron cyclotron frequency. The continuity of phase between the incident wave (ω_0, k_0) and one of the upshifted (or downshifted) transmitted waves (ω, k) gives

$$(\omega + \beta ck) = (\omega_0 + \beta ck_0) = (1 + \beta)\omega_0 \approx 2\omega_0,$$

or

$$\omega(1 \pm \beta\sqrt{\varepsilon}) = (1 + \beta)\omega_0, \quad \text{i.e.} \quad \frac{\omega}{\omega_0} = \frac{1 + \beta}{1 \pm \beta\sqrt{\varepsilon}}. \tag{3}$$

Substituting either eq. (1) or (2) for $\sqrt{\varepsilon}$ into Eq. (3) provides the frequencies for the transmitted modes.

2.1. *Frequency upshift*

When the front velocity is near the speed of light ($\beta \approx 1$, $\gamma \gg 1$), we substitute $ck = 2\omega_0 - \omega$ for eq. (3) into eqs (1) and (2) to obtain

$$\left[\omega^3 - \left(\omega_0 + \frac{\omega_p^2}{4\omega_0}\right)\omega^2 - \omega_h^2\omega + \left(\omega_0\omega_h^2 + \frac{\omega_p^2}{4\omega_0}\right)\right] = 0, \tag{4}$$

and

$$\omega^2 - \left(\omega_0 + \frac{\omega_p^2}{4\omega_0} \pm \omega_c\right) \cdot \omega \pm \omega_0\omega_c = 0, \tag{5}$$

where $\pm$ refer to the R/L waves, respectively. Solving Eq. (4) and (5), we obtain the frequencies of the transmitted waves. We have previously shown [5] that there are four solutions in either case. In the perpendicular case, they are denoted as X_1, X_2, X_3, and X_s, where X_s represents the free streaming mode. In the parallel case, the four waves are denoted as R_1, R_2, L_1, and L_2. The former two modes are the R-waves in a magnetized plasma, while the latter two modes are L-waves [6]. It is also found [3], [5] that the group velocities of some transmitted modes could be negative (i.e. the wave follows the front to the left). For example, the X_1 wave has a negative phase and group velocity as long as $(1 + \beta)\omega_0 \approx 2\omega_0 < \omega_R$, while the X_2 wave has a negative group velocity when $2\omega_0 < \omega_L$, where ω_R and ω_L are defined as:

$$\omega_R = \frac{\omega_c + (\omega_c^2 + 4\omega_p^2)^{1/2}}{2},$$

$$\omega_L = \frac{-\omega_c + (\omega_c^2 + 4\omega_p^2)^{1/2}}{2}.$$

Useful expressions for the upshifted modes are

$$\omega = \omega|_{B_0=0} = \frac{\omega_p^2}{4\omega_0}\left(\frac{\omega_c^2}{\omega^2 - \omega_h^2}\right) \quad \text{for } X_1 \text{ mode,} \tag{6}$$

and

$$\omega_{R1} \approx \omega|_{B_0=0} + \omega_c \quad \text{for } R_1 \text{ mode,} \tag{7}$$

where $\omega|_{B_0=0} = \omega_0 + \omega_p^2/4\omega_0$.

2.2. *Transmission coefficients*

The reflection and transmission coefficients can be obtained by matching boundary conditions at the moving front. The common boundary conditions are that $\boldsymbol{E}$ tangential, $\boldsymbol{E}$ normal and $\boldsymbol{B}$ tangential are continuous in the absence of surface charge and current densities. In addition, $\boldsymbol{J}$ tangential and ρ are zero at the boundary because electrons and ions are born at rest. These provide two additional boundary conditions (from Faraday's law and Gauss' law). Therefore the boundary conditions for the system geometry are the continuity of (1) E_y, (2) B_z, (3) E_x, (4) $\partial E_y/c\,\partial t + \partial B_z/\partial x$ (=0) and (5) $\partial E_x/\partial x$ (=0). For the parallel case the incident wave can be decomposed into right and left circularly polarized waves. Each polarization interacts separately. In each case only three boundary conditions actually exist ((1), (2), and (4)) because E_x vanishes everywhere. Therefore, besides the incident R or L wave only three waves are excited. The reflection and transmission coefficients are defined as

$$r = \frac{E_{\text{tang(reflected)}}}{E_{\text{tang(incident)}}}, \tag{8.1}$$

$$t_1 = \frac{E_{\text{tang}(R_1, L_1)}}{E_{\text{tang(incident)}}}, \tag{8.2}$$

$$t_2 = \frac{B_{\text{tang}(R_2, L_2)}}{E_{\text{tang(incident)}}}, \tag{8.3}$$

where "r" denotes the reflection coefficient and is approximately zero for most underdense cases. "t_1" and "t_2" denote the transmission coefficients for R_1 mode and R_2 mode, respectively. "t_2" is defined in term of magnetic field because R_2 and L_2 waves degenerate to the free streaming mode as the D.C. magnetic field is turned off.

For the perpendicular case all five boundary conditions are required and therefore six waves exist (i.e. incident, reflected, three transmitted modes, and a free streaming mode). The reflection and transmission coefficients in the lab frame are defined in a similar way as

$$r = \frac{E_{y\text{(reflected)}}}{E_{y\text{(incident)}}}, \tag{9.1}$$

$$t_i = \frac{E_{y\text{(transmitted)}}}{E_{y\text{(incident)}}}, \quad \text{for } i = 1, 2, 3 \tag{9.2}$$

and

$$t_s = \frac{B_{z\text{(streaming)}}}{E_{y\text{(incident)}}}. \tag{9.3}$$

Again, "r" goes to zero in most underdense cases and "t_s" is defined as the ratio of magnetic field to incident electric field because the E_y component of this mode vanishes in the lab frame. Solutions for Eqs. (8) and (9) are given in Ref. [5].

2.3. *Density ripple in the perpendicular case*

Although the free streaming mode ($\omega = 0$) has been known for a long time, it has never been detected in a laboratory experiment for two reasons. First, a stationary plasma driven at frequency ω responds at various k-values but all at the same frequency ω. Thus the $\omega = 0$ mode is not excited. Second, the mode is difficult to detect (it has zero group

velocity and remains in the plasma). However, recently it was shown [5] that a static density modulation associated with this mode can be generated in the plasma when a perpendicular D.C. magnetic field is applied. This may enable detection by laser scattering in a laboratory plasma. The size of the density modulation can be estimated from Gauss' law

$$\nabla \cdot \boldsymbol{E} = 4\pi\rho = -4\pi e\,\Delta n. \tag{10}$$

This gives

$$\left|\frac{\Delta n}{n_0}\right| = \frac{k_s}{4\pi e n_0}\,|E_x|, \tag{11}$$

where k_s is the wave number of the free streaming mode and is approximately equal to $2k_0$; E_x is the longitudinal electrical field of this mode and can be obtained as follows; Since $dV_x/dt = 0 = -e/m(E_x + V_y B_0/c)$, $E_x = V_y B_0/c$. V_y follows from Ampere's law: $\nabla \times \boldsymbol{B}_s = (4\pi/c)\boldsymbol{J}_s$ or $ik_s B_s = 4\pi n_0 e V_y/c$. Substituting this expression for V_y and E_x into eq. (11) gives:

$$\left|\frac{\Delta n}{n_0}\right| = 4\left(\frac{\omega_c}{\omega_p}\right)^2\left(\frac{\omega_0}{\omega_p}\right)^2 \frac{I \cdot t_s}{B_0}, \tag{12}$$

where $B_s = It_s$ by definition; I is the incident wave amplitude and t_s is the transmission coefficient for the free streaming mode.

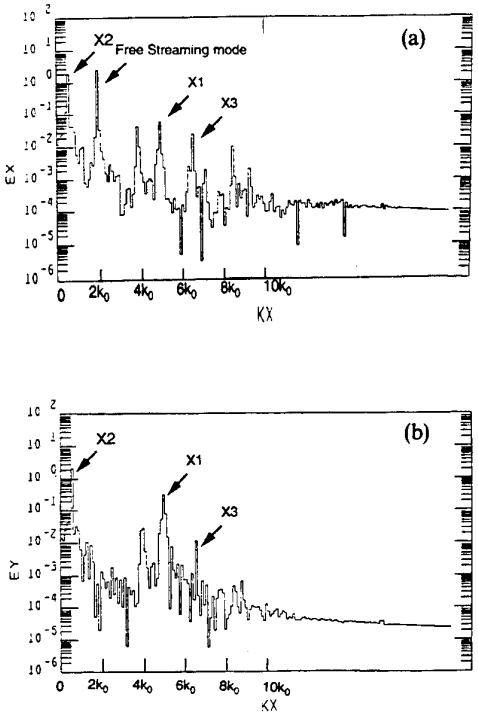

Fig. 2a, b. The spatial power spectrums of E_x and E_y for the perpendicular case. $\omega_c/\omega_p = 1$, $\gamma = 1000$.

3. Simulation results

We use the particle-in cell code WAVE in 1-3/2D (one spatial and three velocity components) to confirm the above analysis. In our simulations, the incident wave, linearly polarized in the y-direction, has a frequency of $\omega_0 = 0.25\omega_p$ and an amplitude of $1.2\,m\omega_0 c/e$. The front moves from right to left towards the incident wave with $\beta = 0.9999$, as shown in Fig. 1. The D.C. magnetic field is in the z-direction for the perpendicular case or in the x-direction for the parallel case.

In Figs 2–5 we plot results from simulations for the perpendicular case with $\omega_c = \omega_p$. The spatial power spectrums of E_x and E_y are plotted in Fig. 2(a) and 2(b), respectively. These plots reveal clearly that four modes are generated in the plasma. (The other two modes-incident and reflected-exist ahead of the front in vacuum). The X1, X2, and X3 modes have both E_x and E_y components while the free streaming mode only has an E_x component. Unlike the unmagnetized case, where the upshifted radiation piles up immediately behind the front [3], in this case the transmitted radiation is spread out behind the front because of the disparate group velocities of each mode. This is shown in Fig. 3 where the E_x and E_y fields are plotted at the instant the front has reached the left hand boundary. To compare with theory, we plot in Fig. 4 the frequency shifts and transmission coefficients obtained from simulations in which ω_c/ω_p was varied. The solid lines are the theoretical curves from Eqs. (3), (4) and Ref. [5] and the dots are simulation results.

In Fig. 5 we plot the spatial electron density spectrum. At $k = k_s = 2k_0$, there is a peak, which is the evidence of density ripple for the free streaming mode. For $\omega_c = \omega_p$, the theoretically predicted value for $\Delta n/n_0$ is $4.2 \cdot 10^{-3}$ which is very close to the simulation. In Fig. 6 we present results from the parallel case. We found four transmitted waves excited behind the front by a linearly polarized incident wave, two for R-waves and the other two for L-waves. In contrast to the perpendicular case, the E_y component of the incident wave couple to E_y and E_z, instead of E_y and E_x. The free streaming mode and the static density ripple associated with it disappear. In Figs. 6(a) and 6(b) the frequency upshifts and transmission coefficients *vs.* ω_c/ω_p are plotted. Once again excellent agreement is obtained between theory and simulation.

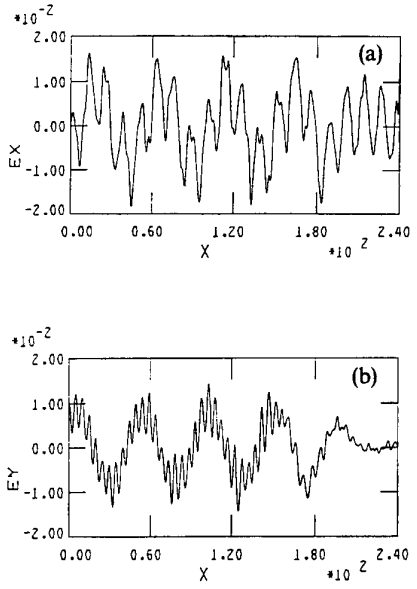

Fig. 3a, b. The E_x and E_y components of transmitted waves behind the front at the instant the front has reached the left hand boundary.

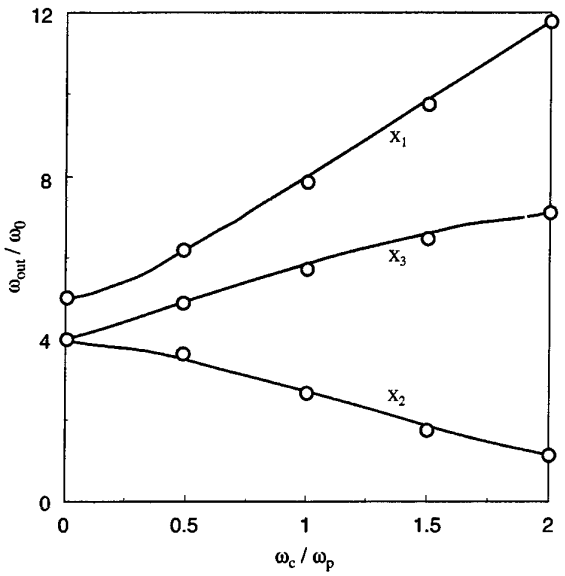

Fig. 4a. Frequency upshift ratios in a perpendicular D.C. magnetic field as a function of ω_c/ω_p. The solid curves are theoretical predictions and the dots are simulation results $\omega_0/\omega_p = 0.25$, $\gamma = 1000$.

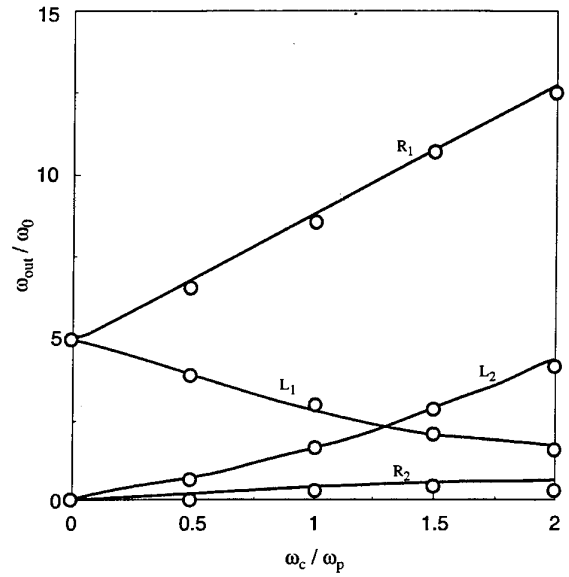

Fig. 6a. Frequency upshift ratios in a parallel D.C. magnetic field as a function of ω_c/ω_p. The solid curves are theoretical predictions and the dots are simulation results $\omega_0/\omega_p = 0.25$, $\gamma = 1000$.

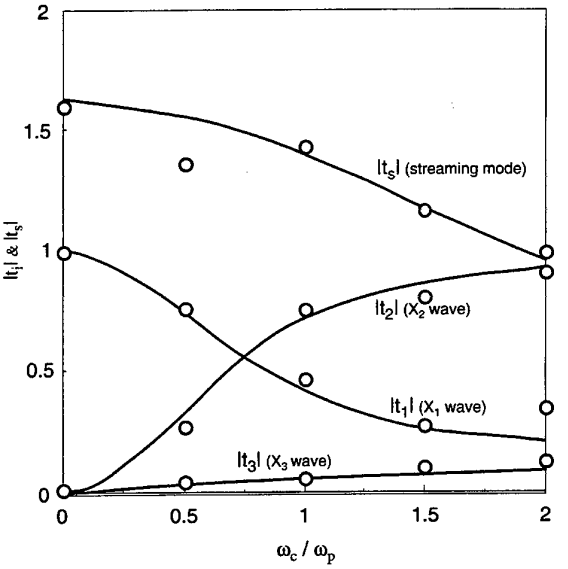

Fig. 4b. The transmission coefficients for the three XO waves ($|t_1|$, $|t_2|$, $|t_3|$) and the free streaming mode ($|t_s|$) *vs.* ω_c/ω_p. The solid curves are theoretical predictions and the dots are simulation results. $\omega_0/\omega_p = 0.25$, $\gamma = 1000$.

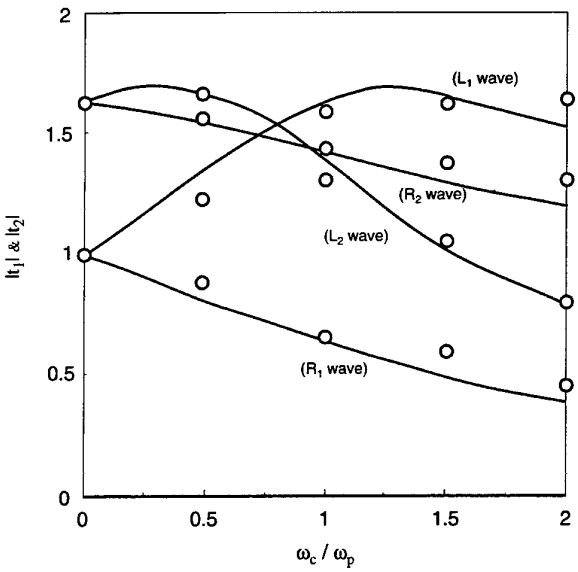

Fig. 6b. The transmission coefficients for the R and L waves *vs.* ω_c/ω_p. The solid curves are theoretical predictions and the dots are simulation results. $\omega_0/\omega_p = 0.25$, $\gamma = 1000$.

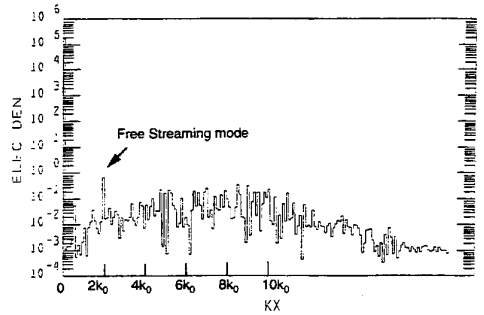

Fig. 5. The spatial electron density spectrum. A peak at $k = 2k_0$ clearly shows the evidence of density ripple for the free streaming mode.

4. Conclusion

The effects of an applied D.C. magnetic field on the interaction between a light wave and a relativistic ionization front was studied by using simulations. As predicted by theory, two more transmitted waves are generated and the frequency upshifts as well as the transmission coefficients are altered due to the D.C. magnetic field. There is excellent agreement between the theoretical predictions and the simulation results for the frequency shifts and transmission coefficients. We also observe the generation of a static density ripple in the perpendicular case. However, the analysis and simulations are based on step function fronts. The condition

for the validity of a step function front analysis is that $\gamma^2\omega_0 L \ll 1$, where L is the scale length of the front. The γ^2 factor comes about because of a Doppler shift to the frequency and Lorentz contraction to the scale length. Preliminary simulation results for continuous fronts indicate that in a magnetic field the transmission coefficients may be significantly altered from those in abrupt fronts. Further work is underway. Finally, we comment that the frequency upshifts of the most upshifted modes (X_1, R_1 in Eqs. (6), (7)) scales as $\omega_c \sim 2.86\,\text{GHz/kG}) \cdot B$ for $\omega_c \gg \omega_p$. Near pulsars, B can be as large as 10^{12} G suggesting that very low frequency signals could be converted into gamma radiation by a relativistic front. Further work is required for this case to include the Compton recoil of the plasma electrons and the discreteness of the plasma fluid (since $\lambda < n_0^{-1/3}$).

Acknowledgement

Work supported by U.S.D.O.E. under grant number DE-FG03-93-ER40776 and DE-FG03-91ER12114.

References

1. Semenova, V. I., Sov. Radiophys. **10**, 599 (1967).
2. Lampe, M., Ott, E. and Walker, J. H., Phys. Fluids **21**, 42 (1978).
3. Mori, W. B., Phys. Rev. **A44**, 5118 (1991).
4. Savage, R. L., Joshi, C. Jr. and Mori, W. B., Phys. Rev. Lett. **68**, 946 (1992).
5. Lai, C. H., Katsouleas, T. C. and Mori, W. B., IEEE Trans. Plasma Sci. **21**, 45 (1993).
6. Chen, Francis F., "Introduction to Plasma Physics and Controlled Fusion" (Plenum, New York 1984), Vol. I., Ch. 4, pp. 122–131.

Physica Scripta. Vol. T52, 87–92, 1994

Lattice of Langmuir Solitons in the Pulsar Magnetosphere

E. Asseo

Centre de Physique Theorique, Ecole Polytechnique, 91128 Palaiseau, Cedex, France

Received November 22, 1993; accepted January 28, 1994

Abstract

From the study of the nonlinear evolution of the relativistic two-stream instability in the physical conditions of the pulsar magnetosphere, that gives rise to strong Langmuir turbulence, we conclude to the probable existence of a lattice of stable Langmuir soliton-like solutions, called "Langmuir microstructures". Such microstructures are associated to three different types of radiation mechanisms. The first mechanism is direct radiation of the microstructures. The second one is curvature radiation of the microstructures moving along the dipolar pulsar magnetic field lines. The third one is related to the acceleration of beam particles in interaction with the lattice of Langmuir microstructures. It can be extremely efficient when some coherence is maintained between the phases of beam particles, for instance by a modulation of the beam. The conditions in which one or the other of these three radiation mechanisms can account for observed pulsar radio luminosities are given.

1. Introduction

It seems reasonable to assume the existence in the pulsar magnetosphere of a lattice of "Langmuir microstructures", all with the same amplitude and fixed with respect to the magnetospheric plasma [1, 2]. Such structures correspond to stable Langmuir soliton-like plasma solutions, that result from the development of strong Langmuir turbulence during the nonlinear evolution of the interaction between a beam and a plasma, both present in the emission region of a pulsar magnetosphere according to standard models. Such a description appears realistic in view of experimental results, obtained by Antipov, Nezlin and Trubnikov [3], that showed the presence of strong Langmuir turbulence in a strongly magnetized plasma triggered by a monoenergetic beam and observed a stable lattice of Langmuir solitons in the plasma.

These Langmuir microstructures can radiate electromagnetic energy by three processes. First, they contain by themselves electromagnetic energy. Second, they may curvature radiate. Indeed, they are dragged along the dipolar magnetic field lines by the plasma motion and have a relativistic motion with respect to the observer's frame. Third, the most energetic beam particles present in the emission region will induce electromagnetic radiation through "turbulent emission" due to their interaction with the assembly of Langmuir microstructures. When the beam is modulated and maintains a degree of phase coherence between its constituent particles, this last linear acceleration mechanism can result in coherent turbulent radiation with an intense level of emission. This kind of process was initially proposed for the interpretation of coherent radio emission from jets [4]. What is new here is that, due to the constraints imposed by the extremely strong pulsar magnetic field, linear acceleration of the beam particles is dominant, whereas it was considered negligible in [4].

Acceleration of particles to very high energies and turbulent emission has already been observed in laser experiments and analysed [5–9]. Also, recent numerical simulations ensure the generation of electromagnetic radiation by a strong Langmuir turbulence [10].

2. Physical conditions in the pulsar magnetosphere

The physical conditions in the pulsar magnetosphere are those of the classical standard model [11], that describes the generation of a primary weakly dense beam of very energetic positrons (and/or electrons) and a plasma of pairs of electrons and positrons, less energetic than the primary beam but with a higher density. This arises just above the polar cap of the neutron star, in the region where the dipolar pulsar magnetic field is extremely strong. Both the beam and the plasma are in relativistic bulk motion along the bundle of open magnetic field lines that delimit the active region of the pulsar magnetosphere. The interaction between the beam and the plasma results in the development of the two-stream instability.

In fact, the electrons and the positrons of the plasma, although created with the same initial velocity, acquire relative drift motions while moving along the magnetic field lines and constitute in this way two different populations of particles [12]. The fastest particles form the "beam", the slowest ones form the "plasma". In these conditions, the contribution of the very energetic primary beam to the dispersion features is negligible and the most efficient two-stream instability arises between the electrons and the positrons of the plasma itself. Thus in what follows, we represent the physical situation in the plasma rest frame of the pulsar magnetosphere as correctly accounted for by a weakly relativistic "plasma" pervaded by an ultrarelativistic beam [2].

3. Characteristics of the "Langmuir Microstructures"

The analysis of the development of a hydrodynamical beam-plasma instability for the interaction between the weakly relativistic magnetospheric plasma and the ultrarelativistic beam and of its nonlinear evolution towards Langmuir soliton-like solutions are at the basis of our interpretation of the observed pulsar radio radiation [1, 2]. Similar results were obtained [13–16] but, what is important here, is that

we are able to specify in more detail the properties of the Langmuir soliton-like solutions.

We have shown in [17] that in general, for a beam and a plasma immersed in a magnetic field of arbitrary strength, the stability of these Langmuir soliton-structures only depends on the sign of the parameter

$$s = \frac{\omega_c^2}{\omega_p^2 - \omega_c^2}. \tag{1}$$

(Here, ω_p is the plasma frequency and $\omega_c = eB/mc$ is the gyrofrequency). If $s < 0$, these Langmuir solitons are stable, if $s > 0$, they are unstable and collapse. Obviously, in the region of the pulsar magnetosphere inside the light cylinder, $\omega_c \gg \omega_p$, and the Langmuir solitons generated in this region are stable. They are the so-called "Langmuir microstructures" that form the small-scale texture in the region of the pulsar magnetosphere where radio emission processes can take place. Each elementary microstructure is characterized by (1) the electromagnetic components associated to it, (2) the corresponding density well, (3) its amplitude and spatial widths, and (4) the resulting electric charge.

3.1. *Electromagnetic field components*

The parallel electric field component of one Langmuir wave-packet, or Langmuir soliton, has an envelope, $\varepsilon_{\|}$, that slowly varies with space and time and is the solution, at rest in the plasma frame, of a modified nonlinear Schrödinger equation.

$$E_{\|} = \varepsilon_{\|} \cos \omega_p t = 2e_{\|} \operatorname{sech} a(x_{\|} - x_0) \cos \Omega_p t. \tag{2}$$

Here, $e_{\|} = 4\sqrt{3}\,(\pi n_p k_B T_p)^{1/2} a\lambda_D$ is the parallel electric field amplitude, a is the soliton amplitude, inversely proportional to the soliton width Δ, a_0 its saturated value, $\Omega_p = \omega_p(1 - \lambda_D^2 a_0^2/2)$ is the shifted oscillation frequency of the Langmuir soliton, $\lambda_D = v_{th,p}/\omega_p$ the Debye length and $v_{th,p}$ the plasma thermal velocity.

The perpendicular electric field component, $E_\perp$, is obtained from a wave-like equation, $E_{\|}$ acting as a source for its generation,

$$E_\perp = E_\perp^+ + E_\perp^-, \tag{3}$$

$$E_\perp^\pm = e_\perp \cos \Omega_p\left(t_+^- \frac{x_{\|} - x_0}{c}\right) \quad \text{and} \quad e_\perp = e_{\|}\left(\frac{\nabla_\perp a}{a^2}\right). \tag{4}$$

The transverse magnetic field component, B_t, is easily derived from Maxwell's equations. $E_\perp$ and B_t, having a propagative character, lead to a radiation process. The radiated power depends on the perpendicular irregularities of Langmuir soliton electromagnetic components, through the term $(\nabla_\perp a/a^2)^2$ (see Ref. [1]). However, if $|\nabla_\perp| \approx k_\perp$ is too small, more efficient radiation processes can be active. Also, let us mention that, for sufficiently small $k_\perp$, $E_\perp$ can be considered negligible compared to $E_{\|}$, since the ratio $e_\perp/e_{\|} \approx k_\perp/a \approx 10k_\perp \lambda_D$, is then much smaller than unity.

3.2. *The corresponding density wells*

The solutions for $E_{\|}$ and $E_\perp$ show localized regions of intense electric field. As long as there is some relativistic drift between the electrons and the positrons of the plasma, the ponderomotive force is effective, even in the case of an electron-positron plasma, and will induce nonlinear density perturbations. In the case of an extremely strong magnetic field, only the parallel component of the soliton electric field contributes to the density perturbations, $\delta n_\pm$, that result from the relativistic ponderomotive effect,

$$\frac{\delta n_\pm}{n_p} \approx -\frac{1}{32\pi} \frac{|\varepsilon_{\|}|^2}{n_p k_B T_p} \frac{\omega_{p,\pm}^2}{\omega^2} \frac{1}{\gamma_\pm} \tag{5}$$

and density wells form that correspond to the localized Langmuir soliton electric fields.

3.3. *Amplitude and spatial extent associated to the Langmuir microstructures*

Because a balance will exist between beam instability and Landau dissipation, the amplitude of the Langmuir microstructures is limited and it is possible to estimate its saturated value, a_0 [17]. For Langmuir solitons at rest in the plasma, $a_0 \approx 1/10\lambda_D$.

The characteristic parallel dimensions of Langmuir microstructures depend on their amplitude, $L_{\|} \approx a_0^{-1} \approx 10\lambda_D$. Only minimum and maximum values can be determined for their perpendicular extent, $L_\perp$, and we assume equivalent perpendicular and transverse dimensions, $L_t \approx L_\perp$. Consequently, there is an extremely large latitude for the choice of the soliton volume, v_s, that has a considerable impact on our numerical estimates. For instance, if at $r = 10^8$ cm, the presumed distance of the pulsar radio emission zone, we have

$$L_{\|} \approx 100\,\text{cm}, \quad L_\perp \approx L_t \approx 10^3\text{–}10^7\,\text{cm},$$
$$10^8\,\text{cm}^3 \leqslant v_s \leqslant 10^{16}\,\text{cm}^3. \tag{6}$$

3.4. *The resulting electric charge*

We consider that the lattice of stable Langmuir microstructures is well described by a succession of elementary positive and negative charges moving along each magnetic field line. This represents density wells with alternately one sign and the opposite one, the whole sequence being neutral. A simple estimate for the electric charge associated to each stable elementary microstructure is obtained by means of the charge density fluctuation derived from the ponderomotive force (5), i.e. $\delta\rho_{FP} = e(\delta n_+ - \delta n_-)$. An integration over the volume of one Langmuir microstructure fixes the charge estimate, Q, between two limits, that depend on the soliton volume. The minimum (maximum) limit corresponds to the minimum (maximum) volume. We have,

$$Q \equiv Q_{FP} = 8 \times 10^{10}\left(\frac{r}{R_*}\right)^{3/2}\left(\frac{v_s}{v_s^{\min}}\right) \text{electrons}. \tag{7}$$

Let us notice that Antipov, Nezlin and Trubnikov [3] observed a stable lattice of solitons in the plasma, fixed with respect to the plasma, with electric field maxima related to their density wells and with longitudinal dimensions of the order of $6\lambda_D$. These solitons showed concentration in wave energy, $W \approx 40\,W_{\text{initial}}$. These experimental results are in good agreement with the characteristics derived above. This strengths our confidence in the probable existence of a lattice of stable Langmuir microstructures in the pulsar magnetosphere, at rest in the plasma, all with the same amplitude and regularly distributed in space. These Langmuir microstructures most likely form the small-scale texture of the pulsar radio emission zone.

4. Lattice of Langmuir microstructures in the pulsar magnetosphere

If a lattice of stable Langmuir microstructures do exist in the pulsar magnetosphere they can radiate electromagnetic energy by various mechanisms. First, the deformations of the structures, in a direction perpendicular to the magnetic field lines, may directly induce electromagnetic radiation from the microstructures themselves. Secondly, these microstructures curvature radiate, being electrically charged and in relativistic motion along the dipolar magnetic field lines. Thirdly, an incoherent or coherent emission result, that depends on the relative phases of the particles, accelerated by the lattice of Langmuir microstructures.

4.1. *Direct emission of electromagnetic energy by Langmuir microstructures*

Direct emission of electromagnetic energy by Langmuir microstructures is associated with perpendicular irregularities of the Langmuir microstructure that induce perturbations of their amplitude. These irregularities diffuse on a time much longer than any other characteristic time and thus sufficiently persist to contribute directly to the radiation process [1, 2]. When each Langmuir microstructure can be considered as an independent emitter, the radiated power in the observer's frame, that depends on the perpendicular gradient of the amplitude, is obtained as

$$P_{\parallel}^{\mathrm{NL}} \approx \gamma_{\mathrm{p}}^2 N \frac{c}{4\pi} e_{\parallel}^2 \left(\frac{\nabla_{\perp} a}{a^2}\right)^2 S_{\perp}. \tag{8}$$

The amplitude is maximum when the Langmuir soliton contains transverse irregularities on the scale $(k_{\perp}^{\max})^{-1}$, with

$$\left|\frac{\nabla_{\perp} a}{a}\right|^2 \approx (k_{\perp}^{\max})^2.$$

If we assume a reasonable number of Langmuir microstructures in the emission region, $N = 10^3$, and usual pulsar parameters, $P_{\parallel}^{\mathrm{NL}} \approx 8 \times 10^{27}\,\mathrm{ergs\,s^{-1}}$. Thus, as long as $k_{\perp} \approx k_{\perp}^{\max}$, direct emission of electromagnetic energy from Langmuir microstructures is important and is sufficient to account for pulsar radio luminosities, $L(\mathrm{radio}) \approx 10^{26}$–$10^{30}\,\mathrm{ergs\,s^{-1}}$. However, it is insufficient when $k_{\perp} < k_{\perp}^{\max}$ or even $k_{\perp} \ll k_{\perp}^{\max}$. Then, the two other mechanisms described below, in 4.2 and 4.3, are worth consideration.

4.2. *Curvature radiation from Langmuir microstructures*

Strong Langmuir turbulence in the pulsar magnetospheric plasma has been related to a succession of stable and charged Langmuir microstructures that move relativistically with respect to the observer's frame, in the direction of the magnetic field lines and curvature radiate [2]. The power associated to each elementary charged Langmuir microstructure is simply obtained from classical formulae [18], as

$$P_{\mathrm{c}}^{1s} = \frac{2}{3}\frac{Q^2 c}{R_{\mathrm{c}}^2}\gamma_{\mathrm{p}}^4. \tag{9}$$

The charge Q, given in (7), corresponds to the density fluctuations induced by nonlinear effects through the ponderomotive force, $R_{\mathrm{c}} = (4/3) r^{1/2} R_{LC}^{1/2}$ is the radius of curvature of the magnetic field line, and γ_{p} the Lorentz factor associated to the plasma motion. Using (6) for the estimates of the soliton volume, we have

$$4 \times 10^9\,\mathrm{ergs\,s^{-1}} \leqslant P_{\mathrm{c}}^{1s} \leqslant 6 \times 10^{21}\,\mathrm{ergs\,s^{-1}} \tag{10}$$

at the presumed distance of the radio emission zone, $r = 10^8\,\mathrm{cm}$, while closer to the star

$$4 \times 10^5\,\mathrm{ergs\,s^{-1}} \leqslant P_{\mathrm{c}}^{1s} \leqslant 6 \times 10^{17}\,\mathrm{ergs\,s^{-1}}. \tag{11}$$

Consequently, if the Langmuir microstructures were generated at $r = 10^8\,\mathrm{cm}$, one should require a large number of such Langmuir microstructures, at least $N \approx 10^6$, all with the maximum volume, to reach the high level of radio luminosity observed from pulsars. If this mechanism is to happen close to the star surface, its contribution is less efficient, unless it occurs in the most extreme conditions in the region where the radius of curvature of the field lines should be considered as quite small, i.e. $R_{\mathrm{c}} \approx R_{*}$ (for a pulsar period $P = 1\,\mathrm{s}$). This last possibility, although marginal here, would give strength to the attractive interpretation given by Gil *et al.* [19–21] for the characteristic features of core single or triple profiles classified by Rankin [22–26] for series of observed pulsars, as due to curvature radiation of bunches of particles located close to the star.

4.3. *Acceleration and radiation of relativistic particles interacting with the lattice of Langmuir microstructures*

While the interaction is treated in the plasma rest frame, the estimate for the available radiated power is given in the observer's frame.

Since the lattice can be represented by a succession of Langmuir microstructures, regularly spaced, the associated parallel electric field, $E_{\parallel}^{\mathrm{L}}$, can be obtained from the parallel electric field (2) associated to one Langmuir microstructure. We assume that the distance between two successive maxima of the electric field can be taken as 2Δ, Δ being the width of the Langmuir wave-packet itself. Then,

$$E_{\parallel}^{\mathrm{L}} = \sum_{l=0}^{N} 2e_{\parallel}\ \mathrm{sech}\ a[(x_{\parallel} - (x_0 + 2l\Delta)]\cos\Omega_{\mathrm{p}} t \tag{12}$$

or, representing the function sech by its Fourier series and performing straightforward calculations,

$$\begin{aligned} E_{\parallel}^{\mathrm{L}} \approx{}& 2e_{\parallel}(N+1) b_0 \cos\left(\Omega_{\mathrm{p}} t + \frac{\pi}{2}\right) \\ &\times e_{\parallel} \sum_{j=1}^{\infty} \mathrm{sech}\,\frac{\pi}{2}\frac{j\omega}{ac}\,\frac{\sin\left(N+1\right)\frac{j\omega}{ac}}{\sin\frac{j\omega}{ac}} \\ &\times \left\{\cos\left[\Omega_{\mathrm{p}} t - \frac{j\omega}{c}(x_{\parallel} - (x_0 + N\Delta))\right]\right. \\ &\left. + \cos\left[\Omega_{\mathrm{p}} t + \frac{j\omega}{c}(x_{\parallel} - (x_0 + N\Delta))\right]\right\}. \end{aligned} \tag{13}$$

This parallel electric field is thus equivalent to an oscillating electric field plus a sum of travelling waves. The only travelling component that can have a true effect for particle acceleration and radiation towards the observer is the one travelling in the positive direction, with $j = 1$. Indeed, due to the factor sech $(\pi j\omega/2ac)$, the other travelling wave contributions are smaller and can be considered negligible below.

Doing this, we implicitly assume that the ratio

$$R_{\sin}(j) = \frac{\sin (N+1)\dfrac{j\omega}{ac}}{\sin \dfrac{j\omega}{ac}}$$

is finite.

4.3.1. *Turbulent incoherent particle acceleration in the parallel electric field associated with the lattice.* The variation of the momentum induced by the oscillating part of the electric field, of the type $e_1 \cos \Omega_p t$, cancels when averaged over the oscillation period. The relativistic motion of the beam particle in the travelling wave of the lattice electric field, written as

$$e_2 \cos\left[\Omega_p t - \frac{\omega}{c}(x_\parallel(x_0 + N\Delta))\right],$$

is derived from the simultaneous variation of the momentum and of the phase, ϕ, of the particle, in the case where radiation reaction is negligible. For an electron, it can be written:

$$\frac{dp}{dt} = -ee_2 \cos \phi \tag{14}$$

and

$$\phi = \omega t - \frac{\omega}{c}[x_\parallel - (x_0 + N\Delta)], \tag{15}$$

where $p = m\gamma v$, $\gamma = [1 - (v^2/c^2)]^{-1/2}$ and $\Omega_p \approx \omega$. Writing $v/c = \cos \alpha$ and $p = (mc/\tan \alpha)$, and taking the derivative of eq. (15) with respect to time, this system of eqs (14) and (15), is equivalent to the system

$$\frac{d\alpha}{dt} = \frac{ee_2}{mc} \cos \phi \sin^2 \alpha \tag{16}$$

and

$$\frac{d\phi}{dt} = \omega(1 - \cos \alpha). \tag{17}$$

A combination of these equations yields, after a straightforward integration,

$$\tan \frac{\alpha}{2} - \tan \frac{\alpha_0}{2} = v_2(\sin \phi - \sin \phi_0) \equiv f_\phi, \tag{18}$$

where α_0 and ϕ_0 correspond to the initial velocity and phase, and $v_2 = ee_2/mc\omega$ is a dimensionless parameter related to the strength of the wave.

From the definition of the momentum,

$$\frac{p - p_0}{mc} = \frac{\Delta p}{mc} = \frac{1}{\tan \alpha} - \frac{1}{\tan \alpha_0}. \tag{19}$$

Combining eqs (18) and (19), $\Delta p/mc$ can be rewritten in terms of f_ϕ and $\tan \alpha_0/2$,

$$\frac{\Delta p}{mc} = -\frac{f_\phi}{2}\left[1 + \frac{1}{\tan \dfrac{\alpha_0}{2}\left(\tan \dfrac{\alpha_0}{2} + f_\phi\right)}\right]. \tag{20}$$

Since

$$\tan \frac{\alpha}{2} = \left(\frac{1 - \cos \alpha}{1 + \cos \alpha}\right)^{1/2} \approx \frac{\varepsilon}{2\gamma} \quad \text{and} \quad \tan \frac{\alpha_0}{2} \approx \frac{\varepsilon_0}{2\gamma_0}, \tag{21}$$

where $\varepsilon = \pm 1$, $\varepsilon_0 = \pm 1$ and $\gamma = \gamma_0 + \Delta\gamma$, we have

$$f_\phi \approx \frac{\varepsilon}{2\gamma} - \frac{\varepsilon_0}{2\gamma_0} \approx \frac{1}{2\gamma_0}\left[\varepsilon\left(1 - \frac{\Delta\gamma}{\gamma_0}\right) - \varepsilon_0\right]. \tag{22}$$

Four different values for f_ϕ are obtained, that depend on the relative values of ε and ε_0. Since $\Delta\gamma \approx \beta_0(\Delta p/mc)$, the corresponding solutions for $\Delta p/mc$, and thus the possibility of acceleration in these four different cases, are obtained from eq. (20). Then in the most favourable case,

$$\varepsilon = \varepsilon_0 = -1 \quad \text{and} \quad \Delta\gamma \approx \frac{\Delta p}{mc} \approx \gamma_0\left(\frac{1 + \beta_0}{\beta_0}\right) \approx 2\gamma_0.$$

It represents the maximum of acceleration acquired by one relativistic beam particle, when moving through the lattice of Langmuir microstructures. The resulting acceleration, being in the direction of the magnetic field to which the longitudinal electric field of the lattice is parallel, it is a linear acceleration mechanism. The available radiated power is then simply

$$P_{T,I}^{1,N} \approx \frac{2}{3}\frac{e^2}{c}\left(\frac{\Delta p}{mc}\right)^2 \Delta t_{\text{interaction}}^{-2}. \tag{23}$$

If the interaction occurs all over the length, L, of the radio emission zone, $\Delta t_{\text{interaction}} = L/c \approx 10^{-5}$ s. Assuming that the whole number of relativistic beam particles present in the radio emission zone interact with the lattice of Langmuir microstructures, but radiate independently, we obtain in [2] that the "incoherent turbulent emission" associated with the relativistic beam particles, is insufficient to account for L(radio).

4.3.2. *Turbulent coherent particle acceleration.* Following recent arguments by Weatherall and Benford [4] in a different astrophysical context, one realizes that some phase coherence can be maintained between the beam particles, at least by the beam itself. Indeed, the beam is modulated by the unstable Langmuir wave at about the plasma wavelength, $\lambda = c/\omega_p$ and some phase coherence between beam particles can thus be expected on distances of this order. The turbulent emission is then coherent and can reach a very important level. An analysis of the acceleration and subsequent radiation of the whole beam particles is made to take into account the phase of each charged particle. This phase depends on the time at which the particle intersects one particular Langmuir microstructure. Including the phase factor in the relativistic equation of motion, the radiated power is

$$P_{T,C} = \frac{2}{3}\frac{e^2}{m^2c^3}\left|\sum_i \frac{dp_i}{dt}\right|^2, \tag{24}$$

or

$$P_{T,C} = \frac{2}{3}\frac{e^2}{m^2c^3}\left|\sum_i eE_\parallel \exp(-i\omega t_i)\right|^2.$$

Here, $\phi_i = \omega t_i$ represents the phase of the ith charged particle. Then,

$$P_{T,C} = \frac{4}{3}\frac{e^4 e_\parallel^2}{m^2c^3} \times \left|\sum_i \sum_{l=0}^{N} \operatorname{sech} a(x_i - (x_0 + 2l\Delta)) \exp i(\Omega_p - \omega)t_i\right|^2, \tag{25}$$

or

$$P_{\mathrm{T,C}} = \frac{4}{3}\frac{e^4 e_\parallel^2}{m^2 c^3} I.$$

We use the free-streaming trajectory of the ith relativistic particle to represent the intersection of the particle with the Langmuir microstructure. Then, t_i is replaced by x_i/c and the sum over the assembly of beam charged particles can be written as an integral over the beam density or even as a double integral since, in the extremely strong pulsar magnetic field, the beam density only varies in the direction of the magnetic field itself. Then,

$$I = (L_\perp L_t)^2 \int\cdot\int \mathrm{d}x_1\,\mathrm{d}x_2\, n(x_1)n(x_2) \times \sum_{l=0}^{N}\sum_{l'=0}^{N} \operatorname{sech} a(x_1 - (x_0 + 2l\Delta)) \times \operatorname{sech} a(x_2 - (x_0 + 2l'\Delta)) \times \exp \mathrm{i}\left(\frac{\Omega_\mathrm{p} - \omega}{c}\right)(x_1 - x_2). \quad (26)$$

Since the Langmuir microstructures are localized, the limits of integration can be taken as infinite. The product $n(x_1)n(x_2)$ is expressed in terms of the correlation of the density fluctuations, $N(x_1, x_2)$

$$n(x_1)n(x_2) = N(x_1, x_2) + n_\mathrm{b}^{(\mathrm{pl})2}. \quad (27)$$

If $N(x_1, x_2)$ only depends on the separation between x_1 and x_2, we may change the variables x_1 and x_2 to $X = x_1 - x_2$, $X^* = X + 2(l' - l)\Delta$ and $Y = x_2 - (x_0 + 2l'\Delta)$. Then, if we assume that density fluctuations that arise at the resonant plasma wavelength induce a monochromatic spectrum for beam density fluctuations,

$$N(X) = \left(\frac{\Delta n_\mathrm{b}^{(\mathrm{pl})}}{n_\mathrm{b}^{(\mathrm{pl})}}\right)^2 n_\mathrm{b}^{(\mathrm{pl})2} \exp(ikX). \quad (28)$$

After straightforward integrations over Y and X, we have

$$P_{\mathrm{T,C}} \approx \frac{8\pi^2}{3}\frac{e^4 e_\parallel^2}{m^2 c^3}(L_\perp L_t a^{-1})^2 n_\mathrm{b}^{(\mathrm{pl})2} N^2 \times \left\{\operatorname{sech}^2\frac{\pi}{2}\left(\frac{\Omega_\mathrm{p} - \omega}{ac}\right) + \left(\frac{\Delta n_\mathrm{b}^{(\mathrm{pl})}}{n_\mathrm{b}^{(\mathrm{pl})}}\right)^2 \times \operatorname{sech}^2\frac{\pi}{2}\left(\frac{2\Omega_\mathrm{p} - \omega}{ac}\right)\right\}. \quad (29)$$

Here, $(L_\perp L_t a^{-1})$ represents the soliton volume v_s, the factor $(n_\mathrm{b}^{(\mathrm{pl})} v_\mathrm{s})^2$ accounts for coherency of the particle radiation and we assume that $R_{\mathrm{sin}}^2 \approx (N+1)^2 \approx N^2$.

Then, in the observer's frame, the available radiated power can be written:

$$\Pi_{\mathrm{T,C}} \approx 3 \times 10^{23} N^2 \frac{\gamma_\mathrm{p}^2}{\gamma_\mathrm{b}^{(\mathrm{pl})6}}\left(\frac{v_{\mathrm{th,p}}}{c}\right)^6\left(\frac{v_\mathrm{s}}{v_\mathrm{s}^{\mathrm{min}}}\right)^2 \times \left[\operatorname{sech}^2\frac{\pi}{2}\left(\frac{\Omega_\mathrm{p} - \omega}{ac}\right) + \left(\frac{\Delta n_\mathrm{b}^{(\mathrm{pl})}}{n_\mathrm{b}^{(\mathrm{pl})}}\right)^2 \times \operatorname{sech}^2\frac{\pi}{2}\left(\frac{2\Omega_\mathrm{p} - \omega}{ac}\right)^2\right]. \quad (30)$$

Different ensembles of reasonable values for the parameters in the pulsar magnetosphere lead us to an order of magnitude for $\Pi_{\mathrm{T,C}}$, comparable to the observed pulsar radio luminosities, $L(\mathrm{radio}) \approx 10^{26} - 10^{30}\,\mathrm{ergs\,s^{-1}}$. For instance, choosing $N = 10^3$, $v_{\mathrm{th,p}}/c \approx 0.13$, $\gamma_\mathrm{p} \approx 10^2$, $\gamma_\mathrm{b}^{(\mathrm{pl})} \approx 2$, $v_\mathrm{s}/v_\mathrm{s}^{\mathrm{min}} = 10^2$ and with an estimate for beam density fluctuations.

$$\left(\frac{\Delta n_\mathrm{b}^{(\mathrm{pl})}}{n_\mathrm{b}^{(\mathrm{pl})}}\right)^2 \approx 3 \times 10^{-3},$$

obtained from linear calculations [1],

$$\Pi_{\mathrm{T,C}} \approx 5 \times 10^{29}\left[\operatorname{sech}^2\frac{\pi}{2}\left(\frac{\Omega_\mathrm{p} - \omega}{ac}\right) + 3 \times 10^{-3} \times \operatorname{sech}^2\frac{\pi}{2}\left(\frac{2\Omega_\mathrm{p} - \omega}{ac}\right)\right]\mathrm{ergs\,s^{-1}}. \quad (31)$$

The available radiated power from the interaction of relativistic beam particles with the lattice of Langmuir microstructures present in the emission region is then easily of the order of the observed radio luminosities. Moreover, the function sech being maximum when its argument is zero, the turbulent coherent power is emitted by relativistic beam particles, either directly at the plasma frequency or at twice the plasma frequency for the emission of particles imparted by beam density fluctuations or both. There are no means to decide, from radio observations, between emission at the plasma frequency or at its second harmonic since only rough estimates are deducible for the value of the plasma density from observations and models. Emission at the plasma frequency may be favoured considering that the interaction of the beam particles with the Langmuir microstructures is forced at the very frequency of the Langmuir solitons.

5. Summary

The presence of a lattice of Langmuir microstructures in the pulsar magnetosphere is very important. Indeed, the strong Langmuir turbulence which develops in the physical conditions expected around pulsars will give rise to an electromagnetic emission 1, directly through the emission of electromagnetic radiation from the Langmuir microstructures themselves; 2, through curvature radiation of the Langmuir microstructures that move along the open and curved magnetic field lines; 3, through "incoherent turbulent emission"; or 4, through "coherent turbulent emission", from the relativistic beam particles interacting with the lattice of Langmuir microstructures. Processes 1 and 4 are the most efficient ones.

References

1. Asseo, E., Pelletier, G. and Sol. H., Mon. Not. R. Astron. Soc. **247**, 529 (1990).
2. Asseo, E., 1993, Mon. Not. R. Astr. Soc. **264**, 940.
3. Antipov, S. V., Nezlin, M. V. and Trubnikov, A. S., Physica **3D**, 1&2, 311 (1981).
4. Weatherall, J. C. and Benford, G., Astrophys. J., **378**, 543 (1991).
5. Chen, P., Dawson, J. M., Huff, R. W. and Katsouleas, T., Phys. Rev. Lett. **54**, 693 (1985).
6. Katsouleas, T., Phys. Rev. **A/33**, 2056 (1986).
7. Mora, P. and Amiranoff, F., J. Appl. Phys. **66**, 3476 (1989).
8. Bulanov, S. V., Kovrizhnykh, L. M. and Sakharov, A. S., Physics Reports, **186**, 1 (1990).
9. Mora, P., in "Proc. Cargese International Workshop 1991, Collective Accelerations in Collisionless Plasmas" (Edited by D. Lequeau, A.

Roux and D. Gresillon) (Les Editions de Physique, France 1992), p. 171.
10. Akimoto, K., Rowlands, H. L. and Papadopoulos, K., Phys. Fluids **31**, 2185 (1988).
11. Ruderman, M. A. and Sutherland, P. G. Astrophys. J., **196**, 51 (1975).
12. Cheng, A. F. and Ruderman, M. A., Astrophys. J. **212**, 800 (1977).
13. Lominadze, Dzh. G., Mikhailovskii, A. B. and Sagdeev, R. Z., Sov. Phys. JETP, **50**, 927 (1979).
14. Lominadze, Dzh. G. and Mikhailovskii, A. B., Sov. Phys. JETP **49**, 483 (1979).
15. Onishchenko, O. G., Sov. J. Plasma Phys. **7**, 722 (1981).
16. Lominadze, Dzh. G., Machabeli, G. Z., Melikidze, G. I. and Pataraya, A. D., Sov. J. Plasma Physics **12**, 712 (1986).
17. Pelletier, G., Sol, H. and Asseo, E., Phys. Rev. **A/38**, 2552 (1988).
18. Jackson, J. D., "Classical Electrodynamics" (Wiley and Sons, New York 1962).
19. Gil, J. A. and Snakowski, J. K., Astron. Astrophys. **234**, 237 (1990).
20. Gil, J. A. and Snakowski, J. K., Astron. Astrophys., **234**, 269 (1990).
21. Gil, J. A., Kijak, J. and Zycki, P., Astron. Astrophys. (to be published, 1993).
22. Rankin, J. M., Astrophys. J. **274**, 333 (1983).
23. Rankin, J. M., Astrophys. J. **274**, 359 (1983).
24. Rankin, J. M., Astrophys. J. **301**, 901 (1986).
25. Rankin, J. M., Astrophys. J. **352**, 247 (1990).
26. Rankin, J. M., Astrophys. J. **352**, 258 (1990).

Physica Scripta. Vol. T52, 93–95, 1994

Relativistic Magnetic Reconnection

Eric. G. Blackman and George B. Field

Harvard-Smithsonian Center for Astrophysics, 60 Garden Street, Cambridge, MA 02138, U.S.A.

Received November 22, 1993; accepted January 28, 1994

Abstract

We study the kinematics of the relativistic Sweet-Parker and Petschek reconnection models for a magnetically dominated relativistic pair plasma and find that the steady state inflow velocity to the resistive region can approach the relativistic Alfvén speed when the outflow velocity does. This allows for a much faster rate of energy conversion than in the non-relativistic regime and may be important in astrophysical settings.

1. Introduction

In both the Sweet-Parker [1] (hereafter SP) and Petschek [2] (hereafter PK) models of magnetic annihilation and reconnection shown in Fig. 1, flows of plasma with oppositely directed magnetic fields meet along the x-axis in a thin resistive dissipation region (DR), and outflow perpendicular to the inflow ensues. The important difference between the two models is that length w, of the DR satisfies $w = L$ for SP and $w \ll$ L for PK, where L is the characteristic field gradient length scale of the inflow. Outside of the resistive rectangle, in the PK outflow region, the field reconnects, and its tension thrusts the plasma away from the x-point along the x-axis (Fig. 1).

The length of the DR in PK is then determined by the distance from the origin for which the Alfvén velocity associated with the normal component of the proper frame magnetic field is large enough to balance the inflow velocity. From each corner of the diffusion region, standing Alfvén waves separate the inflow and outflow regions.

For non-relativistic flows, PK provides a faster rate of reconnection for a given outflow velocity than SP. We shall see however, that for extremely relativistic outflows, both pictures can provide relativistic energy conversion rates.

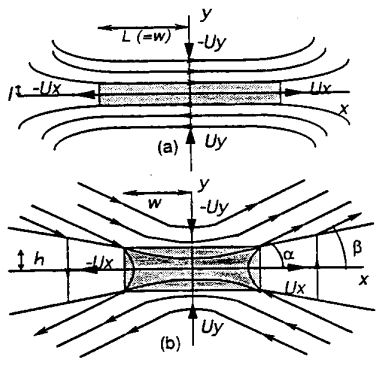

Fig. 1. Physical configuration. We consider magnetized pair plasma inflow toward the origin, along the y-axis and outflow away from the origin along the x-axis. (a) Sweet-Parker picture, with a null line along the x-axis. (b) Petschek picture; here the gain in plasma kinetic energy at the x-point and across the shocks is absorbed into the outflow plasma, reducing the magnetic flux there. The resistive regions are shaded.

When the magnitude of the magnetic energy density of the inflow plasma region is larger than the plasma density times c^2, the kinetic energy of the ejected plasma will be relativistic even if the inflow plasma is not. We recognize that the conditions under which various models of magnetic reconnection occur are not agreed upon [3] but suggest that including relativity does not add significantly more uncertain physics *per se*, in the kinematic picture.

In this paper we assume that the collisional term dominates synchrotron radiation losses in the Boltzmann equation and that the charge density, mean velocity density, and mean momentum density vanish in the proper frame. Quantities measured in this frame are labeled with a superscript *. For PK we also assume that the outflow field is very small compared to the inflow field, and that the inflow 4-velocity is much less than the outflow 4-velocity. These are mutually consistent assumptions.

We employ Ohm's law, the magnetic induction equation, and the continuity equation to obtain the steady state SP inflow velocity as a function of resistivity and outflow velocity by setting $w = L$. Then we proceed to use energy-momentum conservation, and the field solution in this order to obtain the PK solution by requiring $w \ll L$.

2. Relativistic SP and PK inflow velocities

Blackman and Field [4], show that Ohm's law for a relativistic pair plasma under fairly general conditions has the MHD form

$$\mathbf{F}^{\mu\nu}\boldsymbol{U}_\nu = \eta(\boldsymbol{j}^\mu + \boldsymbol{U}^\nu \boldsymbol{j}_\nu \boldsymbol{U}^\mu). \tag{1}$$

where $\boldsymbol{j}^\mu$ is the current density, $\mathbf{F}^{\mu\nu}$ is the electromagnetic tensor, η is the resistivity and $\boldsymbol{U}^\mu$ is a frame 4-velocity. We shall assume that the inflow and outflow velocities are approximately constant and uniform so that the inflow and outflow regions each have unique proper frames and field gradients occur primarily in the DR of Fig. 1.

Using (1) and Maxwell's Equations, the lab frame magnetic induction equation is given by

$$-\partial^2\boldsymbol{B}/\partial t^2 + c^2\nabla^2\boldsymbol{B} = (4\pi\gamma_y/\eta)(\partial\boldsymbol{B}/\partial t - \nabla \times [\boldsymbol{V} \times \boldsymbol{B}]). \tag{2}$$

Let us approximate the derivatives over small scales by the inverse of their size scales. Thus, Δt is the timescale for flux dissipation and $\Delta x = h$, the height of the DR. Writing out explicitly the components which are relevant for our y-influx, and rearranging, we obtain

$$U_y \sim \eta c/(8\pi\gamma_y^2 h) = \eta c/(8\pi h^* \gamma_y), \tag{3}$$

where U_y is the inflow 4-velocity. (3) can also be derived from the Ohm's law and the 0th component of energy-momentum conservation.

For the very small DR, integrating the continuity equation over the four volume and using Gauss' Theorem gives

$$U_y/U_x = \Delta y^*/\Delta x^* = h^*/w^*. \tag{4}$$

To obtain the SP inflow velocity, we set $w^* = L$ in (4) and combine with (3) to obtain

$$U_y/U_x = [\eta c/(8\pi U_x L\gamma_y)]^{1/2}. \tag{5}$$

Since the maximum outflow velocity is the Alfvén velocity ($\sim c$) we have

$$\gamma_y^{1/2} U_y/U_{x\,\max} \sim R_0^{-1/2}, \tag{6}$$

Where R_0 is the Reynolds number of the outflow region. (6) shows that even though the ratio of inflow to outflow momenta may be small ($R_0 \gg 1$ for astrophysical plasma), the ratio of velocities can approach 1 if $V_x/c \sim 1$. For $R_0 \sim 10^5$ the ratio of velocities is plotted in Fig. 2 for SP and PK. We shall now derive the latter.

Consider PK as in Fig. 1(b). Assuming that all of the variation in the inflow wedge takes place across the DR in the y-direction, and along the small x-direction in the outflow region, we change the partial derivatives to total derivatives and write the y-component of energy-momentum conservation for the inflow region as

$$\mathrm{d}P + U_y^2\,\mathrm{d}(\varepsilon^* + P) + 2U_y(\varepsilon^* + P)\,\mathrm{d}U_y = -B_x/(4\pi)\,\mathrm{d}B_x, \tag{7}$$

where ε^* is the energy density in the proper frame, and P is the scalar pressure. We have assumed magnetic energy is converted into either scalar pressure or bulk flow. $\mathrm{d}U_y$ cannot absorb the change in B_x since plasma is flowing in from both sides of the x-axis. The change must be accounted for by an increase in plasma pressure. Then, (7) becomes

$$\mathrm{d}P + U_y^2\,\mathrm{d}(\varepsilon^* + P) = -B_x/(4\pi)\,\mathrm{d}B_x. \tag{8}$$

Using the ultrarelativistic approximation to the equation of state for low densities and high temperatures [5], $P = 1/3\varepsilon^*$, and integrating (8) we get

$$P_0 - P_{\mathrm{in}} = B_L^2/(8\pi[1 + 4U_y^2]), \tag{9}$$

where P_0 is the plasma pressure at the x-point, P_{in} is the plasma pressure in the inflow wedge far away from the DR, where $B = B_L$.

We assume that any change in magnetic field in the outflow wedge is small. Performing a similar analysis as above, for the x-component energy-momentum conservation in the outflow, gives

$$P_0/P_{\mathrm{ot}} = 1 + 4U_x^2, \tag{10}$$

where P_{ot} is the plasma pressure in the outflow wedge.

All of the magnetic energy is converted to plasma kinetic energy at the x-point. The simplest case, and the one which maximizes the outflow velocity, is when all of the magnetic energy is converted into bulk kinetic energy. In this case, $P_{\mathrm{ot}} = P_{\mathrm{in}}$, and we can substitute (9) into (10) to obtain

$$U_{x\,\max}^2 = B_L^2/(32\pi[1 + 4U_y^2]P_{\mathrm{in}}). \tag{11}$$

We assume that most of the change in $\boldsymbol{B}$ occurs within the small resistive region, so that, outside that region, $\boldsymbol{B} = \nabla\psi$ and

$$\partial_i\partial^i\psi = 0 = \partial_\mu\partial^\mu\psi, \tag{12}$$

in the steady state. Define $r^2 = (x^2 + y^2)$ and $\theta = \tan^{-1} y/x$. Our boundary conditions are $\boldsymbol{B} = \nabla\psi = 0$ at $r = 0$, $\boldsymbol{B} = \nabla\psi = B_L$ at $r = L$, and $B_\theta = 0$ at $\theta = \beta$, where β is the angle between the x-axis and the field in the inflow wedge shown in Fig. 1(b). The appropriate solution of (12) in polar coordinates [6] is

$$B_r = B_L(r/L)^{2\beta/(\pi - 2\beta)} \cos(\theta - \beta)/(1 - 2\beta/\pi), \tag{13}$$

$$B_\theta = B_L(r/L)^{2\beta/(\pi - 2\beta)} \sin(\theta - \beta)/(1 - 2\beta/\pi). \tag{14}$$

The presence of stationary shocks in PK requires the relativistic Alfvén velocity associated with the proper frame field normal to the shock, to balance the parallel component of the inflow velocity in the lab frame. For $h \ll w$, the angles are small, and this equality is given by

$$U_y^2 = (\alpha^* - \beta^*)^2 B_L^{*2}(w^*/L)^{4\beta^*/(\pi - 2\beta^*)}/[12\pi P_{\mathrm{in}}], \tag{15}$$

where α is the angle between the x-axis and the shock shown in Fig. 1(b). Note that $B_L^{*2} = \gamma_y^2 B_L^2$, since $E_x = E_y = 0$, and $V_y \perp B_L$. Then using (10), (11) and (15), we obtain in the small angle approximation

$$U_y/\gamma_y(1 + 4U_y^2)^{1/2} = (8/3)^{1/2} U_{x\,\max}(w^*/L)^{2\beta^*/(\pi - 2\beta^*)}(\beta^* - \alpha^*). \tag{16}$$

We can obtain another relating U_y to $U_{x\,\max}$ by considering the field at the top center of the DR, ($x = 0$, $y = h$, $\theta = \pi/2$). From (11), (4), and (14) we have in the small angle approximation,

$$U_y/U_{x\,\max} = \alpha^*(h^*/L)^{2\beta^*/(\pi - 2\beta^*)}. \tag{17}$$

In the small angle limit, (16) and (17) give,

$$U_y = U_{x\,\max}\alpha^*(w^*/L)^{2\beta^*/(\pi - 2\beta^*)}. \tag{18}$$

Equations (16) and (17) also give

$$0.77 \leqslant \alpha^*/\beta^* \leqslant 1.0, \tag{19}$$

since $0 \leqslant V_y/c \leqslant 1$. Thus α^* has a nealrly constant relation to β^* over a full range of inflow velocities. We write

$$\alpha^* \sim k\beta^*, \tag{20}$$

where k is approximately constant.

Using (3), (4), and (18), we obtain

$$U_y/U_{x\,\max} = (R_0)^{-2\beta^*/\pi}(k\beta^*)^{(1 - 4\beta^*/\pi)}. \tag{21}$$

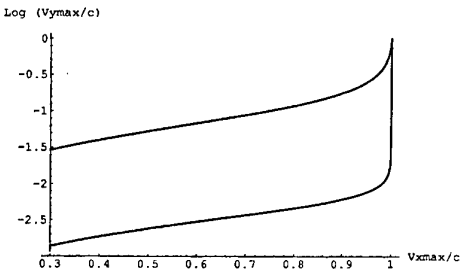

Fig. 2. Summary of results. Inflow velocity *vs.* outflow velocity for relativistic steady state Petschek and Sweet-Parker reconnection. Relativistic reconnection allows for rapid conversion of magnetic energy because although the ratios of inflow momenta to outflow momenta are small, as in the non-relativistic regime, the relativistic momentum of velocity allows the ratios of inflow to outflow velocities to approach 1. As the Alfvén velocity approaches c. The top curve is the Petschek result [eq. (7.10)] and the bottom curve is the Sweet-Parker result [eq. (4.50)].

Define $\bar{R}_0 \equiv k^2 R_0$. Then maximizing the l.h.s as a function of β^* gives:

$$U_{y\,\max}/U_{x\,\max} \sim \frac{k}{\ln\left[\gamma_{y\,\max}\bar{R}_0\right]}. \tag{22}$$

Figure 2 shows how the PK $V_{y\,\max}$ can be relativistic for even smaller $V_{x\,\max}$ than the SP result for the same Reynolds number. Since the steady state can maintain relativistic inflows, the rate of magnetic energy conversion into plasma kinetic energy is relativistic as well. We have not discussed the details of the DR which are more important to SP than PK, since the latter solution for the inflow velocity depends only logarithmically on the resistivity, and has a much smaller fraction of the energy conversion occurring in the DR.

3. Applications

Relativistic reconnection may be operating in Active Galaxies (AG) in several contexts. In models of active galactic nuclei (AGN) for which energy and angular momentum transfer from an accretion disk occurs by strong-field magnetic dissipation in a pair plasma corona [7], reconnection in a relativistic plasma is likely occurring, and relativistic reconnection increases the efficiency of this energy conversion.

In addition, in those AG which have relativistic jets of plasma, part of the energy in any relativistic jet lepton population is likely produced by local acceleration processes in order to maintain the observed power law distribution over kiloparsec scales [8]. This *in situ* acceleration has been thought to be due to either stochastic or diffusive oblique shock acceleration [8], but the latter hs been shown to be ineffective in pair plasmas [9]. Thus, if jets are composed primarily of pair plasma, relativistic reconnection could provide an alternative to shock acceleration. Since we have shown that the steady state conversion of magnetic energy to plasma kinetic energy can occur relativistically, significant reacceleration by reconnection could be operating as the relativistic leptons stream. Jet particles could then continue to radiate, without significant losses over the travel time corresponding to the jet length. Further work should be done to understand the outflow particle power spectrum from relativistic reconnection.

Another possible role of relativistic reconnection is as an aide to radiative acceleration of pair plasmas. Such a mechanism may be at work in the hydromagnetic jets of AGN. Relativistic reconnection can account for a rapid formation of pair plasma blobs from unstable open loop configurations [10] and the subsequent skewing of the distribution function toward higher energies required [11] for radiative acceleration to operate over parsec scales. The presence of a tangled magnetic field in the bulk accelerating plasma can also reduce the "drag" effect resulting from dilation of the source photons [12] if the synchrotron cross-section dominates the Thomson cross-section.

References

1. Sweet, P. A., Proc. IAU Symp. No. 6, 123, (1958); Parker, E. N., J. Geophys. Res. **79**, 1558, (1957).
2. Petschek, H. E., AAS-NASA Symp. on Phys. of Solar Flares, NASA SP-50, 425 (1964).
3. Priest, E. R., in "Basic Plasma Processes on the Sun" (Edited by E. R. Priest and V. Krishnan) IAU Symposium, (1990b); see also Priest, E. R., in "Solar Flare Magnetohydrodynamics" (Edited by E. R. Priest and V. Krishnan) (IAU Symposium (1990a); Parker, E. N., J. Plasma Physics **9**, 1, 49 (1973).
4. Blackman, E. G., and Field, G. B., Phys. Rev. Lett. **71**, 3481 (1993).
5. Pathria, R. K., "Statistical Mechanics" (Pergamon Press, Oxford 1972).
6. Parker, E. N., "Cosmical Magnetic Fields" (Oxford University Press, New York 1979).
7. Field, G. B. and Rogers, R., Astrophys. J. **403**, 94 (1993).
8. Achterberg, A., in "Astrophysical Jets and Their Engines" (Edited by W. Kundt) NATO series C, vol. 208, (1987); Eilek, J. A. and Hughes, P. A., in "Beams and Jets in Astrophysics (Edited by P. A. Hughes) (Cambridge, 1991).
9. Hoshino, M., *et al.*, Astrophys. J. **390**, 454 (1992).
10. Low, B. C., Ann. Rev. of Astron. and Astrophys. **28**, 491 (1990).
11. Phinney, E. S., Mon. Not. R. Astron. Soc. **198**, 1109 (1982).
12. Ghisellini, G., *et al.*, Astrophys. J. **401**, 87 (1992).

Physica Scripta. Vol. T52, 96–105, 1994

Acceleration in Astrophysics

Stirling A. Colgate

MS B275, LANL, Los Alamos, NM 87545, U.S.A.

Received November 22, 1993; accepted April 22, 1994

Abstract

The origin of cosmic rays and applicable laboratory experiments are discussed. The principle problems of shock acceleration for the production of cosmic rays in the context of astrophysical conditions are found to be: (1) The presumed unique explanation of the power law spectrum is shown instead to be expected as a universal property of all accelerators with high loss; (2) The extraordinary isotropy of cosmic rays and the limited diffusion distances implied by supernova induced shock acceleration requires a more frequent and space-filling source than supernova; (3) Near perfect adiabaticity of reflection by strong hydromagnetic turbulence is required in order to accelerate the particles. In each doubling in energy roughly 10^{5-6} scatterings are required with negligible energy loss. This seems most unlikely by strong hydromagnetic waves; (4) The evidence for acceleration due to quasi-parallel heliosphere shocks is weak. There is small evidence for the expected strong hydromagnetic turbulence, and instead, only a small number of particles are observed to be accelerated after only a few shock traversals; (5) The acceleration of electrons in the same collisionless shock that accelerates ions is difficult to reconcile with the theoretical picture of strong hydromagnetic turbulence that reflects the ions. The hydromagnetic turbulence will appear adiabatic to the electrons at their much higher Larmor frequency and so the electrons should not be scattered incoherently as they must be for acceleration. Therefore the electrons must be accelerated by a different mechanism. This is unsatisfactory, because wherever electrons are accelerated these sites, observed in radio emission, may accelerate ions more favorably. Because of these difficulties, an alternate explanation is given where reconnection of twisted magnetic fields (from gravitational condensation, accretion, and conservation of angular momentum) accelerates particles along field lines. The acceleration is coherent provided the reconnection is coherent, in which case the total flux, as for example of collimated radio sources, predicts single charge accelerated energies significantly greater than observed. The same acceleration process should occur during the formation of stars associated with the T-Tauri phase and bi-polar outflows. Because of the ubiquitous nature of matter condensations in the universe, and the near universal excess of angular momentum, the acceleration is inherently isotropic and space-filling in nature. Four laboratory experiments are suggested that would form the basis of a substantiated science of plasma processes of acceleration. These include an α–ω dynamo using liquid sodium, a one-ended plasma pinch that simulates the formation of collimated radio sources or bi-polar out-flows, reconnection or current interruptions in a tokamak, which simulates acceleration by coherent reconnection, and finally a collisionless shock experiment to simulate the classical shock acceleration process.

1. Introduction

Cosmic Rays are the extremum of non-thermal phenomena within the Galaxy as well as within the universe. The present upper energy limit of the most energetic event, observed at the Fly's Eye corresponds to $3 \cdot 10^{20}$ eV or $\Gamma = 3 \cdot 10^{11}$. When one compares this to the 3 degree cosmic background radiation, the ratio becomes $1.6 \cdot 10^{24}$, an awesome departure from thermal equilibrium. There are only a few proposed mechanisms of acceleration by which this extraordinary departure from equilibrium can likely arise. Among these are:

(1) The stochastic processes, the Fermi mechanism, where a single particle can scatter elastically and randomly off of individual, more massive units of matter. The units of matter may be either magnetized moving galactic or metagalactic clouds or hydromagnetic waves induced by magnetized collisionless shocks.

(2) The purely hydrodynamic relativistic shock acceleration that occurs when a strong shock in a supernova propagates in the decreasing density gradient of the envelope of a star during the supernova explosion.

(3) The coherent acceleration of particles by electric fields parallel to the local magnetic field as for example occurs in reconnection or by hydromagnetic waves that coherently accelerate particles along field lines.

The most generally accepted mechanism is the collisionless shock (here after CS) in galactic and intergalactic space. The reason for this wide acceptance is the almost universal intuitive acceptance of a mechanism that produces a power-law (in energy) because of diffusion in energy space. The tacit assumption that, in general, "a power law is unlikely" is false and instead a power law occurs naturally in many circumstances as we shall discuss. Since there are many unresolved questions even insuperable difficulties to applying the CS mechanism universally to cosmic ray acceleration, there is a strong motive to consider all other possibilities and how we can possibly resolve this major and dramatic phenomena. Towards this end, the CS mechanism and its limitations will be reviewed in Section 2 leading to why additional mechanisms are needed. The remaining two mechanisms will then be discussed in Section 3 and 4. The second mechanism, the relativistic hydrodynamic shock ejection of supernova envelopes will be rejected for nearly the same reasons as the rejection of the CS mechanism, leaving only the coherent magnetic reconnection mechanism as the likely universal explanation of cosmic rays. In order to help resolve this difficult question, five laboratory experiments will be suggested in Section 5 to help substantiate physical modeling. The conclusion argues for the experiments.

2. Power laws, isotropy and collisionless shock acceleration

2.1. *Power-law spectrum*

The accepted theory of cosmic ray acceleration is shock wave acceleration in the ISM driven by supernova (Axford, Leer, and Skadron, [1]; Bell, [2] Blanford and Ostriker, [3]). As Hillas [4] points out "This acceptance has been largely based upon the good agreement between the universal power-law spectrum predicted by shock acceleration."

colgate@eagle.lanl.gov

i.e. the power-law index becomes:

$$s = (\mathrm{d} \ln N)/(\mathrm{d} \ln E) \sim -(2 + \varepsilon)$$

depending only on the Mach number and the observed or inferred particle spectra. (see Blanford and Eichler [5], for a review, and many papers by P. Biermann for a more accurate comparison.) This belief that a nearly correct power-law spectral index alone is unique is instead, a less restrictive condition than commonly believed. Any accelerator for which a fractional gain in energy, (d ln E), by a few particles is accompanied by a significantly larger fractional loss, $-$(d ln N), in number of the remainder will give a power-law:

$$\mathrm{d}\, N/N = -s(\mathrm{d}\, E/E).$$

The fractional loss for a fractional gain in energy is what would be expected for a rigidity dependent loss mechanism where the probability of a relativistic particle being scattered out of an acceleration region is inversely proportional to its energy or rigidity.

For values of $s < \sim 2$, i.e. a smaller fractional loss, the integral energy becomes asymptotically large, $\int_{E_0}^{E} E\, \mathrm{d}N \sim E^{-s+2}$ and at some energy will truncate or limit the acceleration mechanism, destroying the confinement and hence the accelerating mechanism itself. Hence, it is not likely that at any one time we should see many such accelerators occurring naturally in the Galaxy. On the other hand accelerators with $s \gg 2$ will produce a spectrum so steep that, relative to another less steep one, will not be observed above some critical energy at which the two mechanisms give the same flux. Hence it is likely that the spectrum of any observed mechanism should be close to $s = 2 + \varepsilon$. The conclusion of this argument is that a power law distribution of energy or rigidity *vs.* number is expected for many natural acceleration mechanisms.

2.2. *Why do we need a new Theory of the Origin of Cosmic Rays?*

(1) The spectral argument for shock acceleration is not compelling.

(2) The observed isotropy requires a space-filling mechanism, or if supernova shocks are the sources, that the diffusion mean-free path after acceleration must be very long, >1 kpc, in order that the spatial fluctuations due to a small number of contributing supernova be averaged out and furthermore that the surrounding "leaky box" be extraordinarily isotropic.

(3) The plasma physics of the required scattering mechanism is uncertain in that $\sim 3(v_{\mathrm{shock}}/c)^2 \sim 10^5$ to 10^6 scatterings per particle must occur from strong, self-excited hydromagnetic waves per doubling in energy and yet with negligible damping. Furthermore the hydromagnetic turbulence must be "strong" in order that a particle be scattered with a mean free path not too many Larmor orbits in dimension.

(4) The evidence for acceleration due to quasi-parallel heliosphere shocks is weak, in some cases with small or no evidence for the expected strong hydromagnetic turbulence, and where acceleration is demonstrated, with only a few shock traversals by the accelerate particles implied.

(5) The acceleration of electrons in the same collisionless shock that accelerates ions is difficult to reconcile with the theoretical picture of hydromagnetic turbulence, self-excited by the anisotropic streaming of energetic accelerated ions. This hydromagnetic turbulence will appear adiabatic to the electrons at their much higher Larmor frequency, and so the electrons should not be scattered incoherently as they must be for acceleration. Therefore the electrons must be accelerated by a different mechanism. This is unsatisfactory, because wherever electrons are accelerated, these sites, observed in radio emission, may accelerate ions more favorably.

2.3. *Isotropy*

The shocks in the ISM that would produce the bulk of the cosmic rays up to an energy of $\sim 10^{14}$ eV (Lagage and Caesarsky [6], are presumably derived from supernova. The energy of the supernova explosion, $\sim 10^{51}$ ergs produces a shock of sufficient strength out to a radius of roughly 100 pc or the half thickness of the Galaxy. Any mechanism for accelerating cosmic rays that depends primarily upon supernova will have a problem producing the necessary isotropy presently observed (Osborne [7]). From a TeV to 10 to 100 times greater, where shower arrays are most sensitive to anisotropy, this anisotropy is now less than 10^{-3}. The lifetime, τ, of cosmic rays is assumed to be $\leqslant 10^7$ years from the measurements of the decay of ^{10}Be and the nuclear spallation arguments leading to the "leaky box" model of cosmic rays in the Galaxy. For a diffusion coefficient, D, for particles of a given rigidity there is a characteristic distance, d, within which particles can diffuse to the observer. (It is usually believed that such a diffusion coefficient will be rigidity dependent, but in the CS mechanism the set of all hydromagnetic waves that scatter the particles must scatter effectively over at least six orders of magnitude in rigidity. Hence, in a CS dominated Galaxy, it is likely that most particles wil be localized to a dimension, d, independent of rigidity.) The anisotropy of the diffusive flux will be of the order of the maximum fractional differences of the source distribution of $N_{\mathrm{supernova}}$ number of events averaged over the time, τ. This fractional difference is of order $(N_{\mathrm{sn}})^{1/2}$. If all the supernova within the galaxy at a maximum rate of 1/30 years in the life time of 10^7 years, or $3 \cdot 10^5$ supernova were all equally contributing to the local flux, then the anisotropy would be of the order $(3 \cdot 10^5)^{-1/2} = 1.8 \cdot 10^{-3}$ a value somewhat larger than observed. The diffusion distance, d, must then be significantly greater than the dimension of the galaxy, 30 kpc. Under these circumstances the diffusion coefficient must be greater than $3 \cdot 10^{31}$ cm^2/s or a mean free path for scattering greater than 1 kpc. This is $3 \cdot 10^4$ greater than what is assumed for the necessary scattering for the diffusive shock mechanism where the mean free path is frequently assumed to be roughly 10 Larmor radii at 10 TeV. If this difference in scattering length indeed occurs due to a decrease in hydromagnetic turbulence after the passage of the shock, then one is faced with the further difficulty that the cosmic rays would escape from the galaxy unless the whole galaxy were surrounded by a near perfect "leaky box" with an anisotropic imperfection of diffusive loss of less than 10^{-3}. This is hard to imagine in view of current galactic dynamo theory where a dipole field surrounds the Galaxy yet at the same time inside the box cosmic rays diffuse rela-

tively easily. If a smaller diffusion coefficient, D, is imagined, then in a flat Galaxy, $N_{sn} \sim d^2 \sim D$ and the probable anisotropy due to fluctuations becomes large, proportional to $D^{-1/2}$. Hence an unlikely circumstance must exist of first a very small diffusion coefficient for CS, then a very large one for isotropy, and finally a near perfectly symmetric surrounding leaky diffusive box of our Galaxy.

2.4. *Particle scattering losses*

It is well recognized that in diffusive shock acceleration a particle must traverse the shock many times, $c/v_{shock} \sim 300$ in order to double in energy. However, in order to return to the shock this number of times by random scattering, the mean number of scattering events becomes the square of this number of crossings, or 10^5 scatterings. One recognizes that the accelerated particles are likely to be the exceptional ones that cross the shock the requisite number of times with fewer scatterings, but exceptional in this case is a fraction less than the total number of particles only by the fraction $1/s$ per doubling where s is the above exponent of the power law. Hence, the fractional energy loss per scattering must be very small for the average particle, which is the particle "lost" from acceleration by diffusion in space, down stream in the shock fluid to convection at each energy. Hence, recognizing the many orders of magnitude of acceleration required, in order not to modify the power-law exponent below the good agreement with theory, the fractional irreversible loss per scattering must be less than $\sim 10^{-5}$ to $^{-6}$. This is an extraordinarily small loss in the presence of what must be strong turbulence in order to have the short scattering lengths required (~ 10 Larmor orbits) to reach the highest energies (Lagage and Caesarsky [6]). One suspects the excitation of at least one mode of non-linear damping of the hydromagnetic waves at this level. Such non-linear damping induces heating and hence damping of those particles furthest ahead of the shock that excite the waves in the first place. The particles furthest ahead are those of greatest rigidity and therefore most sensitive to modifying the spectrum.

2.5. *Particle acceleration by magnetospheric shocks*

Particle acceleration in quasi-parallel magnetospheric shocks as well as the expected hydromagnetic turbulence have been observed by space craft but at intensity levels that are as low as 10^{-4} of the values both expected and necessary for shock acceleration (Sarris and Krimigis [8], and Krimigis [9]). The perpendicular shocks on the other hand show significant acceleration as one would expect by trapped Larmor orbits (Colgate [10]). These accelerated particles, however, represent a small fraction of the necessary acceleration for explaining cosmic rays. One suspects that a lower law spectrum of non relativistic particle velocities is not sufficiently narrow in phase space to excite the hydromagnetic turbulence necessary for back scattering the particles repeatedly across the shock front. On the other hand in the relativistic case of high energy cosmic rays, the variance in rigidity should lead to a variance in frequency, which should play a similar damping role.

2.6. *Acceleration of electrons by collisionless ion shocks*

The plasma turbulence associated with the scattering of the accelerated ions back and forth across the shock is presumed to be excited by the anisotropy of the momentum distribution of the ions forming the shock. This "current" of ions is subject to a local channeling instability where a local current density, in the z direction, gives rise to a local component of the magnetic field in the ϕ-direction. Hence locally a small region of combined z and ϕ field or helical field or torsional Alvén, or hydromagnetic wave is created. The dimension of these helices is of the order of an ion Larmor orbit, so that the time of the existence of such a wave is of the order of an orbit time. Therefore the phases of individual ions will be scrambled and hence, a random group of such waves at the strong turbulence limit should scatter ions in the z-direction back and forth along (in the z-direction) in some 10 Larmor orbits. This is the usual thickness assumed for the front of the collisionless shock. The question is how can such a picture be made consistent with electron acceleration when the momentum and the orbit time of the electrons is less by the mass ratio? The point is that one would expect electrons to follow along the field lines regardless whether the lines are wrapped up in a helix or not. The electrons would remain adiabatic, not change their magnetic moment stochastically like the ions, and so would proceed out ahead of the collisionless shock. Naturally, if many electrons proceeded ahead of the ions, a strong electric field of charge separation would develop, the ambipolar field. The integral of this field along the line, or potential, however, is limited to some ten times the thermal energy of the electrons, not enough to reflect a few exceptional accelerated electrons that might be reflected back and forth across the shock. Therefore it seems unlikely that a collisionless shock in the lowest order description should accelerate electrons.

Galeev [11] has discussed the acceleration and heating of electrons in collisionless shocks and finds that one must rely upon the excitation of strong ion sound waves by the streaming ions in order to back scatter energetic electrons. The problem of the excitation of strong ion sound waves by streaming ions has had a long history, and it has never been shown theoretically or experimentally that such excitation takes place.

A laboratory plasma experiment was performed to observe the effect of a strong current in a plasma by transmission of a short pulse, 10^{-8} s, of energetic, 0.5 MeV, electrons. The plasma current, a linear stabilized pinch, was strong enough to excite hydromagnetic turbulence sufficient to scramble the magnetic flux surfaces as would be expected for an ensemble of torsional hydromagnetic waves (Birdsall *et al.* [12] and see Appendix Colgate [13]. However, despite the extreme random distortion of the magnetic surfaces, the high energy electron beam was transmitted through the hydromagnetic turbulence unattenuated. Electron acceleration by collisionless shocks is therefore conceptually a very questionable process.

3. The supernova envelope shock origin of cosmic rays

The explosion of Type 1 supernova leads to a collisional hydrodynamic shock in the envelope of the star, (Colgate and Johnson [14], Colgate and White [15], Colgate, McKee and Blivens [16], Colgate and McKee [17], Colgate [18], Colgate and Petschek [19], and a review, Colgate [20, 21].) The spectrum produced by the relativistic shock is one

power of E steeper than observed. (The differential exponent s is ~ 3.5 rather than the observed 2.6) and so is unlikely to be the primary source of cosmic rays. On the other hand the possibility of accelerating ultrahigh energy particles to $> 10^{18}$ eV is significantly greater than by collisionless shocks in the ISM driven by supernova. The non-relativistic hydrodynamic supernova shock becomes relativistic at an external mass fraction of $(1 - F) = 3 \cdot 10^{-6}$ of the star. The resulting ejected relativistic matter energy, $(1 - F)M_0 c^2 = 6 \cdot 10^{48}$ ergs per SN. This is only about $\frac{1}{5}$ of what is necessary to explain the galactic cosmic rays energy.

The heavy nuclei are partially spalled in the shock transition and partially resynthesized in the post shock expansion for $E < 10^{15}$ eV, depending upon the large number of pairs in the post-shock fluid. Above this energy the shock progresses in the magnetized photosphere, but still as a pair dominated collisional shock. At some point the expanding relativistic matter escapes into the ISM. There have been arguments both for the escape of the accelerated matter (Holman, Ionson and Scott [22], and Colgate [20, 21]) and against by adiabatic expansion in the ISM (Kulsrud and Zweibel [23], Kulsrud [24, 25]). The adiabatic expansion argument depends upon the existence of a collisionless shock which contains the relativistic shock ejected matter. The existence of such a collisionless shock in the ISM has the same uncertainties as the above arguments for acceleration by the CS mechanism. Regardless, the prediction of a too steep spectrum, too little total energy, and a non standard nuclear composition argue strongly against this mechanism. In addition the supernova envelope shock suffers a similar difficulty from anisotropy limited by diffusion in the ISM. In summary a different mechanism is needed for acceleration of cosmic rays that is isotropic, space-filling and extends over the full observed spectrum.

4. Acceleration of CR by reconnection of magnetic helicity

There is a need for a mechanism to accelerate cosmic rays universally over the full energy spectrum, isotropically, and space filling. A theory based upon a series of mechanisms, patched to fit various spectral regions is less satisfactory than a single mechanism that takes place in different circumstances throughout the universe. Furthermore any mechanism that results in a fractional loss in number of particles for a given fractional gain in energy results in a power-law. I believe that the force-free reconnection of magnetic field twisted by the vorticity motion of all accretion or gravitational condensations both within the Galaxy as well as the metagalaxy is a universal circumstance to expect such acceleration. Mass condensations always occur with finite angular momentum. The winding number occurring during the dissipation of this angular momentum assures that all imbedded flux will undergo continuous winding until either the angular momentum is dissipated or reconnection takes place. This assures that at least several orders of magnitude of twist, i.e. a winding number of at least several hundred or greater will take place. The transition between this picture of transient, multiple, highly twisted, flux-tubes within our galaxy (and between galaxies) and the observed state of relatively ordered flux must occur by reconnection. It is this reconnection of force-free field that of necessity must lead to E-parallel acceleration. The acceleration of cosmic rays in this picture is then a sum of both individual particles that are accelerated in single coherent regions of high winding number and particle that undergo random diffusion in energy space. These are particles that stochastically traverse many coherent regions of E-parallel acceleration and deceleration.

An important distinction exists between this picture of acceleration by force free reconnection and acceleration by reconnection in a turbulent plasma. Matthaeus *et al.* [26] and Ambrosiano *et al.* [27] have suggested the acceleration of particles by reconnection in a turbulent plasma in the ISM and recently to very high energies, 10^{16} eV, with Goldstein *et al.* [28]. The general picture of hydromagnetic turbulence is one where turbulent mass motions induce a stochastic distortion of the magnetic field. Here the mass and the field motions are at the characteristic hydromagnetic velocity and the currents are therefore primarily perpendicular to the local magnetic field in order to generate the pondermotive forces. In the force-free reconnection acceleration mechanism the currents are primarily parallel to the field by definition. This circumstance arises because of the relatively slow twist of the flux tubes by gravitationally condensing mass, but limited in the rate of condensation by the transport of angular momentum. The advantage to acceleration of force-free reconnection is that the electric field of reconnection is necessarily along the field lines rather than across the field. This allows coherent acceleration over great distances as compared to a stochastic diffusion in energy space with relatively small steps of the order of a ~ 1000 Larmor orbits.

4.1. *The reconnection theory of acceleration*

The specific angular momentum of matter in the galaxy rotating at an $\omega = 10^{-8}$ per year and a local radius corresponding to roughly one solar mass, (~ 3 pc) is $3 \cdot 10^{22}$ cm^2/s. This is some $2 \cdot 10^4$ larger than the Keplerian orbit at a solar radius. This large factor of excess angular momentum must be exchanged with the Galaxy as a whole in order to form a star, and still more angular mometum must be removed in order to collapse to a neutron star. The most likely mechanism for the transport of this angular momentum is by a turbulent, α-viscosity in the disk-like accretion of a star through the T-tauri stage. (If the torque is transmitted by magnetic stress, this makes the following effects even larger.) Similarly, the magnetic flux threading the original matter at the density of the ISM is also orders of magnitude, $\times 300$, larger than the flux that would allow compression to a solar radius. Furthermore the observed external flux of the Sun and typical other stars is 10^{-6} to $^{-7}$ times less than this formation limit. Hence magnetic flux must also be expelled from the condensing matter as well. Therefore this flux, in order to escape the matter, must undergo reconnection during the process of condensation. However the subsequent winding or twisting of this residual flux requires a far larger reconnection process since the winding produces a far larger total flux than the original flux.

The picture at every stage of condensation is that of a helical, twisted flux tube that extends some 50 to 100 turns beyond the source. The number of turns is intepreted observationally from the topology of the "jets" or collimated radio sources which are presumed to be just these helical flux tubes from accretion onto the black holes of AGN.

They become illuminated in the radio by the accelerated electrons due to the reconnection of the force-free flux of the twisted flux tube. The same picture applies to the bi-polar flows observed in star formation. The relation between the number of turns and the angle of the "jet" is that the minimum energy force-free field of the helix is close to a 45 degrees where the ϕ and z components of the field are equal. Hence the number of turns, n, will be of the order (1/jet angle) $\times$ ln (L_{max}/R_{min}), or several hundred.

It is assumed that the reconnection dissipates the total current associated with the B_ϕ component of the field. If this current is interrupted as a sequence of multiple reconnection events, but phased along a local flux surface at c by the accelerated particles themselves, the total potential becomes of the order:

$$V = nB_{max}R_{min}\,300(2\pi \ln n) = 2 \cdot 10^{22}\ \text{eV}.$$

where $B_{max} = 10^3$ gauss, the limiting magnetic field around an AGN black hole and at six times the Schwartzschild radius, and $R_{min} = 1$ AU.

Accretion onto neutron stars, cataclysmic variables, and T-tauri stars will all lead to tearing mode reconnection associated with all mass condensations. The bi-polar flows that are now frequently observed in the radio maps of star forming regions correlate with this process. The energy of these condensations alone is sufficient by many orders of magnitude to maintain the cosmic rays of our Galaxy. Let us assume that the star formation rate is $10\,M_0$ per year and that magnetic field decouples from the accreting matter at a disk radius of 1 AU where pressure support of the forming star would become comparable to the α-viscosity. Then the energy released by star formation at this decoupling radius becomes;

$$\dot{E} = \dot{M}\frac{MG}{R} = 2 \cdot 10^{47}\ \text{ergs year}^{-1}.$$

In the life-time of cosmic rays of 10^7 years this rate corresponds to $2 \cdot 10^{54}$ ergs. This is equal to that required to make the CR flux corresponding to a total cosmic ray energy content of the Galaxy of $2 \cdot 10^{54}$ ergs. In addition the wrapping up of the flux generated by the dynamo of each star during its life time should increase the available magnetic field energy by 10 to 100 fold, and by neutron stars a further factor of 100. Finally if the magnetic field of the Galaxy is conductively attached to a larger mass of matter in the IGM, a comparable energy in helical sheared field will be created. Therefore the free energy in force free magnetic field stress should be many orders of magnitude larger than necessary to accelerate the cosmic rays.

5. Experiments

In order to choose which of the many complicated processes are primary in producing the acceleration of cosmic rays, we need some guidance from the laboratory experiments. Since every proposed mechanism for the acceleration of cosmic rays depends upon the existence of relatively strong magnetic fields, either stellar or Galactic, where "strong" implies equipartition between dynamical stress and magnetic field stress, the most fundamental process is the dynamo itself. Although a large amount of effort has been spent on the theory and numerical modeling of the dynamo process (see Roberts and Soward [29] for a current review), no experiment has yet been able to demonstrate that the models are correct. In preparation for this meeting, such an experiment was designed.

There are two kinds of proposed dynamos: the first is the so-called fast dynamo originally proposed in part by Alvén [30] and in the more complete form by Vainshtein and Zeldovich [31]. Here a loop of flux, fully imbedded in a conducting medium is first stretched, twisted, folded and reconnected. See current work by Childress *et al.* [32] and Finn *et al.* [33]. The second kind of dynamo is the so-called α–ω dynamo. I believe that it is more applicable to a star or the conducting interior of a planet because of the physical deformations of the fluid. Here the ω deformation is the continuous internal wrap up of a bias field by a differential rotation of the bulk motion of the interior of the star. This wrap up produces an increase in the toroidal field entirely interior to the conducting media. The bias field is a poloidal field that has the special feature that it extends external to the conducting media and is therefore observed. The bias field also experiences the special condition of reconnection both at the surface separating the conducting media from an external partially insulting "vacuum" region and within the partially insulating medium. The α deformation converts a small fraction of the amplified internal toroidal field into the poloidal bias field.

The importance of plume type convection to the "α" deformation of the α–ω dynamo is just now recognized. The convective motions of the convective region of a star are primarily large bubbles or plumes that because of rapid expansion and small entrainment, approximately preserve both entropy and angular momentum. In a rotating body and because of the partial conservation of the angular momentum, the plume rotates more slowly as it expands. This twist relative to the bulk motion and the buoyancy driven vertical motion constitute the "α" deformation.

The combination of these motions for producing an α–ω dynamo allows the possibility of an experimental analog using the hydromagnetic fluid of the liquid metal sodium or sodium–potassium alloy, called "NaK". Similarly we can perform laboratory plasma experiments to observe reconnection in the near vacuum limit and the resulting parallel electric field and hence acceleration. Without laboratory experiments, shock acceleration is uncertain because of nonlinear plasma effects. A partial list of astrophysical experiments relevant to acceleration follows:

(1) A mock-up of the α–ω dynamo process using liquid Na as a hydromagnetic fluid. The origin of the α component of dynamo theory in real circumstances like stars, galaxies, and planets is questionable. An experiment can demonstrate that a diverging plume in a rotating frame produces the necessary α effect whereas smaller scale uniform turbulence is unlikely to.

(2) A plasma "pinch" experiment can be done that simulates the formation of a collimated radio source originating from an accretion disk. The presumed collimated helical magnetic field structure can be formed by either an accretion disk around a black hole or by an accretion disk at an early stage of star formation. Both the hydromagnetic configuration of a force-free helical field as well as the expected acceleration due to reconnection should be observable in a laboratory plasma experiment. A plasma code, numerical

simulation would give a greater degree of confidence of extending the experimental results to astrophysical circumstances.

(3) The self-triggering of a reconnection event in a force free, sheared (current carrying) plasma by relativistic run-away electrons. This would simulate one explanation of the acceleration of the highest energy cosmic rays. This needs to be done in a tokamak that has been retired from active fusion research. The interruption events in Tokamaks are well recognized to result in the confined acceleration of a run away beam of multi-MeV electrons that can severely damage the metal vacuum liner.

(4) The formation of a strong hydromagnetic shock in the laboratory with enough Larmor orbits in dimension (about 100). This would allow the investigation of the first order Fermi shock acceleration process. The presumed excitation of the pre-shock hydromagnetic waves can be diagnosed by a pulsed electron beam that maps the shear in a bundle of lines or flux tube on which torsion hydromagnetic waves, which are self excited by anisotropic high energy ions. These flux lines would be those that threaded along the oblique lines of force.

5.1. *The dynamo experiment*

An α–ω dynamo is characterized by a "dynamo number" defined by the product of the two Reynolds numbers, R_ω of the ω deformation and R_α of the α deformation, or $R_\omega R_\alpha$. This product has been estimated by Parker [34] as required to be ~ 1000 in order to achieve positive gain, i.e. to make a dynamo work. However, the minimum value of this number depends upon the ratio of the characteristic dimensions of the two different deformations. These two Reynolds numbers can be defined in terms of the magnetic diffusion coefficient, D_{Na}, of the liquid metal at 100 °C or of D_{plasma} of

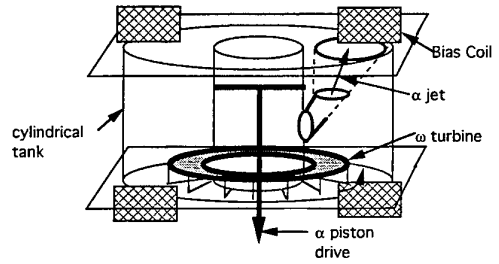

Fig. 1. The liquid sodium α–ω dynamo experiment. Here, meridianal circulation within a cylindrical tank of liquid sodium is driven by a turbine at one end. A piston within a smaller diameter cylinder drives axial jets. These jets in turn create axial plumes directed towards the opposite end of the tank.

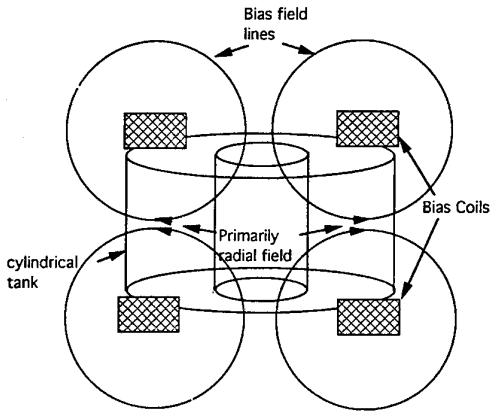

Fig. 2. The field created by the bias coil. This field is poloidal and is primarily radial in the central region where meridional flow creates a region of differential rotation. The bias field is a convenience for measurements and does not play a fundamental role.

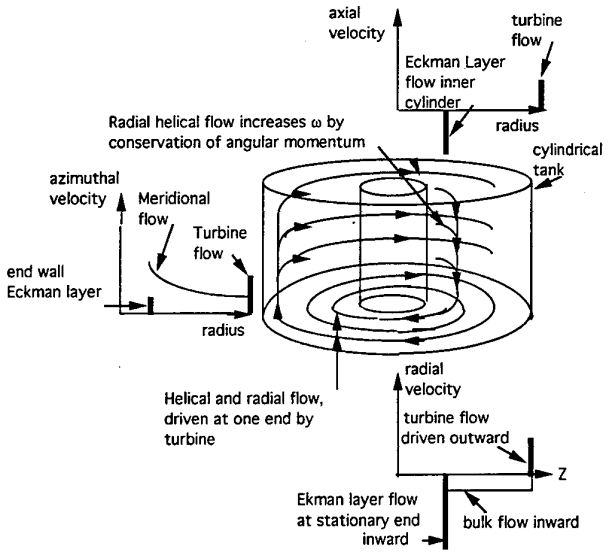

Fig. 3. The meridional flow with the azimuthal velocity component proportional to r^{-1} or ω proportional to r^{-2}. This flow is driven at one end by the turbine with excess angular momentum, and a small, non-rotating Eckman* layer flow at the opposite end short circuits some of the turbine driving flow. The axial flow is shown as thin Eckman layers at the non-rotating surfaces. The radial flow is comprised of the turbine flow at one end, a smaller oppositely directed Eckman layer flow at the opposite end, and an average radial inward flow throughout the volume.

* An Eckman layer is a layer of fluid separating a rotating fluid from a stationary (different rotational velocity, ω) boundary. Viscosity produces a layer of fluid with different ω and hence with different buoyancy relative to the main flow. The buoyancy drives a rapid circulation of the fluid of the layer; the viscous drag is a slow diffusion. Hence the layer is thin.

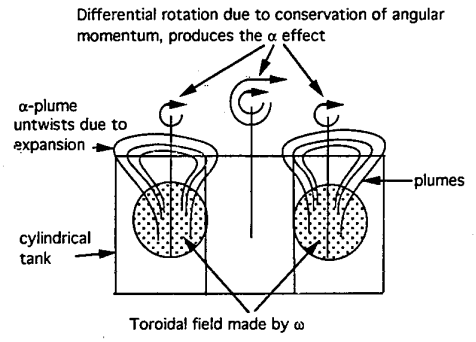

Fig. 4. The increased toroidal field due to "wrapping up" or twisting of the radial bias field. Axial jets are also shown that diverge as plumes when they reach the end wall. They carry a fraction of the toroidal flux to the end wall where the divergence of the flow both exposes the trapped flux to the lower conductivity (or insulator) of the end wall allowing a fraction of the flux loop to escape the tank as a potential field. A twist of the loop occurs because the plume increases in radius as it diverges at the end wall. At roughly constant angular momentum, the angular velocity decreases relative to the parent fluid so that the ω of the plume is roughly $\frac{1}{2}$ to $\frac{1}{4}$ of the ω of the meridional flow. This differential rotation is depicted by the fewer circulation arrows of the plumes relative to the main flow. The relative twist produced by this difference in ω rotates the loop of flux into the poloidal plane. The merging of these poloidal loops adds to the original, poloidal, bias field.

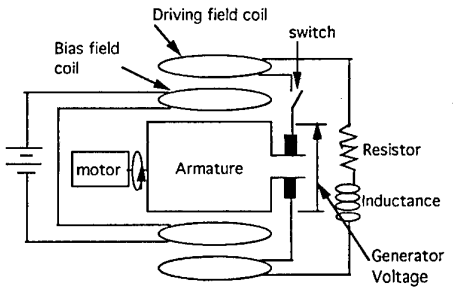

Fig. 5. An analog of the dynamo experiment. A d.c. generator has two sets of field coils. One set, which corresponds to the d.c. bias field of the dynamo experiment is driven by a battery producing a bias field current. This current, I_0, produces an output voltage, V_0, where $V_0 = \Gamma I_0$ and where Γ is a gain factor. If the armature were short circuited on itself, the resulting current and magnetic field would be the analog of the dynamo meridional circulation, which wraps up the bias field into a large toroidal field. In addition a second set of field coils, the generator coils, with the same gain factor, Γ, are connected in series through a switch with the armature, which is driven at constant speed by the motor. This connection and the output voltage due to the increase in the total field, is the analog of the "α" part of the dynamo. This generator is built similar to the older electric starter motor in your automobile. The bias field is the residual magnetism of the field core iron. The voltage generated by the generator coils with current, I, is $V = \Gamma I$. This set of coils and armature have a lumped series resistance R and an inductance L. If the inductance is neglected and if $\Gamma/R < 1$, then the voltage at steady state becomes $V = V_0/(1 - \Gamma/R)$. If the inductance is included, then when the switch is closed the voltage becomes;

$$V = \frac{V_0}{1 - \Gamma/R}(1 - e^{(-tR/L)}).$$

In other words the voltage approaches the same steady state with the characteristic time constant L/R. The absolute value of the voltage depends only upon the ratio, Γ/R. If this ratio is equal to unity, the generator output increases until the power is limited by the motor. This is then the analog of a successful self-generating dynamo. On the other hand, if Γ/R is small compared to unity, there will be a small fractional incremental increase in voltage (above V_0) of order Γ/R. There will also be a small fractional increase in the total field current, I. Similarly for a dynamo with small or marginal gain, there will be a small increase in the external bias field. It is this case of small gain that we expect for the initial experiment. This small increase in the external poloidal field indicates partial gain. This partial gain should then depend upon velocity, plume frequency, and plume initial angular momentum in a fashion predictable by modeling and theory. A larger size, higher velocity, more efficient plumes will then presumably lead to a dynamo with $\Gamma/R \geqslant 1$.

a plasma or D_{copper} etc. Here, $D = \eta_{\text{emu}}/4\pi$, where $\eta_{\text{emu}} = 10^9\eta_{\text{ohms}}$. In cgs units: $D_{\text{Na}} = 716$, $D_{\text{copper}} = 135$ and $D_{\text{plasma}} = 2.0 \cdot 10^6 Z T_{\text{eV}}^{-3/2}\,\text{cm}^2\,\text{s}^{-1}$. (Here, $\ln\Lambda$ is chosen = 10.) Liquid sodium is the optimum analog, or experimental hydromagnetic fluid because of density and electrical resistivity (Colgate, Furth and Haliday [35]). The alkali metal alloy, Na plus K, is more convenient to use because it is a liquid at room temperature, but its resistivity is more than four times greater than that of liquid Na at its melting point of 100 °C. Using Na for the experimental fluid, the magnetic Reynolds number becomes:

$$R_{\text{mag}} = vr/D; \quad \text{using } D_{\text{Na}} \quad \text{then } R_{\text{mag}} = vr/716,$$

where v and r are the characteristic velocity and dimension of the respective flows, α and ω.

5.2. *Fluid friction*

In order to maximize R_{mag}, a high velocity of the fluid is required, but this increases the fluid friction and hence the power required to drive the fluid motions. If the boundary of the flow has a dimension L then the dissipation due to fluid friction over the surface area, ($A \sim 4\pi L^2$) becomes:

$$\textit{power} = AC_f\rho v^3/2.$$

If the flow dimensions corresponding to α and ω are a fraction, δ, of the boundary dimensions such that $r = \delta L$, then the power becomes

$$\textit{power} = 2\pi(R_{\text{mag}} D_{\text{Na}}/\delta)^3 C_f/L.$$

For liquid sodium, $\rho = 1$, and the coefficient of fluid friction, C_f, is approximately 1/400, corresponding to high (fluid) Reynolds number flow and neglecting the enhanced friction due to Eckman layer flow. Also for the ω-flow one might achieve $\delta = \frac{1}{2}$. Then

$$\textit{power} = 5 \cdot 10^{-3} R_\omega^3/L \text{ kW}.$$

For example a 120 cm diameter cylinder, 60 cm in length driven by 2.5 kW of power might achieve a value of $R_{\text{mag}} = 32$ for the ω term.

The α flow is created by episodic plumes or jets of dimension $r/4$ at a velocity of roughly $2v$. Hence, $R_\alpha = 16$. The product of the two magnetic Reynolds numbers, the dynamo number, is 500, somewhat less than presumed to be required, ~ 1000, but the frequency of the episodic plumes is an additional variable that can decrease this limit.

The experiment would use a finite bias poloidal magnetic field so that the magnetic sensors are less expensive, but in addition if the dynamo gain is less than unity, then a very much smaller gain, less than 1%, can be detected as an incremental change, or increase in the poloidal field. Therefore, one can explore dynamo action on very much smaller scales provided the goal of large gain is given up. Figures 1–5 illustrate such an experiment including a standard d.c.-generator which is an analog of the dynamo experiment.

5.3. *The plasma pinch/collimated radio source experiment*

The helical hydromagnetic field structure produced by an accretion disk is shown in Fig. 6. Here an initial bias through the disk is wound up many turns by the Keplerian orbital motions of the disk. The minimum force-free field configuration is a diverging helix. The limiting extent is primarily determined by the reconnection of the various flux surfaces comprising the helix. An experiment to produce this field configuation is shown in Figs 7 and 8. The objective of the design is to minimize the cost and yet maintain a high enough magnetic Reynolds number that the conducting limit is achieved. The limiting temperature in a laboratory experiment of a one-ended pinch is discussed in the context of solar flares in Colgate [13] and references are given to the corresponding laboratory work. The agreement between the laboratory scale and the solar flare scale gives confidence to the scaling parameters. Hence, one can estimate a mean plasma temperature of roughly 20 eV where ionization of a hydrogen plasma is complete. (Neutral atoms strongly damp the desired hydromagnetic effects because of charge exchange). Then, the magnetic diffusion coefficient of the plasma becomes,

$$D_{\text{plasma}} = 2.0 \cdot 10^6 Z T_{\text{eV}}^{-3/2}\,\text{cm}^2\,\text{s}^{-1} = 2 \cdot 10^4\,\text{cm}^2\,\text{s}^{-1}$$

so that $R_{\text{em}} = rv/D = 5.4 \cdot 10^3$ for $r = 30$ cm and $v = 3 \cdot 10^7\,\text{cm}\,\text{s}^{-1}$. These values are chosen on the assumption

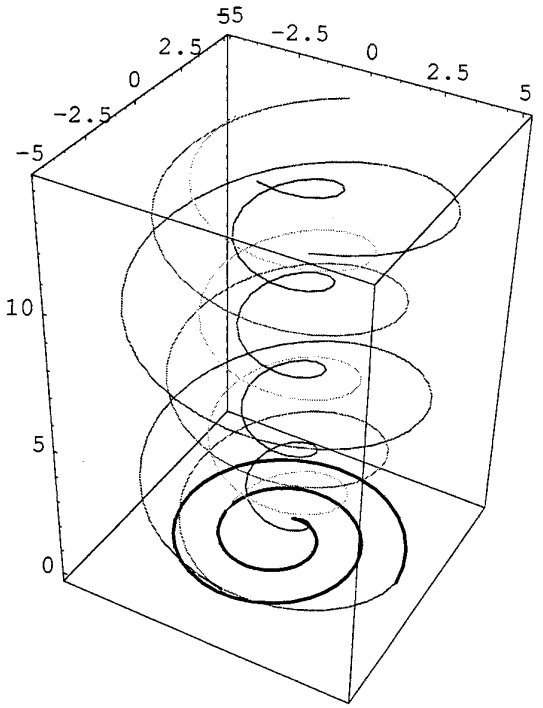

Fig. 6. The hydromagnetic field configuration produced by a poloidal bias magnetic field convected by the accreting plasma of an accretion disk as for example around a star or black hole. The vertical helical structure is the nested twisted flux tubes produced by the lines of force threading the accretion disk. The differing pitch of the lines of force is due to both the force-free field condition as well as the radially differing Keplerian orbital velocities. (Figure by Ramond Laflamme, T-6, LANL).

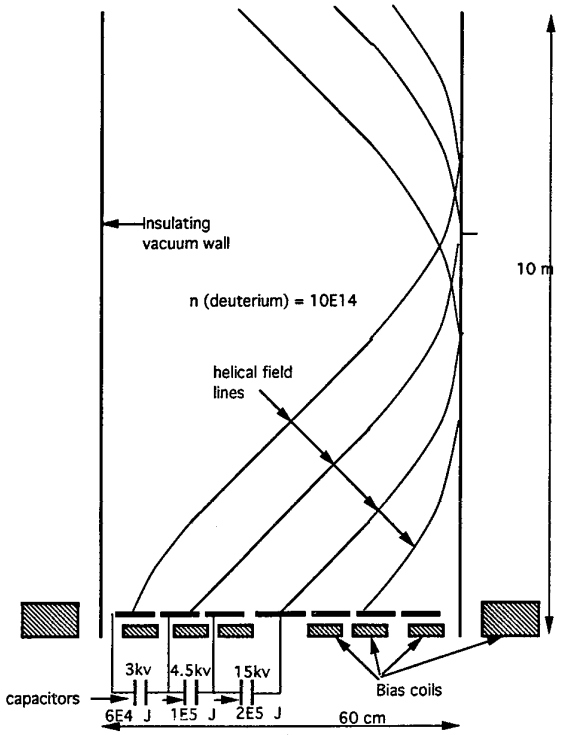

Fig. 7. A laboratory plasma physics experiment that should permit the observation of the helical flux surfaces produced by an accretion disk. The bias field coils are arranged so that the poloidal field strength simulates the axial field component expected, $B = B_0 r^{-3/2}$. The bias field flux lines close outside the insulating walls of the vacuum system. The electrodes are rings connected to a series of condenser banks. The respective voltages and the resulting electric fields, $E = E_0 r^{-2}$, produce the azimuthal velocities corresponding to the Keplerian orbits of an accretion disk. The length of the actual experiment should be enough to demonstrate roughly 10 turns of the inner half diameter, or 16 diameters.

that the experimental values of $B \sim 5000$ gauss and that $n_D = 10^{14}\,\mathrm{cm}^{-3}$. The resulting capacitor bank energy is then $3 \cdot 10^5$ joules if the length is 10 meters. This is sufficiently large so that one might observe a winding number of $R_{em}/(3 \cdot 2\pi) = 200$ turns. Here, the factor of $\frac{1}{3}$ is an estimate of the radius where the inner half of the current flows. The reason for choosing such a high axially velocity of the helix (figuratively the velocity of the jet) is that one desires a velocity high enough so that the initial neutral gas will be ionized by the electron drift energy (Colgate [36]) which in turn is due to the kinetic energy of the ions. At $3 \cdot 10^7\,\mathrm{cm\,s}^{-1}$ the kinetic energy of a deuterium ion, the preferred ion, is 1000 eV. This is high enough to ensure complete ionization, as well as make up for losses. Since the magnetic helix is presumed to be force free in the astrophysical circumstance, in the experimental case, the hydromagnetic velocity must be larger than the axial velocity, or roughly $v_{\mathrm{hydmag}} = 3 \cdot 10^7\,\mathrm{cm\,s}^{-1}$. This large hydromagnetic velocity means that the density must be low, or the field strength large. If the field strength is large, the magnetic energy supplied by the capacitors must be large and therefore the cost will be excessive. A low density, on the other hand, is limited by the electron velocity of the current carriers that would induce Alvén instabilities. A compromise of all these factors suggests an electron or ion density of $n_e = 1$ to $2 \cdot 10^{14}\,\mathrm{cm}^{-3}$. A gradient of the initial gas density (as from a pulsed valve), allows the initial discharge to form at higher density, but then the helix should progress ahead of this higher density plasma into a region of lower density where the force-free condition is more closely met. In addition the run-away condition (i.e. acceleration) would take

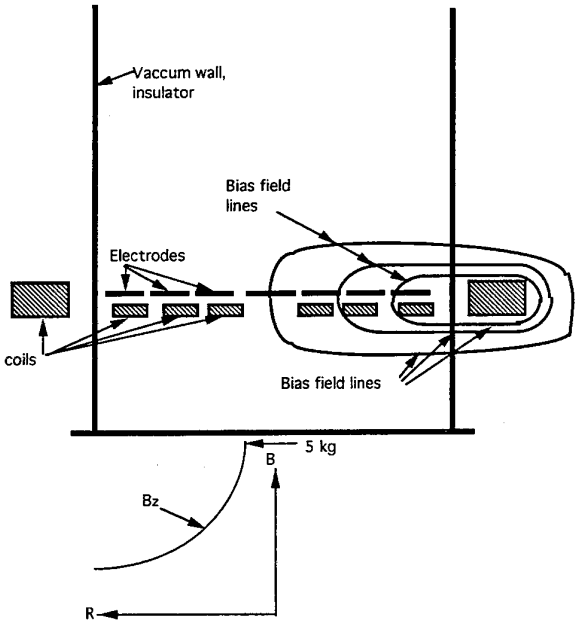

Fig. 8. The bias field lines for the above one-ended plasma pinch. The magnetic field distribution is shown below the coils and bottom electrodes. A peak field of roughly 5 kg falls off as $r^{-3/2}$ in order to simulate the axial field advected in and diffused outward in an accretion disk (G. Willett, private communication). The values chosen for the voltage and stored energy of the capacitor banks in Fig. 7 are chosen to simulate the Keplerian velocity of an accretion disk at various radii, proportional to $r^{-1/2}$.

place due to the lower density as well as reconnection instabilities.

5.4. *Tokamak run-away acceleration experiment*

As the density of the plasma decreases in a tokamak discharge due to diffusion processes, the current must be carried by a smaller number of electrons. The inductive energy or magnetic energy of this current then accelerates fewer and fewer electrons to higher energy. Because of the high degree of perfection of the magnetic surfaces, the run-away particle confinement is good and the accelerated electrons remain within the field configuration. Hence their energies can become very great, 10 to 100 MeV, and the total energy of the run-away beam is enough to do damage to the walls of the confinement vessel (Wesson *et al.* [37] and Gill [38]). This damage is expensive to repair, a hole melted through the vacuum vessel liner, and so the circumstances of this "fault" occur rarely and in successful machines not at all. This process is therefore to be avoided with great care in the usual plasma experiments. A pulsed gas valve ensures that the density never falls low enough to approach the run-away condition. On the other hand, this is just the circumstance that is most likely to demonstrate acceleration in astrophysics. Nearly all of the free energy of the field configuration is transformed to accelerated particles.

This condition can be induced and experimentally investigated in a tokamak machine that is no longer dedicated to fusion plasma confinement experiments. Of course, care would be needed to prevent a concentrated dumping of the accelerated beam energy at one point on the liner, but coils that destroy the perfection of the magnetic surfaces should allow a more gradual and more dispersed in area dumping of the beam. One should then be able to investigate the process of an induced tearing mode instability, phased by the accelerated particles themselves

5.5. *Collisionless shock acceleration experiment*

A collisionless shock experiment in the laboratory requires driving a strong shock into a pre-ionized magnetized plasma. The only practical piston is another rapidly rising magnetic field. The constraints that must be met are:

(1) The number of Larmor orbits in dimension must be large enough to make a valid test of collisionless shock theory, a number of the order of 100.

(2) The damping by collisions must be small enough so that velocity phase space instabilities are not stabilized by isotropization. The number of collisions should then be less than 1/(number of Larmor orbits).

(3) The cost determines feasibility. The cost is nearly proportional to the magnetic energy, or in turn to the size of the capacitor bank required to supply the energy. A reasonable goal for a university scale experiment is a total capacitor bank energy less than several times 10^5 J.

Let the distance the shock traverses be L, measured in Larmor orbits, R_L, so that $L = \Gamma R_L$ where Γ is the primary measure of the test of the plasma physics of the experiment. In addition the preferred ion is deuterium, because it has the minimum scattering cross section for maximum mass and minimum radiation loss. Then

$$L = \Gamma R_L = 200\ \Gamma E_{eV}^{1/2}/B \text{ cm}.$$

Since the build-up of velocity phase space instabilities is likely to be very sensitive to the velocity distribution function and therefore to the collisional damping, the number of scattering events in the distance L, should be of the order $1/\Gamma$, so that the mean free path, λ, should be

$$\lambda = \Gamma^2 R_L.$$

Since the Coulomb cross section is a function of energy and only weakly, logarithmically, a function of density, it can be approximated to give

$$\lambda = 1.6 \cdot 10^{12} E_{eV}^2/n_D \text{ cm},$$

where n_D is the plasma number density.

The shock must be driven at a velocity, v_s, such that the particle pressure is approximately the magnetic pressure, or equivalently, that the shock speed is the hydromagnetic speed. This gives the relation that

$$\rho v_s^2 = B^2/8\pi.$$

With these relationships and expressing the results in terms of $\Gamma = 100$, or Γ_{100} and the kinetic energy of the ions in units of a keV, one obtains:

$$L = 3.3 E_{keV}^{-2} \Gamma_{100}^3 \text{ m}$$

$$B = 1.9 E_{keV}^{5/2} \Gamma_{100}^{-2} \text{ kg}$$

$$n_D = 4.8 \cdot 10^{13} E_{keV}^4 \Gamma_{100}^{-4} \text{ cm}^{-3}.$$

The total energy, W, becomes

$$W = 13 E_{keV}^{-1} \Gamma_{100}^5 \text{ MJ},$$

and the time for the shock to traverse the dimension, L, becomes

$$t_s = 10 E_{keV}^{-5/2} \Gamma_{100}^3 \ \mu\text{s}.$$

For $\Gamma = 100$, the energy is of the order of the "Zeus" capacitor bank at Los Alamos, dismantled several years ago, but for $\Gamma = 50$, and $E = 300$ eV the dimensions and energy are feasible. The turbulence excited on the field lines by the anisotropic velocity distribution of the shocked particles can be measured by a pulsed electron beam as in Colgate [13] and Birdsall *et al.* [12]. Therefore a modest test of particle acceleration by a collisionless shock can be performed in the laboratory, but the relativistic, truly collisionless case is uniquely the domain of astrophysical space.

6. Summary

Five problems of shock acceleration for the production of cosmic rays have been discussed in the context of astrophyisical conditions. Because of these difficulties, an alternate explanation has been given where reconnection of twisted magnetic fields (from condensation, accretion, and conservation of angular momentum) accelerates particles along field lines. The acceleration is coherent provided the reconnection is coherent, in which case the total flux, as for example of collimated radio sources, predicts single charge accelerated energies much greater than observed. The same acceleration process should occur during the formation of stars associated with the T-tauri phase and bi-polar outflows. Because of the ubiquitous nature of matter condensations in the universe, the acceleration is inherently isotropic and space-filling in nature.

Four laboratory experiments are suggested that would form the basis of a substantiated science of plasma processes of acceleration. These include an α–ω dynamo using liquid sodium, a one-ended plasma pinch that simulates the formation of collimated radio sources or bi-polar out-flows, reconnection in a tokamak which simulates acceleration by coherent reconnection, and finally a collisionless shock experiment to simulate shock acceleration.

Acknowledgements

It is a pleasure to acknowledge the stimulation of this conference on Acceleration Processes in Astrophysics organized by Tom Katsouleas and Andrew Sessler. Conversations during the Cosmic ray conference in Calgary, '93 with N. Duric, R. Jokopi, H. Volk, and many others has added to this understanding. Particularly work in progress on plume convection with Greg Willett has led to the recognition of the α-effect due to conservation of angular momentum.

References

1. Axford, W. I., Leer, E. and Skadron, G., 15th Proc. Int. Cosmic Ray Conf. **11**, 132 (1977).
2. Bell, A. R., Mon. Not. R. Astron. Soc. **182**, 147 (1978).
3. Blanford, R. D. and Ostriker, J. P., Astrophys. J., **221**, L29 (1988).
4. Hillas, A. M., Ann Rev. Astron. Astrophys. **22**, 425 (1984).
5. Blanford, R. D. and Eichler, D., Physics Reports **154**, 1 (1987).
6. Lagage, P. O. and Caesarsky, C. J., Astron. Astrophys. **125**, 249 (1983).
7. Osborne, J. L., "Origin of Cosmic Rays", Proc of NATO Conf., Durham, England, (Edited by J. L. Osborne and A. W. Wolfendale) (Reidel 1974), p. 203.
8. Sarris, E. T. and Krimigis, S. M. Astrophys. J., **298**, 676 (1985).
9. Krimigis, S. M., Space Sci. Rev. **59**, 167 (1992).
10. Colgate, S. A., Phys. Fluids **2**, 495 (1959).
11. Galeev, A. A., Adv. Space. Res. **4**, 255 (1984).
12. Birdsall, D. H., Furth, H. P., Hartman, C. W. and Spoerlein, R. L., Nuclear Fusion, Suppl. Pt. **3**, 955 (1962).
13. Colgate, S. A., Astrophys. J., **221**, 1068 (1978).
14. Colgate, S. A. and Johnson, M. H., Phys. Rev. Lett. **5**, 235 (1960).
15. Colgate, S. A. and White, R. H., Astrophys. J., **143**, 681 (1966).
16. Colgate, S. A., McKee, C. R. and Blevins, B., Astrophys. J., **173**, L91 (1972).
17. Colgate, S. A. and McKee, C. R. Astrophys. J., **181**, 903 (1973).
18. Colgate, S. A., Phys. Rev. Lett. **34**, 1177 (1975).
19. Colgate, S. A. and Petschek, A. G., Astrophys. J., **229**, 682 (1979).
20. Colgate, S. A., "Origin of Cosmic Rays" (Edited by J. L. Osborne and R. W. Wolfendale), NATO Study, Durham, England (Reidel 1974), p. 425.
21. Colgate, S. A., Adv. Space Res. **4**, 367 (1984).
22. Holman, G. D., Ionson, J. A. and Scott, J. S., Astrophys. J., **228**, 576 (1979).
23. Kulsrud, R. M. and Zweibel, E. G., 14th Int. CR Conf., Munich, 0-9-1-12 (1975).
24. Kulsrud, R. M., 16th Int. CR Conf. Kyoto **12**, 128 (1979).
25. Kulsrud, R. M., Physica Scripta **T2/1**, 177 (1982).
26. Matthaeus, W. H., Ambrosiano, J. J. and Goldstein, M. L., Phys. Rev. Lett. **53**, 1449 (1984).
27. Ambrosiano, J. J., Matthaeus, W. H. and Goldstein, M. L., J. Geophys. Res. **93**, 14, 383 (1988); Phys. Rev. Lett. **53**, 1449 (1984).
28. Goldstein, M. L., Dury, L. O'C., Matthaeus, W. H. and Gray, P. C., "On the Possibility of Accelerating Cosmic Rays in the Galaxy and in the IGM by Turbulent Reconnection", preprint, Bartol Res. Inst., U. Delaware, MD (1944).
29. Roberts, P. H. and Soward, A. M., Ann Rev. Fluid Mech. **24**, 459 (1992).
30. Alvén, H., Tellus **2**, 74 (1950).
31. Vainshtein, S. I. and Zeldovich, Ya. B., Sov. Phys. Usp. **15**, 159 (1972).
32. Childress, S., Collet, P., Frish, U., Gilbert, A. D., Moffatt, H. K. and Zaslavsky, G. M., Geophys. Astrophys. Fluid Dyn. **52**, 263 (1990).
33. Finn, J. M., Hansen, J. D., Kan, I. and Ott, E., Phys. Rev. Lett. **62**, 2965 (1989).
34. Parker, E. N., "Cosmical Magnetic Fields, their Origin and their Activity" (Clarendon, Oxford 1979).
35. Colgate, S. A., Furth, H. P. and Halliday, F. O., Rev. Mod. Phys. **32**, 744 (1960).
36. Colgate, S. A., Proc of Symposium on "Electromagnetics and Fluid Dynamics of Gaseous Plasma", Polytechnic Inst. of Brooklyn, 373 (1961).
37. Wesson, J. A., *et al.*, Nuclear Fusion **29**, 641 (1989).
38. Gill, R. D., "Generation and Loss of Runaway Electrons following Disruptions in Jet", preprint, JET, UK, 1993).

Physica Scripta. Vol. T52, 106–109, 1994

Processes of MHD-Wave Radiation and of Cosmic Ray Flux Focusing in the Galaxy

V. A. Dogiel,[1,2] A. V. Gurevich[1] and K. P. Zybin[1]

[1] P. N. Lebedev Physical Institute, 117924 Moscow, Russia
[2] Max-Planck-Institut für Extraterrestrische Physik, Garching b. München, Germany

Received November 22, 1993; accepted January 28, 1994

Abstract

Nonlinear kinetic equations describing cosmic ray propagation in a scattering medium are analyzed. The scattering is determined by cosmic ray interactions with MHD-fluctuations. We consider a self-consistent model in the framework of MHD-wave radiation by the cosmic rays. Our investigations show that in the model the region in which cosmic rays are confined occurs naturally around the disk of cosmic ray sources. Beyond the boundary the scattering is not effective giving rise to the run-away flux of cosmic rays. This process of cosmic ray flux focusing just describes particle excape from the Galaxy.

The propagation of fast particles in the interstellar medium is mainly determined by their interaction with the electromagnetic fields excited in the cosmic plasma. The most important feature of this interaction of the particles with the waves is its resonance character, i.e. the frequency of the wave is a multiple of the frequency of the cyclotron rotation of the particle in the regular magnetic field $\boldsymbol{H}_0$. One of the sources of these resonance waves is the flux of cosmic rays itself. This flux generates (radiates) MHD-waves in the interstellar medium by amplifying weak initial fluctuations. So the process of cosmic ray propagation is described by a complex system of kinetic equations describing processes of charge particle scattering and wave radiation. The analysis of these equations, however, is rather difficult and the processes of cosmic ray (CR) propagation in the interstellar medium is usually investigated in the framework of different phenomenological models such as the leaky-box model, diffusion or convective models, etc (see, for details, Berezinsky *et al.* [1]) in which processes of CR propagation and escape from the Galaxy are described by some phenomenological parameters. For instance the escape processes are characterized either by the CR lifetime in the Galaxy or by the effective outflow velocity due to convection or diffusion. The region of diffusion-convective propagation is usually assumed to be bounded by a surface from which particles escape into the metagalactic medium. However, the problem of the galactic boundary and conditions on it, is in some sense open in these models till now. We also don't know if particles of different energies, masses and charges escape from the same boundary or not, what kind of boundary conditions we should put at the bondary, etc.

To analyze these problems we try to investigate the kinetic model of CR propagation in the Galaxy.

As we have mentioned already the character of CR propagation in the Galaxy is caused by particle scattering on MHD waves. There are many potential sources of the MHD turbulence in the Galaxy however most of them (supernova, stellar winds) are concentrated in the galactic disk. In the region of our interests (far away from the disk) MHD waves are excited by the CR flux itself [2]. It means that the distribution function of CRs, $f(r, p)$, and the level of MHD turbulence, $W(r, k)$, are not independent on each other. Here, p is the particle momentum, r-space coordinate, and k the wave number of MHD waves.

Then, the system of kinetic equations describing particle propagation and wave excitation can be written as

$$\frac{\partial f}{\partial t} + v\frac{\partial f}{\partial r} = I(f) + Q(r, p)$$

$$\frac{\partial W}{\partial t} + \frac{\partial \omega}{\partial k}\frac{\partial W}{\partial r} - \frac{\partial \omega}{\partial r}\frac{\partial W}{\partial k} = (\sigma - \Gamma)W. \tag{1}$$

Here, v is the particle velocity, $Q(r, p)$ is the CR source distribution which is approximated by a δ-function (for distances larger than the source region scale),

$$Q(r, p) = Gp^{-\gamma_0}\,\delta(r).$$

We notice here that the results of our investigations are also applicable for the case of CR flux propagation along divergent magnetic flux tube (see [3]). This case was also investigated by J. A. Earl (see e.g. [4, 5]).

The integral of particle scattering over pitch-angles due to particle collisions with magnetic inhomogeneities $I(f)$ at the frequency $\nu(r, p, \mu)$ (here, μ is the cosine of the particle pitch angle) has the form

$$I(f) = \frac{\partial}{\partial \mu}\left[\nu(r, p, \mu)(1 - \mu^2)\frac{\partial f}{\partial \mu}\right]. \tag{2}$$

The increment of MHD-waves, σ, for the stream instability is equal to [6]:

$$\sigma(k, r) = \frac{\pi^2 V_A}{c^2}\int_p p^2\,\mathrm{d}p\int_\mu v(1 - \mu^2)\,\mathrm{d}\mu\delta\left(p|\mu k| - \frac{eH_0}{c}\right) \times\left(\frac{\partial f}{\partial \mu} + \frac{V_A}{v}p\frac{\partial f}{\partial p}\right). \tag{3}$$

The nonlinear wave decrement, Γ, to their decay we take from Berezinsky *et al.* [1]:

$$\Gamma(k, r) = 4\pi V_{th}k^2\frac{W(k)}{H_0^2}. \tag{4}$$

Here, V_A is the Alfvén velocity, V_{th}-thermal velocity of the gas particles, H_0 is the large scale magnetic field strength, $\omega = kV_A$.

The frequency $\nu(r, p)$ for resonant particle scattering on MHD-waves can be written as

$$\nu(r, p) = 2\pi^2\Omega_H \frac{k_{res} W(k_{res}, r)}{H^2}, \tag{5}$$

where

$$\Omega_H \simeq \frac{eH}{p} \tag{6}$$

and

$$k_{res} = \frac{eH}{pc|\mu|}. \tag{7}$$

Inserting (5) and (6) into eq. (4) we obtain that

$$\nu(r, p, \mu) = \frac{2\pi^2 e^2}{p^2 c|\mu|} W(r, p, \mu). \tag{8}$$

As one can see from eq. (1) the problem is characterized by the dimensionless parameter δ

$$\delta = \frac{\nu}{c\left|\frac{\partial \ln f}{\partial r}\right|}, \tag{9}$$

where c is the light speed.

If $\delta \gg 1$ then the function f is quasi-isotropic and it is represented as

$$f(r, p, \mu) = \sum_{n=0}^{\infty} \delta^{-n} f_n(r, p, \mu), \tag{10}$$

i.e. in this quasi-isotropic case (see [1]):

$$f \simeq f_0(r, p) \quad \text{and} \quad f_1(r, p, \mu) \simeq \frac{v}{2\nu}\frac{\partial f_0}{\partial r}\mu.$$

The isotropic part of the distribution function, f_0, is described by the diffusion-convective equation

$$\nabla(D\nabla f_0 - V(r) f_0) + Q(r, p) = 0, \tag{11}$$

with the spatial diffusion coefficient

$$D(r, p) = \frac{v^2 p^2 c}{16\pi^2 e^2} \int_{-1}^{1} \frac{|\mu|(1-\mu^2)\,d\mu}{W(k_{res})} \sim \frac{c^2}{\nu} \tag{12}$$

and with the convective velocity, V.

We see from eq. (9) that in the case of MHD-wave radiation by the flux of cosmic rays we expect a change of the CR propagation if the parameter δ decreases in the region of diffusion-convective cosmic ray propagation and its value passes through the point $\delta = 1$.

The key point of the analysis is the value of $\partial f/\partial\mu$ in eq. (3) for this self consistent model. The problem is that while cosmic rays stream along the magnetic field they make waves moving at Alfvén speed, V_A, in the direction in which cosmic rays diffuse. Formally, it means that cosmic rays are also convectively transported by the waves with velocity (see e.g. [1]):

$$V = V_A \int_0^1 d\mu \frac{3(1-\mu^2)}{2} \frac{(\nu_\mu^+ - \nu_\mu^-)}{(\nu_\mu^+ + \nu_\mu^-)}, \tag{13}$$

where ν_μ^+ and ν_μ^- are scattering rates of cosmic rays by Alfvén waves propagating along the field outward (+) from and inward (−) toward the Galaxy.

For the case considered above only outward (+) waves are generated by the outcoming cosmic ray flux. As a result

$$V = V_A. \tag{14}$$

So, we have

$$\frac{\partial f}{\partial \mu} \sim \frac{v}{2\nu}\frac{\partial f_0}{\partial r} - \frac{V_A}{v} p \frac{\partial f_0}{\partial p}, \tag{15}$$

where f_0 is the isotropic part of the distribution function, f, in the case of high isotropy. As Chin and Wentzel [7] have pointed out, however, under conditions of fully ionized plasma, wave-wave interaction implies the existence of waves propagating in both directions even for the case of an asymmetric distribution of Alfvén waves generated by outcoming cosmic ray flux. A forward (+) Alfvén wave (travelling in the direction of cosmic ray flux) decays into a dissipative magnetosonic wave plus a backward (−) travelling Alfvén wave with a slightly larger wave length and a slightly smaller energy.

Skilling [8–10] showed in a series of papers that the pure diffusion regime and free streaming regime of CR propagation are possible for the case of fully ionized plasma (see cases 3 and 4 in [8], just these cases are analyzed in our paper).

For some parameters (see Section IV in [9], and the self-consistent solution for the case of moderately damped sound and symmetric waves in [10]) the equality

$$\nu_\mu^+ \sim \nu_\mu^- \sim \text{const}. \tag{16}$$

is realized even under conditions of Alfvén wave generation by the cosmic-ray flux. In this case [see eq. (13)]

$$V \sim 0 \tag{17}$$

and for

$$\frac{\partial f}{\partial \mu} \simeq \frac{v}{2\nu}\frac{\partial f_0}{\partial r} \tag{18}$$

the spectrum of MHD-waves far away from the source region has the form

$$W(k, r) \simeq \frac{\frac{a_1 c^3}{4a_3\pi^2 V_A(r) r}\left(\frac{eH(r)}{k}\right)^2}{\left[1 + \frac{c}{4G\pi^4 a_3 \gamma_0}\left(\frac{e}{c}\right)^{\gamma_0 - 4} \frac{rH^{\gamma_0 - 2}(r)}{V_A(r)} k^{3-\gamma_0}\right]}. \tag{19}$$

where a_1 and a_3 are some numerical values.

If $\gamma_0 = 4$ one can see from eq. (19) that:

(a) the function W decreases with distance for reasonable values of the problem;

(b) there is a break in the spectrum W. The dependence of W on k changes from $W \propto k^{-1}$ for small k to $W \propto k^{-2}$ for larger k;

(c) the position of the break shifts to smaller k with increasing of distance r.

Now let us investigate the spatial dependence of $W(k_{res})$ which just determines the efficiency of particle scattering [eq. (5)]. From eq. (19) we have ($\gamma_0 = 4$)

$$W(k_{res}) = \frac{a_1 c^3 (p\mu)^2 / 4a_3\pi^2\gamma_0 e^2 V_A r}{1 + (c^2 rH/4\pi^4 G\gamma_0 a_3 eV_A)(p\mu)}. \tag{20}$$

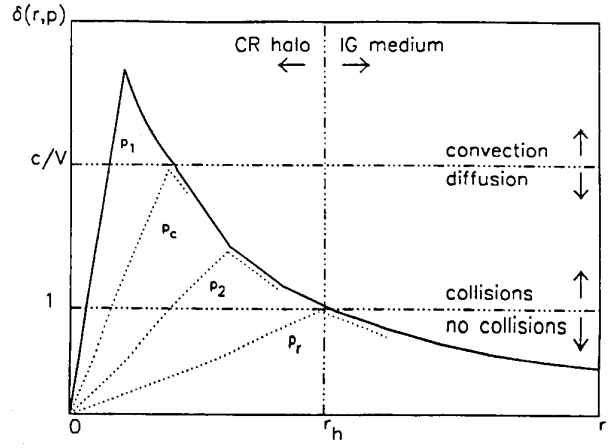

Fig. 1. Spatial dependence of the parameter $\delta(r, p)$.

The spatial dependence of the function $W(k_{res})$ changes at the momentum $p_b(r)$

$$p_b(r) \sim \frac{4G\pi^4\gamma_0 a_3 e}{c^2}\frac{V_A(r)}{rH(r)}. \tag{21}$$

The function decreases with distance if $p < p_b(r)$,

$$W(k_{res}) \simeq \frac{a_1(p\mu)^2 c_3}{4\pi^2 a_3 \gamma_0 e^2 r V_A}. \tag{22}$$

For $p > p_b(r)$ it is independed of space coordinates,

$$W(k_{res}) \sim \frac{a_1 Gcp\mu\pi^2}{er^2 H(r)}. \tag{23}$$

From these equations we find that the scattering frequency equals

$$\nu \simeq \begin{cases} \dfrac{a_1}{a_3}|\mu|\dfrac{c^2}{\gamma_0 r V_A(r)}, & \text{if } p < p_b; \\ \dfrac{4a_1\pi^4}{Gpr^2H(r)}, & \text{if } p > p_b. \end{cases} \tag{24}$$

and, as a result, we get from eqs (9)

$$\delta(\mu = 1) \sim \begin{cases} \dfrac{a_1 c}{a_3\gamma_0 V_A(r)}, & \text{if } p < p_b; \\ \dfrac{4a_1\pi^4}{GprH(r)c}, & \text{if } p > p_b. \end{cases} \tag{25}$$

We see that the parameter δ decreases, in the collisional region, with distance and at some point it equals unity.

In the case ($\delta \ll 1$) (in the run-away region) the solution for the distribution function can be written as

$$f(r, p, \mu) = \frac{G' p^{-\gamma_0}}{\tau + \omega}\exp\left(-\frac{1-\mu}{\tau+\omega}(r/r_H)^2\right) \tag{26}$$

where

$$\tau = 4\int_{r_h}^{r} \nu(r', p)(r'/r_h)^2\, dr',$$

and the parameter ω is chosen from the matching condition of solutions at the boundary $\delta = 1$.

So

$$\frac{\partial f}{\partial \mu} = \frac{G' p^{-\gamma_0}}{(\tau+\omega^2)}(r/r_h)^2\exp\left(-\frac{1-\mu}{\tau+\omega}(r/r_h)^2\right) \tag{27}$$

From these equations we can show that in the range $\delta < 1$ the scattering is not effective enough to make the function f isotropic and as a result the "run-away" flux of particles takes place in the regions where $\delta \ll 1$.

In other words, in the volume where $\delta \gg 1$ the distribution function is quasi-isotropic and particle propagation is described as diffusion. In the peripheral volume where $\delta \ll 1$ the cosmic rays are focused into the run-away flux and the particle propagation there is completely different from diffusion.

From the analysis of particle propagation in the regions $\delta > 1$ and $\delta < 1$ we see that the function W drops in space fast enough, the region of particle sources should be surrounded by the "runaway" boundary.

Thus, in the initially boundless problem we can establish the boundary $\delta \approx 1$ surrounding the source, across which the character of particle propagation changes. Further, the surface defined the condition $\delta \approx 1$ will be taken as the boundary of the cosmic ray halo. We don't present here the calculations themselves (see [11]) but discuss only a few results of these calculations.

1. The scale of the collisional region (halo) r_h determines by the equality

$$V_A(r_h) = \frac{c}{4\gamma_0|\ln(\mu_*)|},$$

which follows from the condition $\delta(r_h) = 1$.

Here, the magnitude of μ_* is estimated from the truncation conditions at pitch angles close to $\pi/2$ (for details see [1]). So at distances where the Alfvén velocity reaches a value as large as several times 10^8 cm/sec we can expect a transition to the collisionless regime of particle propagation. This result is also valid for one-dimensional CR flux propagation along divergent magnetic flux tubes.

2. Low energy particles ($p > p_c$) may also be transported by the galactic wind with a velocity $V(r)$. The condition for the CR galactic wind transport is $\delta(r, p) > [c/V(r)]$. Nevertheless, at large enough distances the type of motion changes to diffusion and then, at larger distances, these particles run away into the intergalactic medium.

Only in the case when the velocity of convective transport weakly depends on spatial coordinates do we expect another scenario of CR propagation in the Galaxy. According to the numerical calculations of Breitschwerdt *et al.* [12] we can expect this only at distances as large as 100 kpc.

3. Particles of very high energies ($E_r = p_r c > 10^6$ GeV) freely leak out of the sources without scattering everywhere in space. These particles are not able to produce the MHD-turbulence needed for particle scattering, i.e. these particles are not confined in the halo. It means that the parameter $\delta < 1$ everywhere in space for particle momenta $p > p_r$.

Just near this energy there is a break in the CR spectrum observed near the Earth. We suppose that this break may be due to the transition from collisional propagation of particles to collisionless propagation in the halo.

4. For the peculiar case $\gamma_0 = 4$ [we use here the normalization condition $N(>p) = \int_p f(p)p^2\, dp$] the coordinate of the "runaway" boundary does not depend on the particle energy. So all particles which are in the collisional regime of propagation ($E < 10^6$ GeV) escape into the intergalactic space from the same boundary. If the injection index γ is larger than four, however, (it is often supposed that $\gamma = 4.3$)

the escape boundary position depends on the particle energy: the smaller energy the larger scale of the galactic halo. This effect may be essential for analysis of observational data.

5. Figure 1 shows the spatial dependence of the parameter $\delta(r, p)$ on the distance from CR sources for different particle momenta. Here, $p_i < p_c < p_2 < p_r$, the spectral index γ_0 is taken to be 4.

References

1. Berezinsky, V. S. *et al.*, "Astrophysics of Cosmic Rays" (Edited by V. L. Ginzburg) (North-Holland 1990).
2. Kulsrud, R. M. and Pearce, W. F., Astrophys. J. **156**, 445 (1969).
3. Dogiel, V. A., Gurevich, A. V. and Zybin, K. P., Astron. Astrophys. **268**, 356 (1993).
4. Earl, J. A., Astrophys. J. **205**, 900 (1976).
5. Earl, J. A., Astrophys. J. **251**, 739 (1981).
6. Wentzel, D., Annual Review Astronomy and Astrophysics **12**, 71 (1974).
7. Chin, Y. and Wentzel, D., Astrophys. J. **16**, 465 (1972).
8. Skilling, J., Mon. Not. R. Astron. Soc. **172**, 557 (1975).
9. Skilling, J., Mon. Not. R. Astron. Soc. **173**, 245 (1975).
10. Skilling, J., Mon. Not. R. Astron. Soc. **173**, 255 (1975).
11. Dogiel, V. A., Gurevich, A. V. and Zybin, K. P., Astron. Astrophys. **281**, 937 (1994).
12. Breitschwerdt, D., McKenzie, J. F. and Völk, H. J., Astron. Astrophys. **245**, 79 (1991).

Physica Scripta. Vol. T52, 110–114, 1994

High Energy Gamma Rays from Active Galactic Nuclei

Demosthenes Kazanas

Laboratory for High Energy Astrophysics, NASA/Goddard Space Flight Center, Code 665, Greenbelt, MD 20771, U.S.A.

Received November 22, 1993; accepted January 28, 1994

Abstract

Orders of magnitude and the basic processes associated with Active Galactic Nuclei (AGN) are outlined. Particular emphasis is given on the recent high energy (100 MeV–1 TeV) γ-ray observations from radio loud AGN and is argued that AGN can, in principle, be the sites of acceleration of particles to energies in excess of 1 TeV. It is indicated that the observed γ-ray emission cannot originate in a stationary plasma but from plasma in bulk relativistic motion with $\Gamma \gtrsim 10$ and arguments are given as to the dynamical origin of such relativistic outflows.

1. Introduction

Active Galactic Nuclei (hereafter AGN) are, as the term indicates, the central regions of certain galaxies in which there is apparent activity, that is emission, which can rival or even surpass the total power output of the entire galaxy by as much as a thousand fold. What makes AGN particularly exceptional is the fact that all the power is emitted from a region which is quite small by galactic standard, and whose size is of the order of that of our solar system.

AGN come under a host of names depending on their total luminosity, morphology and frequency band in which they were first discovered or studied. The most familiar to the non-expert name is that of "quasar", denoting a class of objects, controversial at the time of their discovery, precisely because of their prodigious power requirements, if they indeed were at the distances indicated by their redshifts. We now know that quasars are but the brightest members in the AGN class, which in the meantime came to include other objects known as Seyfert galaxies. The difference between a quasar and a Seyfert is their absolute luminosity and their distance to the observer: Because they are very far away and much brighter than the host galaxy, it is almost impossible to detect the associated (but much fainter) galaxy, thus giving the impression that they represent "naked" sources of energy output.

To appreciate the extreme conditions associated with AGN, the following scaling analogy is instructive: If the electric power output of a major metropolitan area (e.g. Athens, London, or Boston) represents the light distribution in a galaxy, then a Seyfert nucleus would represent the same power output from the volume smaller than the head of a pin, while a quasar in the same scale would emit as much power as all of Europe from the volume of a basketball. It becomes thus apparent that in AGN we deal with extremes of power output density, higher than those which could be attributed to nuclear reactions. It was precisely these power density requirements that associated controversy with the name of quasars and AGN in general. The absolute values of the power associated with AGN are then $\sim 10^{11} L_\odot =$ $10^{44}\,\mathrm{ergs\,s^{-1}}$ for a Seyfert and 10^2–10^3 times higher for a quasar.

The requirement for such tremendous power density outputs does not leave but one choice for the source that powers AGN: gravity. It was proposed that by radiatively releasing the energy available from the accretion of matter into a deep gravitational potential one could achieve efficiencies approaching mc^2 (in contrast, nuclear reaction efficiencies cannot exceed $10^{-3}mc^2$). The required deep potential well however can only be found near the horizon of a black hole. It has been therefore accepted, and it is generally agreed within the community that AGN are powered by matter accretion onto a black hole. Though the source of energy is agreed upon by almost everyone, that is where the agreement, for the most part, stops. The particular details of the accretion process and the energy release remains elusive and despite the over twenty year study of these objects, their study still yields surprises as it will become apparent later in this document.

The contents of this review do not necessarily represent the most popular, politically correct, current views concerning AGN, but rather they reflect to a certain degree the personal prejudices of the author. At the same time, being intended for an audience interested primarily in astrophysical processes involving high energies (i.e. particles, photons and neutrinos in excess of 1 GeV), it weighs heavily toward the non-thermal AGN models and the description of the associated non-thermal radiation processes. The author therefore feels that the non-expert reader should be warned about the possibility of imbalance in the contents of this review.

2. The physics of AGN

This section presents a very rough and incomplete summary of the physics of AGN necessary to a non-specialist so that he can develop a general feeling of the order of magnitude of the physical quantities involved and begin to form an opinion of the issues involved and the importance and observational significance of the various processes associated with the emission of high energy radiation in photons and neutrinos.

2.1. *The physical quantities*

The assumption that AGN are powered by accretion of plasma onto a black hole does provide estimates of the order of magnitudes of the various quantities associated with the accretion in terms of the mass of the black hole, M, and the accretion rate, $\dot{M}$.

1. Length: The size of the black hole horizon sets the natural unit of length in the problem. The length of the Schwarzschild radius in cm is given in terms of the black hole mass by

$$R_S = 3 \times 10^{14} M_9 \,\mathrm{cm} \tag{2.1}$$

where M_9 is the mass of the black hole in units of $10^9 M_\odot$. With this unit of length one can scale the radial distance, r, by defining the dimensionless radial coordinate $x = r/R_S$.

2. Velocity and time scales: The characteristic velocities and time scales usually quoted in association with AGN variability are the free-fall velocity $v_{\mathrm{ff}} \simeq (2GM/r)^{1/2} = c/x^{1/2}$ and the free-fall time scale $t_{\mathrm{ff}} \simeq r/v_{\mathrm{ff}} \simeq 10^4 x^{3/2} M_9$. These expressions are usually employed when trying to estimate the size of the AGN "central engine" region, and then the mass of the putative black hole responsible for powering the AGN. It should be cautioned that in the most popular models, namely those involving accretion disks and viscous dissipation of energy, the associated time scales are much longer than the above estimates (see below, item 3).

3. Accretion rate: As a unit of accretion rate in AGN one uses (arbitrarily) one solar mass per year because the observed AGN luminosities imply accretion rates which range from a few orders of magnitude smaller to roughly 100 times this value; this value hence lies roughly in the geometric mean of the range of this quantity. The luminosity corresponding to the unit of accretion rate at efficiency of energy conversion into radiation equal to mc^2, is $5 \times 10^{46}\,\mathrm{ergs\,s^{-1}}$. It is certain that the efficiency is less than one and it is loosely assumed that it is $\simeq 0.1$ so that $\dot{M} = 1$ provides roughly $10^{46}\,\mathrm{ergs\,s^{-1}}$. A more natural unit for the accretion rate will be discussed later on in this section.

4. Particle density: The density of matter in the vicinity of the accreting black hole apparently depends on both the aaccretion rate, $\dot{M}$, the mass, M_9, and the dimensionless distance, x, from the black hole. Unfortunately, it also depends on the speed with which matter is accreted onto the black hole which is very poorly determined. A lower limit on the density can nonetheless be obtained by assuming the highest possible accretion speed, which in the case of accretion is given by the free-fall velocity, i.e. assuming a largely spherically symmetric free-fall accretion. Under this assumption the density of the accreting matter is

$$n(x) \simeq 10^9 x^{-3/2} \frac{\dot{M}}{M_9^2}\,\mathrm{cm^{-3}}. \tag{2.2}$$

Different assumptions about the mode of accretion can lead to vastly different estimates for the values of the particle density in the vicinity of the black hole. In particular, in the popular accretion disk models, the accretion of matter (and for that reason, the rates of energy release per unit mass) takes place over the (largely unknown) viscous time scales leading to much different values and functional dependences for the particle density [1].

5. Luminosity: The fact that AGN are powered by accretion induced by gravity provides a natural scale for the luminosity of these objects the so-called Eddington luminosity, L_{Edd}, given the requirement that the radiation pressures does not overcome the force of gravity. This yields,

$$\frac{GMm_{\mathrm{p}}}{r^2} = \frac{L}{4\pi r^2 c}\,\sigma_{\mathrm{T}} \tag{2.3a}$$

or

$$L_{\mathrm{Edd}} = 4\pi GMm_{\mathrm{p}} c\sigma_{\mathrm{T}} \simeq 1.3 \times 10^{38} M_0 = 1.3 \times 10^{47} M_9\,\mathrm{ergs\,s^{-1}}. \tag{2.3b}$$

Because both forces, for spherically symmetric geometry, fall like r^{-2}, the condition of balance between radiation pressure and gravity does not depend on the radius but only on the mass of the accreting object. The existence of this characteristic luminosity then allows the definition of an equivalent accretion rate, the so-called Eddington accretion rate through the relation

$$\dot{m}_{\mathrm{Edd}} \equiv L_{\mathrm{Edd}}/c^2 \simeq 2M_9\,M_\odot\,\mathrm{yr^{-1}}. \tag{2.4}$$

6. Energy density: Estimates of the particle energy density suffer from the same uncertainties as their number density. In the case of quasi-spherical accretion in which the density can be estimated rather accurately and the velocity dispersion of the accreting matter is of the same order as the free-fall velocity, the energy density, similar in magnitude to the ram pressure, is

$$P \simeq \rho v_{\mathrm{ff}}^2 \simeq nm_{\mathrm{p}} c^2 (v_{\mathrm{ff}}/c)^2 \simeq 1.5 \times 10^6 x^{-5/2} \dot{M} M_9^{-2}\,\mathrm{erg\,cm^{-3}}. \tag{2.5}$$

In the case of a thin accretion disk one has to bear in mind that the ambient density $n(x)$ can be much higher and that the velocity dispersion can be much less than the azimuthal velocity $v_\phi \simeq v_{\mathrm{ff}}$.

7. Magnetic field: This is the most poorly determined parameter associated with AGN. Its knowledge is of importance because in many cases it is believed that the continuum emission is due to synchrotron radiation. The magnitude of this parameter is simply determined from equipartition arguments, i.e. by equating the energy density associated with a magnetic field, B, $U_{\mathrm{mag}} = B^2/8\pi$ with another characteristic energy density; as such a "characteristic energy density" it is typically used the photon energy density $L/4\pi R^2 c$ (mainly because it can be easily estimated from the observed luminosity and the variability of a source which provides an estimate of R). An upper limit to the mean magnetic field value in quasi-spherically symmetric accretion can be obtained by using instead the ram pressure (as given above). These considerations yield values for the magnetic field which scale inversely with the mass of the black hole, $B \sim 1 - 100 M_9^{-1}$ Gauss.

2.2. *The physical processes*

This section deals with several of the physical processes associated with AGN. The list is by no means complete and particular weight (maybe unwarranted) is given again to models of non-thermal emission from AGN, as it is the most relevant to the topic of this workshop. The processes to be discussed include dynamics, radiation processes, the opacities of high energy radiation, and the effect of relativistic beaming on the emission from AGN.

1. The dynamics of accretion: The notion that the prodigious energy output of AGN is due to accretion onto a compact object (most likely a massive black hole) dates back to the late sixties. The model of accretion in these earliest models was considered to be spherical accretion. However, it was soon realized [2] that spherical accretion

coupled only with free-free emission by the compressed and heated gas is a very inefficient way for radiation production, mainly because of the very low radiative efficiency of the particular radiative process; most of the available thermal energy is in fact advected into the black hole and never really emitted.

The problem of low radiative efficiency prompted the consideration of disk rather than spherical accretion as a means for providing the required radiative efficiency. In the case of disk accretion, matter is considered to be in Keplerian orbit, slowly sinking toward the black hole by dissipating and radiating away its azimuthal kinetic energy. The difference between this and the spherical mode of accretion is that in this latter case matter can accrete only by losing (radiatively) energy, thus guaranteeing high efficiency for this mode of accretion. The major problem with disk accretion is that the viscosity responsible for the dissipation is completely unkown, a fact that makes quantitative predictions of this type of model very unlikely (for more details on disk accretion the reader is referred to the text of Ref. [1]).

An alternative class of models, based mainly on the spherical mode of accretion is that given in Refs [3–6]. These type of models use a standing shock surrounding the black hole as a means for randomizing the accretion kinetic energy and slowing down the infall, thereby increasing the radiative efficiency. The problem with these models is that formation of a shock in spherical accretion requires a boundary condition on the horizon other than simple free-fall. The model of Ref. [3] does address this issue by providing for the required back-pressure for shock formation with a sufficiently high concentration of relativistic protons which do not feel the pull of gravity and do not necessarily fall into the black hole; these relativistic protons are thought to be produced by the Fermi acceleration mechanism at the same shock whose existence guarantee by their presence. Protons are necessary for such a model as relativistic electrons suffer losses on time scales much shorter than the free-fall time and cannot provide the required back-pressure to ensure that formation of such a shock. The interesting feature of this type of model is that once a mechanism can convert a sizable fraction of the accretion power into relativistic protons, the subsequent formation of the shock is almost inevitable; in addition, the dissipation of energy is in this case very well understood and the dissipation time-scale, the proton–proton collision time scale $t_{pp} = 1/n(r)c\sigma_{pp}$, is computable from the first principles once the density of the ambient gas is given. The position of the shock is then set at $r_s \simeq v_{ff} t_{pp}$. It is easy then to see that in this case $r_s/R_S \equiv x_s \propto M_9/\dot{M}$, i.e. the postion of the shock (in units of the Schwarzshild radius) depends only on one parameter $M_9/\dot{M}$ or $\dot{m}_{Edd}/\dot{M}$. Indeed, Fig. 5 of Ref. [3] indicates that AGN cover a rather limited range in this parameter, despite the wide range of their luminosities.

2. The γ-ray opacities: The extremely high radiation energy densities expected in the vicinity of an AGN "central engine" in conjunction with the possible production of γ-rays of energy greater than $m_e c^2$, provides the possibility for a process not encountered in other astrophysical sources: the absorption of γ-rays and their conversion into e^+e^- pairs. The cross section for this process is that of Thomson, σ_T, and it is therefore possible that the opacity of radiation to this process be extremely high. Given a source of luminosity L_γ in the MeV region of the spectrum, the opacity to pair production for a spherically symmetric source of radius, R, is roughly $\tau_{\gamma\gamma} \simeq n_\gamma \sigma_T R$, where n_γ is the photon density; expressing the latter in terms of the luminosity, L_γ, one gets

$$\tau_{\gamma\gamma} \simeq \frac{L_\gamma}{\pi R^2 m_e c^3}\sigma_T R = \frac{L\sigma_T}{\pi R m_e c^3} \simeq \frac{L/R}{10^{29}\,\mathrm{ergs\,s^{-1}\,cm^{-1}}}. \quad (2.6)$$

One sees, therefore, that the photon–photon opacity depends on only the combination L/R of the source parameters called the compactness of the source. It is roughly one for $L/R \simeq 10^{29}\,\mathrm{erg\,s^{-1}\,cm^{-1}}$. This is a very high compactness, it corresponds to having a solar luminosity emitted from a room of size of a few tens of meters.

The estimate of the opacity given above was made under the assumption that the relevant photon energies were in the MeV range. In cases in which one is interested in the opacities of photons of energy $\varepsilon_\gamma \gg m_e c^2$, one has to bear in mind: (a) that there is a threshold condition for pair production namely, $\varepsilon_\gamma \varepsilon_1 > (1 - \cos\theta)$ (θ is the angle between the photons and their energies are measured in units of $m_e c^2$); (b) for $\varepsilon_\gamma \varepsilon_1 \gg 1$ the process is in the Klein–Nishina regime and the cross section decreases like $1/\varepsilon_\gamma \varepsilon_1$. Thus, most of the opacity for photons of energy ε_γ is effected by photons of energy $1/\varepsilon_\gamma$. In this respect then the opacity expression above has to be modified to

$$\tau_{\gamma\gamma}(\varepsilon_\gamma) \simeq \frac{L(1/\varepsilon_\gamma)\sigma_T}{R m_e c^3}. \quad (2.7)$$

Because in AGN the number of photons is a decreasing function of frequency, the higher the γ-ray energy, the higher is the number of soft target photons that fulfill the threshold condition and consequently the higher the opacity of the γ-ray.

The magnitude of the γ-ray opacity to photon–photon interactions can be estimated by looking at the normalization of the expression given above

$$\frac{L\sigma_T}{R m_e c^3} = \frac{2\pi}{3}\left(\frac{m_p}{m_e}\right)\frac{L}{L_{Edd}}\left(\frac{3R_S}{R}\right). \quad (2.8)$$

As it is apparent from this expression, the photon opacity in a source that emits close to its Eddington luminosity from a region of size similar to the least stable orbit around a black hole is the order of a thousand. This is very important as γ-ray radiation emitted from such a small volume would never escape but it would be converted into e^+e^- pairs, whose presence could influence the emerging radiation spectra significantly. The subject of such spectral effects due to the presence of e^+e^- pairs in AGN has been the subject of intense research in the past few years.

It is appropriate at this point to also calculate the cooling time in the AGN environment of the relativistic electrons that would produce these γ-rays; for that one has to bear in mind that the energy loss rate is

$$\dot{\gamma} = -\left(\frac{4}{3m_e c^2}\right)\sigma_T \rho_{rad}\gamma^2 \quad \text{with } \rho_{rad} = \frac{L}{\pi R^2 c} \quad (2.9)$$

yielding

$$t_c = \frac{\gamma}{\dot{\gamma}} \simeq \frac{R}{c}\frac{1}{\gamma_e}\left[\frac{L/R}{10^{29}\,\mathrm{erg\,s^{-1}\,cm^{-1}}}\right]. \quad (2.10)$$

The similarity with the expression for the photon opacity expression should not surprise the reader as both processes have the same cross section, namely that of Thomson, σ_T. What is crucial to note is that for sources with high γ–γ opacity the electron loss time scale is shorter than the light crossing time across the source, indicating that under such circumstances relativistic electrons lose their energy before they have time to escape from the source.

3. Relativistic beaming: The term "relativistic beaming" is used to indicate the perceived amplification of the radiation emitted by plasma moving with a bulk Lorentz factor $\Gamma \gg 1$, when viewed at a sufficiently small angle, θ, with respect to its direction of motion (typically $\theta \lesssim 1/\Gamma$). Light travel time effects then cause any intrinsic variability of the emission to be shortened by one power of the Doppler factor, $\delta \equiv [\Gamma(1 - \beta \cos \theta)]^{-1}$, while conservation of the photon phase space implies an increase of the observed radiation flux density by $\delta^{3+\alpha}$ (where the intrinsic emission has an intensity of the form $F_\nu \propto \nu^{-\alpha}$) and also an increase in the observed bolometric luminosity by δ^4 (see e.g. Ref. [7]). Thus emission from plasma in bulk relativistic motion could appear extremely luminous and yet vary on time scales short compared to the light travel time across the emitting source. In addition, it is easy to show that if a "blob" of plasma moves relativistically at an angle $\theta \simeq 1/\Gamma$ with the observer's line of sight, its apparent transverse velocity will be $v_{app} = \Gamma c$, i.e. it will appear moving superluminally on the plane of the sky.

3. The γ-ray emission and the acceleration challenge

Armed with the broad picture of the AGN physical setup and the most relevant processes we can now discuss in more detail the data with particular emphasis in the γ-ray observations to see how the notions discussed above are applied in AGN modeling and what constraints they put in our understanding of particle acceleration in the AGN environment.

Figure 1 presents the spectrum of a particular AGN namely, 3C 279, in a νF_ν *vs.* ν diagram, i.e. in a diagram in which the luminosity per decade is plotted as a function of frequency from radio to γ-rays as detected recently by *EGRET* aboard the *Compton Gamma Ray Observatory* (*CGRO*). There are several features in this class of objects (in addition to those mentioned in the introduction, i.e. the emission of large luminosity from very small volumes) which set it apart from that of normal galaxies which are apparent already in this figure. One such feature is the extent of the observed spectrum of this object in particular (it covers more than 12 decades in frequency) and generally of the class of radio loud AGN.† An additional feature related to the spectral distribution of these objects is the fact that the energy is distributed roughly equally among the 14 or so decades of frequency. By contrast, normal galaxies cover roughly three decades in frequency with very little emission beyond that contributed by their stars. Finally, and most amazing, the flux in the >100 MeV γ-rays outshines that in any other band by a factor of 10–30.

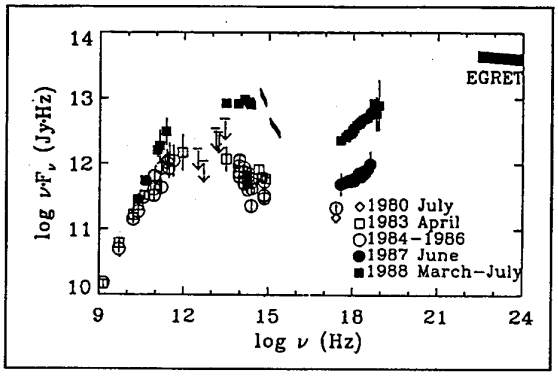

Fig. 1. The energy distribution from radio to γ-rays in the radio loud quasar 3C 279 (from Ref. [9]). The *EGRET* results are not simultaneous with those at other frequencies. The X-ray flux during the *EGRET* observations was closer to that of the June 1987 observation.

The observed γ-ray flux, if isotropic, would correspond, given the object's redshift $z = 0.54$, to a γ-ray luminosity of the order of $10^{48}\,\mathrm{erg\,s^{-1}}$. At the same time the γ-ray is variable with characteristic time scale of a few days suggesting that the size of the emitting region cannot be much larger than 10^{16} cm, yielding a compactness for this object of the order of $10^{32}\,\mathrm{erg\,s^{-1}\,cm^{-1}}$ which would result to an optical depth of several thousand at 100 MeV. Under these circumstances the γ-rays shown in Fig. 1 should be completely absorbed due to the γ–γ opacity.

The apparent absence of γ–γ absorption in the >100 MeV spectrum of 3C 279 (as well in the spectra of 30 or so additional radio loud AGN detected by *EGRET* to date) clearly leaves relativistic beaming of the γ-ray emission as the only logical account of this emission. It can be shown that the optical depth to the γ–γ opacity is a very sensitive function of the beaming parameter delta (actually $\tau_{\gamma\gamma}(\varepsilon_\gamma) \propto \varepsilon_\gamma^\alpha \delta^{-(4+2\alpha)}$, where $\alpha \sim \frac{1}{2}$ is the spectral index in the X-ray band [10]) and thus a value of $\delta \simeq 10$ could render the γ-ray emission optically thin up to energies of several GeV, in accordance with observations.

One thus is led by the γ-ray observations to consider emission by a plasma which is emitting γ-rays of energies 100 MeV–10 GeV and it is therefore composed of electrons with individual Lorentz factors 10^3–10^4, and which at the same time is moving with bulk Lorentz factor, $\Gamma \simeq 10$. However, as discussed above, electrons of such high energies would suffer catastrophic radiative losses on time scale much shorter (by factors of thousands) than the light crossing time scales. The problem is in fact even more severe. The additional constraints come from the lower frequency (10^9–10^{16} Hz) spectral distribution in these objects. As pointed out above, the spectrum in this range is smooth and continuous over this entire range, indicating a single emission mechanism, thought to be synchrotron emission by a population of relativistic electrons (in contrast with the X-ray and γ-ray emission which is thought to be due to inverse Compton scattering of the synchrotron photons by the same relativistic electrons). However, it can be easily shown that the radio emission must originate in a volume much larger than that of γ-rays because otherwise it would have suffered

† We mention parenthetically here that there are two broad and distinct classes of AGN, the radio loud (containing ~10% of all AGN) and radio quiet ones (with ~90% of them; see Ref. [8] for a review), distinguished mainly on the basis of their radio properties. The spectra of the radio quiet AGN cut-off at frequencies $\nu \lesssim 10^{12}$ Hz, while the radio loud ones have spectra which are continuous and smooth from the 10^9–10^{15} Hz. We will be mainly dealing at present with the radio loud class.

self-absorption at a frequency $\sim 10^{12}$ Hz. The smooth, continuous spectrum is thus considered to be emission from a distribution of relativistic electrons that extends several orders of magnitude both in energy and radius. Then one can reproduce the obsrved spectra as the superposition of emission over this entire radial range [11].

The combination of radio, IR, optical, UV, and γ-ray observations lead us then to a picture of an inhomogeneous electron distribution spanning several decades in radius, from a few Schwarzshild radii to a few parsecs ($\sim 3 \times 10^{18}$ cm), consisting of electrons with individual Lorentz factors of the order of 10^3–10^4 and even up to 10^6 [12] (much too high to have their origin in the vicinity of the black hole), with this entire distribution outflowing relativistically with bulk Lorentz factor $\Gamma \sim 10$–20. In addition, in order that the spectrum have the form observed in the radio 10^9–10^{11} Hz the relativistic electron spectrum and normalization cannot be arbitrary but of rather well contrained form. Can such a distribution be materialized in some realistic dynamical scenario? The answer is not obvious as yet to the author. One can, of course, parametrize it but one soon finds out that the number of parameters quickly becomes very large [13]. On the other hand, statistical surveys and model fits to the observations indicate that the number of parameter necessary to fit the continuum spectrum of radio loud AGN is rather small, in fact of order 1 (Ref. [14]), indicating that these parameters are constrained by unknown hitherto physics. One hopes that the study and detailed modeling of the γ-ray emission from these objects, because of the much stringent constraints that presents to these models will lead to a much deeper understanding of the conditions that prevail in the vicinity of the black holes responsible for the AGN phenomenon, and will allow us to uncover these sought after physics.

In connection with the issue of bulk relativistic motion, it should be noted that simple arguments can indicate the parameters that would lead to such outflows and that these can in fact be materialized by the model of Refs [3, 4]. This model as discussed above, relies in hadronic collisons of shock accelerated protons as a means for dissipating the accretion kinetic energy. It is well known that such collisions produce 50% of the time neutrons in the charge exchange reaction $pp \rightarrow pn\pi^+$. Thus a flux of relativistic neutrons is expected to be emitted continuously from the AGN central sources within this model. The neutrons escape from the system, not held in by the turbulent magnetic field that restricts the escape of protons, they decay after they travel on the average $c\tau_n \gamma_n \sim 3 \times 10^{13} \gamma_n$ cm (with $\tau_n \sim 10^3$ sec being the neutron lifetime and γ_n the neutron Lorentz factor), whereby they reconvert by their decay into protons. If the size of the source is $R \gg 3 \times 10^{13}$ cm, only neutrons with mean energy $E \sim (R/c\tau_n) m_p c^2$ will escape the source, and under these conditions we will have the continuous injection of a relativistic proton gas in virtually empty space. Energy conservation then implies that upon its expansion, this gas will convert its internal energy into directed motion achieving bulk Lorentz factors $\Gamma \sim R/c\tau_n$. It is therefore a prediction of the model that relativistic outflows should appear only in the most luminous objects, i.e. in AGN with black hole masses larger than 10^8 solar masses. It is interesting to examine whether the data support this simple origin of the relativistic AGN outflows.

References

1. Shapiro, S. L. and Teukolsky, S. A., "White Dwarfs, Neutron Stars, Black Holes, The Physics of Compact Objects" (Wiley, New York 1983).
2. Shapiro, S. L., Astrophys. J. **240**, 246 (1974).
3. Kazanas, D. and Ellison, D. C., Astrophys. J. **304**, 178 (1986).
4. Kazanas, D. and Ellison, D. C., Nature **319**, 380 (1986).
5. Mesźaros, P. M. and Ostriker, J. P., Astrophys. J. (Lett.) **273**, L59 (1983).
6. Babul, A. *et al.*, Astrophys. J. **347**, 59 (1989).
7. Rybicki, G. B. and Lightman, A. P., "Radiative Processes in Astrophysics" (Wiley, New York 1979).
8. Osterbrock, D. E., Rep. Prog. Phys. **54**, 579 (1991).
9. Hartman, R. C. *et al.*, Astrophys. J. (Lett.) **385**, L1 (1992).
10. Mattox, J. R. *et al.*, Astrophys. J. **410**, 609 (1993).
11. Marscher, A. P., Astrophys. J. **216**, 244 (1977).
12. Punch, M. *et al.*, Nature **358**, 477 (1992).
13. Ghisellini, G. and Maraschi, L., Astrophys. J. **340**, 181 (1989).
14. Landau, R. *et al.*, Astrophy. J. **308**, 78 (1986).

Physica Scripta. Vol. T52, 115–117, 1994

Reflection of Radio Radiation at Ionization Fronts in Emission Line Regions and Accretion Disks of Active Galactic Nuclei

Vinod Krishan*

Indian Institute of Astrophysics, Bangalore – 560 034, India

Received November 22, 1993; accepted January 28, 1994

Abstract

It is known that high frequency short duration electromagnetic pulses can be generated by reflection of low frequency radiation off relativistically moving ionization fronts. In addition, a part of the incident electromagnetic energy is converted into a spatially periodic static magnetic field. Here, we investigate this phenomenon in the emission line region (ELR) and accretion disks of active galactic nuclei (AGN) where relativistically moving ionization fronts are created by the ionizing continuum. It is suggested that this process may play an essential role in (1) causing rapid correlated variability in radio radiation and high frequency parts of the nonthermal spectrum; (2) generating high frequency radiation through scattering of relativistic electrons off the spatially periodic magnetic field, a byproduct of the reflection process; (3) the diagnostic of the emission line region; and (4) absorption of the radio radiation. The anomalous absorption of radio radiation in ELR through parametric decay instabilities has been pointed out earlier. Interaction of radio radiation with ionization fronts further strengthens the case for the existence of strong correlation between the nonthermal radio continuum and the ELR phenomena as the multi-wavelength observations of AGN are beginning to do.

1. Introduction

Active galactic nuclei and quasars emit a strong nonthermal continuum almost over the entire electromagnetic spectrum with a flux F_ν that varies as $\nu^{-\alpha}$, where ν is the frequency and α is the spectral index which varies with the frequency. Over the continuum are superimposed bumps in the blue and bends in the radio region. In addition to the continuum, quasars show a complex line spectra whose interpretation has given rise to the cloud model of the emission line regions. The exceptionally broad emission lines are believed to result from the collective motions of a large number of clouds. This picture is supported by the photoionization models in which emission line spectra are calculated from finite regions of gas irradiated by the nonthermal continuum. A typical cloud has a dimension of 10^{12} cm, an electron density of $\approx 10^{10}\,\mathrm{cm}^{-3}$, an electron temperature $\approx 10^4$ K and is situated about a parsec or less from the central ionizing source. However electron densities $\geqslant 10^{13}\,\mathrm{cm}^{-3}$ have been necessitated for the interpretation of broad emission lines in some active galaxies [1]. The geometrical distribution of emission line gas has been deduced to vary from a random distribution of clouds to rotating accretion disks with various inclinations to the central source [2–4].

Most of the effort in the study of the emission line regions is spent in calculating the line ratios, their widths and asymmetries within the framework of photoionization models, in order to match with observed profiles. Not much attention has been paid to the possible role of the radio radiation in the establishment of the emission line regions in spite of the facts that the two are almost cospatial and the electron plasma frequencies of the emission line regions lie in the radio region. Under these circumstances, the strong radio radiation is capable of exciting nonlinear instabilities which can heat the plasma to much higher temperature in much shorter times as compared to the collisional absorption [5, 6]. A preliminary proposal for the microwave ionization of hydrogen in the highly excited hydrogen region of the ELR has also been made.

In this paper, we investigate the reflection of radio radiation off a relativistically moving ionization front [7, 8]. The ionization front is produced by the ultraviolet radiation from the central source and may exist either in individual clouds or in accretion disks. Since the nonthermal radio emitting region almost overlaps the emission line region, the incidence of radio radiation on the neutral side of the ionization front is highly probable. Thus, in this first instance, we assume an ionization front propagating at the group velocity of the ultraviolet photons, upon which impinges the strong nonthermal radio radiation. Several issues related to the geometrical aspects of the plasma-neutral gas distribution as well as the spectral width of the radio radiation will be addressed in more detail, later on. Here, we illustrate the essential physics of the reflection process and its ensuing consequences for AGN environs. The frequency up-conversion; formation of short duration pulses and their relationship to rapidly variable emission; excitation of spatially periodic static magnetic fields and their possible use for inverse Compton and Raman scattering of electron beams and all of this taking place at the ionization fronts can give up a wealth of information about quasar atmospheres in general and signatures of cloud formation in the variability of radio radiation in particular.

2. Frequency up-conversion, pulse compression and magnetic field generation

Consider an ionization front created by ultraviolet photons of frequency ω_u. The speed, V_0, of the ionization front is the group velocity, V_g, of the ultraviolet photons in the just-made plasma of density n, so that $V_g = c[1 - \omega_p^2/\omega_u^2]^{1/2} \approx V_0$, where $\omega_p = [4\pi ne^2/m]^{1/2}$ is the electron plasma frequency and e, m are the charge and mass of an electron. Let radio radiation of frequency ω_i, wavevector $\boldsymbol{K}_i$ and electric field $\boldsymbol{E}_i$ be incident on the neutral side of the ionization front, Fig. 1.

* Visiting the Lawrence Berkeley Laboratory, October 14, 1993–Janauary 15, 1994.

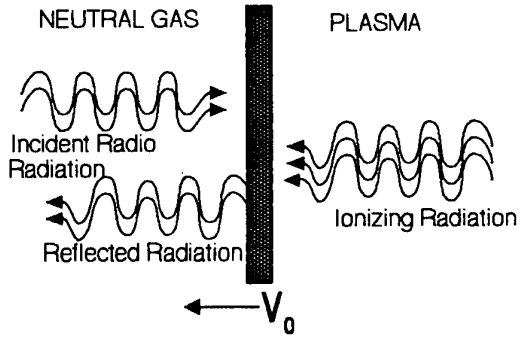

Fig. 1. Reflection of radio radiation on a moving ionization front.

One is familiar with the phenomenon of reflection and transmission at a di-electric boundary. In the case of reflection of an ionization front, an additional magnetic wave is excited as has been emphasized by Lampe, Ott and Walker [7]. The origin of this wave lies in the requirement of zero transverse current of the just born electrons at the ionization front. In the frame of the ionization front, the front is stationary and the plasma and the neutral gas are moving to the right with speed V_0 (Fig. 1). The transverse modes of the plasma are obtained by the standard procedure except that one must use the initial condition of zero transverse velocity of electrons. The dispersion relation of the transverse waves is given by

$$\left[K_f^2 - \frac{\omega_f^2 - \omega_p^2}{c^2}\right]\left[K_f - \frac{\omega_f}{V_0}\right] = 0, \tag{1}$$

where the subscript f denotes a quantity in the front frame. Thus, there are four waves at the front: (1) the incident wave of Doppler-shifted frequency $\omega_f = (1 + V_0/c)\gamma_0\,\omega_i \approx 2\gamma_0\,\omega_i$, the wavevector $K_f = \omega_f\,\varepsilon/c$ and the electric field I_f; (2) the reflected wave of frequency ω_f, wave vector $K_f = \omega_f\,\varepsilon/c$ and the electric field R_f; (3) the transmitted wave of frequency ω_f, wavevector $K_{tf} = (\omega_f^2 - \omega_p^2)^{1/2}/c$ and electric field T_f; and (4) the new magnetic wave of frequency ω_f, wavevector $K_{Bf} = \omega_f/V_0$ and electric field N_f. Note that all waves have the same frequency, ω_f, in the front's frame (stationary boundary) though their wave vectors are determined by their respective dispersion relations. Their magnetic fields are determined from

$$\nabla \times \boldsymbol{E} = -\frac{1}{c}\frac{\partial \boldsymbol{B}}{\partial t}.$$

The fields on the two sides of the ionization front can be written as: for $x > 0$,

$$E_{yf} = I_f \exp i(\omega_f t - K_f x) + R_f \exp i(\omega_f t + K_f x) + C.C.,$$

$$B_{zf} = I_f \exp i(\omega_f t - K_f x) - R_f \exp i(\omega_f t + K_f x) + C.C.,$$

for $x < 0$,

$$E_{yf} = T_f \exp i(\omega_f t - K_{tf} x) + N_f \exp i(\omega_f t - \omega_f/V_0\, x) + C.C.,$$

$$B_{zf} = T_f \frac{cK_{tf}}{\omega_f} \exp i(\omega_f t - K_{tf} x) + N_f \frac{c}{V_0} \exp i(\omega_f t - \omega_f/V_0\, x) + C.C.,$$

and the transverse current,

$$\frac{4\pi J_{yf}}{c} = i[cK_{tf}^2/\omega_f - \omega_f/c]T_f \exp i(\omega_f t - K_{tf} x) + i[c\omega_f/V_0^2 - \omega_f/c]N_f \exp i(\omega_f t - \omega_f x/V_0) + C.C.,$$

where $K_{tf}^2 c^2 = \omega_f^2 - \omega_p^2$ and c is the speed of light. The transmission and reflection coefficients can be obtained by using the three boundary conditions: (1) continuity of $\boldsymbol{E}$; (2) continuity of $\boldsymbol{B}$; and (3) vanishing of $\boldsymbol{J}$, at the front. The fields and the frequencies can be transformed back to the laboratory frame in which the electric field, E_t, of the transmitted wave is found to be:

$$E_t = \frac{2E_i}{1 + \varepsilon_f^{1/2}}, \quad \varepsilon_f = \frac{K_{tf}^2 c^2}{\omega_f^2},$$

the frequency:

$$\omega_t = \gamma_0(\omega_f - V_0 K_{tf}) \approx 4\gamma_0^2\,\omega_i,$$

and the wavevector:

$$K_t = \frac{(\omega_t^2 - \omega_p^2)^{1/2}}{c}.$$

The electric field, E_R, of the reflected wave is given by:

$$E_R = \frac{1 - \varepsilon_f^{1/2}}{1 + \varepsilon_f^{1/2}} E_i,$$

with the frequency of $\omega_R \approx 4\gamma_0^2\,\omega_i$ and the wavevector $K_R = \omega_R\,\varepsilon/c$. The magnetic field, B_n, of the new mode is (its electric field vanishes in the laboratory frame):

$$B_n = 2\beta_0 E_i \frac{1 - \sqrt{\varepsilon_f}}{1 - \beta_0\sqrt{\varepsilon_f}},$$

with the frequency $\omega_B = \omega_f - K_f V_0 = 0$ and the wavevector $K_B = V_0 K_i/(c + V_0)$. The magnitudes of the fields E_t, E_R and B_n can be investigated for the overdense and the underdense regimes defined by requiring $\omega_p > \omega_f$ and $\omega_p < \omega_f$, respectively. In the overdense case, i.e. $\omega_p > \omega_f = 2\gamma_0\,\omega_i$; $c^2K_{tf}^2 < 0$, the transmitted wave is evanescent. The amplitudes of the reflected and the incident waves are equal. The up-shifted frequency $\omega_R \approx 4\gamma_0^2\,\omega_i < 2\omega_u$ due to the overdense condition, where $\gamma_0^2 = \omega_u^2/\omega_p^2$. The magnitude of the static magnetic field is twice that of the incident field. The energy conservation tells us that the static magnetic field exists over a region half as big as that of the incident field. In conclusion, in the overdense case one gets a reflected wave of much higher frequency ω_R and of much shorter duration τ_R since $\omega_R/\omega_i = \tau_i/\tau_R$, where τ_i is the pulse duration of the incident radiation. In the underdense case, $\omega_f = 2\gamma_0\,\omega_i = 2\omega_u\,\omega_i/\omega_p > \omega_p$. The frequency ω_t of the transmitted wave in the laboratory frame is $\omega_t = \gamma_0(\omega_f - V_0 K_{tf}) \approx \omega_i(1 + \omega_p^2/4\omega_i^2)$. Thus, $\omega_t \gg \omega_i$ for $\omega_p^2/4\omega_i^2 \gg 1$, though $\omega_p^2/4\omega_i^2 < \gamma_0^2$. The transmission coefficient, $|t| \to 1$, the magnetic field coefficient $n = B_n/E_i \to 2$ for $\omega_p^2/4\omega_i^2 \gg 1$. The combination $|t| \to 1$ and $n \to 2$ does not cause any violation of energy convervation. In the laboratory frame, the group velocity of the transmitted wave is given by:

$$V_g = V_{gf} - V_0 = c(1 - \omega_p^2/\omega_f^2)^{1/2} - V_0 \approx (1 - \omega_p^2/4\omega_i^2)/2\gamma_0^2 < 0,$$

also the wave vector, $K_t = \omega_i(1 - \omega_p^2/4\omega_i^2)/c < 0$. The transmitted wave, thus, carries energy in the direction of the reflected wave.

3. In AGN

We choose the typical values of the various quantities as: the frequency ω_u of the ionizing photons $= 10^{15}\omega_{15u}\,\mathrm{sec}^{-1}$; the electron density, n, in the plasma of accretion disks or emission line region $= 10^{10}n_{10}\,\mathrm{cm}^{-3}$. This gives us $\omega_p^2 = 3 \times 10^{19}n_{10}\,\mathrm{sec}^{-2}$, $\gamma_0^2 = 10^{13}\omega_{15u}^2/3n_{10}$. Let the frequency of the incident radiation $\omega_i = 10^9\omega_{9i}\,\mathrm{sec}^{-1}$. In the overdense case, the up-converted reflected wave has a frequency $\omega_R = 1.33 \times 10^{22}\omega_{15u}^2\omega_{9i}/n_{10}$ which must be less than $2\omega_u$ so that $(\omega_{15u}\omega_{9i}/n_{10}) < 1.5 \times 10^{-6}$. Thus, for $n_{10} \approx 10^5$, $\omega_{15}^u = \omega_{9i} = 1$, the GHz radiation can be converted into infrared radiation at $\omega_R \approx 10^{15}\,\mathrm{sec}^{-1}$, with energy density $|E_R|^2 = |E_i|^2$ and the pulse duration reduced by a factor $\approx 10^6$.

In the underdense case, the transmitted wave has a frequency $\omega_t = \omega_{9i}[10^9 + 0.75n_{10}/\omega_{9i}^2]$ along with the conditions that

$$\frac{n_{10}^2}{\omega_{9i}^2 * \omega_{15u}^2} < \frac{4}{9} \times 10^{10}$$

and

$$\frac{n_{10}}{\omega_{9i}^2} \gg \frac{4}{30}$$

or

$$\frac{4}{30} < \frac{n_{10}}{\omega_{9i}} < \frac{2\omega_{15u}}{3} \times 10^5,$$

One notes that this range of electron densities includes almost every value suggested either by accretion disks, partially ionized dense gas blobs or emission line regions. In conclusion, the reflection of radio radiation off the ionization fronts can generate high frequency and short duration localized pulses. Could it be that the part of the rapid correlated variability in the radio to optical region is triggered by the onset of ionization of the gas clouds? The conversion of radio radiation to higher frequencies and the generation of high frequency radiation by Compton and Raman scattering of fast electrons off the newly generated spatially periodic magnetic field, can significantly contribute to the time variability of AGN emission.

Acknowledgement

Part of this work was done at the International Centre for Theoretical Physics, Trieste during my visit as an associate (July 14–August 28, 1993).

References

1. Guilbert, P. W. and Rees, M. J., Mon. Not. Roy. Astron. Soc. **223**, 475 (1988).
2. Osterbrock, D. E., in "Astrophysics of Active Galaxies and Quasi-stellar Objects" (Edited by J. S. Miller) (Oxford University Press, Oxford 1985), p. 111.
3. Ferland, G. J. and Shields, G. A., in: "Astrophysics of Active Galaxies and Quasi-stellar Objects" (Edited by J. S. Miller) (Oxford University Press, Oxford 1985), p. 157.
4. Mathews, W. G. and Capriotti, E. R., in "Astrophysics of Active Galaxies and Quasi-stellar Objects" (Edited by J. S. Miller) (Oxford University Press, Oxford 1985), p. 185.
5. Krishan, V., Mon. Not. Roy. Astron. Soc. **226**, 629 (1987).
6. Krishan, V., Mon. Not. Roy. Astron. Soc. **231**, 353 (1988).
7. Lampe, M., Ott, E. and Walker, J. H., Phys. Fluids **21**, 42 (1978).
8. Mori, W. B., Phys. Rev. **A44**, 5118 (1991).

Physica Scripta. Vol. T52, 118–122, 1994

Role of Plasma Processes in Astrophysics

Vinod Krishan

Indian Institute for Astrophysics, Bangalore – 560 034, India

Received November 22, 1993; accepted January 28, 1994

Abstract

The universe is made up of plasmas and fluids. The plasma phenomena exhibits itself through electromagnetic processes and the fluid through configurational processes. I shall try to illustrate both these aspects by taking examples from the observable universe.

1. Introduction

Plasmas are so prevalent throughout the cosmos that it is the "Plasma Universe", a term first coined by the Nobel Laureate Hannes Alfvén, that we are trying to observe and understand. You may find it disconcerting that our awareness of the three common states is barely adequate to comprehend about one percent of the universe, the other 99 percent being in the plasma state.

Since most of the universe is in the plasma state, I guess knowing plasmas would help us to understand some of the workings of the universe. Of course, it is the thermonuclear fusion that is the preoccupation of most of the laboratory plasma physicists. Plasma physics has also drawn the attention of the people seeking the ultimate accelerators. But man does need bread to live and that takes him into the realm of technological applications of plasma from communication to dyeing to deposition of ions on materials.

Filamentary structures of all sizes and shapes are observed on all scales in the universe. Be it stellar and planetary atmospheres, supernovae ejecta, planetary nebulae, galactic environment or extragalactic realms. The macroscopic stability of these structures is studied using single and the two-fluid description of a plasma. This description relates the size, the pressure, the fields and the flows in a plasma structure.

One learns about these structures through the characteristics of radiation that propagates through or generated in them. For example, quasiperiodic time variations in the radiation flux may indicate an oscillatory state of the emitting region. Similarly, one can learn about the medium through which the radiation propagates. For example, the observed delay in the arrival time of pulses of different frequencies from a pulsar, is attributed to the dispersion properties of the interstellar medium. This time delay can be related to the electron density, the magnetic field and the size of the intervening interstellar medium. The nonthermal radio emission from the Sun reveals the density, temperature, magnetic field and geometrical nature of the solar corona. It is through the absorption and scattering of electromagnetic radiation in the emission line regions of a quasar that we hope to learn about the invisible central object, suspected to be a black hole.

2. Plasmas as sources of coherent radiation

A source of radiation is coherent if its size is smaller than the wavelength of the radiation it emits, for then one can neglect the differences in the retarded times of the various parts of the source. It is in the realm of coherent sources of electromagnetic radiation that plasmas exhibit their versatility, the most. Plasmas are good at fast and large releases of energy. This is possible as it can store free energy in several forms, either as gradients in configuration and/or gradients in velocity space. Thus, large departures from equilibrium are allowed to grow which, then are permitted relaxation in an explosive manner. Solar flares are one such phenomenon where a complex configuration of magnetic and velocity fields becomes unstable and the relaxation occurs through a release of kinetic and electromagnetic energy. Most of the strong radio sources involve nonthermal (non-Maxwellian) distributions of energetic particles which relax by a combination of single particle and plasma processes, the latter being always more efficient and faster, if and when they happen. Often, the radiation observed from astrophysical sources has several components in it. There may be a steady emission over which is superimposed a fast varying or a quasi-periodic component, or the contribution of thermal to nonthermal may vary in different parts of a single source; or the emission may appear as absorption at some parts of the spectral region. All these situations involve a host of wave–particle and wave–wave interaction processes which can enhance or eliminate certain spectral regions. Therefore, the generation and propagation characteristics of radiation are the diagnostics of the physical conditions in the distant objects.

3. Nonlinear plasma processes

A plasma, by nature is hyperactive. More often than not, it responds violently to external stimuli in an attempt to attain equilibrium. When subjected to strong radiation fields, it exhibits a variety of nonlinear processes which modify its parameters as well as those of the radiation. When the size of the plasma region disturbed by an electromagnetic wave is much larger than the mean free path of an electron, an electron can gain enough energy before suffering collisions with other ions and neutrals. Further the large mass difference between electrons and other particles hinder the transfer of energy from electrons to the heavy particles. Thus the electric field of the electromagnetic wave heats the electrons preferentially, as a result of which the dielectric constant, ε, and the conductivity, σ, of the plasma become functions of the electromagnetic field and a nonlinear relation between the electric field, $\boldsymbol{E}$, and the current density, $\boldsymbol{J} = \sigma(\boldsymbol{E})\boldsymbol{E}$, is set up. In the opposite case, when the size of the disturbed

plasma region is much smaller than the mean free path of an electron, the inhomogeneous electric field of the electromagnetic wave exerts a pressure on the electrons, creating compressions and rarefactions. Then, the dielectric constant begins to depend on the electromagnetic field and the plasma again becomes a nonlinear medium. Summarizing a collisional plasma becomes nonlinear mainly through the dependence of electron temperature on the electromagnetic field and a collisionless plasma becomes nonlinear mainly through the dependence of electron density on the electromagnetic field.

In such a nonlinear medium an electromagnetic wave undergoes anomalous absorption, anomalous scattering, modulation and polarization changes through the excitation of parametric instabilities. Here, the driving energy is contained in a finite amplitude wave, electrostatic or electromagnetic that impinges on a plasma. It then couples with other waves in the plasma and drives them unstable. These unstable waves may eventually undergo dissipation and heat or accelerate plasma particles. This class of instabilities also plays an important role in the generation of high frequency radiation from the low frequency radiation, e.g. through a process called Stimulated Raman Scattering where low frequency radiation by scattering on the electron plasma wave of a high energy electron beam is converted into a high frequency radiation, a process akin to inverse Compton scattering but with the important difference that a single electron in the Compton scattering is substituted by an electron plasma wave in the Raman scattering. Both these processes have been applied to explain the properties of quasar nonthermal radiation.

In the reflection region an incident electromagnetic wave ($\boldsymbol{k}_0, \omega_0$) can decay into an electron plasma wave ($\boldsymbol{k}_1, \omega_1$) and an ion–acoustic wave ($\boldsymbol{k}_i, \omega_i$) leading to the anomalous absorption instead of reflection. On the other hand in the underdense region ($\omega_0 > \omega_{pe}$), the incident radio wave can decay into an electron plasma wave ($\boldsymbol{k}_1, \omega_1$) and an electromagnetic wave ($\boldsymbol{k}_s, \omega_s$) leading essentially to backscattering. Thus, the underdense region becomes a reflecting medium instead of a transparent medium. At a special site in an underdense region, known as the quarter critical region, where $\omega_0 = 2\omega_{pe}$, the incident wave can undergo anomalous absorption by decaying into two electron plasma waves or scattering by decaying into an electron plasma wave and an electromagnetic wave. The growth rates and the thresholds then determine the dominance or otherwise of the two processes. Parametric instabilities have been widely studied in the Earth's ionospheric plasmas as well as in the solar corona.

4. Fast plasma processes in quasars

We have attempted to understand the generation of the quasar continuum radiation and its interaction with the surrounding plasma, particularly emphasizing the role of plasma processes, which being coherent in nature, enhance the scattering and absorption rates, sometimes by several orders of magnitude, over the ones obtained from single particle processes.

The continuum emission of a quasar is in the form of a power law, $F_\nu \propto \nu^{-\alpha}$, consisting of several components: in the low frequency ($\nu \leqslant 1$ GHz) radio region, $\alpha \approx 0.1$; in the X-ray region $\alpha \leqslant 0.7$. The entire spectrum when fitted with an average value of $\alpha = 1$ shows bends in the radio, bumps in the blue and distinct variations in the hard X-ray and γ-ray regions. The continuum originates very near the black hole and then interacts with the surrounding plasma, which, as a result, exhibits phases of diverse temperatures and densities.

The earlier proposals of the continuum emission include synchrotron process for the radio radiation, which is upshifted to optical and X-rays by the inverse Compton scattering.

There are three ways by which the scattering of radiation in a plasma can occur: (*i*) the Stimulated Raman Scattering (SRS), where a strong electromagnetic wave is scattered off a weakly damped electron plasma wave ($k \ll k_D$), (*ii*) the stimulated Compton scattering (SCS), where a strong electromagnetic wave is scattered of a highly damped electron-plasma wave ($k \geqslant k_D$) and (*iii*) the Compton scattering (CS), where the electromagnetic radiation is scattered by single electrons (Fig. 1). Here, k_D is the Debye wave vector and k is the wave vector of the electron plasma wave. While estimating the up conversion of radio radiation the elders included the contribution only of the process (*iii*) (CS).

We have investigated the role of stimulated scattering processes in the generation of quasar continuum. In addition to accounting for the general features of a typical quasar continuum, we have been able to reproduce almost the entire spectrum of the quasar 3C 273 (Fig. 2) by suitably combining SRS and SCS. In particular, we have suggested that the bump in the blue region may be due to a change of process from SRS to SCS. In the process of reproducing the

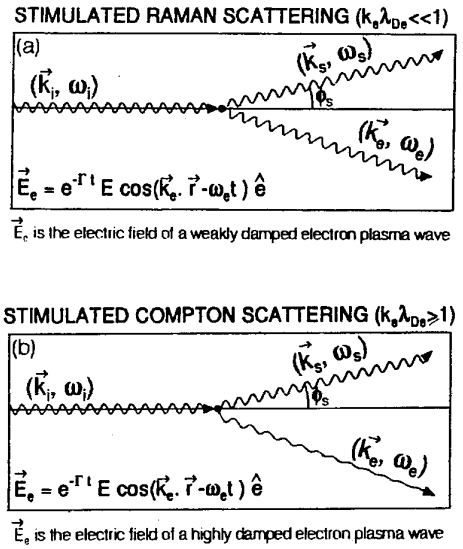

Fig. 1. The scattering of an electromagnetic wave ($\boldsymbol{k}_i, \omega_i$) in a plasma medium.

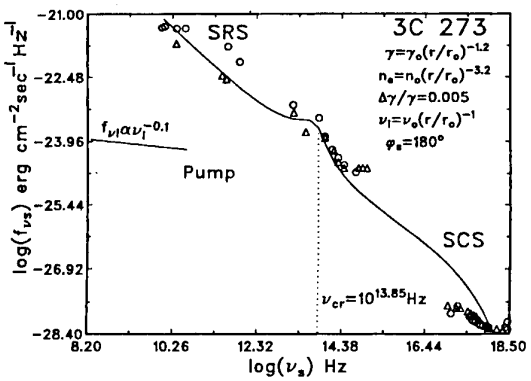

Fig. 2. The spectrum of the quasar 3C 273. The solid lines represent the calculated spectrum and the spectrum of the pump wave. The observed points, ○ (February 1984) and △ (February 1986) by Courvoisier *et al.* [22], are also plotted. The constants are: $\gamma_0 = 3 \times 10^3$, $n_0 = 9.24 \times 10^{17}\,\mathrm{cm}^{-3}$, $\nu_0 = 4 \times 10^{10}\,\mathrm{Hz}$ and $f_0 = 7.1 \times 10^{-25}\,\mathrm{erg\,cm}^{-2}\,\mathrm{sec}^{-1}\,\mathrm{Hz}^{-1}$.

observed spectrum we are able to derive the spatial variations of the plasma parameters in the emission region. One has to check if these variations are compatible with the geometry and stability of the accretion flows [1–5].

If the electron energy is converted into radiation via the extremely fast processes of SRS and SCS, then it must also be replenished at a comparable rate for the sustained emission from quasars. We have suggested that electrons can gain energy through an equally fast process of Raman Forward Scattering in which the electron–plasma waves produced by the beating of the cyclotron lines provide the necessary electric fields. Several issues related to the efficiency of these processes in the rather inhomogeneous and variable environment of a quasar, need to be investigated in-depth [4].

5. Anomalous absorption of the quasar radiation

The electron densities of the thermal plasma in the environs of a quasar are such that the corresponding electron plasma frequencies lie in the range of radio frequencies. This opens up several avenues by which the radio radiation can be absorbed in the thermal plasma by processes more efficient than the collisional. Again, through the processes of the parametric decay instability and the stimulated Raman and Compton scattering followed by the damping of the electron plasma and the ion acoustic waves, the plasma can be heated to much higher temperatures in much shorter times. The plasma temperature is one of the most important factors in the emission of continuum and line radiation and is also responsible for the inhomogeneous distribution of the gas [3, 5, 6].

These absorption processes also modify the spectral distribution of the emitted radio radiation. The bends in the radio continuum of a quasar could therefore be in part account for by the plasma absorption processes [7].

The 21 cm radio radiation is always associated with the spin–flip transition of neutral hydrogen atoms. Therefore the absorption feature at 21 cm from a quasar is attributed to the neutral hydrogen clouds which can exist only far beyond the reach of the ionizing continuum of a quasar.

We have shown that the radio continuum around the 21 cm will be anomalously absorbed via the plasma processes in the ionized regons lying much closer to the central object. If so, only the part of the 21 cm radiation that tunnels in between the ionized filaments, will be available for absorption in neutral hydrogen clouds. This would put constraints upon the positions, sizes and densities of neutral hydrogen regions [8].

We have also investigated the potential of plasma processes in explaining the apparent superluminal motion of compact radio sources as well as the extremely rapid changes in the polarization properties of the radiation [5, 9].

The modulational instability of a large amplitude electromagnetic wave propagating in an electron–positron plasma is investigated by Gangadhara, Krishan and Shukla [10]. It is shown that the observed time variability in the radiation from active galactic nuclei and pulsars may be explained through the excitation of the modulational instability.

In astrophysical situations, ionization of hydrogen is believed to be due to the stellar ultra-violet radiation, cosmic rays and X-rays. Recently laboratory experiments have shown the possibility of ionizing hydrogen by microwave radiation. It is a stochastic excitation process and is associated with the destruction of the invariant tori of a chaotic system. We have explored the role of this process in the ionization and the production of extremely highly excited states of hydrogen, since recombination lines corresponding to very high values of the principal quantum number have been observed [11].

6. More on frequency upconversion and variability

It is known that high frequency short duration electromagnetic pulses can be generated by reflection of low frequency radiation off relativistically moving ionization fronts [12, and references therein]. In addition, a part of the incident electromagnetic energy is converted into a spatially periodic static magnetic field. This phenomenon has been investigated (this conference proceedings) in the emission line region (ELR) and accretion disks of active galactic nuclei, where relativistically moving ionization fronts are created by the ionizing continuum. It is suggested that this process may play an essential role in: (1) causing rapid correlated variability in radio radiation and high frequency parts of the non-thermal spectrum; (2) generating high frequency radiation through scattering of relativistic electrons of the spatially periodic magnetic field, a by-product of the reflection process; (3) the diagnostics of the emission line region; and (4) absorption of the radio radiation. The anomalous absorption of radio radiation in ELR through parametric decay instabilities has been pointed out earlier. Interaction of the radio radiation with ionization fronts further strengthens the case for the existence of strong correlation between the nonthermal radio continuum and the ELR phenomena as the multiwavelength observations of AGN are beginning to do.

7. Nonthermal emission from dust

An electron moving with the superluminal velocity in a dielectric medium gives rise to the spontaneous Cerenkov radiation. If, instead of a single electron, a high density superluminal electron beam is made to pass through the

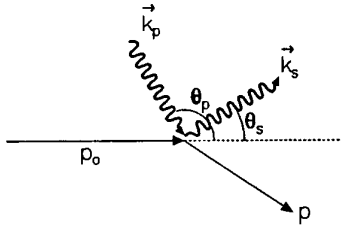

Fig. 3. Cerenkov–Raman scattering.

dielectric, the spontaneously generated radiation can undergo exponential amplification and is known as stimulated Cerenkov–Compton radiation. If, in addition, an incident electromagnetic field interacts with a strong superluminal or subluminal electron beam, a frequency upconverted stimulated scattered radiation is produced, which by analogy to a similar process in vacuum with subluminal electron beams is known as Cerenkov–Raman radiation. We explore and point out the role of these processes in the dust environs of AGN. Since, the refractive index of the dust matter is a key factor in these processes, their inclusion links the properties of the dust grains with the characteristics of the non-thermal continuum especially in the infrared and ultraviolet range, which, the observations show to be particularly bumpy and could be additonal contributions over the thermal.

Dust, in the universe, is best kown for its reddening and polarization properties. It absorbs ultraviolet radiation, becomes hot and reradiates the thermal spectrum corresponding to its temperature. The highest temperature, it can attain before sputtering is ~ 2000 K, which gives, from the Wien's displacement law, the maximum wavelength $\lambda_m \approx 1.5\,\mu$m. Evidence for the presence of dust in AGN comes from the strong thermal infrared, the 3.3 μm emission, the 10 μm silicate absorption and polarization of the continuum and the lines. The composition of the dust in AGN is suspected to be different from that of the circumstellar and the interstellar dust. This is inferred from the near absence or weakness of the 2200 A absorption feature, though this is also true for stars seen in the Magellanic clouds. A dust-to-gas ratio of ~ 10 percent of the galactic interstellar medium has been inferred from a comparison of resonance and non-resonance lines. A disk-like or a toroidal distribution with 10–20 times the dimensions of the flattened broad line emitting region has been necessitated for explaining the asymmetric line profiles and reddening. The dust particle sizes have been deduced to be much smaller than the sizes of the interstellar grains.

8. Stimulated Cerenkov emission

The intensity of radiation of frequency ω produced per unit path length (z) per uniqut frequency interval by a single electron of velocity $\beta c\hat{z}$ travelling in a medium of dielectric constant $\varepsilon(\omega)$ is given by [13]

$$\frac{dI(\omega)}{dz} = \frac{e^2\omega}{c^2}\left(1 - \frac{1}{\beta_0^2\,\varepsilon(\omega)}\right). \tag{1}$$

The spontaneous Cerenkov radiation, being proportional to the number of electrons, is a weak process. It can be strengthened if the prebunched electron beam of bunch size smaller than the wavelength of the radiation is sent through the medium. The stimulated processes achieve bunching of electrons through the excitation of electron plasma waves.

In a dielectric, a low frequency (ω_i) radiation can be upconverted to a high frequency (ω_s) radiation through a process known as the Cerenkov–Raman in analogy with the stimulated Raman scattering in a vacuum or a plasma [14]. The change in the frequency of radiation due to its scattering off fast electrons in the presence of a dielectric of refractive index, $n(\omega)$, can be determined from kinematic relations of energy and momentum conservation and is given as [15]

$$\frac{\omega_s}{\omega_i} = \frac{1 + \beta_0\, n(\omega_i)\cos\theta_i}{\beta_0\, n(\omega_s)\cos\theta_s - 1} \quad \text{for } \beta_0\, n(\omega_s) > 1,$$

$$= \frac{1 + \beta_0\, n(\omega_i)\cos\theta_i}{1 + \beta_0\, n(\omega_s)\cos\theta_s} \quad \text{for } \beta_0\, n(\omega_s) < 1. \tag{2}$$

Here, θ_i and θ_s are the incident and scattering angles as shown in Fig. 3. Since $n(\omega_s) > 1$, one can have large amplification for smaller values of β_0 as compared to the vacuum case. The dynamics of this process involve three-wave scattering where the incident mode, ω_i, is scattered off the collective mode of the beam electrons into the scattered radiation (ω_s). It can be shown that the phase matching conditions for the three-wave process are identical to the kinematic relations. The growth rate for this process can be calculated by using the standard techniques of the parametric instabilities.

We stress that the inclusion of stimulted processes in plasmas and dust could alleviate many of the spectral and time variability problems of AGN, in addition to providing correlated nonthermal radiation over a broad spectrum.

9. Large scale structure of the universe

The formation of the observed hierarchy of large scale structures [16] in the universe remains a challenging problem in cosmology. The distribution of galaxies does not appear as a random sprinkling. Galaxies are seen held together in clusters and superclusters of a few Mpc size as well as in sheets and arcs of sizes as large as ≈ 100 Mpc.

The gravity of the visible matter by itself appears to be too weak to form such large structures from the initial density perturbations in time scales comparable with the Hubble age. The conventional understanding of the clustering of galaxies rests on the wishful existence of several types of dark matter [17]. The nature of the invisible matter is only one of the many issues that these theories have to settle. The one-way turbulence theory by which large structures decay into small ones, was forsaken sometime ago due to the rather large hydrodynamic time scales and the – "bottom-up", i.e. small structures were formed first, dictates of the observations.

The "bottom-up" is precisely what can be achieved by an inverse cascade of energy. We have proposed that the supercluster and the giant clusters like the Great Wall form from the elementary structures like galaxies or small clusters of galaxies [18]. Velocities and sizes of the large scale structures derived from the inverse cascade process are consistent with the observations. In fact, the energy spectrum shown in Fig. 4 is applicable to solar granulation [19] as well as to

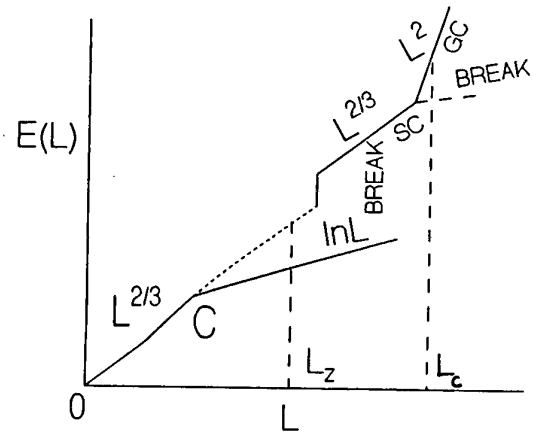

Fig. 4. Turbulent energy spectrum, L_z = scale of the break due to buoyancy, L_c = scale of the second break due to the Coriolis force, C = cluster or granule, SC = super-cluster or super-granule and GC = giant-cluster or giant cell.

the large scale structure of the universe with the appropriate scaling. The energetics indicates that turbulent velocities of $\approx 300\,\mathrm{km\,sec^{-1}}$ at the galactic scale (≈few kpc) are sufficient to form structures of a few Mpc with peculiar velocities of a few thousand km $\mathrm{sec^{-1}}$, in a time-scale of $\approx 3 \times 10^9$ years. Further, the [ln (L)] branch of the energy spectrum lies exactly at a scale (i.e. between clusters and superclusters) where a paucity of structures was seen observationally. We have successfully modelled the flat rotation curves of many galaxies combining the effects of rigid rotation, gravity and inverse cascades in a turbulent medium [20]. Of course, the final verdict about the success of inverse cascade can only be given after enough information on peculiar motion of these objects becomes available. We have also considered the large scale structure of the universe by the Navier–Stokes way [21].

The modification, that may arise due to the universe being in a state of expansion, is being worked out.

Based on these preliminary results, we have put-forward the following suggestions:

(*i*) The universe has distinct regions of rotational and potential flow. The phenomenon of clustering takes place in the rotational flow regon through the inverse cascade of energy.

(*ii*) In the irrotational or the potential flow dominated regions, the organized structures cannot form. The fluid elements are in a random state of small scale motions, which may appear as a continuum and this is what we may be interpreting as voids. Thus, contrary to the popular belief, voids are not empty. In fact they may contain motions which are more compressible than the ones associated with the clustering phenomenon.

(*iii*) The seemingly disparate phenomenon of (*a*) non-equilibrium motions on stellar surfaces, (*b*) the generation of large scale magnetic field; and (*c*) the large scale structure of the universe have their origin in the inverse cascade of energy leading to self-organization in an otherwise turbulent medium.

I have indicated some of the exciting and essential roles that the plasma processes play in astrophysics. We have made a small beginning and a lot more remains to be done for as Nietzsche says "It is not sufficient to prove a case, we must also tempt or raise men to it; Hence the wise man must learn to convey his widsom; and often in such a manner that it may sound like foolishness."

References

1. Krishan, V., Astrophys. Lett. **23**, 133 (1983).
2. Krishan, V., Astrophys. Space Sci. **115**, 119 (1985).
3. Krishan, V., Mon. Not. Roy. Astr. Soc. **234**, 79 (1988).
4. Krishan, V., and Wiita, P. J., Mon. Not. Roy. Astr. Soc. **246**, 597 (1990).
5. Gangadhara, R. T. and Krishan, V., Mon. Not. Roy. Astr. Soc. **256**, 111 (1992).
6. Krishan, V., Mon. Not. Roy. Astr. Soc. **226**, 629 (1987).
7. Krishan, V., Mon. Not. Roy. Astr. Soc. **230**, 181 (1988).
8. Krishan, V., Mon. Not. Roy. Astr. Soc. **231**, 353 (1988).
9. Krishan, V., J. Astrophys. Astr. **9**, 231 (1988).
10. Gangadhara, R. T., Krishan, V. and Shukla, P. K., Mon. Not. Roy. Astr. Soc. **262**, 151 (1992).
11. Krishan, V., "Microwave Excitation and Ionization of Hydrogen" (Preprint) (1990).
12. Mori, W. B., Phys. Rev. A **44**, 5118 (1991).
13. Melrose, D. B., "Plasma Astrophysics" (Gordon and Breach Science, New York 1982), Vol. 1, p. 62.
14. Krishan, V., Current Science **64**, 301 (1993).
15. Walsh, J. E., in "Physics of Quantum Electronics" (Edited by S. F. Jacobs *et al.*) (Addison-Wesley, Massachusetts 1980), Vol. 7, p. 255.
16. Huchra, J. *et al.*, Astrophys. J. Suppl. **52**, 89 (1983).
17. Kolb, W. E. and Turner, M. S., "The Early Universe" (Addison-Wesley, Massachusetts 1990).
18. Krishan, V. and Sivaram, C., Mon. Not. Roy. Astr. Soc. **250**, 157 (1991).
19. Krishan, V., Mon. Not. Roy. Astr. Soc. **250**, 50 (1991).
20. Prabhu, R. D. and Krishan, V., Astrophys. J. (in press) (1994).
21. Krishan, V., Mon. Not. Roy. Astr. Soc. **264**, 257 (1993).
22. Courvoisier, T. J.-L. *et al.*, Astr. Astrophys. **176**, 197 (1987).

Physica Scripta. Vol. T52, 123–131, 1994

Plasma Configurations and Particle Acceleration Associated with Rotating Cosmic Magnets[1]

K. O. Thielheim

Institut für Reine und Angewandte Kernphysik, Abteilung Mathematische Physik, University of Kiel, Otto Hahn Platz 3, 24118 Kiel, Germany

Received November 22, 1993; accepted April 5, 1994

Abstract

Rotating cosmic magnets, rotation-powered radio pulsars, for example, can accelerate electrically charged particles to very high energies. In this paper, I shall discuss some of the physical mechanisms at work in this type of cosmic accelerators.

The Lorents-Dirac-Landau equation governing the development of particle orbits and of particle energy is reproduced from Maxwell's tensor using arguments of causality and self-consistency. Special attention is given to the role of radiation pressure.

In the immediate vicinity of the surface of a magnetized sphere, rotating with its vector of magnetic dipole moment μ inclined or orthogonal to its vector of angular velocity ω, charge clouds are found to be formed under the influence of the force-free surface FFS. Preliminary results of numerical iterations deliver a detailed picture of these plasma configurations characterized by global charge separation.

If the velocity of rotation is sufficiently high and if the magnetic dipole moment is sufficiently strong the formation of an evacuated region around the rotating magnet is predicted in a fully ionized, thin ambient plasma. Correspondingly, two classes of objects are distinguished according to whether an evacuated region of acceleration does or does not exist. Preliminary results of relativistic N-body plasma simulations confirm these predictions.

1. High energy particles in pulsar magnetospheres

The present work is directed to the understanding of fundamental electromagnetic processes evolving in rotating, strongly magnetized objects rather than to the reproduction and phenomenological description of data observed from individual cosmic objects.

In Part 2 classical equations of motion which (together with Maxwell's equations) govern individual particle dynamics will be discussed.

Well known arguments, reproduced in Section 2.1, lead to the conclusion that the Lorentz-Dirac equation (L-D equation) cannot be the correct equation of motion.

A deduction of the so-called Lorentz-Dirac-Landau equation (L-D-L equation) from Maxwell's tensor using causality and self-consistency arguments is given in Section 2.2.

The role of radiation pressure in the generation of radiation reaction force is demonstrated in Section 2.3. This mechanism will be illustrated by particle acceleration through radiation pressure.

In Part 3 the formation of plasma configurations around rotating cosmic magnets will be discussed.

For methodical reasons this work was done in two stages. "Stage one" is devoted to the dynamics of just one particle of mass m and electric charge e within the electromagnetic vacuum fields of a rotating, homogeneously magnetized sphere.[2] On "stage two" work is extended to configurations consisting of a rotating magnet embedded in an ambient plasma and bestowed with an outflow of electrically charged particles from the rotating magnet.

In order to produce a coherent picture of the scenario, most of the numerical results accomplished are based on a standard set of parameters believed to be typical of pulsars. This standard set of parameters is compiled in Table I.

It is of advantage to substitute parameters ω and μ by two other parameters, each with the dimension of a length. One is the radius of the light cylinder $r_L = c/\omega$ characterizing the state of rotation. This so-called light radius is about $r_L = 5000\,\mathrm{km}$ for the standard set of parameters, that is almost about equal to the radius of the Earth.

Another parameter relevant for particle dynamics in the fields of a rotating magnet is the typical radius $r_T = (e\mu/mc^2)^{1/2}$ characterizing the electromagnetic properties of the system. Since the mass of the particle under consideration enters into this parameter, there are two typical radii, one for electrons and one for protons. Of these the typical radius for protons is the main interest here. For the standard set of parameters, the typical radius for protons is about $r_T \cong 5\,\mathrm{Mio\,km}$ that is about ten times the radius of the Sun.

Outside the transition zone, separating the near zone from the wave zone, the local amplitude of the vacuum wave field at a distance r_0 from the orthogonal rotator ($\chi = \pi/2$) is $E = H = 2^{1/2}\mu/r_L^2 r_0 = f_0 mc^2/er_L$ with $f_0 = 2^{1/2} r_T^2/r_L r_0$, along the axis of rotation ($\Theta = 0,\ \pi$), i.e. for circular polarization.[3]

Table I. *Standard set of parameters for rotating, magnetized neutron star (considered to be typical for pulsars)*

Parameter	Numerical value
Radius	$r_N = 10^6\,\mathrm{cm} = 10\,\mathrm{km}$
Mass	$M_N = M_S = 1.98 \times 10^{33}\,\mathrm{g}$
Angular velocity of rotation	$\omega = 20 \times \pi\,\mathrm{s}^{-1} = 10\,\mathrm{Hz}$
Magnetic dipole moment	$\mu = 10^{30}\,\mathrm{G\,cm}^3$
Angle of inclination	$\chi = \angle\{\omega, \mu\} = \pi/2$

[1] Lecture delivered to the Int. Workshop on Acceleration and Radiation Generation in Space and Laboratory Plasmas, Kardamyli, Greece, Aug. 29–Sept. 4 (1993).

[2] A review of conclusions reached on "stage one" is given in [1]. Most of our results on charged particle dynamics in the fields of rotating cosmic magnetics are based on the L-D-L equation.

[3] In the general case, for arbitrary latitudinal angle Θ, the dimensionless amplitude is $f_0 = (r_T^2/r_L r_0)(1 + \cos^2\Theta)^{1/2}$. Especially, in the equatorial plane of rotation, $f_0 = r_T^2/r_L r_0$, in agreement with {69} of [2]. (Formulae given in [2] are quoted here in curled brackets, {#}).

In Section 3.1 recent results of numerical iterations concerning the formation of space charges under the influence of the force-free surface (FFS) will be reproduced.

Particle decoupling from spherical wave fields is of relevance for processes in the outer regions of rotating cosmic magnets where, if particles have decoupled, the electromagnetic field is a vacuum wave field. This will be discussed in Section 3.2.

As will be shown in Section 3.3, within a certain range of parameter space, the formation of an evacuated region and, as a consequence, of a plasma border (PB) is predicted from the osculation theorem.

Correspondingly, two classes of cosmic accelerators may be distinguished, one by which a PB is formed and another by which this is not the case. Estimates on the location of the PB are given for the case of comparatively low ambient plasma density and, alternatively, for the case of comparatively high ambient plasma density, in Section 3.4. These two regimes are separated by the typical plasma density N_T related to plasma frequency of the ambient medium. Preliminary results of relativistic N-body simulations largely confirm these predictions, as demonstrated in Section 3.5.

2. Equations of motion

2.1. *The Lorentz-Dirac equation*

The classical equation of motion of an electrically charged particle, an electron for example, within an external electromagnetic field due to all other electrically charged particles around, incorporating radiation reaction may be written [3]

$$du_j/d\tau = \eta_0 F_{jk} u^k + \tau_0 G_{jk} u^k, \tag{1}$$

where $\eta_0 = e/mc$ are the contravariant components of four-velocity and F_{jk} is the field tensor of the external field. G_{jk} is the radiation force tensor. Latin indices run from 0 to 3. In the case of the L-D equation based on the works of H. A. Lorentz [28], M. Abraham [29, 30] and M. Laue [31, 32], the radiation force tensor

$$G_{jk} = G_{jk}^{\text{L-D}} = ([d^2u_j/d\tau^2]u_k - u_j[d^2u_k/d\tau^2])/c^2 \tag{2}$$

is constructed from the second kinematic acceleration $d^2u_j/d\tau^2$. $\tau_0 = 2e^2/3mc^3$ is the radiation constant.

The proof suggested by P. A. M. Dirac [4] essentially is based on the use of advanced together with retarded Green's functions. C. Teitelboim [5] and others have further developed this approach using subtraction techniques for mass renormalization. Several authors have tried to overcome the problem of divergencies by postulating finite particle extension suggesting an internal structure [6, 7] or by applying the De-Broglie-Schrödinger wave picture to the electron, for example, [8]. Approaches were also made to prove the Lorentz-Dirac equation on the basis of quantum electrodynamics making use of perturbative methods [9]. It will not be possible to discuss this extensive research work in detail here.

The L-D equation, unfortunately, also describes runaway solutions. For vanishing external fields, $F_{jk} = 0$, eq. (1) with (2) after multiplication with $du^j/d\tau$ reduces to

$$d\{|\underline{du}/d\tau|^2\}/d\tau = 2|\underline{du}/d\tau|^2/\tau_0 \tag{3}$$

with the (unphysical) solution

$$d\log\gamma/d\tau = (d\log\gamma/d\tau)_{\tau=0}\exp(\tau/\tau_0). \tag{4}$$

These difficulties have widely been discussed in literature. Obviously, they arise, since the radiation force tensor (2) is defined by means of the kinematic acceleration.

Runaway solutions can be avoided, for example, by an appropriate choice of initial conditions for acceleration. But then the question of the stability of these solutions arises.

As a consequence there is good reason to believe that the L-D equation is not the correct classical equation of motion for an electrically charged particle.

2.2. *The Lorentz-Dirac-Landau equation*

Runaway solutions can also be avoided by using iterated forms of the L-D equation. In the case of the L-D-L equation [10] the radiation force tensor is

$$G_{jk} = G_{jk}^{\text{L-D-L}} = \eta_0 u^l d_l F_{jk} + (u_j^{\text{LL}} u_k - u_j u_k^{\text{LL}})/c^2 \tag{5}$$

where $u_j^{\text{LL}} = \eta_0^2 F_{jk} F^{kl} u_l$ is an abbreviation for the second Lorentz acceleration. The first term on the right side of (5), gives rise to a third order contribution of the interaction constant e to radiation reaction force. The second term[4] on the right side of (5) gives rise to fourth order contributions of the interaction constant e to radiation reaction force. It contains two contributions, neither of which may separately be considered as a force. The first of these two contributions, is related to what sometimes is called the Schott term, while the second contribution may be called the Larmor term since it incorporates Larmor's radiation formula.

In the momentary rest system of reference (MRS), the L-D-L equation reduces to

$$d\boldsymbol{v}_{\text{MRS}}/dt = c\eta_0 \boldsymbol{E}_{\text{MRS}}^{\text{EXT}} + c\tau_0\eta_0\, d\boldsymbol{E}_{\text{MRS}}^{\text{EXT}}/dt + c\tau_0\eta_0^2[\boldsymbol{E}_{\text{MRS}}^{\text{EXT}}, \boldsymbol{H}_{\text{MRS}}^{\text{EXT}}], \tag{6}$$

where $\boldsymbol{E}_{\text{MRS}}^{\text{EXT}}$ and $\boldsymbol{H}_{\text{MRS}}^{\text{EXT}}$ is the electric and magnetic vector, respectively, of the external field[5].

But since we have concluded that the L-D equation (1) with (2) cannot be correct and since the L-D-L equation (1) with (5) is understood as an iterative approximation to the L-D equation, the L-D-L equation in so far also cannot be seen to rest on solid grounds unless a stringent proof is found.

In view of the importance of the L-D-L equation for theoretical studies on particle dynamics in extremely strong electromagnetic fields a deduction of the L-D-L equation from Maxwell's tensor based on causality and self-consistency arguments [11] will be given here.

For this purpose it is useful to consider, in its MRS, a particle of mass m and electric charge e within an external (given) electromagnetic field represented by the vectors $\boldsymbol{E}_{\text{MRS}}^{\text{EXT}}$ and $\boldsymbol{H}_{\text{MRS}}^{\text{EXT}}$, respectively. Then the total electric field is described by the electric vector

$$\boldsymbol{E}_{\text{MRS}} = \boldsymbol{E}_{\text{MRS}}^{\text{EXT}} + \boldsymbol{E}_{\text{MRS}}^{\text{RAD}} + \boldsymbol{E}_{\text{MRS}}^{\text{COUL}} \tag{7}$$

[4] The corresponding component of radiation "reaction" force may be referred to as the Thomson force for reasons discussed in Section 2.3 of this lecture.

[5] Gaussian units will be used throughout this paper so that both the electric as well as the magnetic field strength are measured in units of $1\,\text{G} = 300\,V/c$. Brackets (,) are for the scalar, [,] for the vector product.

where

$$\boldsymbol{E}_{\mathrm{MRS}}^{\mathrm{COUL}} = e\boldsymbol{R}_0/R^2 \tag{8}$$

is the Coulomb field of the particle under consideration. R is the distance from the particle to the point at which the field is considered. $\boldsymbol{R}_0$ is the corresponding unit vector.

The particle is subject to a (total) force $\boldsymbol{K}_{\mathrm{MRS}}$ and therefore to the acceleration $\mathrm{d}\boldsymbol{v}_{\mathrm{MRS}}/\mathrm{d}t = \boldsymbol{K}_{\mathrm{MRS}}/m$. As a consequence of its acceleration the particle is expected to "create" a radiation field as described by the Liénard-Wiechert potential or by the corresponding electric and magnetic vectors

$$\boldsymbol{E}_{\mathrm{MRS}}^{\mathrm{RAD}}(t) = (\eta_0/cR)[\boldsymbol{R}_0, [\boldsymbol{R}_0, \boldsymbol{K}_{\mathrm{MRS}}]]_{\mathrm{RET}} \tag{9}$$

and

$$\boldsymbol{H}_{\mathrm{MRS}}^{\mathrm{RAD}}(t) = (\eta_0/cR)[\boldsymbol{R}_0, [\boldsymbol{R}_0, [\boldsymbol{R}_0, \boldsymbol{K}_{\mathrm{MRS}}]]]_{\mathrm{RET}}, \tag{10}$$

respectively. (The subscript $_{\mathrm{RET}}$ stands for retardation.) Then the total magnetic field is described by the vector

$$\boldsymbol{H}_{\mathrm{MRS}} = \boldsymbol{H}_{\mathrm{MRS}}^{\mathrm{EXT}} + \boldsymbol{H}_{\mathrm{MRS}}^{\mathrm{RAD}}. \tag{11}$$

Maxwell's tensor is

$$\sigma_{\mathrm{MRS}\,\mu\nu} = \varepsilon_{\mathrm{MRS}}\,\delta_{\mu\nu} - (1/4\pi)(E_{\mathrm{MRS}\,\mu}\,E_{\mathrm{MRS}\,\nu} + H_{\mathrm{MRS}\,\mu}\,H_{\mathrm{MRS}\,\nu})_{\text{"RET"}} \tag{12}$$

where Greek indices are running from 1 to 3 and

$$\varepsilon_{\mathrm{MRS}} = (1/8\pi)(\boldsymbol{E}_{\mathrm{MRS}}^2 + \boldsymbol{H}_{\mathrm{MRS}}^2)_{\text{"RET"}} \tag{13}$$

is the total energy density of the electromagnetic field. ("RET" now has been put into apostrophes meaning that retardation applies only to contributions to the fields originating from the particle.)

Integration of Maxwell's tensor (12) for the total field over the surface of a sphere in the limit of vanishing radius, $R \to 0$, delivers the total electromagnetic force acting on the particle

$$\boldsymbol{K}_{\mathrm{MRS}} = \left\{ -\oint_{R\to 0} \varepsilon_{\mathrm{MRS}}\,\mathrm{d}^2\boldsymbol{o} + (1/4\pi)\oint_{R\to 0} \boldsymbol{E}_{\mathrm{MRS}}(\boldsymbol{E}_{\mathrm{MRS}}, \mathrm{d}^2\boldsymbol{o}) + (1/4\pi)\oint_{R\to 0} \boldsymbol{H}_{\mathrm{MRS}}(\boldsymbol{H}_{\mathrm{MRS}}, \mathrm{d}^2\boldsymbol{o}) \right\}_{\text{"RET"}}. \tag{14}$$

When evaluating this result most of the contributions appearing in the integrals on the right side of (14) are found to vanish except those arising from the dyadic products $\boldsymbol{E}_{\mathrm{MRS}}^{\mathrm{EXT}} \otimes \boldsymbol{E}_{\mathrm{MRS}}^{\mathrm{COUL}}$ and $\boldsymbol{E}_{\mathrm{MRS}}^{\mathrm{RAD}} \otimes \boldsymbol{E}_{\mathrm{MRS}}^{\mathrm{COUL}}$.

The first of these two contributions, resulting from $\boldsymbol{E}_{\mathrm{MRS}}^{\mathrm{EXT}} \otimes \boldsymbol{E}_{\mathrm{MRS}}^{\mathrm{COUL}}$, is nothing but the Lorentz force

$$\boldsymbol{K}_{\mathrm{MRS}}^{\mathrm{LOR}} = mc\eta_0\,\boldsymbol{E}_{\mathrm{MRS}}^{\mathrm{EXT}}, \tag{15}$$

which is easily transformed from the MRS into an arbitrary inertial system of reference (IS)

$$K_{\mathrm{MRS}\,j}^{\mathrm{LOR}} = m\eta_0\,F_{jk}\,u^k \tag{16}$$

The second contribution resulting from $\boldsymbol{E}_{\mathrm{MRS}}^{\mathrm{RAD}} \otimes \boldsymbol{E}_{\mathrm{MRS}}^{\mathrm{COUL}}$, is identified as the radiation "reaction" force

$$\boldsymbol{K}_{\mathrm{MRS}}^{\mathrm{RAD}} = (1/4\pi)\oint_{R\to 0} \boldsymbol{E}_{\mathrm{MRS}}^{\mathrm{RAD}}(\boldsymbol{E}_{\mathrm{MRS}}^{\mathrm{COUL}}, \mathrm{d}^2\boldsymbol{o})_{\text{"RET"}}. \tag{17}$$

Evaluation delivers $(\boldsymbol{E}_{\mathrm{MRS}}^{\mathrm{COUL}}, \mathrm{d}^2\boldsymbol{o}) = e \sin\vartheta\,\mathrm{d}\vartheta\,\mathrm{d}\varphi$, where the "latitudinal" angle ϑ is measured against and the "longitudinal" angle φ is measured around the vector of the total force $\boldsymbol{K}_{\mathrm{MRS}}$.

Contributions to $\boldsymbol{E}_{\mathrm{MRS}}^{\mathrm{RAD}}$ are taken into account which originate from the charged particle during a time interval $(t, t + \Delta t)$, while the particle rests in configuration space (MRS) and moves from 0 to $(\mathrm{d}\boldsymbol{v}_{\mathrm{MRS}}(t)/\mathrm{d}t)\,\Delta t$ in velocity space. In what follows, the corresponding contribution (17) to momentum flux onto this particle during the same time interval $t, t + \Delta t$ is calculated.

To begin with, the momentum flux through a spherical surface of sufficiently (small) Radius $R > 0$ around that particle during a time interval $(t', t' + \Delta t)$ with $t' = t + \delta t \geqslant t$, may be written

$$\boldsymbol{K}_{\mathrm{MRS}}^{\mathrm{RAD}}(t', R)\,\Delta t = (1/4\pi)\oint_{R>0} \boldsymbol{E}_{\mathrm{MRS}}^{\mathrm{RAD}}(\boldsymbol{E}_{\mathrm{MRS}}^{\mathrm{COUL}}, \mathrm{d}^2\boldsymbol{o})_{\text{"RET"}}\,\Delta t. \tag{18}$$

For $\delta t = R/c$

$$\boldsymbol{K}_{\mathrm{MRS}}^{\mathrm{RAD}}(t + R/c, R) = (c/R)\tau_0\,\boldsymbol{K}_{\mathrm{MRS}}(t), \tag{19}$$

while for $\delta t = 0$ causality requires

$$\boldsymbol{K}_{\mathrm{MRS}}^{\mathrm{RAD}}(t, R) = 0 \tag{20}$$

for $R > 0$. With the Taylor expansion

$$0 = \boldsymbol{K}_{\mathrm{MRS}}^{\mathrm{RAD}}(t, R) = \boldsymbol{K}_{\mathrm{MRS}}^{\mathrm{RAD}}(t + \delta t, R) - \delta t \cdot \mathrm{d}\boldsymbol{K}_{\mathrm{MRS}}^{\mathrm{RAD}}(t + \delta t, R)/\mathrm{d}t + \cdots \tag{21}$$

and with (19) one arrives at

$$\boldsymbol{K}_{\mathrm{MRS}}^{\mathrm{RAD}}(t + R/c, R) = \tau_0\,\mathrm{d}\boldsymbol{K}_{\mathrm{MRS}}(t)/\mathrm{d}t \tag{22}$$

which is found to be independent of R so that

$$\boldsymbol{K}_{\mathrm{MRS}}^{\mathrm{RAD}}(t) = \tau_0\,\mathrm{d}\boldsymbol{K}_{\mathrm{MRS}}(t)/\mathrm{d}t. \tag{23}$$

This expression has to be Lorentz transformed from the MRS into an arbitrary IS. For this purpose it is useful to remember that the norm of the (four-) vector of velocity $\underline{u}$ is constant and equal to the velocity of light $\|\underline{u}\|^2 = (u^0)^2 - (\boldsymbol{u})^2 = c^2$, so that $u^0 = (c^2 + \boldsymbol{u}^2)^{1/2} = c\gamma$, where γ is the Lorentz factor of the particle under consideration. Thus the (relativistic three-) vector of velocity $\boldsymbol{u}$ is constituting a (3-dimensional Riemannian) velocity space $R_3(\boldsymbol{u})$ which is associated with the (4-dimensional pseudo-Euklidean) Minkowski space $R_4(\boldsymbol{x})$. With the help of $\mathrm{d}u^0 = (\boldsymbol{u}, \mathrm{d}\boldsymbol{u})/c\gamma$, the metric of $R_3(\boldsymbol{u})$ may be written

$$(\mathrm{d}\lambda)^2 = \gamma_{\mu\nu}\,\mathrm{d}u^\mu\,\mathrm{d}u^\nu = -\|\mathrm{d}\underline{u}\|^2, \tag{24}$$

with the metric tensor

$$\gamma_{\mu\nu} = \delta_{\mu\nu} - \beta_\mu\beta_\nu, \tag{25}$$

where $\beta_\mu = u_\mu/c\gamma$. The inverse metric tensor is

$$\gamma^{\mu\nu} = \delta^{\mu\nu} + \gamma^2\beta^\mu\beta^\nu. \tag{26}$$

Christoffel symbols

$$\gamma_{\mu\nu}^{\rho} - (\gamma/c)\beta^\rho\gamma_{\mu\nu} \tag{27}$$

are used to evaluate the covariant derivative, in this case, of the (relativistic three-) vector of force in $R_3(\mathbf{u})$

$$\mathrm{D}\boldsymbol{K}/\mathrm{d}\tau = \mathrm{d}\boldsymbol{K}/\mathrm{d}\tau + \boldsymbol{u}\|\underline{\mathrm{K}}\|^2/mc^2 \tag{28}$$

which may be completed by the appropriate zero-component to obtain the causal derivative [11]

$$\mathrm{D}\underline{\mathrm{K}}/\mathrm{d}\tau = \mathrm{d}\underline{\mathrm{K}}/\mathrm{d}\tau + \underline{\mathrm{u}}\|\underline{\mathrm{K}}\|^2/mc^2. \tag{29}$$

From (28) and (23) one is led to the following expression for the radiation reaction force

$$\underline{K}^{RAD} = \tau_0 \, D\underline{K}/d\tau. \tag{30}$$

With the projection operator $\underline{P} = \underline{1} - \underline{u} \otimes \underline{u}/c^2$, which provides for the projection on the hyperplane that is orthogonal to $\boldsymbol{u}$, the radiation reaction force is

$$\underline{K}^{RAD} = \tau_0 \, \underline{P} \, d\underline{K}/d\tau. \tag{31}$$

For self-consistency postulate, when the total force $\underline{K}$ is due to electromagnetic interaction and restricting further to the lowest order contributions of the interaction constant e, one is led to

$$K_j^{RAD} = m\tau_0 \, G_{jk}^{L\text{-}D\text{-}L} \, u^k \tag{32}$$

which reproduces the L-D-L equation.

While traditionally in Maxwell theory, the acceleration dv_{MRS}/dt occurring in Liénard-Wiecert's potential, is interpreted as the kinematic acceleration without specifying the force by which acceleration is effected[6] we find that the reproduction of the L-D-L equation requires that acceleration is produced by an external electromagnetic field [13].

2.3. *Particle acceleration by radiation pressure*

In his Presidential Address to the Physical Society on February 10, 1905 J. H. Poynting described certain didactic difficulties when he discussed the introduction of radiation pressure in a theory based on the concept of wave propagation: "A hundred years ago, when the corpuscular theory held almost universal sway, it would have been much more easy to account for and explain the pressure of light than today, when we all are certain that light is a form of wave motion" [16]. In our days, while we are familiar with the duality of the quantum and wave pictures for the electromagnetic field didactic difficulties still seem to arise when it comes to the suggestion that (at least part of) radiation "reaction" force is nothing but radiation pressure acting on the individual electron, for example.[7]

The mechanism of momentum transfer from wave fields through many-photon Thomson scattering has been discussed earlier by L. D. Landau and E. M. Lifschitz [10] and in subsequent work [17–19]. It has already been noted in some of this preceding work that, within the MRS, the resulting rate of (three-) momentum transfer $\sigma^T S_{MRS}^{EXT}/c$ from the external wave field to the electron is in agreement with the third term appearing on the right side of the L-D-L eq. (6), so that the latter may be written

$$dv_{MRS}/dt = c\eta_0 \, E_{MRS}^{EXT} + c\tau_0 \eta_0 \, dE_{MRS}^{EXT}/dt + \sigma^T S_{MRS}^{EXT}/mc, \tag{33}$$

where

$$\sigma^T = 8\pi e^4/3m^2c^4 \tag{34}$$

is the total cross-section for Thomson scattering and

$$S_{MRS}^{EXT} = (c/4\pi)[E_{MRS}^{EXT}, H_{MRS}^{EXT}] \tag{35}$$

is the Poynting vector of the external (given) field.

If the external field is a wave field, radiation reaction force, in so far, is the knock-on force produced by the incoming photons. The situation of the particle can thus be seen in analogy to that of a massive dust particle subject to friction in a stream of gas molecules [13–15].[8]

This mechanism may be chosen as a starting point to deduce, by Lorentz transformation, (at least part of) radiation reaction force assuming (as a classical model) that the latter is created by radiation pressure [14].

This interpretation is also possible (in the quantum wave picture) for the more general case of an *arbitrary* external field.

Maxwell's equations are known to fit the structure of quantum wave mechanics in having a form which is isomorphic to *de Broglie and Schrödinger*'s wave formalism. As I will illustrate here (at least for the fourth order term), this isomorphism allows the deduction of the radiation reaction force. For this purpose it is useful to consider *self-consistent Maxwell theory* [13–15], in which what conventionally is referred to as the "creation" of electromagnetic radiation through particle acceleration can be seen, alternatively, as *Thomson* scattering of photons while radiation reaction, essentially, is understood as the knock-on force produced in that scattering.

Schrödinger's wave equation for the photon is

$$i\hbar\partial_t \psi = H_M \psi - 4\pi i\hbar\chi, \tag{36}$$

with $(\nabla, \psi) = 4\pi\rho$ for the three-component, complex *photon wave function* $\psi = C(\boldsymbol{E} + i\boldsymbol{H})$. $\chi = C(\boldsymbol{j}^e + i\boldsymbol{j}^m)$ represents the electric and magnetic charge currents and $\rho = \rho^e + i\rho^m$ incorporates the electric and magnetic charge densities, respectively, through which the photon is scattered. $C = 1/\int_V \{\mathbf{E}^2 + \mathbf{H}^2\}^{1/2} d^3\boldsymbol{x}$ is a normalisation constant,[8] providing for

$$\int_V \psi^+ \psi \, d^3\boldsymbol{x} = 1 \tag{37}$$

V is in the normalisation volume. $\psi^* = C^*(\boldsymbol{E}^T - i\boldsymbol{H}^T)$ is the adjoint wave function. ^{T} stands for transposition. The *Hamiltonian* of the photon $H_M = -i(\varepsilon, c\boldsymbol{p})$ is defined with the help of the *Levi Civita* symbols $\varepsilon = ((\varepsilon_\lambda)_{\mu\nu}) = (\varepsilon_{\lambda\mu\nu})$. As usual, $\boldsymbol{p} = -i\hbar\nabla$ is the momentum operator. Obviously, $c^2\boldsymbol{p}^2 = H_M^2$ and consequently, $c^2\langle \boldsymbol{p}^2 \rangle = \langle H_M^2 \rangle$. Multiplying Schrödinger's equation (36) with ψ^+ and the adjoint equation with ψ after subtraction delivers the continuity equation

$$\partial_\mu w_\mu + \partial_t w = 0, \tag{38}$$

where $\chi = 0$ and $w = (\psi^*, \psi) = |C|^2\{\boldsymbol{E}^2 + \boldsymbol{H}^2\}$ is the *position probability density* and $\mathbf{w} = (w_\mu) = -i[\psi^*, \psi] = 2|C|^2[\boldsymbol{E}, \boldsymbol{H}]$ is the *position probability current* of the photon field.

Without loss of generality, photon scattering may be described in the MRS of the scattering particle, so that $\boldsymbol{j}^e = \boldsymbol{j}^m = 0$, since it is always possible by *Lorentz* transform-

[6] For example in [12], Chapter 14.

[7] K. O. Thielheim, "Radiation Reaction as Many Photon Thomson Scattering", paper submitted to Astrophys. J.

[8] In a more elaborate deduction, to avoid infinities, it is necessary also to use a Schrödinger wave function ϕ for the scattering particle, so that $\chi = Ce\phi^* v\phi$ and $q = Ce\phi^*\phi$, where e is the electric charge and v is the velocity operator of the scattering particle.

ation to pass to an arbitrary inertial frame of reference IS. Also, $\rho^e = e\delta^3(x - x')$ and $\rho^m = 0$.

It is not necessary to solve here, explicitly, *Schrödinger*'s equation for the case of photon scattering. Instead, it is possible to make use of the above-mentioned isomorphism with *Liénard* and *Wiechert*'s problem for the *radiating electron*, so that $\psi_{MRS} = \boldsymbol{E}^{EXT}_{MRS} + \boldsymbol{E}^{RAD}_{MRS} + \boldsymbol{E}^{COUL}_{MRS} + i\{\boldsymbol{H}^{EXT}_{MRS} + \boldsymbol{H}^{RAD}_{MRS}\}$.

The quantities w and w_μ, defined above, are functions of the position vector x of the scattering particle as well as of the position vector x' (and time coordinate t') for which one may wish to consider the wave field. In the case of stationary fields, because of (38) with q = 0,

$$0 = -\int_{V'} \partial_{t'} \, d^3x' = \int_{V'} \partial_{\mu'} w_\mu \, d^3x' = \oint_{O(V')} w_\mu \, d^2o'_\mu$$

and, consequently, since "mixed" terms in w_μ do not occur,

$$|w^{EXT}|\sigma^T \overset{DEF}{=} -\int_{V'} \partial_\mu w^{EXT}_\mu d^3x'$$

$$= -\oint_{O(V')} w^{EXT}_\mu d^2o'_\mu = \oint_{O(V')} w^{RAD}_\mu d^2o'_\mu \qquad (39)$$

This expression may serve to reproduce the *Thomson*'s cross-section eq. (34) and to relate classical with quantum mechanical conjectures for the statistics of scattering.

Due to the symmetry properties of w^{RAD}, each of the incoming photons which experiences scattering transfers its total momentum $\langle|p|\rangle \cong |\langle p^2\rangle|^{1/2} = (1/c)\langle H^2_M\rangle^{1/2} \cong (1/c)\langle|H_M|\rangle$ to the particle, so that the rate of increase of particle momentum, i.e. the "knock-on" force, is

$$K^T_{MRS} = N^{EXT}_{MRS} w^{EXT} \sigma^T (1/c)\langle|H_M|\rangle = (\sigma^T/c) S^{EXT}_{MRS}, \qquad (40)$$

where $N^{EXT}_{MRS} = 1/8\pi C^{EXT}\langle|H_M|\rangle^{EXT}$ is the number of photons in the normalization volume calculated from the ratio of the classical field energy in the normalization volume to the quantum mechanical expectation value of photon energy, reproducing thereby in eq. (33) the fourth order contribution to "radiation reaction" force.

I shall illustrate these findings by two examples. The first example concerns the asymptotic energy development of charged particles within strong wave fields (of lasers for example).

The charged particle moves essentially in direction of the Poynting vector S_{MRS}. The latter may be Lorentz transformed from the MRS to the IS. Then $S_{MRS} \to S \cong 4\gamma^2 S_{MRS}$ with $S_{MRS} = \text{const}$. Similarly, the longitudinal component of the (three-) vector of acceleration transforms $(dv/dt)_{MRS} \to (dv/dt) = (1/\gamma^3)(dv/dt)_{MRS}$. Now the differential equation $(dv/dt) = (\sigma^T/4mc)(1/\gamma^5)S$ is easily integrated, leading to the mean asymptotic Lorentz factor

$$\bar{\gamma}_{AS} = \cong (3\tau_0 \eta_0^2/c)^{1/3} E^{2/3} x^{1/3} \qquad (41)$$

in agreement with earlier results [13].

The second example concerns a mechanism which may be at work in the polar region of rotating, magnetised neutron stars, where it can produce an upper limit for the observed intensity of curvature radiation.

I shall consider here the simple configuration of homogeneous and static crossed magnetic and electric fields, where the magnitude of the former is extremely large (typically 10^{12} G), while the latter still is very large though considerably smaller than the former. Under such circumstances an electrically charged particle is moving practically along a magnetic field line, accelerated by the component of the electric vector $\boldsymbol{E}^{EXT}_{\parallel}$ parallel (or antiparallel) to the magnetic vector $\boldsymbol{H}^{EXT}$.

When *Lorentz* transforming the external fields into the MRS, the parallel component of the electric vector, $\boldsymbol{E}^{EXT}_{\parallel}$ does not change. But the transverse component of the electric vector does change, $\boldsymbol{E}^{EXT}_{\perp} \to \boldsymbol{E}^{EXT}_{MRS\perp} = \gamma \boldsymbol{E}^{EXT}_{\parallel}$. Also a transverse component of the magnetic vector, $\boldsymbol{H}^{EXT}_{MRS\perp} = -(\gamma/c)[\boldsymbol{v}, \boldsymbol{E}^{EXT}_{\perp}]$, is produced.

Inserting these fields into (33) produces an upper limit of particle energy

$$\beta\gamma^2 \leqslant (1/\eta_0 \tau_0) \boldsymbol{E}^{EXT}_{\parallel} / (\boldsymbol{E}^{EXT}_{\perp})^2. \qquad (42)$$

3. Plasma configurations associated with rotating magnets

3.1. *Preliminary results of numerical iterations on the formation of charge clouds under the influence of the force-free surface*

Studies performed on "stage one" with respect to the development of particle orbits and energy for individual electrons and protons within the vacuum fields of rotating magnets have revealed different features existing in different regimes of the radial coordinate.[2] Preliminary results obtained on "stage two" which take into account effects of collective particle motion indicate that this is also the case for plasma fields, where different methods are required for different ranges of the radial coordinate. In the second part of this lecture, I shall describe two such features of plasma configuration which have been predicted theoretically and eventually reproduced in computer experiments.

Rotating, homogeneously magnetized spheres are known to own a non-trivial force-free surface FFS [20] (at least as long as the axis of rotation is not parallel or anti-parallel to the magnetic axis) generated by points at which the electric vector is orthogonal to the magnetic vector. For the standard set of parameters, the FFS extends to a distance of about 10 km from the surface of the sphere.

Particle motion in the regime of the FFS, i.e. in the immediate neighbourhood of the rotating magnet, essentially follows magnetic field lines since there the magnitude of the electric vector is much smaller than the magnitude of the magnetic vector. In two opposite quadrants, the projections of the electric vector on the respective magnetic vectors are directed towards the FFS on both sides of the FFS. These segments of the FFS can act as particle traps towards positively charged particles.[9] Analogous statements hold for particles of negative sign in the two alternative quadrants [21]. Consequently, two positive and two negative corotating charge clouds are expected to form in the regime of the FFS.

[9] In the case of the parallel or anti-parallel rotator, the FFS degenerates to the equatorial plane. Rotational symmetry then provides for the conservation of generalized angular momentum thus generating Störmer regions (radiation belts). For the homogeneously magnetized sphere, these trapping regions are modified through the presence of an electric quadrupole moment, as compared with the point dipole [23].

H. Wolfsteller and K. O. Thielheim have verified these predictions in computer experiments [22]. So far, the latter work was intended to clarify conditions for the existence and structural features of quasi-stable configurations and not their dynamical evolution. For that reason, it was not necessary in this context to perform N-body simulations and numerical integrations of the L-D-L equation. Instead, sequences of quasi-static, co-rotating plasma configurations were generated by an iterative method.

In each iteration step, a certain amount of charge was allowed to separate from each segment of the surface and to move along the adjacent magnetic field line (neglecting drift effects) and to settle down, where the electrostatic forces tangent to the magnetic field line vanish. The total electric charge dismissed locally from the surface in each iteration step was chosen to be proportional to the magnitude of the component of the electric vector tangent to the magnetic field line (given the appropriate sign of that component).

Modifications of the electric field (with respect to vacuum fields) due to space charges were taken into account in each iteration step. Modifications of the magnetic field were found to be irrelevant.

A minimum value for the tangent electric component was adopted as a current limiting condition to define the end of the iteration process.

Figure 1 illustrates intermediate charge configurations found after 10 iteration steps (left) of an inclined rotator ($\chi = \pi/3$) and quasi-stable charge configurations established after 50 iteration steps (right). Positive charges (top) are shown as well as negative charges (bottom).

3.2. *Decoupling of particles from spherical wave fields*

The question arises whether charged particles moving outward with the electromagnetic field energy cooperate with the electromagnetic fields in the sense of (possibly non-linear) plasma waves. Results obtained on "stage one" suggest that for the standard set of parameters particles injected into the fields decouple very efficiently.

Particles injected within the regime of the near-field contributions can achieve energies considerably higher than the Gunn-Ostriker energy[10] $\gamma_{GO} mc^2 \cong (9/2)^{1/3}(r_T/r_L)^{4/3} mc^2$ [24, 25].

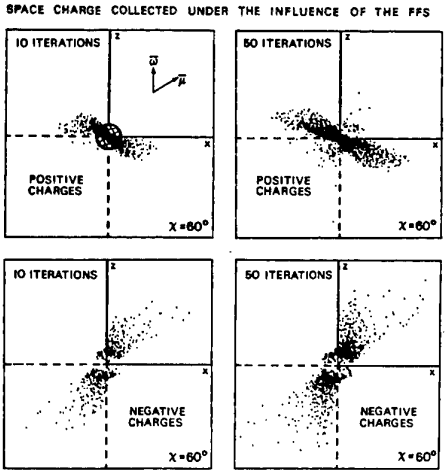

Fig. 1.

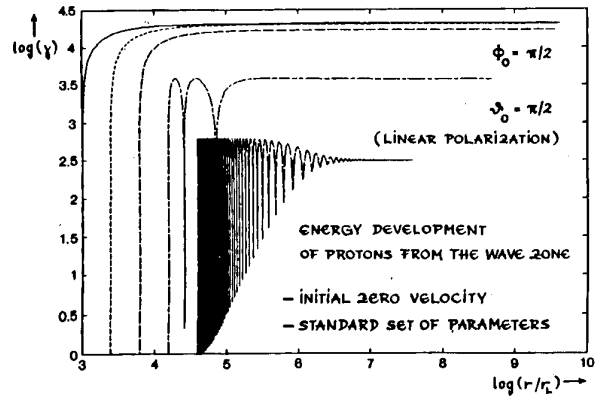

Fig. 2.

Particles injected within the comparatively narrow interval between the transition zone (separating the near zone from the wave zone) and the acceleration boundary[11] $r_B \cong (2\pi)^{1/3} r_L (r_T/r_L)^{4/3}$ gain the Gunn-Ostriker energy, independent of their initial position (at least in the phase average). This is demonstrated by Fig. 2 showing the energy development of individual particles starting from various positions in the equatorial plane of rotation within the wave zone.

There is an acceleration boundary (AB) for electrons and one for protons, indicating a different dynamical behaviour of the two kinds of particles. Here, the AB for protons is of special interest. At the axis of rotation, i.e. for circular polarization and for the standard set of parameters the AB occurs at $r_B \cong 2/3$ AU corresponding to about the orbital radius of the planet Venus.[12]

Particles injected outside the acceleration boundary are accelerated to their local drift energy[13] $\gamma_\infty mc^2 \cong (1/4)(r_L/r_0)^2 (r_T/r_L)^4 mc^2$. The latter is proportional to the inverse square of the initial radial coordinate r_0 so that with a constant source function (outer injection of neutral particles with subsequent ionization) a differential energy spectrum can be generated, which is proportional to $(\gamma_\infty mc^2)^{-2.5}$ [1]. This is illustrated by Fig. 3 representing asymptotic particle energy as a function of initial position within the wave zone.

[10] For the standard set of parameters, $\gamma_{GO} \cong 1.3 \times 10^4$, for millisecond pulsars with the same magnetic dipole moment $\gamma_{GO} \cong 5.8 \times 10^6$. Erratum: In [2], the Gunn-Ostriker energy lacks the exponent 4/3 in formula {89} and in Fig. 18. (A reproduction of the deduction of the Gunn-Ostriker energy using the nomenclature of [2] is offered in [26]). In [2], the expression following {10} should read $\underline{\dot{u}} = r_L \, d\underline{u}/c^2 \, dt$.

[11] Figure 18 and {69} of [2] is for linear polarization. For arbitrary latitudinal angle Θ {78} of [2] becomes: $\bar{u}^1 = (1/4)(r_T^2/r_L r_0)^2 (1 + \cos^2\Theta)^{-1} \{(1 + \cos^2\Theta)^2 + 4\cos^2\Theta\}$. The acceleration boundary (defined with respect to one period in [2]) in generalization of {79} reads $r_B = (\pi/2)^{1/3} r_L (r_T/r_L)^{4/3} (1 + \cos^2\Theta)^{-1/3} \{(1 + \cos^2\Theta)^2 + 4\cos^2\Theta\}^{1/3}$.

[12] $r_B = 1/3$ AU corresponding to about the orbital radius of the planet Mercury in the case of linear polarization.

[13] This fact has already been remarked by J. E. Gunn and J. P. Ostriker [24, 25]. The acceleration boundary r_B corresponds to the limit given by these authors for the applicability of the constant-phase approximation. Also, the typical radius r_T is related to Störmer's unit of length: $a = r_T(\beta\gamma)^{-1}$ [C. Störmer, Z. Astrophys., **1**, 237 (1930)].

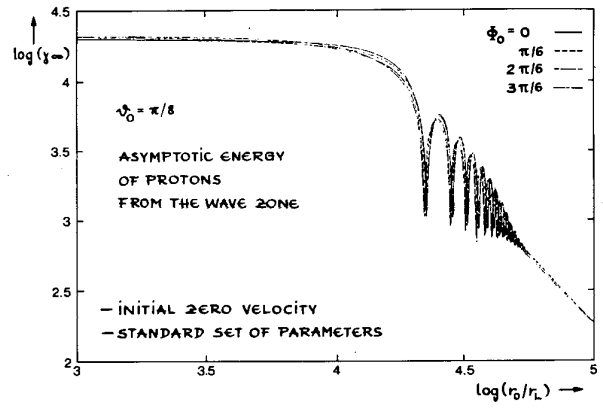

Fig. 3.

3.3. *Theoretical predictions on the existence of a plasma border*

Rotating magnets embedded in an ambient, fully ionized plasma are predicted to clean a certain region of surrounding space from all electrically charged particles, if the angular velocity of rotation ω is sufficiently high and if the magnetic dipole moment μ is sufficiently strong and if these two vectors are not parallel (or anti-parallel) and if the ambient plasma density is sufficiently low [1–3].

Correspondingly, two classes of configurations are expected to exist, one in which all the above mentioned conditions are fulfilled so that an evacuated region of acceleration can be formed and another class, in which this is not the case. The question arises whether both classes of configurations occur with rotating magnetized neutron stars and how they distinguish for an observer.

The formation of an evacuated region would create a boundary layer, at a certain distance r_P from the centre of the rotating magnet [1–3]. This plasma border (PB) would separate evacuated inner regions from plasma-filled outer regions at the utmost extension of the cosmic accelerator in space. The PB is also expected to be a source of synchrotron radiation. This scenario is shown schematically in Fig. 4.

In the case of comparatively low ambient plasma density, the formation of a plasma border may be understood as a consequence of the scattering of individual electric monopoles by a massive, rotating magnetic dipole [1].

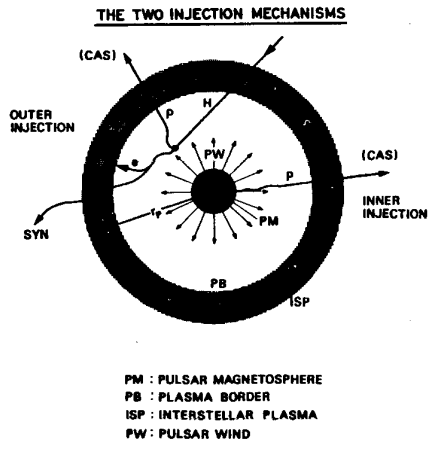

Fig. 4.

For a given distribution of particle energy, (taken for practical reasons at the point of reflection) the plasma border is generated as the inner envelope of all possible particle orbits.

The radial distance r_P of the PB from the rotating magnet is calculated by means of the osculation theorem [2]. The latter suggests that reflection takes place where the (physical) orbit in the given spherical wave field is osculated by a (hypothetical) closed orbit in the corresponding plane wave field.

The application of the osculation theorem may be illustrated for regions near to the axis of rotation. There, the corresponding plane wave field is circularly polarized. Consequently, closed orbits are of circular shape. The velocity vector $\boldsymbol{v} = \boldsymbol{\beta} c = \boldsymbol{\beta}_0 \beta c$ of the particle, in this case, is orthogonal to the electric vector $\boldsymbol{E} = \boldsymbol{E}_0 E = \boldsymbol{E}_0 \mu / r_L^2 r_0$ of the circularly polarized wave and parallel (or anti-parallel) to the magnetic vector $\boldsymbol{H}$. The equation of motion $\mathrm{d}(m\boldsymbol{v}\gamma)/\mathrm{d}t = \pm e\ \boldsymbol{E}$, therefore, reduces to $\mathrm{d}\boldsymbol{\beta}_0/\mathrm{d}t = [\boldsymbol{\omega},\ \boldsymbol{\beta}_0] = \pm \boldsymbol{E}_0 (1/\beta\gamma)(r_T/r_L)^2 (c/r_0)$ so that[14]

$$r_P^{VAC} = (\beta\gamma)^{-1} \cdot r_L (r_T/r_L)^2 \,. \tag{43}$$

There is a PB for electrons and one for protons, indicating that effects of charge separation may occur also in that region. For the following considerations, the PB for protons is of interest. For $\beta\gamma = 1$, the latter amounts to $r_P \cong 45\,\mathrm{AU}$ (that is about the orbital radius of the planet Pluto), at the axis of rotation i.e. for circular polarization.[15]

At comparatively high ambient plasma density, particles react collectively rather than individually towards the electromagnetic wave fields of the rotating magnet. Radiation pressure is exerted on the total inner surface of the PB and not just on the Thomson cross-sections of individual plasma particles. Then, the plasma border originates from a compensation of the kinetic pressure of plasma particles on one side and of the kinetic pressure of photons on the other side. While plasma particles by reflection deliver twice their momentum, photons through their scattering are expected to deliver at least their total momentum. This estimate suggests that the PB acts as a "black wall" towards the outgoing spherical wave field. Thus, it delivers a lower limit for the location of the PB in the case of comparatively high ambient plasma density. (Alternatively, photons through their reflection may be expected to deliver at most twice their total momentum. Then the PB acts as a "mirror" towards the outgoing spherical wave field.)

The flux of field momentum from the rotating magnet is calculated with the help of Maxwell's tensor for the spherical wave field $\sigma_{\mu\nu} = \varepsilon^{EXT}\delta_{\mu\nu} - (1/4\pi)\{E_\mu^{EXT} E_\nu^{EXT} + H_\mu^{EXT} H_\nu^{EXT}\}$ which, in the wave zone, reduces to $\sigma_{\mu\nu} = \varepsilon^{EXT}\delta_{\mu\nu} = (1/8\pi)\ \{(\boldsymbol{E}^{EXT})^2 + (\boldsymbol{H}^{EXT})^2\}\ \delta_{\mu\nu} = (\boldsymbol{E}^{EXT})^2 \delta_{\mu\nu}/4\pi = (1/4\pi)\delta_{\mu\nu}(\mu/r_L^2 r)^2$.

[14] In the general case, for arbitrary longitudinal angle Θ, {70} of [2] generalizes to $v_0 = \{1 + (1/2)(r_T^2/r_L r_0)(1 + \cos^2\Theta)\}^{1/2}$ and the location of the vacuum plasma border {71} of [2] generalizes to $r_P^{VAC} = 2^{-1/2}(\beta\gamma)^{-1} \cdot r_L (r_T/r_L)^2 (1 + \cos^2\Theta)^{1/2}$. In the equatorial plane of rotation, $\Theta = \pi/2$, i.e. for linear polarization, $r_P^{VAC} = 2^{-1/2}(\beta\gamma)^{-1} \cdot r_L (r_T/r_L)^2$, in agreement with {71} of [2].

[15] $r_P^{VAC} \cong 30\,\mathrm{AU}$ that is about the orbital radius of the planet Neptune in the equatorial plane of rotation, i.e. for linear polarization.

The kinetic pressure of electrons and protons[16] is $4mc^2N\gamma$.

Equalizing the two pressures delivers the following (rough) estimate for the PB in the case of a relativistic ambient plasma of comparatively high density

$$r_P^{PL} \leqslant (16\pi r_e \gamma N)^{-1/2}(r_T/r_L)^2. \tag{44}$$

A typical plasma density[17]

$$N_T = (1/16\pi)\gamma(1/r_e r_L^2) \tag{45}$$

separates the regime of comparatively low ambient plasma density $N \ll N_T$ from the regime of comparatively high ambient plasma density $N \gg N_T$. For the standard set of parameters the typical plasma density is $N_T \cong 5.7 \times 10^{-4}\gamma_P\,\mathrm{cm}^{-3}$. This is well below the plasma density of about $1\,\mathrm{cm}^{-3}$ plausible for the surroundings of a rotating magnetized neutron star (with the standard set of the parameters) so that (44) is expected to apply in that case. But the situation would be different for a millisecond pulsar (with the same magnetic dipole moment) where $N_T \cong 5.7 \times \gamma_P\,\mathrm{cm}^{-3}$ so that (43) should be applicable.

Within the regime of comparatively high ambient plasma density, practically all energy of the outgoing spherical wave is expected to be converted into synchrotron radiation within the boundary layer between the evacuated region of acceleration and the ambient plasma so that for a rough estimate (in the sense of an upper limit) $L_{PB}^{SYN} \leqslant (2/3)(c/r_L)mc^2(r_T^4/r_e r_L^3) \leqslant (2/3)\omega^4\mu^2/c^3$.

The PB for comparatively low density (at the axis rotation) and the upper limit of the PB for comparatively high density are shown schematically in Fig. 5.

3.4. *Preliminary results of computer experiments on the formation of a plasma border*

In order to verify the above mentioned predictions concerning the formation of a PB and to investigate in greater detail the conditions for its stability, its structure and the generation of synchrotron radiation relativistic N-body simulations[18] are performed by C. Greve, H. Laue and K. O. Thielheim.

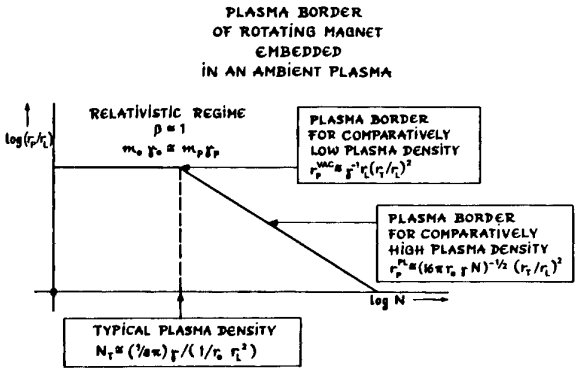

Fig. 5.

In preliminary runs, a reduced value of the magnetic dipole moment of $\mu = 10^{26}\,\mathrm{G\,cm}^3$ was adopted,[20] as compared with $\mu = 10^{30}\,\mathrm{G\,cm}^3$ for the standard set of parameters.

The simulation volume is a spherical shell with the rotating magnetic dipole at its centre. The inner and outer radii of the spherical shell are chosen so that according to theoretical predictions the plasma border can be expected to be located between them.

A large number of particles is randomly and continuously injected into the simulation volume through its outer surface, directed towards the rotating magnet and allowed to interact with the spherical wave field of the rotating magnet and with the additional field created by the particles. We have adopted $\beta\gamma = 1.0$ for protons and $\beta\gamma = 2000.0$ for electrons.[20]

Preliminary results are shown in Fig. 6. The four diagrams depict projections of spatial particle distributions from thin layers orthogonal to one of the coordinate axis at a certain instant of time. Only a small fraction of all particles is shown to give an impression of the density distribution. The two pictures on the left reproduce density distributions from a layer orthogonal to the y-axis, which is perpendicular to both, the magnetic (horizontal) as well as the rotational (vertical) axis. The two pictures on the right reproduce density distributions from a layer orthogonal to the z-axis, which is the axis of rotation. The two pictures at the top are for protons while the two pictures at the bottom are for electrons.

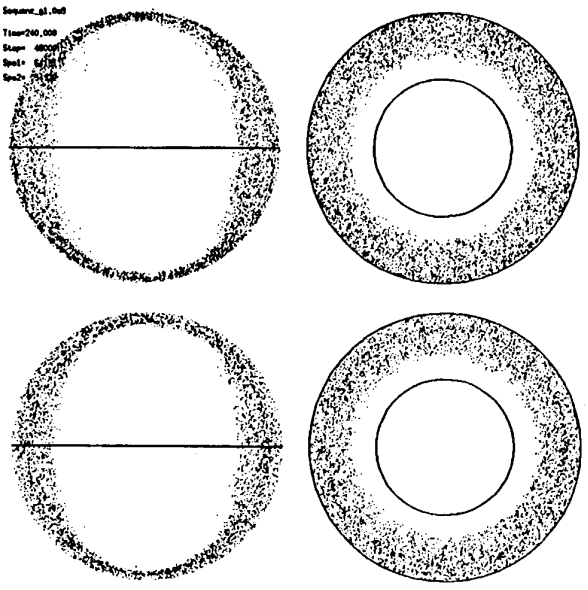

Fig. 6.

[16] Within this rough estimate it is justified to neglect the effect of the directional distribution of plasma particles.

[17] (45) essentially corresponds to the definition of the plasma frequency. Correspondingly, in generalization of the osculation theorem, plasma oscillations would characterize collective particle motion at the PB in the case of wave reflection.

[18] To be published.

[19] For comparison: the magnetic dipole moment of the Earth is $\mu_E = 8.1 \times 10^{25}\,\mathrm{G\,cm}^3$.

[20] It is adopted here that the mean energies of electrons and protons are equal at the point of reflection $m_e c^2\langle\gamma_e\rangle \cong m_P c^2\langle\gamma_P\rangle = mc^2\gamma$ and that both are in the relativistic regime $\langle\beta_e\rangle \cong \langle\beta_P\rangle \cong 1$, so that the mean absolute values of the momenta of electrons and protons are also equal at the point of reflection, $m_e c\langle\beta_e\gamma_e\rangle \cong m_P c\langle\beta_P\gamma_P\rangle = mc\gamma$. The vacuum plasma borders for the two kinds of particles then are also equal, $r_P^{VAC,e} \cong r_P^{VAC,P} = r_P$. I shall further adopt that the mean number densities of electrons and protons in the ambient plasma are equal $\langle N_e\rangle = \langle N_P\rangle = N$ providing for global charge neutrality.

These preliminary results confirm theoretical predictions for the location of the plasma border [1, 3, 27] in the case of comparatively low ambient plasma density as given by (37). Also, there are indications for the beginning of a contraction of the plasma border with increasing ambient plasma density.

References

1. Thielheim, K. O., Fundamentals of Cosmic Physics, **13**, 35 (1989).
2. Thielheim, K. O., Proc. 12th ECRS, Nottingham, Nucl. Phys. B (Proc. Suppl.) **228**, 60 (1991).
3. Thielheim, K. O., Proc. Advanced Accelerator Physics Course, CERN Accelerator School, Berlin, 23 (1987).
4. Dirac, P. M. A., Proc. Roy. Soc. (London) **A164**, 148 (1938).
5. Teitelboim, C., Phys. Rev. **D1** No. 6, 1572 (1970).
6. O'Connel, R. F. and Ford, G. W., Phys. Lett. **157A**, 217 (1991).
7. O'Connel, R. F. and Ford, G. W., Phys. Lett. **174A**, 182 (1993).
8. Monitz, E. J. and Sharp, D. H., Phys. Rev. **D15**, 2850 (1977).
9. Krivitskij, V. S. and Tystovich, V. N., Usp. Fiz. Nauk **161**, 125 (1991).
10. Landau, L. D. and Lifschitz, E. M., "The Classical Theory of Fields", Pergamon Press (1959).
11. Thielheim, K. O., Il Nuovo Cimento B, **109**, 103 (1994)
12. Jackson, J. D., "Classical Electrodynamics" (Wiley, New York 1975).
13. Thielheim, K. O., Proc. Particle Accelerator Conference, Washington, D.C., 17–20 May, **1**, 276 (1993).
14. Thielheim, K. O., Proc. Journeés Relativistes, Bruxelles, Belgium, 5–10 April, World Scientific, 289 (1993).
15. Thielheim, K. O., Proc. Second Tallin Symposium on Neutrino Astrophysics, Lohusalu, Estonia, 5–8 October, 138 (1993).
16. Poynting, J. H., Phil. Mag., and Journ. of Sci., Ser. **6**, Vol. **9**, 393 (1905).
17. Anderson, J. J., Phys. Lett., **18**, 114 (1965).
18. Kibble, T. W. B., Phys. Lett., **20**, 627 (1966).
19. Schmitd, G., Phys. Lett., **74A**, 222 (1979).
20. Jackson, E. A., Astrophys. J. **222**, 675 (1978).
21. Thielheim, K. O. and Wolfsteller, H., Astrophys. J. Suppl., **71**, 583 (1989).
22. Thielheim, K. O. and Wolfsteller, H., Astrophys. J., in press (1994).
23. Thielheim, K. O. and Wolfsteller, H., Journ. Phys. **A23**, 593 (1990).
24. Ostriker, J. P. and Gunn, J. E., Astrophys. J. **157**, 1395 (1969).
25. Gunn, J. E. and Ostriker, J. P., Astrophys. J. **156**, 523 (1971).
26. Thielheim, K. O., Proc. II Int. Conf. on Trends in Astroparticle Physics, Aachen, Germany, Oct. 10–12, 58, Teubner (1991).
27. Thielheim, K. O., "Cosmic Gamma Rays, Neutrinos and Related Astrophysics" (NATO ASI series) **270**, 523 (1989).
28. Lorentz, H. A., Enzykl. d. math, Wissensch. V, 1, 188 (1903).
29. Abraham, M., Ann. der Physik (4) **14**, 236 (1904).
30. Abraham, M., Theorie der Elektrizität, Verlag B. G. Teubner, Leipzig, (1. Auflage) Bd. 2. § 15 (1905).
31. Laue, M., Verh. d. deutschen physikalischen Gesellschaft **10**, 838 (1908).
32. Laue, M., Ann. d. Phys. **28**, 436 (1908).

Physica Scripta. Vol. T52, 132–134, 1994

Nonlinear Neutrino Plasmas Interactions

J. J. Su,* R. Bingham,† J. M. Dawson,‡ and H. A. Bethe§

* Institute of Space Science, National Central University, Chung-Li, Taiwan.
† Rutherford Appleton Laboratory, Chilton, Didcot, Oxon, OX11 0QX, U.K.
‡ University of California, Los Angeles, Physics Department Los Angeles, CA 90024-1547, U.S.A.
§ Physics Department, Cornell University, Ithaca, New York, U.S.A.

Received March 2, 1994; accepted March 23, 1994

Abstract

A new interaction mechanism is described between neutrinos and dense plasmas. With the unification of the electromagnetic and weak forces, analogous processes should occur for intense neutrino fluxes as for photon fluxes. Intense EM waves excite parametric instabilities in nonlinear media and plasma in particular. Therefore, sufficiently intense neutrino fluxes should also cause similar parametric instabilities in dense plasmas. An important example is the production of Langmuir plasmons and lower energy neutrinos. In plasma physics, for electromagnetic waves, the process is known as stimulated Raman scattering and it greatly increases the interaction of the light with the plasma. We propose that the analogous process, for neutrinos, occurs in the plasma surrounding the core of a supernova due to the immense neutrino flux there and the fact that at some distance from the core the flux is strongly unidirectional. We develop a theory for stimulated scattering of neutrinos in plasmas based on the index of refraction for neutrinos which depends on electron density, conservation of energy and momentum for neutrinos plus plasmons and wave damping; we estimate approximate growth rates.

1. Introduction

The interaction of neutrinos with matter is an important topic in high energy astrophysics. The question about how supernova explode is still an unsolved problem and depends critically on the transport of neutrinos within the star. During the implosion phase or collapse electron capture occurs, i.e. a proton and electron coalesce to yield a neutron and a neutrino. The super-dense core is optically thick (larger than an absorption length) to the neutrinos and a thermal distribution results with a temperature of about 20 MeV. Due to the density fall-off as one leaves the core, there is a surface (known as the neutrino sphere [1]), which radiates neutrinos more or less like a black body. The neutrinos carry away energy and entropy allowing the collapse process to accelerate. It is widely recognized [1] that more than 1% of the total neutrino energy flux must be absorbed by electrons in the layers surrounding the super-dense core of the star to produce sufficient electron pressure to eject the outer part of the star leaving only enough mass to form a neutron star. Otherwise no supernovae would occur and only black holes would result. Previous studies [2] have concentrated on collisional energy losses between neutrinos and fermions, the loss rate, however, is marginal to produce the required electron heating. In this paper we propose an entirely new neutrino interaction mechanism based on the coupling between the neutrinos and collective plasma oscillations in the dense plasma surrounding the core, namely stimulated neutrino-plasmon scattering. The interactions between electrons and neutrinos takes place through the electroweak interaction [3], the electrons interacting via both electromagnetism and weak interactions and the neutrinos interacting only through the weak interaction. The stimulated scattering process described in this paper has an analogue with laser plasma interactions [4], in this case the intense photon field of the laser couples to plasma oscillations producing effects such as stimulated Raman and Brillouin scattering [4] and the parametric decay process [4] where a photon is annihilated. Processes such as self-focusing and filamentation instabilities belong to the class of modulational instabilities, are also possible, and are described in terms of a nonlinear refractive index or susceptibility. In fact all material substances interact nonlinearly with intense radiation and the interaction with an intense neutrino flux should follow similar ideas.

The many body interactions between neutrinos and electrons in a plasma is no exception and results in polarization effects allowing the possibility of collective interactions between electron plasma oscillations and the neutrino fields. Stimulated scattering of neutrinos in a dense plasma into either a lower energy neutrino of the same type or a different neutrino and a photon or plasma oscillation is a strong possibility provided the neutrino flux is intense enough to overcome damping of the wave modes. In other words the growth rate of this nonlinear instability must be greater than a threshold value determined by the damping of the resultant modes. In such stimulated scattering processes the neutrino energy flux will decrease while conserving total lepton number, the interaction being determined by the following energy and momentum relationships,

$$\omega_{\nu 0} = \omega_{\nu 1} + \omega_{\mathrm{p}}, \quad \boldsymbol{k}_{\nu 0} = \boldsymbol{k}_{\nu 1} + \boldsymbol{k}_{\mathrm{p}}, \tag{1}$$

where ω and $\boldsymbol{k}$ are the frequencies and wavenumbers of the wave fields (for the neutrino and Langmuir plasmons) subscripts $\nu 0$, $\nu 1$ and p refer to the incident neutrino scattered neutrino and the plasma wave, respectively. The interaction we consider is described by a three point interaction as opposed to the more common four-point interaction.

The nonlinear coupling between the neutrino field and the Langmuir plasmon field is easily obtainable from the dispersion relation given by eq. (5) of Bethe [5] which is

$$E^2 - p^2c^2 - m^2c^4 - 2EV = 0, \tag{2}$$

where E is normalized energy, p is normalized momentum, m is the normalized neutrino rest mass, and V is equivalent to a potential energy $V = G\sqrt{2}\,n_{\mathrm{e}}$ (where n_{e} is the electron number density) and G is the Fermi constant of the weak interaction. The effects of linear dispersion and amplitude nonlinearity can be studied within the framework of a nonlinear Klein-Gordon equation obtained by making the

following substitutions

$$p \to -\mathrm{i}\hbar \frac{\partial}{\partial x}, \quad E \to \mathrm{i}\hbar \frac{\partial}{\partial t},$$

in eq. (4) forming the following wave equation for the neutrino field $\delta\Psi$

$$\left(\hbar^2 c^2 \frac{\partial^2}{\partial x^2} - m^2 c^4 - \hbar^2 \frac{\partial^2}{\partial t^2}\right)\delta\Psi = 2\mathrm{i}V\hbar \frac{\partial \delta\Psi}{\partial t}, \tag{3}$$

where V is now determined by n_e (electron number density per unit volume) and is related to the refractive index of the medium. $\delta\Psi$ is the neutrino amplitude wave function normalized so that the neutrino energy density is $|\delta\Psi|^2/4\pi$, ($|\delta\Psi|^2$) is proportional to the neutrino density times their energy ($\hbar\omega$). Equation (3) is the Kelin-Gordon equation describing the neutrino field coupling into the plasma medium through the potential V, it is similar to the wave equation for electromagnetic waves coupling to a plasma medium.

Writing $\delta\Psi = \delta\Psi_0 + \delta\Psi_1$, where subscript 0, 1 refers to the incident and scattered field, and using the conservation relations, eq. (1).

Equation (3) can be written in the form

$$\left(\hbar^2 c^2 \frac{\partial^2}{\partial x^2} - \hbar^2 \frac{\partial^2}{\partial t^2} - \tilde{m}^2\right)\delta\Omega_1 = \mathrm{i}2\sqrt{2}\, G\delta n_e \hbar \frac{\partial \delta\Psi_0}{\partial t}, \tag{4}$$

where δn_e is the perturbed electron density ($n_e = n_0 + \partial n_e$) varying as $\sim e^{\mathrm{i}(k_p x - \omega_p t)}$. Equation (5) describes the nonlinear interaction between the incident neutrino field, $\delta\Psi_0$, and the plasma wave, δn_e, producing a scattered signal at $\delta\Psi_1$ and $\tilde{m}^2 = m^2c^4 + 2V_0\hbar\omega_1$, with $V_0 = \sqrt{2}\,Gn_0$ being the potential associated with the mean plasma density, n_0.

From eq. (4) and assuming the amplitudes can be written as a slowly varying part, due to the nonlinear interaction, times a high frequency phase, the time derivative of the slowly varying part of the amplitude, $\delta\Psi_1$ is given by

$$\hbar \frac{\partial \delta\Psi_1}{\partial t} = -\mathrm{i}\sqrt{2}\, G\delta n_e^* \delta\Psi_0 \tag{5}$$

where we have assumed $\omega_{v0} \simeq \omega_{v1}$ and * denotes complex conjugate.

We can also obtain an analogous equation for $\partial\delta n_e/\partial t$ in terms of $\delta\Psi_{1,0}$ by using eq. (5) and conservation of momentum. From conservation of momentum (in the case of forward scattering, i.e., $k_p = k_{v0} - k_{v1}$), using the fact that the plasma waves with phase velocity $\sim c$ has energy and momentum densities $n_0 m_e c^2 \delta n_e^2/n_0^2$ and $n_0 m_e c \delta n_e^2/n_0^2$.

$$\delta\Psi_1 = \sqrt{4\pi m_e c^2 n_0}\, \frac{\omega_0}{\omega_p} \frac{\delta n_e}{n_0}. \tag{6}$$

Using eqs (5) and (6) we get

$$\frac{\partial \delta n_e}{\partial t} = \frac{-\mathrm{i}\sqrt{2}\, n_0 G\omega_p}{4\pi m_e c^2 \hbar \omega_0} \delta\Psi_1^* \delta\Psi_0. \tag{7}$$

From eqs (5) and (6) we obtain the growth rate of stimulated scattering of neutrinos on plasma oscillations.

$$\gamma = \sqrt{2}\, \frac{G}{\hbar} \sqrt{\frac{n_0 |\delta\Psi_0|^2 \omega_p}{4\pi m_e c^2 \omega_0}}. \tag{8}$$

To determine the threshold of the instability we have to add the dissipation term to eqs (5) and (7).

These equations then become

$$\frac{\partial \delta\Psi_1}{\partial t} + \gamma_v \delta\Psi_1 + \frac{\mathrm{i}\sqrt{2}\, G\delta n_e^* \delta\Psi_0}{\hbar} = 0, \tag{9}$$

$$\frac{\partial \delta n_e}{\partial t} + \gamma_p \delta n_e + \frac{\mathrm{i}\sqrt{2}\, n_0^2 G\delta\Psi_1^* \delta\Psi_0}{4\pi\hbar m_e n_0 c^2} \frac{\omega_p}{\omega_0} = 0, \tag{10}$$

where γ_v is the damping frequency for the neutrino waves [$= G^2(KT)^5 c/4\pi^2\hbar^7 c^7$] and γ_p is the damping rate of the plasma oscillations.

The damping of the Langmuir plasmons, γ_p, is the sum of collisional damping and Landau damping. For forward scattering, Landau damping is unimportant since the phase velocity of the plasma wave is close to c which is necessary to maintain phase coherence with the neutrino field. Equations (10) and (11) give the solubility determinant as

$$\begin{vmatrix} \gamma + \gamma_v & \dfrac{-\mathrm{i}\sqrt{2}\, G\delta\Psi_0}{\hbar} \\ \dfrac{-\mathrm{i}\sqrt{2}\, n_0^2 G\delta\Psi_0}{4\pi m_e n_0 c^2 \hbar(\omega_0/\omega_p)} & \gamma + \gamma_p \end{vmatrix} = 0 \tag{11}$$

which yields the following growth rate with damping included

$$\gamma = \tfrac{1}{2}\{-(\gamma_v + \gamma_p) \pm \sqrt{(\gamma_v - \gamma_p)^2 + \alpha|\delta\Psi_0|^2}\}, \tag{12}$$

where $\alpha = n_0 \omega_p G^2/2\pi m_e c^2 \omega_0 \hbar^2$. Setting $\gamma = 0$ gives the threshold for stimulated scattering of neutrinos off Langmuir plasmons

$$|\delta\Psi_0|^2 = \frac{4\gamma_p \gamma_v}{\alpha}. \tag{13}$$

The true damping of the neutrino field is of course negligibly small if we only consider electron-neutrino scattering, resulting in an unrealistically low threshold and high growth rate. However, there is an effective damping rate due to dephasing of the neutrino field with the generated plasma wave. The neutrino field has a broad frequency spectrum since it is a thermal spectrum. Dephasing is very rapid except for forward scattering, where the scattered wave moves along with the incident wave (both at essentially the speed of light) and so phase coherence can be maintained for long times. In the forward direction there is still an important phase slippage due to the angular spread in the propagation direction for the neutrinos. This gives them a spread in velocities along the radial (forward) direction which is $c\Delta\theta^2$. We have recently completed an analysis of the effects of a broadband neutrino distribution [6] and find that the process is still viable. The forward scattering for $\omega_0 \gg \omega_p$ should also include the up-shifted sideband we have neglected this but included it in a more rigorous treatment [6] involving the neutrino transport equation.

In this article we describe a new nonlinear coupling between neutrinos and dense plasmas which may be important in supernovae explosions.

Acknowledgements

This work was supported by NATO CGR 910316 and NSF PHY 91-21052. One of us (Su) would like to acknowledge the hospitality of Rutherford Appleton Laboratory where much of the early stages of this work was done. He also wants to acknowledge his visit to CERN where he had many interesting discussions.

References

1. Bethe, H. A., Rev. of Modern Physics **62**, 801 (1990).
2. Bethe, A. H. and Wilson, J. R., Astrophys. J. **295**, 14 (1985).
3. Weinberg, S., Phys. Rev. Lett. **19**, 1264 (1967).
4. Kaw, P. K., Kruer, W. L., Liu, C. S. and Nichikawa, K., "Advances in Plasma Physics" (John Wiley and Sons 1986), Vol. **6**, Part 1.
5. Bethe, H. A., Phys. Rev. Lett. **56**, 1305 (1986).
6. Bingham, R., Dawson, J. M., Su, J. J. and Bethe, H. A., submitted to Phys. Rev. Lett.

Physica Scripta. Vol. T52, 135–138, 1994

Superthermal Ion Cyclotron Harmonic Emission from Fusion and Space Plasmas: a Single Physical Mechanism

R. O. Dendy, C. N. Lashmore-Davies, K. G. McClements and K. F. Kam

AEA Technology, Fusion, Culham, Abingdon, Oxfordshire, OX14 3DB, UK (Euratom/UKAEA Fusion Association)

and

G. A. Cottrell

JET Joint Undertaking, Abingdon, Oxfordshire, OX14 EA, UK

Received November 22, 1993; accepted January 28, 1994

Abstract

A common mechanism for the observed excitation of waves at sequential multiple ion cyclotron harmonics in the JET tokamak and in various space plasmas is proposed. It is suggested that, in each case, waves on the fast Alfvén-ion Bernstein branch are excited by the magnetoacoustic cyclotron instability, which is driven by an energetic ion distribution with a local maximum at $v_\perp \neq 0$, where $v_\perp$ is the velocity component perpendicular to the magnetic field.

1. Introduction

In both fusion and space plasmas, intense superthermal radiation at sequential multiple ion cyclotron harmonics has been detected. There is strong observational and theoretical evidence that the same emission mechanism operates in both cases. This mechanism – the so-called magnetoacoustic cyclotron instability, whose original theoretical identification pre-dates the observations – involves the excitation of waves on the quasi-perpendicular fast Alfvén-ion Bernstein branch, due to cyclotron resonance with an energetic ion population which has anisotropic or inverted structure in velocity-space.

This paper is organized as follows. In Section 2 we briefly review the nature of the radiation of interest which has been detected in fusion experiments, and in Section 3 we do the same for space plasmas. The velocity-space distribution of energetic ions in the emitting region in fusion and space plasmas is discussed in Sections 4 and 5, respectively. In Section 6, we outline the theory of the common emission mechanism, and in Section 7 we present our conclusions.

2. Ion cyclotron emission from fusion plasmas

Superthermal ion cyclotron emission (ICE) has been observed in JET, using antennae which are designed to transmit fast Alfvén waves [1, 2]. The ICE intensity is proportional to measured fusion reactivity in a database which covers six decades in signal intensity, and spectral peak frequencies (see Fig. 1) match successive local ion-cyclotron harmonics at the outer mid-plane edge. There are correlations between the time-evolution of the ICE signal and that of the neutron flux during the discharge. These observations, obtained initially in so-called ohmic discharges where there is no attempt to create significant deviation from the Maxwellian in the ion population by external means, motivated a simple leading hypothesis: that ICE is due to cyclotron resonant collective excitation of fast Alfvén waves by the energetic ion products of fusion reactions. Later experiments using tritium [2], which involved $\simeq 13$ MW of neutral beam injection, leading to the creation of an energetic beam ion population additional to the fusion products, tended to support this hypothesis. In particular, by comparing otherwise similar discharges with high and low reactivity, it was possible to eliminate beam ions as a source of the observed ICE. Quantitative investigation of candidate emission mechanisms requires information on the velocity-space distribution of fusion products in the emitting region, which we shall discuss in Section 4.

3. Ion cyclotron emission from space plasmas

An excellent example of sequential multiple harmonic superthermal ion cyclotron emission, detected by the GEOS 2 spacecraft in the vicinity of the Earth's dayside geomagnetic equator at L-values between 4 and 8, is shown in Fig. 2 (taken from Ref. [3]). Measurements of the relative strength of the parallel and right and left circularly polarized components of the magnetic field unambiguously identify the

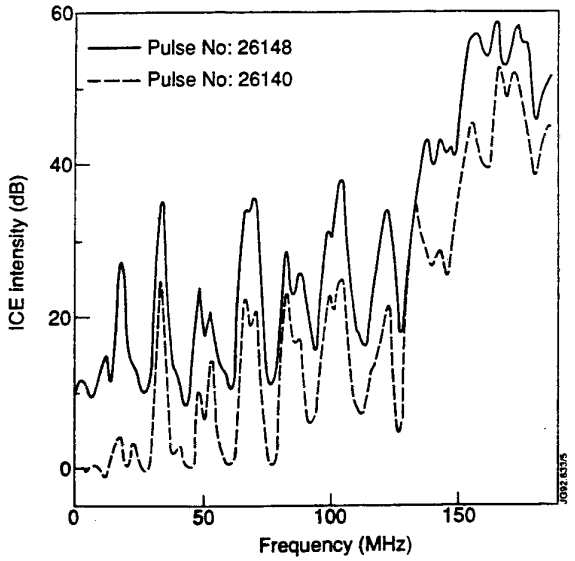

Fig. 1. Example of ion cyclotron emission spectra from JET deuterium-tritium (solid line) and deuterium-deuterium (dashed line) discharges. Peak frequencies are harmonics of the local alpha particle/deuteron cyclotron frequency [2].

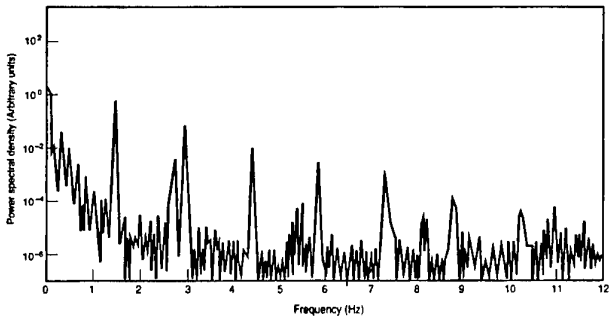

Fig. 2. Example of ion cyclotron emission spectra measured by the GEOS 2 spacecraft in the Earth's radiation belts. The wave magnetic field is predominantly aligned with the ambient field, indicating the presence of a quasi-perpendicular fast Alfvén wave [3].

wave as the quasi-perpendicular fast Alfvén mode. Frequency-matching of spectral peaks shows that they correspond to local ion cyclotron harmonics at somewhat higher L-values than those at which the observations were made.

4. Energetic ion velocity distributions in fusion plasmas

The observations described in Section 2 suggest that the fusion ion distribution in the edge plasma of JET is uniquely unstable. It was shown in Ref. [2] that a certain subgroup of centrally born fusion ions, restricted to a specific narrow range of pitch-angles and energies, make large drift orbit excursions which carry them to the outer mid-plane edge (Fig. 3). These particles are much more numerous than fusion ions born locally, and consequently dominate the fusion ion velocity distribution in the ICE emitting region. The predicted velocity-space distribution at the outer mid-plane edge, shown in Fig. 4, is wedge-shaped, and has a finite drift along the magnetic field. The total number density of fusion ions is predicted to fall off rapidly with major radius.

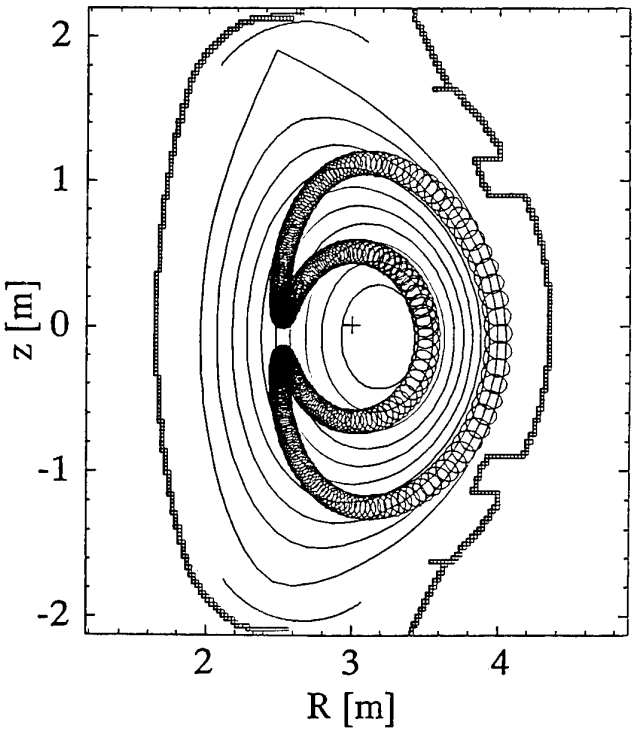

Fig. 3. Poloidal projection of a trapped alpha particle orbit in the flux surface geometry of the JET tritium experiment. Such orbits, which carry fusion alpha particles from the plasma centre to the outer edge plasma, only exist for pitch angles in the range 55°–65° [2].

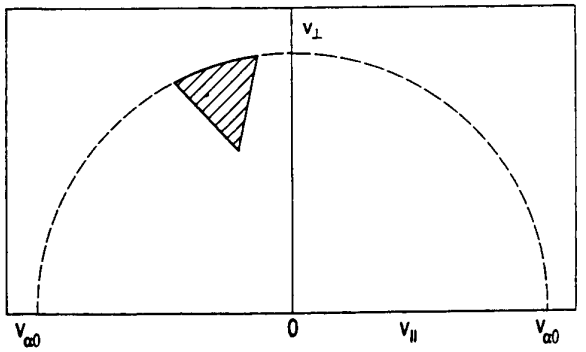

Fig. 4. The ring-like region of velocity space occupied by centrally-born alpha particles with large excursion orbits at major radius $R = 4.0$ m in the outer mid-plane edge plasma in JET [2].

5. Energetic ion velocity distributions in space plasmas

Several spacecraft have provided detailed information on the energy spectra and pitch angle distributions of energetic particles in the Earth's radiation belts. Anisotropic ions have been observed over a broad range of energies from below 1 keV to several MeV, the degree of anisotropy increasing with both energy and geocentric distance [4, 5]. It is particularly significant in the present context that radiation belt proton distributions are often observed to have broad peaks in the perpendicular direction, with local maxima occurring at energies of about 10 keV and above [3, 6]. An example is shown in Fig. 5. Anisotropic and ring-like proton distributions have also been detected by the AMPTE/IRM spacecraft downstream of the Earth's bow shock [7]. In the Earth's central plasma sheet, the ISEE-1 spacecraft has revealed a series of peaks and valleys in quiet-time ion energy spectra [8], implying that the three dimensional velocity distribution consists of several concentric shells or rings.

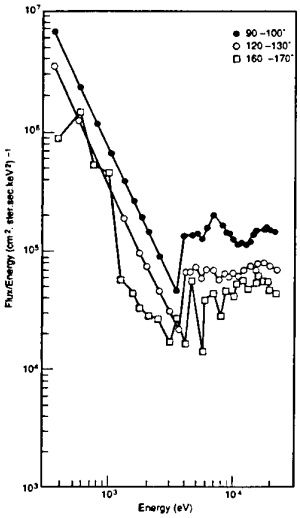

Fig. 5. Energy spectra of protons in the Earth's radiation belts, obtained using the GEOS 1 spacecraft. The three sets of data points correspond to different pitch angle ranges. The distribution peaks at an energy of 7.1 keV and a pitch angle of ~90° [3].

6. Emission mechanism

We propose that the wave data described in Sections 2 and 3 can be understood in terms of a common mechanism, the so-called magnetoacoustic cyclotron instability [9–11]. This involves the excitation of waves on the quasi-perpendicular fast Alfvén-ion Bernstein branches, at frequencies lying close to harmonics of the cyclotron frequency of an energetic ion species. Instability can only occur if there is a local maximum in the ion velocity distribution at $v_\perp \neq 0$, where $v_\perp$ is the velocity component perpendicular to the magnetic field. The particle distributions discussed in Section 4 and 5 have this particular non-Maxwellian feature in common.

The instability can be described in terms of the dielectric tensor ε_{ij}, which in general contains contributions from electrons, bulk ions, and energetic ions, labelled respectively by e, i and α:

$$\varepsilon_{ij} = \delta_{ij} + \varepsilon^{e}_{ij} + \varepsilon^{i}_{ij} + \varepsilon^{\alpha}_{ij}, \tag{1}$$

where δ_{ij} is the unit tensor. The other terms in eq. (1) are defined in terms of kinetic integrals over the particle distribution functions, f_e, f_i and f_α. We assume that the wave electric field is approximately polarized in the plane perpendicular to the magnetic field direction, **z**, so that electron Landau damping can be neglected. In such cases we only require the (x, x), (x, y) and (y, y) components of ε_{ij}.

In the case of quasi-perpendicular propagating waves with frequencies in the ion cyclotron range, the electrons are effectively cold [10]. We assume that the bulk ions have a bi-Maxwellian distribution:

$$f_i = \frac{n_i}{\pi^{3/2} v_{i\parallel} v_{i\perp}^2} \exp\left(-\frac{v_\parallel^2}{v_{i\parallel}^2} - \frac{v_\perp^2}{v_{i\perp}^2}\right), \tag{2}$$

and that the energetic ions have an extended ring distribu-

$$f_\alpha = \frac{n_\alpha}{2\pi^2 u v_r^2} \exp\left[-\frac{v_\parallel^2 + (v_\perp - u)^2}{v_r^2}\right]. \tag{3}$$

In eqs (2) and (3) n_i and n_α denote the number densities of bulk and energetic ions; $v_\parallel$ is the velocity component parallel to the magnetic field; and $v_{i\parallel}$, $v_{i\perp}$, u and v_r are constant speeds. The normalization in eq. (3) is only strictly correct if $\exp(-u^2/v_r^2) \ll 1$.

For a wave propagating in the (x, z) plane, Maxwell's equations yield the relation [12, 13]

$$\left(\varepsilon_{xx} - \frac{k_z^2 c^2}{\omega^2}\right)\left(\varepsilon_{yy} - \frac{k^2 c^2}{\omega^2}\right) = -\varepsilon_{xy}^2, \tag{4}$$

where ω is the complex wave frequency, $\boldsymbol{k}$ is the wave vector and c is the speed of light. Substituting the appropriate expression into eq. (4), we obtain a dispersion relation which simultaneously describes fast Alfvén waves, cyclotron harmonic (Bernstein) waves, and (when $k_z \neq 0$) cyclotron damping. Instability of quasi-perpendicular propagating waves ($k_z \ll k$) is predicted to occur under certain conditions. These are: that u is greater than the Alfvén speed c_A; that v_r/u is sufficiently small; and, in the case of $k_z \simeq 0$, that the energetic ion concentration is sufficiently high.

Using realistic parameter values, we have found that our model predicts the excitation of sequential multiple ion cyclotron harmonics, both in the edge plasma of JET [2, 10, 11] and in various space plasmas [14–16]. Figure 6, taken from Ref. [2], shows the linear growth rate due to the magnetoacoustic cyclotron instability under the conditions of the JET tritium experiment. In the case of oblique propagation ($\theta = 85°$), all cyclotron harmonics from $\ell = 1$ upwards are linearly unstable. Corresponding results for the Earth's bow shock are shown in Fig. 7 [15]. In this case, $u = 2c_A$, $n_\alpha/n_i = 10^{-2}$, $v_{i\perp}^2/v_{i\parallel}^2 = 3$, and $\beta_{i\perp} = 0.15$

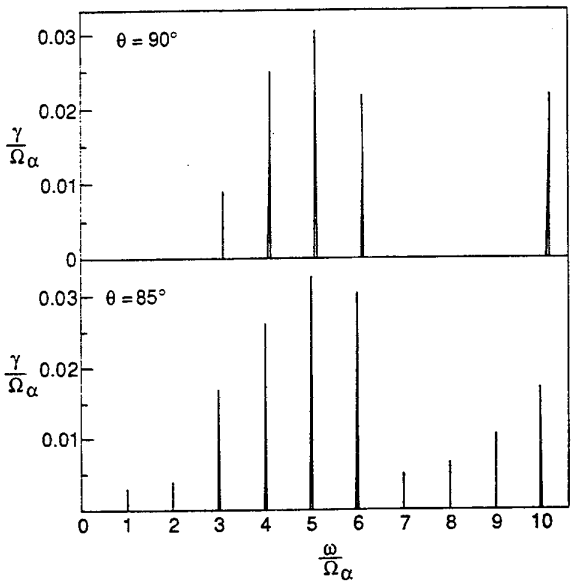

Fig. 6. Calculated linear growth rates at alpha particle cyclotron harmonics due to the magnetoacoustic cyclotron instability under JET conditions. The angle θ defines the propagation direction of the wave with respect to the magnetic field. The model parameters are: $u = 1.67c_A$, $n_\alpha/n_i = 1.5 \times 10^{-4}$, $v_{i\perp} = v_{i\parallel}$, and $\beta_{i\perp} = 1.6 \times 10^{-3}$ [2].

7. Conclusions

A single physical mechanism, the magnetoacoustic cyclotron instability, appears to be responsible for multiple ion cyclotron harmonic emission (ICE) in JET and in space plasmas.

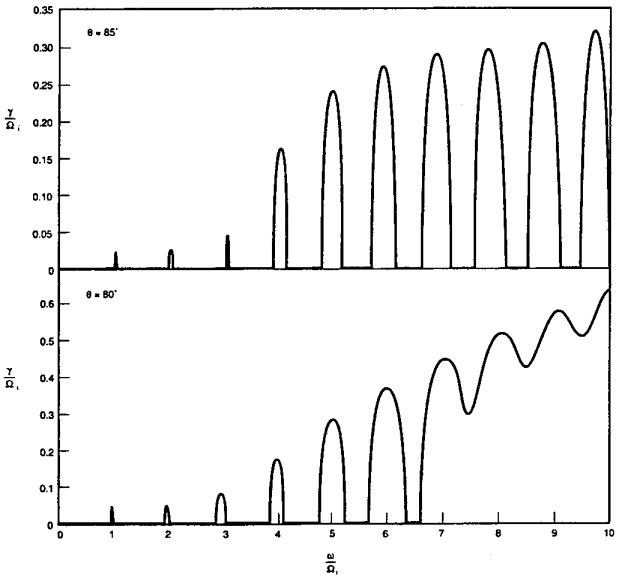

Fig. 7. Calculated linear growth rates at proton cyclotron harmonics due to the magnetoacoustic cyclotron instability under bow shock conditions. The model parameters are: $u = 2c_A$, $n_\alpha/n_i = 10^{-2}$, $v_{i\perp}^2 = 3v_{i\parallel}^2$, and $\beta_{i\perp} = 0.15$ [15].

ICE provides an important diagnostic of fusion ions in thermonuclear terrestrial plasmas, in which direct *in situ* measurements of particle distributions cannot be made. In the case of space plasmas, observations of ring-like or shell-like ion distributions in conjunction with wave emission in the ion cyclotron range provide strong evidence that the waves are driven by the magnetoacoustic cyclotron instability. We conclude from this that ICE is not peculiar to any particular magnetic field geometry.

Acknowledgements

We are grateful to Alain Roux for permission to reproduce Figs 2 and 5. This work was funded by the UK Department of Trade and Industry, by Euratom, and by the Commission of the European Communities under contract SCI*-CT92-0773.

References

1. Cottrell, G. A. and Dendy, R. O., Phys. Rev. Lett. **60**, 33 (1988).
2. Cottrell, G. A., *et al.*, Nucl. Fusion **33**, 1365 (1993).
3. Perraut, S., *et al.*, J. Geophys. Res. **87**, 6219 (1982).
4. Fritz, T. A. and Spjeldvik, W. N., J. Geophys. Res. **84**, 2608 (1979).
5. Lui, A. T. Y., McEntire, R. W., Sibeck, D. G. and Krimigis, S. M., J. Geophys. Res. **95**, 20839 (1990).
6. Kistler, L. M., *et al.*, J. Geophys. Res. **94**, 3579 (1989).
7. Sckopke, N., Paschmann, G., Brinca, A. L., Carlson, C. W. and Lühr, H., J. Geophys. Res. **95**, 6337 (1990).
8. Chen, J., Burkhart, G. R. and Huang, C. Y., Geophys. Phys. Lett. **17**, 2237 (1990).
9. Belikov, V. S. and Kolesnichenko, Ya. I., Sov. Phys. Tech. Phys. **20**, 1146 (1976).
10. Dendy, R. O., Lashmore-Davies, C. N. and Kam, K. F., Phys. Fluids **B4**, 3996 (1992).
11. Dendy, R. O., Lashmore-Davies, C. N. and Kam, K. F., Phys. Fluids **B5**, 1937 (1993).
12. Stix, T. H., "The Theory of Plasma Waves" (McGraw-Hill, New York 1962).
13. Sharma, O. P. and Patel, V. L., J. Geophys. Res. **91**, 1529 (1986).
14. McClements, K. G. and Dendy, R. O., J. Geophys. Res. **98**, 11689 (1993).
15. Dendy, R. O. and McClements, K. G., J. Geophys. Res. **98**, 15531 (1993).
16. McClements, K. G. and Dendy, R. O., in "Spatio-Temporal Analysis for Resolving Plasma Turbulence" (ESA WPP-047, 1993), p. 137.

Physica Scripta. Vol. T52, 139–141, 1994

A Possible Synchrotron Radiation Instability in JET Post Disruption Discharges

C. N. Lashmore-Davies and D. C. McDonald*

AEA Technology, Fusion, Culham, Abingdon, Oxfordshire OX14 3DB, U.K.; (Euratom/UKAEA Fusion Association)

Received November 22, 1993; accepted January 28, 1994

Abstract

Gill [JET-P(93)28(1993)] has noted the existence of a population of 35 MeV electrons in JET post disruption discharges. A preliminary consideration of the effect of such a population of relativistic electrons on electron cyclotron emission is described. It is shown that a collective synchrotron instability is possible. The presence of the background plasma causes the low harmonics to be stable but a large number of high harmonics could be unstable.

1. Introduction

It is well known that one of the effects of a major disruption in a tokamak is a large drop in the electron temperature with the result that the plasma becomes highly resistive. Under these conditions a large increase in the loop voltage has been measured and a population of runaway electrons is produced. A study of the behaviour of runaway electrons in post disruption discharges on JET has recently been reported by Gill [1]. Gill [1] noted that the discharge following the disruption supports a current ~ 1 MA which is carried substantially by the runaway electrons. Similar effects have been observed on TORE SUPRA where the limitation of the runaway energy was attributed by Laurent and Rax [2] to a stochastic instability in which the runaway electrons emitted electromagnetic radiation by interacting with the toroidal field ripple in the manner of a free electron laser. In both JET and TORE SUPRA the runaway electrons reach energies ~ 30 MeV. In this note we consider the effects of such electrons on the cyclotron emission from such a discharge.

2. The dispersion relation for a relativistic beam in a hot plasma

Zayed and Kitsenko [3] discussed the stability of a gyrating, relativistic electron beam in a cold magnetized plasma. In this paper we consider the effect of a hot background plasma on the stability of such a beam. We use the same equilibrium distribution function to describe the relativistic electrons as in Ref. [3].

$$f_{ob} = \frac{n_{ob}}{2\pi p_{\perp 0}} \delta(p_\perp - p_{\perp 0})\delta(p_z - p_{z0}). \tag{1}$$

Zayed and Kitsenko [3] showed that for the above distribution function the ordinary and extraordinary waves are both unstable at the fundamental and harmonics of the electron cyclotron frequency for perpendicular propagation. They also showed that obliquely propagating waves can be unstable. However, since these authors assumed a cold background plasma they did not include the important effects of cyclotron damping by the background plasma, or equivalently, mode coupling to cyclotron harmonic waves [4] supported by the background plasma. In order to include these effects a hot, background plasma must be used. We therefore combine the dielectric tensor for the relativistic, gyrating electrons given by Zayed and Kitsenko [3] with the standard dielectric tensor for a hot background plasma in which the bulk electrons have a Maxwellian distribution given, for example, by Stix [5]. In this note we shall confine our attention to the case of the ordinary mode propagating perpendicular to the uniform magnetic field in a uniform plasma. For this case the dispersion relation is

$$\frac{c^2k^2}{\omega^2} = 1 - \frac{\omega_{pe}^2}{\omega}\exp(-\lambda)\sum_{n=-\infty}^{\infty}\frac{I_n(\lambda)}{(\omega - n\Omega_0)} - \frac{\omega_{pb}^2}{\omega^2} - \sum_{l=-\infty}^{\infty}\frac{v_{z0}^2}{v_{\perp 0}^2}\omega_{pb}^2\frac{2kv_{\perp 0}}{\Omega_e}\frac{J_l(kv_{\perp 0}/\Omega_e)J_l'(kv_{\perp 0}/\Omega_e)}{\omega(\omega - l\Omega_e)} + \sum_{l=-\infty}^{\infty}\frac{v_{z0}^2}{c^2}\omega_{pb}^2\frac{J_l^2(kv_{\perp 0}/\Omega_e)}{(\omega - l\Omega_e)^2}, \tag{2}$$

where $\lambda = k^2v_T^2/\Omega_0^2$, $\Omega_0 = |e|B_0/m_0$, $\Omega_e = |e|B_0/\gamma_e m_0$,

$\gamma_e = (1 - v_{z0}^2/c^2 - v_{\perp 0}^2/c^2)^{-1/2}$, $\omega_{pe}^2 = \dfrac{n_{0e}e^2}{\varepsilon_0 m_0}$, $\omega_{pb}^2 = \dfrac{n_{ob}e^2}{\varepsilon_0\gamma_e m_0}$,

and v_T is the thermal speed of the bulk electrons. The dispersion relation given by eq. (2) reduces to that of Zayed and Kitsenko [3] when $\lambda = 0$.

Now consider the hot plasma case for which λ is finite. In order to illustrate the key effects we consider the following special case. We assume that the relativistic electrons have an energy such that

$$m\Omega_e = \Omega_0. \tag{3}$$

In other words, $\gamma_e = m$. Thus, the mth cyclotron harmonic of the relativistic electrons is degenerate with the fundamental cyclotron frequency of the bulk electrons. In addition, we also assume the resonance condition

$$(\omega_{pe}^2 + \omega_{pb}^2 + c^2k^2)^{1/2} = m\Omega_e, \tag{4}$$

i.e. the ordinary electromagnetic wave is in cyclotron resonance with the bulk and the relativistic electrons. We may now solve eq. (2) by a perturbation procedure, keeping only the resonant terms in the infinite summations and assuming

$$\omega = m\Omega_e + \delta\omega. \tag{5}$$

* Department of Mathematical and Computational Sciences, University of St. Andrews, St. Andrews KY16 9SS, Scotland.

With the aid of eqs (3)–(5), the dispersion relation, eq. (2), reduces to

$$(\delta\omega)^3 - \left(\omega_{pe}^2 \frac{\lambda}{4} + \omega_{pb}^2 \frac{v_{z0}^2}{v_{\perp 0}^2} \frac{kv_{\perp 0}}{\Omega_e} J_m J'_m\right)\delta\omega + \frac{\omega_{pb}^2}{2} m\Omega_e \frac{v_{z0}^2}{c^2} J_m^2 = 0. \quad (6)$$

The criterion for instability given by eq. (6) is

$$\left(\frac{1}{2}\omega_{pb}^2 \Omega_e \frac{v_{z0}^2}{c^2} J_m^2\right)^2 > \frac{4}{27}\left(\omega_{pe}^2 \frac{\lambda}{4} + \omega_{pb}^2 \frac{v_{z0}^2}{v_{\perp 0}^2} \frac{kv_{\perp 0}}{\Omega_e} J_m J'_m\right)^3. \quad (7)$$

A number of points are clear from eq. (7). First, as expected, the relativistic electrons will drive the O-mode unstable if their number density is high enough, if their parallel velocity is large enough (in comparison with the velocity of light in vacuum) and if their perpendicular velocity is large enough, also in comparison with c. However, unlike the cold plasma case discussed by Zayed and Kitsenko, there is now a threshold for instability given by the density and temperature of the bulk electrons. This effect is described by the first term on the r.h.s. of eq. (7). The second term on the r.h.s. of eq. (7). can be either stabilizing or destabilizing, depending on the sign of $J_m J'_m$ which in turn will depend on the magnitude of the argument $kv_{\perp 0}/\Omega_e$ and on the harmonic number, m. In any case, since the density of the relativistic electrons is usually much smaller than the density of the bulk electrons, $\omega_{pb}^2 \ll \omega_{pe}^2$, the second term on the r.h.s. of eq. (7) can usually be neglected.

It will be noticed that the case we have considered [defined by eqs (3) and (4)] corresponds to the situation where the stabilizing effects are maximized. However, eq. (3) describes a very special case. For almost all cases γ_e will not be an integer, so that a given cyclotron harmonic for the relativistic electrons will be locally unstable since the bulk electrons will not be simultaneously resonant. This is equivalent to the statement that regions of cyclotron damping by the bulk electrons are physically separate from regions of cyclotron instability of the relativistic electrons. In a plasma where the equilibrium magnetic field varies in space the unstable cylotron radiation may still be reabsorbed by the bulk electrons at another location but such instabilities could provide a mechanism for relaxation of the relativistic electrons.

There is another important point which is illustrated by the resonance condition given by eq. (4). The usual laboratory situation is such that $\omega_{pe}^2 \gg \omega_{pb}^2$. For very energetic electrons no instability will be possible for those harmonics where $\omega_{pe} > m\Omega_e$ since the ordinary mode will not propagate at these relativistically down-shifted frequencies.

Let us now apply the above analysis to the case of the JET post disruption discharges [1]. The parameters for these discharges are somewhat uncertain but Gill [1] gives the following set for the stage of the discharge when a steady current ~ 1 MA is carried by a population of runaway electrons whose energy ~ 35 MeV. Assuming the current flows in a cross section $\sim 1\,m^2$, we obtain for the density of relativistic electrons, $n_{ob} \sim 2 \times 10^{16}\,m^{-3}$. The parameters of the background plasma are $B_0 = 2.7$ T, $n_{0e} \simeq 2 \times 10^{19}\,m^{-3}$ and $T_e \simeq 25$–50 eV. For 35 MeV electrons we take $\gamma_e = 70$. In addition, we assume $v_{\perp 0} \sim v_{z0} \sim c$. For the above parameters, $\omega_{pe} \simeq 2.5 \times 10^{11}$ rads/sec and $\Omega_0 = 4.7 \times 10^{11}$ rads/sec and clearly $\omega_{pb} \ll \omega_{pe}$. The first propagating harmonic of the relativistic electrons is given by the condition $m = 70\omega_{pe}/\Omega_0$ which yields $m = 38$. Thus, the first 37 harmonics are stable. The harmonics from $m = 38$ to (say) $m = 65$ will be unstable. For these the radiation may either be reabsorbed by the bulk electrons or may be emitted from the plasma depending on the location of the relativistic electrons. The harmonics close to $m = 70$ will be subject to cyclotron absorption by the bulk electrons (or equivalently, mode coupling) at the fundamental cyclotron frequency of these electrons. In this case we must use eq. (7) to calculate the threshold for the JET post disruption conditions. In order to carry out this calculation we obtain an approximate value of $J_{70}(kv_{\perp 0}/\Omega_e)$ as follows. For $\omega > \omega_{pe}$ we approximate $k \sim m\Omega_e/c$ so that $kv_{\perp 0}/\Omega_e \sim m$ since we have assumed $v_{\perp 0} \sim c$. We use the asymptotic expression, for large m [6]

$$J_m(m) \sim \frac{\Gamma(\frac{1}{3})}{48^{1/6}\pi m^{1/3}} \quad (8)$$

to obtain approximate values for J_{70} and J'_{70}. We note that the second term on the r.h.s. of eq. (7) is now destabilizing but is small compared with the stabilizing term of the bulk electrons, due to the smallness of J'_{70}. Substituting the above results into the other two terms in eq. (7) we find that the $m = 70$ harmonic is also unstable.

In view of eq. (8) all harmonics up to $m = 140$ will also be unstable. Since the cyclotron damping of the ordinary mode at the second harmonic of the bulk electrons is much weaker than that at the fundamental, the ordinary wave will also be unstable at this frequency. All higher harmonics will be unstable since the cyclotron damping of the bulk electrons will be negligible. Unlike the instabilities resulting from weakly relativistic electrons, the instability of the ordinary mode for strongly relativistic electrons (tens of MeV) is shifted to very high harmonics, characteristic of synchrotron radiation [7, 8]. For a relativistic beam of the type discussed in this note the synchrotron radiation could be significantly enhanced by the collective nature of the beam plasma interactions.

Since the JET post disruption plasma has an electron temperature ~ 25–50 eV we also compare the electron-ion collision frequency with the growth rate at the fundamental of the bulk electrons. For a density $n_{oe} \sim 2 \times 10^{19}$ and the above bulk electron temperature we obtain $\nu_{ei} \sim 2 \times 10^6\,sec^{-1}$. Since the instability is well above threshold we estimate the growth rate $\gamma \sim 10^9\,sec^{-1}$ which is much greater than ν_{ei}.

3. Conclusion

We have considered the stability of a relativistic, gyrating, electron beam in a hot magnetized plasma. We have discussed only the special case of the ordinary mode propagating perpendicular to the magnetic field. For highly relativistic electrons $\gamma_e \gg 1$ the cyclotron emission in the ordinary mode becomes unstable and is shifted to very many high harmonics. This can be described as a collective synchrotron instability and could result in a much enhanced synchrotron radiation, and be a possible mechanism for slowing down of such a beam. In contrast to the alternative mechanism described by Laurent and Rax [2], we have

included the effect of the background plasma on the synchrotron instability. We reiterate that we have only discussed the special case of the ordinary mode for perpendicular propagation. It is evident that the extraordinary mode would also be expected to be unstable as would waves propagating obliquely [3]. Clearly, much more analysis remains to be done in order to clarify the relevance of such instabilities to situations such as the JET post disruption discharges [1].

Acknowledgements

This work was funded jointly by the U.K. Department of Trade and Industry and Euratom. We would like to thank Chippy Thyagaraja for helpful discussions.

References

1. Gill, R. D., Nuclear Fusion **33**, 1613 (1993).
2. Laurent, L. and Rax, J. M., Europhysics Letters **11**, 219 (1990).
3. Zayed K. E. and Kitsenko, A. B., Plasma Phys. **10**, 147 (1968).
4. Cairns, R. A. and Lashmore-Davies, C. N., Phys. Fluids **25**, 1605 (1982).
5. Stix, T. H., "Waves in Plasmas" (American Institute of Physics, New York 1992), Chap. 10.
6. Watson, G. N., "Theory of Bessel Functions", 2nd Edition (Cambridge University Press 1958), Chap. 8, Sec. 8.2, p. 231.
7. Feynman, R. P., "Lecture Notes in Physics" (Addison-Wesley Inc., Reading, Massachusetts 1966), Vol. 1, Chap. 34.
8. Bekefi, G., "Radiation Processes in Plasmas" (John Wiley Inc., New York 1966), p. 191.

Physica Scripta. Vol. T52, 142–151, 1994

Dominant Acceleration Processes of Energetic Protons at the Earth's Bow Shock

G. C. Anagnostopoulos

Department of Electrical Engineering, Demokritos University of Thrace, 67100 Xanthi, Greece

Received November 22, 1993; accepted January 28, 1994

Abstract

We examined magnetic field and energetic ($E \geqslant 30$ keV) proton and ($E \geqslant 220$ keV) electron observations obtained by the spacecraft IMP-6, 7, and 8 in the vicinity of both the (quasi-) parallel and (quasi-) perpendicular bow shock of the Earth. The observations analysed show that: (a) for a quasi-perpendicular ($45 \leqslant \theta_{Bn} < 90°$) region of the bow shock, the downstream proton fluxes are higher (lower) than the upstream fluxes, at low (high) energies, (b) for an oblique ($30 \lesssim \theta_{Bn} < 70°$) bow shock there exists a strong positive correlation of the ($\lesssim 30$ keV) beam events published by Paschmann *et al.* [15] with the ambient solar ~50 keV proton flux, and similar positive correlation with the value of the induced electric field $\boldsymbol{E} = -\boldsymbol{U}_{SW} \times \boldsymbol{B}$ (c) for parallel or quasi-parallel shocks and strong upstream magnetic wave activity, the presence of upstream >50 keV ion events is not a continuous phenomenon, but is strongly correlated with the substorm activity of the magnetosphere. The above observations along with other previously published observations are discussed in the context of the Shock Drift Acceleration (SDA) and the Diffusive (1st order Fermi) acceleration theories. We infer that: (a) a seed population of superthermal (energetic) protons are accelerated to higher energies at the oblique (quasi-perpendicular) bow shock via the SDA process, and (b) there is no convincing evidence for acceleration of either the solar wind or ambient energetic ions to energies $\gtrsim$30–50 keV via the Fermi acceleration process.

1. Introduction

The particle acceleration at MHD shocks is a principal process for accelerating particles to higher energies in the universe. Particles are accelerated within our solar system at interplanetary blast and corotating waves, and at planetary bow shocks [1, 2]; various sites of particle acceleration within the heliosphere are presented in Fig. 1. Given that there has been a series of spacecraft, which have crossed the earth's bow shock and supplied us with an enormous amount of field and particle data, it is implied that the earth's bow shock is an excellent chance for researchers to test the operation of various particle acceleration models at MHD shocks in general.

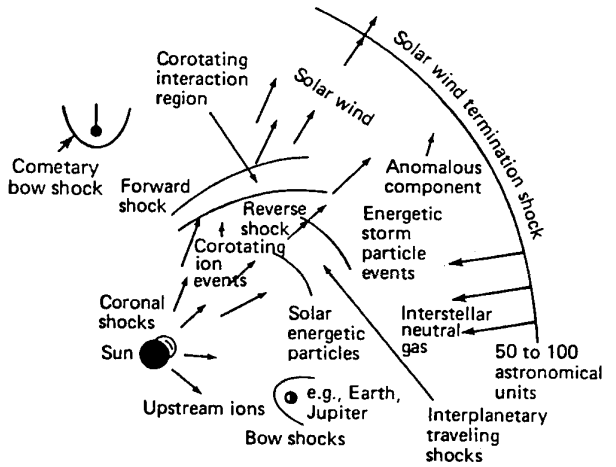

Fig. 1. A schematic view of shock acceleration processes in the Heliosphere (adapted from [2]).

In this work we will concentrate our attention on the acceleration of ions to high ($E \geqslant 30$ keV) energies. This subject has been a controversial one in the scientific community for many years. The capability of the quasi-parallel (dawn) bow shock to accelerate ions to high energies ($E \geqslant$ 30–50 keV) is still under investigation; however, it is widely accepted that the quasi-perpendicular bow shock accelerates ions to very high energies. Two main models have been proposed for explaining the particle and field observations obtained in the vicinity of the bow shock, the Shock Drift Acceleration (SDA) and the diffusive or 1st order Fermi acceleration. In the following Section (2) we will refer to these acceleration models. In Section 3 we will report the characteristics of energetic ions populating the region near the earth's bow shock. Then, in Section 4, we will present some new observations obtained in the same area. Finally, in section 5, we will discuss the ion characteristic in the context of SDA and Fermi models.

2. Theoretical models

2.1. *Shock drift acceleration*

According to the Shock Drift Acceleration model [3] charged particles are accelerated at an MHD shock wave by $\nabla \boldsymbol{B}$ drifting in the presence of the induced electric field $\boldsymbol{E} = -\boldsymbol{U} \times \boldsymbol{B}$, $\boldsymbol{U}$ and $\boldsymbol{B}$ being the plasma velocity and $\boldsymbol{B}$ the magnetic field magnitude, respectively. Computations for particles accelerated at a collisionless shock, either reflected or transmitted (Fig. 2) can easily be made in a frame of reference, the Hoffman-Teller frame, where the induced electric field $\boldsymbol{E}$ is null, i.e. in a frame in which the plasma streams along the magnetic field line. If θ_{Bn} is the angle between the magnetic field direction and the normal bow shock $\hat{\boldsymbol{n}}$ and β is the angle between the plasma velocity $\boldsymbol{U}$ and the normal $\boldsymbol{n}$, the transformation velocity is given by

$$V \equiv U \cos \beta \sec \theta_{Bn}.$$

Computations can easily be carried out if the magnetic moment

$$\mu = mv^2 \sin^2 \alpha / 2B$$

(v and α are the velocity and the pitch angle of a particle) is conserved [4–9]. The SDA is a rapid acceleration process, which predicts efficient acceleration of ions and electrons at

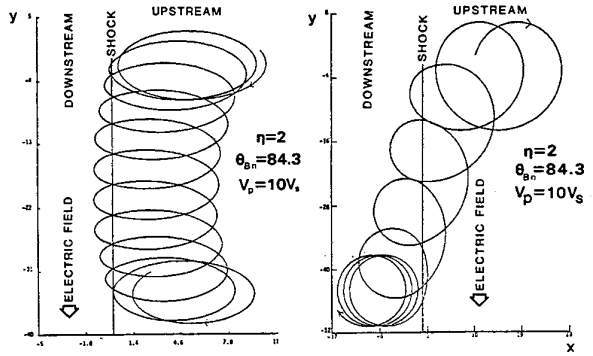

Fig. 2. The x-y plane projection of the motion of a charged particle (a) accelerated and reflected upstream and (b) accelerated and transmitted downstream from a quasi-perpendicular shock of strength $n = 2$. Units of length are V_{shock}/cyclotron frequency (adapted from [3]).

both large angle interplanetary and bow shocks in a few tens of seconds. Figure 3 shows the probability computed for reflection (R), transmission (T) or non-interaction (N) of a particle with the shock. The probability varies with changing the ratio

$$\varepsilon = V/v = U \cos \beta \sec \theta_{Bn}/v$$

At large angle θ_{Bn} or small value of the particle speed v (low energy particle) only transmission is possible. For decreasing (increasing) values of θ_{Bn} the probability of reflection transmission increases (decreases). For $\varepsilon < 1$, both the probability of particle reflection and transmission decrease, and the probability for non-interaction increases [6]. More special predictions of the SDA model will be reported in Section 5 in comparison with bow shock observations. However, we note here, that under solar conditions, which imply in a large value of the induced electric field $\boldsymbol{E} = -\boldsymbol{U}_{SW} \times \boldsymbol{B}$ and a small ratio of the particle gyroradius R_G to the radius of curvature R_C of the bow shock, ions can be accelerated more efficiently at a quasi-perpendicular region of the bow shock, since under such conditions a particle can gain a large amount of energy without leaving the large

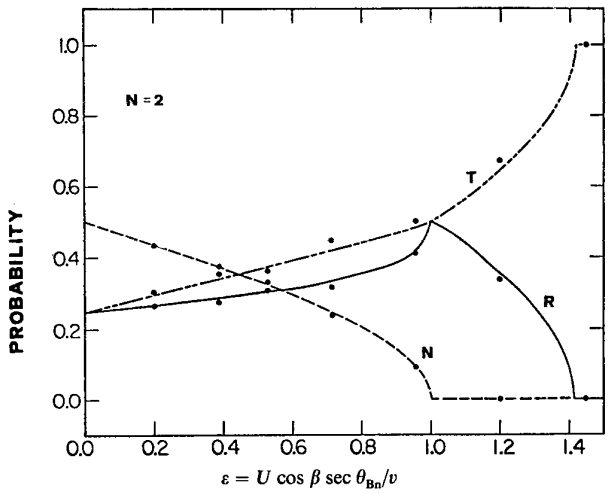

Fig. 3. Reflection (R), Transmission (T) and Non-interaction (N) coefficients *vs.* the ratio $\varepsilon = U \cos \beta \sec \theta_{Bn}/v$ for a quasi-perpendicular shock. N is the ratio of the downstream to the upstream magnetic field magnitude (adapted from [6]).

angle θ_{Bn} region of the shock [10–12]. Significant contribution in understanding the bow shock ion acceleration in terms of the SDA theory has been made by Sonnerup [14], Paschmann *et al.* [15], Burgess [16] and Giacalone [17].

2.2. *Diffusive shock acceleration*

The Diffusive Shock Acceleration or 1st order Fermi acceleration process [18–22] has been applied from a series of researchers to the earth's bow shock [7, 23–29]. According to these models superthermal ions of some keV are accelerated to higher ($\lesssim$150 keV) energies by multiple reflections between converging scattering centres upstream and downstream from the bow shock [24] or waves upstream from the bow shock and the bow shock itself [7]. Fermi acceleration studies have been based on either analytical solutions [26] or Monte Carlo simulations [28] of a convective diffusive transport equation. Particular predictions of these models in comparison with bow shock associated particle observations are reported and discussed in Section 5.

3. Previously published observations

3.1. *Quasi-perpendicular bow shock*

Upstream ions of energies of some keV are almost permanently present at magnetic field lines, which are connected with large angle θ_{Bn} of the earth's bow shock ($30° \leqslant \theta_{Bn} \leqslant 70°$). These ions stream along the interplanetary Magnetic Field (IMF) from the direction of the bow shock [15, 30–32]. However acceleration effects of a quasi-perpendicular bow shock region to energetic ion fluxes have been reported up to energies of $\sim$4 MeV both upstream and downstream from the earth's bow shock in the presence of an ambient energetic particle population of solar origin, i.e. energetic particle population arrived at the position of the earth's magnetosphere after the occurrence of a solar flare [11, 12]. Acceleration effects to the high energy ($E \geqslant 50$ keV) proton fluxes are observed under specific solar wind conditions, which imply in a small ratio R_G/R_C of the proton gyroradius R_G to the local radius of curvature of the bow shock R_C, and large values of the induced electric field $\boldsymbol{E} = -\boldsymbol{U}_{SW} \times \boldsymbol{B}_{IMF}$. Acceleration effects to high energy ions have been observed, in particular, under conditions with large values of the solar wind velocity $\boldsymbol{U}_{SW}$ and of the IMF magnitude B [10].

If the IMF forms a nearly perpendicular structure at a region of the bow shock ($\theta_{Bn} \simeq 90°$), all of the energetic ions are transmitted downstream from the shock, in the magnetosheath. If the IMF forms a quasi-perpendicular ($45° \leqslant \theta_{Bn} < 90°$) bow shock, energetic ($E \geqslant 50$ keV) ions, after their acceleration at the shock front, are either reflected upstream from the bow shock or are transmitted downstream. The reflected ions travel along the direction of the IMF forming angular distributions with strong field aligned anisotropies. The ions, which are transmitted downstream from the bow shock, present double peaked anisotropies at large angles (nearly perpendicular) with the direction of the magnetic field. In some cases the double peaked anisotropy of the ion angular distributions within the magnetosheath are observable at only the higher energy (i.e. $\geqslant$300 keV) ions, because of the Compton-Getting effect, which strongly

affects the angular distributions of the low energy particles [12].

If an ambient solar particle population with an energy spectrum of a power law shape ($dj/dE = K \cdot E^{-\gamma}$) exists, the ions which are accelerated and transmitted downstream from the bow shock present an energy spectrum at low energies, which is parallel to the energy spectrum of the solar background population. Reflected ions of high intensities are observed at intermediate energies, while their spectrum converges to the solar background one at both the low and the high energies.

3.2. *Quasi-parallel bow shock*

The ion behavior in the vicinity of the quasi-parallel side of the bow shock has been the subject of a more intense investigation over the last two decades. Since the IMF forms an $\sim 45°$ angle with the Sun-Earth line at the position of the Earth, it more often forms a parallel shock structure at the dawn side of the bow shock (Fig. 4). Of course, upstream ion events are observed if a detecting spacecraft is magnetically connected with the bow shock. However this is necessary, but not a sufficient condition for detecting $\geqslant 50$ keV ions upstream from the quasi-parallel bow shock [10, 33–36]. From Fig. 4 it is evident that a spacecraft through its trajectory is connected magnetically for a longer period with the quasi-parallel (dawn) bow shock than with the quasi-perpendicular (dusk) side of this shock.

Upstream from the quasi-parallel bow shock the energetic ($E \geqslant 30$ keV) ion fluxes often display broad angular distributions in the presence of large amplitude low frequency plasma and magnetic field waves [37]. However, at the onset phase of an upstream particle event, before the generation of the magnetic wave activity, the energetic ions stream along the IMF direction and present strong field aligned anisotropies in the detecting angular distributions [38].

The energy spectrum of the energetic ions observed upstream from a quasi-parallel region of the bow shock can be well described by a power law shape from ~ 50 keV up to energies as high as ~ 2 MeV [36, 39–41]. At low energies ($E \leqslant 20$–100 keV), both power law [42] and exponential [43, 44] spectra have been reported. In a recent statistics we have shown that the upstream events with significant proton fluxes at intermediate energies (~ 50 keV) have proton spectra, which extend to energies > 300 keV [13].

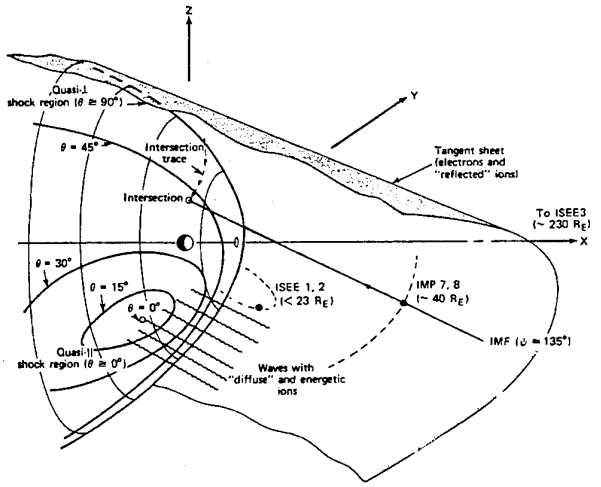

Fig. 4. Schematic indicating the earth's bow shock along with an IMF in the average direction ($\psi = 135°$) and trajectories of the spacecraft ISEE 1, 2 and IMP-7, 8. Contours of constant θ_{Bn} are also sketched on the shock front (adopted from [54]).

With respect to the spatial distribution of ions, a hardening of the spectra toward the dusk magnetopause/bow shock at energies $E \geqslant 30$–50 keV has been confirmed [42, 45, 46]. The ion fluxes decrease with increasing distance from the bow shock in the sunward direction, with an e-folding distance $L \simeq 7R_E (j \propto e^{-x/L})$ according to Ipavich *et al.* [43], but increase downstream, toward the earth magnetopause [47, 48]. Furthermore, a large scale ion intensity gradient from the upstream region toward the earth's magnetotail (plasma sheet) has been confirmed with multi-spacecraft observations [36, 45, 49].

The upstream ion events present either forward (FVD) or inverse (IVD) or not at all (NVD) velocity dispersion [49, 50–52]. Anagnostopoulos [13] recently found a statistical distribution of $\sim 60\%$, $\sim 22\%$ and $\sim 18\%$ for NVD, FVD and IVD, respectively.

The upstream and magnetosheath proton fluxes display a strong positive correlation with substorm activity. This is confirmed by both one case [45, 49, 51, 53] and statistical studies [42, 46, 48, 54]. Furthermore, the proton events are very often (~ 80–90%) accompanied in the upstream region by the presence of energetic ($E \geqslant 220$ keV) electrons, which is a signature of particles of magnetospheric origin [13, 33, 34].

3.3. *Quasi-perpendicular/Quasi-parallel bow-shock: Comparison of simultaneous multispacecraft observations*

Here we report the results from a comparative study of the quasi-perpendicular (dusk) and the quasi-parallel (dawn) side of the earth's bow shock, based on simultaneous measurements obtained by two spacecraft (IMP-7 and IMP-8) with similar energetic particle sensor systems [33]. This study demonstrated that under the same solar wind conditions, the quasi-perpendicular side of the bow shock did produce acceleration effects in the intensities of energetic ($0.050 \leqslant E \leqslant 4.000$ MeV/n) ions, whereas the quasi-parallel side did not [11]. The observations obtained during that time period (intensity-time profiles, energy spectra and angular distributions) in the vicinity of the quasi-perpendicular bow shock, were found in agreement with the predictions of the SDA theory.

4. New observations

4.1. *Quasi-perpendicular bow shock*

In Fig. 5 we present magnetic field (a) and proton (b) observations from the spacecraft IMP-6. The inset in Fig. 5(b) displays the average position of the bow shock and the directions of the IMF $\boldsymbol{B}$ at the times marked a, b and c when IMP-6 crossed the bow shock [normal dashed lines in Fig. 5(b)]. It is evident that in the case of the first bow shock crossing, the IMF formed an oblique bow shock at the position of IMP-6, with significant magnetic field wave activity. Non-observable proton acceleration was detected at energies > 29.3 keV. In the second and third crossings (b and c) the IMF formed an angle θ_{Bn} closer to 90°. Remarkable intensity enhancements were observed by IMP-6 in the three energy ranges (29.3–53.4 keV, 53.4–91.0 keV and 91.0–

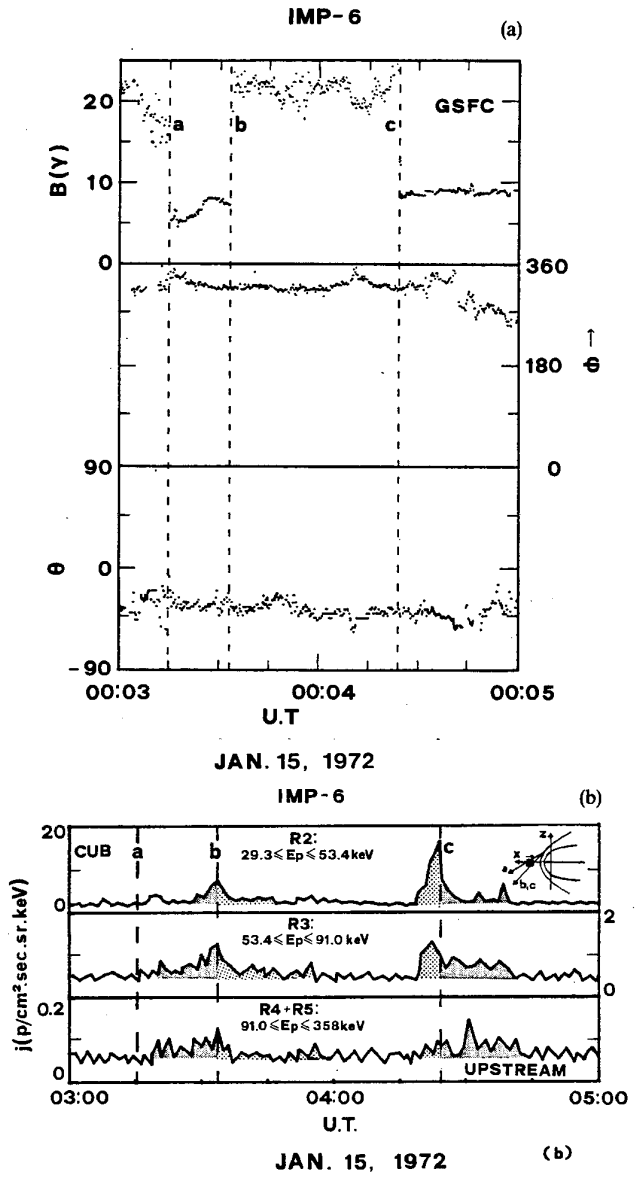

Fig. 5. Magnetic field (a) and energetic proton (b) observations during a time period when the spacecraft IMP-6 crossed the earth's bow shock three times (normal dashed lines marked a, b, c).

358 keV) shown in this figure, with a peak-to-background intensity ratio, which becomes smaller with increasing energy. Furthermore, it is evident that the proton flux peaks downstream from the bow shock at the low energies (29.3–91.0 keV), but it peaks upstream from the bow shock at higher energies ($E \geqslant 91.0$ keV). Such a particle acceleration configuration has been known so far only for interplanetary quasi-perpendicular MHD shocks [56, 57]; it is the first time for which such an ion behaviour is found at the earth's bow shock. We also note that the IMP-6 spacecraft when moved upstream from the quasi-perpendicular bow shock observed first significant high energy proton flux enhancements and at later times the low energy ones (before the bow shock crossing b). Correspondingly, after it left the magnetosheath and entered the interplanetary space (c), it stopped observing the low energy protons first and the high energy ones at later times. During the IMP-6 crossings b and c of the bow shock, the values of both the IMF magnitude and the solar wind speed were somewhat higher than the average ones, i.e. $B_b \simeq 7.5$ nT, $B_c \simeq 9$ nT, and $U_{SW} \simeq 550$ km/sec (instead of $B = 5$ nT, $U_{SW} = 350$ km/sec usually observed).

Figure 6 present energetic ion and solar wind speed observations from the spacecraft IMP-8 for a long time period when this spacecraft crossed the quasi-perpendicular dusk bow shock [10]. In this time period, with exceptional high values of the IMF magnitude ($B = 13$–21.5 nT, see Fig. 6) and solar wind speed ($U_{SW} \geqslant 700$ km/sec), acceleration effects in the proton fluxes were observed up to energies as high as ~4 MeV. Furthermore, acceleration effects were observed to energetic (0.64–1.17 MeV/n) a-particles and energetic (0.77–3.2 MeV/n) nuclei with $Z \geqslant 3$. Forward velocity dispersion was also observed upstream from the bow shock, during the time period examined in Fig. 6 ($\lesssim 10$ UT). The two insets in Fig. 6 display the energy spectra of the proton intensities for two time periods, when IMP-8 was found upstream (~12 : 13 UT) and downstream (~11 : 34 UT) from the bow shock respectively; along with the energy spectrum of the ambient proton population (~12 : 06 UT). These energy spectra correspond to protons reflected upstream (R) and transmitted downstream (T) from the bow

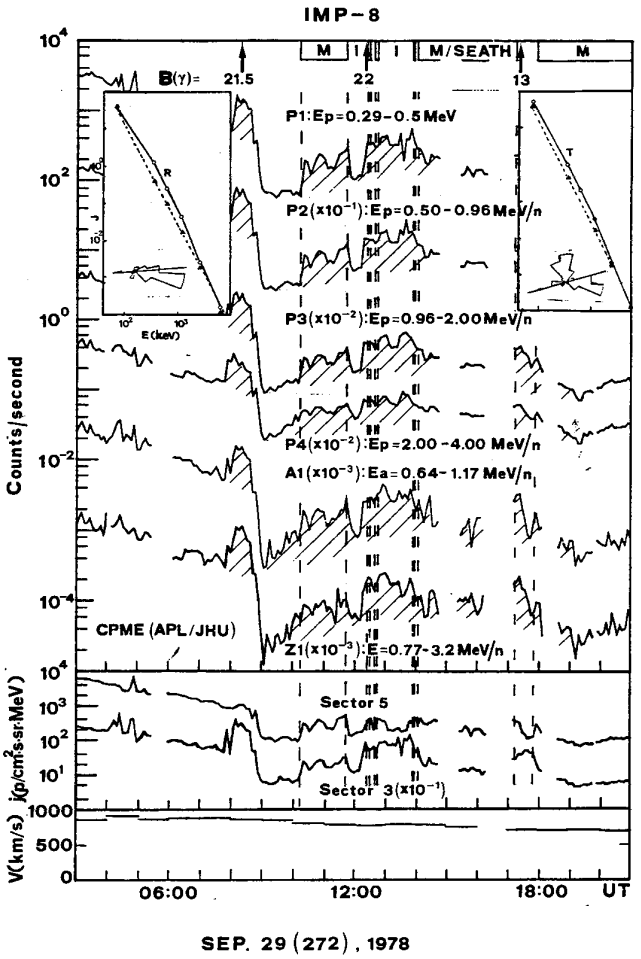

Fig. 6. Energetic observations (two upper panels) and solar wind speed (bottom panel) for a time period when the IMP-8 spacecraft crossed the quasi-perpendicular dusk bow shock several times (normal dashed lines). Intensity enhancements in the sectors 3 and 5 correspond to particles reflected and transmitted, respectively. The two insets in the figure display representative energy spectra for reflected (R) and transmitted (T) particles. Shown are also representative angular distributions.

shock respectively. Angular distributions with field aligned anisotropy for the reflected population and double peaked anisotropy perpendicular to the magnetic field for the transmitted population respectively, are also shown in the insets of Fig. 6.

In the following, we provide some additional observations for 18 beam events of low energies at times when ISEE-1 and 2 were found upstream from a large angle θ_{Bn} ($35° \leqslant \theta_{Bn} \leqslant 80°$–$90°$) region of the bow shock. These beam events were first published and discussed by Paschmann *et al.* [15] and Scholer *et al.* [55]. Table I presents values of some parameters for the times at which the 18 beam events were observed. Figure 7 presents: (a) energetic ion ($E \geqslant 50$ keV/n) and (b) electron ($E \geqslant 220$ keV) observations for the days 182–187, 1978. It is evident that the solar flare of ~09 : 30 UT, on July 2 (183), 1978 emitted energetic particles of high intensity, which were observed at the position of the earth in the following days. During the day July 3 (184), beams of proton and a-particle were observed by ISEE-1 to travel outward from the bow shock along the direction of the IMF (the arrow in Fig. 7(a) indicates the time of beam detection). The observations of Fig. 7 suggest that the acceleration process, which produced the ion beams of energies as high as $E > 60$ keV/q upstream from the large angle θ_{Bn} bow shock, could use a reservoir of ambient energetic ions in order to accelerate these ions to somewhat higher energies. In a further examination of the upstream beam events published by Paschmann *et al.* [15], we also found that the majority of these events were observed under similar solar wind conditions. For instance, most of the 18 beam events discussed by [15] were observed after the occurrence of intense solar flares which produced an energetic particle reservoir in the vicinity of the earth's magnetosphere. In three cases Sudden Storm Commencement effects and/or interplanetary MHD shock waves were observed near the earth.

In Fig. 8 we display the speed of the field aligned protons for the 18 events referred to above *vs.* (a) the angle θ_{Bn} between the IMF direction detected by ISEE-1 and the

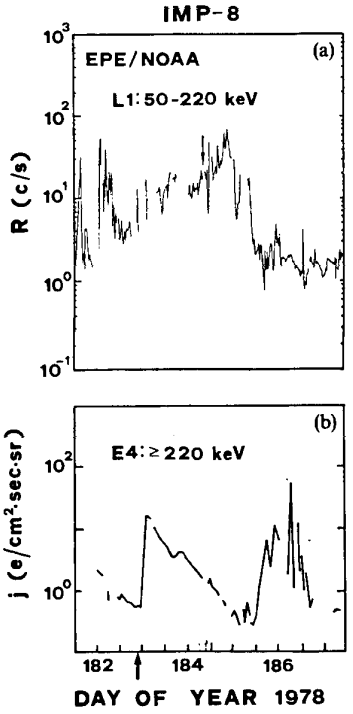

Fig. 7. Energetic (50–220 keV) proton and ($E \geqslant 220$ keV) electron fluxes observed by the spacecraft IMP-8. It is evident that a solar particle event followed the occurrence of a solar flare (N, W 90°) at ~10 : 00 UT, July 2 (183), 1978. The arrow in the upper panel indicates a time period when ion beam events were observed by the ISEE-1 spacecraft in the energy range $10 \lesssim E \lesssim 60$ keV/9 [15, 55].

normal $\hat{\boldsymbol{n}}$ at the bow shock; (b) the ambient solar flux (p/cm² · sec · sr · keV) of ~50 keV proton, as measured by another spacecraft (IMP-8) upstream from the bow shock at the same times; and (c) the magnitude of the interplanetary electric field $|\boldsymbol{E}| = |-\boldsymbol{U}_{SW} \times \boldsymbol{B}| = U_{SW} B \sin\psi$, where $\psi = (\boldsymbol{U}, \boldsymbol{B})$ at the position of ISEE-1. For the values of the angles θ_{Bn} and $\psi_{\boldsymbol{U},\boldsymbol{B}}$ we used the ones computed by [15]. The ~50 keV ambient proton flux of solar origin is used here as an index of the possible presence of less energetic ions, i.e. presence of superthermal (~10 keV) proton population of the same (solar) origin.

Figure 8(a) confirms the dependence of the reflected population in the upstream region on the angle θ_{Bn}. In this case we estimate the Spearman correlation coefficient to be $r_s = 0.4992$, which shows a strong positive correlation between the speed of the reflected beam U_B and θ_{Bn}. However, Figs 8(b) indicates a more impressive characteristic: a very strong positive correlation between U_B and the ambient 50 keV proton flux, with $r_s = 0.8027$ and a critical level $p < 0.0009$. Figure 8(c) also indicates a strong positive relation between reflected speed U_B and the value of the induced electric field E, with $r_s = 0.5906$ ($p < 0.0149$). The very strong correlation of the velocity of the reflected protons with the ambient energetic (superthermal) proton flux is an impressive new observational result, which strongly suggest that the reflected population originates from acceleration of superthermal (not only) solar wind protons.

Table I. *Upstream beam events* [15]

No	Date	Time	Ambient 50 keV proton flux (p/cm² · sec · sr · keV)	θ_{Bn}	E (mV/m)	V_B (km/s)
1	Nov. 8	19 : 23	0.893	36	0.89	420
2	Dec. 7	17 : 10	1.218	48	1.69	740
3	Dec. 18	12 : 05	0.828	49	0.35	435
4	Dec. 25	20 : 04	1.144	36	1.03	380
5	July 3	15 : 35	6.54	71	0.83	1700
6	July 3	23 : 27	22.236	47	5.8	1350
7	July 6	18 : 48	1.394	56	2.41	1050
8	July 6	18 : 57	2.055	51	3.19	1070
9	July 17	23 : 42	6.3	55	2.26	875
10	July 17	23 : 47	6.7 ·	55	2.26	720
11	Aug. 1	01 : 16	0.675	50	0.93	510
12	Aug. 14	10 : 27	4.316	47	1.43	900
13	Aug. 17	17 : 57	1.198	63	2.89	840
14	Aug. 24	19 : 43	1.351	48	1.02	570
15	Aug. 24	19 : 56	1.351	55	0.97	500
16	Aug. 27	03 : 50	264.956	64	3.42	1900
17	Sept. 2	13 : 46	3.018	42	0.86	750
18	Sept. 10	19 : 57	3.058	35	2.06	800

4.2. *Quasi-parallel bow shock*

Figure 9 displays energetic ion and electron observations for a long time period (06–24 UT, Nov. 22, 1977), when a solar particle event was observed by IMP-8 in the vicinity of the

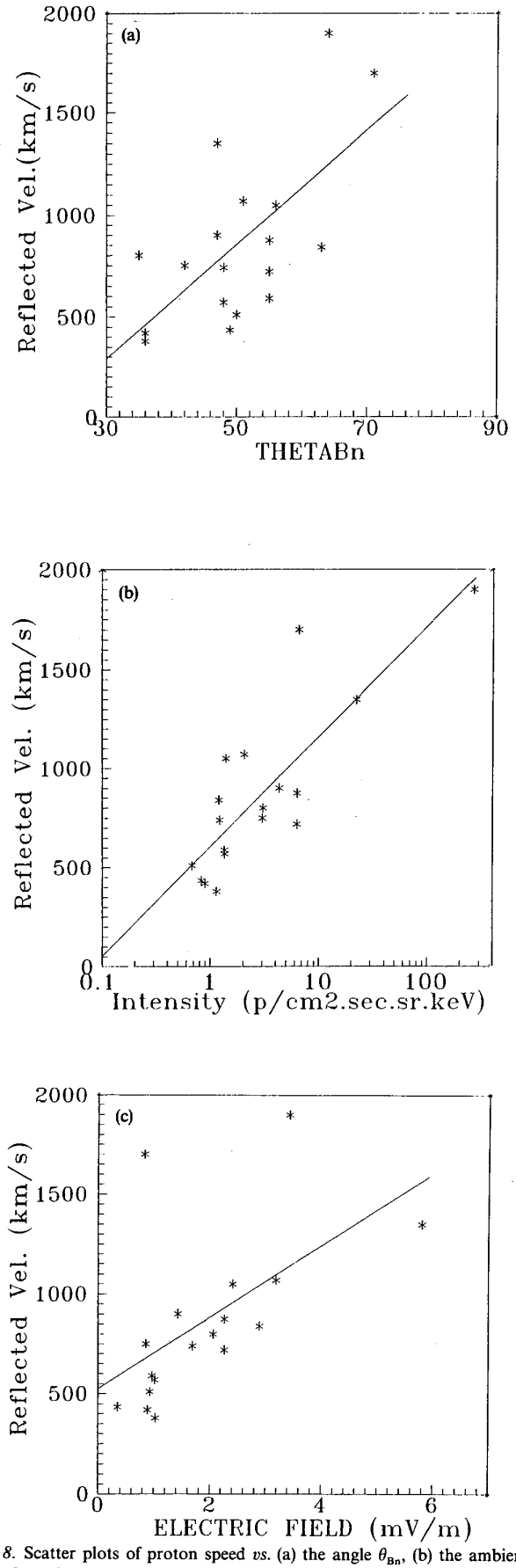

Fig. 8. Scatter plots of proton speed *vs.* (a) the angle θ_{Bn}, (b) the ambient solar flux of 50 keV protons at IMP-8, and (c) the magnitude of the interplanetary electric field $\boldsymbol{E} = |-\boldsymbol{U}_{sw} \times \boldsymbol{B}|$, for 18 ion beam events observed by ISEE-1 [15].

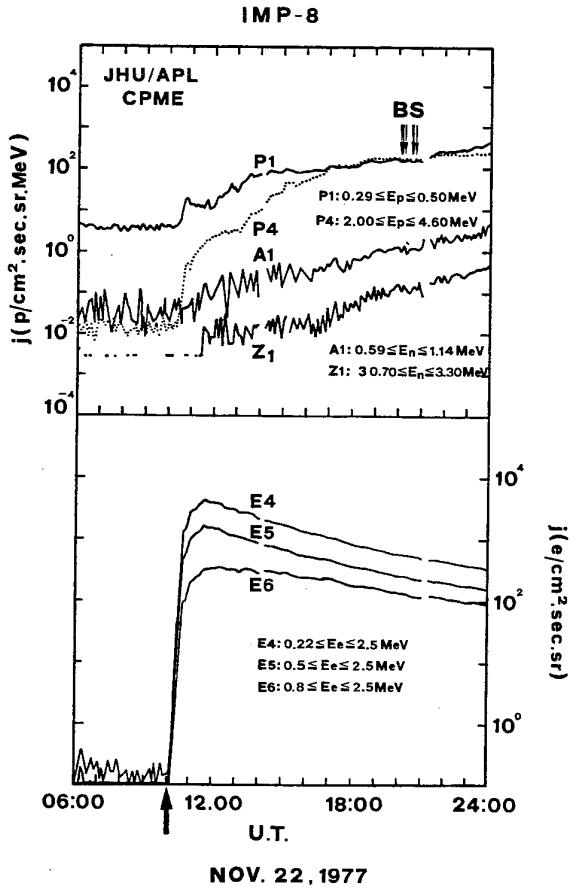

Fig. 9. Energetic ion and electron observations obtained by the spacecraft IMP-8 near the dawn bow shock. The ambient solar particle flux increased after the occurrence of a solar flare (2B, W40). The arrows in the upper right side of the figure indicates times when IMP-8 crossed the dawn bow shock (in the presence of high ion background intensities).

dawn flanks of the earth's bow shock. The arrows on the upper right part of this figure indicate times when IMP-8 crossed the surface of the dawn bow shock. Figure 10 presents energetic (E = 50–220 keV) proton and magnetic field observations with a better time resolution, during a time period when IMP-8 crossed the bow shock seven times successively under a variety of IMF-bow shock configurations. Notice that rich wave activity was present in the cases of the crossings c and e, when the IMF direction formed a nearly parallel bow shock at those times. It is evident that non-observable acceleration effects at energies >50 keV were detected by the IMP-8 spacecraft for all the shock structures shown in Fig. 10, i.e. from nearly parallel to nearly perpendicular (see inset in Fig. 10), under common solar wind conditions $B \lesssim 5$ nT, $U_{sw} = 315$ km/sec observed for that time period.

From the examination of field and particle observations obtained by IMP-8 over the time period of ten years (1974–1984), we found that the absence of $\geqslant 50$ keV protons events upstream from the quasi-parallel bow shock is a common phenomenon under conditions with: (a) no significant substorm activity in the magnetosphere, (b) presence of high solar background flux, which hides the presence of magnetospheric ion events of lower intensities [35]. In the following we will discuss such a representative time period, when IMP-8 was found in the vicinity of the (quasi-) parallel bow shock. In the upper panel of Fig. 11 shown are 50–220 keV

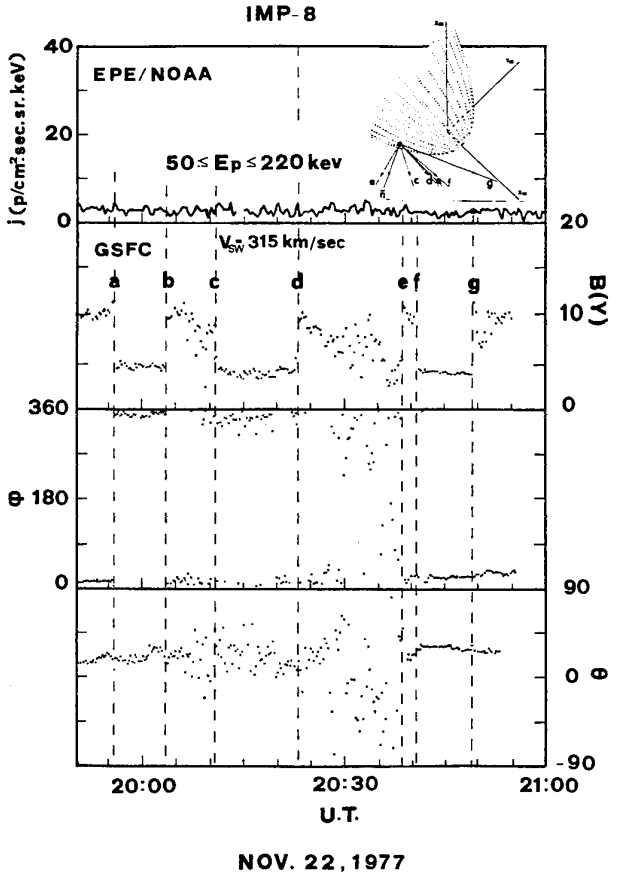

Fig. 10. Energetic (50–220 keV) proton observations of high time resolution for a time period included in Fig. 9. The inset indicates the various IMF-bow shock configurations for this time period. Non-acceleration effects are observable in the ≥ 50 keV proton intensities, all the kinds of the bow shock structure from nearly parallel to nearly perpendicular) for under conditions with small values of the solar wind speed $U_{SW}(=315$ km/sec) and of the IMF B ($\lesssim 5\gamma$).

proton observations from the EPE/NOAA experiment on board the IMP-8 spacecraft, for the day April 18, 1975, and in the second panel the auroral electrojet indices AO, AE, AL, and AU, which indicate the level of substorm activity within the magnetosphere. In the inset of Fig. 11 we display the position of IMP-8 at the time of a bow shock crossing (10 : 30 UT, Apr. 18, 1975) and the position of the earth's bow shock in a plane containing the axis X_{SE} and the spacecraft IMP-8. From Figs 11(a) and 11(b) it is evident that proton flux enhancements were present only after the onset of the substorm activity, i.e. after ~11 : 50 UT, with angular distributions forming a broad shape in the presence of significant magnetic field wave activity [Fig. 11(c)]. We have also found by examining observations (not shown here) obtained by the CPME/APL instrument on board the same spacecraft IMP-8, that ≥ 300 keV protons and ≥ 220 keV electrons were also present over the time period ~12 : 15–14 : 00 UT. Given that protons with an energy spectrum extending up to energies higher than 300 keV and accompanied by the presence of energetic ($E \geq 220$ keV) electrons are a signature of presence of magnetospheric particles [33, 34], we can infer that magnetospheric particles were present at the position of the spacecraft IMP-8 after the onset of the magnetospheric substorm. Figure 11(c) presents magnetic field observations with fine time resolution for both: (a) a

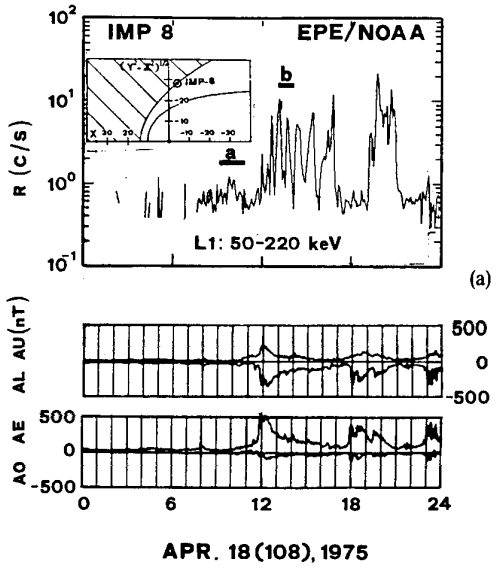

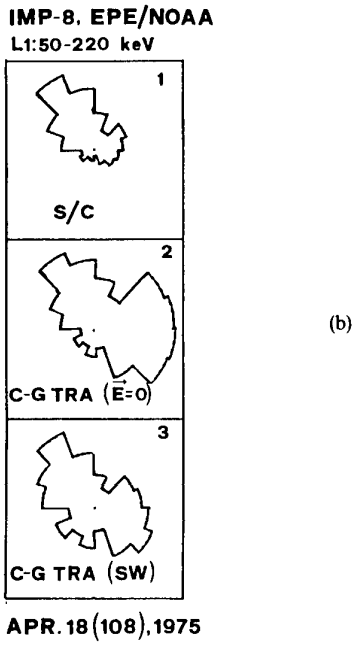

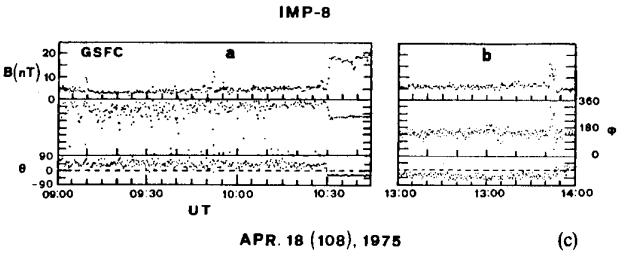

Fig. 11. (a) Fluxes of 50–220 keV protons measured by the IMP-8 spacecraft upstream from the parallel (dawn) side of the bow shock (see inset in the upper left side), along with indices of magnetospheric substorm activity. It is evident that the presence of upstream proton events are closely correlated with enhanced substorm activity. (b) Broad angular distributions of 50–220 keV intensities as observed by IMP-8 in the frame of the spacecraft (1) in the frame of solar wind (2) and in a frame with null electric field ($\boldsymbol{E} = -\boldsymbol{U}_{SW} \times \boldsymbol{B}$). (c) Fine time magnetic field measurements for two time periods with strong (a) and moderate wave activity (b), respectively. Non-acceleration effects in the 50–220 keV proton fluxes were observed during the first period a [see Fig. 11(a)].

time period (09 : 00–10 : 45 UT) before the beginning of the substorm activity [solid bar marked a in Fig. 11(a)], and (b) for a time period (13 : 00–14 : 00 UT) with a turbulent magnetosphere [solid bar marked b in Fig. 11(a)]. We see that at ~10 : 30 UT an IMF discontinuity turned the field direction southward and (most probably) causes an outward motion of the bow shock and a crossing by IMP-8. We note that a southward IMF direction is a preferential one for enhanced substorm activity and ion leakage through the magnetospause [46]. Within the above two periods (a and b) the IMF formed a nearly parallel bow shock ($\theta_{Bn} \simeq 0°$), with strong wave activity in the first case (a) and a moderate wave activity in the second one (b). If an acceleration process depending on the angle θ_{Bn} and the wave activity was in progress, and such an acceleration mechanism contributed in the flux enhancement observed after ~12 UT, we infer that a higher flux enhancement would have been observed during the time period b, in the presence of a similar parallel bow shock and of a stronger wave activity. On the contrary we see that no significant proton activity was present in the first time period a, although the wave activity was more intense than that in the case b, but under conditions of a quiet magnetosphere. Also note that between 09 : 00–10 : 45 UT the IMP-8 spacecraft was found just upstream from the bow shock, where the ion flux expected by Fermi acceleration models are highest [26, 43].

5. Summary of observations and discussion

5.1. *Shock drift acceleration of energetic ions*

We have shown that at quasi-perpendicular ($45° \leqslant \theta_{Bn} < 90°$) regions of the earth's bow shock energetic ($E \geqslant 30$ keV) protons are accelerated and are either reflected upstream or are transmitted downstream from the bow shock. The reflected ions stream along the IMF, whereas the ions transmitted downstream from the bow shock present angular distributions with a double peaked anisotropy at large angles with the bow shock. Furthermore, the reflected ions present forward velocity dispersion when a detecting spacecraft enters the foreshock region from a region which is not connected magnetically with the bow shock.

In this study we have revealed a new characteristic of the upstream ion enhancements observed at quasi-perpendicular regions of the bow shock; the ratio of the upstream proton flux to the flux of the downstream protons increase with increasing energy. This finding is predicted from the SDA theory (Fig. 3), and it has already been confirmed in the case of interplanetary shock waves. The angular distributions and energy spectra observed near the quasi-perpendicular bow shock are also in agreement with the predictions of the SDA theory [3, 6, 9, 58–60]. In Table II we summarize the most characteristic predictions of the SDA theory, which are all found to be confirmed in the case of the bow shock.

Non-acceleration effects at the bow shock, at energies $\geqslant 30$ keV, we found in the following cases for: (a) a quasi-parallel bow shock ($0 \lesssim \theta_{Bn} \lesssim 45°$), even though a rich wave activity existed. (b) a quasi-perpendicular bow shock, but in the presence of small or common values of the solar wind speed U_{SW} and of magnetic field magnitude B, and (c) a quasi-perpendicular bow shock in the absence of an ambient energetic particle population.

Table II. *Shock drift acceleration at the earth's bow shock*

Predictions	Observations
1. Intense acceleration effects under conditions of:	
(a) (Quasi-) perpendicular ($45° \leqslant \theta_{Bn} \leqslant 90°$) shock structure,	Consistent
(b) Large ratio R_G/R_c of the proton gyroradius to the local radius of curvature of the bow shock,	Consistent
(c) Large value of the induced electric field $\lvert E \rvert = \lvert -U \times B \rvert$,	Consistent
(d) Existence of a seed particle popularion	Consistent
2. (a) $\theta_{Bn} \simeq 90°$: T[a]	Consistent
(b) $\theta_{Bn} < 90°$: R[b] & T	Consistent
3. (a) Intense effects to T: at low energies	
(b) Intense effects to R: at high energies	Consistent
4. Energy spectra	Consistent
5. Final (maximum) energy of accelerated:	
(a) solar wind protons: # keV	Consistent
(b) ambient superthermal protons: tens of keV	Consistent
(c) ambient energetic protons: # MeV	Consistent
6. Velocity dispersion of R: Forward	Consistent
7. Angular distributions of	
(a) R: field aligned anisotropy	Consistent
(b) T: double peaked anisotropy perpendicular to the field direction	

[a] T: Transmitted population
[b] R: Reflected population

5.2. *Shock drift acceleration of superthermal ions*

We also found that the low-energy protons, which are observed upstream from the bow shock to travel along the IMF, the so-called reflected population [61], are strongly dependent on three different parameters: (a) the angle θ_{Bn} forming between the IMF direction and the normal to the bow shock front (b) the value of the induced interplanetary electric field $\lvert E \rvert = \lvert -U_{SW} \times B \rvert$ and (c) the presence of an ambient superthermal proton population of solar origin, as possibly suggested by the presence of a high energy ($E \geqslant 50$ keV) tail in the ambient proton spectrum. The occurrence of the reflected beam events in correlation with the coccurrence of a solar flare and the presence of an ambient population of solar origin at low energies confirms the predictions of a relevant numerical study [16], which predicted the SDA as a viable mechanism at oblique shocks for initial energies down to those normally classified as superthermal.

The dependence of the proton beam speed on the value of the induced electric field E is an impressive new result for the low energy ($E \leqslant 30$ keV) reflected population, which further confirms that this population originates from SDA at the bow shock. Large values of the induced electric field E and a small ratio R_G/R_C of the proton gyroradius to the local curvature of the bow shock have been confirmed so far to favour further energization of $E \geqslant 30$ keV protons at the quasi-perpendicular bow shock [10, 11, 17]. Anagnostopoulos and Sarris [10] suggested that under such conditions, an energetic ($E \geqslant 30$ keV) proton could gain a large amount of energy by drifting only a small distance on the shock front, and consequently, without changing the favourable for the SDA quasi-perpendicular structure of the bow shock. However even a proton of a small energy i.e. a proton of initial energy $E_i = 4$ keV, must drift a significant distance of $\sim 8R_E$ along the shock surface in order to accel-

erate to a factor of 7–12 [16]. For such a large removal the characteristic angle θ_{Bn} changes drastically and the acceleration efficiency may be reduced, except that an enhanced electric field and/or a shortening of the ratio R_G/R_C accelerates the proton to high energy, in a shorter distance, in a similar way which favours the acceleration of the energetic (i.e. $\geqslant 30$ keV) protons at the bow shock [10].

Scholer *et al.* [55] noted that at the end of the day July 3, 1978 the ISEE-1 spacecraft detected a beam of $\geqslant 60$ keV/q ions, at a time for which the simple reflection theory [14, 15] predicts reflection of protons with maximum energy of ~ 10 keV. Since, we have confirmed that an ambient proton population of solar origin existed on that day (Fig. 7) with a spectrum extending well above 50 keV, the presence of the ambient superthermal/energetic proton population can successfully explain the presence of high energy ($E \geqslant 60$ keV) protons reflected upstream from the bow shock, through SDA [16, 17].

5.3. *Diffusive acceleration*

The representative observations presented upstream and downstream from a parallel and turbulent bow shock region ($\theta_{Bn} \cong 0°$), further confirms that there exist major inconsistencies of the predictions of the diffusive (1st order Fermi) acceleration models with the observations. Table III displays the major predictions of this theory and the results from a comparison with the observations both presented in this as well as in other relevant studies. We note that, although some investigators claim that diffusive acceleration makes precise predictions for upstream ions [62], this is true only for some of the upstream/downstream characteristics. No consistency is found if predictions of 1st order Fermi acceleration models are compared with the whole body of observations from one spacecraft, i.e. energy spectra north-south and dawn-dusk anisotropies of angular distributions, velocity dispersions, intensity-time profiles, composition of particle events etc. and more if multispacecraft observations be taken into account [36, 49, 51–53].

Table III. *Diffusive (1st order Fermi) acceleration at the earth's bow shock*

Predictions	Observations
1. Intense acceleration effects under conditions of:	
(a) Quasi-parallel ($0° \leqslant \theta_{Bn} \lesssim 45°$) shock structure	consistent (in some cases)
(b) Long connection time t_c of the field line with the bow shock	Consistent (in some cases)
2. Angular distributions: broad	Consistent (at low energies)
3. Proton intensities decrease with increasing distant form the bow shock	
(a) upstream and	Consistent
(b) downstream	Inconsistent
4. Hardening of spectra: toward dawn	Inconsistent
5. Maximum energy: ~ 150 keV	Inconsistent (100%)
6. Velocity dispersion: inverse	Inconsistent ($\sim 80\%$)
7. Presence of energetic electrons: No	Inconsistent ($\sim 92\%$)
8. a-particle to proton ratio a/p: solar	Consistent
9. Direct correlation with magnetospheric subnorm activity: No	Inconsistent

The energetic ($E \geqslant 30$ keV) ion events which are observed upstream or downstream from the quasi-parallel bow shock are most probably of magnetospheric origin [34, 36]. However, ions of lower energies may be accelerated at the bow shock through Fermi acceleration process.

5.4. *Solar cycle dependent acceleration process at the bow shock*

Since, the Shock Drift Acceleration of superthermal or energetic protons to high energies at the bow shock depends on the solar wind speed U_{SW} and the magnitude of the IMF B, we believe that the occurrence of reflected beam events at high energies (i.e. $\geqslant 30$ keV) is a solar cycle dependent phenomenon. Indeed, we have initial results from such a study, which shows a higher occurrence frequency of high energy ($E \geqslant 50$ keV) upstream beam events, during the years 1974–1975 than between 1978–1979.

References

1. Krimigis, S. M., Space Sci. Rev. **59**, 167 (1992).
2. Rosner, R., *et al.* in "Solar-Terrestrial Physics: Present and Future" (Edited by D. Butler and K. Papadopoulos) NASA-PR-1120 (1984).
3. Armstrong, T. P., Pesses, M. E. and Decker, R. B., in "Collisionless Shocks in Heliosphere: Review of Current Research", Geophys. Monogr. Ser. (Edited by B. T. Tsurutani and R. G. Stone) (AGU, Washington, D.C. 1985) p. 271.
4. Hudson, P. D., Mon. Not. R. Astron. Soc. **331**, 23 (1965).
5. Alekseyev, I. I. and Kropotkin, A. P., Geomagn. Aeron. Engl. Transl. **10**, 755 (1970).
6. Pesses, M. E., Ph.D. Thesis, Univ. of Iowa City (1979).
7. Terasawa, T., Planet. Space Sci. **27**, 365 (1979).
8. Toptygin, I. N., Space Sci. Rev. **26**, 157 (1980).
9. Decker, R. B., J. Geophys. Res. **88**, 9959 (1983).
10. Anagnostopoulos, G. C. and Sarris, E. T., Planet. Space Sci. **31**, 689 (1983).
11. Anagnostopoulos, G. C., Sarris, E. T. and Krimigis, S. M., J. Geophys. Res. **93**, 5541 (1988).
12. Anagnostopoulos, G. C. and Kaliabetsos, G. D., J. Geophys. Res. **99**, 2335 (1994).
13. Anagnostopoulos, G. C., Sarris, E. T. and Krimigis, S.M., submitted to J. Geophys. Res., (1994).
14. Sonnerup, B. U. O., J. Geophys. Res. **74**, 1301 (1969).
15. Paschmann, G., Sckopke, N., Asbridge, J. R., Bame, S. J. and Gosling, J. T., J. Geophys. Res. **85**, 4689 (1980)
16. Burgess, D., J. Geophys. Res. **92**, 1119 (1987).
17. Ciacalone, J., J. Geophys. Res. **97**, 8307 (1992).
18. Axford, W. I., Leer, E. and Skadron, G., Conf. Pap. Int. Cosmic Ray Conf. 15th, **11**, 132 (1977).
19. Blandford, R. D. and Ostriker, J. P., Astrophys. J. **237**, 793 (1980).
20. Drury, L. O'C., Rep. Prog. Phys. **46**, 573 (1983).
21. Scholer, M., in "Collisionless Shocks in Heliosphere: Review of Current Research" (Edited by B. T. Tsurutani and R. G. Stone), 287 (1985).
22. Jones, F. C. and Ellison, D. E., Space Sci. Rev. **58**, 259 (1991).
23. Eichler, D., Astrophys. J. **244**, 711 (1981).
24. Scholer, M., Ipavich, F. M., Gloeckler, G. and Hovestadt, D., J. Geophys. Res. **85**, 4602 (1980).
25. Terasawa, T., J. Geophys. Res. **86**, 7595 (1981).
26. Lee, M. A., J. Geophys. Res. **87**, 5063 (1982).
27. Skadron, G. and Lee, M. A., J. Geophys. Res. **88**, 9975 (1983).
28. Ellison, D. C., J. Geophys. Res. **90**, 29 (1985).
29. Ellison, D. C., Mobius, E. and Paschmann, G., Astrophys. J. **352**, 376 (1990).
30. Asbridge, J. R., Bame, S. J. and Strong, I. B., J. Geophys. Res. **73**, 5777 (1968).
31. Greenstadt, E. W., Russel, C. T. and Hope, M., J. Geophys. Res. **85**, 3473 (1980).
32. Thomsen, M. F., Gosling, J. T., Bame, S. J., Feldman, W. C., Paschmann, G. and Sckopke, N., Geophys. Res. Lett. **10**, 1207 (1988).

33. Sarris, E. T., Krimigis, S. M. and Armstrong, T. P., J. Geophys. Res. **81**, 2341 (1976).
34. Sarris, E. T., Bostrom, C. O. and Armstrong, T. P., J. Geophys. Res. **83**, 4289 (1978).
35. Sarris, E. T., Anagnostopoulos, G. C. and Krimigis, S. M., J. Geophys. Res. **97**, 8231 (1992).
36. Anagnostopoulos, G. C., Sarris, E. T. and Krimigis, S. M., J. Geophys. Res. **91**, 3070 (1986).
37. Paschmann, G. N., et al., Geophys. Res. Lett. **6**, 209 (1979).
38. Terasawa, T., Scholer, M. and Ipavich, F. M., J. Geophys. Res. **90**, 249 (1985).
39. West, H. I., Jr. and Buck, R. M., J. Geophys. Res. **81**, 569 (1976).
40. Sanderson, T. R., Reinhard, R., Wenzel, K.-P., Roelof, F. C. and Smith, E. J., J. Geophys. Res. **88**, 85 (1983).
41. Anagnostopoulos, G. C., Sarris, E. T. and Krimigis, S. M., J. Geophys. Res. **92**, 12461 (1987).
42. Lin, R. P., Meng, C.-I. and Anderson, K. A., J. Geophys. Res. **79**, 489 (1974).
43. Ipavich, F. M., Galvin, A. B., Gloeckler, G. Scholer, M. and Hovestadt, D., J. Geophys. Res. **86**, 4337 (1981).
44. Ipavich, F. M., Scholer, M. and Gloeckler, G., J. Geophys. Res. **86**, 11153 (1981).
45. Sarris, E. T., Anagnostopoulos, G. C. and Krimigis, S. M., J. Geophys. Res. **92**, 12083 (1987).
46. Paschalidis, N. P., *et al.*, J. Geophys. Res., in press (1994).
47. Paschalidis, N. P., *et al.*, J. Geophys. Res. **18**, 377 (1991).
48. Kudela, K., Sibeck, D. G., Slivka, M., Fischer, S., Lutsenko, N. V. and Venkatesan, V., J. Geophys. Res. **97**, 14849 (1992).
49. Sibeck, D. G., McEntire, R. W., Krimigis, S. M. and Baker, D. N., J. Geophys. Res. **93**, 14328 (1988).
50. Moebius, E., *et al.*, Geophys. Res. Lett. **13**, 1372 (1986).
51. Krimigis, S. M., Sibeck, D. G. and McEntire, R. W., Geophys. Res. Lett. **13**, 1376 (1986).
52. Kudela, K., Sibeck, D. G., Belian, R. D., Fischer, S. and Lutsenko, V., J. Geophys. Res. **95**, 20825 (1990).
53. Baker, D. N., *et al.*, J. Geophys. Res. **93**, 14317 (1988).
54. Mitchell, D. G. and Roelof, E. C., J. Geophys. Res. **88**, 5623 (1983).
55. Scholer, M., Ipavich, F. M. and Gloeckler, G., J. Geophys. Res. **86**, 4374 (1981).
56. Sarris, E. T., Krimigis, S. M. and Armstrong, T. P., Geophys. Rev. Lett. **3**, 133, (1976).
57. Decker, R. B., J. Geophys. Res. **86**, 4537 (1981).
58. Singer, S. and Montgomery, M. D., J. Geophys. Res. **76**, 6628 (1971).
59. Armstrong, T. P., Krimigis, S. M. and Behannon, K. W., J. Geophys. Res. **75**, 5980 (1970).
60. Pesses, M. E., Van Allen, J. A., Tsurutani, B. T. and Smith, E-J., J. Geophys. Res. **89**, 37 (1984).
61. Gosling, J. T., Asbridge, J. R., Bame, S. J., Paschmann, G. and Scopke, N., Geophys. Res. Lett. **5**, 957 (1978).
62. Ellison, D. C., J. Geophys. Res. **92**, 12458 (1987).

Physica Scripta. Vol. T52, 152–153, 1994

Electron Barkhausen Oscillation as a Possible Source of kHz Radiation from the Neutral Sheet of the Earth's Magnetotail

T. C. Marshall

Department of Applied Physics, Columbia University, New York 10027, U.S.A.

G. Schmidt

Department of Physics, Stevens Institute of Technology, Hoboken NJ 07030, U.S.A.

and

P. Sprangle

Naval Research Laboratory, Washington DC 20375, and Department of Physics and Astronomy, University of Maryland, U.S.A.

Received November 22, 1993; accepted January 28, 1994

Abstract

An analytic estimate is made for radiation from electrons oscillating between magnetic surfaces of the earth's magnetotail. The oscillation is highly anharmonic and occurs within the neutral sheet. An estimate of 4–10 kHz is obtained for the frequency of the electromagnetic radiation from an anisotropic beam of electrons; this radiation grows to appreciable amplitude within ~2 cycles, and results from a phase-bunching instability.

The Barkhausen effect, reported in 1920 [1], originally had to do with the production of high frequency radiation in a radio tube circuit [2]; by appropriate biasing of the grids, an anharmonic oscillation of an electron stream could be set up. This oscillation is now understood [3] as part of a class of radiating instabilities of electron beams in which phase-bunching of the charges occurs (as distinguished from spatial bunching). An important example of this effect is the gyrotron [4].

In this paper, we develop a brief calculation for the oscillating motion of an electron in the neutral equatorial current sheet of the earth's magnetotail, and comment upon the excitation of an electromagnetic wave which may result from the anharmonic Barkhausen-type motion of the electrons. This region of the magnetosphere contains a relatively high concentration of energetic particles and free energy, and therefore it is potentially a source of instabilities and radiation. The model for the system is shown in Fig. 1. The x axis is in the equatorial direction, the y axis is in the vertical or polar direction, and the z direction extends outward from the earth along the magnetotail.

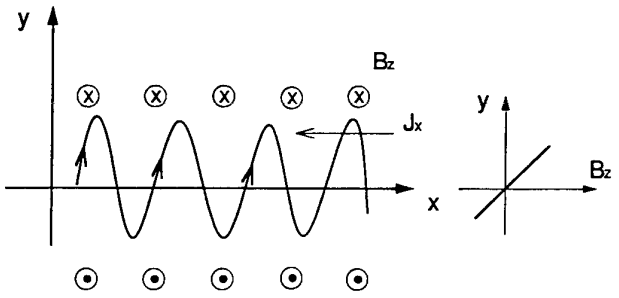

Fig. 1. Model for the electron oscillation with the axes directions indicated.

Table I contains a list of plasma parameters which are generally accepted [5]. However, the sheet width has been more difficult to measure because it varies rapidly, but it is necessary to provide a scale width for the magnetic field variation. The current is such that the directed motion of the electrons within the sheet is of the same order to a factor of two larger than the thermal speed of the electrons.

We begin by taking a simplified form for the variation of $B_z(y)$: Fig. 1 shows this model for the current field of the neutral sheet, which contains the "cross-tail" current $-j_x$:

$$B_z(y) = B_0\, y/L,$$

which provides the vector potential component

$$A_x(y) = \frac{-B_0}{2L}\, y^2.$$

The single electron Hamiltonian, in terms of the electron momenta p_x and p_y (p_z is ignored) is

$$H = \frac{p_y^2}{2m} + \frac{1}{2m}\left(p_x + \frac{eB_0}{2L}\, y^2\right)^2.$$

The model is such that p_x is a constant, which, for simplicity, we take to be zero; then $1/2m[(eB_0/2L)y^2]^2$ is a quartic "effective potential" of the electron. The Hamilton equations

Table I. *Typical numerical values of plasma parameters*

electron density $n \sim \frac{1}{2}\,\mathrm{cm}^{-3}$
electron plasma frequency $f_p = \frac{\omega_p}{2\pi} = \left(\frac{4\pi ne^2}{m}\right)^{1/2} \frac{1}{2\pi} \sim 5\,\mathrm{kHz}$
electron temperature ~5 kV
electron thermal speed $\sim c/10 \sim 3 \times 10^9\,\mathrm{cm/sec}$
random electron thermal current $\sim 2.5\text{–}5.0 \times 10^{-6}\,\mathrm{A/m^2}$
B, magnetic field near sheet ~50 μG
$\omega_c = eB/m \sim 10^3\,\mathrm{sec}^{-1}$
$2L$, sheet width ~10 km – 2 km

for the y-component of motion are

$$\frac{\partial H}{\partial p_y} = \frac{p_y}{m} = V_y \quad \text{and} \quad \frac{\partial H}{\partial y} = -m\dot{V}_y = \frac{1}{2m}\frac{e^2 B_0^2}{L^2}\, y^3,$$

and are nonlinear. We do not integrate these equations, but merely analyze them to find a dimensionally correct "bounce" frequency, f_0, of the electron motion (a spectrum of harmonics may also be anticipated).

Taking $m\dot{V}_y \sim mVf_0$, we find

$$f_0 = \frac{\omega_c^2\sqrt{m}}{2^{3/2}L^2}\left(\frac{8L^2}{m\omega_c^2}\right)^{3/4} E^{1/4}$$

in MKS units, where the characteristic energy, $E = \frac{1}{2}mV_{th}^2$, will define a "turning point" of the motion, y_t, where $V_y = 0$.

$$E = \tfrac{1}{2}mV_{th}^2 \equiv \frac{1}{2m}\frac{e^2 B_0^2}{4L^2}\, y_t^4.$$

Substituting numbers from Table I, we find that $f_0 \sim$ 4–10 kHz, that is, larger than $f_c = \omega_c/2\pi$, and of the same order, or larger than, $\omega_p/2\pi$, the plasma frequency. The turning point of the motion is $\sim$10 km which is $\sim 2L$. A detailed study of orbits of charged particles in a magnetic null has been made by Sonnerup [6].

If the x-component of the electron momentum is not zero, then a distribution of electron momenta will give a spectrum of bounce frequencies. One can estimate the frequency of the "background" of simple harmonic oscillations caused by finite x-momentum of the electron. For the same choice of parameters, it is in the range of 500 Hz, far lower than the bounce frequency.

If phase bunching occurs, an EM wave would grow and have $f \approx f_0$, which corresponds to a wavelength of $\sim$50 km. The bounce motion of an electron would include roughly 10^4 cycles within the magnetospheric region, permitting a gradual interaction with the EM wave.

We next turn to the question of the growth of the EM wave. The dispersion relation of the wave, using a "cold" beam of electrons, is

$$\omega^2 - c^2K_x^2 - c^2K_\perp^2 = \omega_p^2\left[\frac{\omega_0}{\omega - K_xV_x - \omega_0} - \frac{\beta_\perp^2}{2}\frac{c^2K_\perp^2}{(\omega - K_xV_x - \omega_0)^2}\right],$$

where K_x is the wave vector in the sense of the electron motion along the x axis, $K_\perp$ refers to the y direction $\sim 1/L$, and $\beta_\perp$ is the transverse motion $\sim 1/10$. The second term within the brackets is responsible for the instability, and dominates the first term for $\omega \simeq \omega_0 + K_xV_x$. This permits an estimate of the maximum growth rate for the instability of Γ_{max}:

$$\frac{\Gamma_{max}}{\omega_0} = \frac{\sqrt{3}}{2}\left[\frac{1}{2}\left(\frac{\omega_p}{\omega_0}\right)\left(\frac{cK_\perp}{\omega_0}\right)\beta_\perp\right]^{2/3}.$$

We find $\Gamma_{max}/\omega_0 \sim 1/2$, that is, rapid growth. However, a "warm beam" may be expected to provide much less growth [4].

The waves move along the plasma sheet channel, diffract outward, and propagate through the plasma since $\omega_0 \gtrsim \omega_p$ and $\omega_0 \gg \omega_c$. Radiation at kHz frequencies has been observed from the earth's magnetosphric system however it is not known specifically if there is such radiation emerging from the neutral sheet.

Acknowledgements

This research was supported by the ONR and the DOE. The work of one of us (P.S.) was partially supported by NASA-ISPT Grant NAG5-1101.

References

1. Barkhausen, H. and Kurz, K., Phys. Z. **21**, 1 (1920).
2. Morecroft, J. H., in "Electron Tubes and Their Applications" (John Wiley, New York 1993), pp. 329–331.
3. Gaponov, A. V., Petelin, M. I. and Yulpatov, V. K., Izvestiya VUZ. Radiofizika **10**, No. 9–10 (1967).
4. Sprangle, P. and Drobot, A. T., IEEE Trans. Microwave Theory **MTT-25**, 528 (1977).
5. Liu, A. T. Y., "Magnetotail Physics" (Edited by T. Y. Liu Anthony) (Johns Hopkins Press 1987), p. 8.
6. Sonnerup, B. U. Ö., J. Geophysical Res. **76**, 8211 (1971).

Physica Scripta. Vol. T52, 154–156, 1994

Collective Acceleration in Solar Flares

W. Barletta[1], S. S. Gershtein[2], V. Krishan[3], M. Reiser[4], A. M. Sessler[1] and M. Xie[1]

[1] Lawrence Berkeley Laboratory, University of California, Berkeley, CA 94720, U.S.A.
[2] Institute of High Energy Physics, Protvino, Russia
[3] Indian Institute of Astrophysics, Bangalore 560034, India
[4] Laboratory for Plasma Research, University of Maryland, College Park, MD 20742, U.S.A.

Received November 22, 1993; accepted January 28, 1994

Abstract

Solar flare data are examined with an eye to seeing if they suggest collective acceleration of ions. That, in fact, seems to be the case. The collective acceleration mechanism of Gershtein is reviewed and the possibilities of the mechanism are discussed.

1. Introduction

We have examined the solar flare data and note that there are a number of aspects of the data that suggest collective acceleration. In particular, timing data, energy spectrum data, and the flux data are all at least consistent with, and in a way most suggestive of, a collective mechanism of acceleration.

Following a review of the data in Section 2, we discuss very briefly the mechanism proposed by Gershtein [1] in Section 3. In Section 4 we make some remarks concerning the possibilities of the mechanism.

2. Solar flare data

Timing data of solar flares have been studied by Forrest and Chupp [2], and they conclude that "the simultaneous starting times of X-rays >40 keV and γ-ray emission show that electrons and ions were accelerated within seconds of each other".

The energy spectrum data of ions from solar flares have been studied by Reames, Richardson and Wenzel [3]. We reproduce, as Table I a representative sample of these data. Notice that the spectral indices are essentially the same for ^{3}He, ^{4}He, O, Fe.

Assuming the ratio of proton and electron energy is given by the present collective acceleration model, i.e. $E_{\text{proton}}/E_{\text{electron}} \cong M/m$ where M and m are the masses of proton and electron respectively, the ratio of the flux of proton to electron can be seen in Fig. 1, taken from the work in Ref. [4]. From these data one observes that the ratio of the number of accelerated protons to the number of accelerated electrons is roughly 10^{-4}. The ratio is more or less independent of the particular flare.

Table I. *Spectral Indices for Various Particle Species*

^{3}He	3.4 ± 0.2
^{4}He	3.3 ± 0.7
O	3.4 ± 0.5
Fe	3.4 ± 0.4

3. Collective acceleration

The collective acceleration works by having ions trapped in the space charge field of a collection of moving electrons. As the electrons are accelerated to high enegy the ions are dragged along at the same velocity. In this way the acceleration of both electrons and ions is simultaneous. Provided

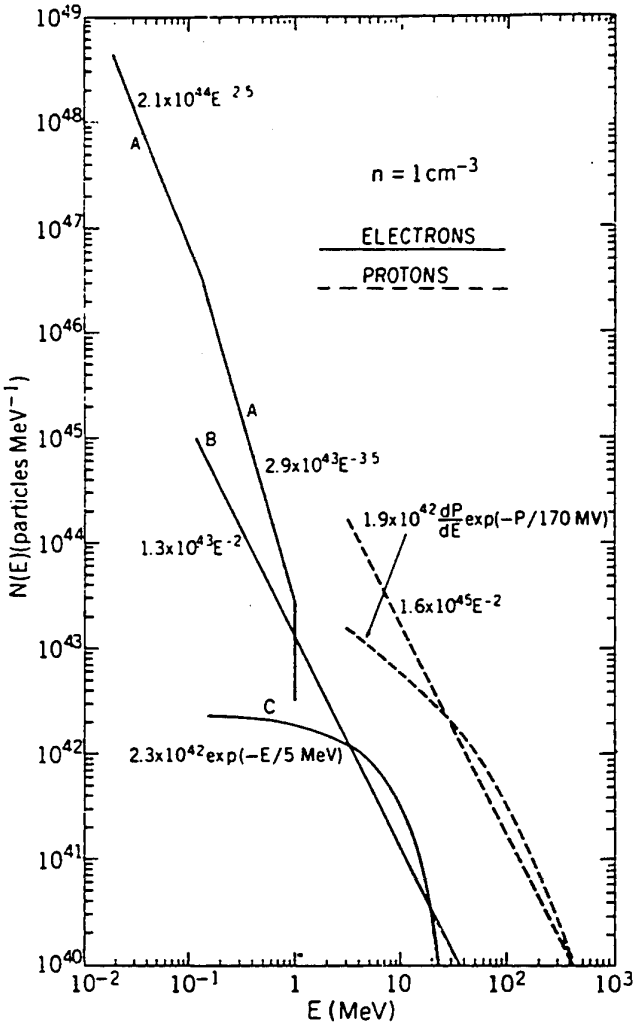

Fig. 1. Flux of electrons and protons as a function of their kinetic energy.

E-mail: MINGXIE@LBL.GOV

the ions are not left behind while the electrons continue to be accelerated, the energy spectra of the ions and electrons will be similar, and so are the energy spectra of various species of ions. Finally, the ratio of ion to electron energy should be proportional to the ratio of ion to electron mass, and the ratio of ion to electron flux must be less than ratio of electron to ion mass.

All of these general features are essentially present in the data. We cannot argue that the data "prove" that the collective acceleration mechanism is valid, but they certainly are consistent with the hypothesis and, we might add, most suggestive of the mechanism.

The mechanism considered by Gershtein [1] is similar to the electron ring accelerator (ERA), as originally proposed by V. I. Veksler [5]. There might be other collective acceleration mechanisms relevant to solar flares. Nevertheless, we follow, here, the discussion of Gershtein. In an ERA, we have initially a rotating ring of electrons with no longitudinal motion (a ring at rest). The ring is "loaded" with a small fraction of ions. A spatially decreasing magnetic field will convert the electron's transverse (ring/cyclotron) energy into longitudinal energy, and the ring will accelerate along the field lines. In this process (called "magnetic expansion" in the ERA literature) the ions will be dragged along.

From the adiabatic magnetic flux conservation law

$$BR^2 = B_0 R_0^2,$$

and the velocity relations

$$v_\parallel^2 = v_0^2 - v_\perp^2, \quad v_\perp = \frac{eBR}{\gamma_0 mc}, \quad v_0 = \frac{eB_0 R_0}{\gamma_0 mc},$$

one obtains for the longitudinal velocity of the electron

$$v_\parallel^2 = v_0^2\left(1 - \frac{B}{B_0}\right),$$

where B_0, R_0, v_0 are the initial values for the magnetic field, electron's gyroradius and velocity, respectively. Assuming that the ion moves with the same longitudinal velocity, $v_\parallel$, as the electrons, the relativistic energy of the ion is given by:

$$E = Mc^2 \frac{\gamma_0 m}{\left[m^2 + \beta_0^2 \gamma_0^2 m^2 \frac{B}{B_0}\right]^{1/2}}.$$

In the ERA literature this formula is usually evaluated in the relativistic limits, so

$$E = Mc^2 \sqrt{\frac{B_0}{B}},$$

but for solar flares a non-relativistic approximation is (almost always) valid, and we obtain

$$T = \frac{M}{m}\left(1 - \frac{B}{B_0}\right)T_e,$$

where T is the kinetic energy of the ion and T_e is the initial transverse kinetic energy of the electron.

The magnitude of the electric field produced by a ring containing N electrons may be estimated by its maximum value at the edge of the ring tube

$$E = \frac{eN}{\pi Ra},$$

where a and R are the minor and major radius of the electron ring, respectively. The energy gain of an ion of charge q and moving a distance Δz in the space charge field of the electron ring is given by

$$q\left(\frac{eN}{\pi Ra}\right)\Delta z.$$

This must be equal to or larger than the kinetic energy gain of the ion:

$$T_e \frac{M}{m}\left|\frac{1}{B_0}\frac{dB}{dz}\right|\Delta z,$$

if the ion is to remain trapped in the field of the electron ring, i.e.

$$\frac{Nqe}{\pi Ra} \geqslant \frac{M}{m} T_e \left|\frac{1}{B_0}\frac{dB}{dz}\right|,$$

which gives, in terms of the electron density, n, in the electron ring

$$n[\mathrm{cm}^{-3}] \geqslant 10^{15} \frac{T_e[\mathrm{MeV}]}{a[\mathrm{cm}] L_B[\mathrm{cm}]},$$

where we have assumed the ion to be a proton, and

$$L_B \equiv \frac{1}{\left|\frac{1}{B_0}\frac{dB}{dz}\right|}.$$

Taking typical values of the magnetic field and its gradient inside solar flares, $B_0 \sim 100$ Gauss, $dB/dz \sim 10^{-6}$ Gauss/cm, and assuming $T_e \sim 100$ keV and $a \sim 1$ cm, we have $n > 10^6\,\mathrm{cm}^{-3}$. This condition is easily satisfied in solar flares. The major radius of the electron ring, taken to be the electron gyroradius given by $R[\mathrm{cm}] = 1.7 \times 10^3(\gamma^2 - 1)^{1/2}/B_0[\mathrm{Gauss}]$, is about 11 cm.

4. Remarks on electron ring formation

In the previous section we have considered the acceleration of ions by well-formed electron rings. The model, however, is silent on the subject of electron ring formation. To trap and accelerate ion effectively a few conditions are required in the ring formation. First, there must be a rotating clouds of energetic electrons accelerated along the magnetic field lines, second, the electrons must be bunched to proper scale longitudinally, and third, the bunching structure must be preserved long enough along the passage of beam propagating through ambient solar plasma.

We could say the following on the first condition: when solar flares erupt, magnetic flux is created by circulating currents in the solar surface. The associated flux lines fan out into space (often as far as the planetary regions) and then return to the sun. During the initial period where the magnetic flux is increasing with time electrons in the solar plasma are accelerated by the inductive electric field in orbits perpendicular to the flux lines (Faraday's law). After this initial acceleration phase is over (i.e. the magnetic flux reached its peak in time) these electron clouds are moving in the direction of the diverging flux away from the sun. Their orbital kinetic energy perpendicular to the flux lines is thereby converted into axial kinetic energy (parallel to the flux lines). The energetic bursts of electrons and synchrotron

radiation due to electron gyration are indeed observed during solar flares.

We may also contemplate the following bunching mechanism for the second condition. In the solar atmosphere, the accelerating electron clouds have to travel in an ambient plasma of density $n_0 \sim 10^{12}\,\mathrm{cm}^{-3}$, thus Langmuir waves could be excited, for example, by beam-plasma instability. As a result, the traveling electron clouds become longitudinally bunched, providing an acceleration field for the ions following each bunch.

To estimate the acceleration field, let us consider the field amplitude given by the wave breaking limit,

$$eE\left[\frac{\mathrm{eV}}{\mathrm{cm}}\right] \approx \sqrt{n[\mathrm{cm}^{-3}]}.$$

Assuming $n \approx 10^8\,\mathrm{cm}^{-3}$ for the electron beam and the Langmuir wave has an amplitude of, say, 10% of the value at the wave breaking limit, to accelerate protons to 100 MeV requires that the Langmuir waves be coherent for 1000 m. Of course, since $\mathrm{d}B/\mathrm{d}z$ is so small, the Langmuir wave amplitude can be even less, but then the coherence length must be longer.

The bunching scale in this model must be of the order of λ, the Langmuir wavelength. For effectively excited Langmuir waves it is required that $\lambda \gg \lambda_D$, where λ_D is the electron Debye length. At a typical temperature of 100 eV in solar flare the Debye length is about 10^{-2} cm. The minor radius of 1 cm we took for the electron ring seems to be a reasonable number in this regards.

What we have seen is that a fairly strong acceleration field for ions may indeed by generated by the excitation of Langmuir waves in solar plasma. The next question is whether the acceleration could be maintained long enough by this process. According to the linear theory of the beam-plasma instability [6], the growth rate of the Langmuir waves given by $0.7\omega(n/n_0)^{1/3}$ is around $10^9\,\mathrm{sec}^{-1}$, where ω is the background electron plasma frequency. At this rate the beam would lose its energy and become thermalized in 10^{-9} sec, which is extremely fast compared to 10^{-5} sec, the time it takes to accelerate protons to 100 MeV. Of course, this estimate is only an extrapolation based on the linear theory, in fact a whole host of nonlinear phenomena may take place well before the Langmuir waves reach the wave breaking limit. Therefore to really answer the question on the stability of electron ring one has to pursue a nonlinear analysis, which is beyond the scope of the present paper.

However we may point out that similar issues have been raised for electron beams traveling far in the corona. There, as supported by the observations of type III solar radio bursts, the plasma oscillations excited by traversing electron beams have been known to last much longer than that predicted by the quasi-linear theory. We may also resort to an explanation proposed for this process, the beam recycling mechanism [7], which shows that beams highly inhomogeneous in their density and velocity structure could maintain themselves against quasi-linear diffusion and therefore sustain the excitation of the Langmuir waves.

Acknowledgement

This work was partially supported by the US Dept. of Energy under contract No. DE-AC03-76SF00098 with the Lawrence Berkeley Laboratory.

References

1. Gershtein, S. S., Geomagnetism and Aeronomia **19**, 202 (1979); Proc. XVII Int. Cosmic Ray Conf. **3**, 419 (1981); Fiorentini, G. and Gershtein, S. S., Phys. Lett. **B307**, 128 (1993).
2. Forrest, D. J. and Chupp, E. L., Nature **305**, 291 (1983).
3. Reames, D. V., Richardson, I. G. and Wenzel, K.-P., Astrophys. J. **387**, 715 (1992).
4. Ramaty, R., Kozlovsky, B. and Lingehfelter, R. E. Space Sci. Rev. **18**, 341 (1975).
5. Veksler, V. I., *et al.*, Proc. of the 6th Int. Conf. on High Energy Accelerators, Cambridge Electron Accelerator Report, CEAL-2000 (1967) p. 289.
6. Mikhailovskii, A. B., Theory of Plasma Instabilities (1974) Vol. I.
7. Zaitsev, V. V., Mityakov, N. A. and Rapoport, V. O., Solar Physics **24**, 444 (1972).

Physica Scripta Reprint Series

RS1 **Perspectives in Condensed Matter Physics,** Trieste Lectures in Theoretical Physics, 20th Anniversary Workshop 1984. Published in Physica Scripta vol 32, 1985. 33 pages, price SEK 50 or USD 5.

RS2 **Nonlinear Waves in Plasmas,** Riso National Laboratory, Roskilde, Denmark, August 13–16, 1985. 135 pages, price SEK 270 or USD 40. Editor: H. L. Pécseli.

RS4 **Contributed papers to the 8th International Conference on Vacuum Ultraviolet Radiation Physics,** Lund, Sweden, August 4–8, 1986. 276 pages, price SEK 530 or USD 88. Editors: P.-O. Nilsson and J. Nordgren.

RS5 **Colloquium on Atomic Spectra and Oscillator Strengths for Astrophysics and Fusion Research,** Toledo, Ohio, August 11–13, 1986. 89 pages, price SEK 180 or USD 30. Editors: L. J. Curtis and L. S. Anderson.

RS6 **18th Conference of EGAS, European Group for Atomic Spectroscopy,** Marburg, Germany, July 8–11, 1986. 80 pages, price SEK 150 or USD 25. Editors: M. Elbel and H. Hühnermann.

RS7 **Relativistic Many-Body Problems,** Trieste, Italy, June 30–July 4, 1986. 240 pages, price SEK 480 or USD 80. Editor: I. Lindgren.

RS8 **Dynamical Screening and Spectroscopy of Surfaces,** Trieste, Italy, June 24–27, 1986. 170 pages, price SEK 340 or USD 57. Editors: M. Sunjić and S. Lundqvist.

RS9 **Quantum Chaos and Physics of Structure and Complexity,** Trieste, Italy, June 17–20 and September 1–5, 1986. 200 pages, price SEK 400 or USD 67. Editors: G. Casati, M. C. Gutzwiller, K.-E. Eriksson, H. Haaken and T. Arecchi.

RS10 **Environmental Physics – Atmospheric Aerosols,** Trieste, Italy, July 22–25, 1986. 112 pages, price SEK 220 or USD 40. Editors: H. Morinaga and E. Selin.

RS12 **19th Conference of EGAS, European Group for Atomic Spectroscopy,** NIHE Dublin, Ireland, July 14–17, 1987. 76 pages, price SEK 140 or USD 30. Editors: T. Andersen, E. T. Kennedy and G. O'Sullivan.

RS13 **Contributed papers to the 7th General Conference of the Condensed Matter Division of the EPS,** Pisa, April 7–10, 1987. 512 pages, price SEK 800 or USD 130. Editors: F. Bassani, G. Grosso, G. Pastori Parravicini and M. P. Tosi.

RS14 **The NORDITA-DIKU Conference on Vision,** Copenhagen, August 1986. 76 pages, price SEK 140 or USD 30. Editors: J. Hertz, P. Lennie, N. Graham and P. Johansen.

RS15 **Frontiers in Atomic Structure Calculations and Spectroscopy,** Lund, Sweden, May 25–26, 1988. 96 pages, price SEK 200 or USD 40. Editor: I. Martinson.

RS16 **Nonlinear Phenomena in Plasmas,** Roskilde, Denmark, August 8–12, 1988. 216 pages, price SEK 300 or USD 50. Editor: H. L. Pécseli.

RS17 **Contributed papers to the Conference on Soft Magnetic Materials 8,** Badgastein, Austria, September 1–4, 1987. 264 pages, price SEK 350 or USD 55. Editor: R. Wäppling.

RS18 **Physics of Atomic Collisions,** Finse, Norway, May 8–11, 1989. 112 pages, price SEK 250 or USD 50. Editors: J. M. Hansteen and I. Singstad.

RS19 **Dusty Plasmas,** Trieste, Italy, June 14–21, 1991. 88 pages, price SEK 200 or USD 40. Editors: P. K. Shukla, U. de Angelis and L. Stenflo.

RS20 **Workshop on Physics with Penning Traps,** Lertorpet, Sweden, June 29–July 1, 1991. 108 pages, price SEK 250 or USD 40. Editors: G. Bollen and C. Carlberg.

RS21 **The 2nd International Conference on Particle Production near Threshold,** Uppsala, Sweden, August 26–29, 1992. 212 pages, price SEK 300 or USD 50. Editors: C. Ekström, B. Höistad, A. Johansson and S. Kullander.

RS22 **Trends in Atomic Structure Calculation and Spectroscopy,** Lund, Sweden, March 3–4, 1993 144 pages, price SEK 220 or USD 30. Editors: J. Carlsson, P. Jönsson and I. Martinson.

Order form: To **The Royal Swedish Academy of Sciences,** Physica Scripta, Box 50005, S-104 05 STOCKHOLM, Sweden

Please send me..... issues of:

RS1 ☐ RS2 ☐ RS4 ☐ RS5 ☐ RS6 ☐ RS7 ☐ RS8 ☐ RS9 ☐ RS10 ☐ RS12 ☐ RS13 ☐ RS14 ☐ RS15 ☐ RS16 ☐ RS17 ☐ RS18 ☐ RS19 ☐ RS20 ☐ RS21 ☐ RS22 ☐

Payment enclosed ☐ Please invoice ☐ Please charge my VISA ☐ MASTERCARD ☐ American Express ☐ card

Card number:

Signature..... Expiry date:

Invoice address

Shipping address (if not invoice address)

Topical Issues in Physica Scripta

Year of Publication	Title	Price per copy in Swedish kronor postage included
1982		
T1	2nd General Conference of the Condensed Matter Division of the European Physical Society. Eds. V. Heine, V. R. Van Doren and J. T. Devreese. 150 pages.	110
T2: I&II	1982 International Conference of Plasma Physics. Ed. H. Wilhelmsson. 600 pages.	450
1983		
T3	Production and Physics of Highly Charged Ions. Ed. L. Liljeby. 260 pages.	195
T4	Nordic Conference on Surface Science. Eds. M. Pessa and R. Nieminen. 215 pages.	160
T5	4th Nordic Meeting on Nuclear Physics. Eds. J. Bondorf and G. Hagemann. 230 pages.	170
T6	Fourth International Workshop on Inelastic Ion-Surface Collisions. Ed. P. Sigmund. 184 pages	140
1984		
T7	European Workshop on Very Hot Astrophysical Plasmas. Eds. L. Koch-Miramond and T. Montmerle. 244 pages	185
T8	Colloquium on Atomic Spectra and Oscillator Strengths for Astrophysics and Fusion Research. Ed. U. Litzén. 152 pages	115
T9	The Physics of Chaos and Related Problems. Ed. S. Lundqvist. 224 pages. (Nobel Symposium 59)	170
1985		
T10	Disordered Systems by J. Hertz. 42 pages.	30
T11	Astrophysical Aspects of the Interstellar Medium and Star Formation. Ed. G. Gahm. 84 pages. (Crafoord Symposium).	65
1986		
T12	Quantum Fields and Laser Spectroscopy. Ed. S. Stenholm. 76 pages.	60
T13	6th General Conference of the Condensed Matter Division of the EPS. Ed. G. Grimvall. 324 pages.	245
T14	Fundamental Effects in Semiconductors. Ed. P. Landsberg. 102 pages.	75
1987		
T15	Unification of Fundamental Interactions. Eds. L. Brink, R. Marnelius, J. S. Nilsson, P. Salomonson and B.-S. Skagerstam. 212 pages. (Nobel Symposium 67).	160
T16	The Role of Alpha Particles in Magnetically Confined Fusion Plasmas. Eds. M. Lisak and H. Wilhelmsson. 178 pages.	135
T17	8th International Conference on Vacuum Ultraviolet Radiation Physics. Eds. P. O. Nilsson and J. Nordgren. 250 pages.	190
T18	6th International Symposium on Solar Terrestrial Physics. Ed. B. Hultqvist. 316 pages.	235
T19A+B	7th General Conference of the Condensed Matter Division of the EPS. Eds. F. Bassani, G. Grosso, G. Pastori-Parravicini and M. P. Tosi. 628 pages.	470
1988		
T20	An Introduction to Nonlinear Dynamics and Chaos Theory by J. L. McCauley. 60 pages.	45
T21	Vacuum in Non-Relativistic Matter-Radiation Systems. Eds. F. Persico and E. A. Power. 128 pages.	95
T22	Workshop and Symposium on the Physics of Low-energy Stored and Trapped Particles. Eds. A. Bárány, A. Kerek, M. Larsson, S. Mannervik and L.-O. Norlin. 330 pages.	250
T23	Trends in Physics EPS–7. Eds. T. Åberg and S. Stenholm. 336 pages.	250
T24	Soft Magnetic Materials 8. Eds. H. Pfützner and R. Wäppling. 74 pages.	55
1989		
T25	8th General Conference of the Condensed Matter Division of the EPS. Eds. F. Beleznay, J. Kollár, I. Kovács, N. Kroo and N. Menyhárd. 376 pages.	280
T26	20th EGAS Conference of the European Group for Atomic Spectroscopy. Ed. L. Windholz. 100 pages	75
T27	Physics of Low-dimensional Systems. Eds. S. Lundqvist and N. R. Nilsson. 168 pages. (Nobel Symposium 73).	125
T28	Carbon and Oxygen Collision Data for Fusion Plasma Research. Ed. R. K. Janev. 112 pages.	85
T29	9th General Conference of the Condensed Matter Division of the EPS. Eds. J. Friedel, J. P. Laheurte and J. P. Romagon. 308 pages.	230
1990		
T30	Large Amplitude Waves and Fields in Plasmas. Eds. R. Bingham, U. de Angelis, P. K. Shukla and L. Stenflo. 232 pages.	175
T31	9th International Conference on Vacuum Ultraviolet Radiation Physics. Eds. D. A. Shirley and G. Margaritondo. 312 pages.	235
T32	6th Nordic Meeting on Nuclear Physics. Eds. G. Lövhöiden, T. F. Thorsteinsen and J. S. Vaagen. 240 pages.	185
T33	Third Nordic Symposium on Computer Simulation in Physics, Chemistry, Biology and Mathematics. Eds. K. Kaski and M. Salomaa. 248 pages.	185
1991		
T34	22nd EGAS Conference of the European Group for Atomic Spectroscopy. Eds. A. Amesen and R. Hallin. 112 pages.	85
T35	10th General Conference of the Condensed Matter Division of the EPS. Eds. A. G. Vallera, J. B. Sousa, A. F. Martins and L. Alcácer. 312 pages.	235
T36	The Birth and Early Evolution of Our Universe. Eds. J. S. Nilsson, B. Gustafsson and B.-S. Skagerstam. 304 pages. (Nobel Symposium 79)	230
T37	Collision Processes of Metallic Ions in Fusion Plasmas. Ed. R. K. Janev. 120 pages.	90

Topical Issues in Physica Scripta

Year of Publication	Title	Price per copy in Swedish kronor postage included
T38	Fourth Nordic Symposium on Computer Simulations in Natural Sciences. Eds. A. Hansen, E. L. Hinrichsen and P. A. Slotte. 124 pages.	95
T39	11th General Conference of the Condensed Matter Division of the EPS. Eds. J. L. Beeby, P. A. Maksym and J. M. McCoy. 400 pages.	300
1992		
T40	23rd EGAS Conference of the European Group for Atomic Spectroscopy. Ed. S. Łęgowski. 80 pages.	120
T41	The 2nd International Workshop on Auger Spectroscopy and Electronic Structure (IWASES–II). Eds. K. Wandelt, C.-O. Almbladh and R. Nyholm. 304 pages.	455
T42	Low Dimensional Properties of Solids. Eds. M. Jonson and T. Claeson. 220 pages. (Nobel Jubilee Symposium)	330
T43	Extragalactic Astronomy including Observational Cosmology. Ed. A. Elvius. 70 pages. (Crafoord Symposium)	105
T44	Contributions to Problems in Statistical Physics Elasticity and Dislocation Theory. Eds. T. Jøssang and D. M. Barnett. 160 pages	240
T45	12th General Conference of the Condensed Matter Division of the EPS. Eds. V. Smid, B. Velický and J. Krištofik. 320 pages.	480
1993		
T46	Heavy Ion Spectroscopy and QED Effects in Atomic Systems. Eds. I. Lindgren, I. Martinson and R. Schuch. 272 pages. (Nobel Symposium 85)	205
T47	4th International Colloquium on Atomic Spectra and Oscillator Strengths for Astrophysical and Laboratory Plasmas. Eds. D. S. Leckrone and J. Sugar. 208 pages.	155
T48	Quantum Phase and Phase Dependent Measurements. Eds. W. P. Schleich and S. M. Barnett. 144 pages.	110
T49A + B	13th General Conference of the Condensed Matter Division of the EPS in conjunction Arbeitskreis Festörperphysik of the DPG. Eds. H. Hoffmann, R. Klein and M. Schwoerer. 752 pages.	565
1994		
T50	Wave-Particle Interaction and Energization in Plasmas. Eds. P. K. Shukla, U. de Angelis, R. Bingham and L. Stenflo. 128 pages.	190
T51	The 25th EGAS Conference of the European Group for Atomic Spectroscopy. Eds. D. Lecler and J. Margerie. 84 pages.	126
T52	Acceleration and Radiation Generation in Space and Laboratory Plasmas. Eds. R. Bingham, J. M. Dawson, T. Katsouleas and L. Stenflo. 160 pages.	240
T53	8th International Seminar on Electron and Ion Swarms. Eds. T. H. Lövaas and H. R. Skullerud. 88 pages.	130
T54	16th Nordic Semiconductor Meeting. Eds. H. P. Gíslason and V. Guðmundsson. 312 pages.	468
T55	14th General Conference of the Condensed Matter Division of the EPS. Eds. J. L. de Segovia, F. Flores and F. Garzía-Moliner. 228 pages.	342

Physica Scripta

Manuscripts
Shall be sent in triplicate – one original and two copies to any of the editors or to the editorial office.

Order form

To **The Royal Swedish Academy of Sciences**
Physica Scripta
Box 50005
S-104 05 STOCKHOLM
Sweden

Please send ..... issues of "Acceleration and Radiation Generation in Space and Laboratory Plasmas". Physica Scripta, Vol. T52, 1994, 160 pages. Price: SEK 240.

Payment enclosed ☐ Please invoice ☐ Please charge my VISA ☐ MASTERCARD ☐ American Express ☐ card

Card number:

Expiry date: ☐☐

Signature: .....

Invoice address

Name: .....

Address: .....

.....

.....

Shipping address (if not invoice address)

Name: .....

Address: .....

.....

.....

Physica Scripta Vol. T52 1994

Contents